NASA Technical Memorandum 84559

Aerodynamic Characteristics of a Series of Twin-Inlet Air-Breathing Missile Configurations

II - Two-Dimensional Inlets at Supersonic Speeds

Clyde Hayes
Langley Research Center
Hampton, Virginia

National Aeronautics
and Space Administration

**Scientific and Technical
Information Branch**

1983

SUMMARY

A series of air-breathing missile configurations has been investigated to provide a data base for the design of such missiles. The model could be configured with either twin axisymmetric or two-dimensional inlets. Three circumferential inlet locations were investigated: 90°, 115°, and 135° from the top center. Two vertical wing locations, as well as wingless configurations, were used. Three tail configurations were formed by locating the tail surfaces either on the inlet fairings or on fairings on the body. The surfaces were deflected to provide pitch control. Two-dimensional inlets with extended compression surfaces, used to improve the angle-of-attack performance of the inlets for wingless configurations, were also investigated. Although the data of this report refer specifically to the two-dimensional inlet configurations, comparison of these data with those for the axisymmetric inlet configurations of NASA Technical Memorandum 84558 indicates that even though individual values and levels of the various curves may differ, where configurations are comparable, the trends are similar and conclusions formed will generally apply to the model with either inlet configuration.

The results of the investigation indicate that the pitching-moment curve, for most configurations, was nonlinear, with a large margin of longitudinal stability at high angles of attack, but with little or no margin of stability near an angle of attack of 0°. The model had marginal lateral-directional stability for most configurations; the X-tail and the inverted tri-tail resulted in lateral-directional stability for the entire range of angle of attack. The model with an inlet orientation angle of 90° could not be trimmed at the maximum angle of attack (20°) with the maximum pitch-control deflection (-20°). Only by increasing the inlet orientation angle to 135° could the model be trimmed at an angle of attack of 20° with a pitch-control deflection of -20° with either tail configuration. Of the three tail configurations, the X-tail had a more linear pitching-moment curve and greater pitch-control effectiveness. The extended two-dimensional inlet configuration without a wing, as with the other inlets, tended to have a nonlinear pitching-moment curve; with the X-tail, the curve was straightened and the configuration was stable throughout the angle-of-attack range and the model could be trimmed at an angle of attack of 20° with a pitch-control deflection of -10°.

INTRODUCTION

During the past several years, several air-breathing missile configurations have been investigated in the Langley Unitary Plan Wind Tunnel. These include one-, two-, and four-inlet configurations with various wing and tail arrangements. The results of these investigations have been reported in references 1 through 7. Although the data from these specific missile programs have contributed to an air-breathing configuration data base, a broader data base is needed to better predict the aerodynamic characteristics of candidate configurations and to better design an air-breathing configuration to meet desired aerodynamic specifications. To provide a broader data base, a series of models, which incorporates a wider range of configuration variables, has been designed and tested.

The model could be configured with axisymmetric or two-dimensional single or twin inlets. The single inlet was located at the bottom of the body, whereas the

twin inlets could be located circumferentially from 90° to 135° from the top center. Two vertical wing locations were available to properly locate the wing relative to the inlets at the 115° and 135° inlet orientation angles to provide favorable interference between the wing and inlet at positive angles of attack. Tail surfaces could be mounted on the inlet fairing and/or on fairings on the body to provide several tail configurations. The tail surfaces could be deflected to provide pitch control. The two-dimensional inlets could be configured with extended compression surfaces intended to improve the angle-of-attack performance of the inlets for the wingless configuration.

The present investigation covers tests of the twin-inlet configurations, both axisymmetric and two-dimensional inlets. The inlets were located at circumferential locations of 90°, 115°, and 135° from the top center. The wing was located above the model center line with the inlets located in the 115° position and at the model center line with the inlets in the 135° position. The wing was not used with the inlets located in the 90° position. Three tail configurations were used. A tri-tail configuration with a vertical surface at the top center of the body and a surface mounted on each of the two inlet fairings was tested at all three inlet orientation angles. With the inlets located in the 135° position, the single vertical surface was replaced by two surfaces in the upper 45° position to form an X-tail configuration. Also, at the inlet orientation angle of 135° and with the two upper surfaces, the two lower surfaces were replaced by a single lower surface to form an inverted tri-tail configuration. The tests included body-inlet, body-inlet-wing, body-inlet-tail, and body-inlet-wing-tail configurations.

The supersonic tests were performed in the high Mach number test section of the Langley Unitary Plan Wind Tunnel at Mach numbers of 2.50, 2.95, 3.50, and 3.95. The inlets were operating with flow through the model to simulate ramjet operation. The subsonic tests were conducted at Mach numbers of 0.60, 0.80, and 0.95 in the 7- by 10-Foot Transonic Wind Tunnel at the David Taylor Naval Ship Research and Development Center. The internal ducts were closed and there was no flow through the model to simulate rocket boost.

Longitudinal aerodynamic characteristics, lateral-directional stability, pitch-control effectiveness, and trim characteristics were obtained.

Because a large volume of data was obtained in this investigation, the data are presented in three reports: Reference 8 covers the twin axisymmetric inlet configurations at supersonic speeds, this report covers the twin two-dimensional inlet configurations at supersonic speeds, and reference 9 covers both inlet configurations at subsonic-transonic speeds. The results of an investigation of the single-inlet configurations are presented in reference 10.

SYMBOLS

The coefficients of forces and moments are referred to both the body axis and stability axis systems, where appropriate. Aerodynamic moments are taken about a point on the model center line at a distance downstream of the model nose equal to 50 percent of the body length (fig. 1). All coefficients are based on the cross-sectional area and the diameter of the body.

A cross-sectional area of basic body, 0.00456 m^2

C_A axial-force coefficient, $\frac{\text{Axial force}}{qA}$

$C_{A,i}$ internal-flow axial-force coefficient, $\frac{\text{Internal-flow axial force}}{qA}$

C_D drag coefficient, $\frac{\text{Drag}}{qA}$

C_L lift coefficient, $\frac{\text{Lift}}{qA}$

C_l rolling-moment coefficient, $\frac{\text{Rolling moment}}{qAd}$

$C_{l_\beta} = \left(\frac{\Delta C_l}{\Delta\beta}\right)_{\beta=0°,3°}$

C_m pitching-moment coefficient, $\frac{\text{Pitching moment}}{qAd}$

C_N normal-force coefficient, $\frac{\text{Normal force}}{qA}$

C_n yawing-moment coefficient, $\frac{\text{Yawing moment}}{qAd}$

$C_{n_\beta} = \left(\frac{\Delta C_n}{\Delta\beta}\right)_{\beta=0°,3°}$

C_Y side-force coefficient, $\frac{\text{Side force}}{qA}$

$C_{Y_\beta} = \left(\frac{\Delta C_Y}{\Delta\beta}\right)_{\beta=0°,3°}$

d body diameter, 0.0762 m

L/D lift-drag ratio

M free-stream Mach number

M.S. model station

m/m_∞ inlet mass-flow ratio (ratio of inlet mass flow to mass flow at free-stream conditions through a stream tube of cross-sectional area equal to inlet projected area)

q free-stream dynamic pressure, Pa

x, y, y_1, y_2, y_3 coordinates of inlet configurations (figs. 1(c) and 1(d))

α angle of attack, deg

β angle of sideslip, deg

δ_p tail deflection in pitch direction, deg (positive deflection with leading edge up)

ϕ_I inlet orientation angle, measured from model top center line, deg (figs. 1(a) and 1(b))

Configuration designations (various components shown in fig. 1):

B_1 body

I_1 twin circular inlets (axisymmetric inlet)

I_2 twin rectangular inlets (two-dimensional inlets)

I_{2c} twin rectangular inlets with inlet covers installed

I_3 twin rectangular extended inlets

I_{3c} twin rectangular extended inlets with inlet covers installed

T tail

T_1 tri-tail, one surface at top center and one on each of the inlet fairings

T_2 X-tail, two surfaces at upper 45° positions and two surfaces at inlet fairing; used only with $\phi_I = 135°$

T_3 inverted tri-tail, two surfaces at upper 45° position and one surface at bottom center line

W_1 wing, located at center-line position for $\phi_I = 135°$ and upper position for $\phi_I = 115°$; not used in combination with $\phi_I = 90°$

MODEL DESCRIPTION

Details of the models are presented in figure 1 and photographs in figure 2. The body was an ogive cylinder approximately 14 diameters long. An inlet of either the axisymmetric or rectangular two-dimensional type was located on each side of the body, separated from the body by boundary-layer diverters. The ducts extended downstream of the inlets to a point where they would turn and dump into the combustor. Beyond this point, the external geometry of the inlets consisted of tapered fairings, which extended back to the model base and provided support for two lower tail surfaces. Other tail surfaces could be attached to the body by means of fairings, which provided the necessary support and represented the volume that would be required for tail control actuators.

The inlet ducts dumped into a common passage within the body. The internal flow was kept separate from the balance cavity to facilitate measurement of the internal flow and the balance-cavity axial-force and drag corrections. A rake at the exit of the duct was used to measure the flow conditions needed to compute the forces due to the internal flow.

The inlets and inlet fairings could be rotated in the circumferential direction about the model center line. The rectangular inlets each had a boundary-layer bleed slot which removed boundary layer from the compression surface and dumped it overboard. The axisymmetric inlets had no boundary-layer control. The wing used in the tests was located so that its pressure field would enhance the angle-of-attack performance of the inlets. The vertical location of the wing depended on the inlet orientation, and for inlets located on each side 90° from the top center line, the wing could not be used.

An extended inlet configuration was also investigated. This configuration consisted of the rectangular two-dimensional inlet with the compression surface extended forward to station 28.829 to enhance the angle-of-attack performance in the absence of a wing. The shorter of the two-dimensional inlet configurations was tested with and without a wing whereas the extended inlets were not tested with the wing.

The airfoil of the wing consisted of an upper surface having a wedge leading and trailing edge with a flat center section and a lower surface that was flat from leading to trailing edge. The airfoils for the tail surfaces were similar, consisting of straight-line segments, but were symmetrical (figs. 1(e) and 1(f)).

Two types of tail surfaces were used: one designed to fit on the inlet fairings and the other to fit to the body in conjunction with a fairing. When the lines of each tail surface type are projected to the body surface (fig. 1(f)), their planforms are identical. The tail arrangements available depended on the inlet orientation. At all inlet orientations, a tri-tail was used, with a surface on each inlet fairing and a top vertical surface. With the inlets located at 135° from the top center, an X-tail configuration was formed by substituting two surfaces at the upper 45° for the single vertical surface. An inverted tri-tail configuration was also formed by substituting a single vertical surface at the bottom for the tail-fairing-mounted surfaces. For pitch-control deflection, all tail surfaces except the vertical surfaces were deflected. The tail-surface deflection angle was measured in the plane normal to the tail-surface hinge line.

TESTS

The supersonic part of the investigation was conducted in the high Mach number test section of the Langley Unitary Plan Wind Tunnel at Mach numbers of 2.50, 2.95, 3.50, and 3.95. The tunnel is of the variable pressure, continuous-flow type and has two test sections, each approximately 1.2 m square and 2.1 m long. The nozzles leading to the test sections are of the asymmetric sliding-block type to allow continuous variation of Mach number. A description of the facility is given in reference 11.

A rake having eight total-pressure tubes and four static-pressure tubes was used to measure the flow conditions at the duct exit. Base pressure measurements were made with the static orifices on the model base, and balance-cavity pressures were measured with two static-pressure tubes attached to the sting and terminating near the balance. Forces and moments were measured with a six-component, sting-mounted, strain-gage balance. Separate runs were made for the internal-flow measurements, but

force data from these runs are not presented. Typical internal-flow data computed from these measurements are presented in figure 3.

Three inlet configurations were tested: axisymmetric I_1, rectangular two-dimensional I_2, and extended two-dimensional I_3. Configurations having inlet orientation angles ϕ_I of 90°, 115°, and 135° were used. Each combination of inlet type and inlet orientation angle was tested with body-inlet, body-inlet-tail, body-inlet-wing, and body-inlet-wing-tail combinations. Exceptions were made for all inlets at $\phi_I = 90°$ and for I_3 at all conditions; these inlets were not tested in conjunction with the wing. Three tail configurations were used and are shown in figure 1(g). Pitch-control deflections of 0°, -10°, and -20° were used primarily, although some configurations were also tested with a pitch-control deflection of +10°.

Tests were made at angles of attack ranging from about -5° to +20°. To obtain lateral-directional stability, runs at angles of sideslip of 0° and 3° were made. Angles of attack and sideslip have been corrected for tunnel flow angularity and for deflection of the sting and balance due to aerodynamic loads. The axial force and drag data have been adjusted to free-stream static pressure acting over the model base and the balance-chamber areas. An adjustment has been made to remove the internal drag, where the internal drag is that drag associated with the momentum and buoyancy acting in the stream direction from the free stream at exit conditions of that flow passing internally. The Reynolds number was maintained constant at 6.56×10^6 per meter. The stagnation dewpoint was maintained below 239 K to avoid condensation effects.

All tests were made with the boundary-layer transition point fixed by means of transition strips. The transition strips were located 3.05 cm aft of the body nose and 1.02 cm in a streamwise direction from the leading edge of the wings, tail surfaces, and inlets. The transition strips consisted of No. 35 sand grains individually spaced.

PRESENTATION OF RESULTS

The results of this investigation are presented in the figures as indicated in the following table:

ϕ_I, deg	Wing	Tail	δ_p, deg	Variable	Effect measured	Figure
Two-dimensional inlets I_2						
Varies	Off	T_1	0	Inlet orientation	Longitudinal	4
Varies	On	T_1	0	Inlet orientation	Longitudinal	5
90	Off	T_1	0	Model components	Longitudinal	6
115	On and off	T_1	0	Model components	Longitudinal	7
135	On and off	T_1	0	Model components	Longitudinal	8
135	On and off	T_2	0	Model components	Longitudinal	9
135	On and off	T_3	0	Model components	Longitudinal	10
135	Off	Varies	0	Tail configuration	Longitudinal	11
135	On	Varies	0	Tail configuration	Longitudinal	12
90	Off	T_1	Varies	Pitch-control deflection	Pitch-control effectiveness	13
115	Off	T_1	Varies	Pitch-control deflection	Pitch-control effectiveness	14
135	Off	T_1	Varies	Pitch-control deflection	Pitch-control effectiveness	15
135	Off	T_2	Varies	Pitch-control deflection	Pitch-control effectiveness	16
135	Off	T_3	Varies	Pitch-control deflection	Pitch-control effectiveness	17
115	On	T_1	Varies	Pitch-control deflection	Pitch-control effectiveness	18
135	On	T_1	Varies	Pitch-control deflection	Pitch-control effectiveness	19

ϕ_I, deg	Wing	Tail	δ_p, deg	Variable	Effect measured	Figure
Two-dimensional inlets I_2						
135	On	T_2	Varies	Pitch-control deflection	Pitch-control effectiveness	20
135	On	T_3	Varies	Pitch-control deflection	Pitch-control effectiveness	21
Varies	Off	T_1	0	Inlet orientation	Lateral-directional	22
Varies	On	T_1	0	Inlet orientation	Lateral-directional	23
90	Off	T_1	0	Model components	Lateral-directional	24
115	On and off	T_1	0	Model components	Lateral-directional	25
135	On and off	T_1	0	Model components	Lateral-directional	26
135	On and off	T_2	0	Model components	Lateral-directional	27
135	On and off	T_3	0	Model components	Lateral-directional	28
135	Off	T_1 and T_2	0	Tail configuration	Lateral-directional	29
135	On	T_1 and T_2	0	Tail configuration	Lateral-directional	30
Two-dimensional extended inlets I_3						
Varies	Off	T_1	0	Inlet orientation	Longitudinal	31
90	Off	T_1	0	Model components	Longitudinal	32
115	Off	T_1	0	Model components	Longitudinal	33
135	Off	T_1 and T_2	0	Model components	Longitudinal	34
90	Off	T_1	Varies	Pitch-control deflection	Pitch-control effectiveness	35
115	Off	T_1	Varies	Pitch-control deflection	Pitch-control effectiveness	36
135	Off	T_1	Varies	Pitch-control deflection	Pitch-control effectiveness	37
135	Off	T_2	Varies	Pitch-control deflection	Pitch-control effectiveness	38
Varies	Off	T_1	0	Inlet orientation	Lateral-directional	39
90	Off	T_1	0	Model components	Lateral-directional	40
115	Off	T_1	0	Model components	Lateral-directional	41
135	Off	T_1	0	Model components	Lateral-directional	42

DISCUSSION OF RESULTS

The effects of inlet orientation angle ϕ_I on the longitudinal aerodynamic characteristics are presented in figures 4 and 5. At all three inlet orientation angles, the model was stable at angles of attack above about 6°. There was very little effect of ϕ_I on the longitudinal characteristics for ϕ_I = 90° and 115° (ϕ_I = 90° could not be tested with a wing). For both values of ϕ_I, the slope of the pitching-moment curves changed abruptly at an angle of attack between 4° and 6°, and the longitudinal stability was less near an angle of attack of 0° than for values of angle of attack above about 6°. Increasing ϕ_I to 135° reduced the longitudinal stability, as well as the slope of the lift curve. At large values of angle of attack, the model was very stable; at angles of attack near 0°, the model was neutrally stable. With the wing in place (ϕ_I = 115° and 135°), the stability level was less. With ϕ_I = 115°, there was near neutral stability near an angle of attack of 0°, and with ϕ_I = 135°, the model was unstable in a range of angle of attack near 0°. As ϕ_I was increased, the planform area of the aft end of the body was decreased; this resulted in decreased longitudinal stability.

The effect of the various model components on the longitudinal aerodynamic characteristics is shown in figures 6 through 10. The body-inlet configurations show a trend towards little or no longitudinal stability near an angle of attack of 0° with a rather large margin of longitudinal stability at high angles of attack. Although increasing ϕ_I decreases the stability level, there was at least some small range of

angle of attack at which the model was stable. Adding tail T_1 increased the longitudinal stability and caused the pitching-moment curve to become more linear. At $\phi_I = 90°$ and $115°$ (figs. 6 and 7), the model was stable through the entire range of angle of attack, whereas at $\phi_I = 135°$ (fig. 8), the model was near neutrally stable near an angle of attack of 0°. Adding the wing to the body-inlet had the effect of decreasing the longitudinal stability and causing the pitching-moment curve to become more nonlinear. Adding the wing to the body-inlet-tail also reduced the longitudinal stability, but retained some of the favorable effect of the tail. This was particularly true with the X-tail, T_2 (fig. 9), which was more effective than T_1.

A direct comparison of the longitudinal characteristics of the model with T_1, T_2, and T_3 is made in figures 11 and 12. Without the wing, the model with T_2 had linear pitching-moment curves, particularly near an angle of attack of 0°. With the wing, T_2 provided a more linear variation of pitching-moment coefficient with angle of attack than with either T_1 or T_3. Near an angle of attack of 0°, the variation of pitching-moment coefficient with angle of attack was similar for T_1 and T_3; at positive angles of attack, the curve for T_1 was located between the curves for T_2 and T_3, whereas at negative angles of attack, the curve for T_3 was located between the curves for T_1 and T_2. This indicates that the windward surfaces were more effective than the leeward surfaces, and that both upper and lower surfaces (as for T_2) were required for the more linear pitching-moment curves.

To consider the effect of the various model components on the lift or normal force, the pitch control and trim characteristics should be considered. Pitch-control data are presented in figures 13 through 21, and include longitudinal characteristics with pitch-control deflection δ_p of 0°, -10°, and -20°, except when limited by balance limits or model fouling. Because of the large margin of longitudinal stability, some configurations could not be trimmed at the maximum angle of attack ($\alpha = 20°$). For instance, at $M = 2.95$ with $\phi_I = 90°$ (fig. 13(b)), the inlet-body-tail model trimmed at $\alpha = 13°$ with a pitch-control deflection of -20°. At these conditions, a value of C_N of 5.5 was achieved. Changing the inlet orientation angle ϕ_I to 135° (fig. 15(b)) decreased the stability level so that the model was trimmed at $\alpha \approx 20°$ at a pitch-control deflection of less than -20°. Although the untrimmed C_N was decreased from about 11 to 9 by the change in ϕ_I, the trimmed C_N increased from about 5.5 to about 7.5. Adding the wing increased the available normal force by the wing lift and by the increased trim angle of attack because of the destabilizing effect of the wing. With the wing on, at $M = 2.95$ with $\phi_I = 115°$ (fig. 18(b)), the model was trimmed at $\alpha = 20°$ with a pitch-control deflection less than -20°, with a resulting C_N of about 11. Increasing ϕ_I from 115° to 135° (fig. 19(b)) decreased the stability, and the model could be trimmed at $\alpha \approx 20°$ with a pitch-control deflection of less than -10°. The corresponding C_N, however, remained at about 11. The smaller value of C_N for the reduced planform area of the configuration with $\phi_I = 135°$ tends to be balanced by the reduced negative normal force C_N due to smaller pitch-control deflection.

The X-tail T_2 configuration (fig. 20), compared with the tri-tail T_1 configuration (fig. 19), had both a greater margin of longitudinal stability and a more linear pitching-moment curve. Trim could be achieved at the maximum angle of attack (20°) with pitch-control deflection of only about -10° since the pitch-control effectiveness is higher. Similarly, tail T_3 provided a different level of stability and control effectiveness (fig. 21). However, with either of the three tails, for both the wing-on and wing-off configurations, the trimmed C_N corresponding to the maximum angle of attack was independent of the tail configuration. Tail T_2, therefore, must be considered to be the better configuration of the three configurations tested, because the pitching-moment curves are more linear.

The data for the two-dimensional extended inlet I_3 are presented in figures 31 through 42. With T_1, the pitching-moment curve exhibited nonlinearity as with I_1 and I_2. With the X-tail T_2 (fig. 34), the pitching-moment curve became more linear and the model was stable throughout the range of angle of attack. With T_2, trim could be achieved at $\alpha = 20°$ with about -10° of pitch-control deflection, as shown in figure 38. The maximum trim normal-force coefficient was generally between that of the I_1 and I_2 configurations.

The change in both planform and lateral area of the aft end of the body which accompanies change in the inlet orientation angle would be expected to change the directional stability as well as the longitudinal stability. This effect is seen in the lateral-directional data shown in figures 22 and 23. As the inlet orientation angle ϕ_I was increased, the change in directional stability was more linear with ϕ_I than the variation of pitching-moment coefficient; there was a significant difference between the C_{n_β} for $\phi_I = 90°$ and 115° (wing-off) data, whereas the difference in the corresponding values of C_m was much smaller. Since the increase in lateral area caused by increasing ϕ_I is below the model center line, increasing ϕ_I would be expected to decrease the lateral stability. This effect is also seen in the data of figures 22 and 23.

The effect of the various model components on the lateral-directional stability is shown in figures 24 through 28. Generally, the body-inlet alone was directionally unstable. At $\phi_I = 90°$ and 115°, the model was laterally stable at moderate angles of attack, but at $\phi_I = 135°$, the body-inlet alone was unstable for the entire range of angle of attack. Adding the wing tended to decrease the directional stability and increase the lateral stability. Adding the tail to the model either with or without a wing resulted in increased directional and lateral stability, but only T_2 and T_3 resulted in a margin of lateral-directional stability for the entire angle-of-attack range.

Comparison of parts (a), (b), (c), and (d) of each data figure gives an indication of the effect of free-stream Mach number. The only effect seems to be an overall reduction of the coefficient values and a somewhat straightening of the pitching-moment curves. The trim angle of attack was generally reduced.

CONCLUDING REMARKS

A series of air-breathing missile configurations has been investigated to provide a data base for the design of such missiles. The model could be configured with either twin axisymmetric or two-dimensional inlets. Three circumferential inlet locations were investigated: 90°, 115°, and 135° from the top center. Two vertical wing locations, as well as wingless configurations, were used. Three tail configurations were formed by locating the tail surfaces on the inlet fairings or on fairings on the body. The surfaces were deflected to provide pitch control. Two-dimensional inlets with extended compression surfaces, used to improve the angle-of-attack performance of the inlets for wingless configurations, were also investigated.

Although the data of this volume refer specifically to the twin two-dimensional inlet configurations, comparison of these data with those for the axisymmetric inlet configurations of NASA Technical Memorandum 84558 indicates that even though individual values and levels of the various curves may differ, where configurations are comparable, the trends are similar and conclusions formed will generally apply to the model with either inlet configuration.

As a result of the investigation, the following general trends may be observed:

1. For most configurations, the pitching-moment curve was nonlinear, with a large margin of longitudinal stability at high angles of attack, but with little or no stability near an angle of attack of 0°.

2. The model had marginal lateral-directional stability for most configurations; the X-tail and the inverted tri-tail resulted in lateral-directional stability for the entire range of angle of attack.

3. The model with the 90° inlet orientation angle could not be trimmed at the maximum angle of attack (20°) with the maximum pitch-control deflection (-20°). Only by increasing the inlet orientation angle to 135° could the model be trimmed at an angle of attack of 20° with less than -20° pitch-control deflection with either tail configuration.

4. Of the three tail configurations, the X-tail had a more linear pitching-moment curve and greater pitch-control effectiveness.

5. The extended two-dimensional inlet configuration without a wing, as with the other inlets, tended to have a nonlinear pitching-moment curve; with the X-tail, the curve was straightened and the configuration was stable throughout the range of angle of attack and the model could be trimmed at an angle of attack of 20° with a pitch-control deflection of -10°.

Langley Research Center
National Aeronautics and Space Administration
Hampton, VA 23665
November 8, 1982

REFERENCES

1. Sawyer, Wallace C.; and Hayes, Clyde: Stability and Control Characteristics of an Air-Breathing Missile Configuration Having a Forward Located Inlet. NASA TM X-3391, 1976.

2. Hayes, Clyde; and Monta, William J.: Aerodynamic Characteristics of a 1/4-Scale Model of MORASS Missile Configurations at Supersonic Speeds. NASA TM X-3354, 1976.

3. Hayes, Clyde: Aerodynamic Characteristics of 1/4-Scale Model of ALRAAM Missile Configuration at Supersonic Speeds. NASA TM-74075, 1977.

4. Hayes, Clyde; and Sawyer, Wallace C.: Aerodynamic Characteristics of a Model Simulating the Gainful (SA-6) Missile at Supersonic Mach Numbers. NASA TM X-3493, 1977.

5. Hayes, Clyde; and Sawyer, Wallace C.: Aerodynamic Characteristics of a Series of Air-Breathing Missile Configurations Investigated as Part of the SASS Program. NASA TM-80139, 1979.

6. Hayes, Clyde: Supersonic Aerodynamic Characteristics of a Twin-Inlet Advanced Intercept Air-to-Air Missile (AIAAM) Configuration. NASA TM-83178, 1981.

7. Hayes, Clyde: Aerodynamic Characteristics of a Supersonic Single-Inlet Missile Configuration Investigated as Part of the Advanced Intercept Air-to-Air Missile (AIAAM) Program. NASA TM-83177, 1981.

8. Hayes, Clyde: Aerodynamic Characteristics of a Series of Twin-Inlet Air-Breathing Missile Configurations. I - Axisymmetric Inlets at Supersonic Speeds. NASA TM-84558, 1983.

9. Hayes, Clyde: Aerodynamic Characteristics of a Series of Twin-Inlet Air-Breathing Missile Configurations. III - Axisymmetric and Two-Dimensional Inlets at Subsonic-Transonic Speeds. NASA TM-84560, 1983.

10. Hayes, Clyde: Aerodynamic Characteristics of a Series of Single-Inlet Air-Breathing Missile Configurations. NASA TM-84557, 1982.

11. Jackson, Charlie M., Jr.; Corlett, William A.; and Monta, William J.: Description and Calibration of the Langley Unitary Plan Wind Tunnel. NASA TP-1905, 1981.

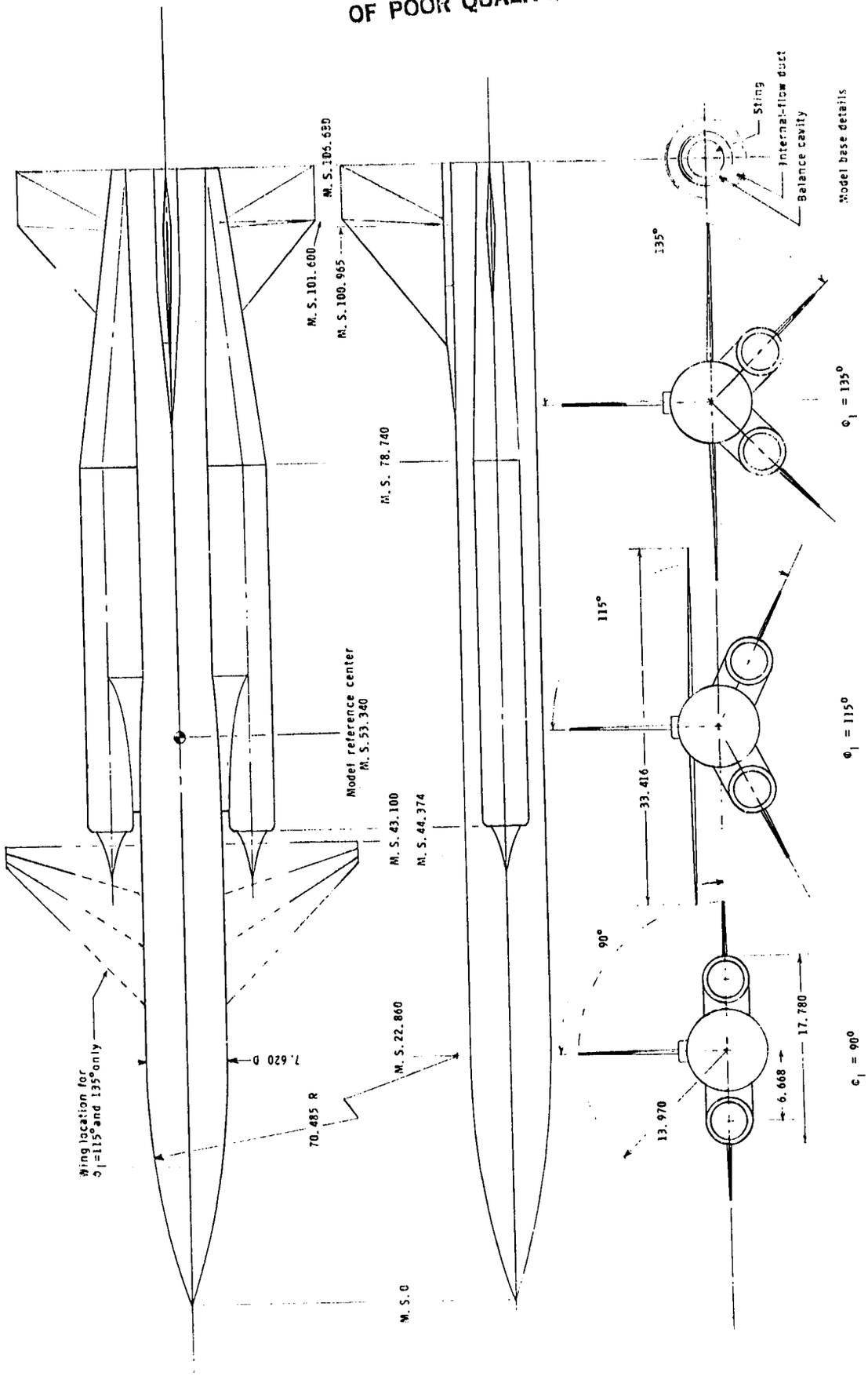

(a) General arrangement of twin axisymmetric inlet I_1 configuration.

Figure 1.- Details of model. All linear dimensions are in centimeters.

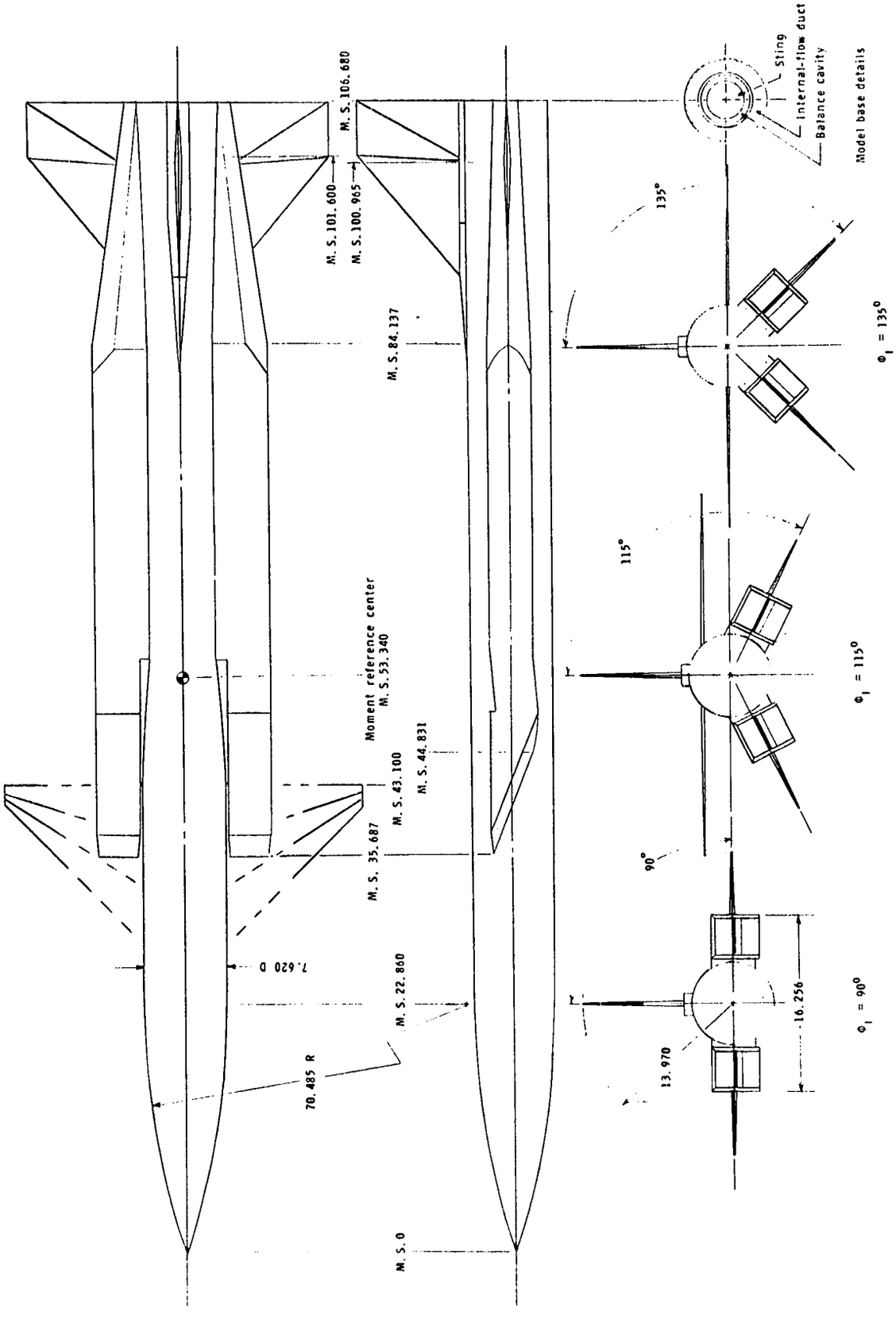

(b) General arrangement of twin two-dimensional inlet I_2 configuration.

Figure 1.- Continued.

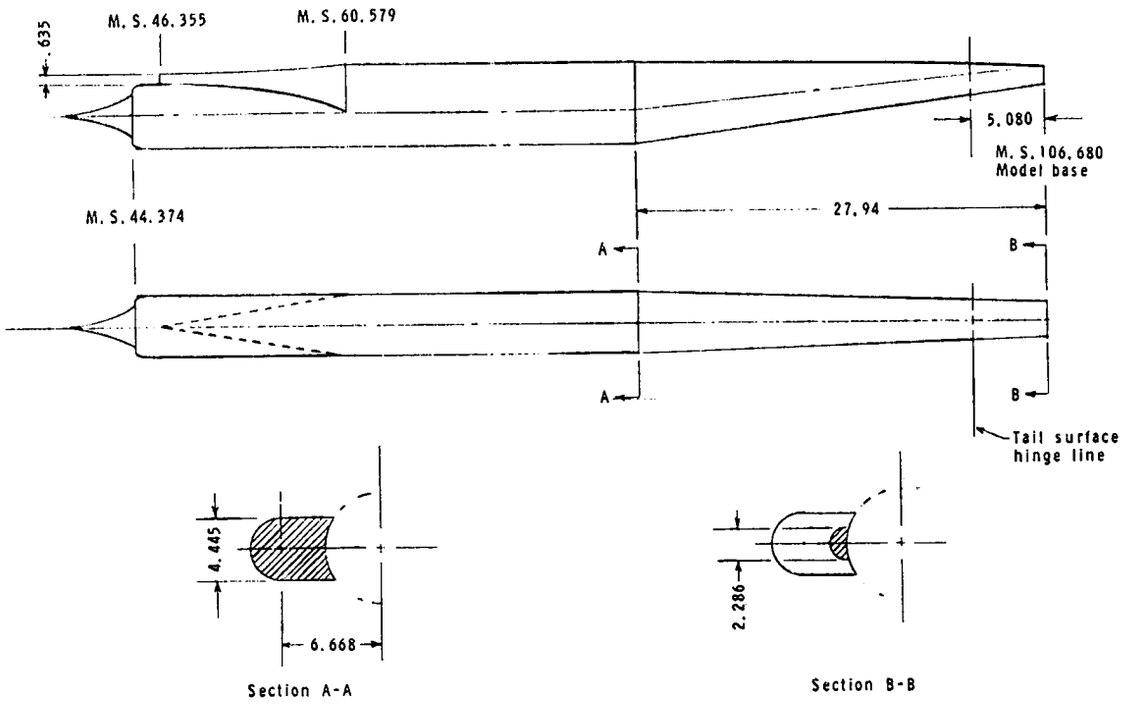

Inlet and inlet fairing

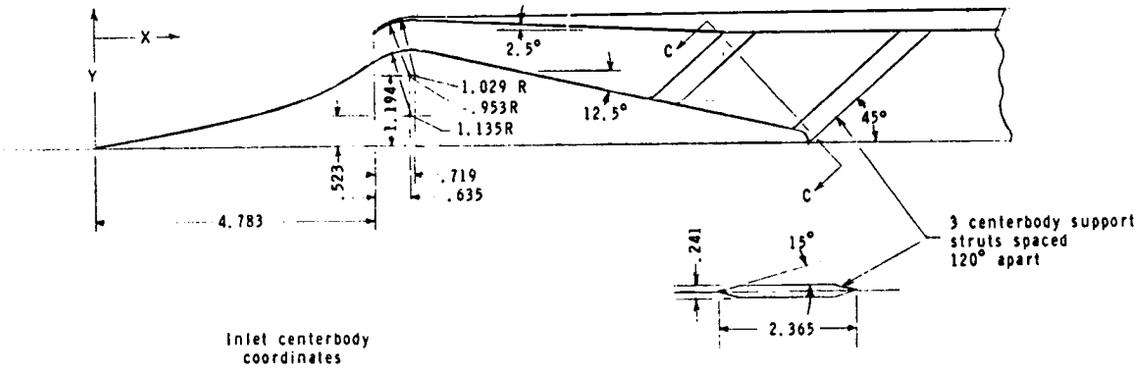

Inlet centerbody coordinates

x	y
.000	.000
1.260	.229
1.712	.325
2.347	.460
2.819	.579
3.185	.688
3.475	.785
3.815	.914
4.061	1.024
4.252	1.128
4.783	1.463
5.664	1.631
13.020	.000

Inlet (x4)

(c) Axisymmetric inlet and inlet fairing.

Figure 1.- Continued.

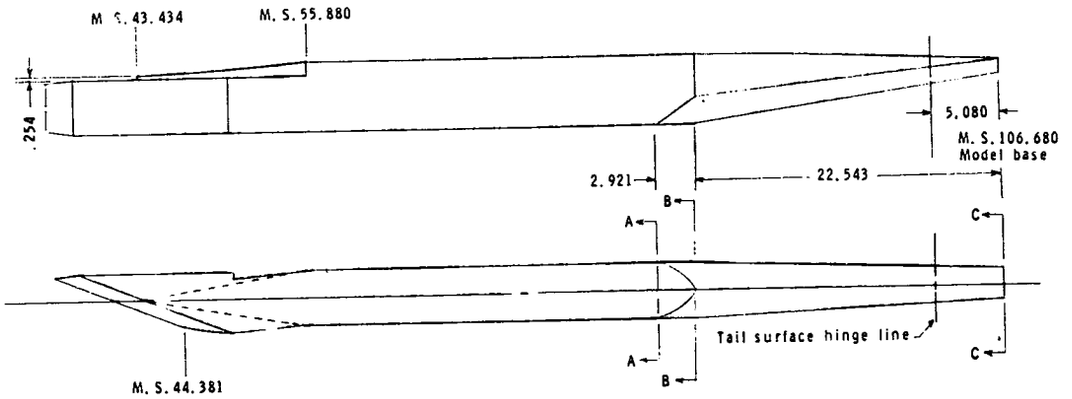

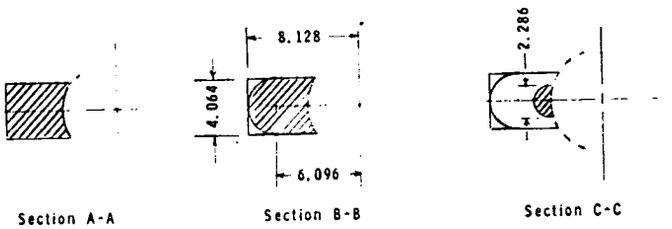

Inlet and inlet fairing

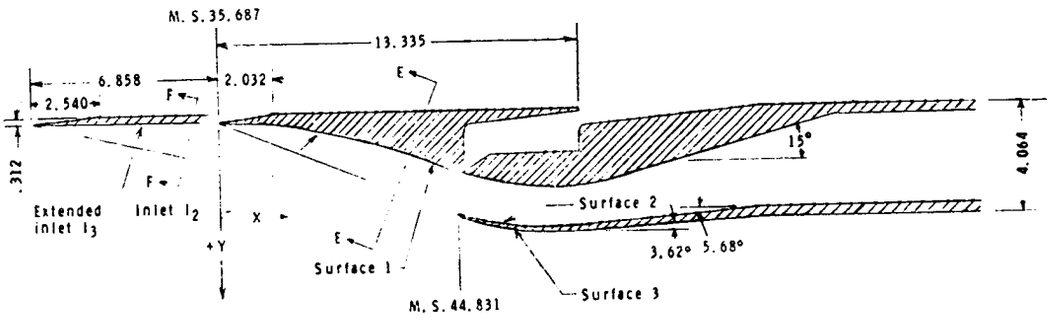

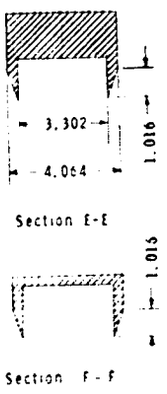

Inlet surface-coordinates

Surface 1		Surfaces 2 and 3		
x	y_1	x	y_2	y_3
000	000	9.144	4.073	4.073
1.920	000	9.502	4.196	4.270
3.861	.340	9.863	4.305	4.412
4.491	.462	10.221	4.399	4.526
5.039	.592	10.582	4.478	4.620
5.519	.716	10.940	4.543	4.699
5.936	.846	11.300	4.592	4.757
6.320	.973	11.659	4.625	4.798
8.964	1.941	12.017	4.646	4.826
9.144	1.981	12.377	4.646	4.844
9.906	2.286	12.736	4.633	4.844
10.922	2.489	14.011	4.600	4.826
11.938	2.515			
12.573	2.477			
13.335	2.388			

Straight line
Boundary layer
Bleed slot

Inlet (x2)

(d) Two-dimensional inlet and inlet fairing.

Figure 1.- Continued.

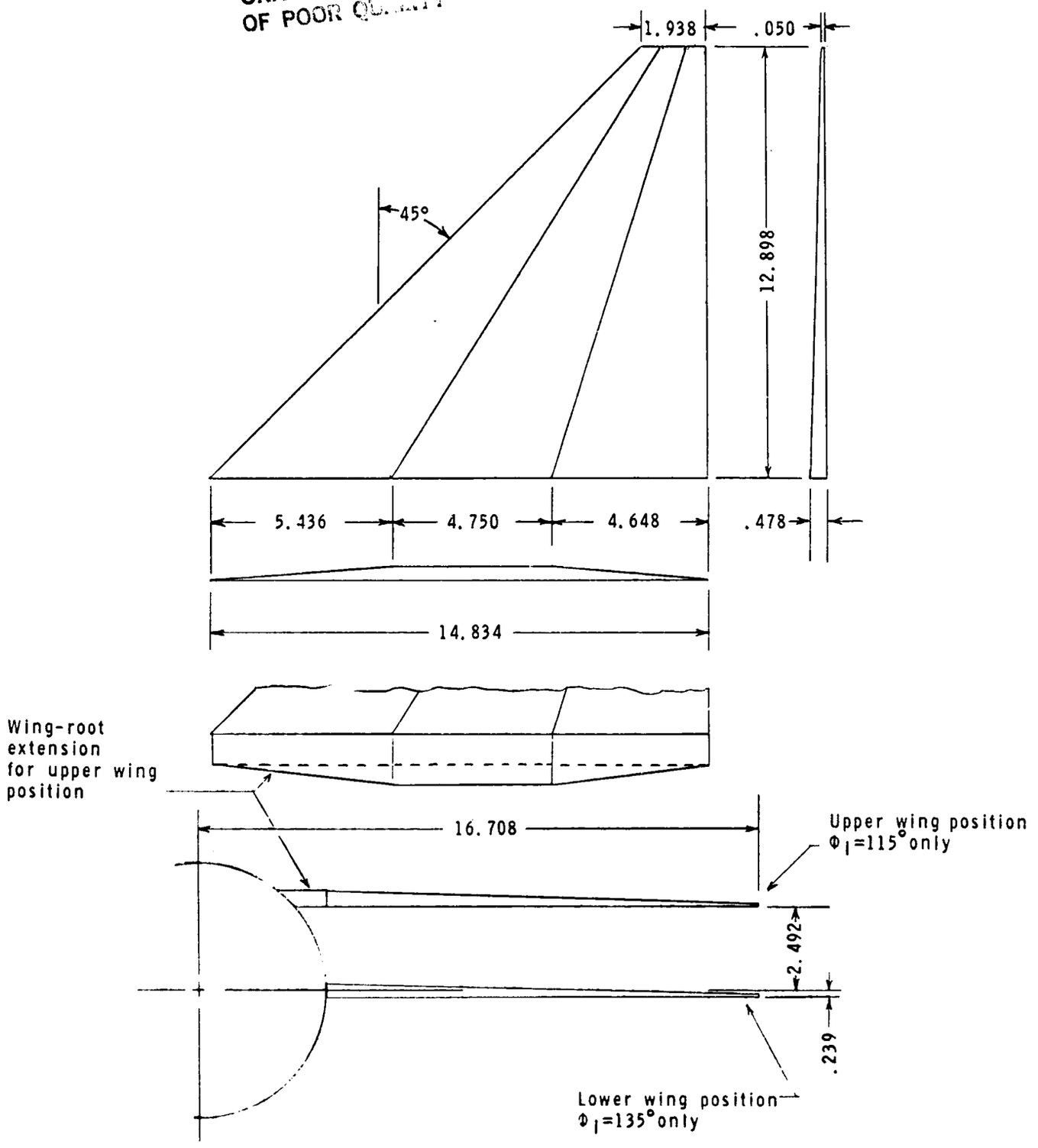

(e) Wing.

Figure 1.- Continued.

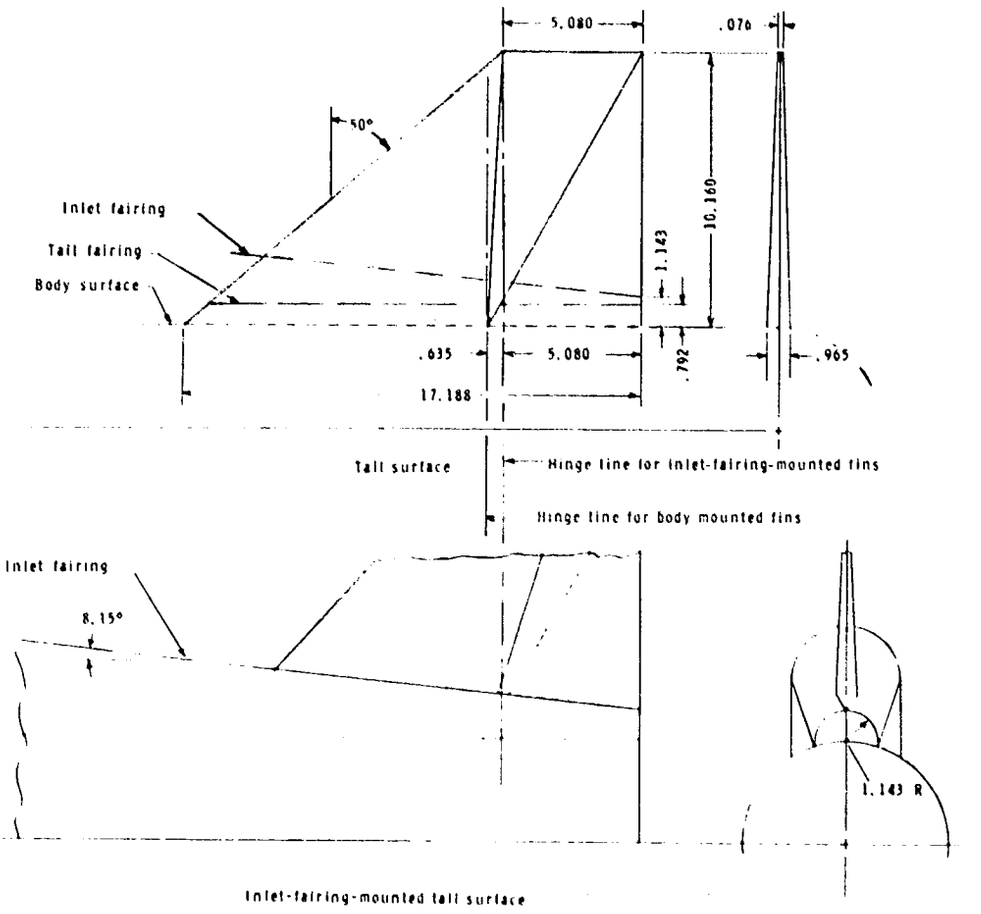

Inlet-fairing-mounted tail surface

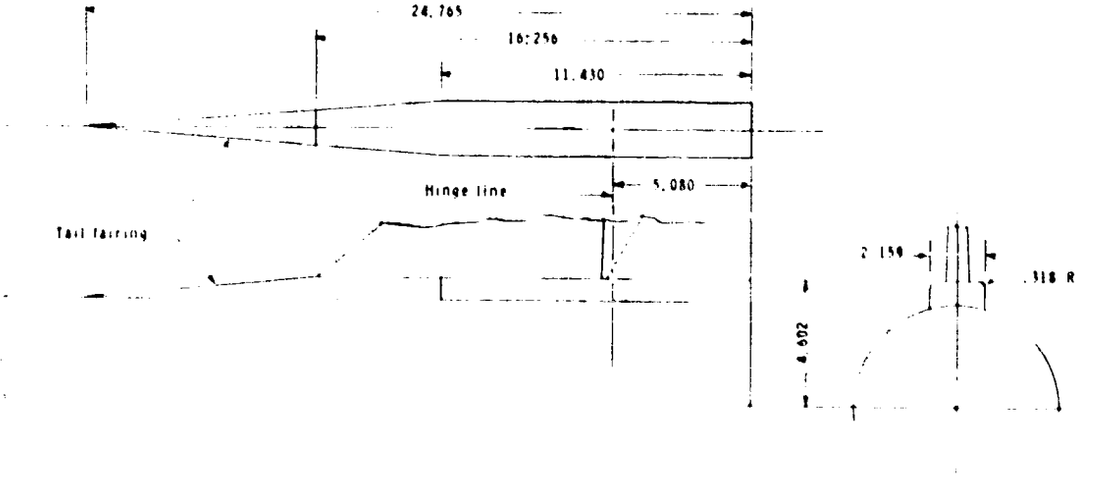

Tail-fairing-mounted tail surface

(f) Tail.

Figure 1.- Continued.

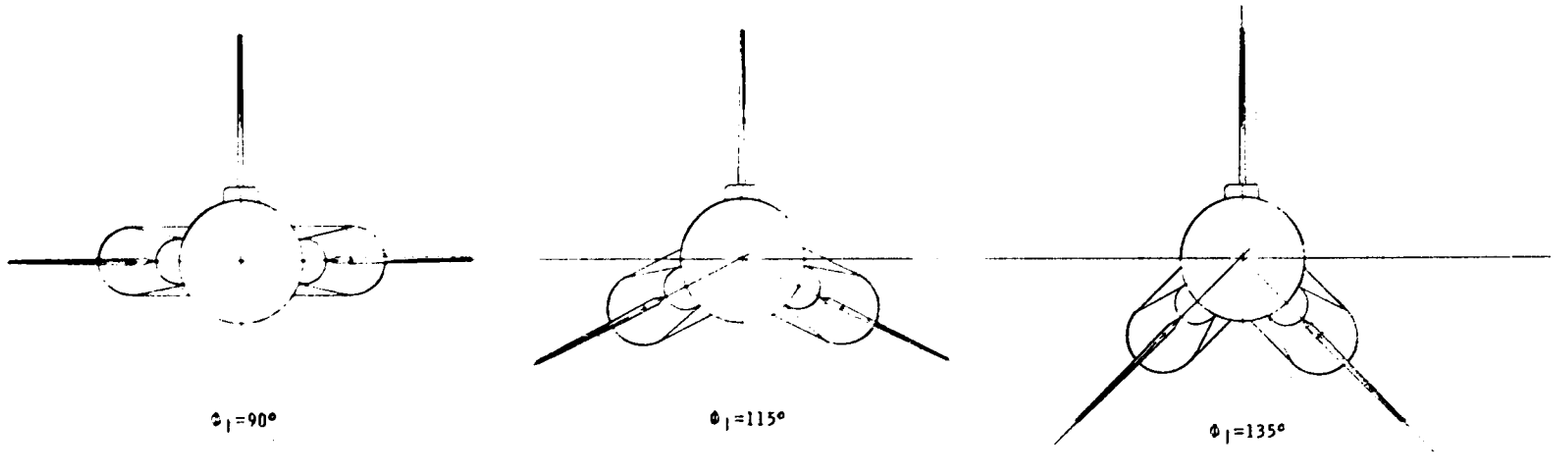

Tail T_1 configuration

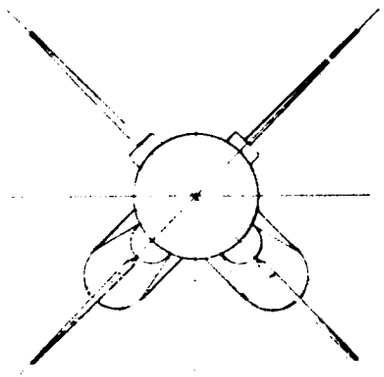

Tail T_2 configuration

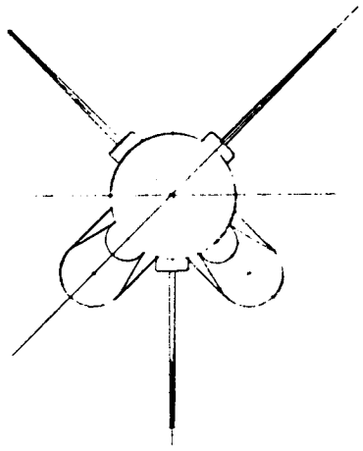

Tail T_3 configuration

(g) Arrangement of tail configurations.

Figure 1.- Concluded.

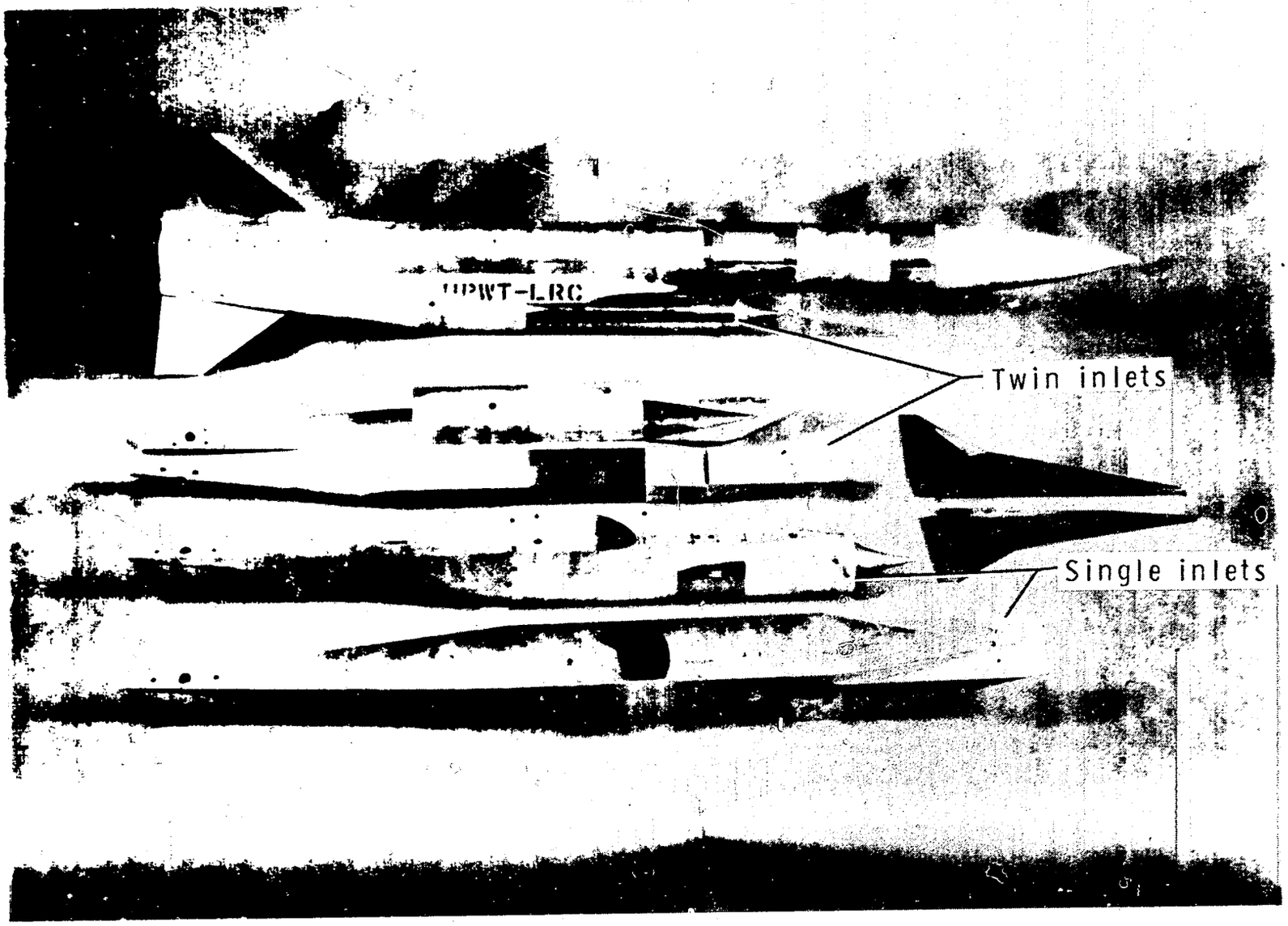

(a) Top view of assembled model.

Figure 2.- Photographs of model. Photographs courtesy of David Taylor Naval Ship Research and Development Center.

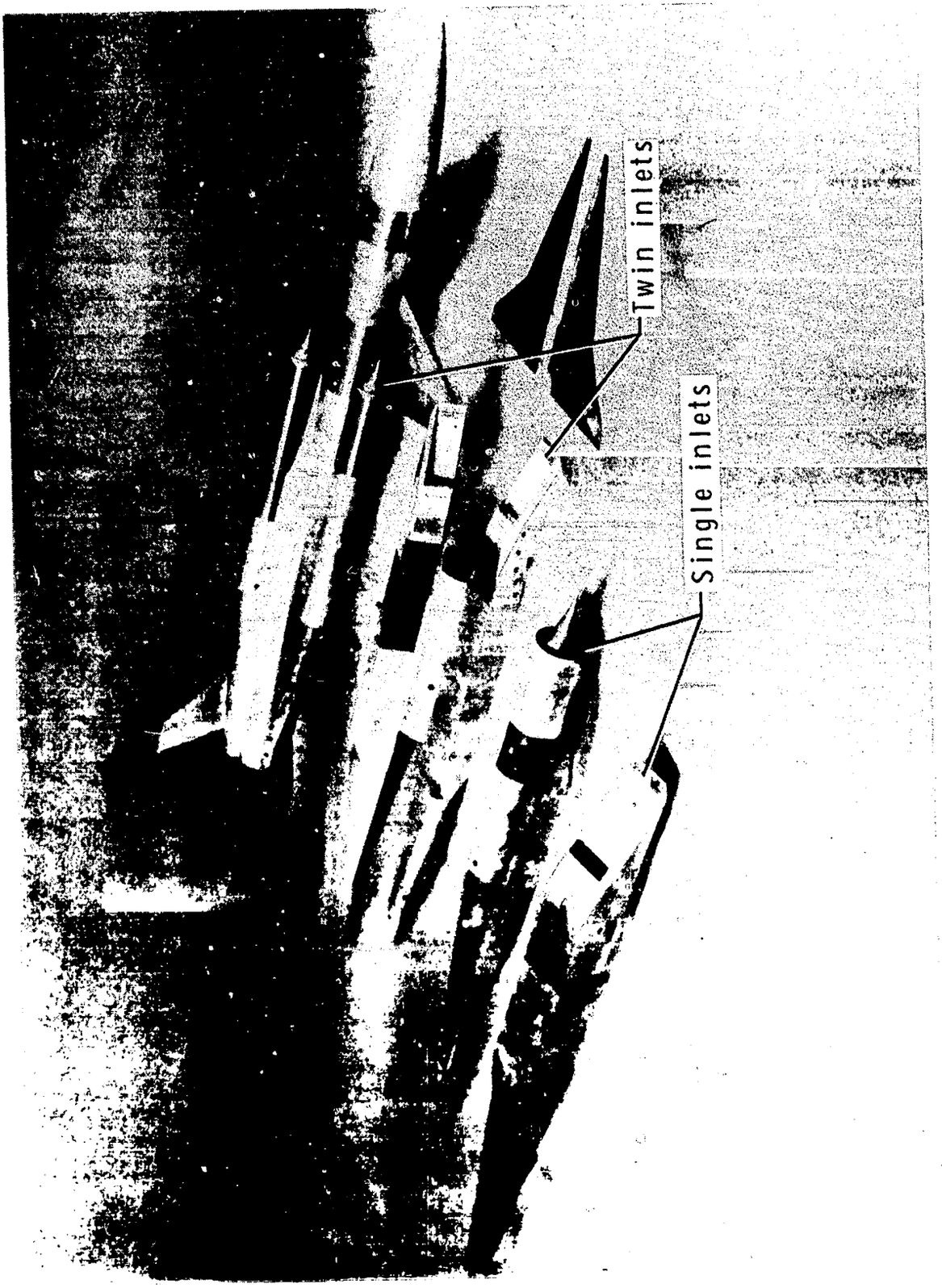

(b) Bottom view of assembled model.

Figure 2.- Concluded.

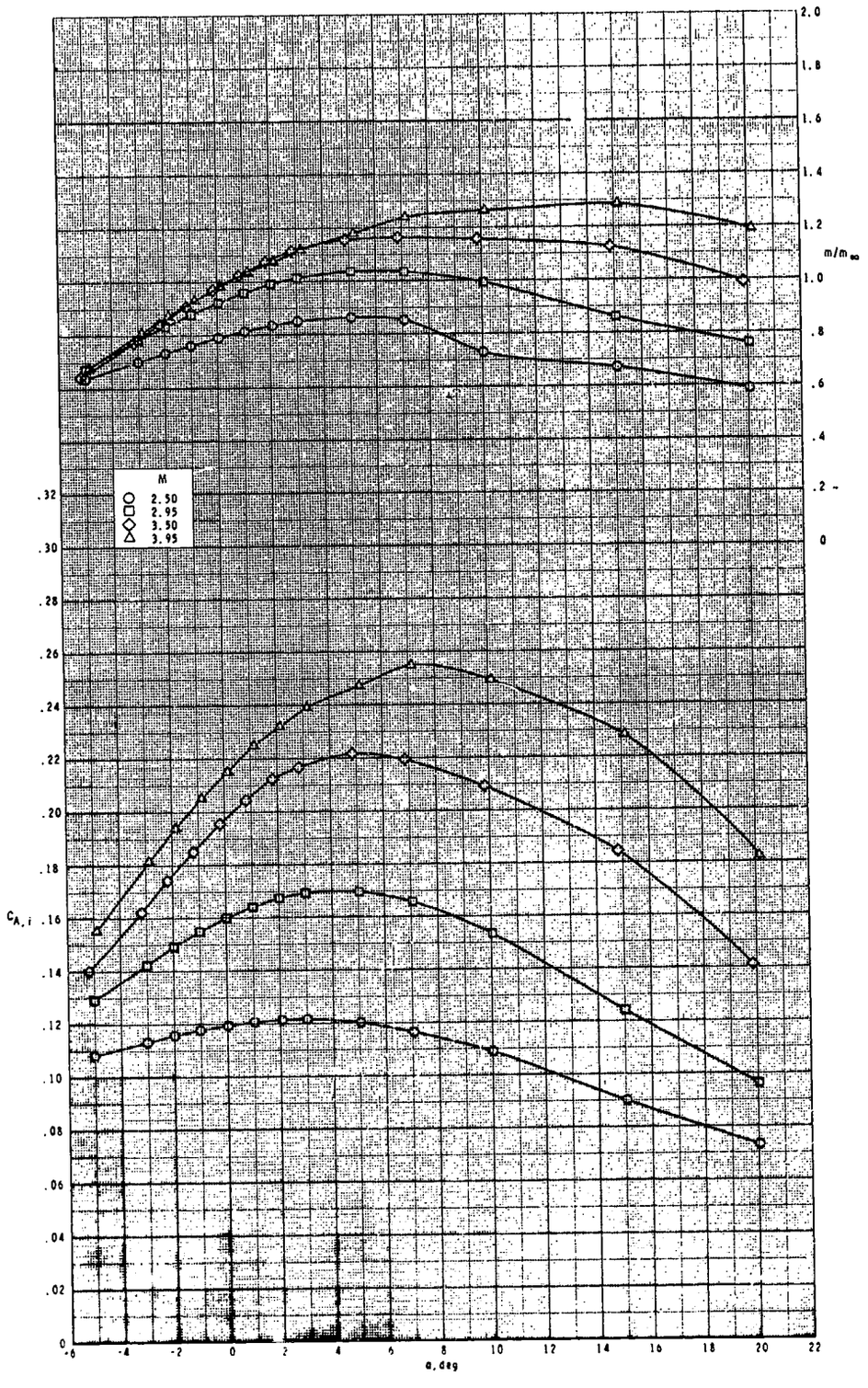

(a) Configuration B_1I_2; $\phi_I = 90°$.

Figure 3.- Internal-flow characteristics of various configurations.

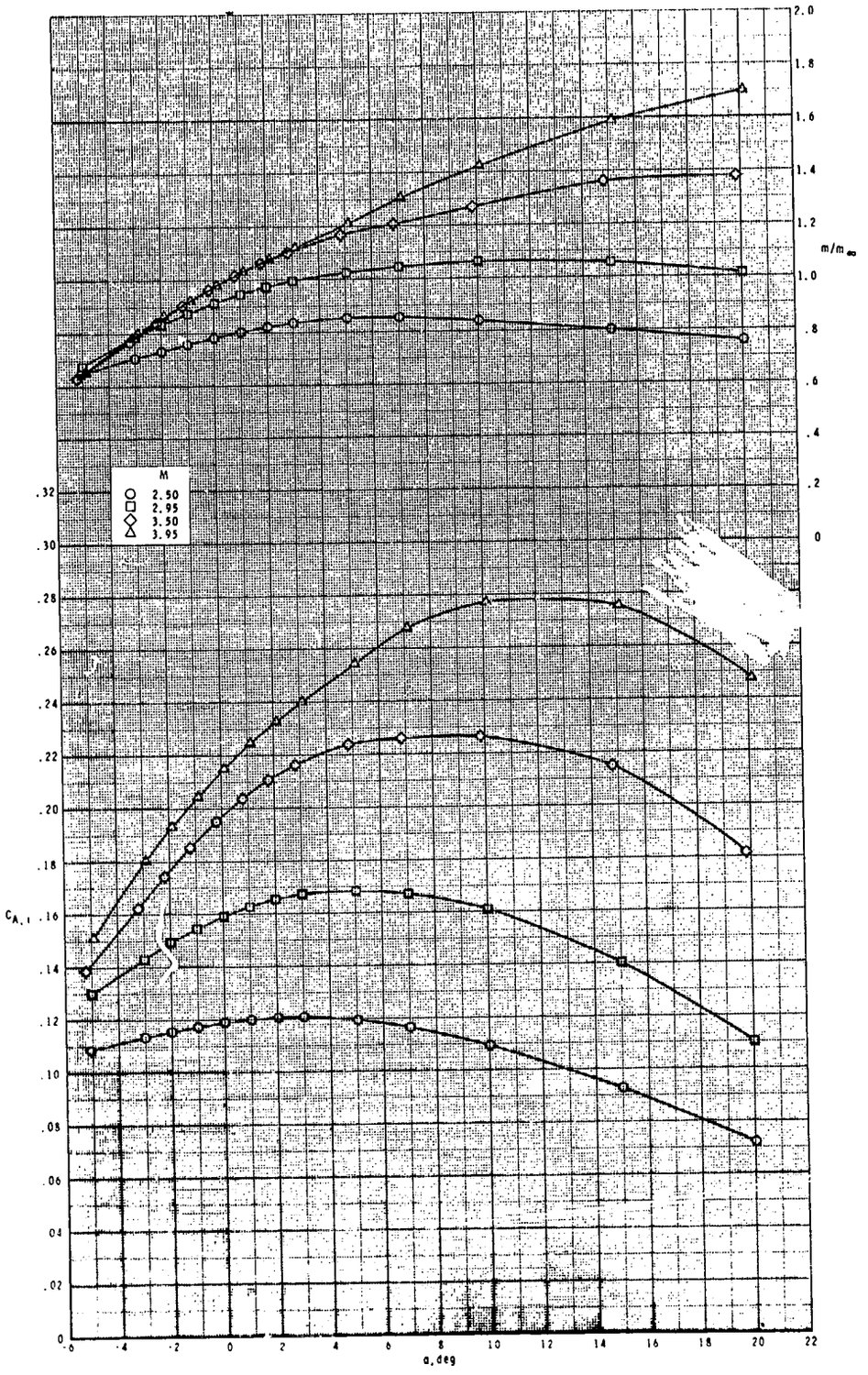

(b) Configuration B_1I_2; $\phi_I = 115°$.

Figure 3.- Continued.

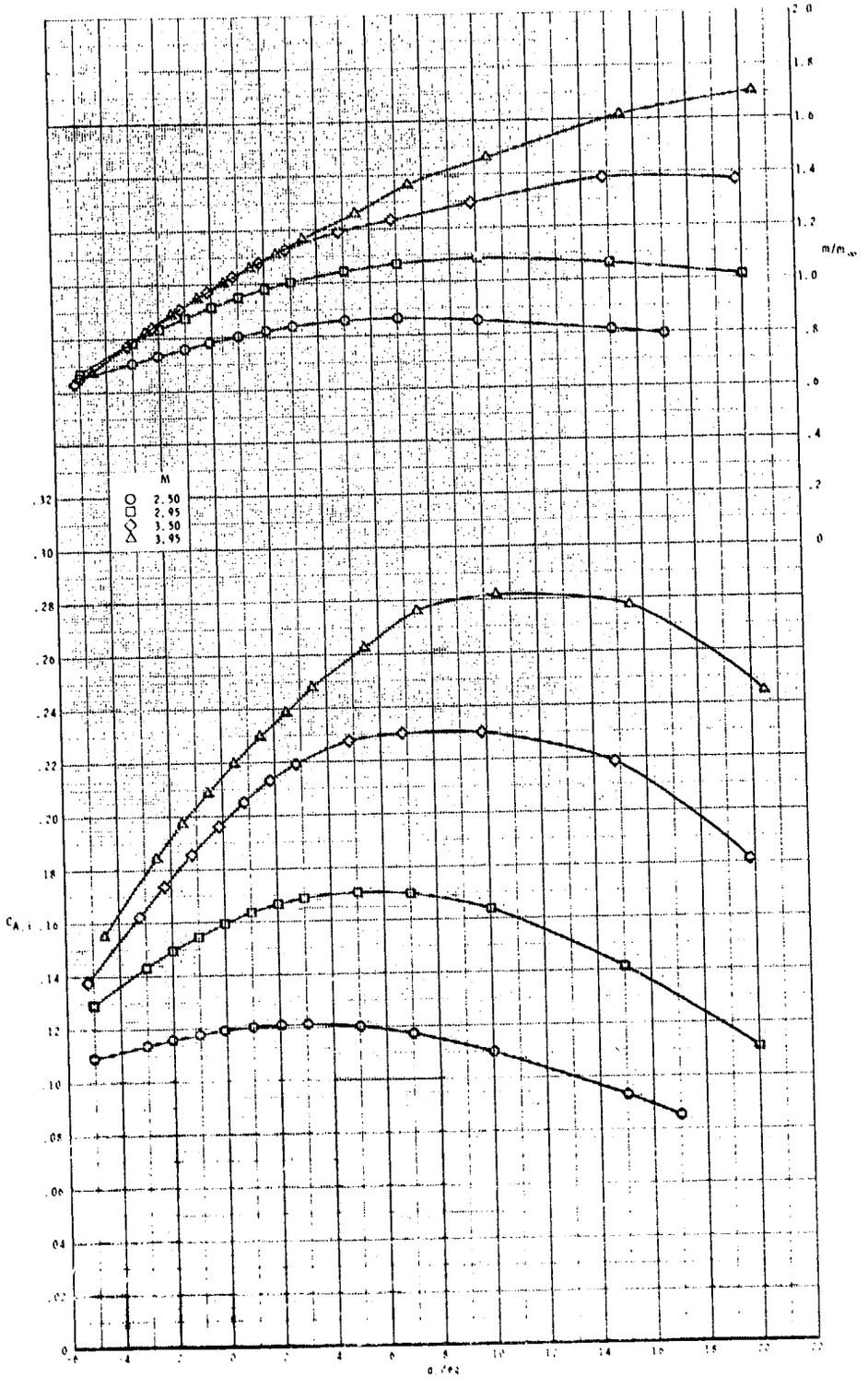

(c) Configuration $B_1I_2W_1$; $\phi_I = 115°$.

Figure 3.- Continued.

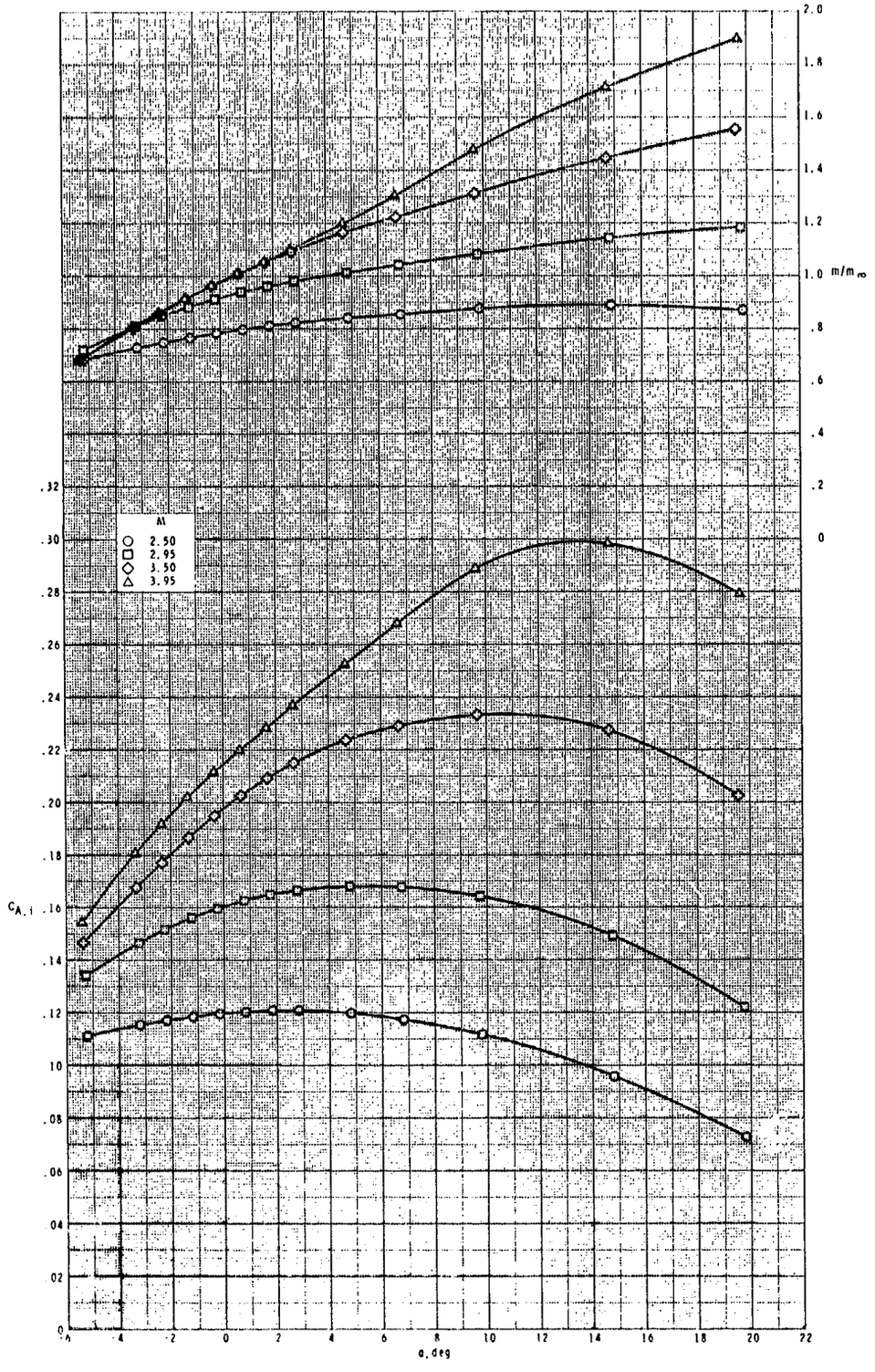

(d) Configuration B_1I_2; $\phi_I = 135°$.

Figure 3.- Continued.

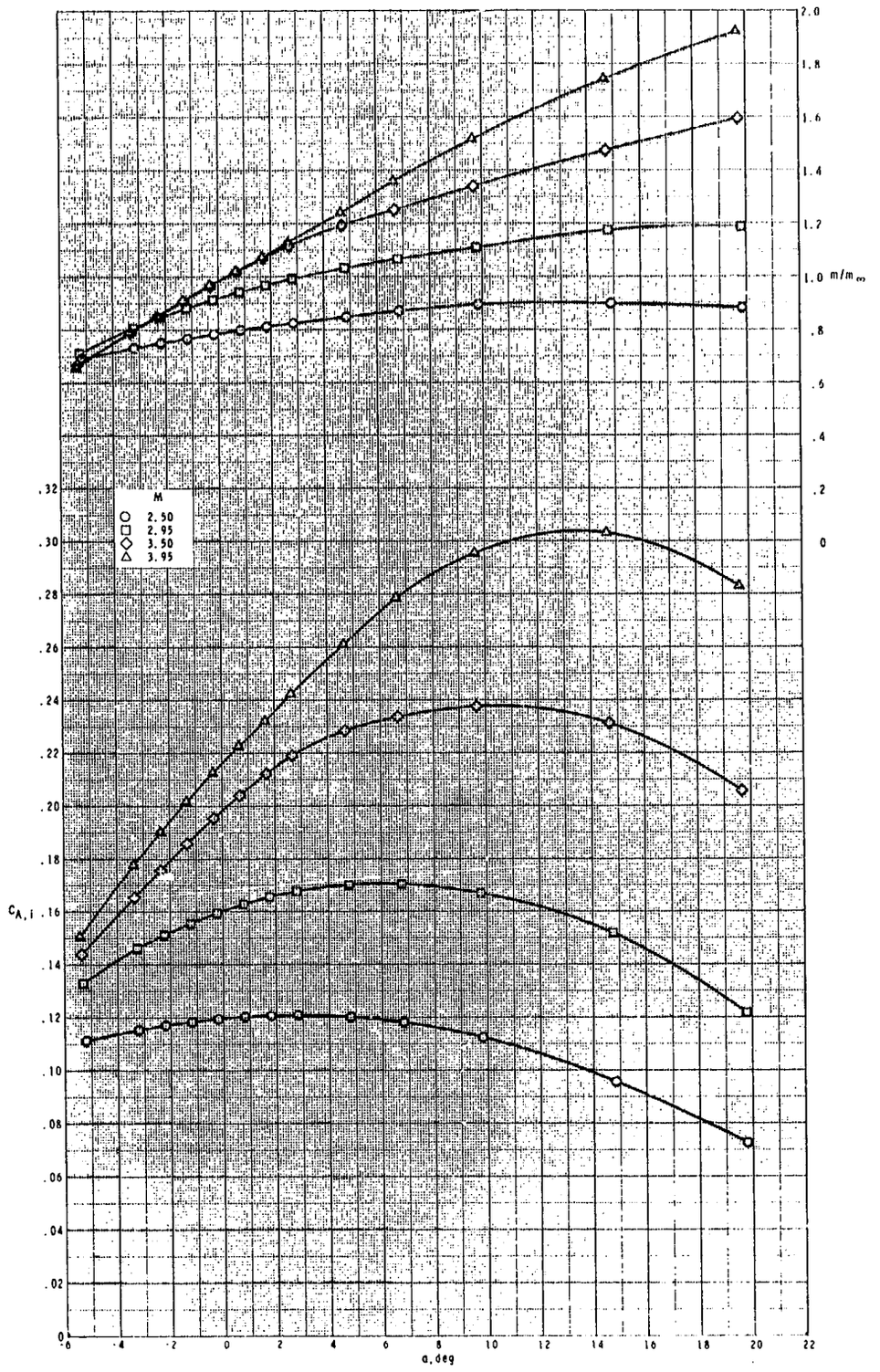

(e) Configuration $B_1I_2W_1$; $\phi_I = 135°$.

Figure 3.- Continued.

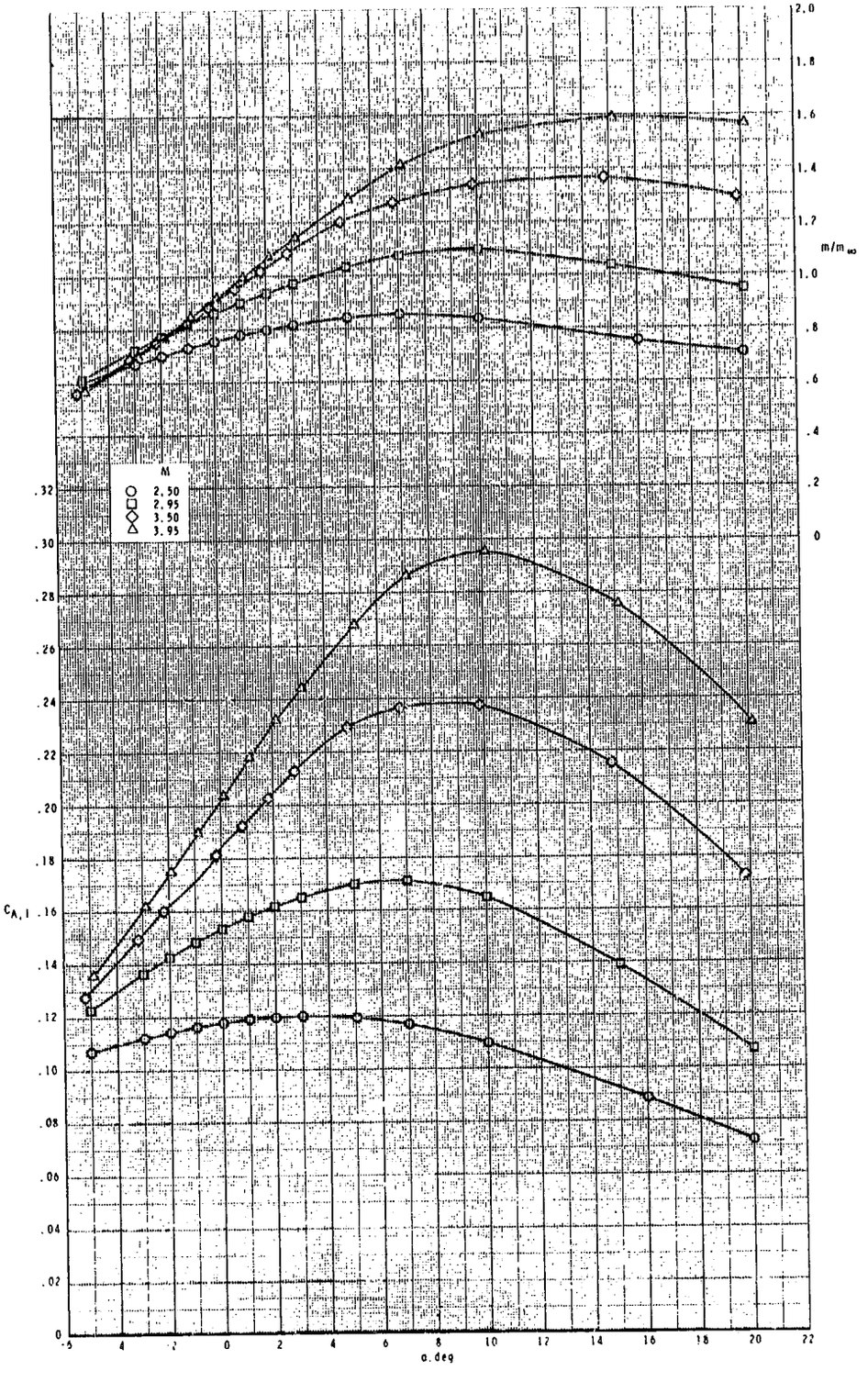

(f) Configuration B_1I_3; $\phi_I = 90°$.

Figure 3.- Continued.

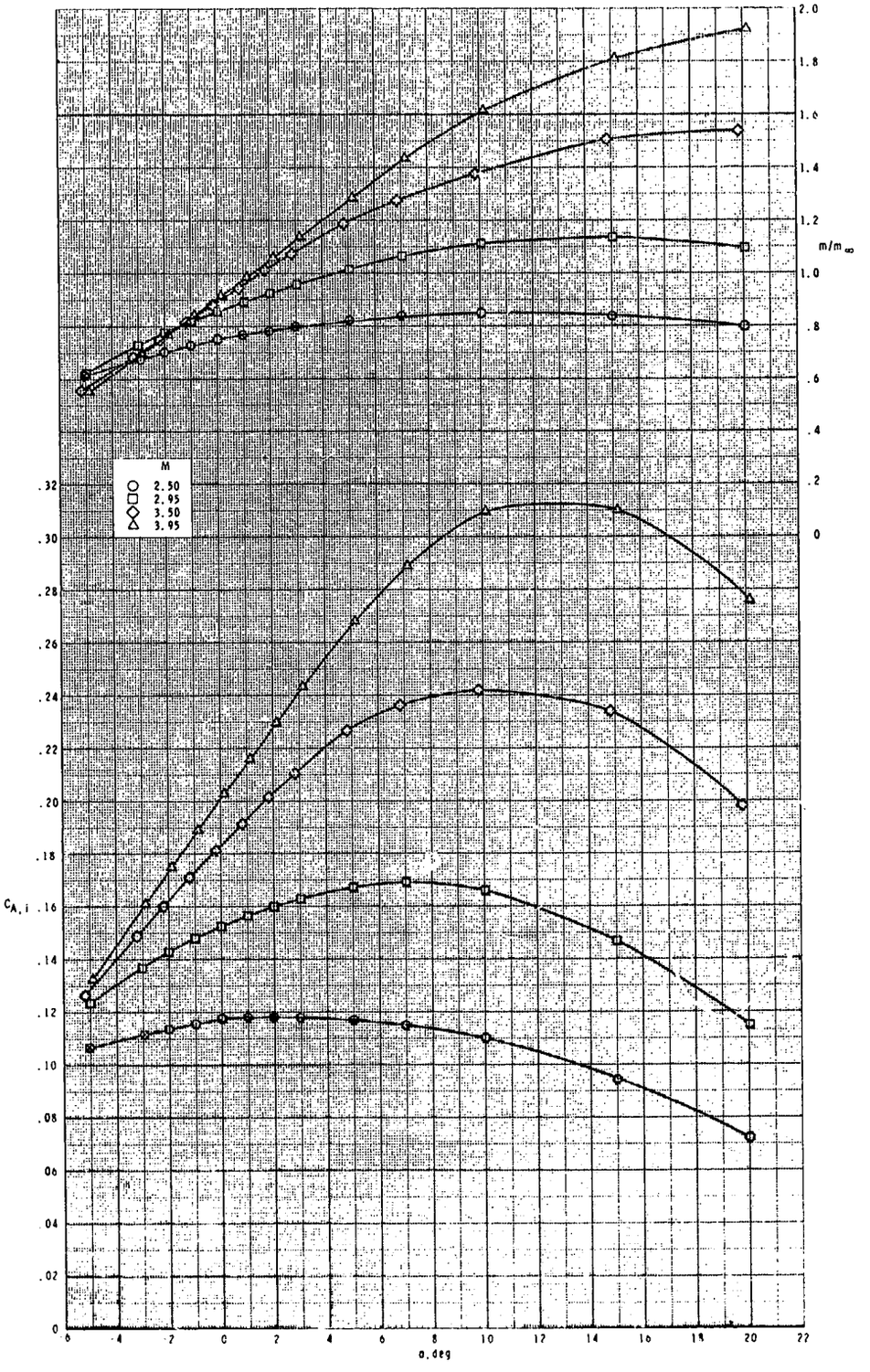

(g) Configuration B_1I_3; $\phi_I = 115°$.

Figure 3.- Continued.

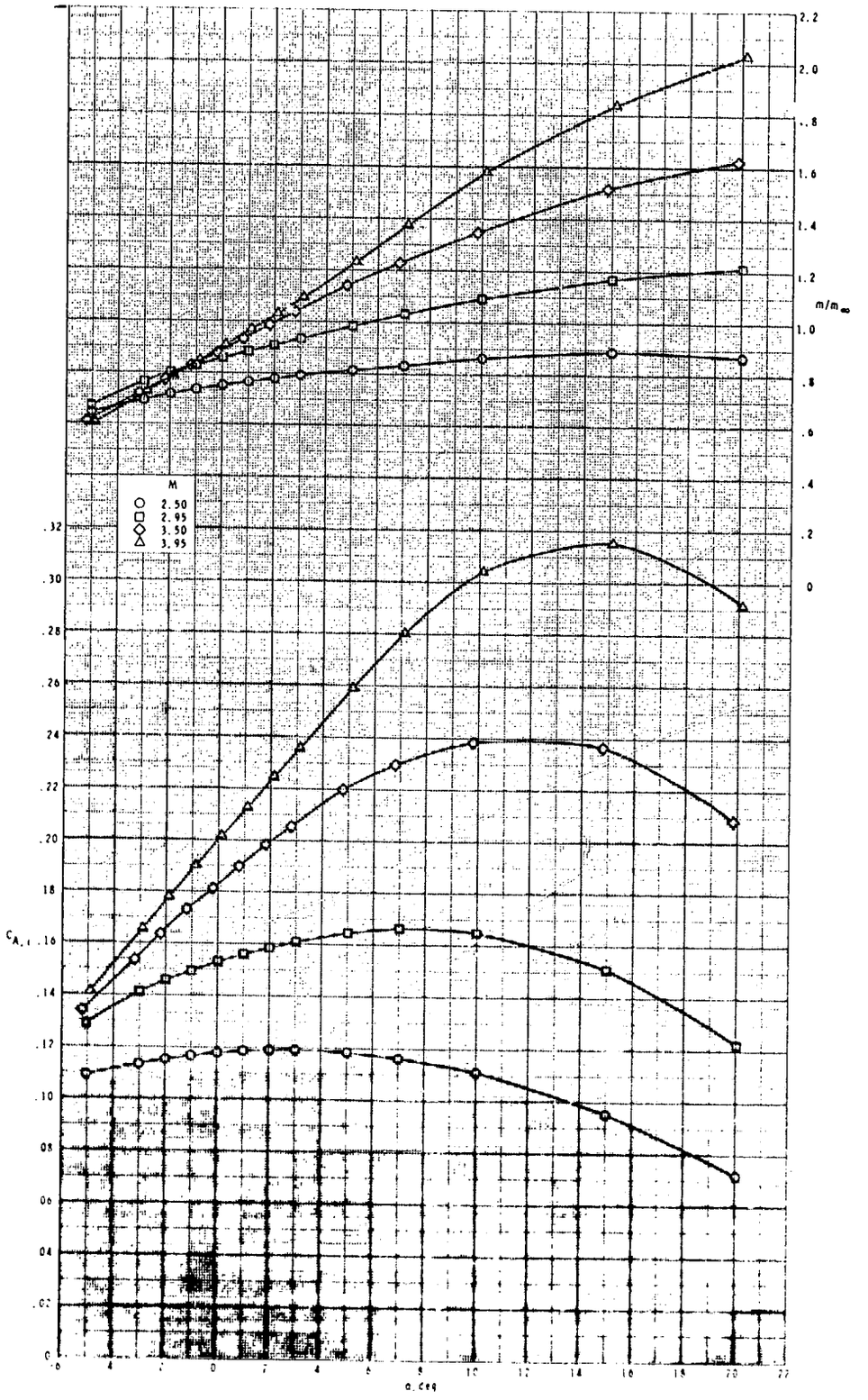

(h) Configuration $B_1 I_3$; $\phi_I = 135°$.

Figure 3.- Concluded.

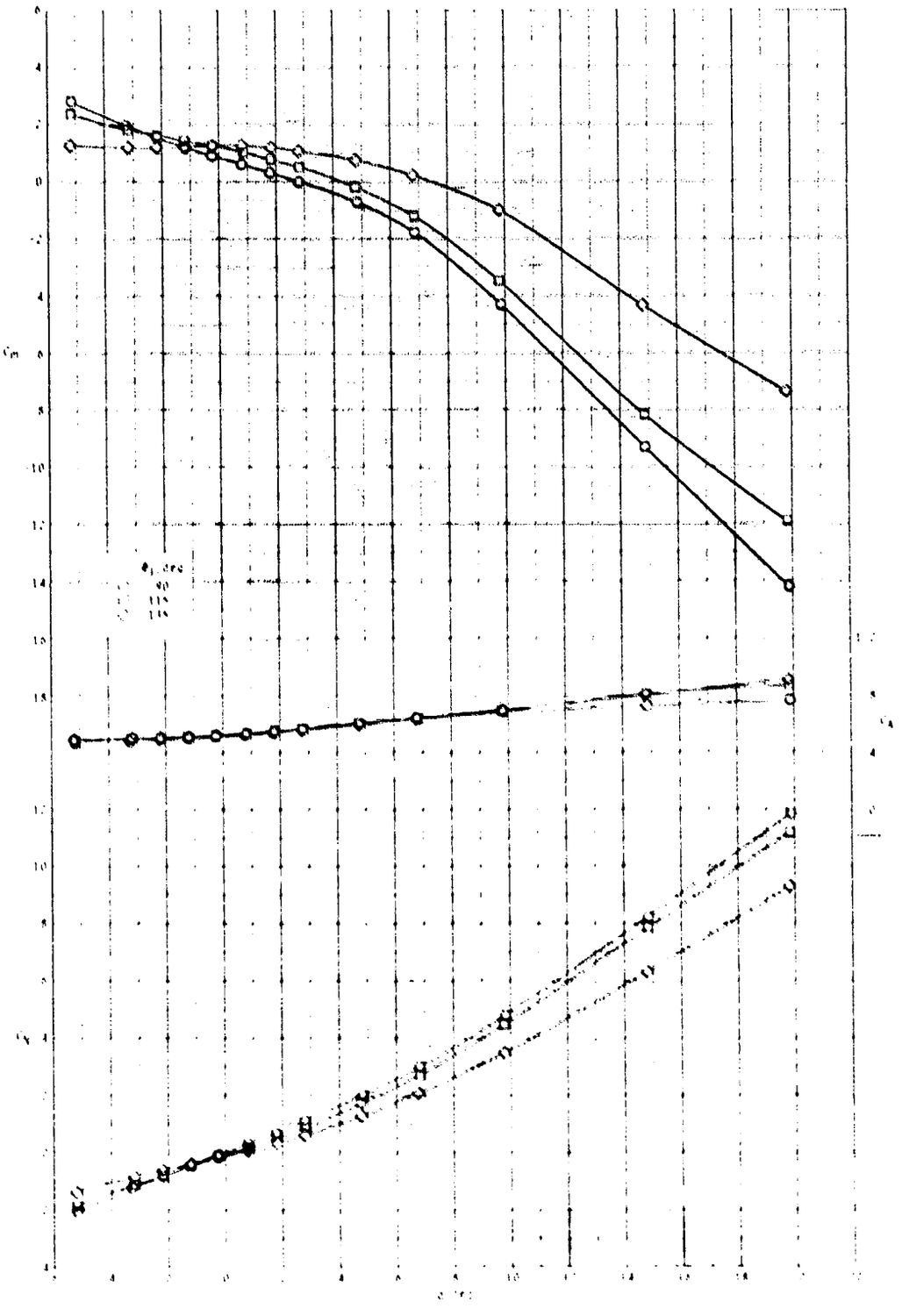

(a) M = 2.50.

Figure 4.- Effect of inlet orientation angle ϕ_I on longitudinal aerodynamic characteristics of configuration $B_1 I_2 F_1$. δ_{te} = 0°.

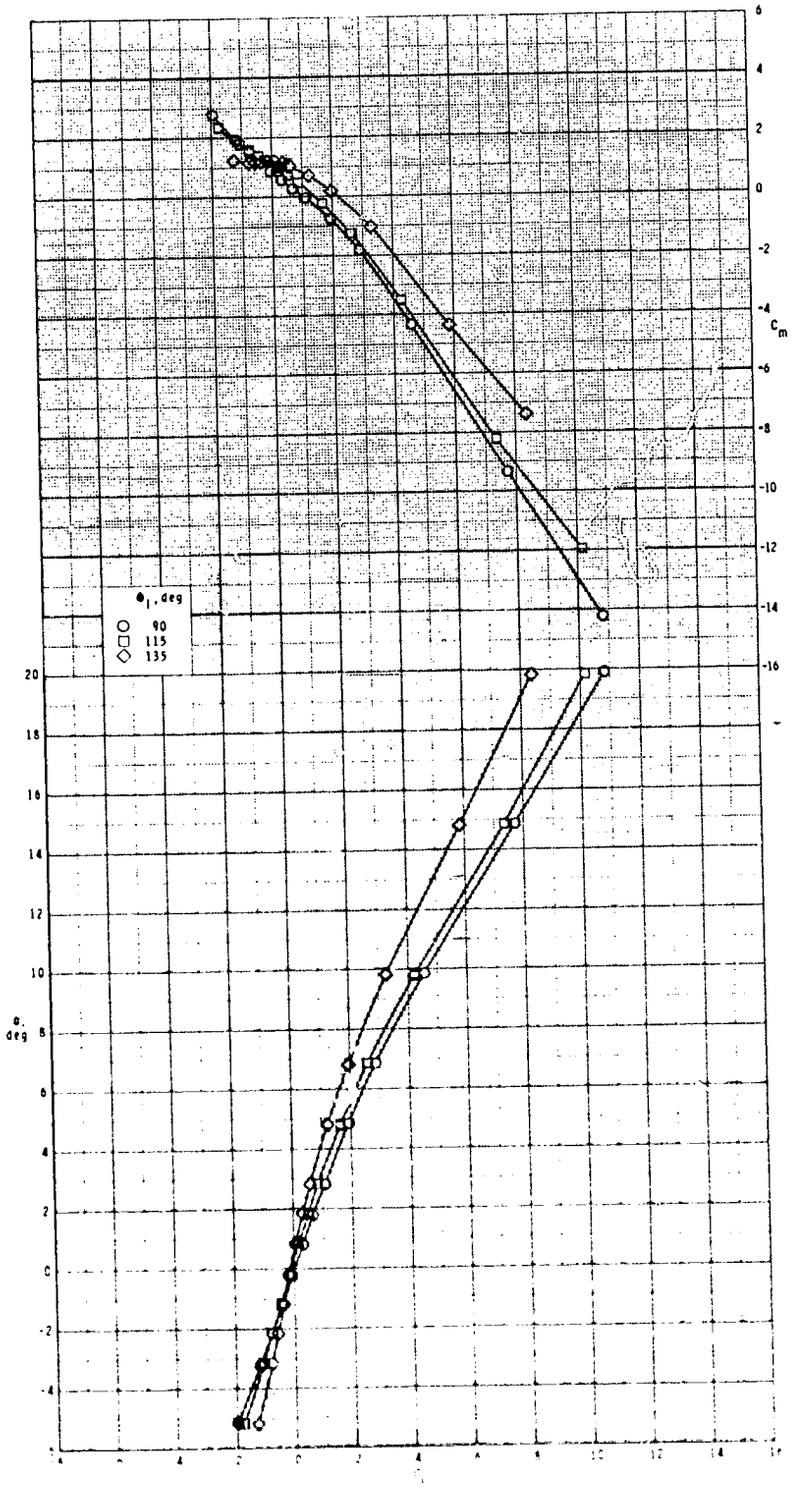

(a) Continued.

Figure 4.- Continued.

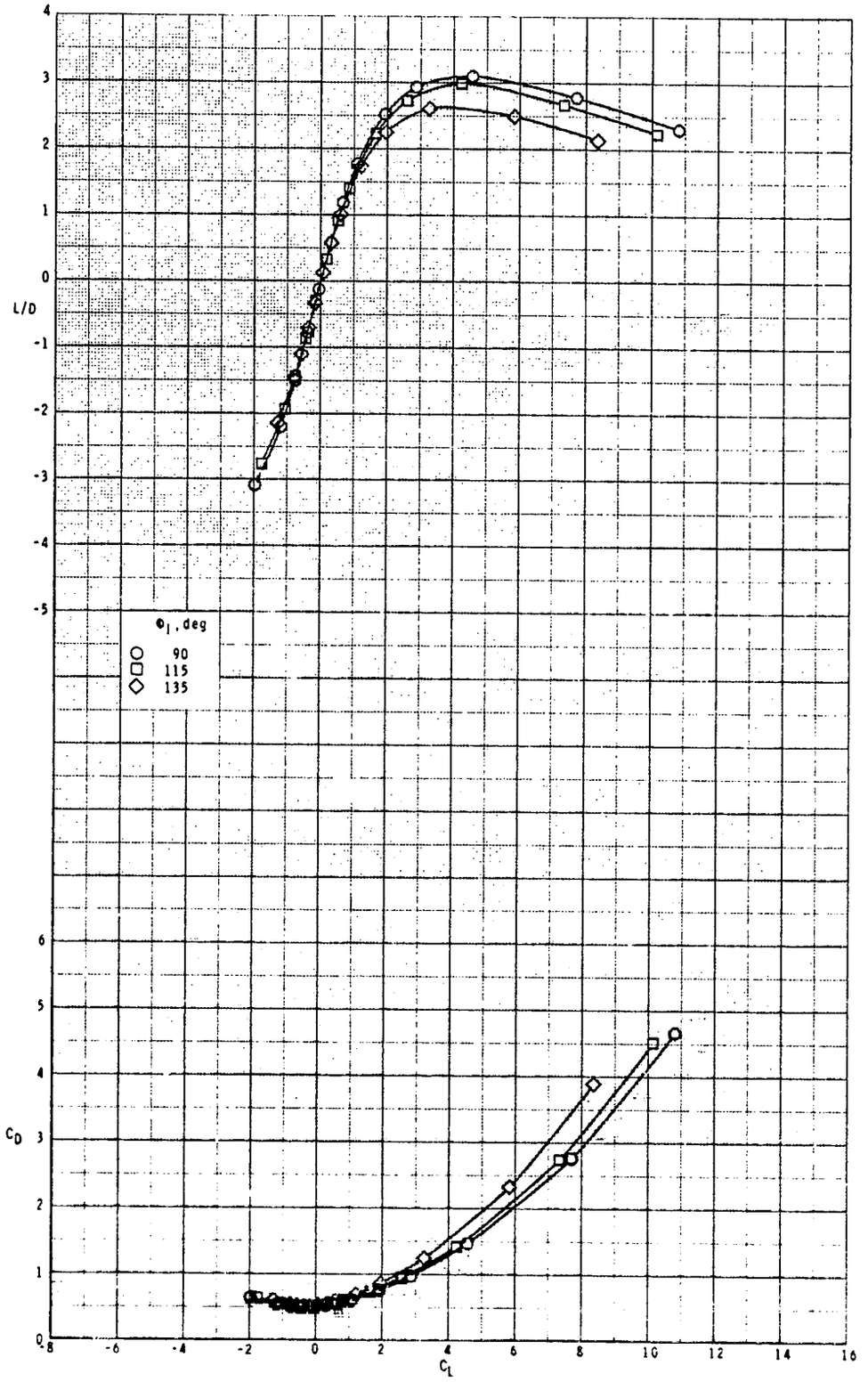

(a) Concluded.

Figure 4.- Continued.

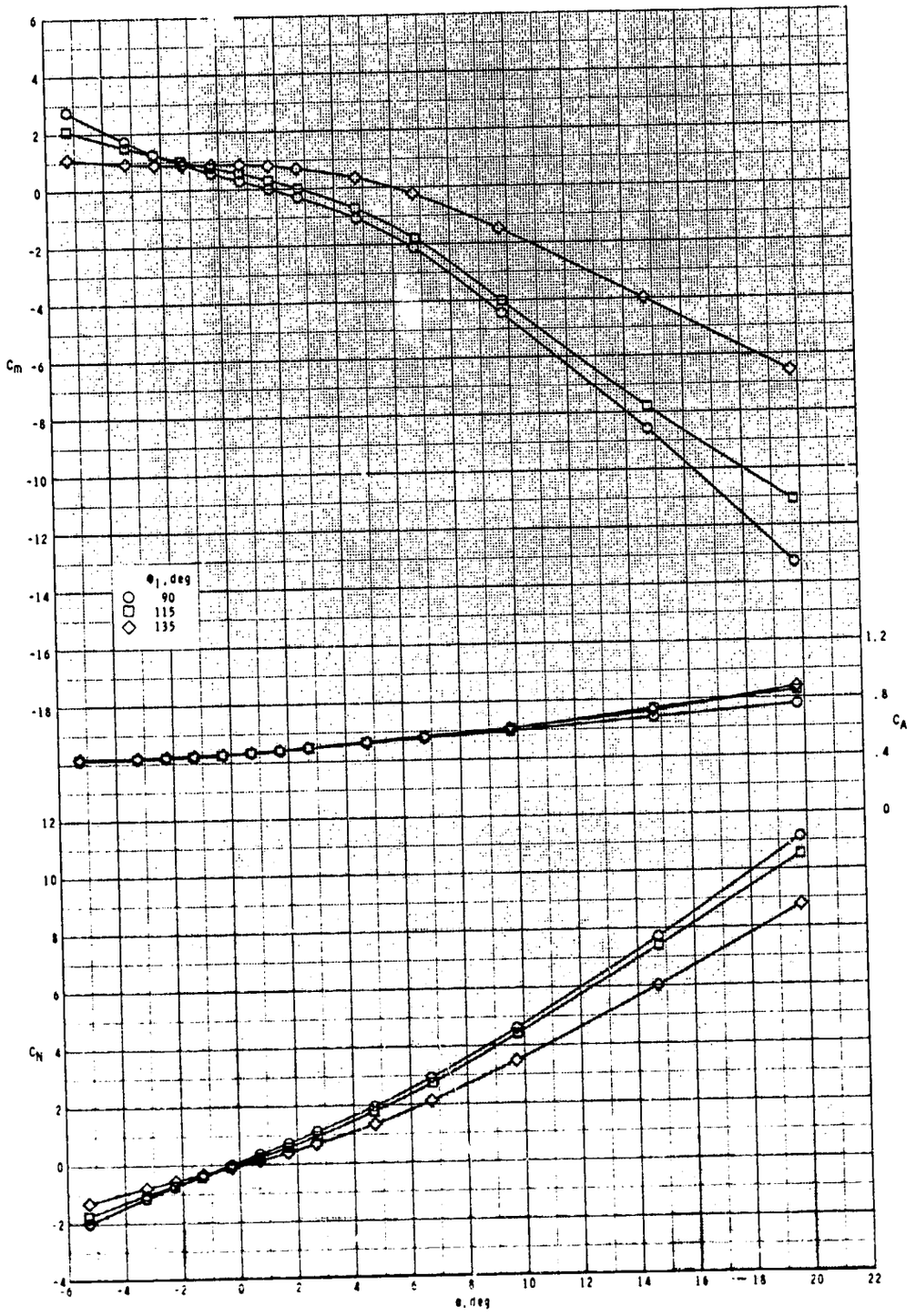

(b) M = 2.95.

Figure 4.- Continued.

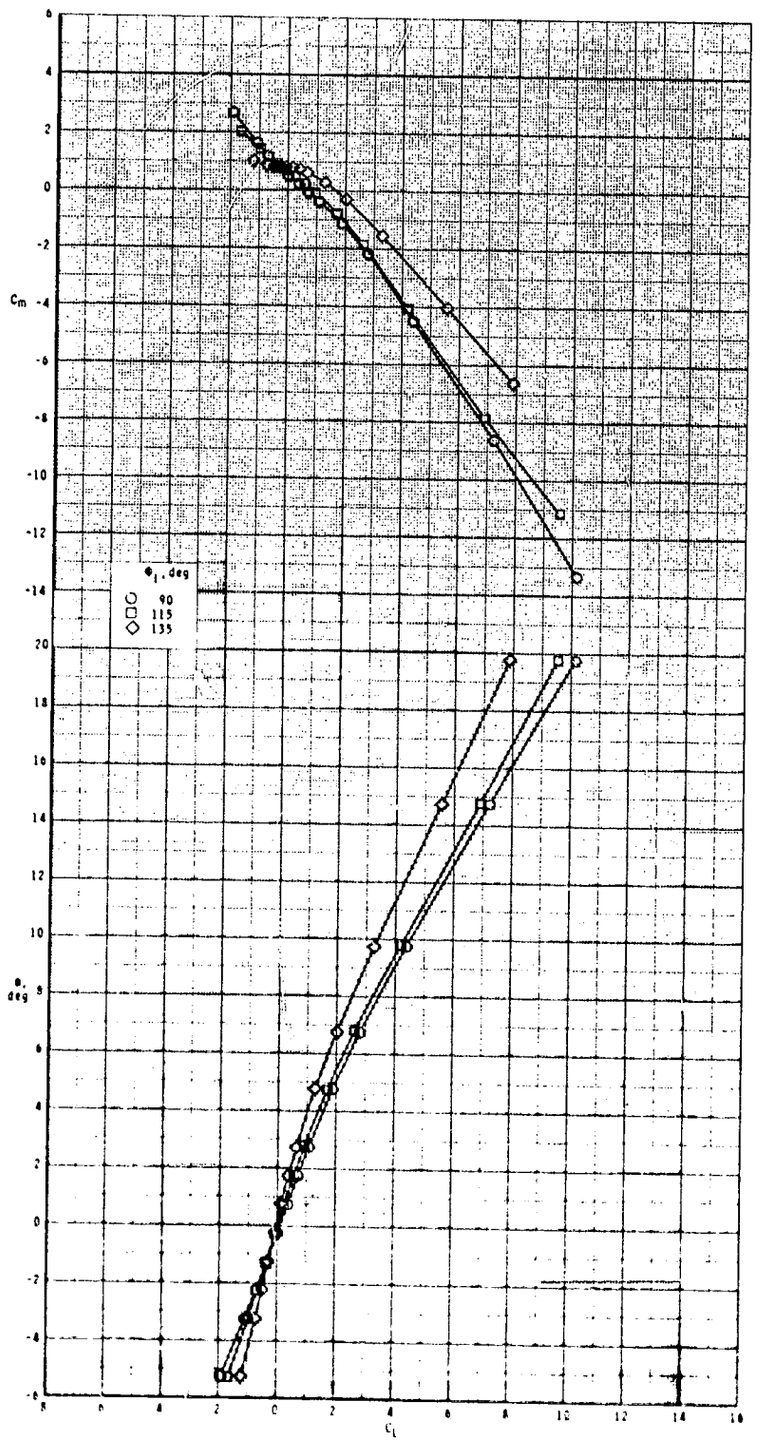

(b) Continued.

Figure 4.- Continued.

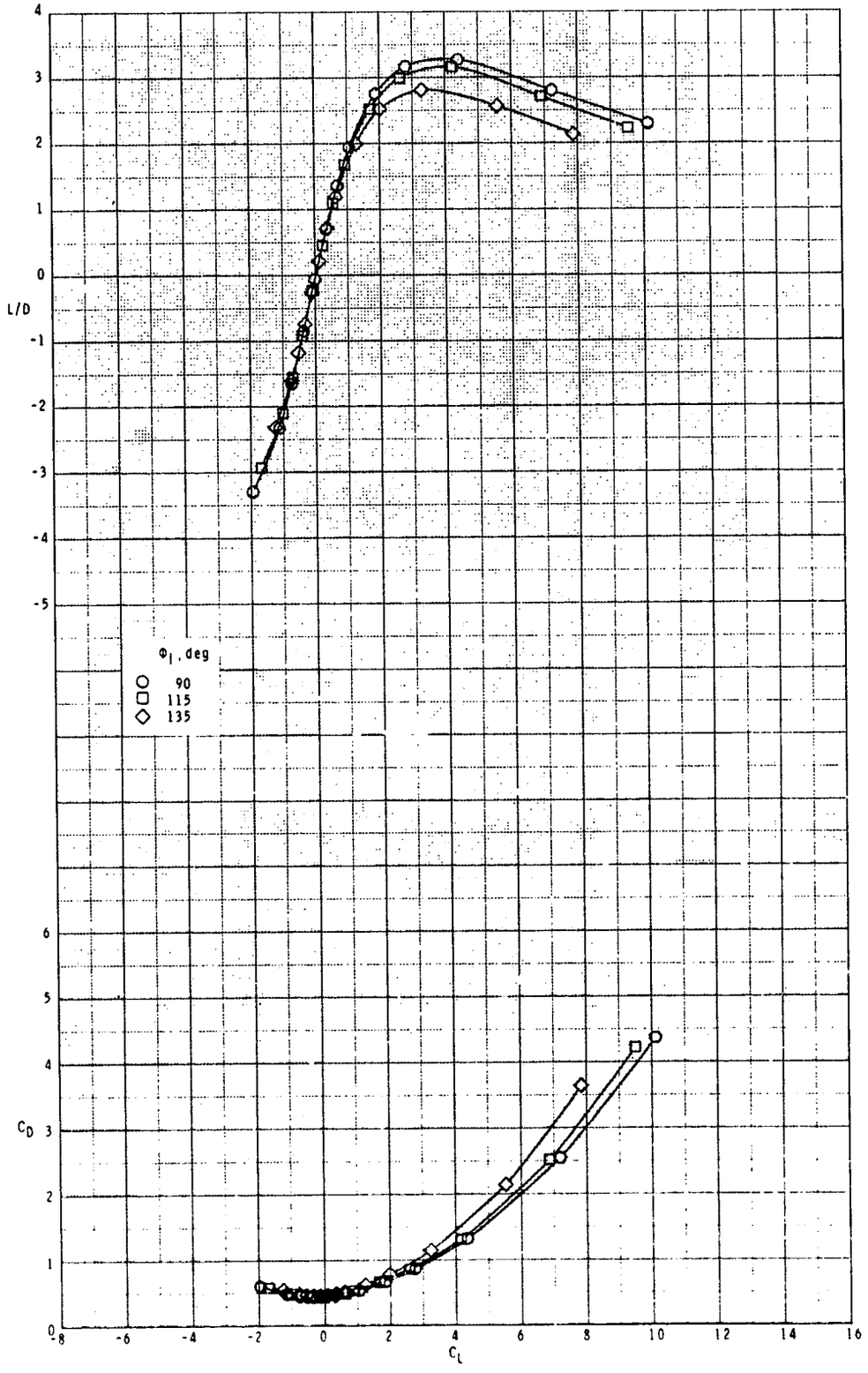

(b) Concluded.

Figure 4.- Continued.

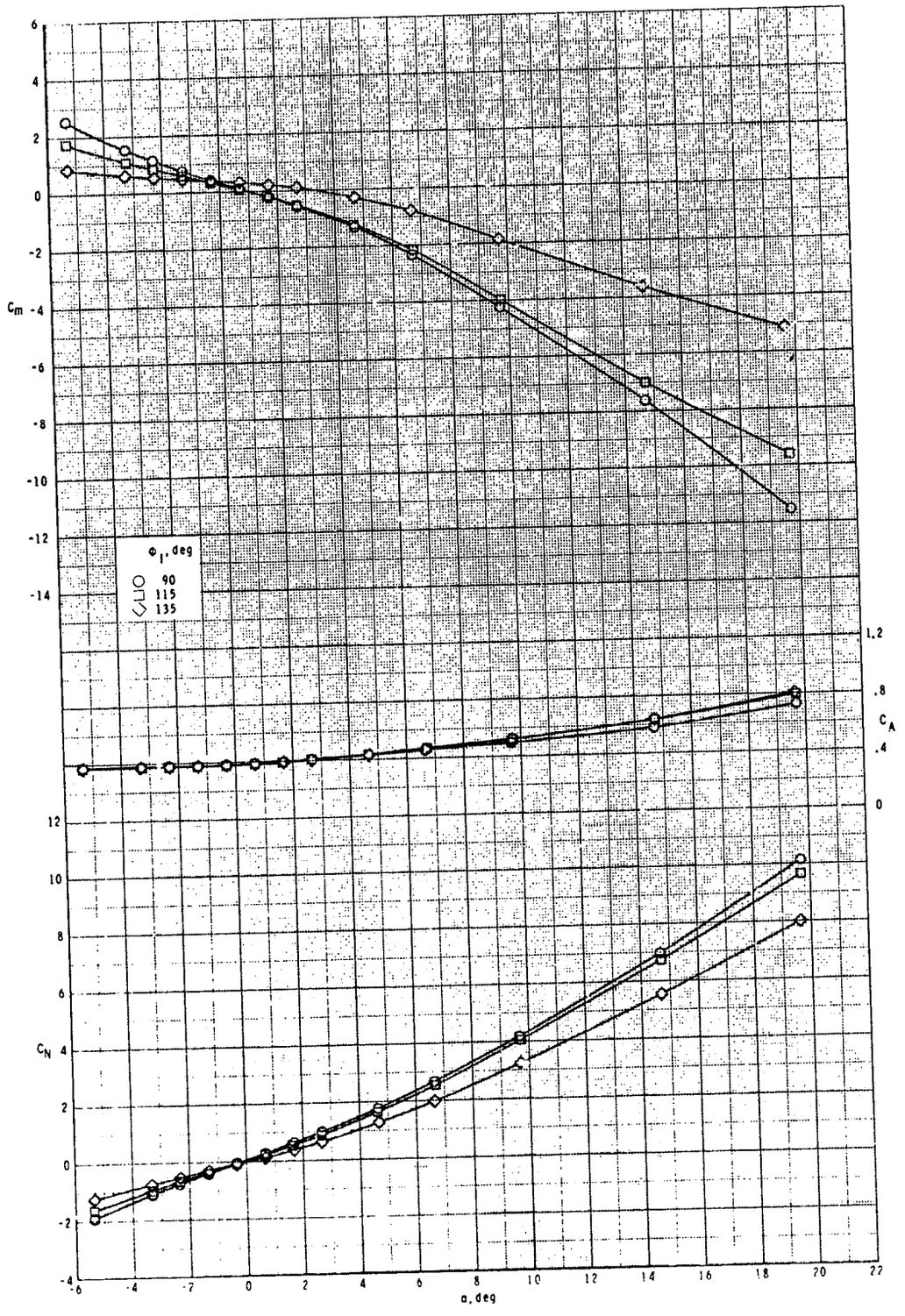

(c) M = 3.50.

Figure 4.- Continued.

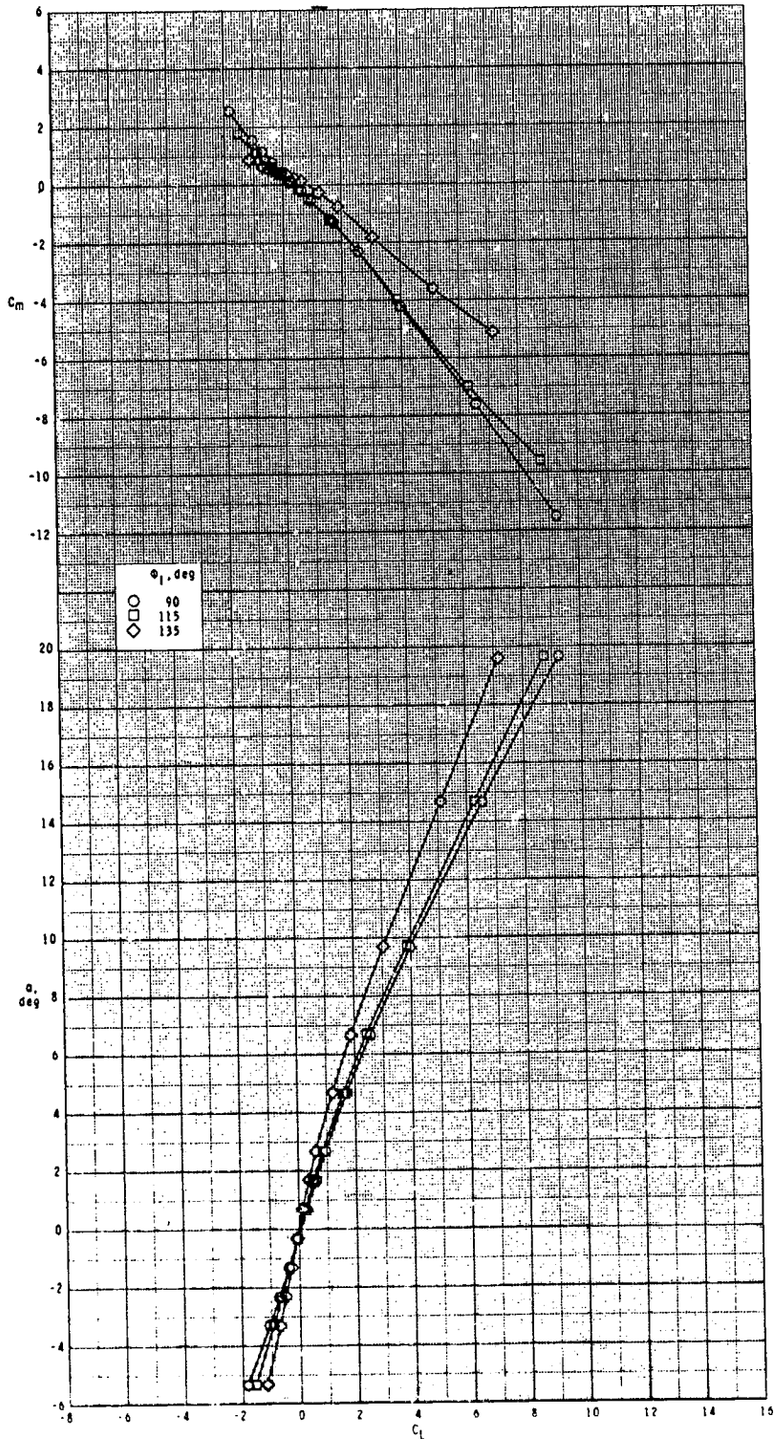

(c) Continued.

Figure 4.- Continued.

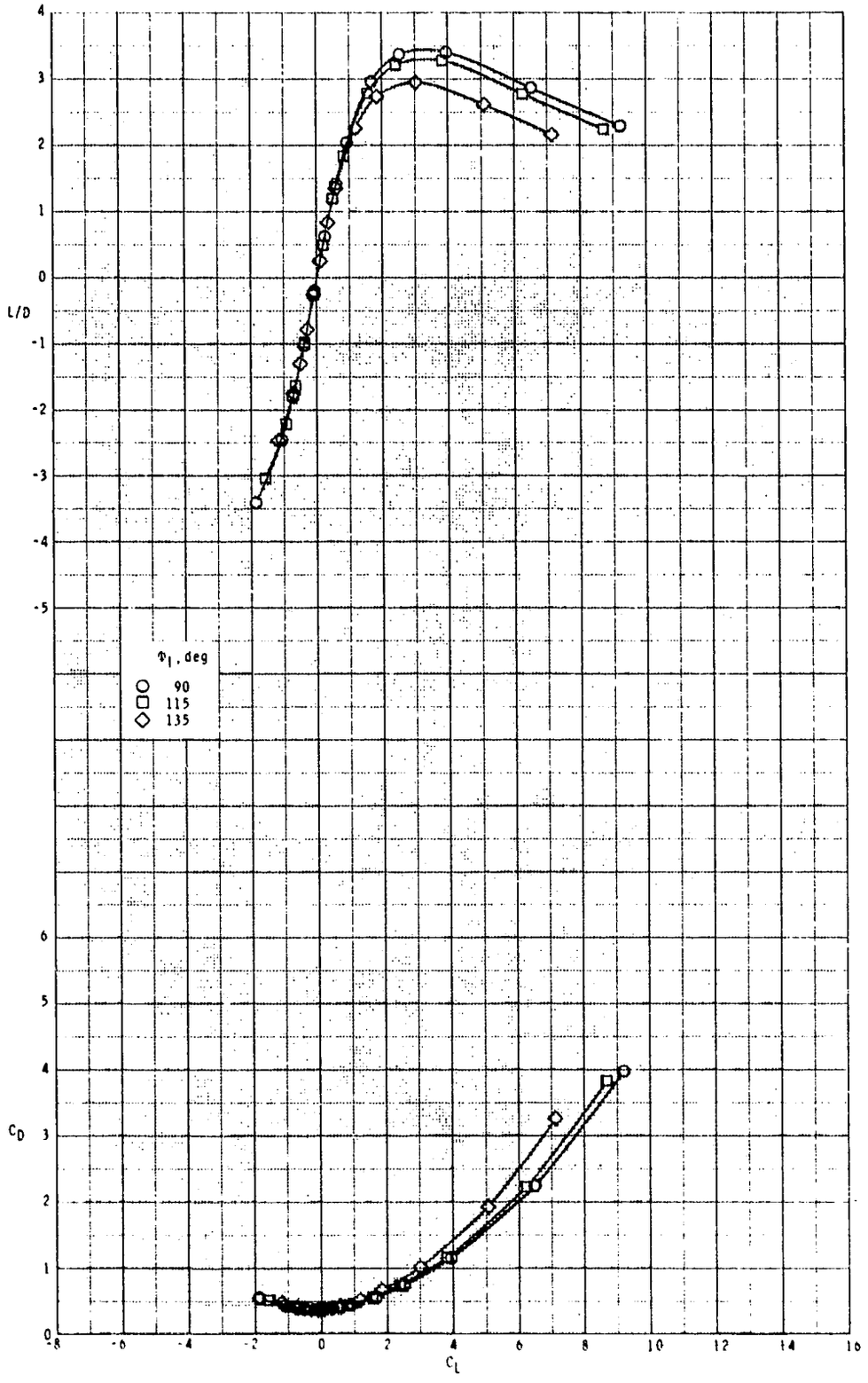

(c) Concluded.

Figure 4.- Continued.

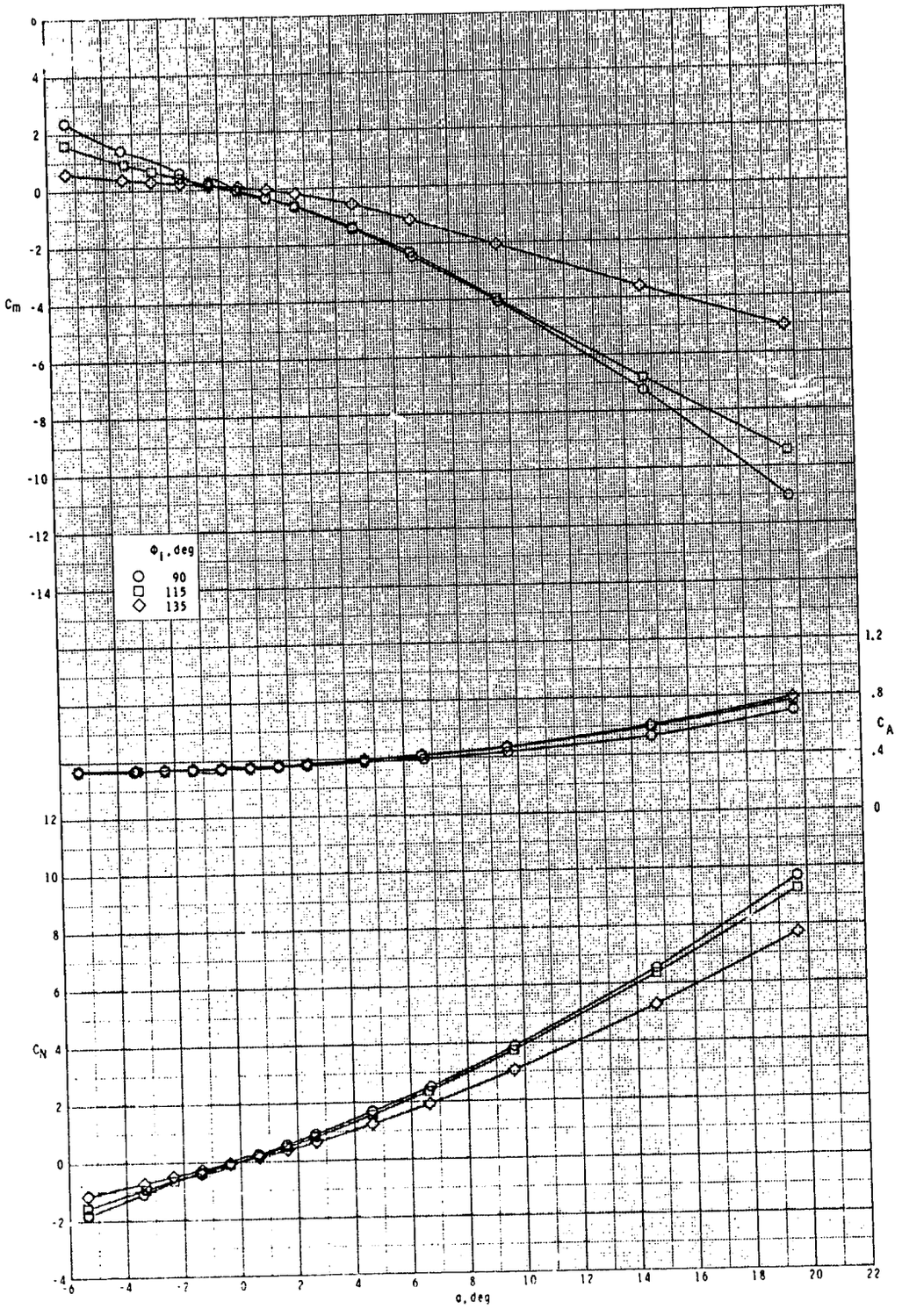

(d) M = 3.95.

Figure 4.- Continued.

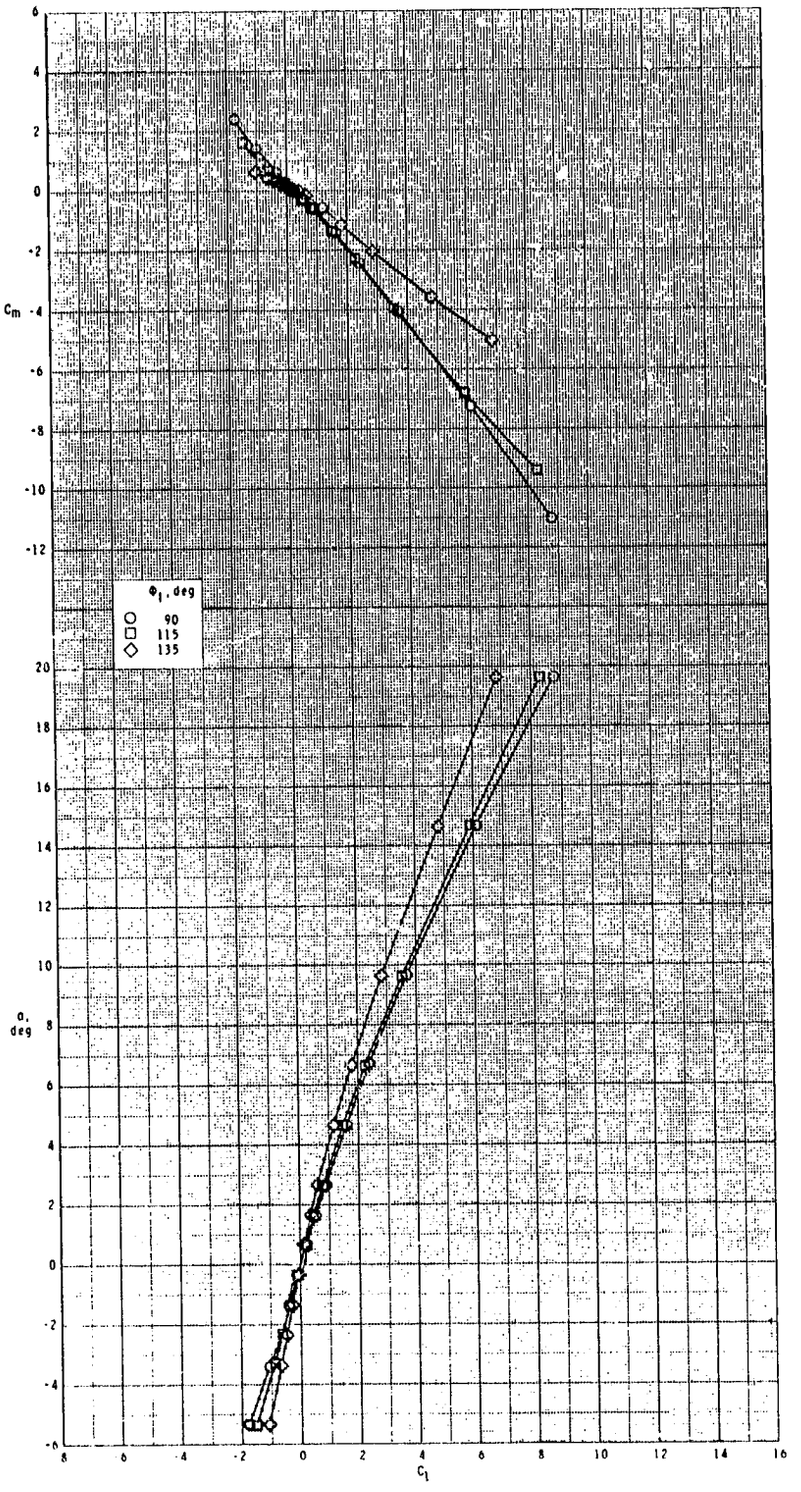

(d) Continued.

Figure 4.- Continued.

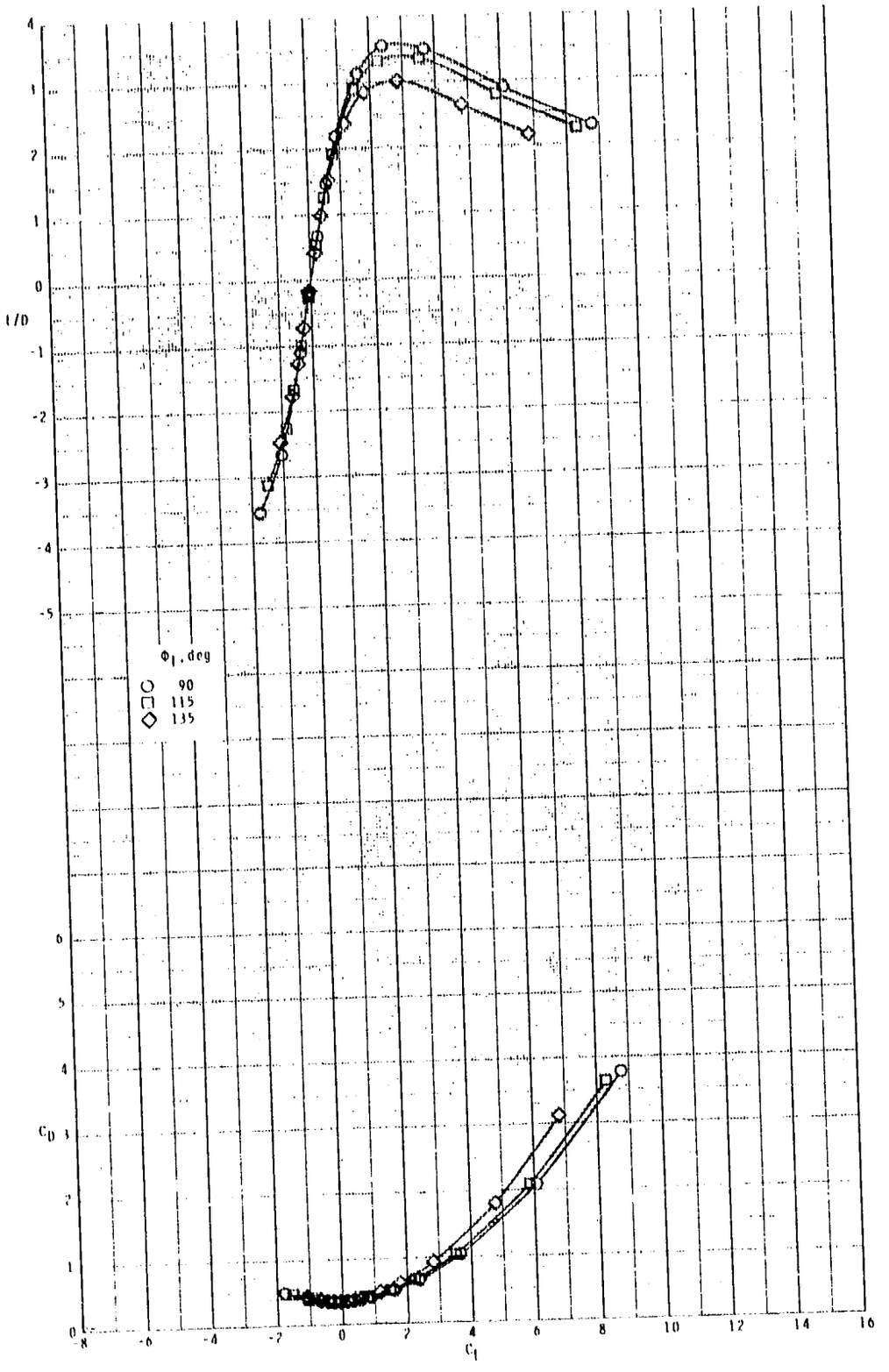

(d) Concluded.

Figure 4.- Concluded.

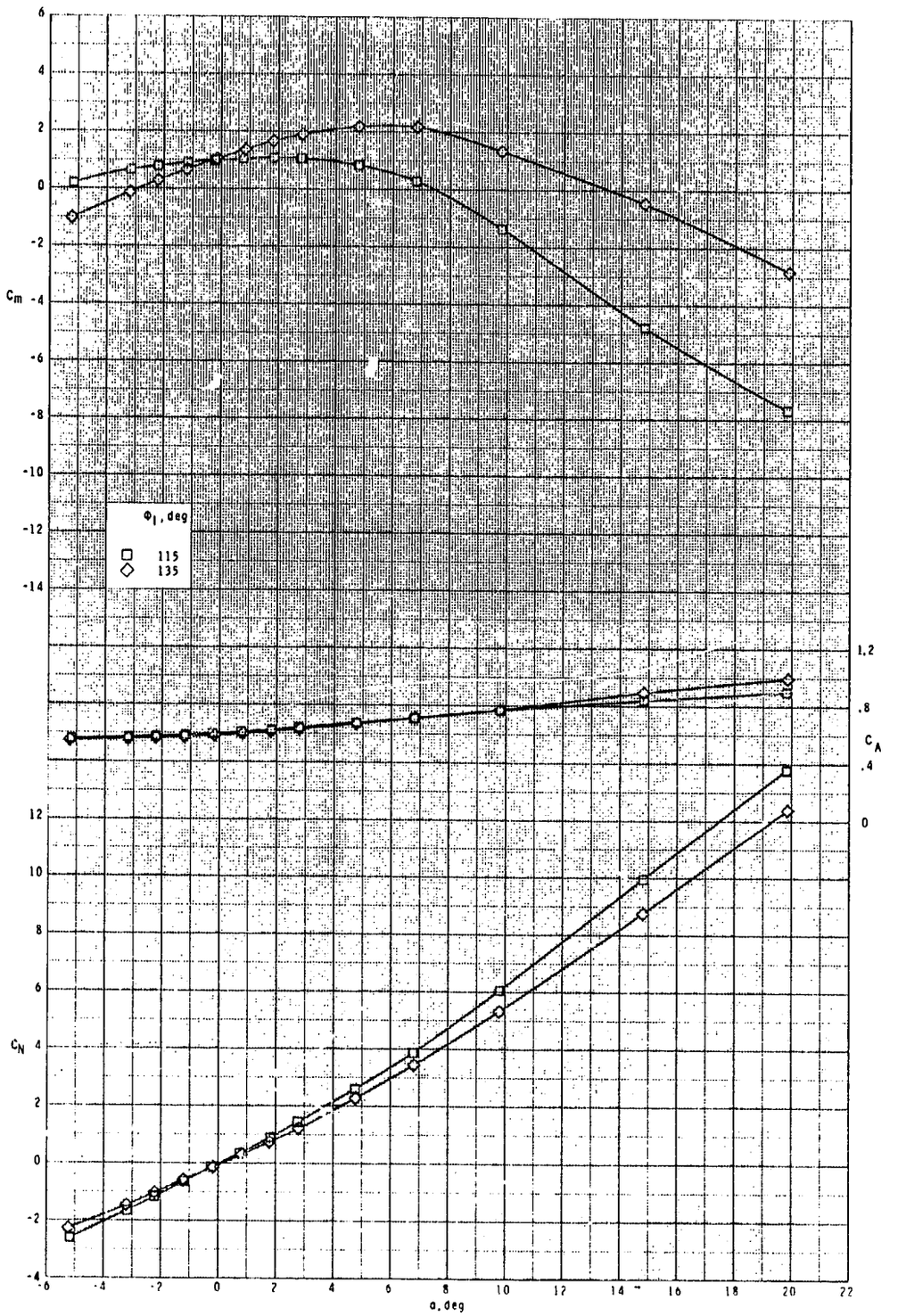

(a) M = 2.50.

Figure 5.- Effect of inlet orientation angle ϕ_1 on longitudinal aerodynamic characteristics of configuration $B_1I_2W_1T_1$. $\delta_p = 0°$.

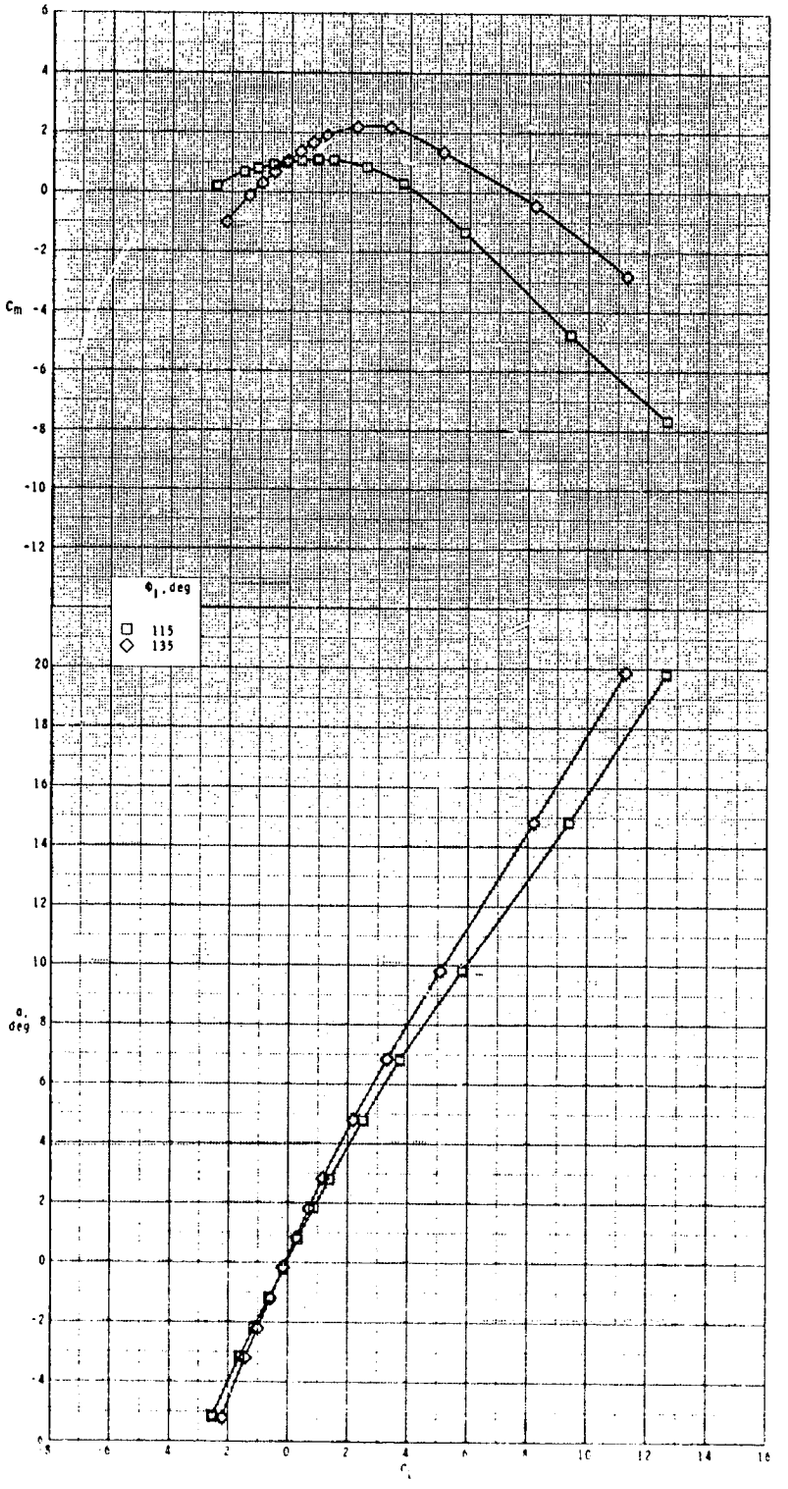

(a) Continued.

Figure 5.- Continued.

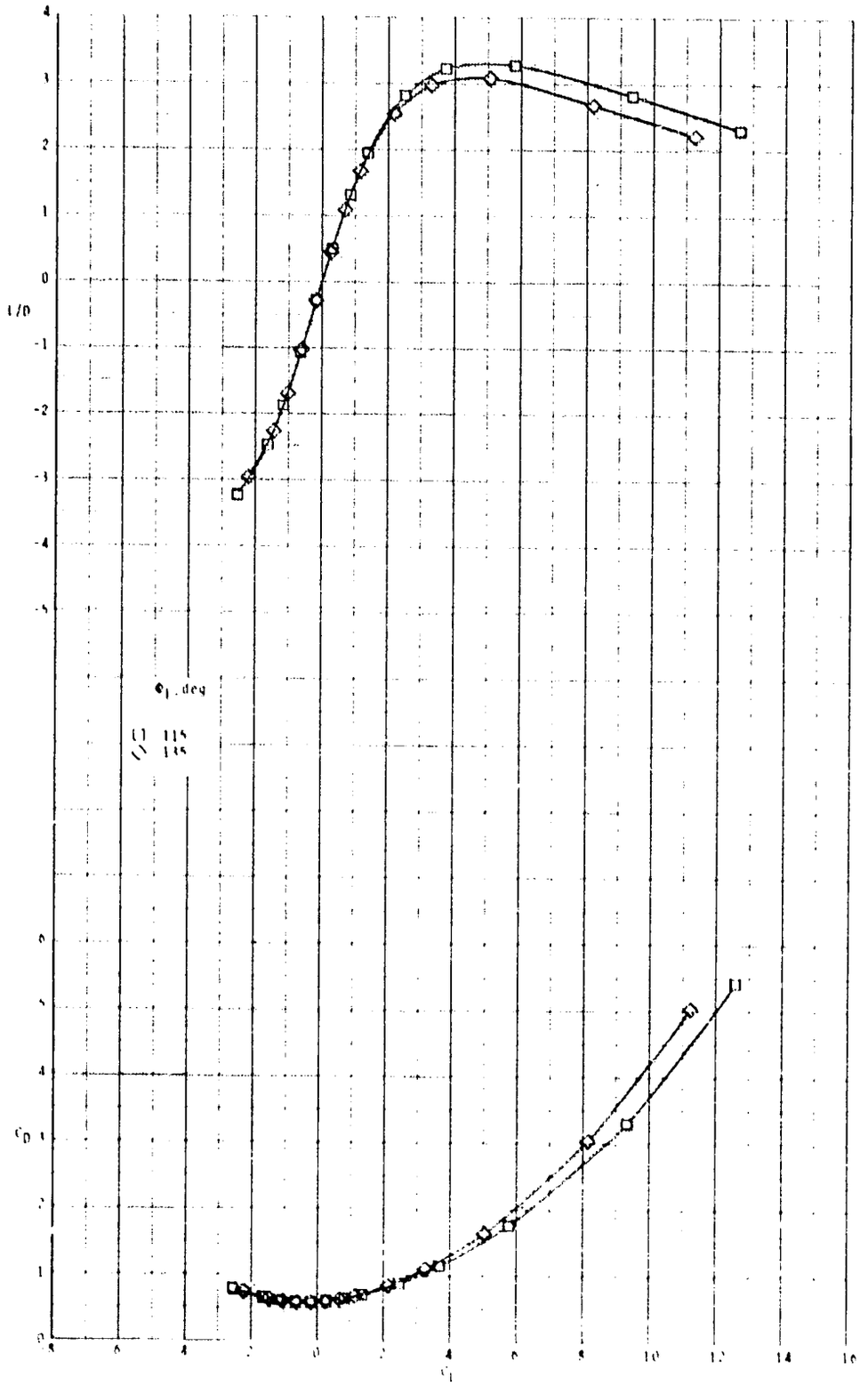

(a) Concluded.

Figure 5.- Continued.

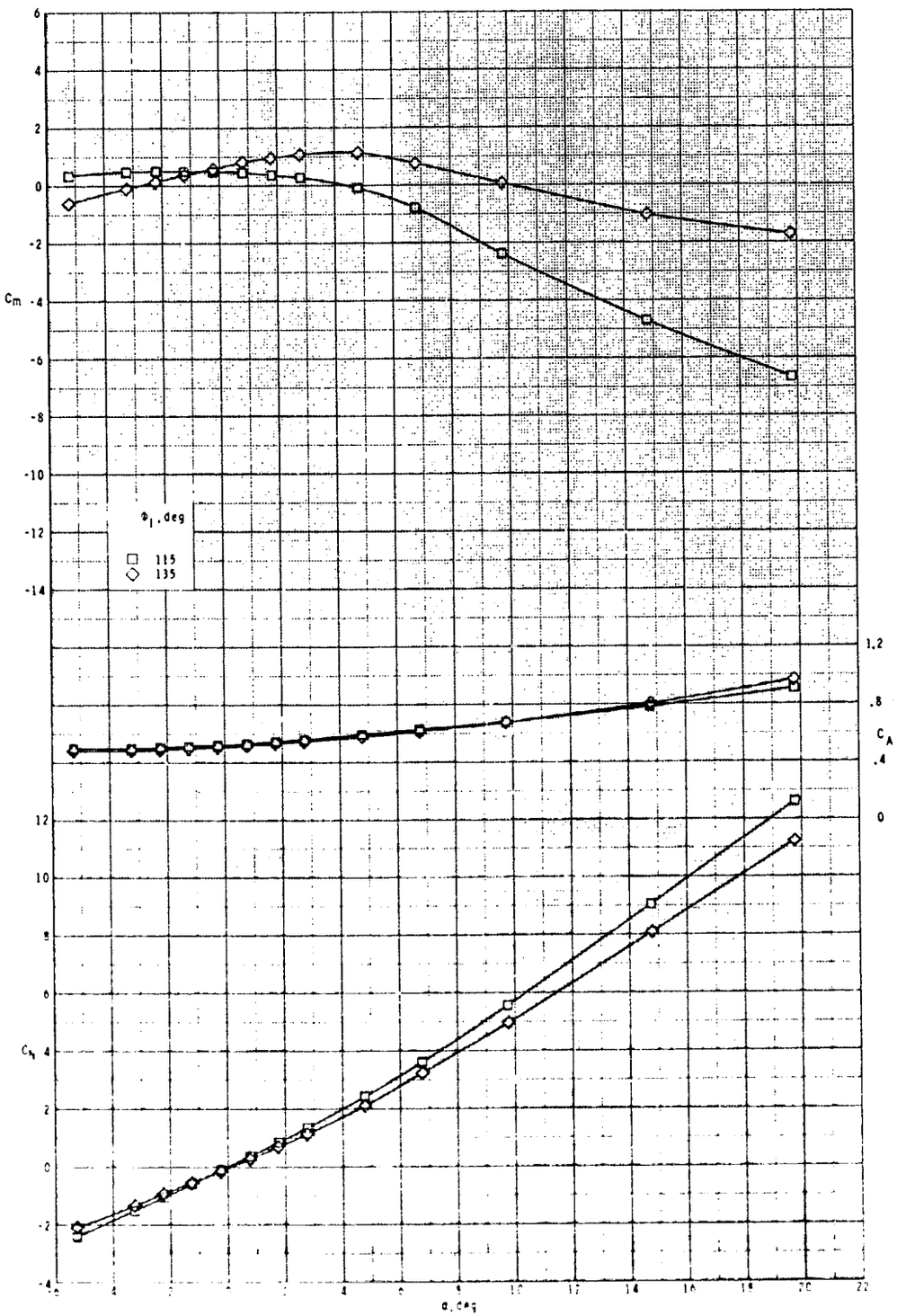

(b) M = 2.95.

Figure 5.- Continued.

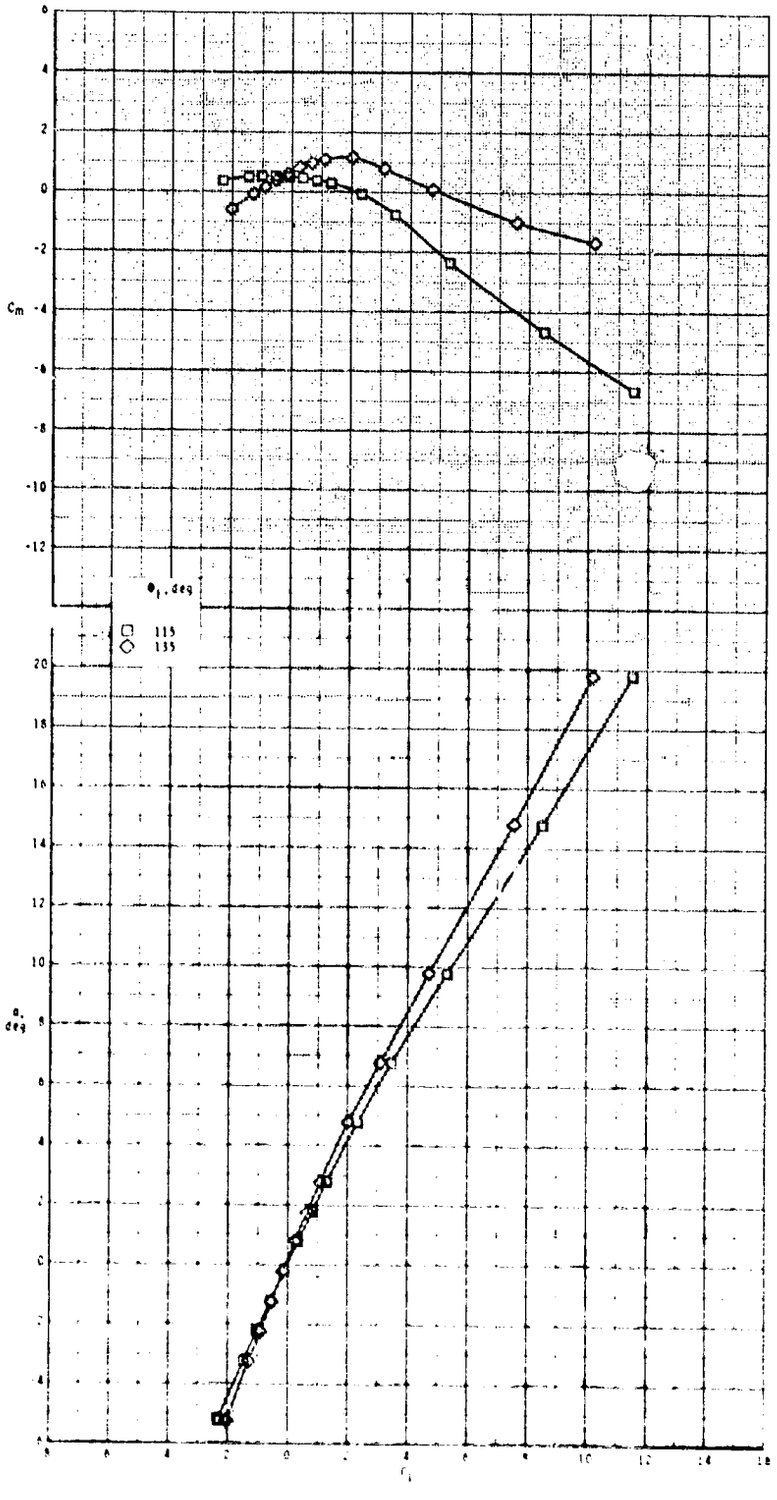

(b) Continued.

Figure 5.- Continued.

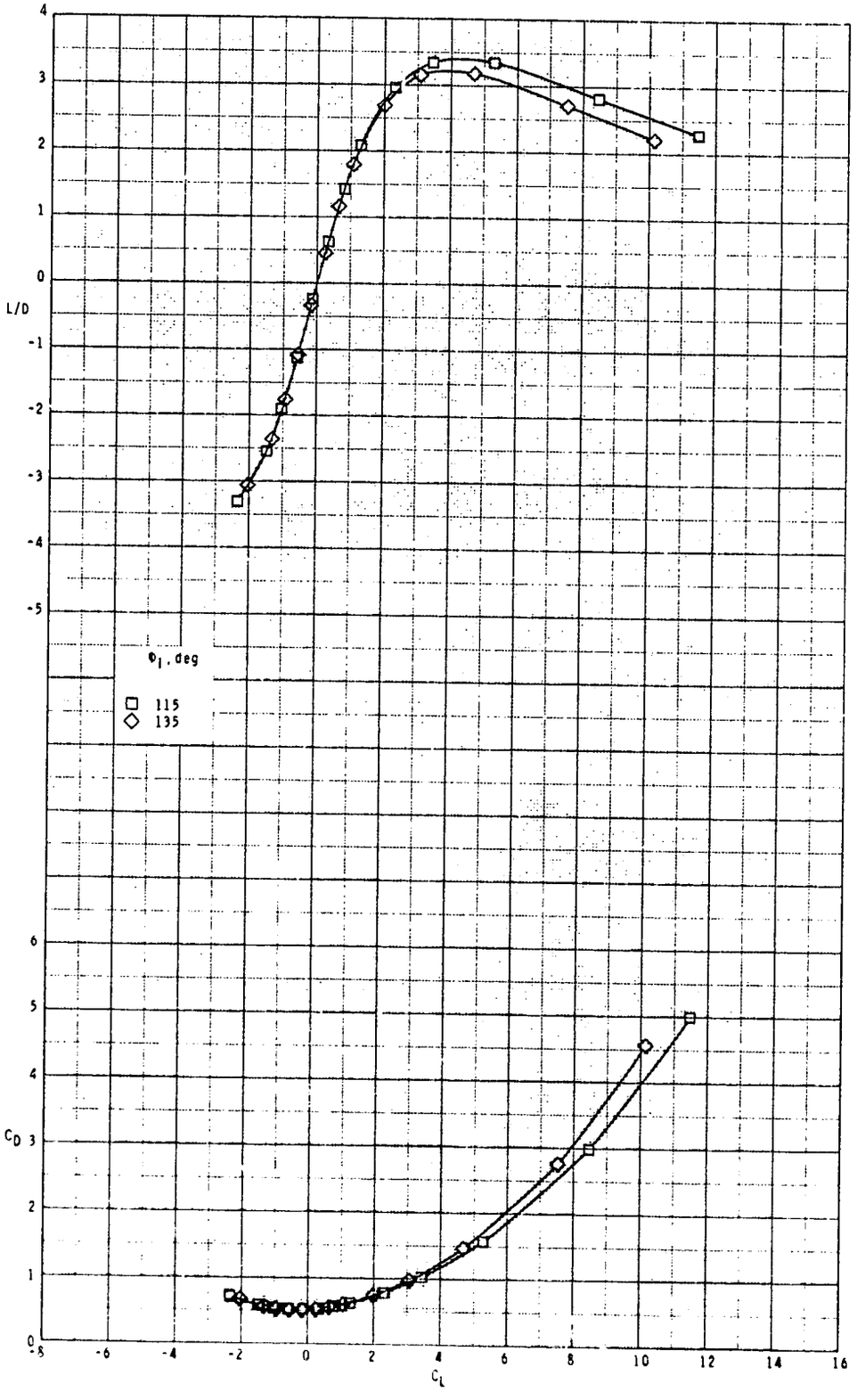

(b) Concluded.

Figure 5.- Continued.

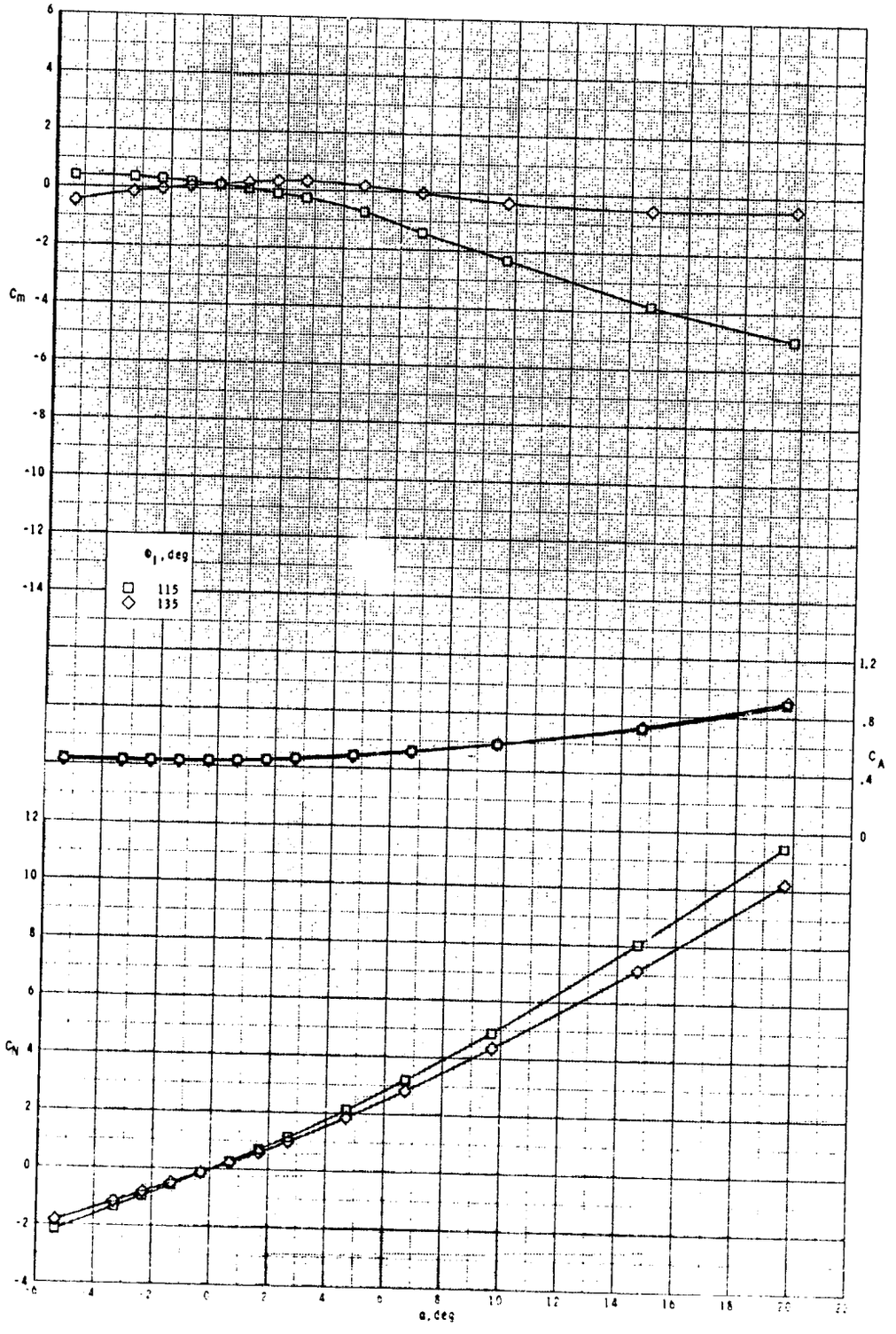

(c) M = 3.50.

Figure 5.- Continued.

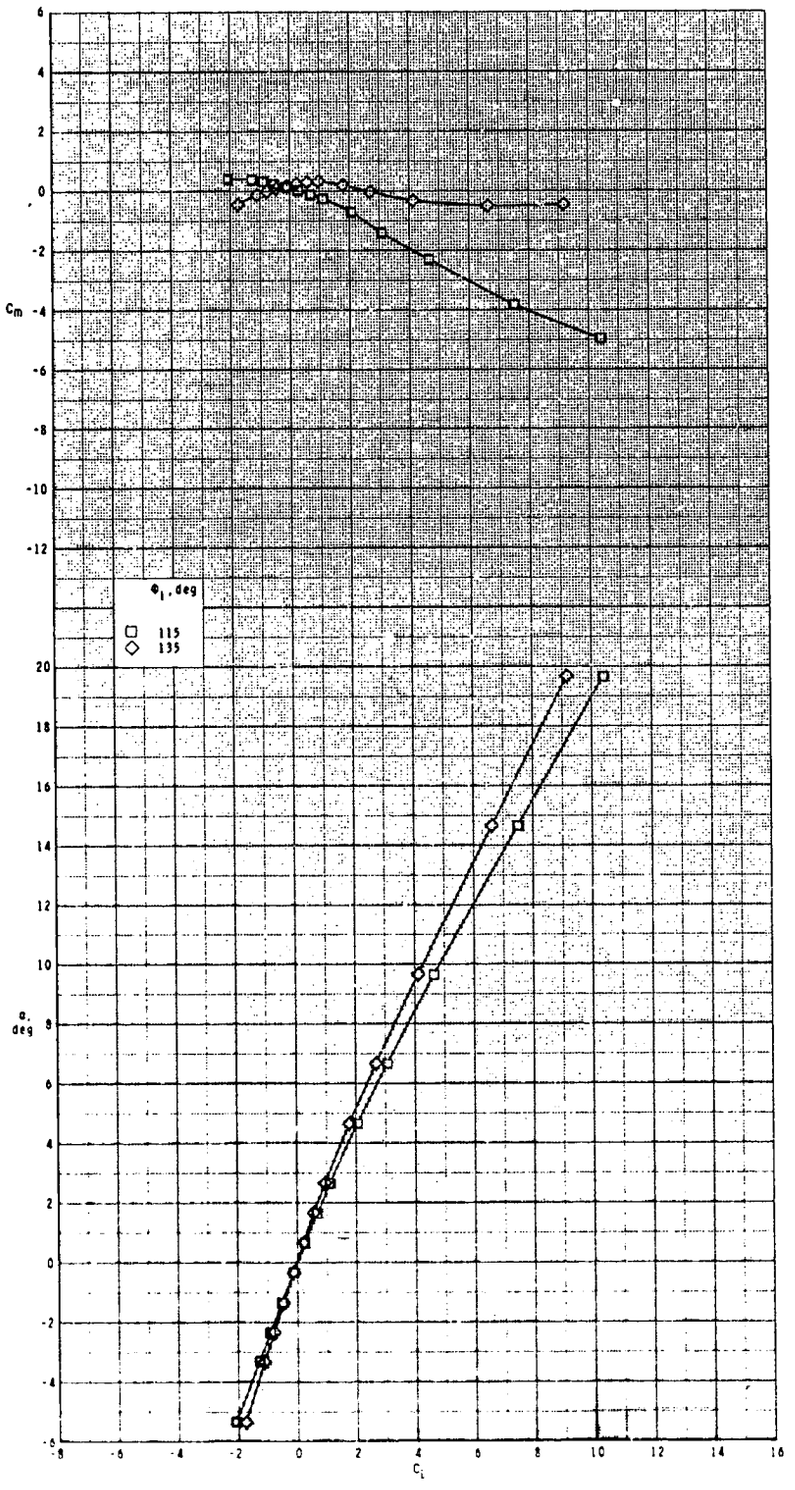

(c) Continued.

Figure 5.- Continued.

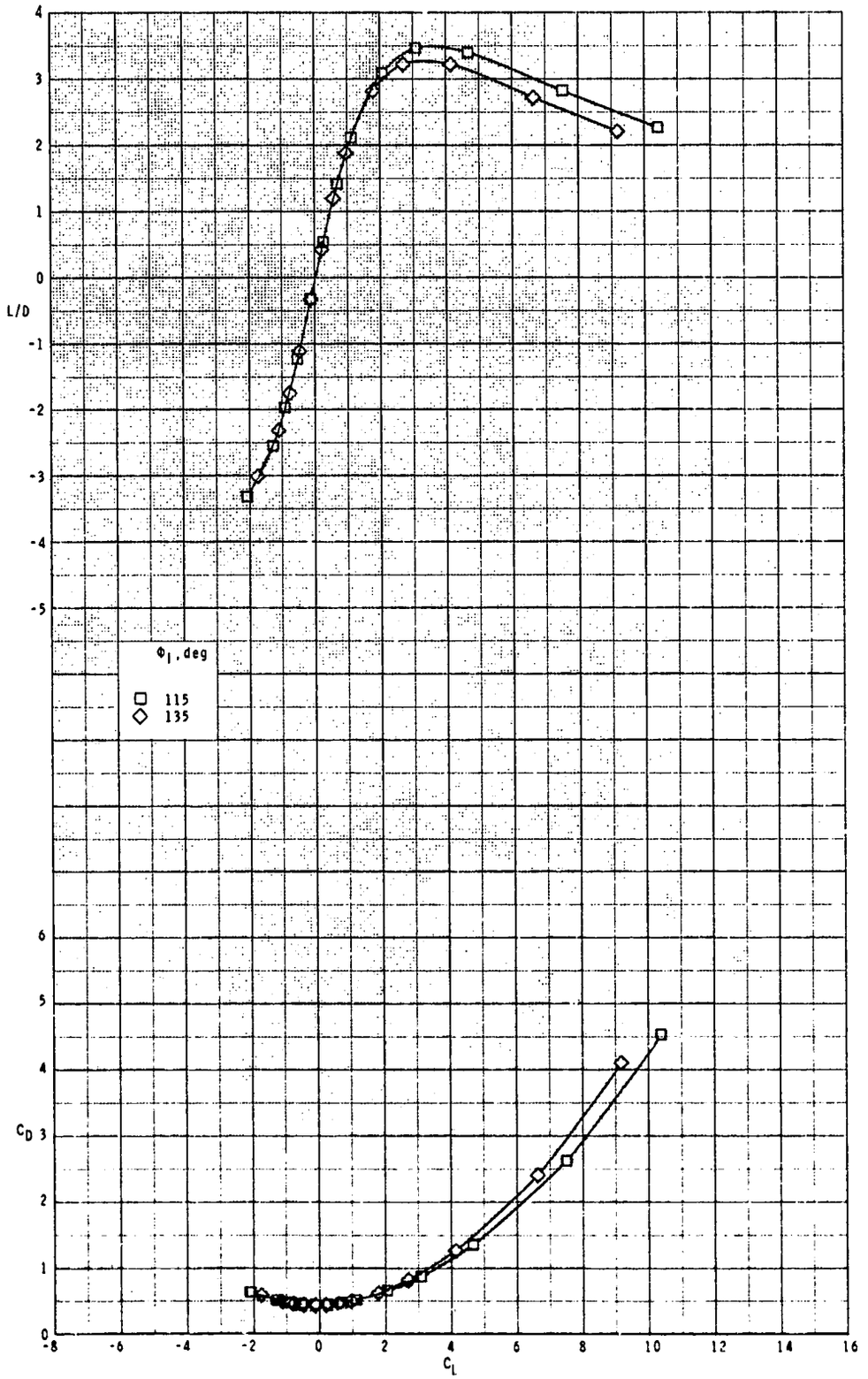

(c) Concluded.

Figure 5.- Continued.

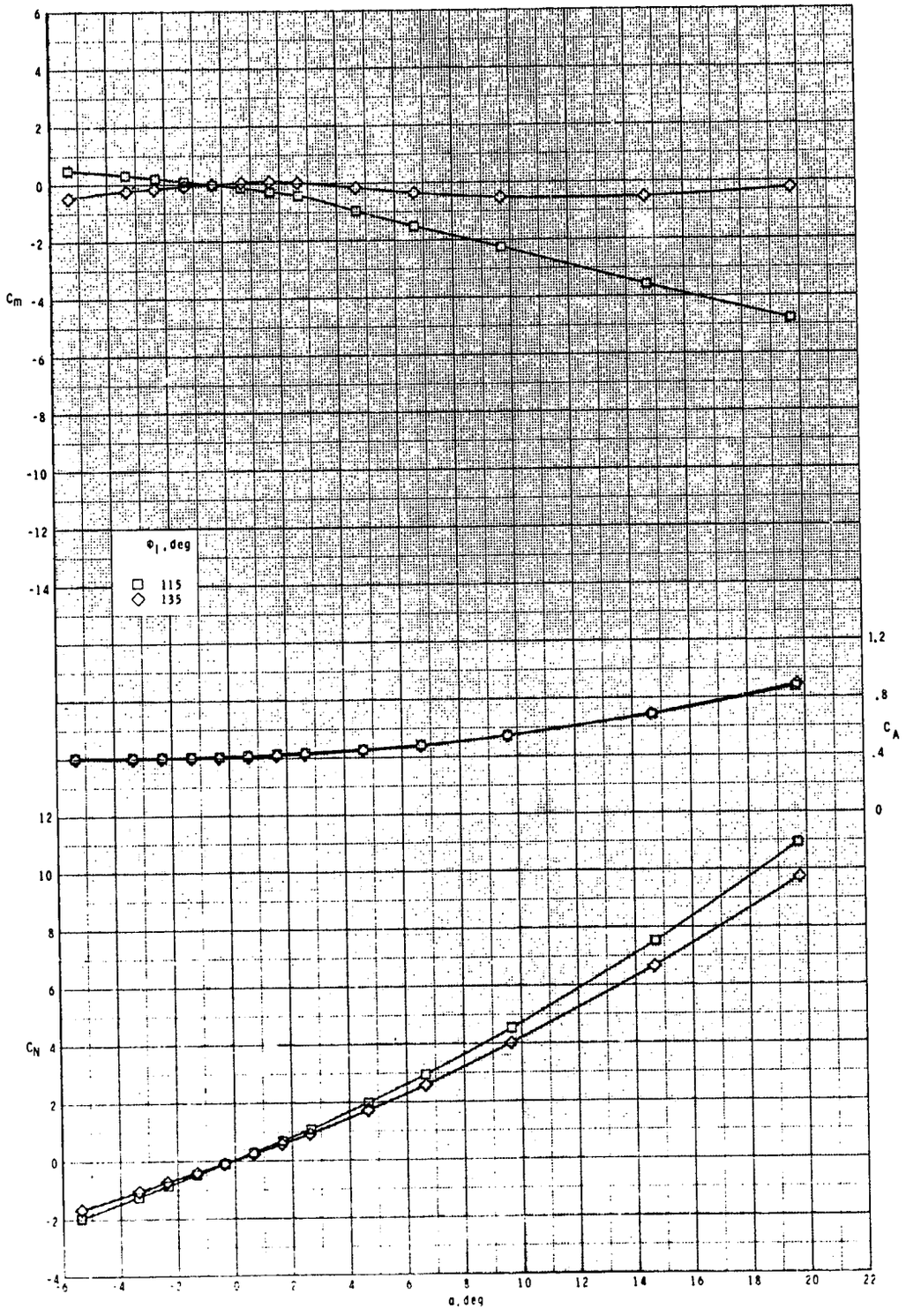

(d) M = 3.95.

Figure 5.- Continued.

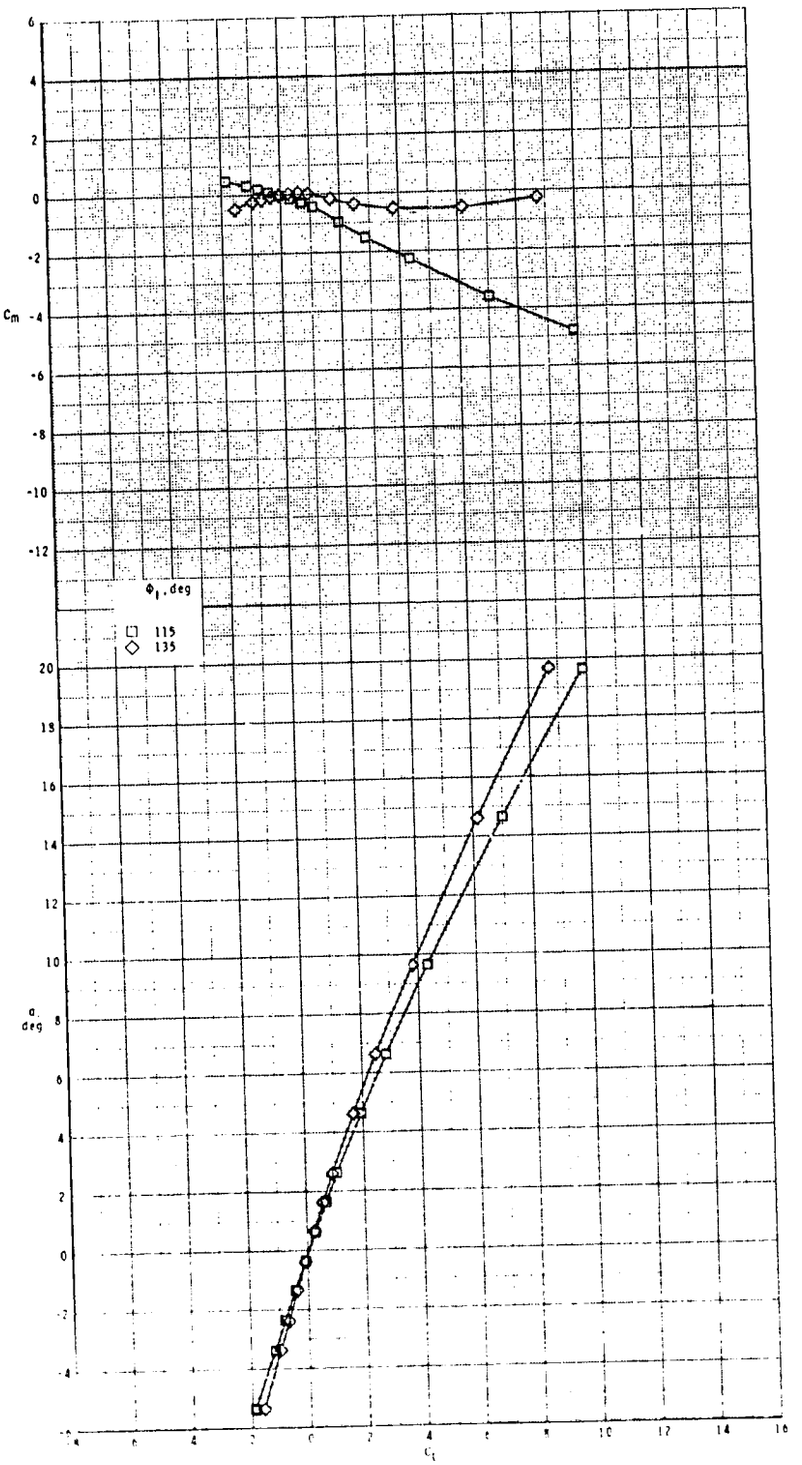

(d) Continued.

Figure 5.- Continued.

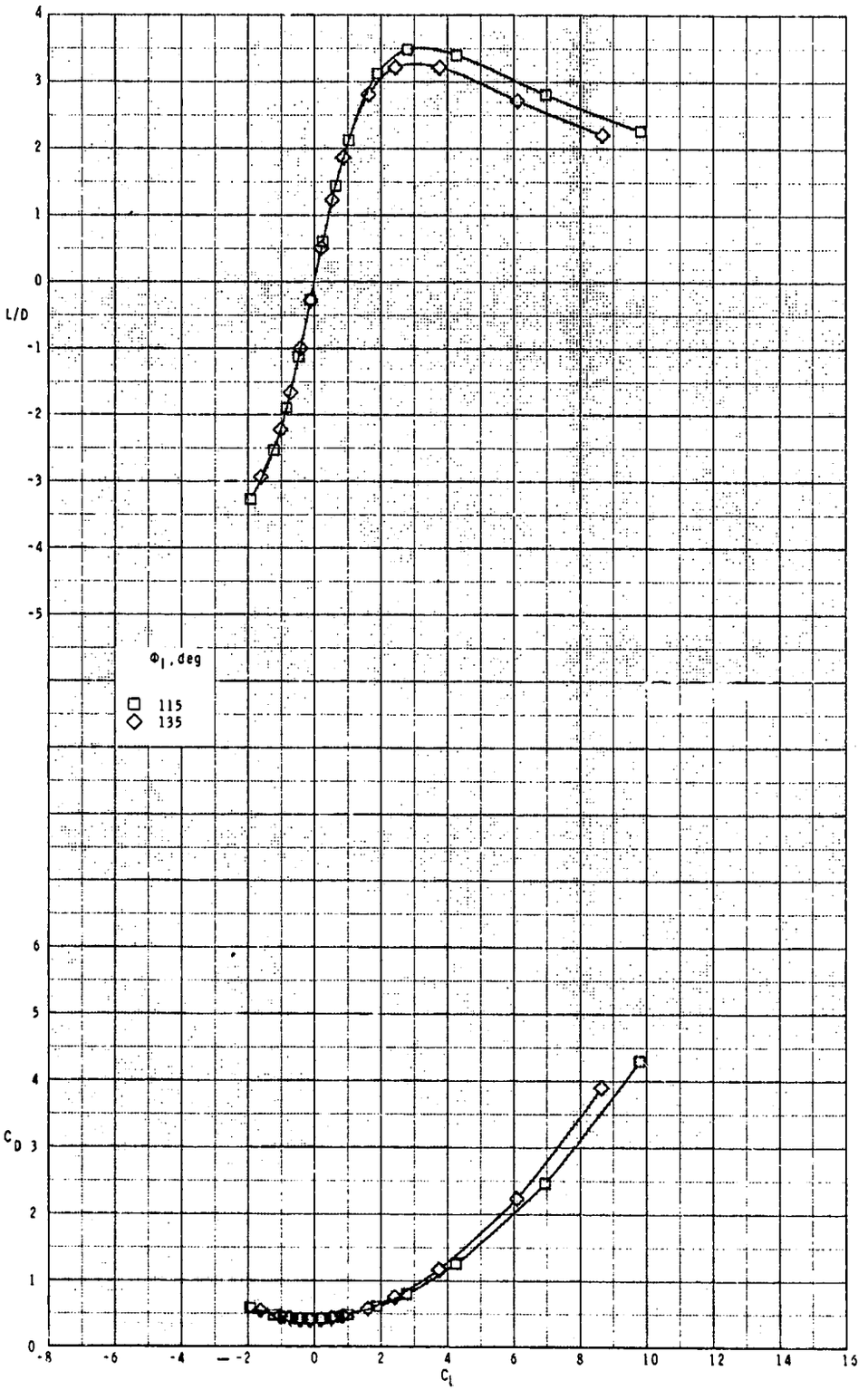

(d) Concluded.

Figure 5.- Concluded.

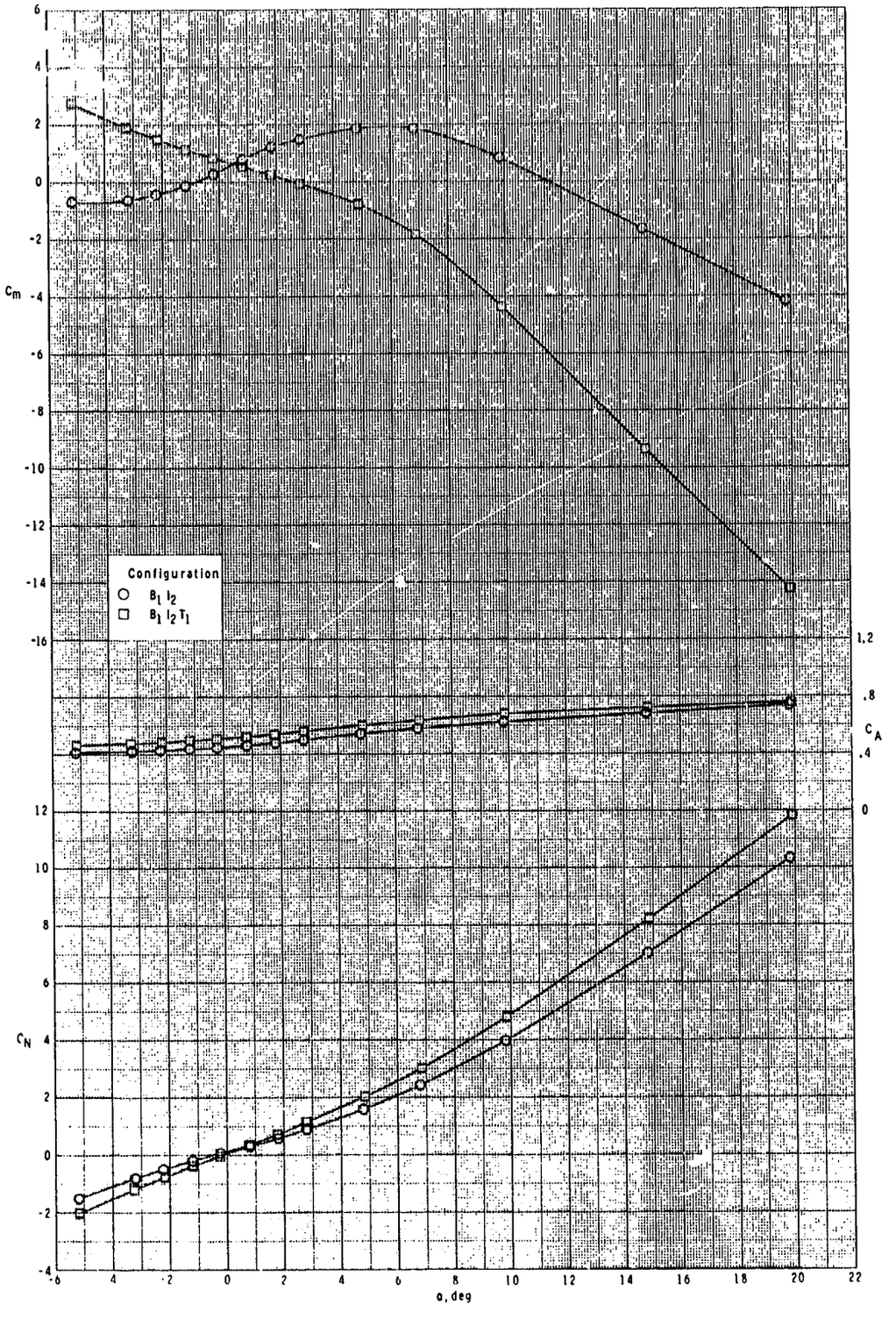

(a) M = 2.50.

Figure 6.- Effect of various model components on longitudinal aerodynamic characteristics for two-dimensional inlets with $\phi_I = 90°$ and $\delta_p = 0°$.

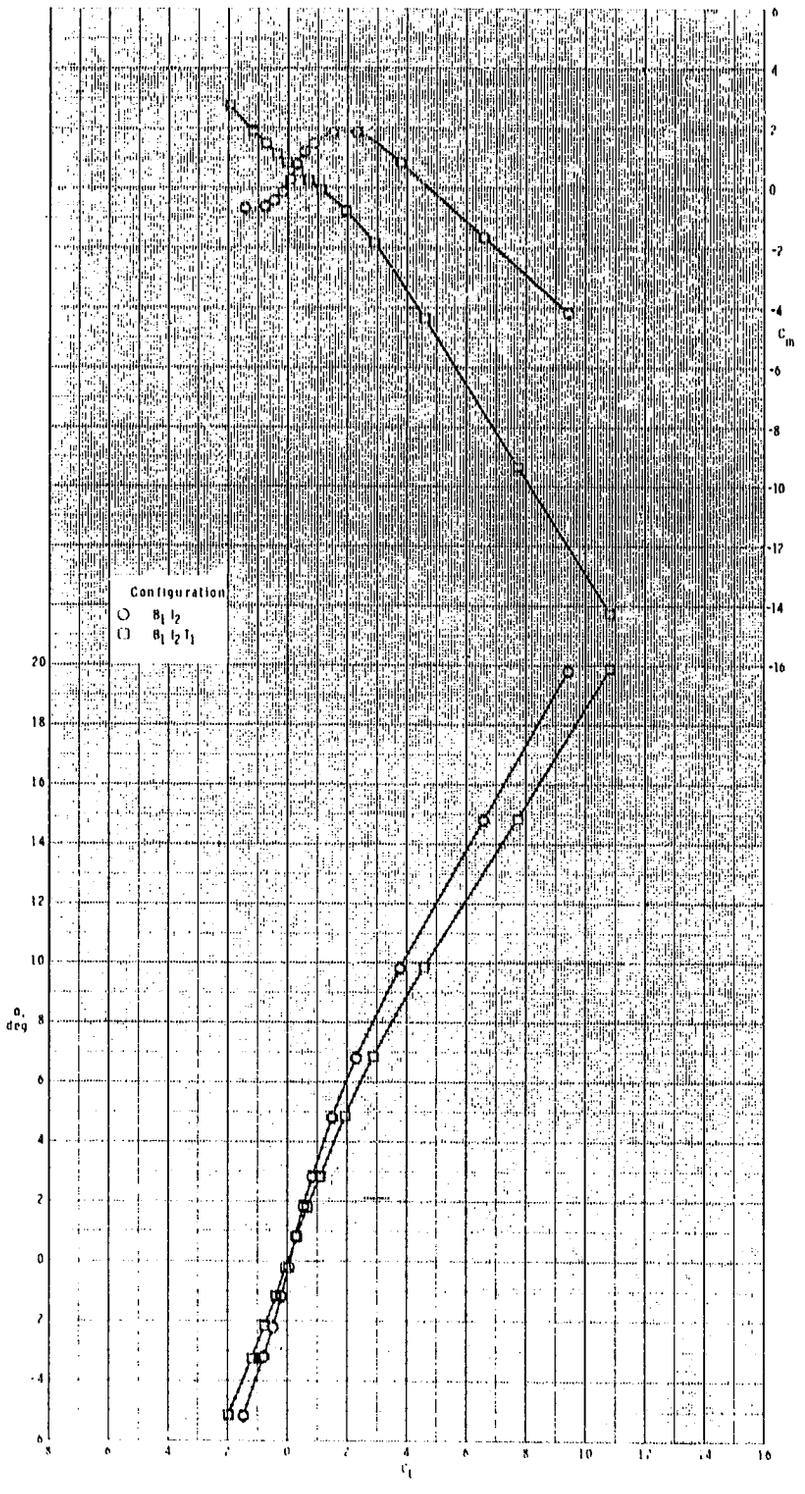

(a) Continued.

Figure 6.- Continued.

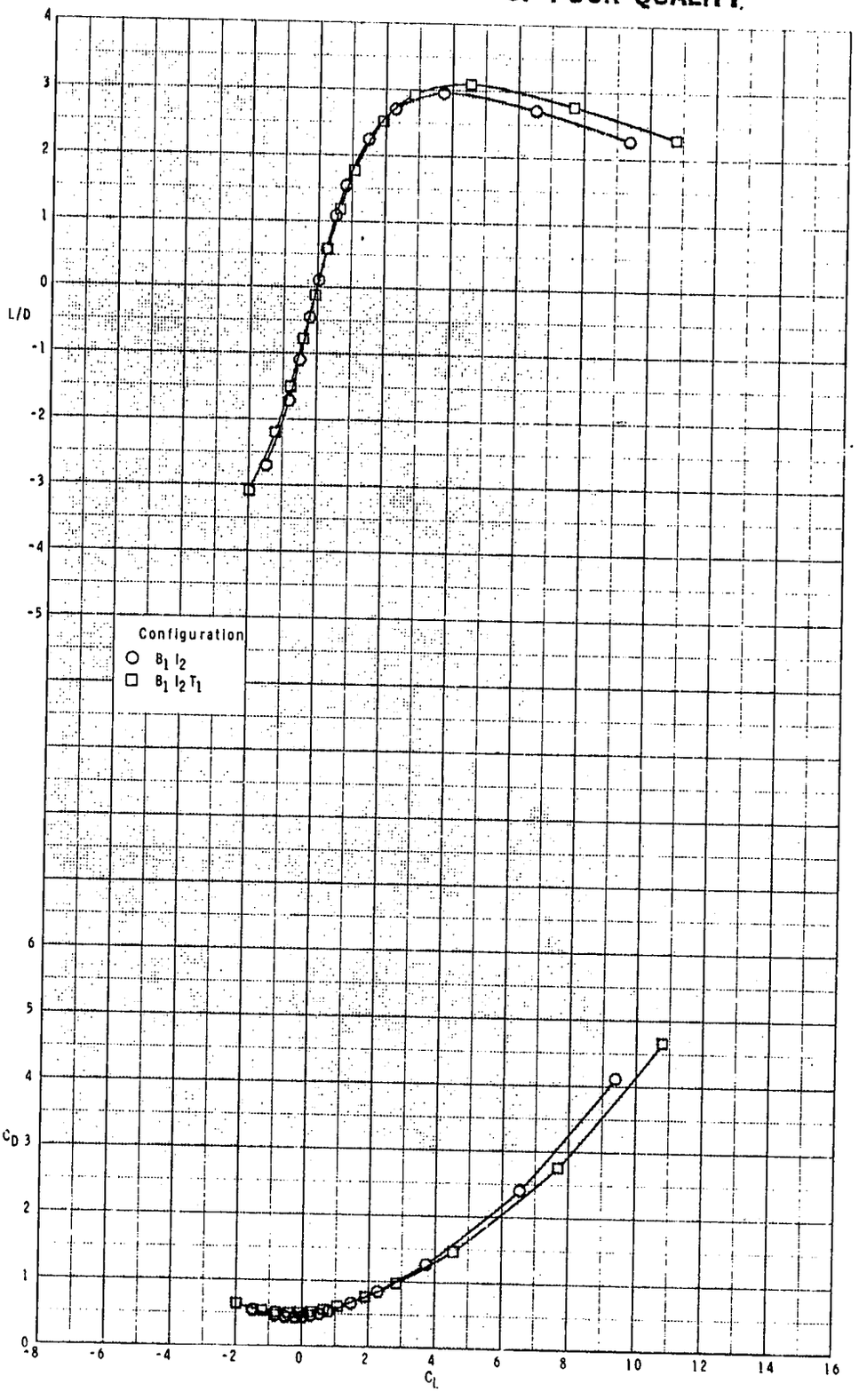

(a) Concluded.

Figure 6.- Continued.

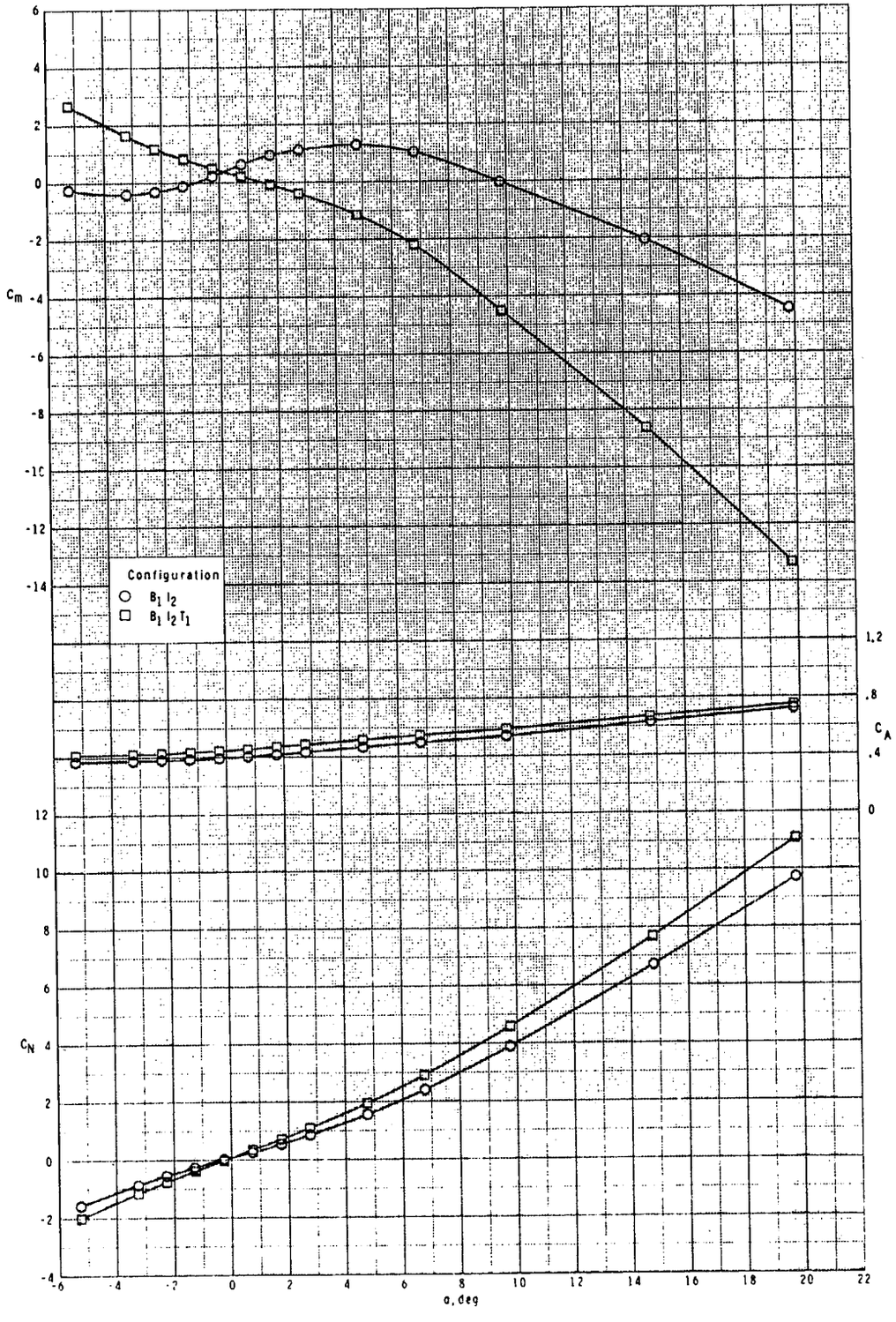

(b) M = 2.95.

Figure 6.- Continued.

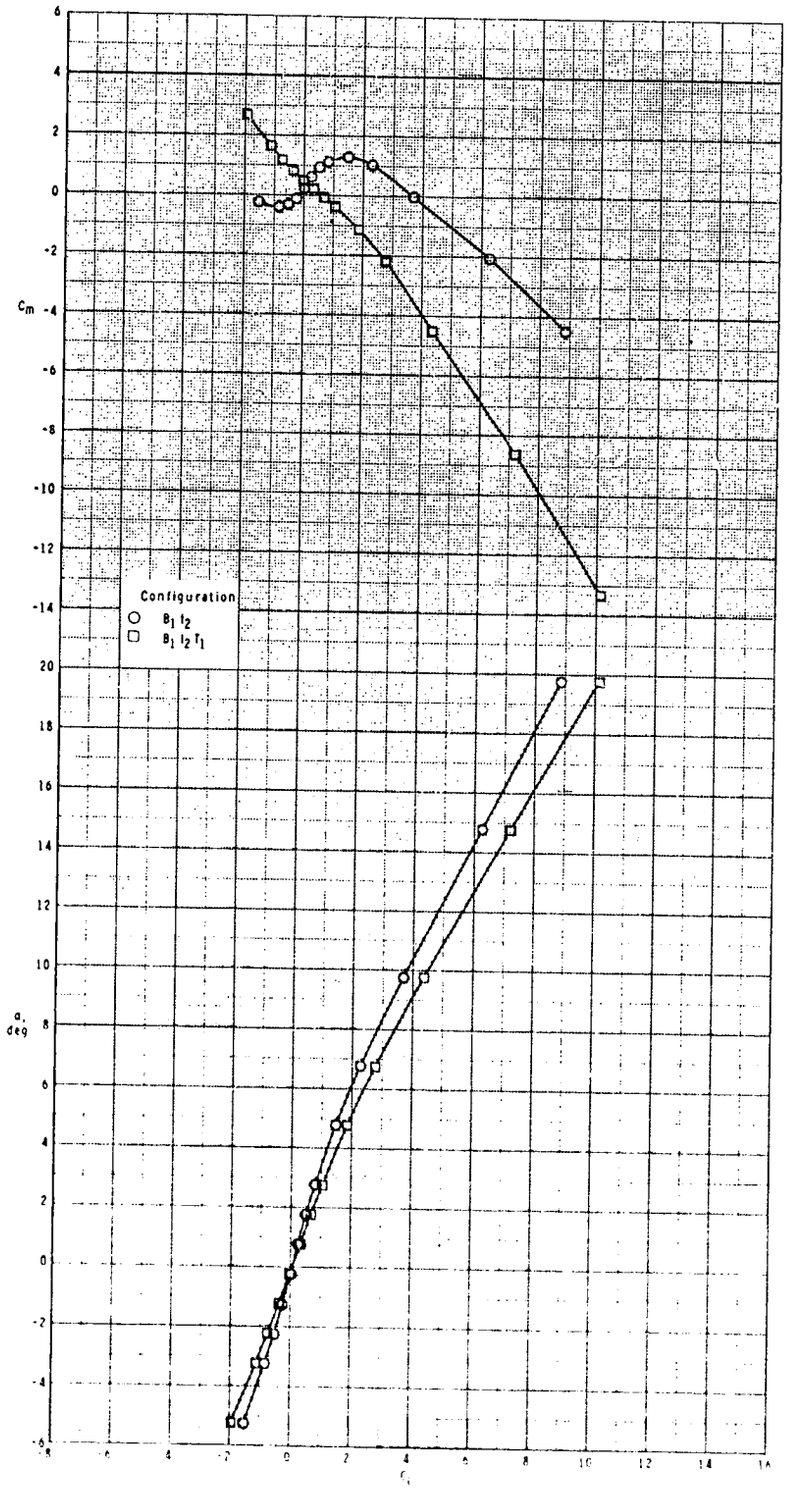

(b) Continued.

Figure 6.- Continued.

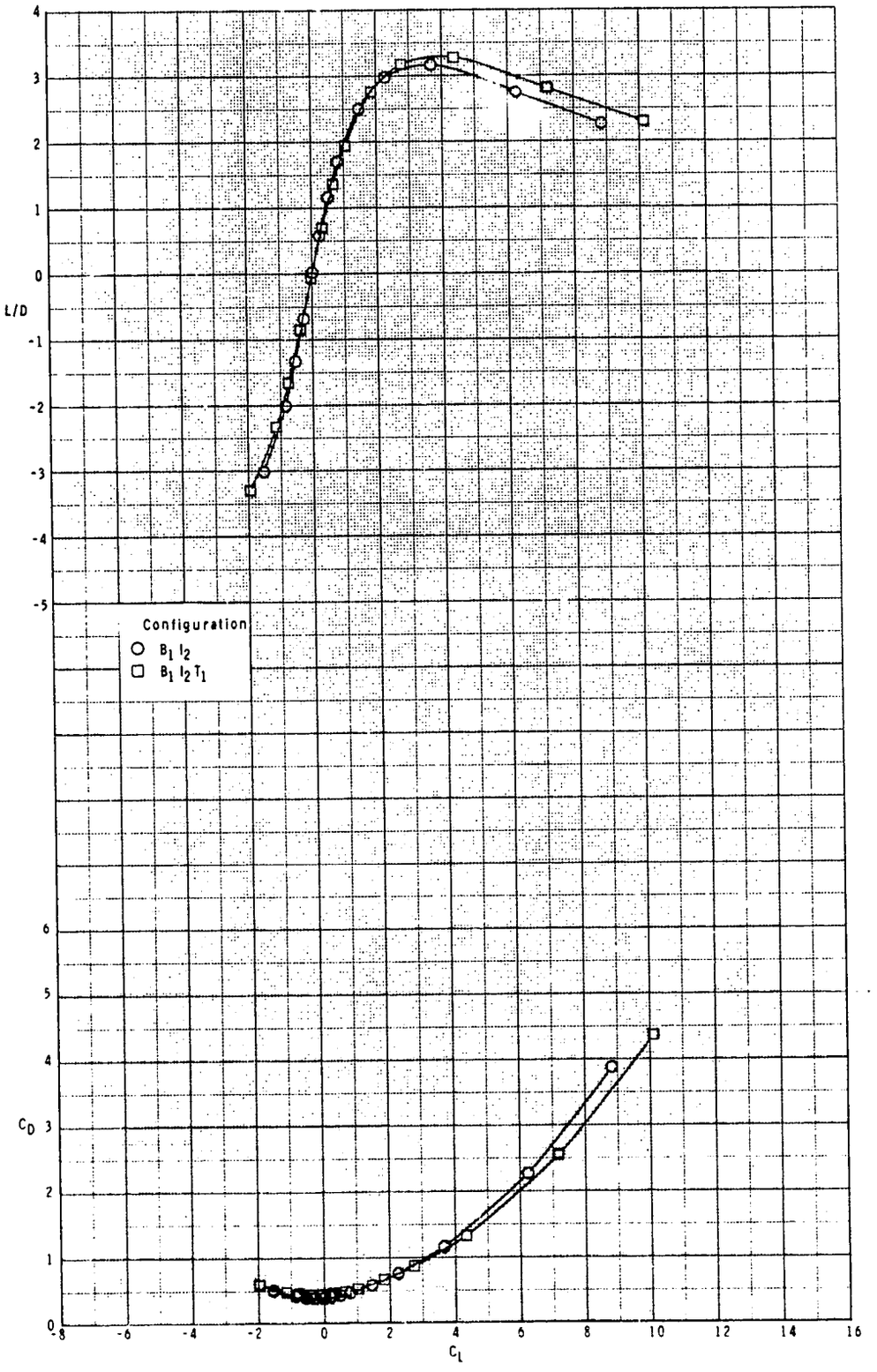

(b) Concluded.

Figure 6.- Continued.

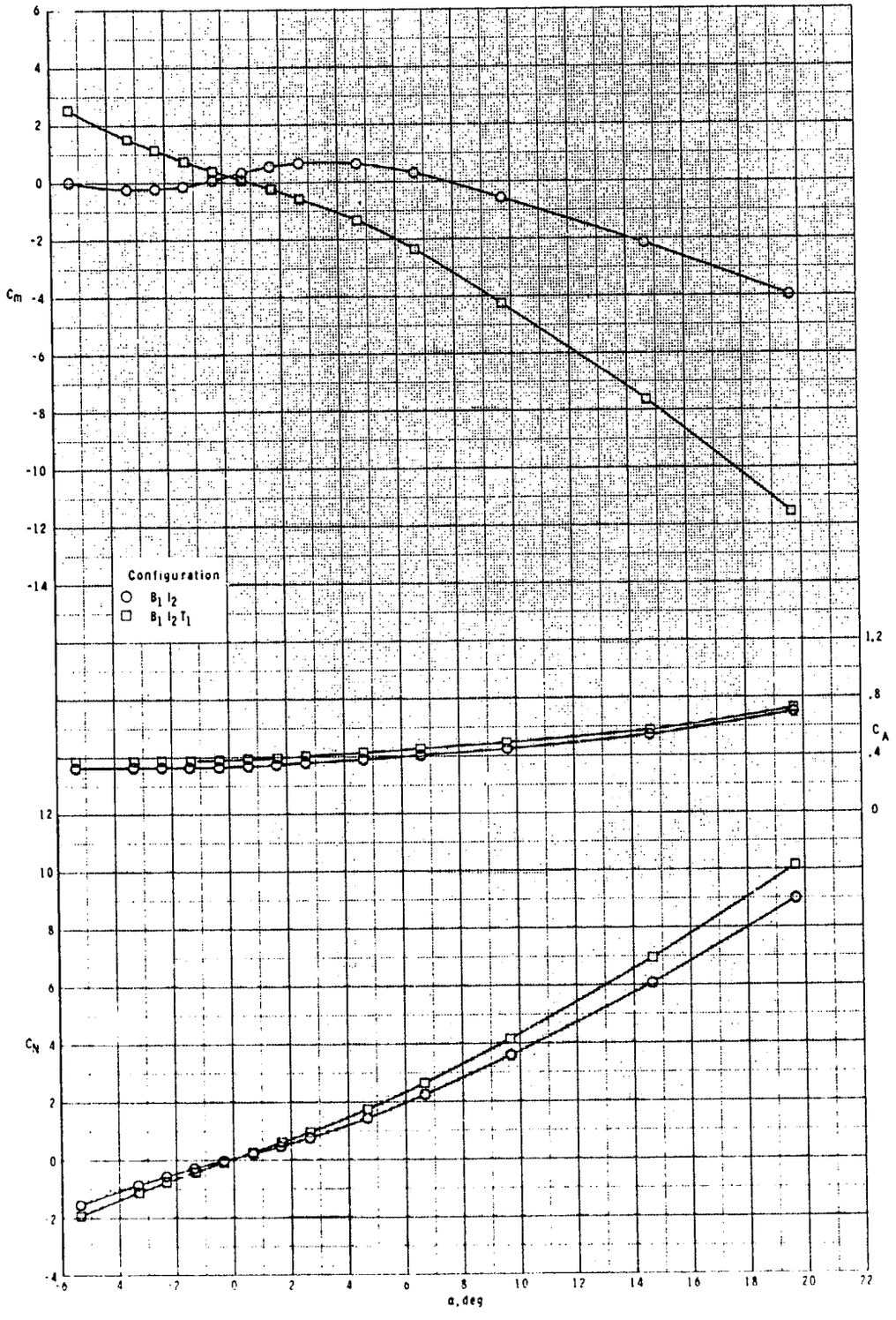

(c) M = 3.50.

Figure 6.- Continued.

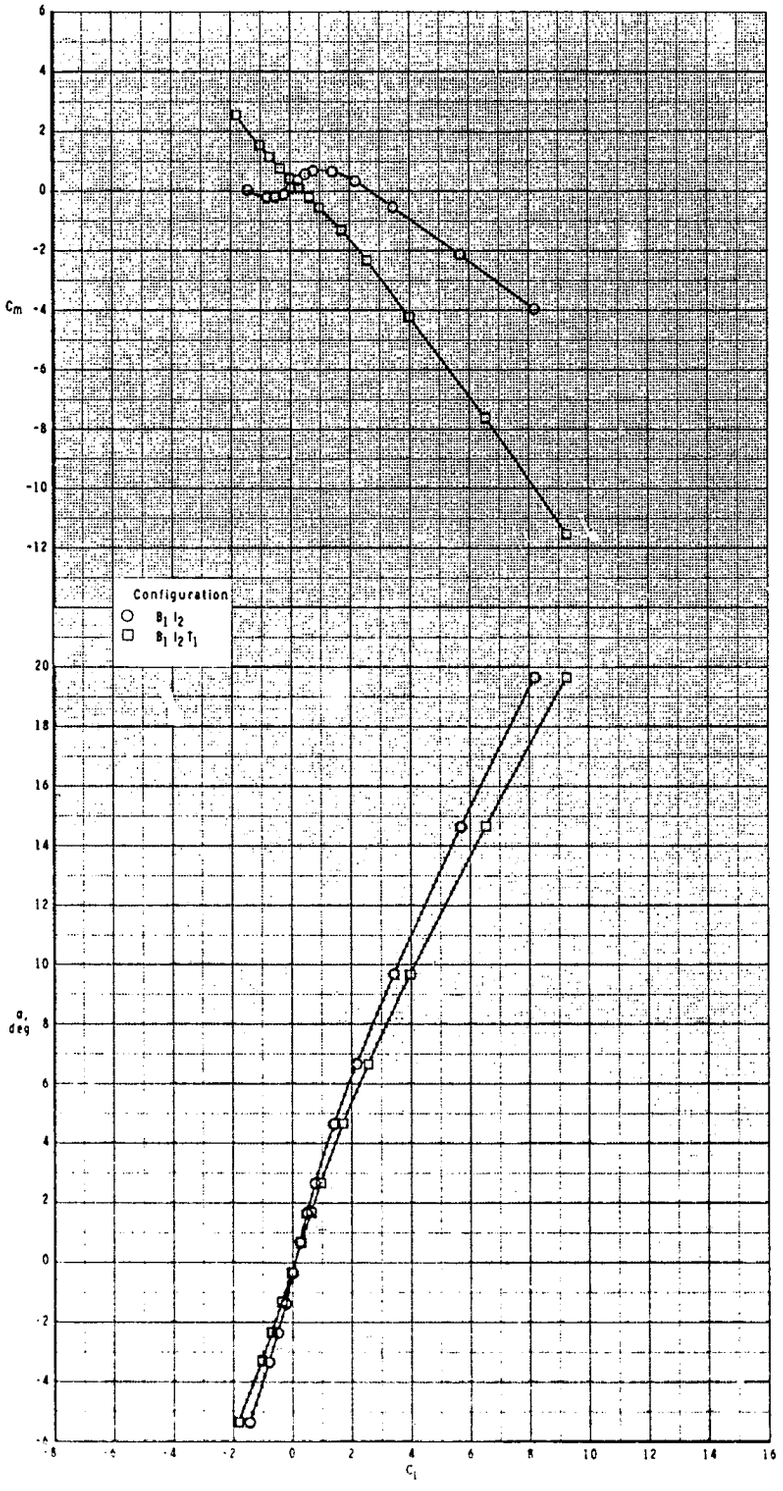

(c) Continued.

Figure 6.- Continued.

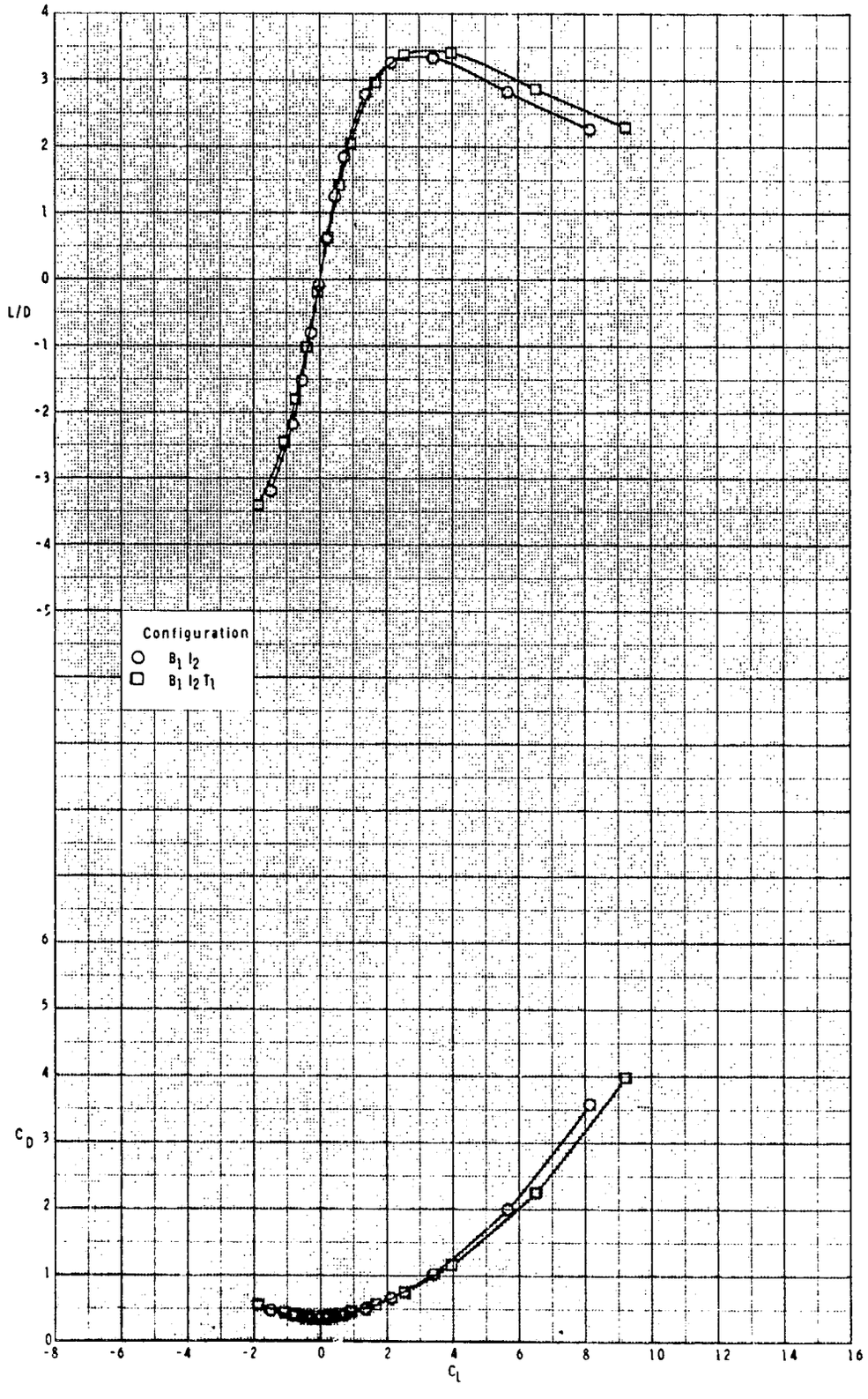

(c) Concluded.

Figure 6.- Continued.

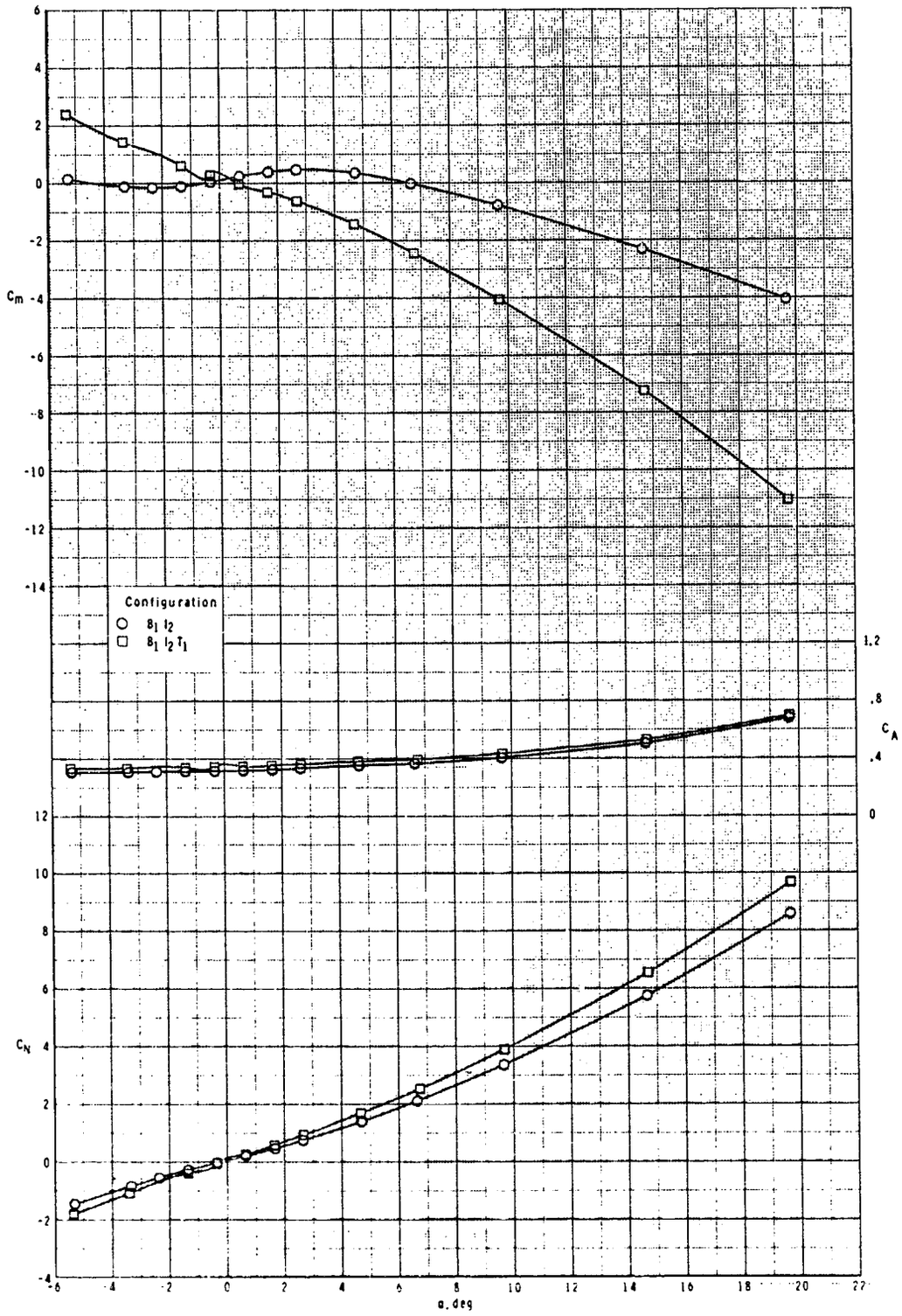

(d) M = 3.95.

Figure 6.- Continued.

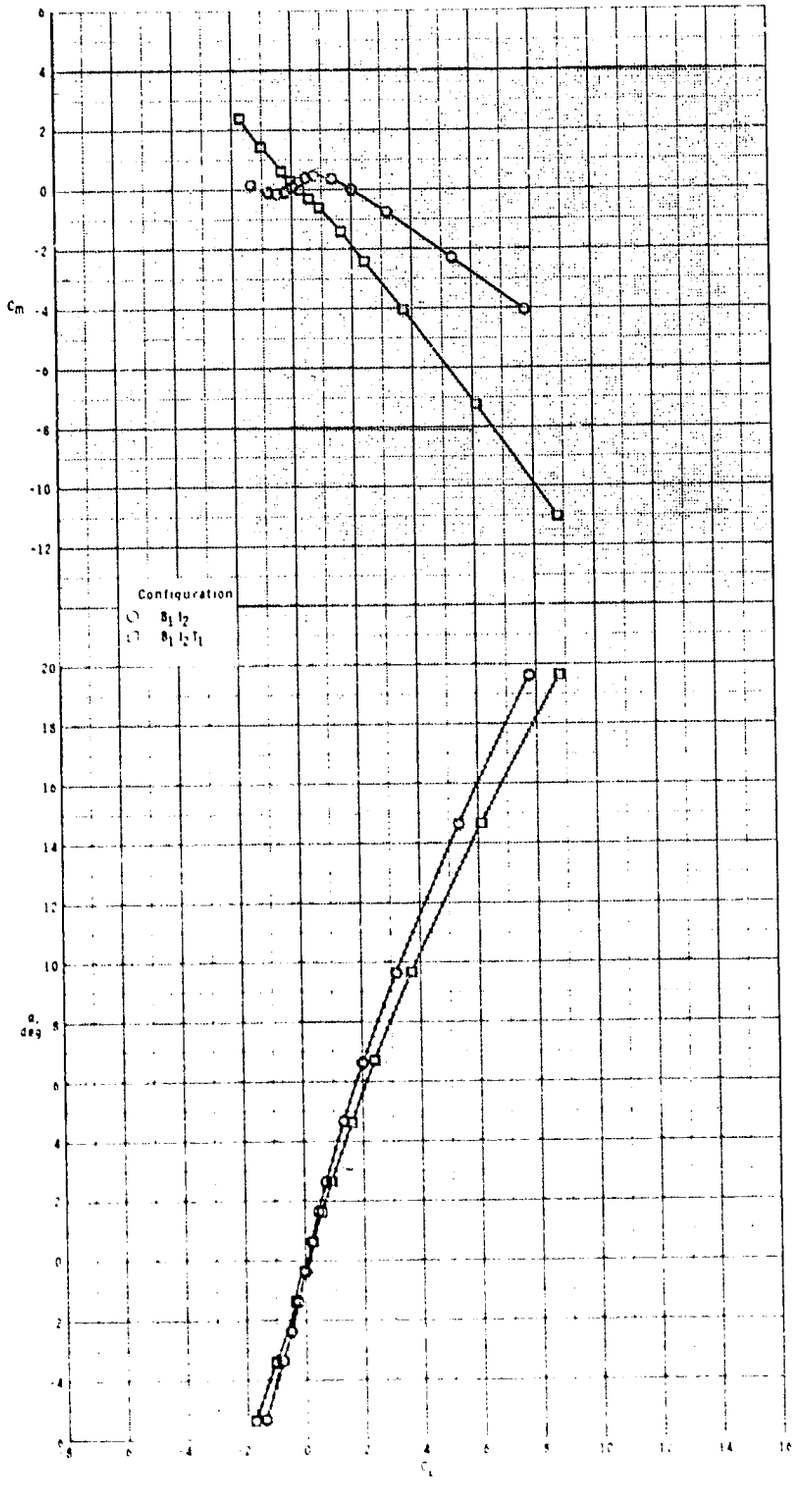

(d) Continued.

Figure 6.- Continued.

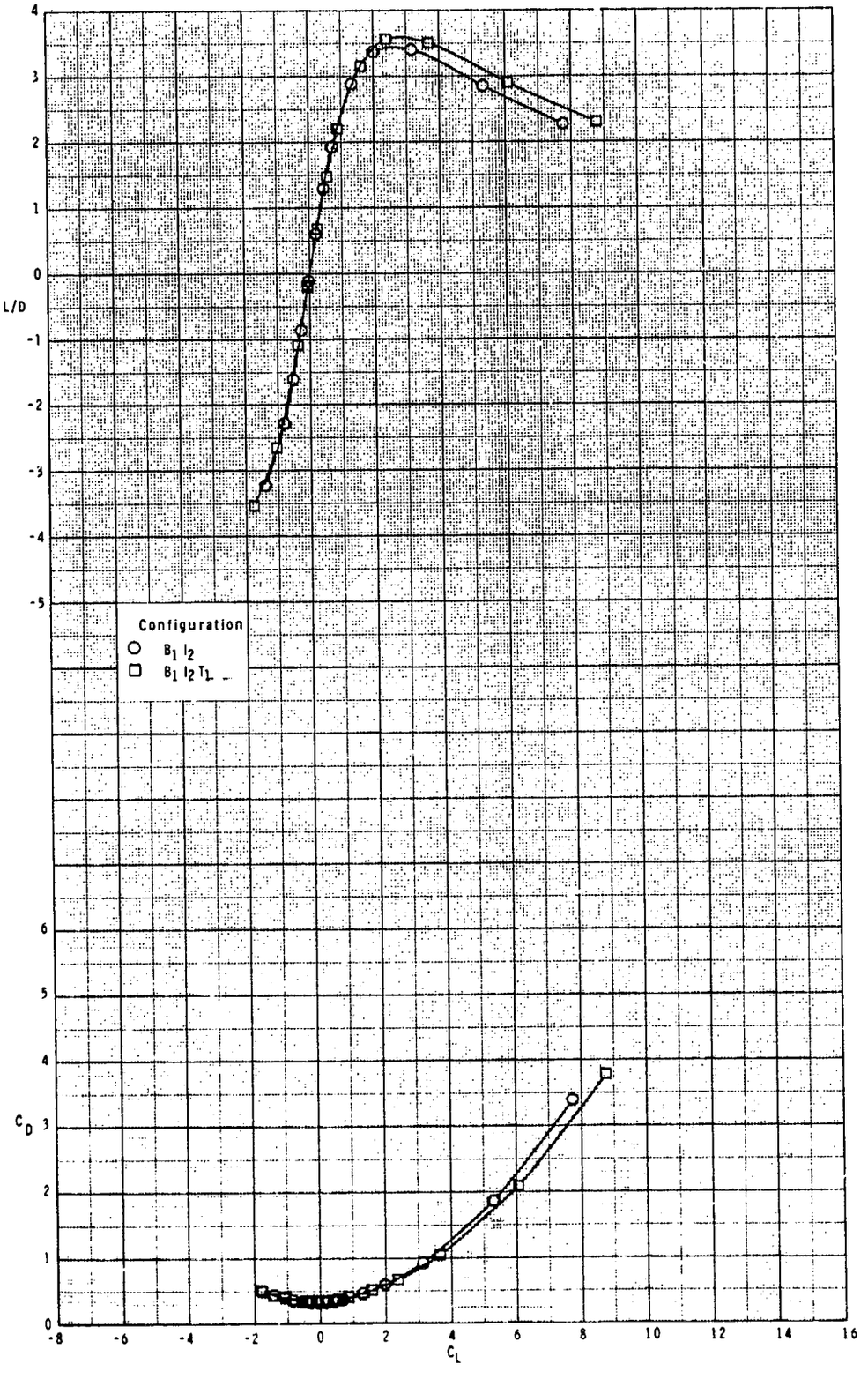

(d) Concluded.

Figure 6.- Concluded.

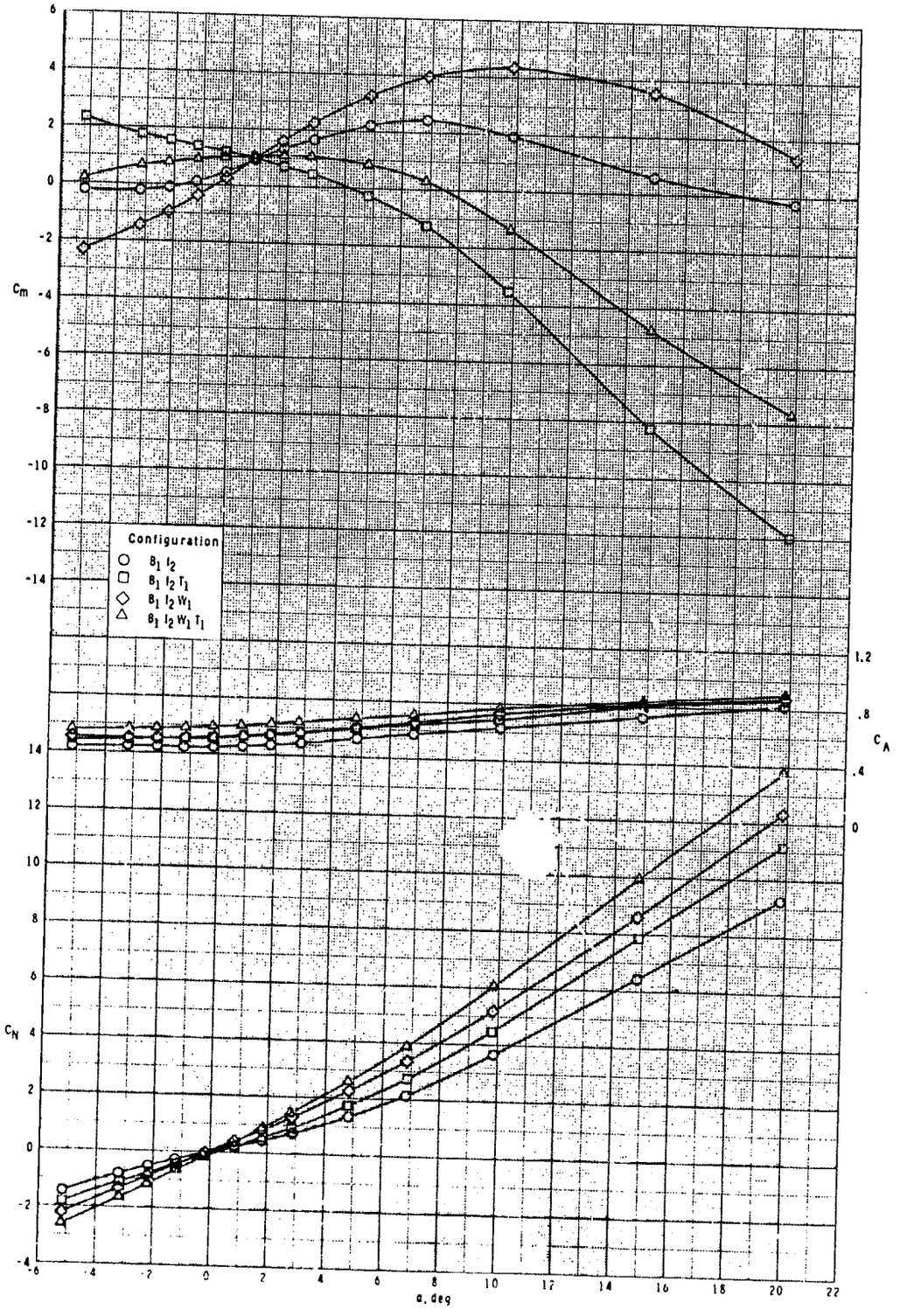

(a) M = 2.50.

Figure 7.- Effect of various model components on longitudinal aerodynamic characteristics for two-dimensional inlets with $\phi_I = 115°$ and $\delta_p = 0°$.

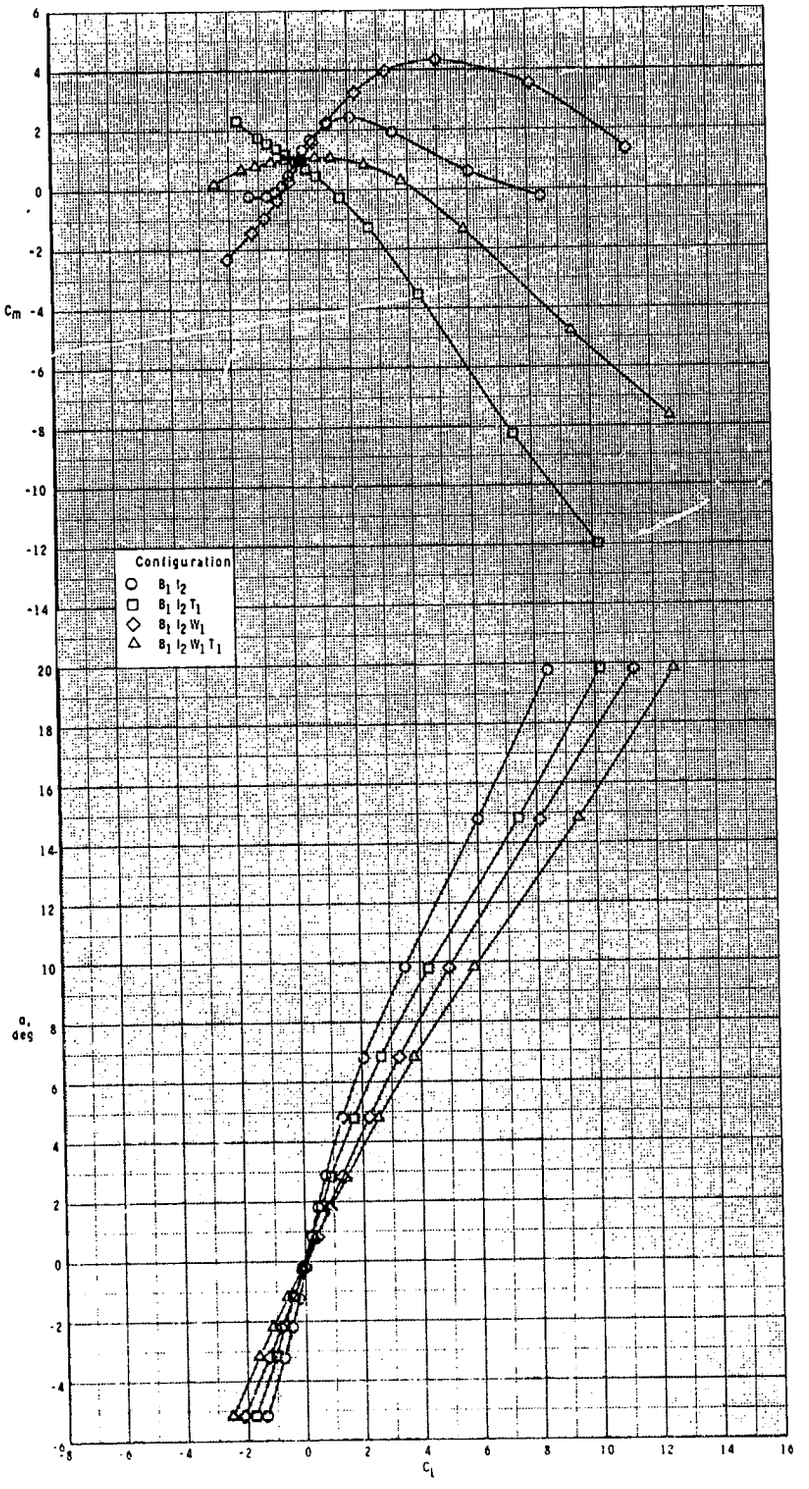

(a) Continued.

Figure 7.- Continued.

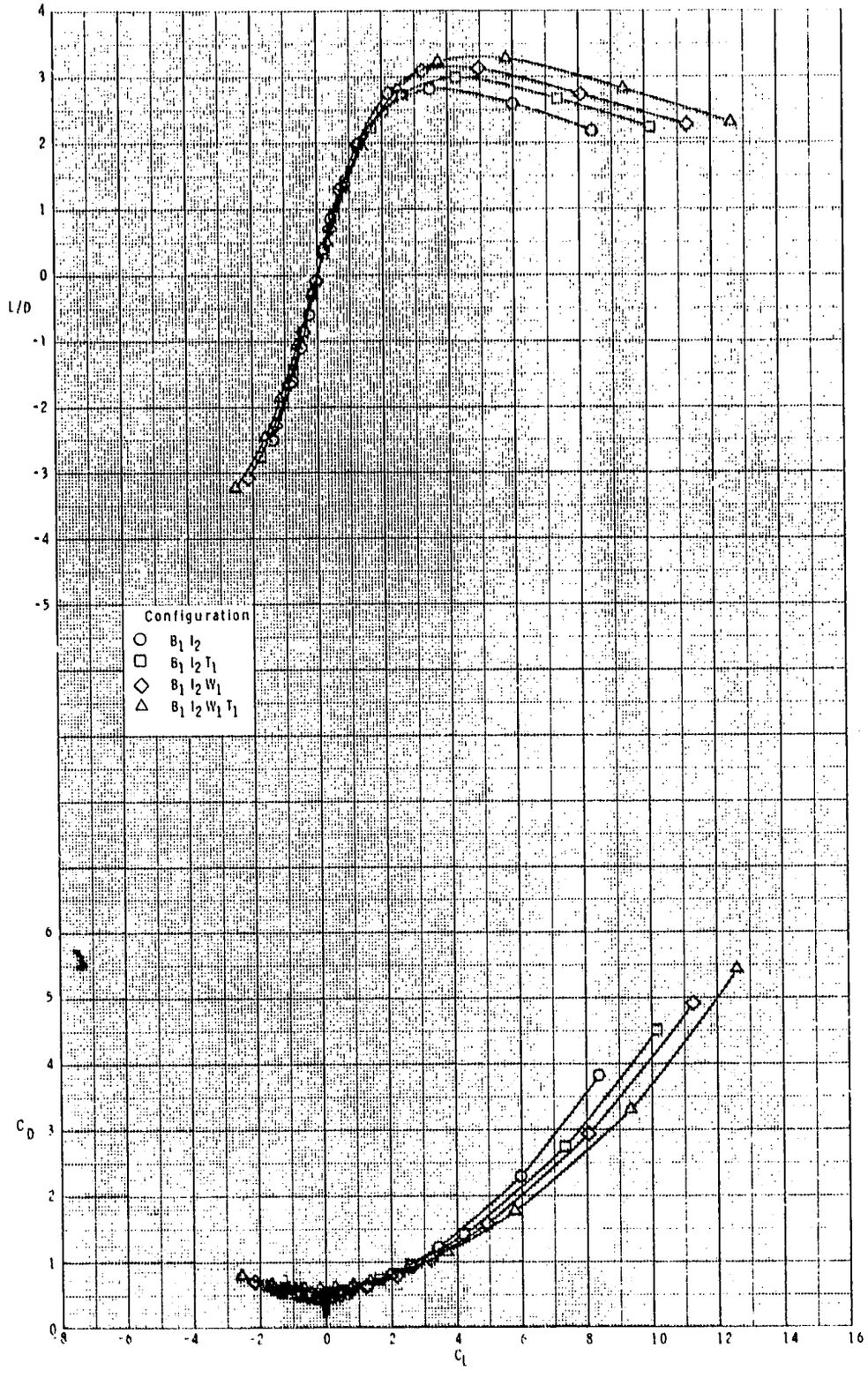

(a) Concluded.

Figure 7.- Continued.

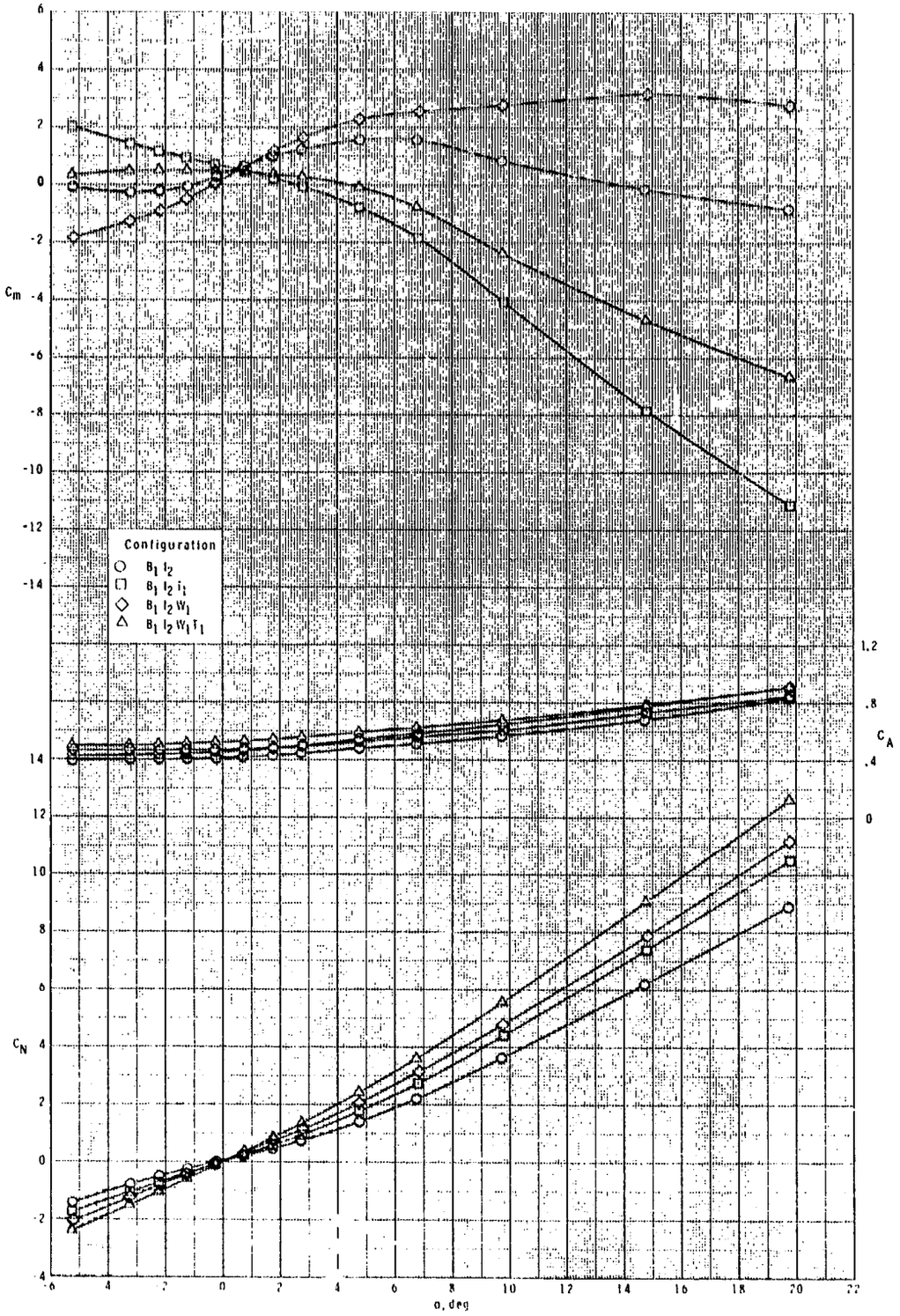

(b) M = 2.95.

Figure 7.- Continued.

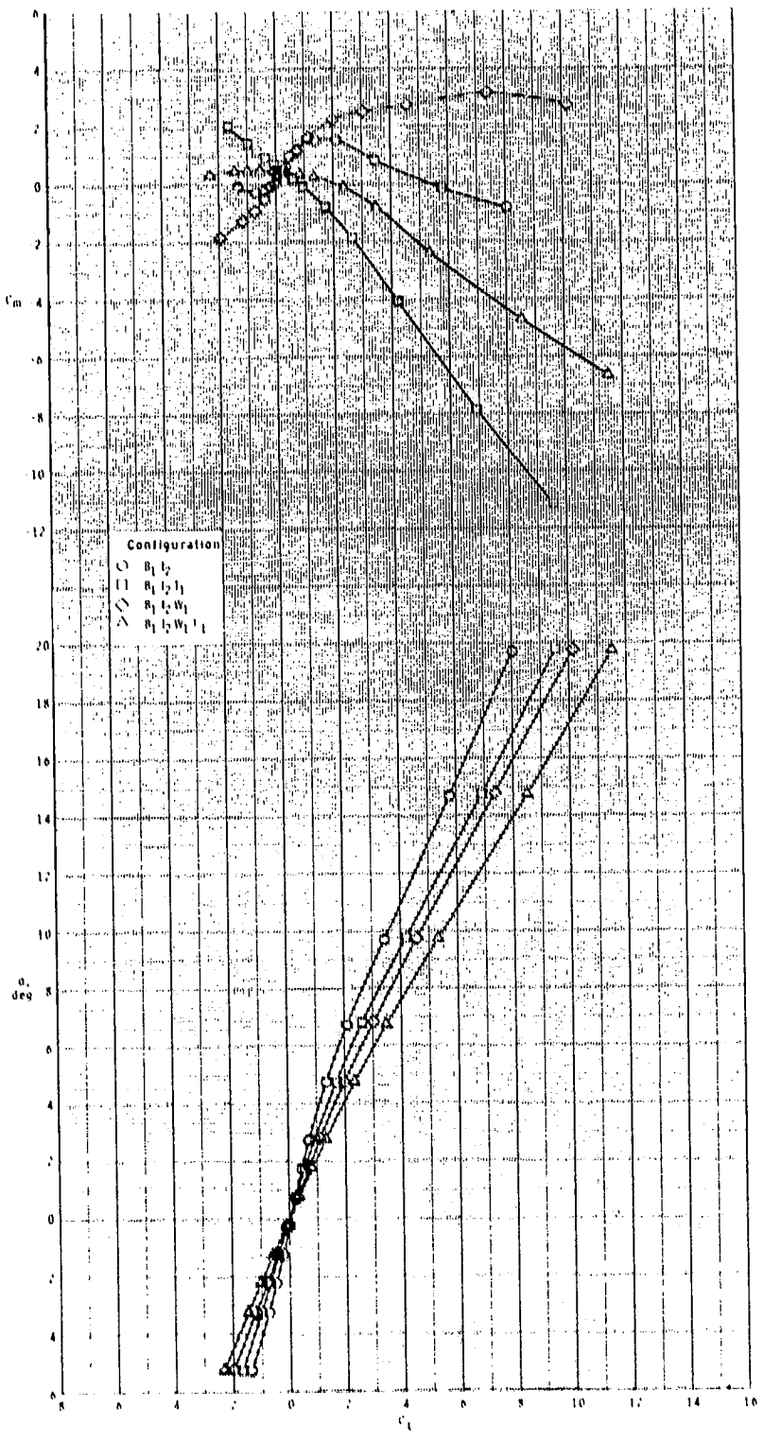

(b) Continued.

Figure 7.- Continued.

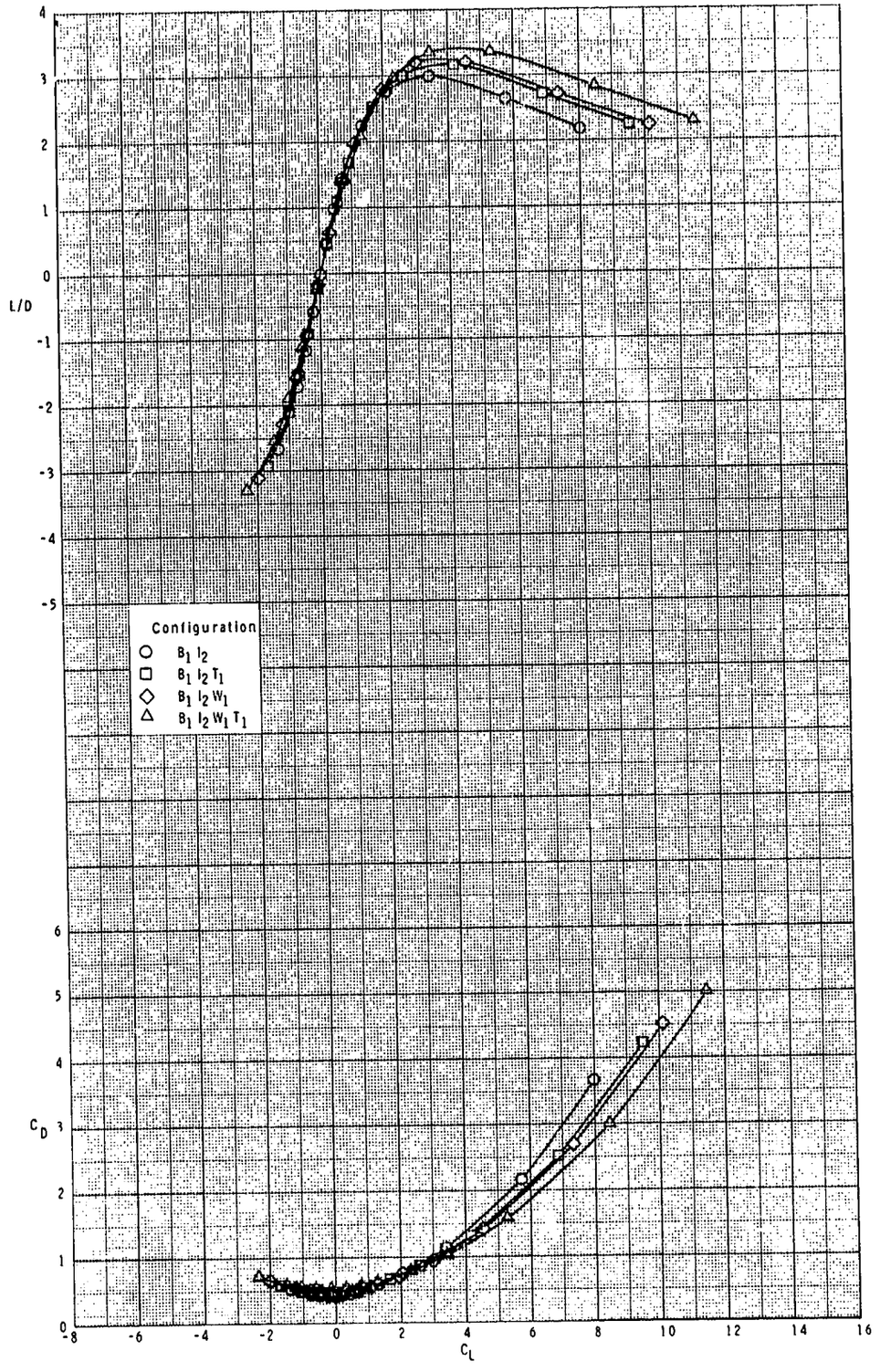

(b) Concluded.

Figure 7.- Continued.

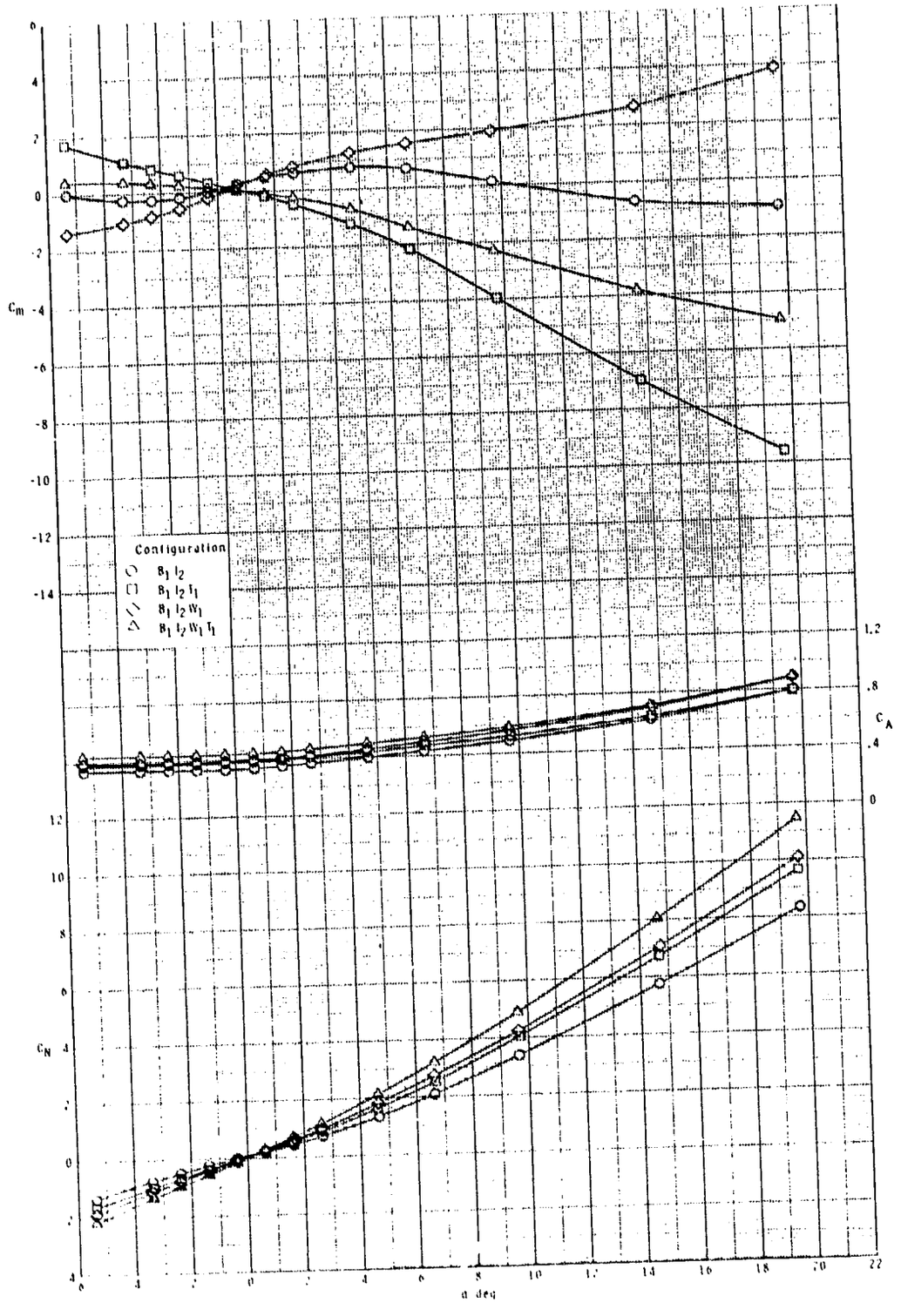

(c) M = 3.50.

Figure 7.- Continued.

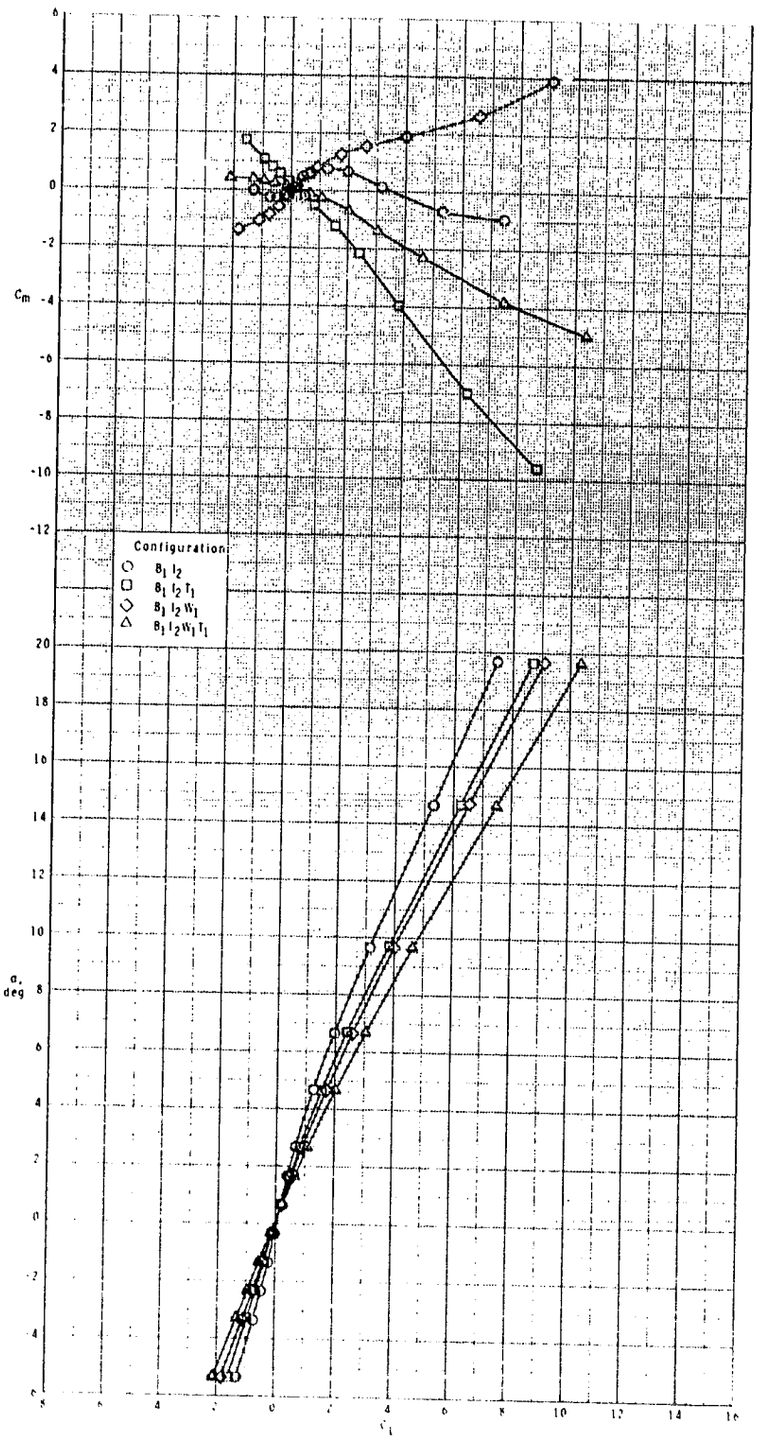

(c) Continued.

Figure 7.- Continued.

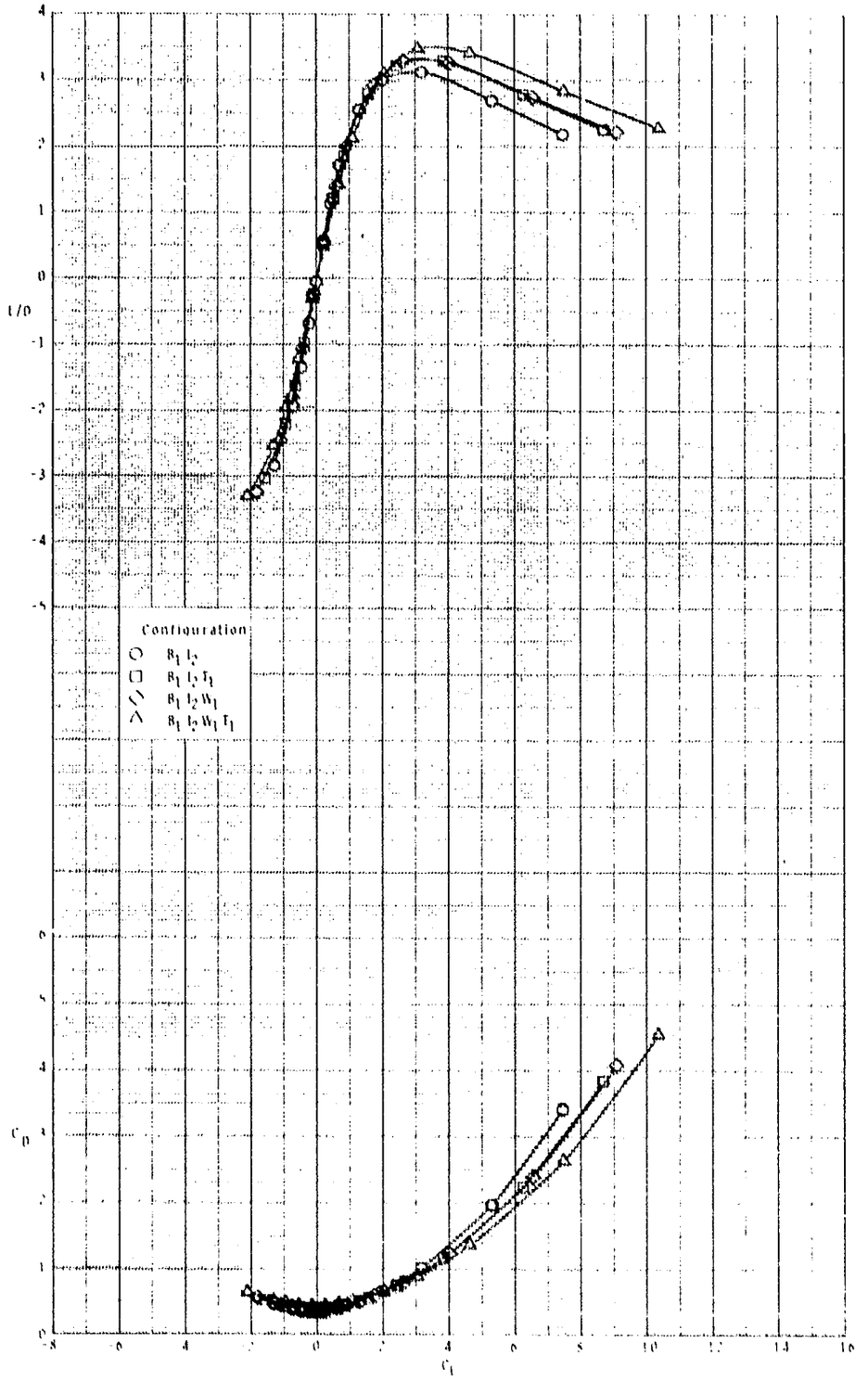

(c) Concluded.

Figure 7.- Continued.

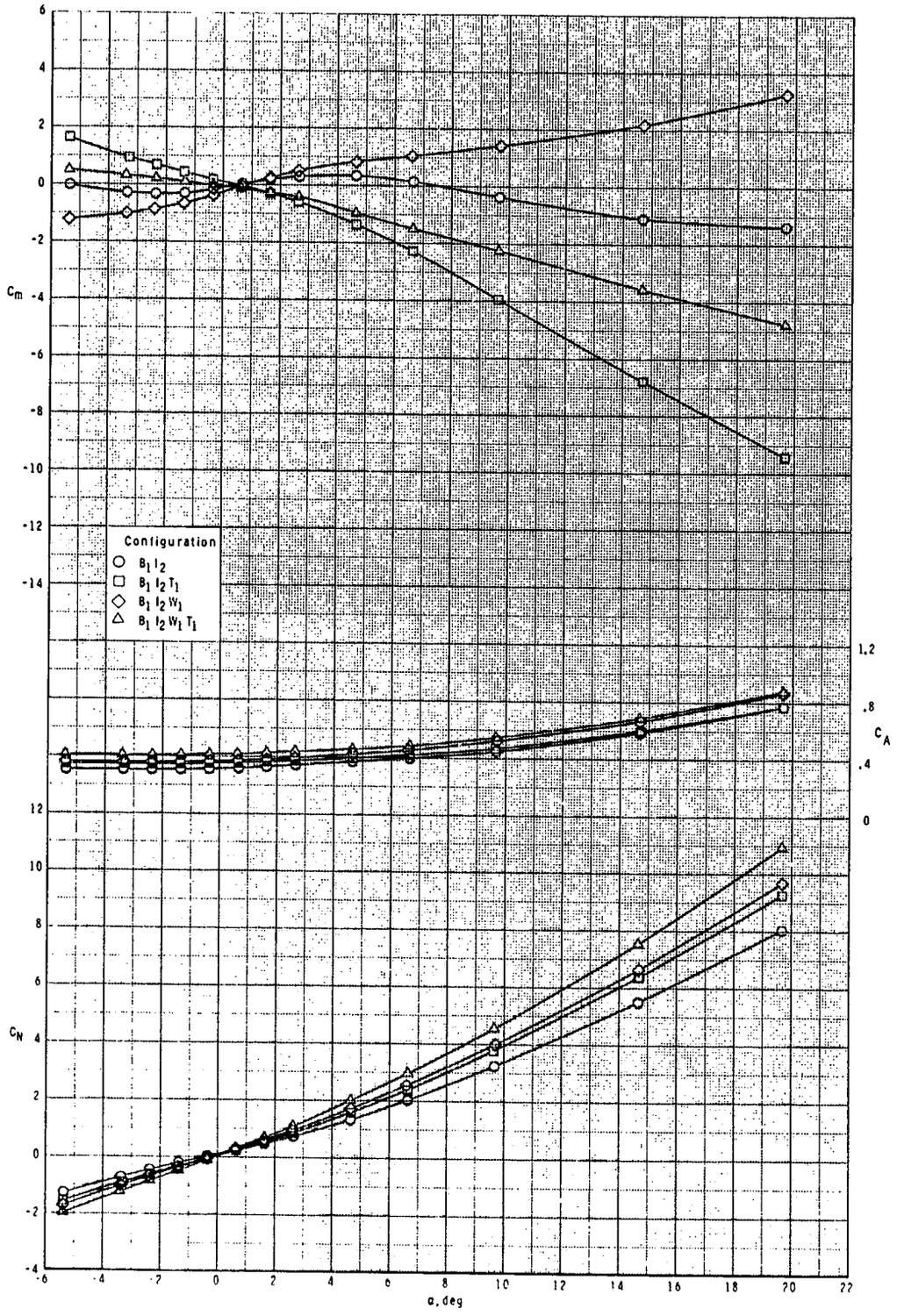

(d) M = 3.95.

Figure 7.- Continued.

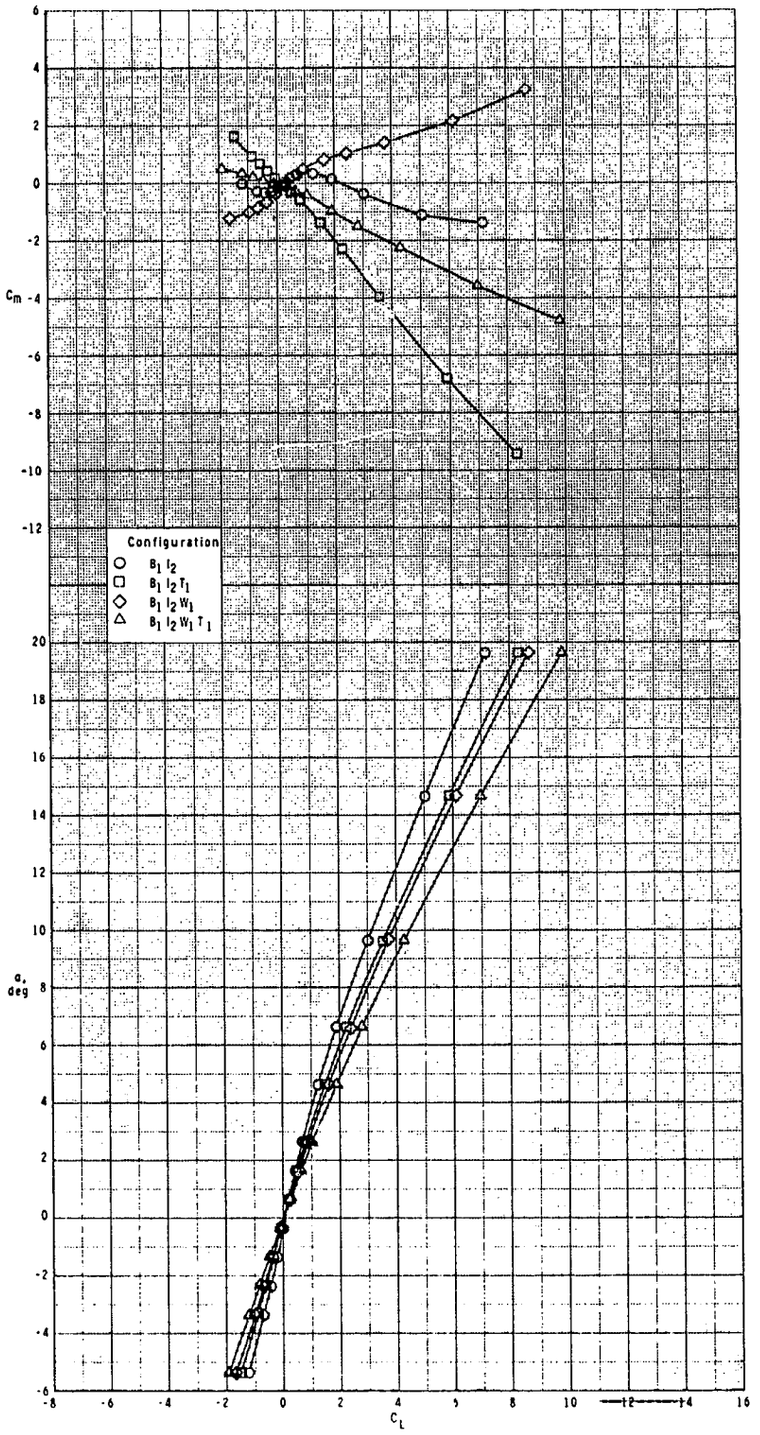

(d) Continued.

Figure 7.- Continued.

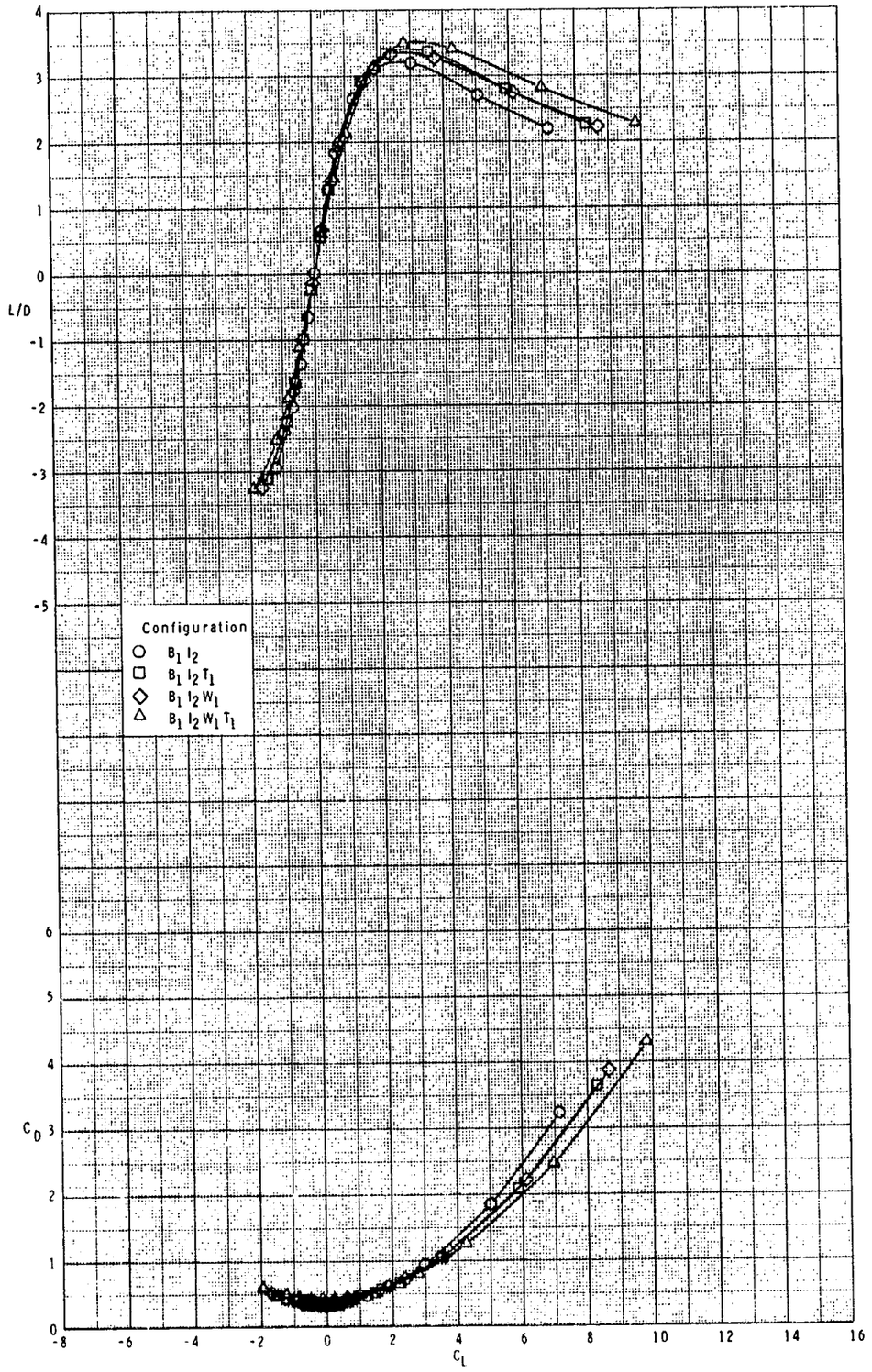

(d) Concluded.

Figure 7.- Concluded.

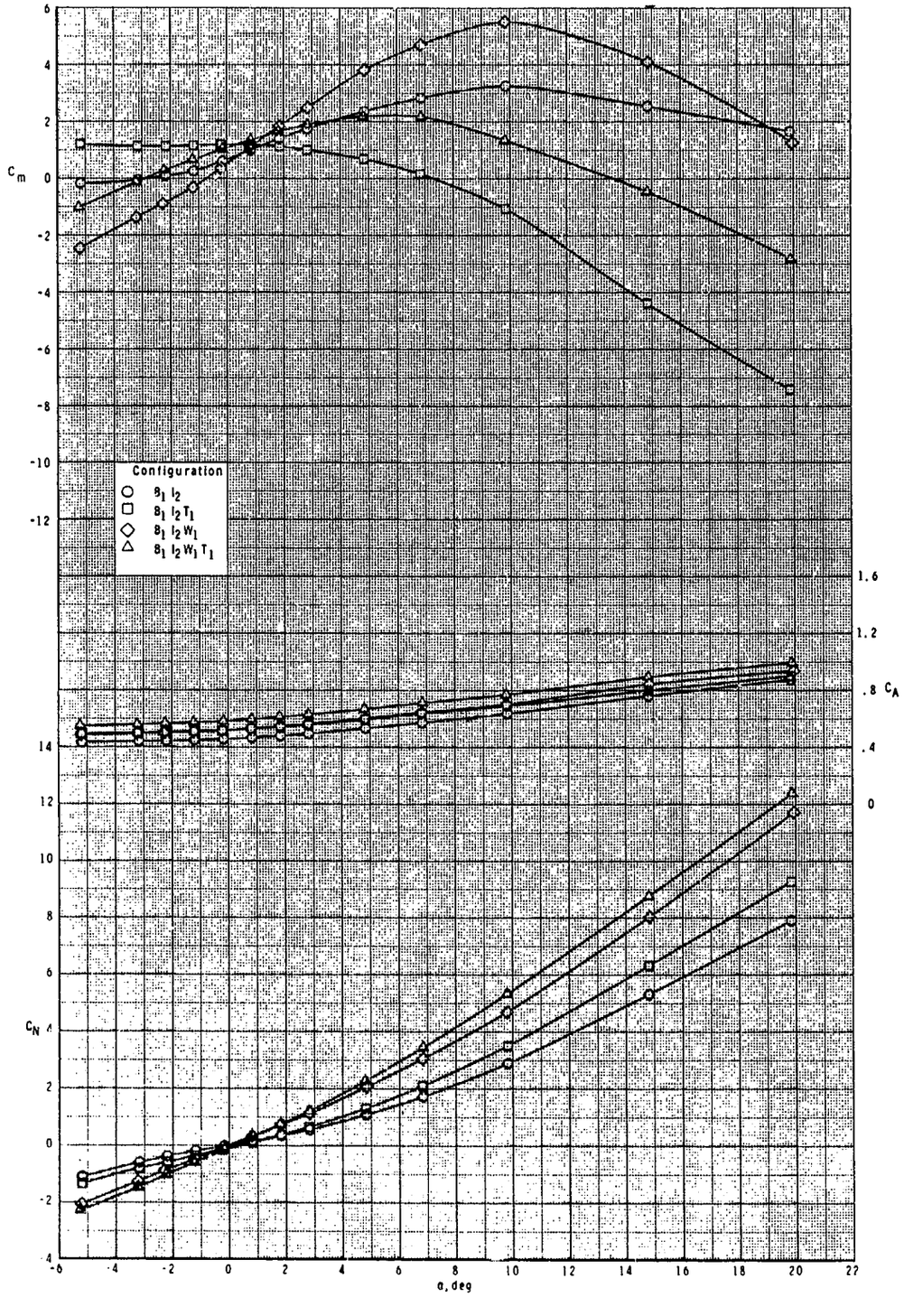

(a) M = 2.50.

Figure 8.- Effect of various model components on longitudinal aerodynamic characteristics for two-dimensional inlets with T_1, ϕ_I = 135°, and δ_p = 0°.

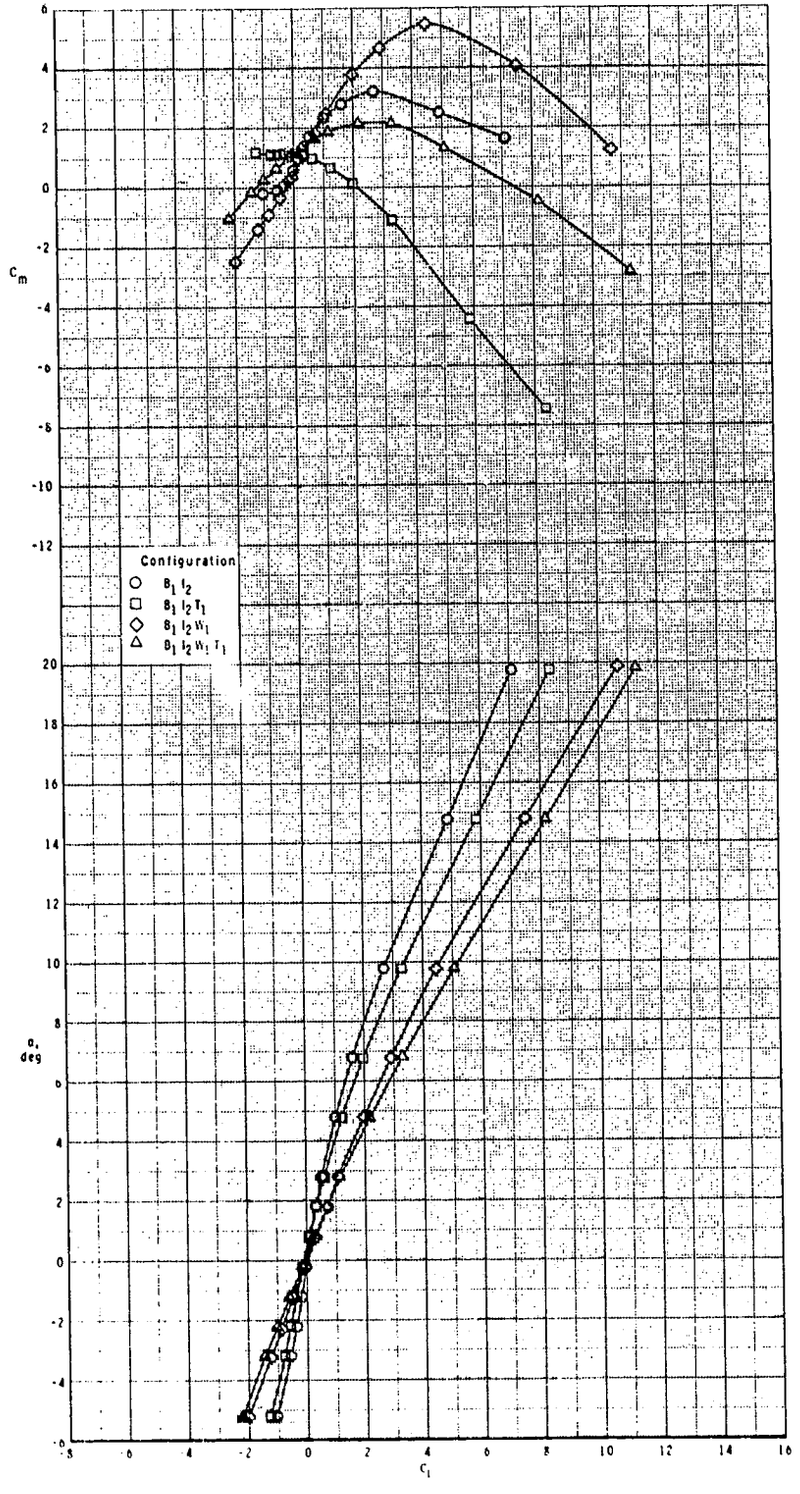

(a) Continued.

Figure 8.- Continued.

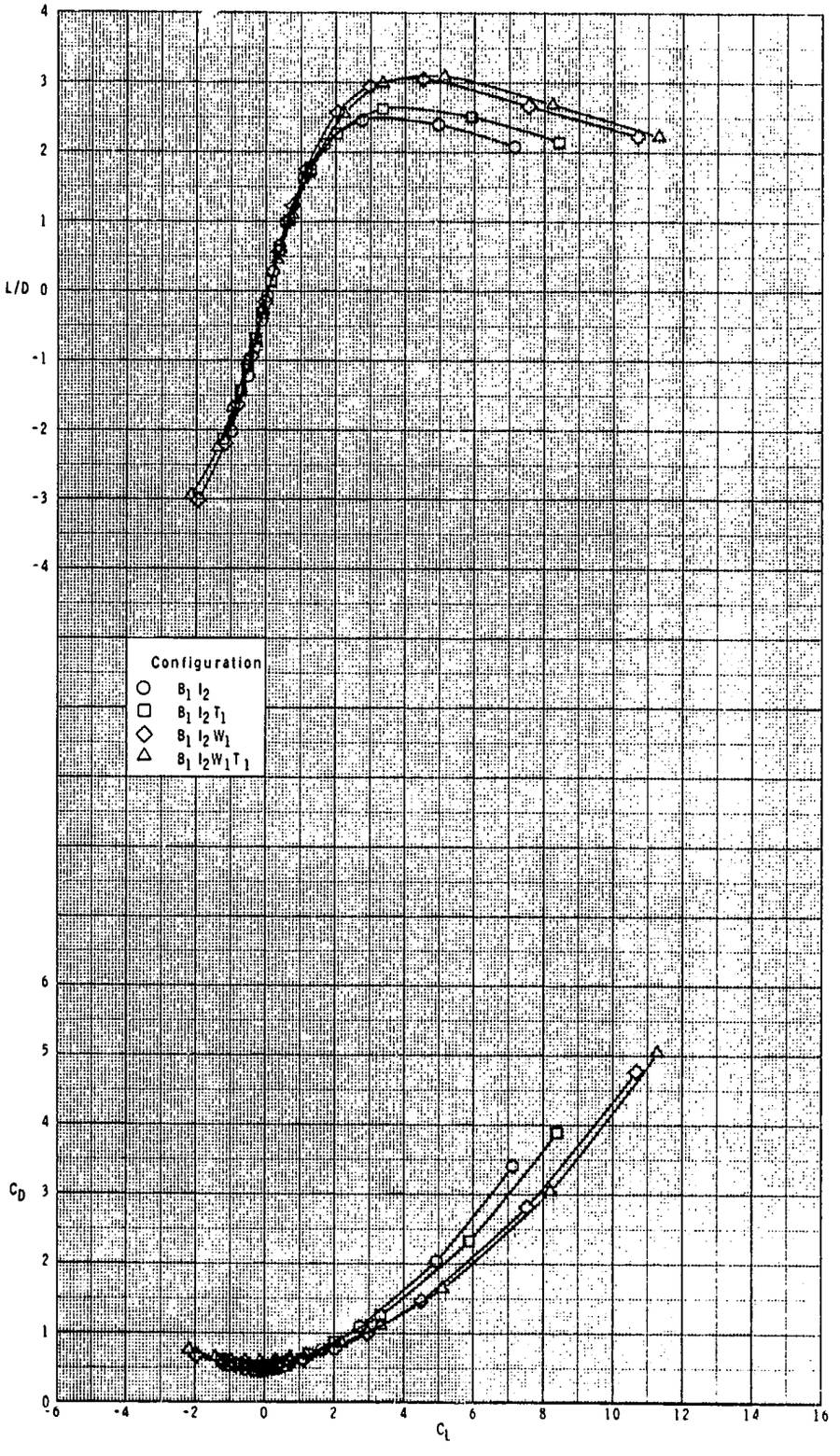

(a) Concluded.

Figure 8.- Continued.

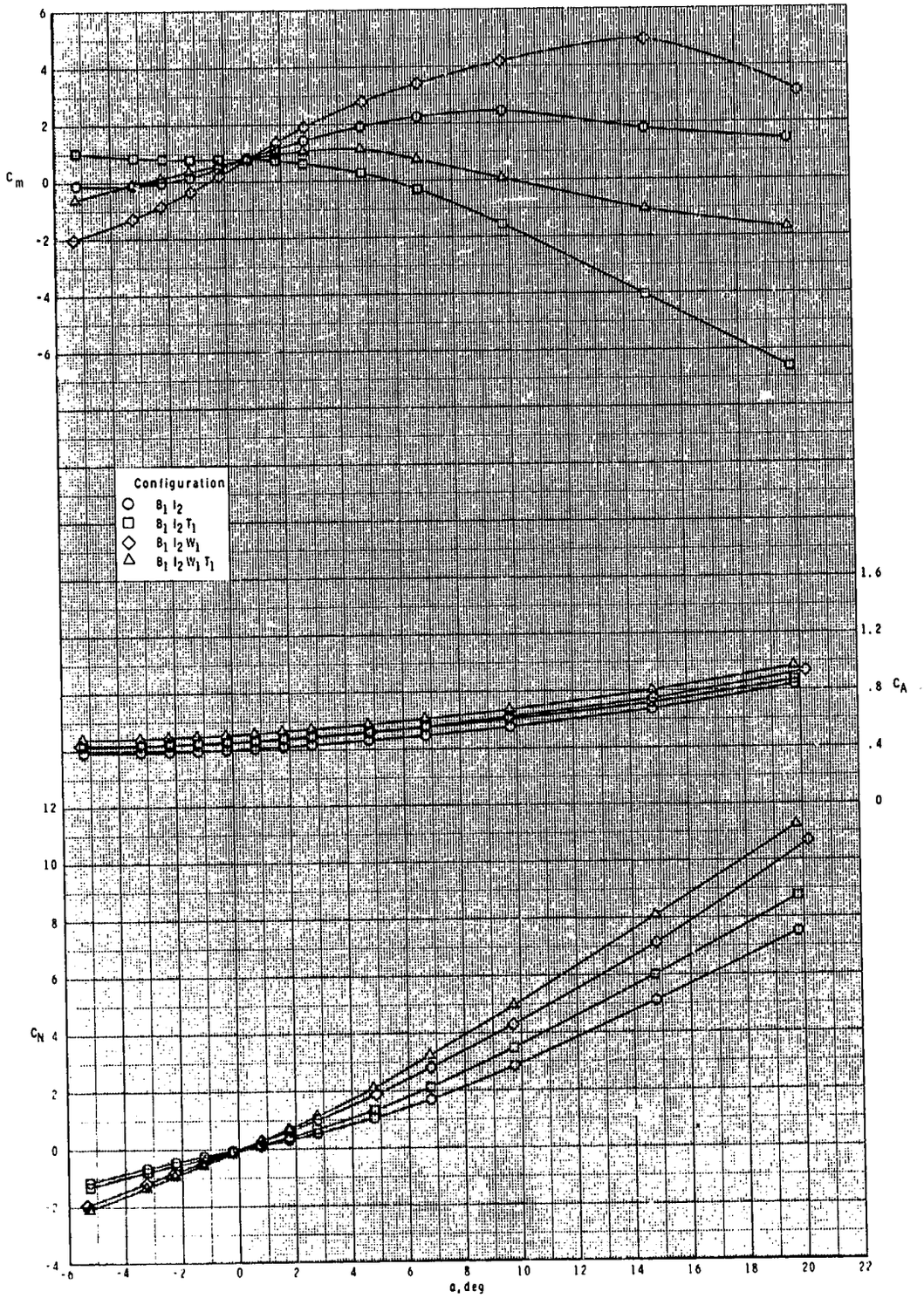

(b) M = 2.95.

Figure 8.- Continued.

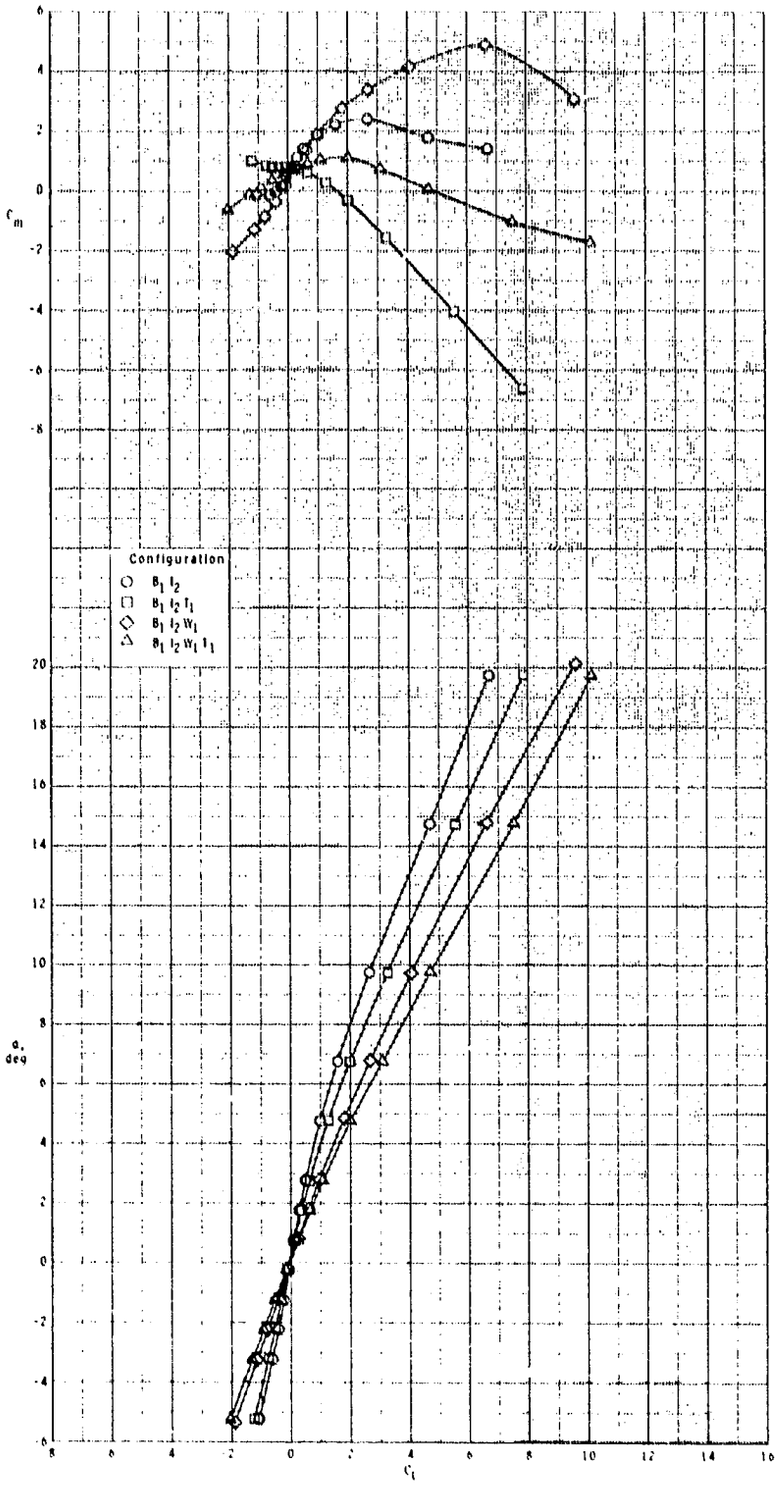

(b) Continued.

Figure 8.- Continued.

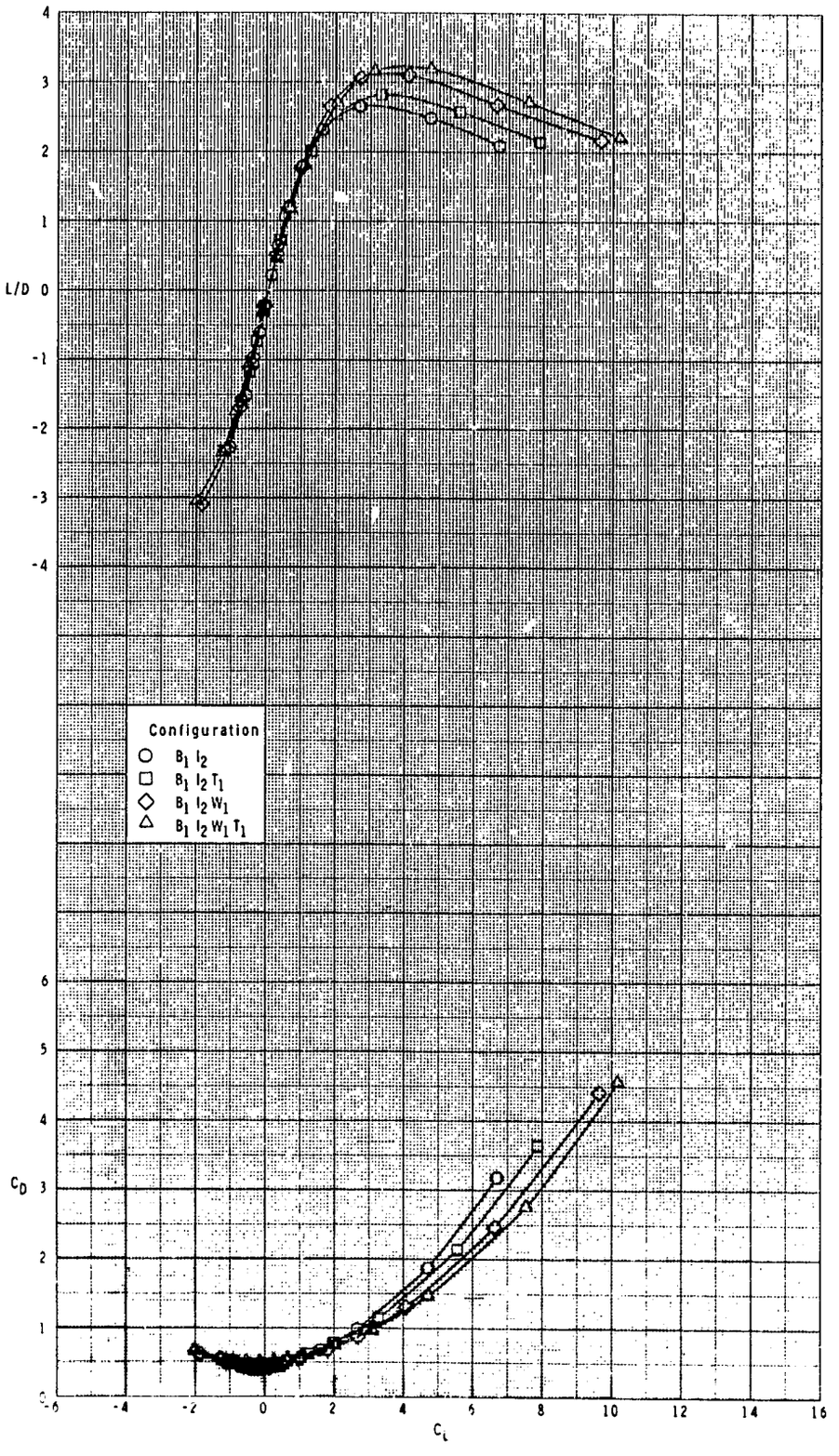

(b) Concluded.

Figure 8.- Continued.

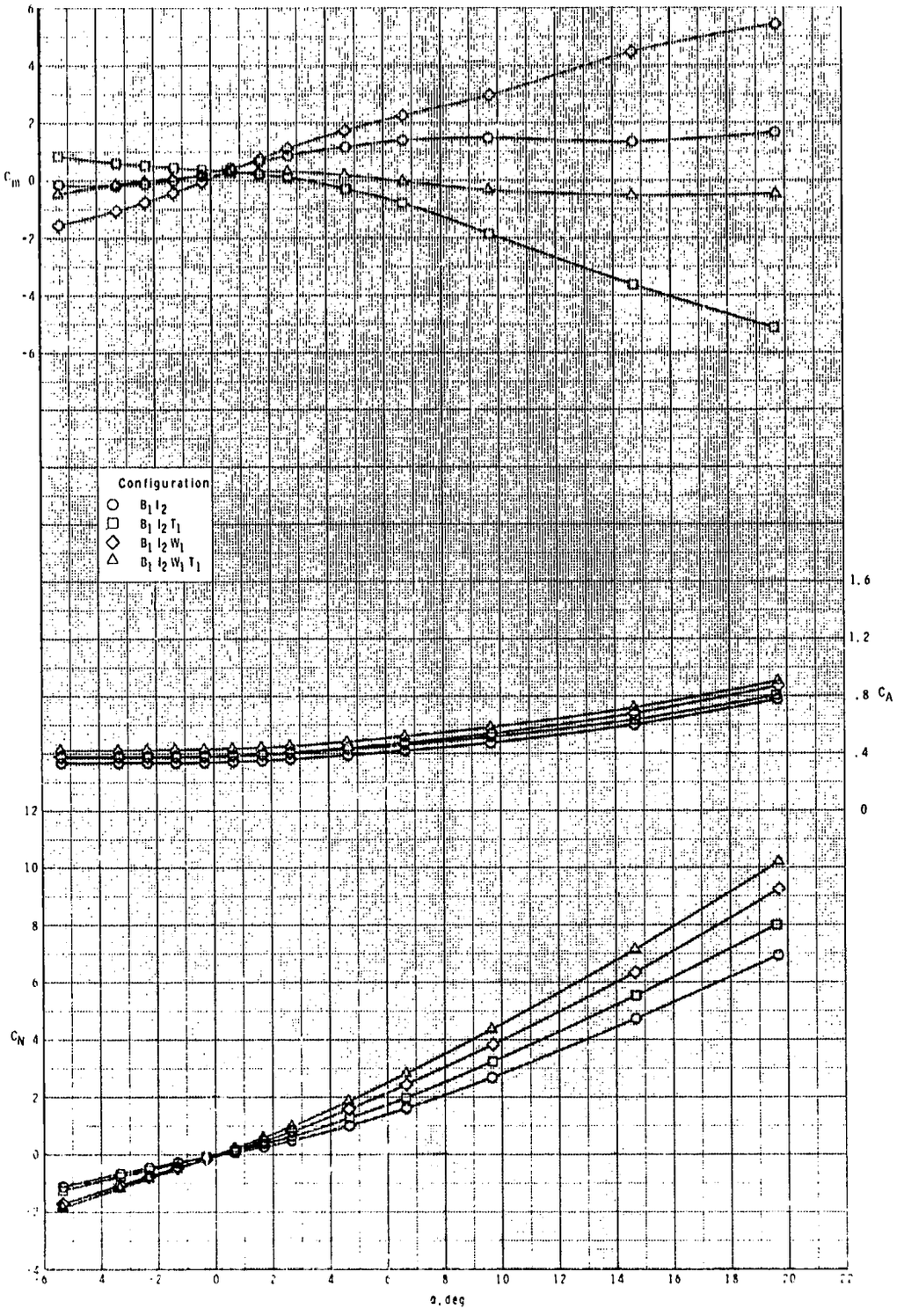

(c) M = 3.50.

Figure 8.- Continued.

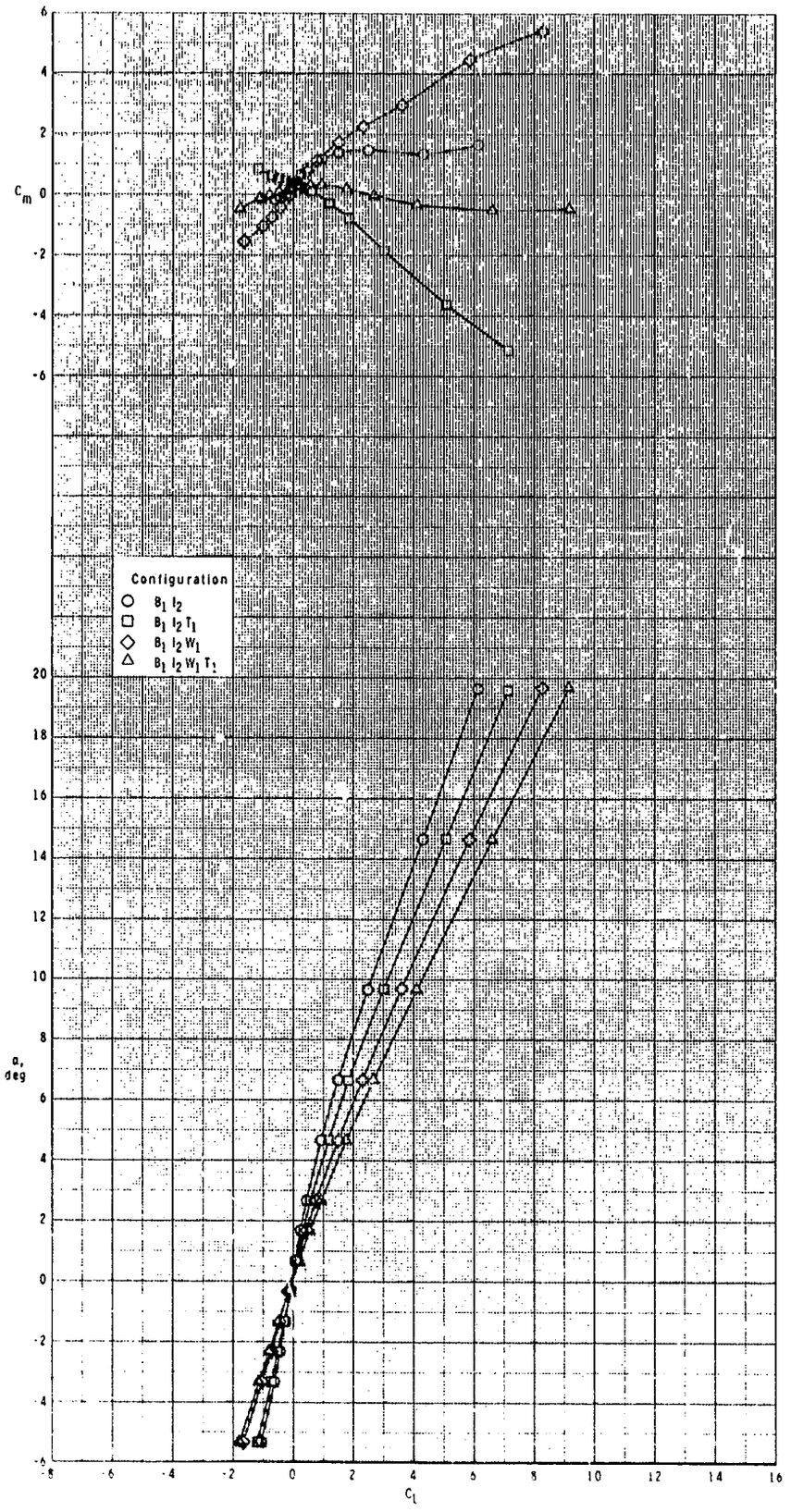

(c) Continued.

Figure 8.- Continued.

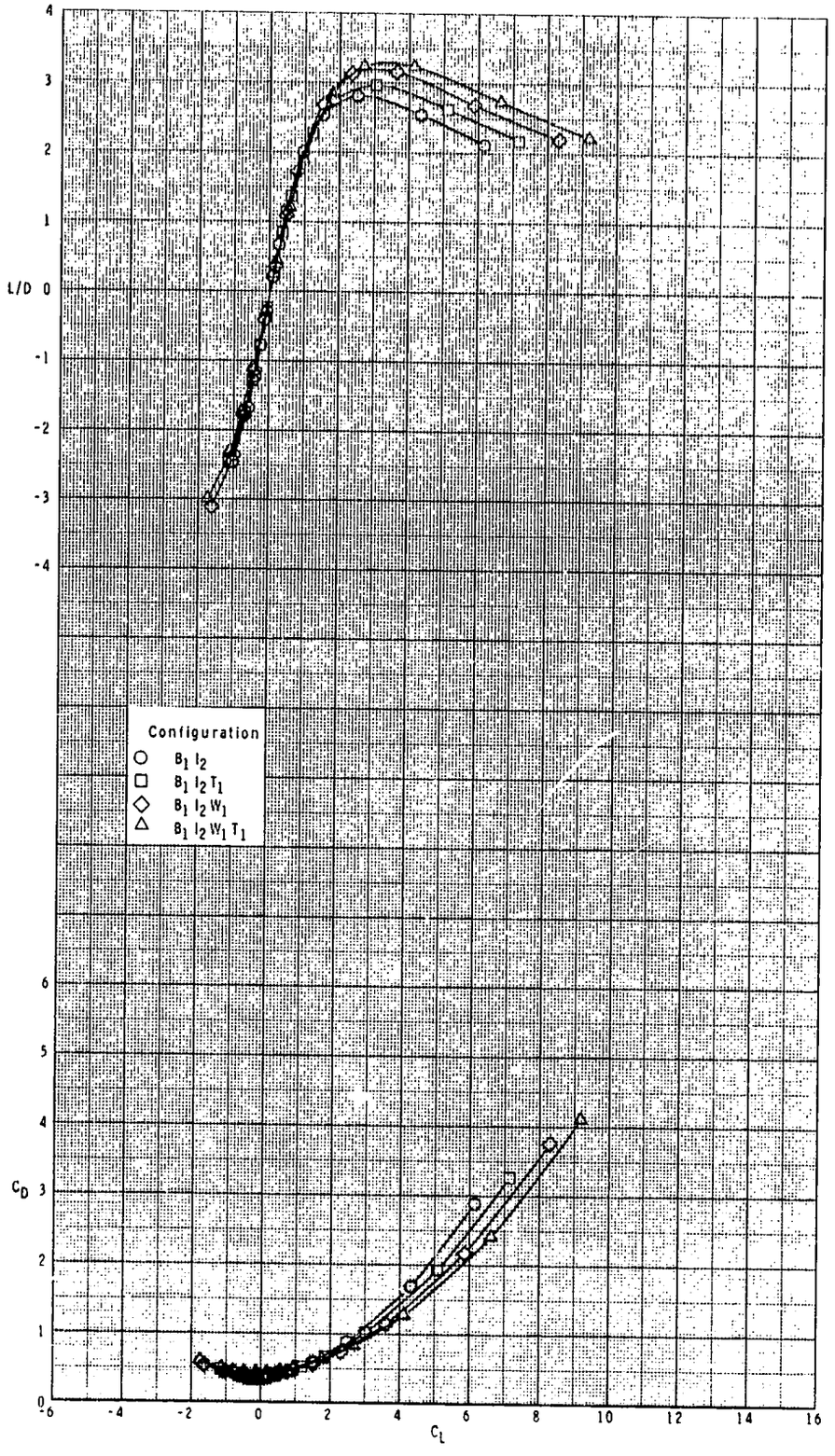

(c) Concluded.

Figure 8.- Continued.

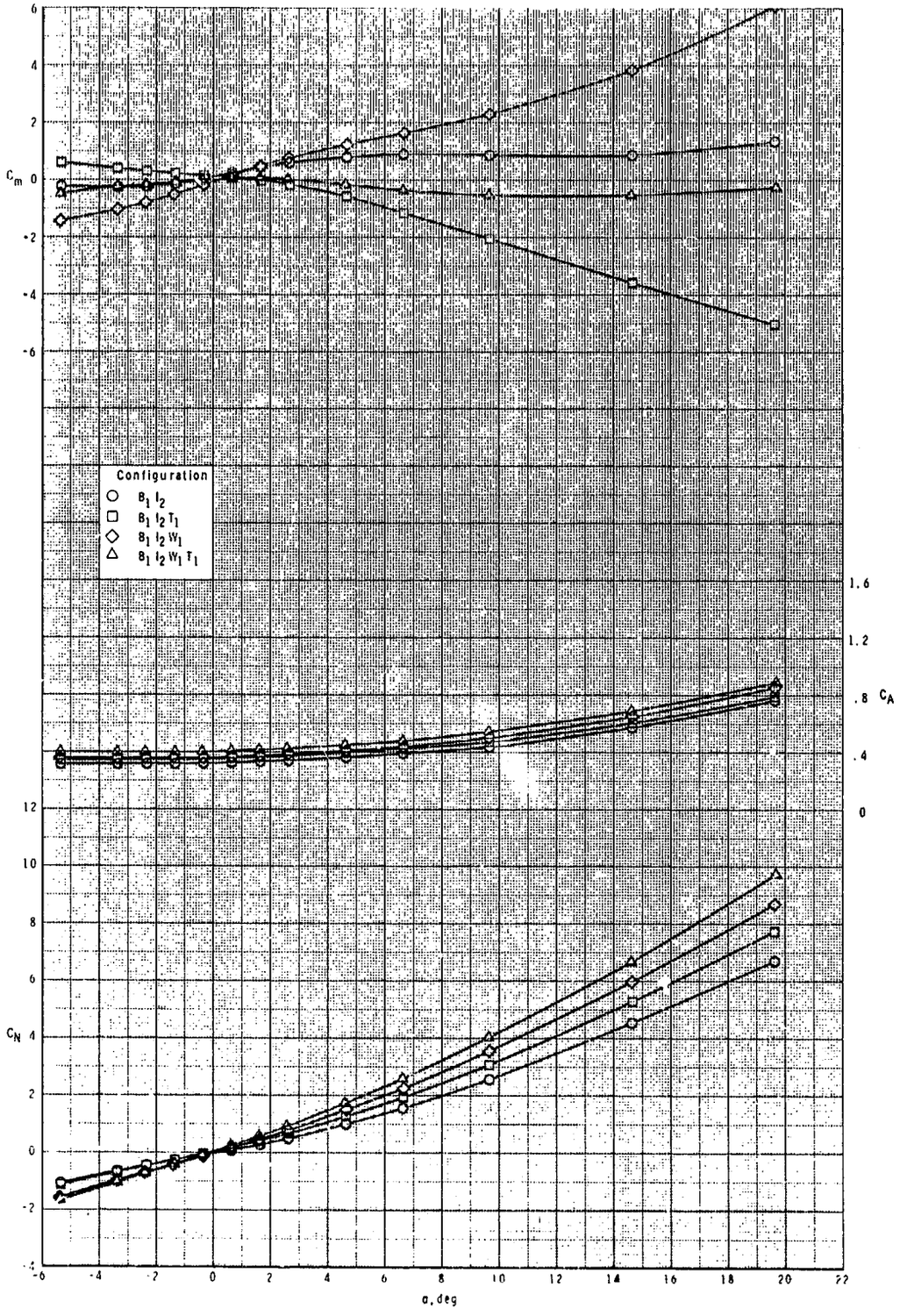

(d) M = 3.95.

Figure 8.- Continued.

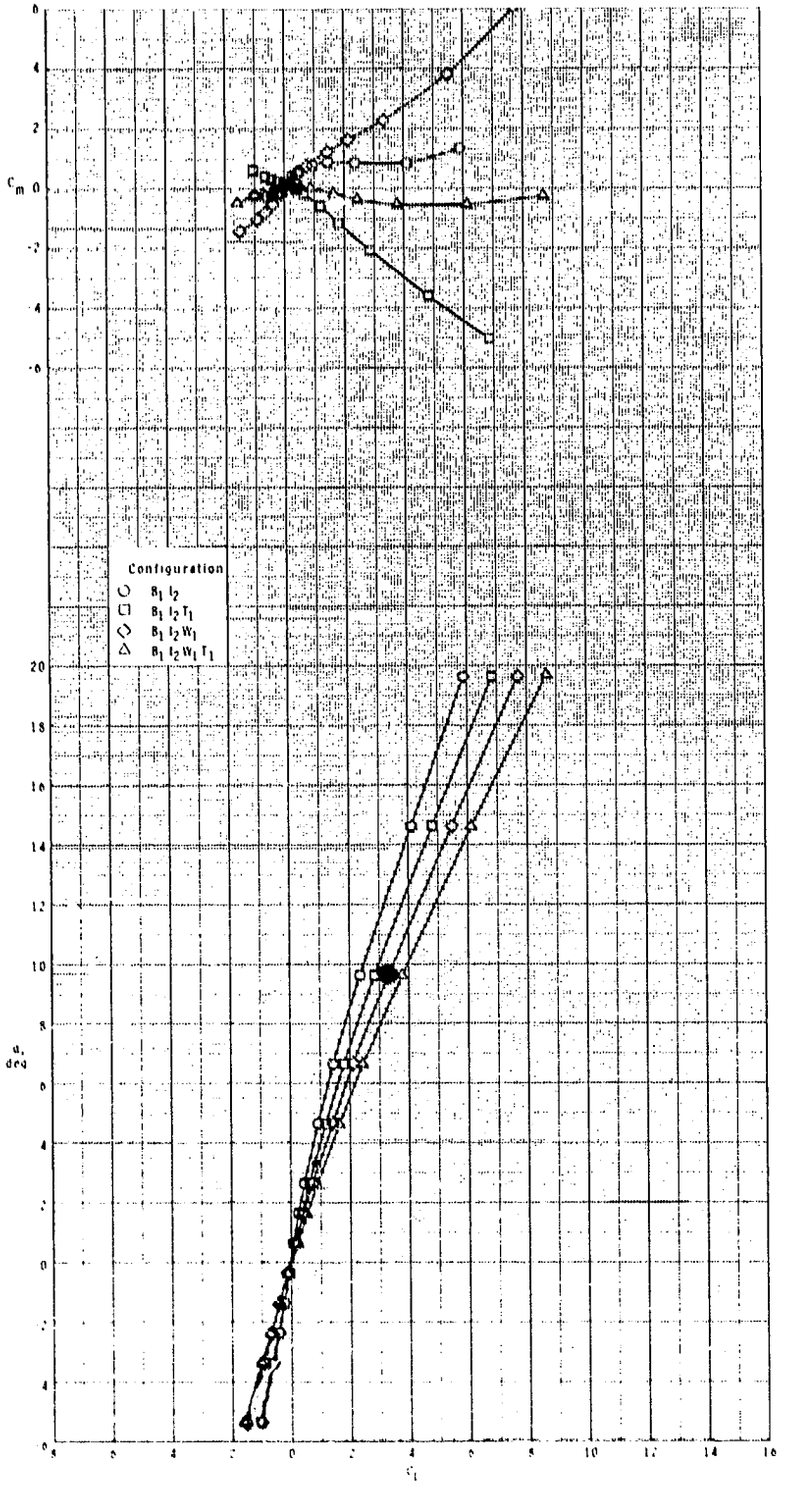

(d) Continued.

Figure 8.- Continued.

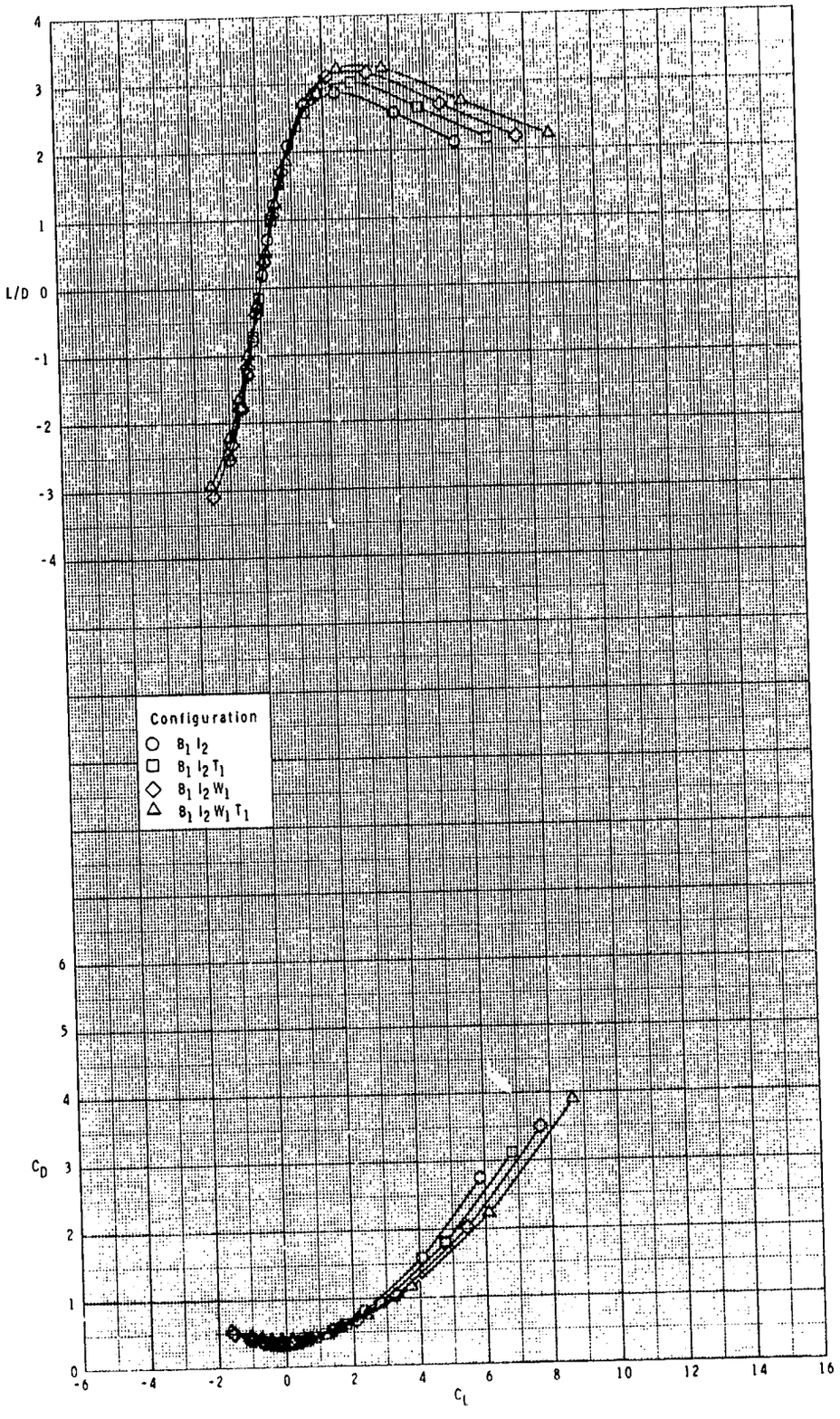

(d) Concluded.

Figure 8.- Concluded.

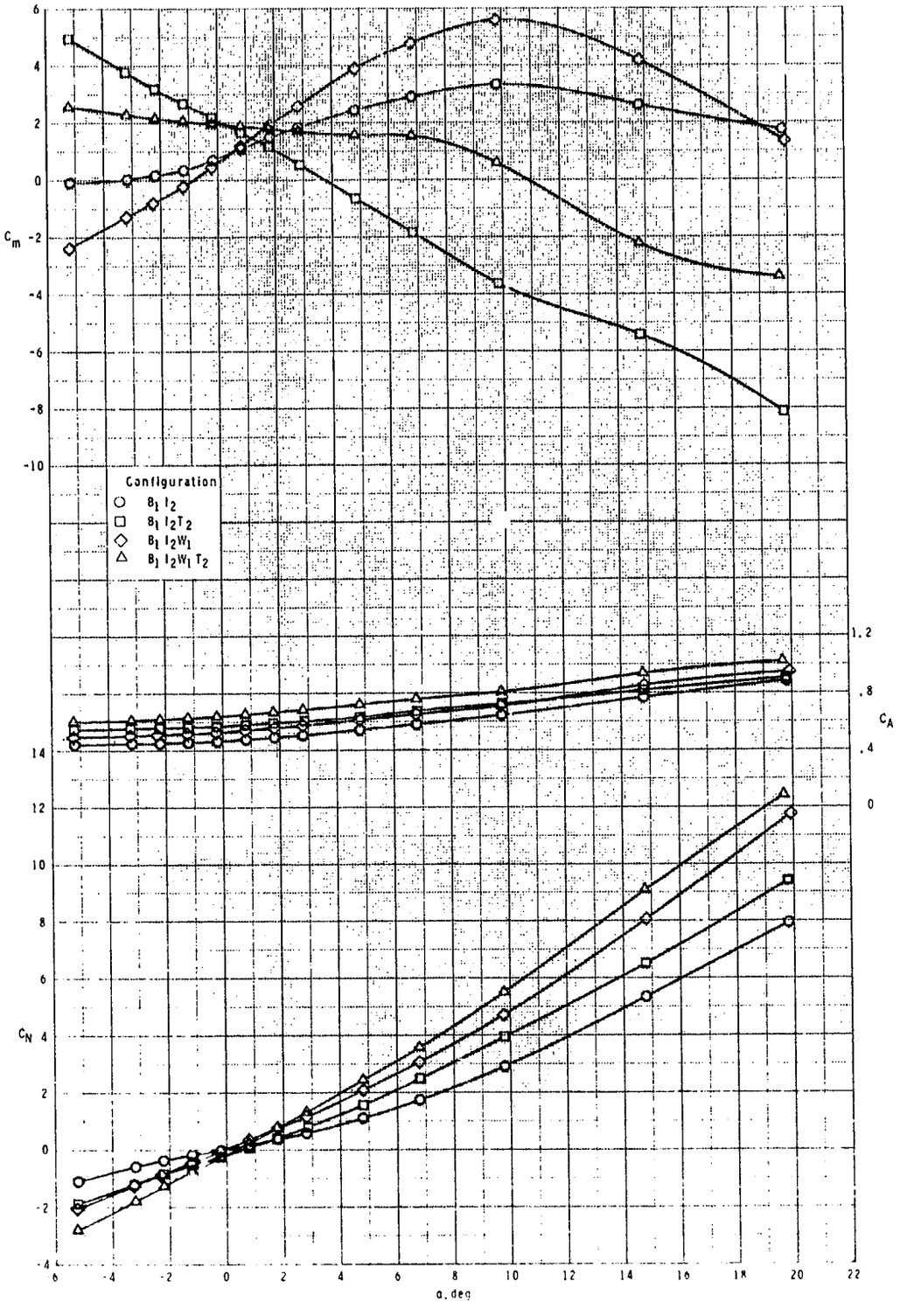

(a) M = 2.50.

Figure 9.- Effect of various model components on longitudinal aerodynamic characteristics for two-dimensional inlets with T_2, $\phi_I = 135°$, and $\delta_p = 0°$.

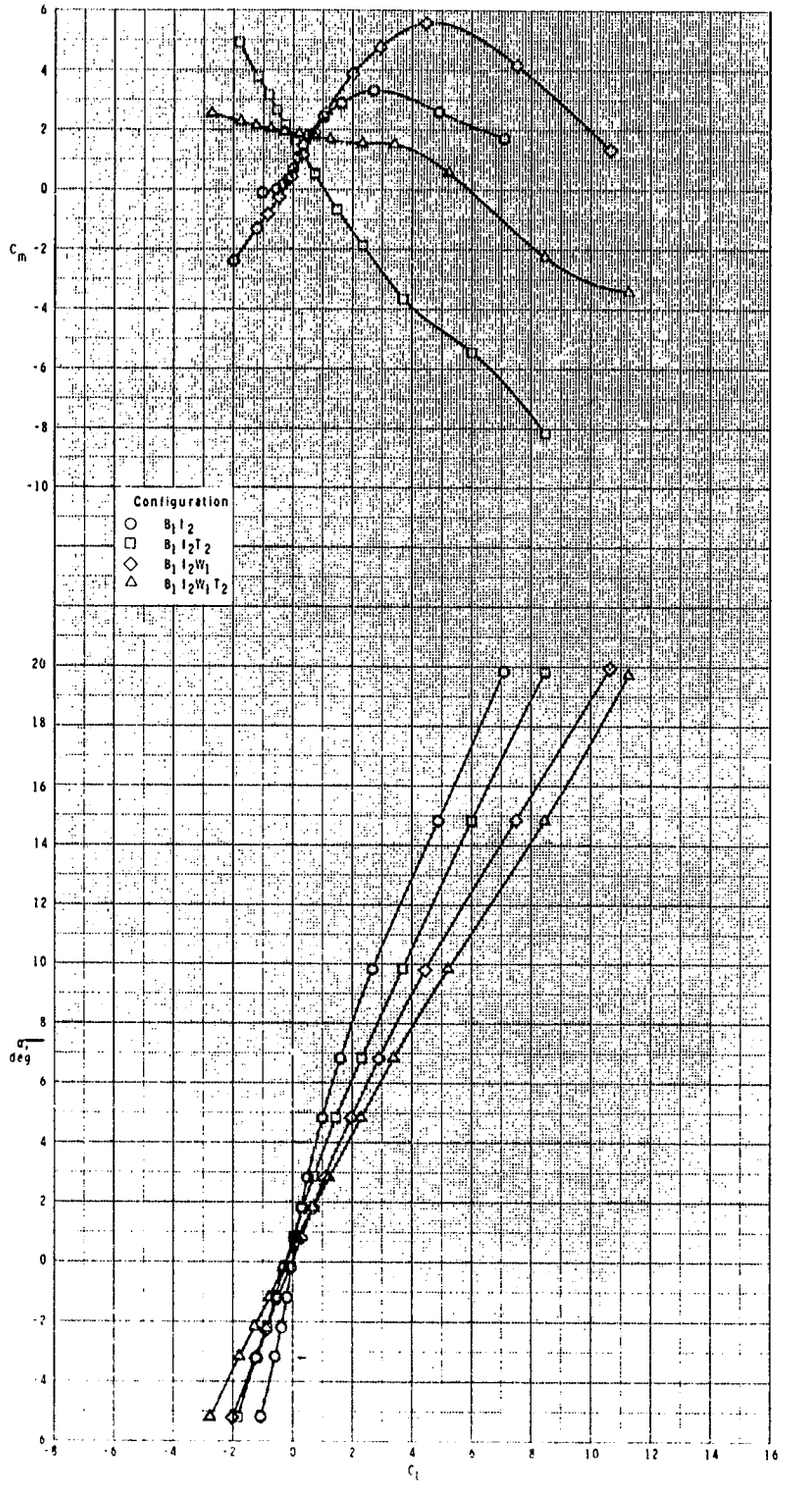

(a) Continued.

Figure 9.- Continued.

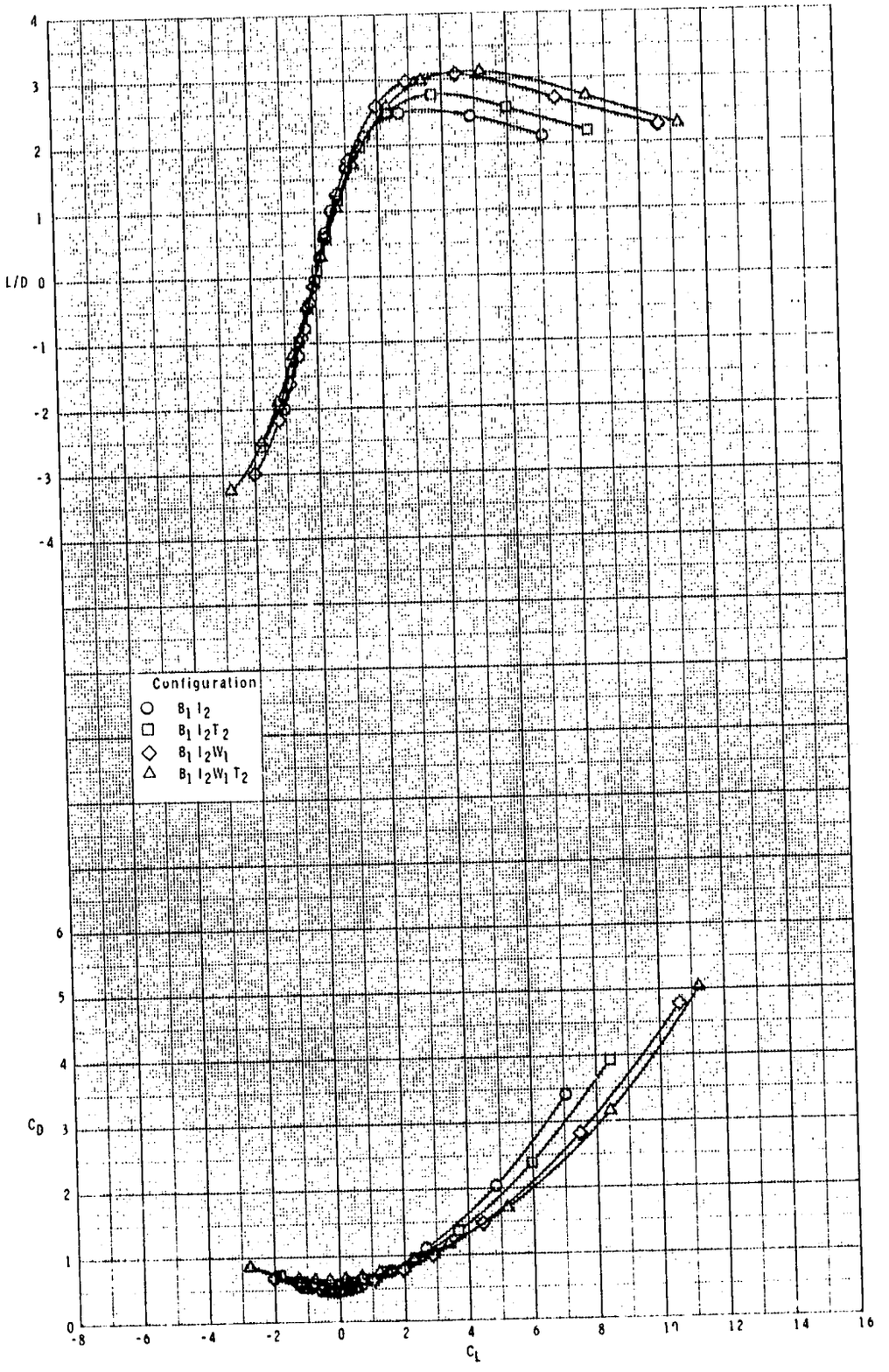

(a) Concluded.

Figure 9.- Continued.

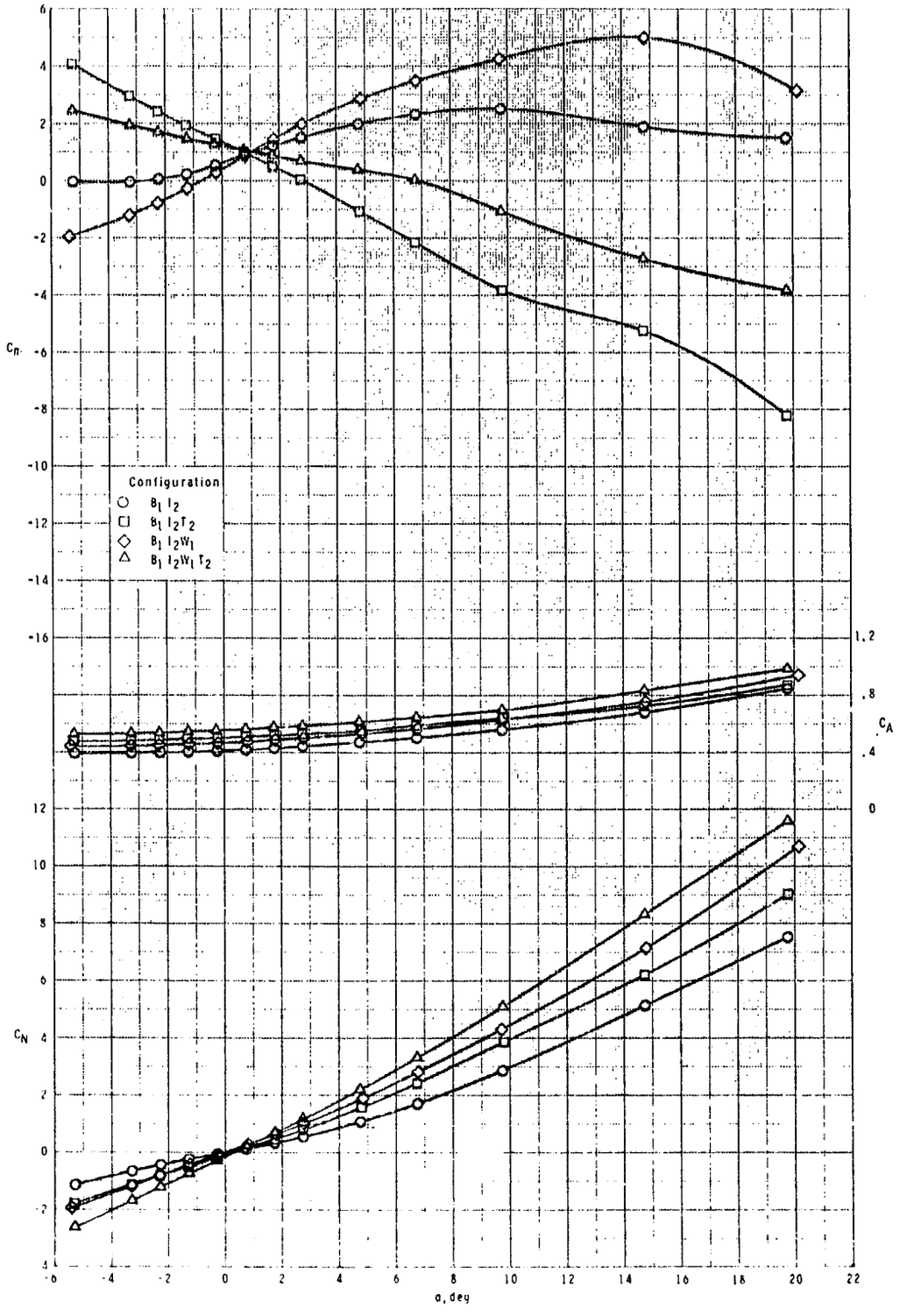

(b) M = 2.95.

Figure 9.- Continued.

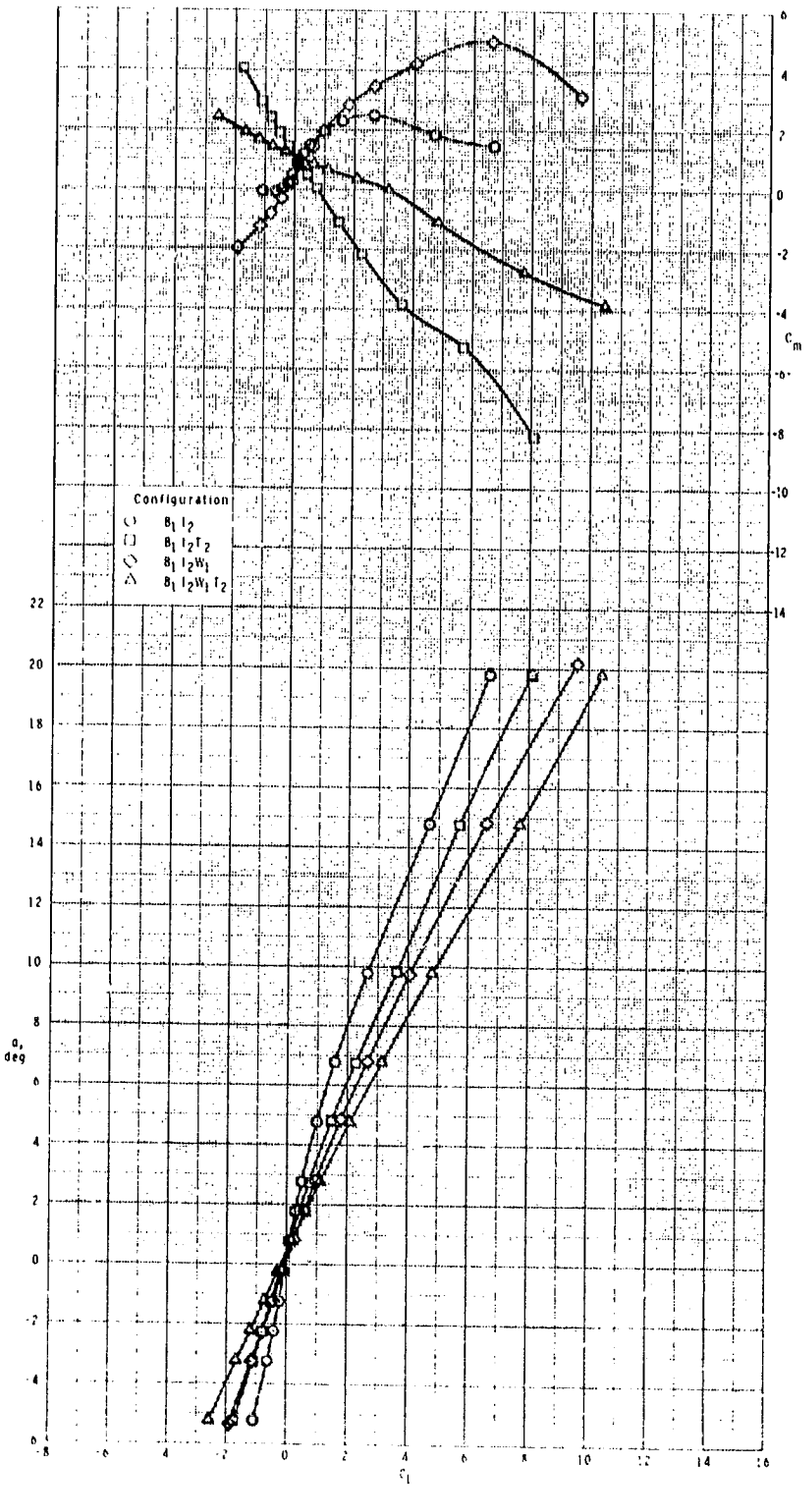

(b) Continued.

Figure 9.- Continued.

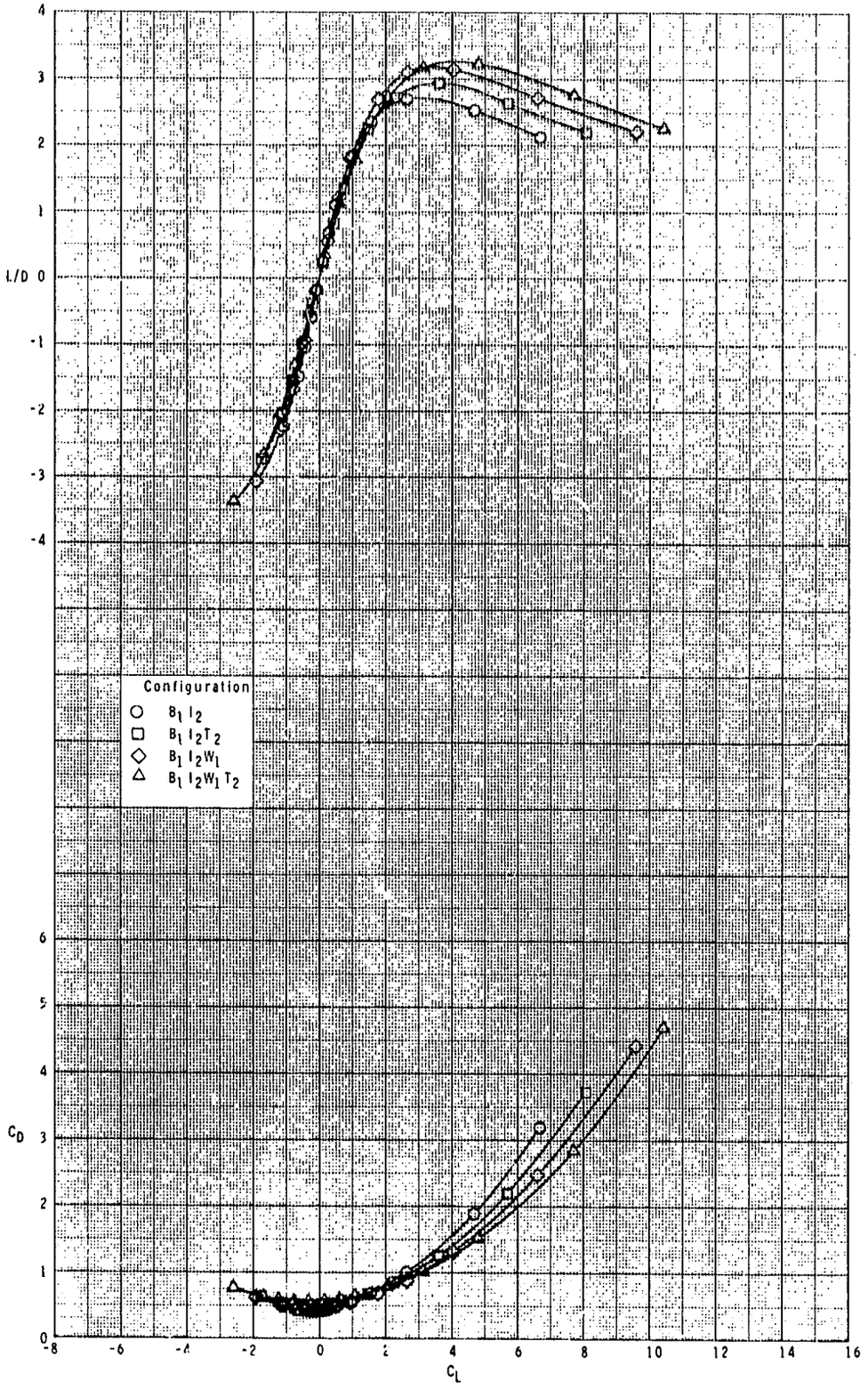

(b) Concluded.

Figure 9.- Continued.

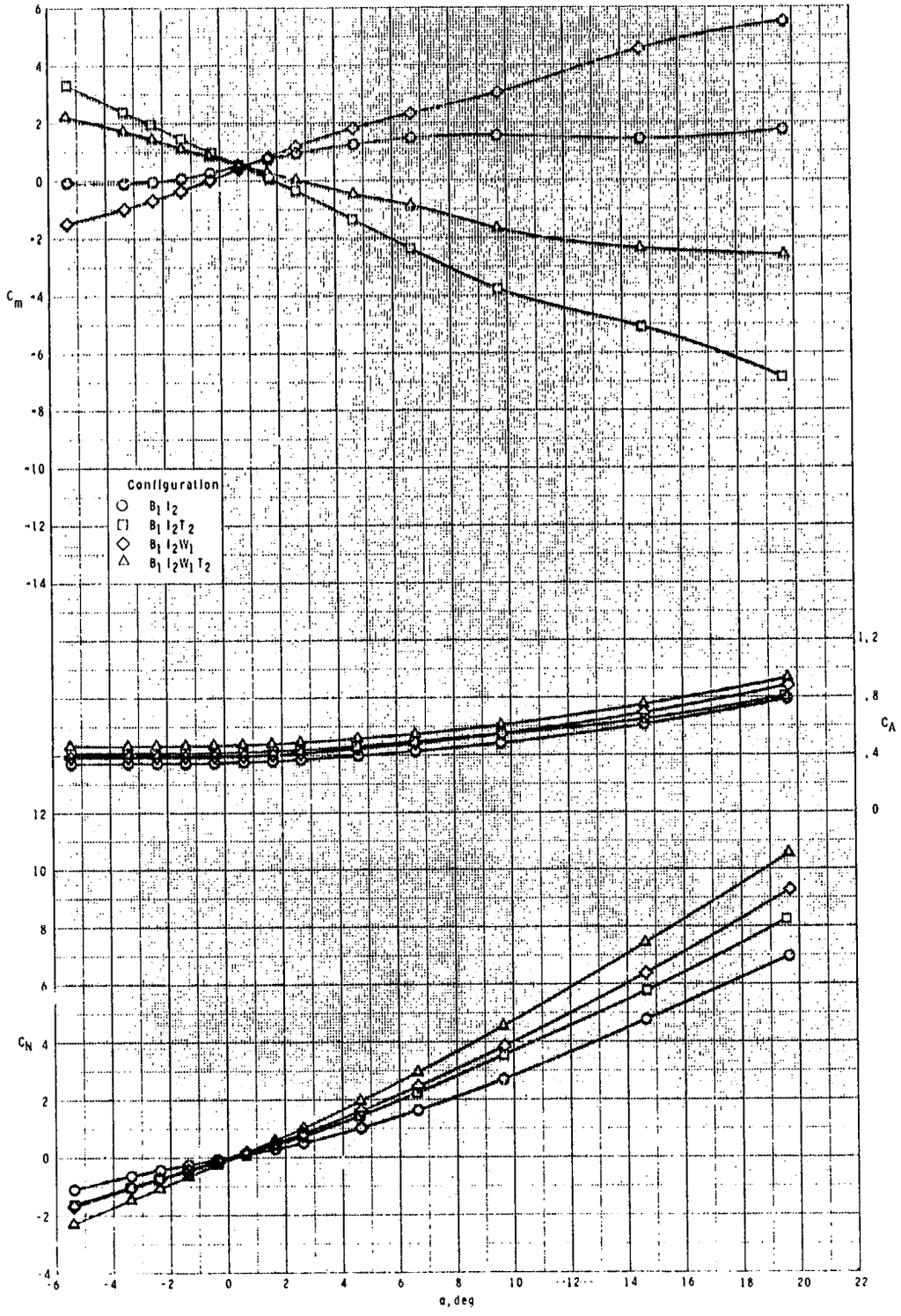

(c) M = 3.50.

Figure 9.- Continued.

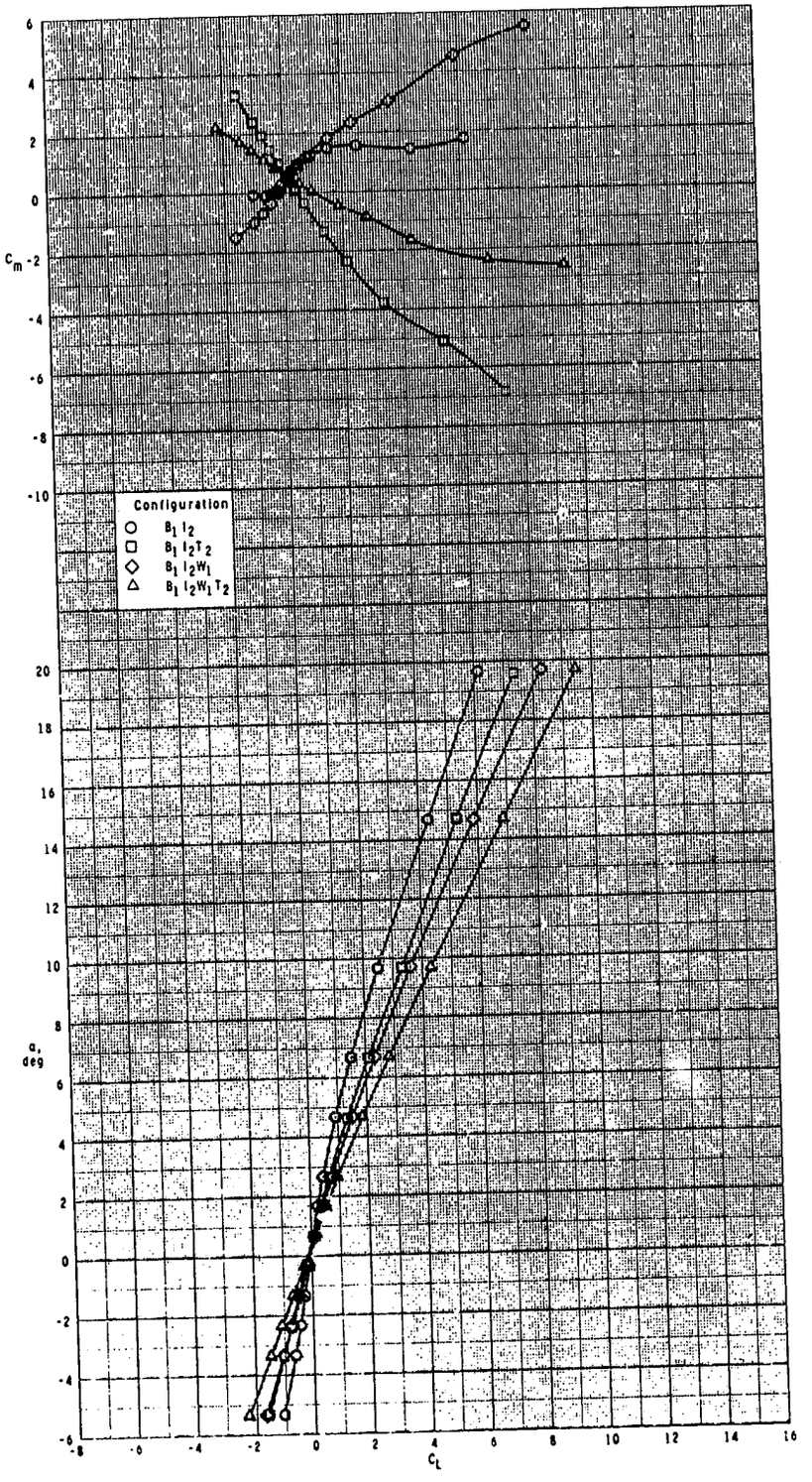

(c) Continued.

Figure 9.- Continued.

C - 2

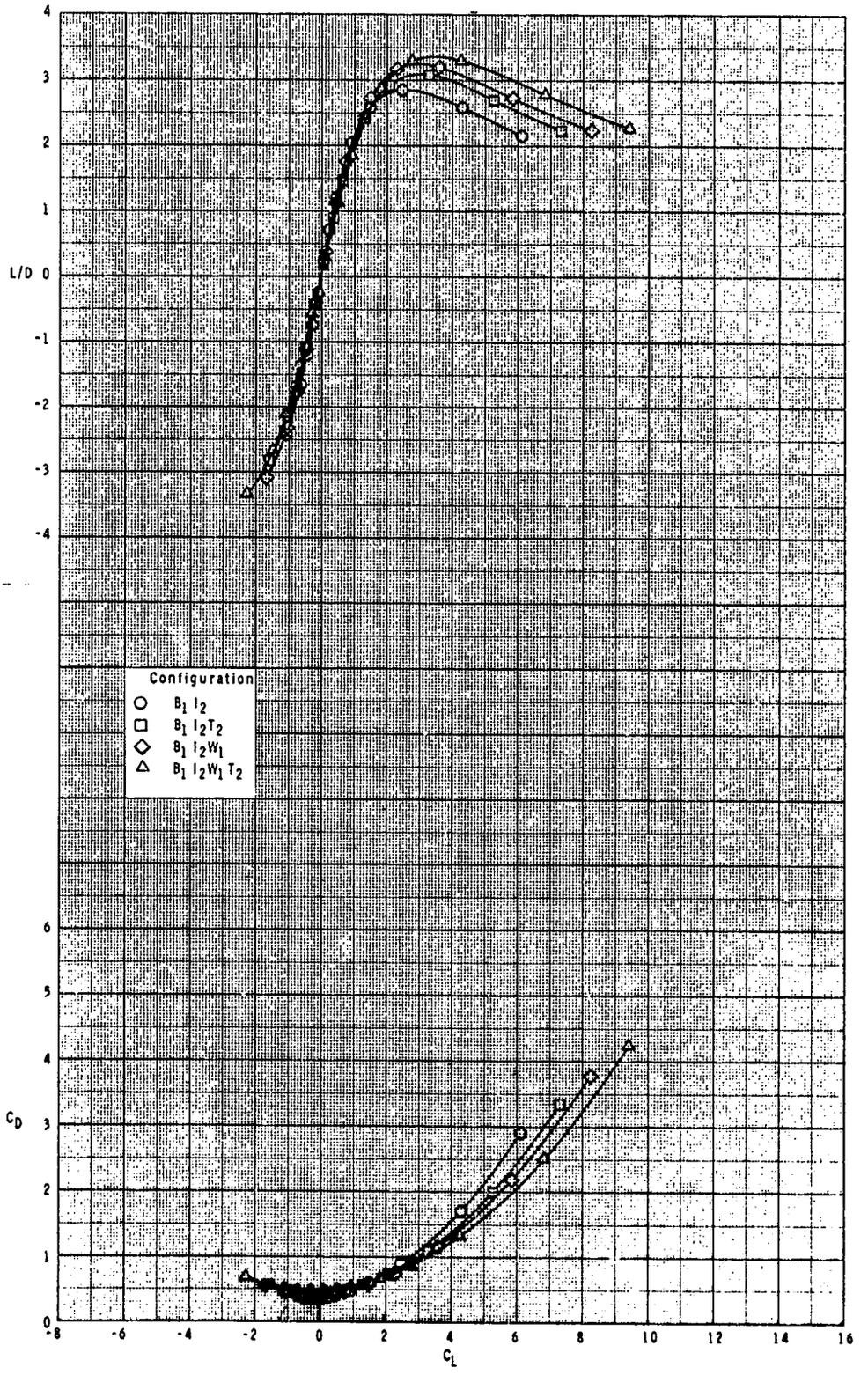

(c) Concluded.

Figure 9.- Continued.

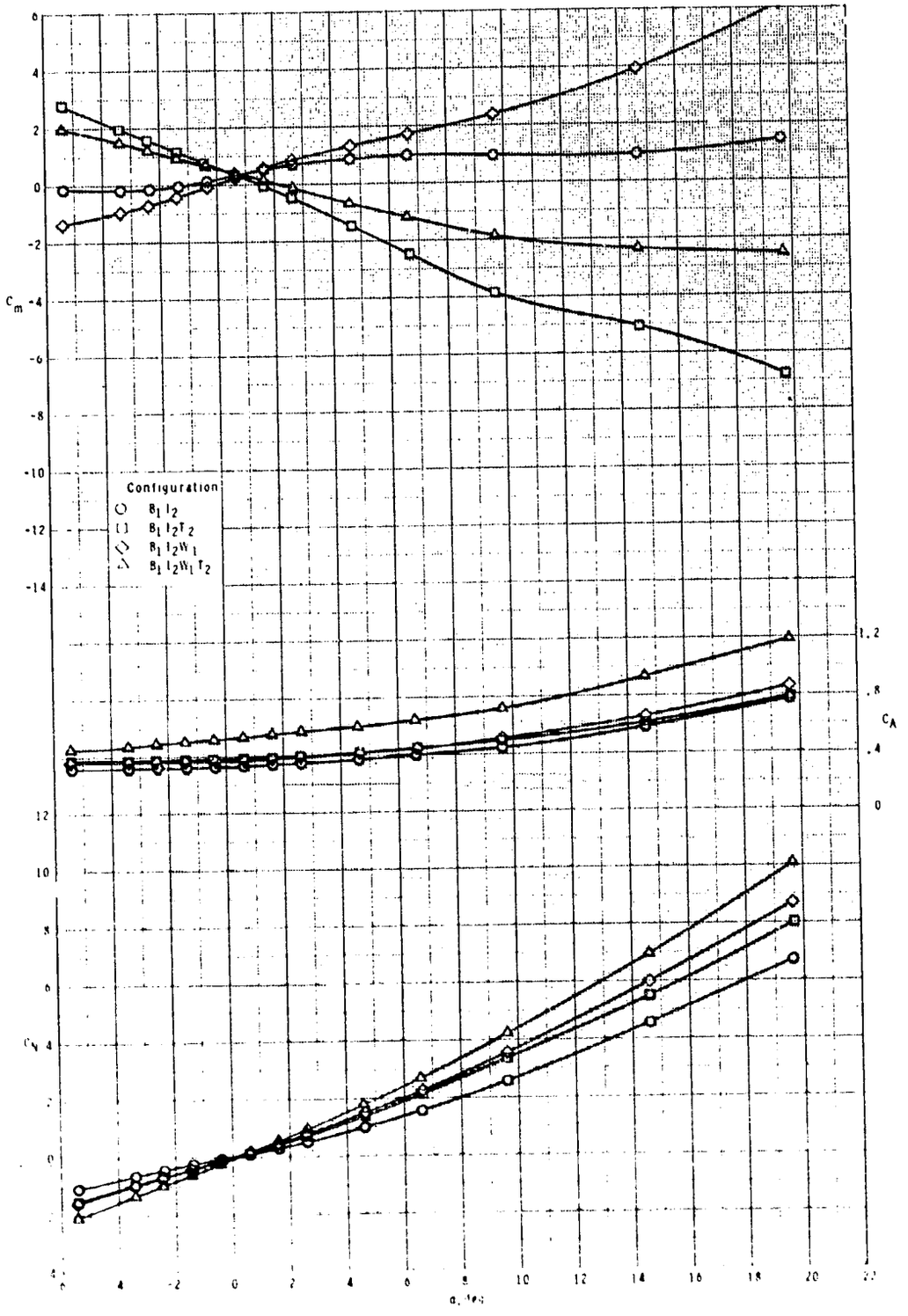

(d) M = 3.95.

Figure 9.- Continued.

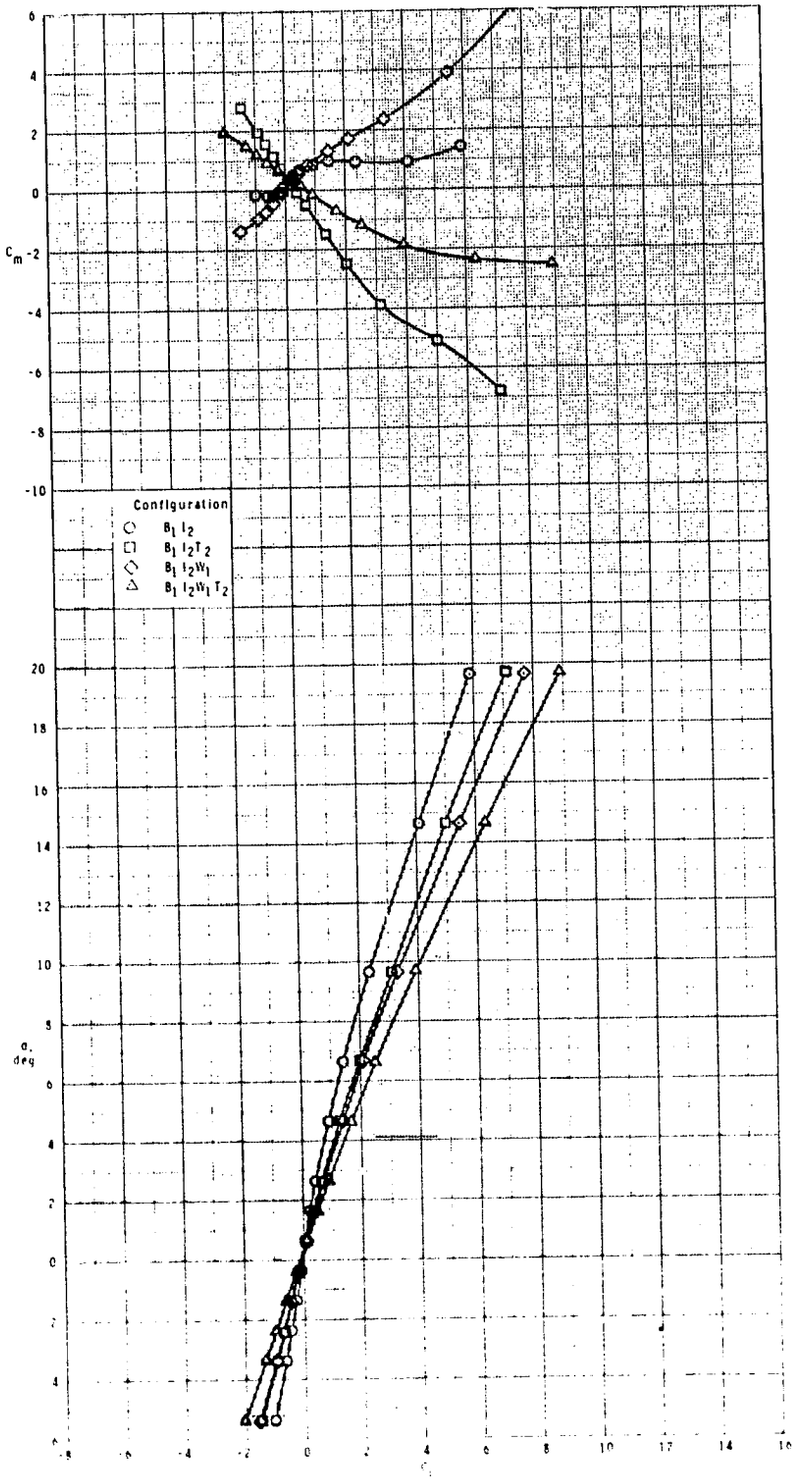

(d) Continued.

Figure 9.- Continued.

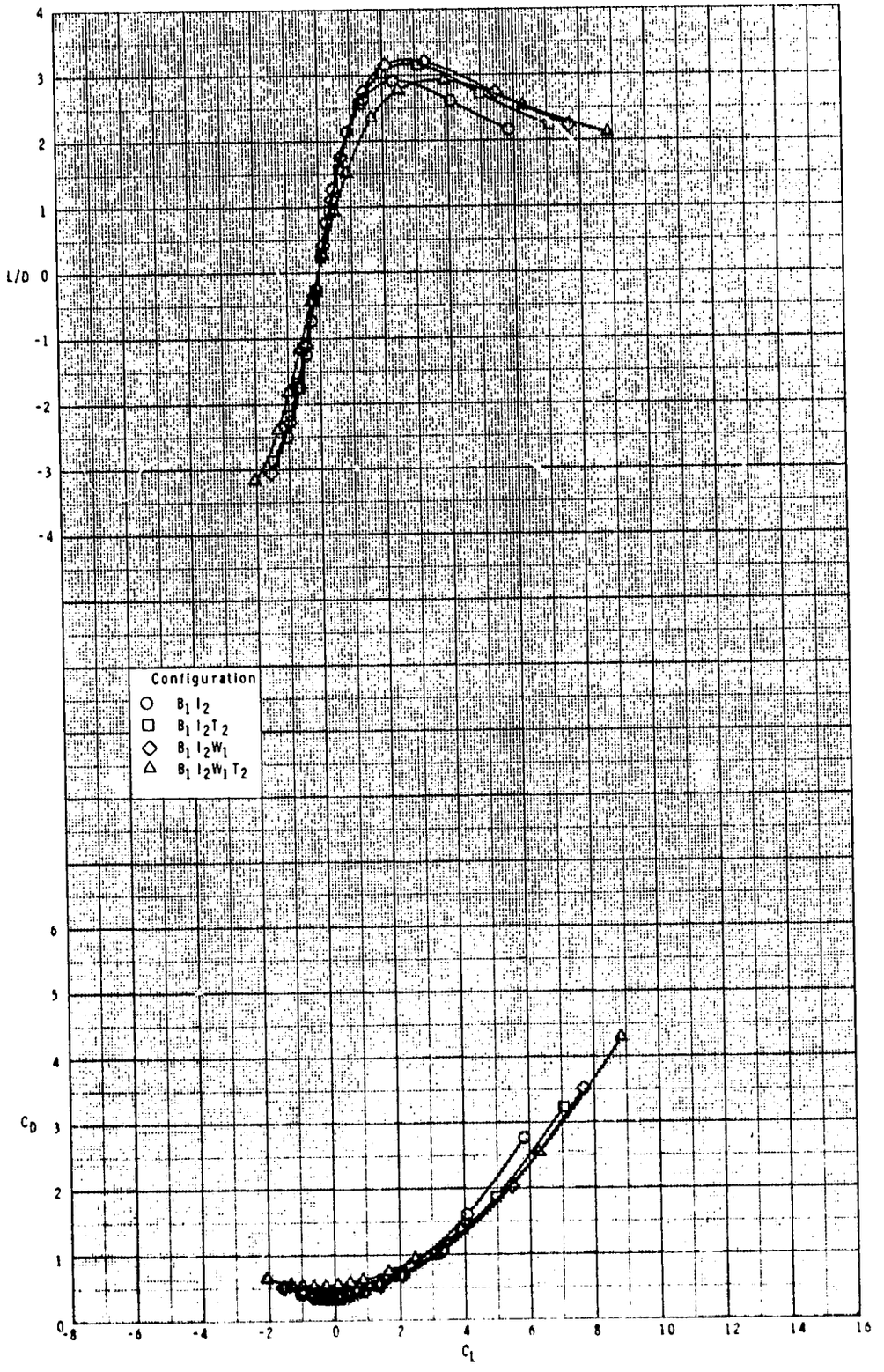

(d) Concluded.

Figure 9.- Concluded.

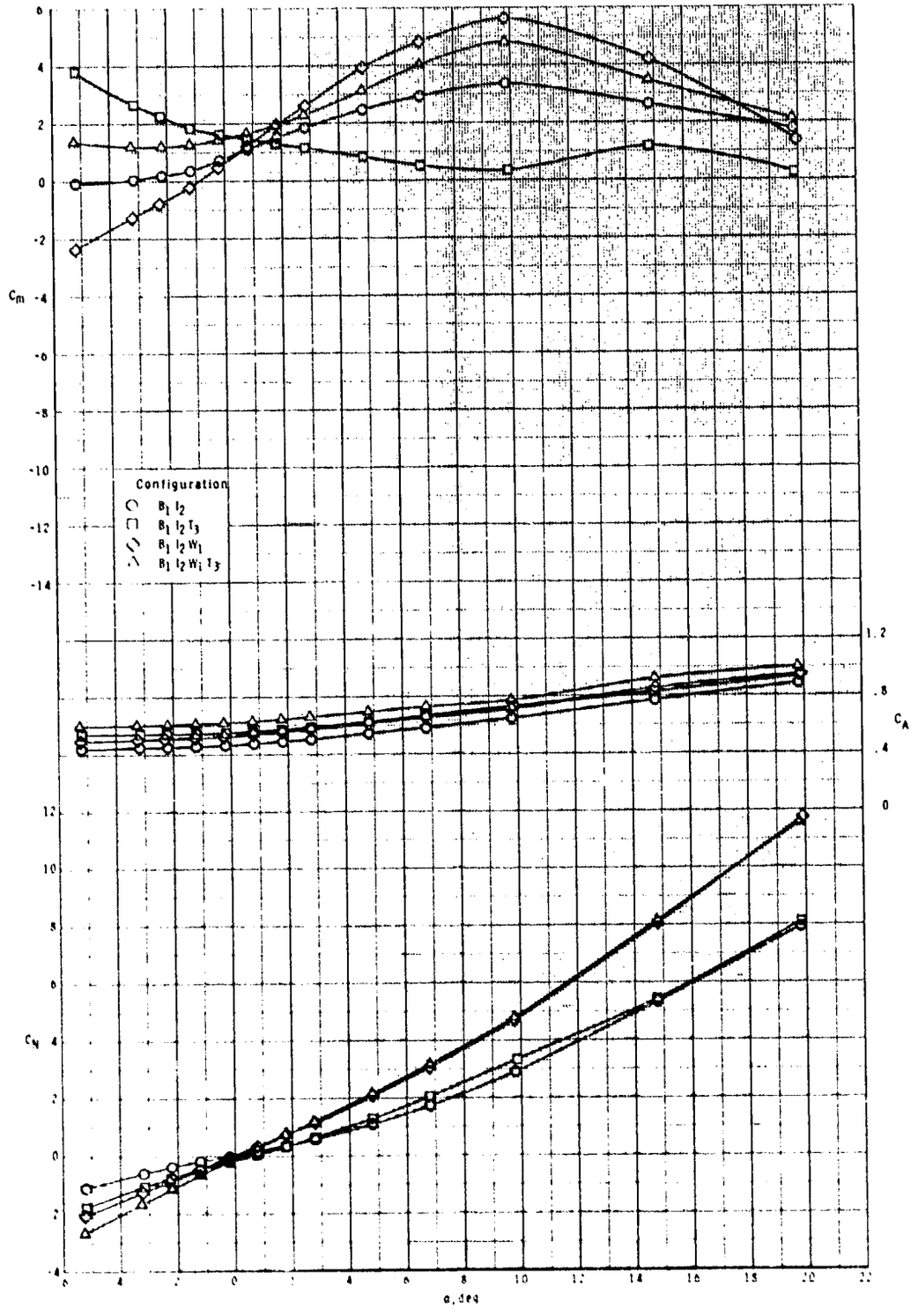

(a) M = 2.50.

Figure 10.- Effect of various model components on longitudinal aerodynamic characteristics for two-dimensional inlets with T_3, $\phi_I = 135°$, and $\delta_p = 0°$.

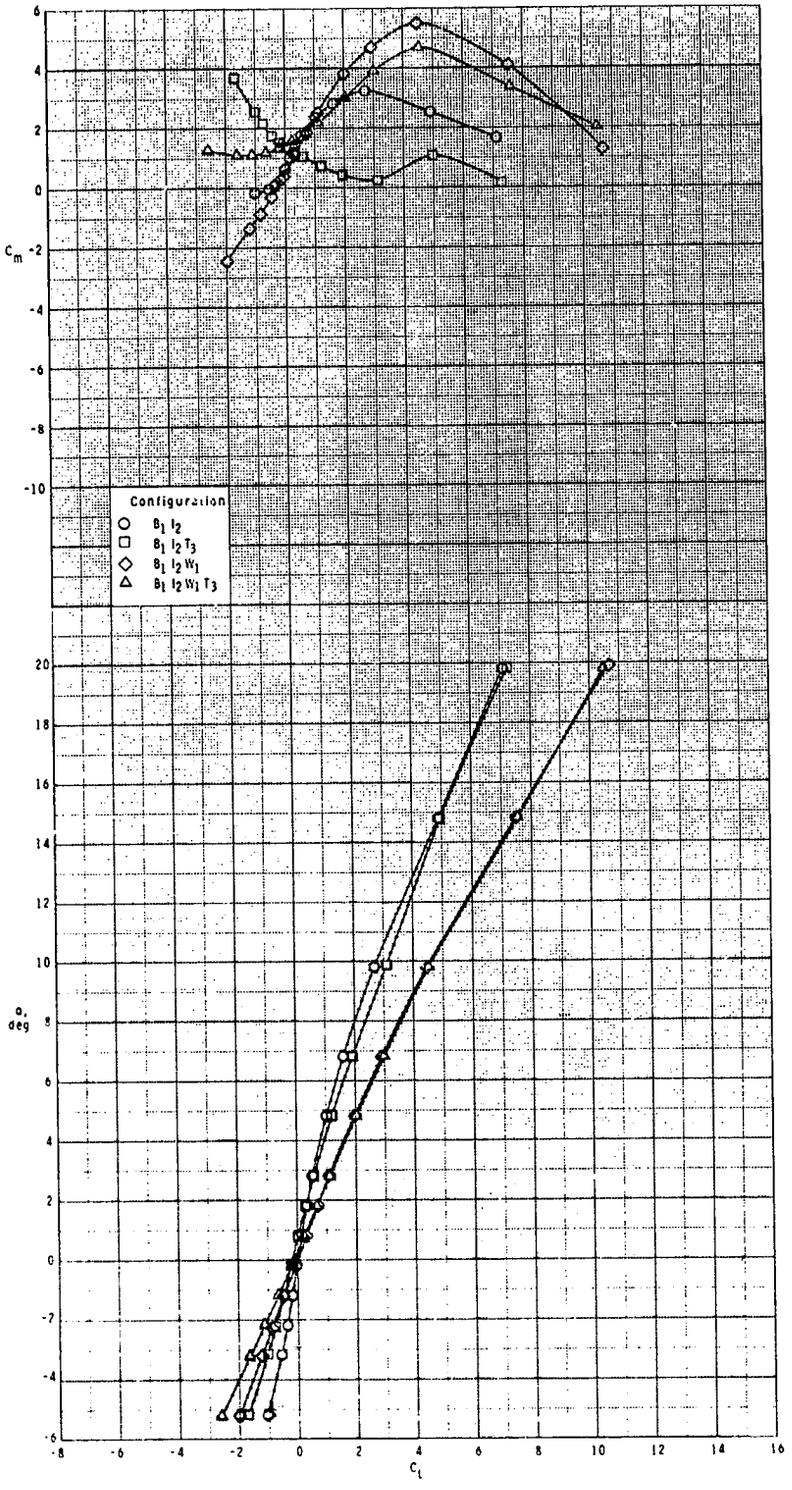

(a) Continued.

Figure 10.- Continued.

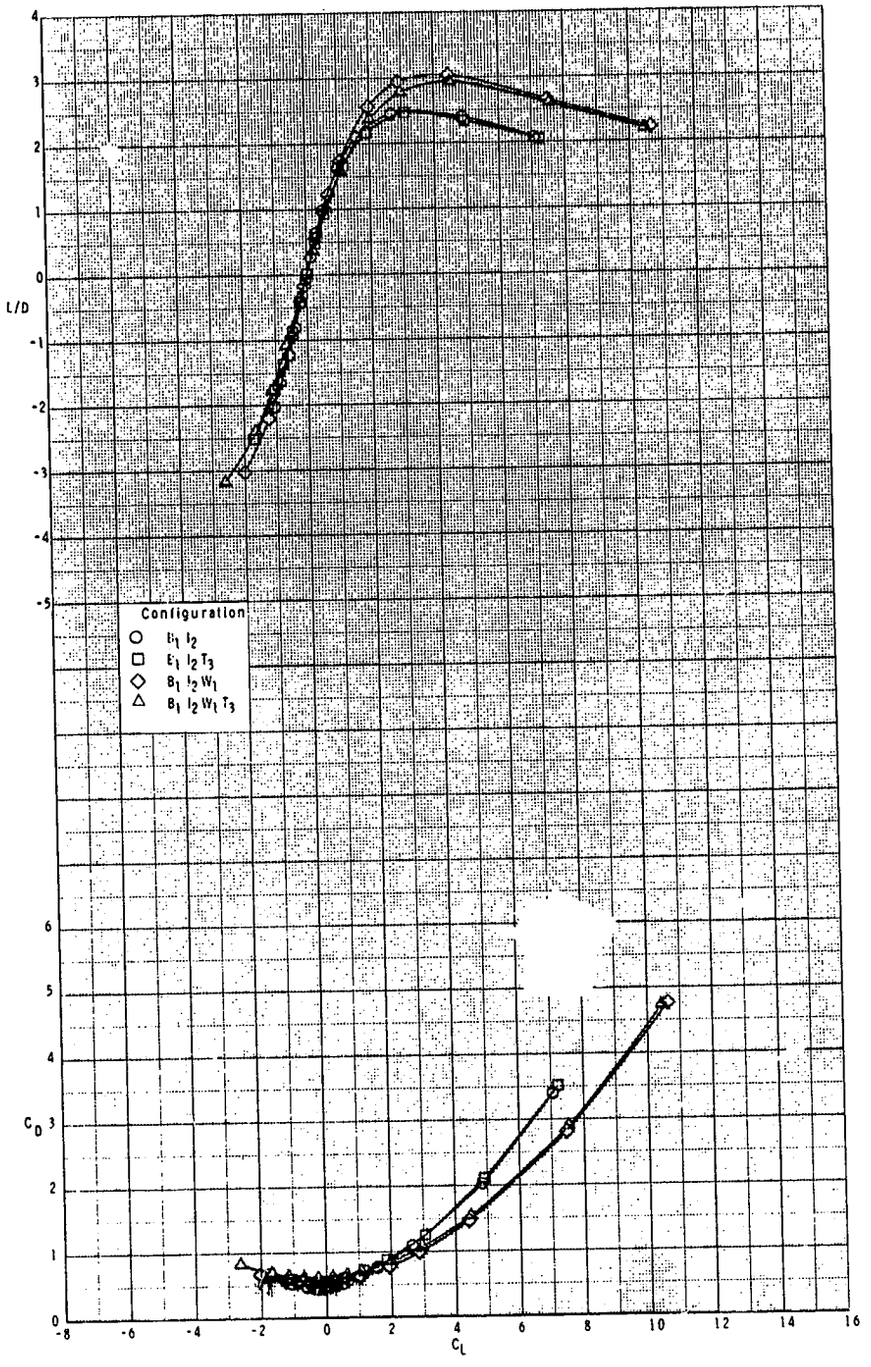

(a) Concluded.

Figure 10.- Continued.

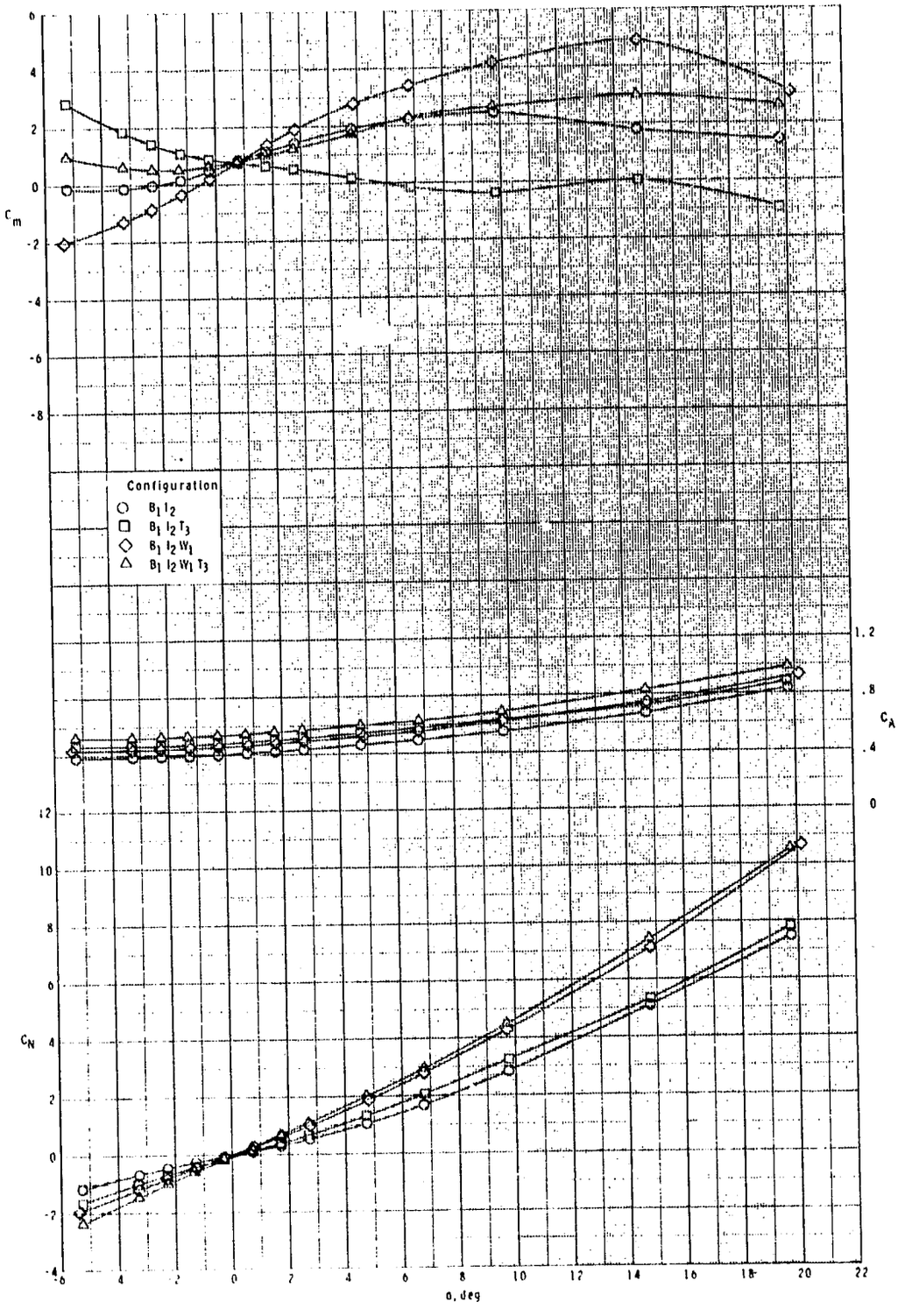

(b) M = 2.95.

Figure 10.- Continued.

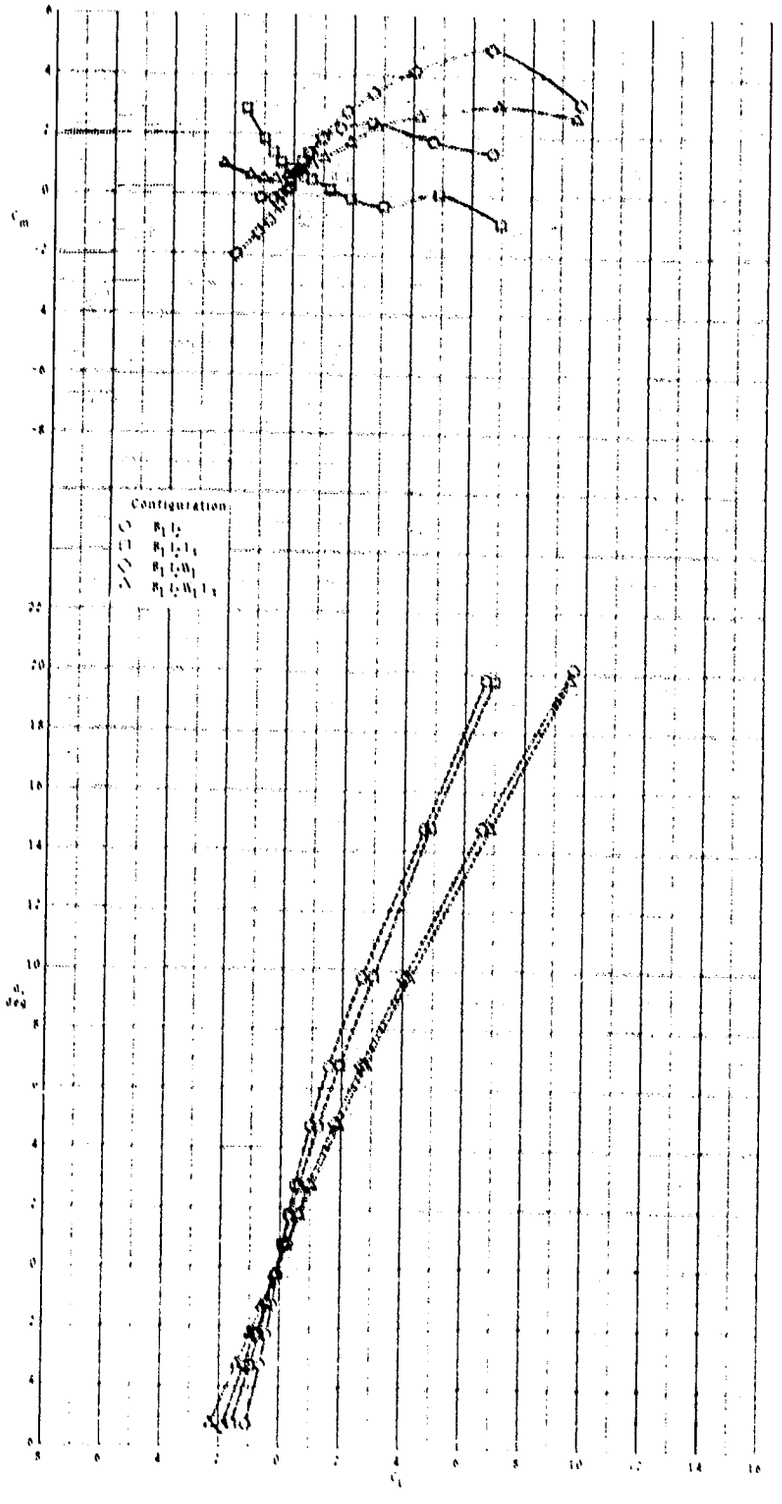

(b) Continued.

Figure 10.- Continued.

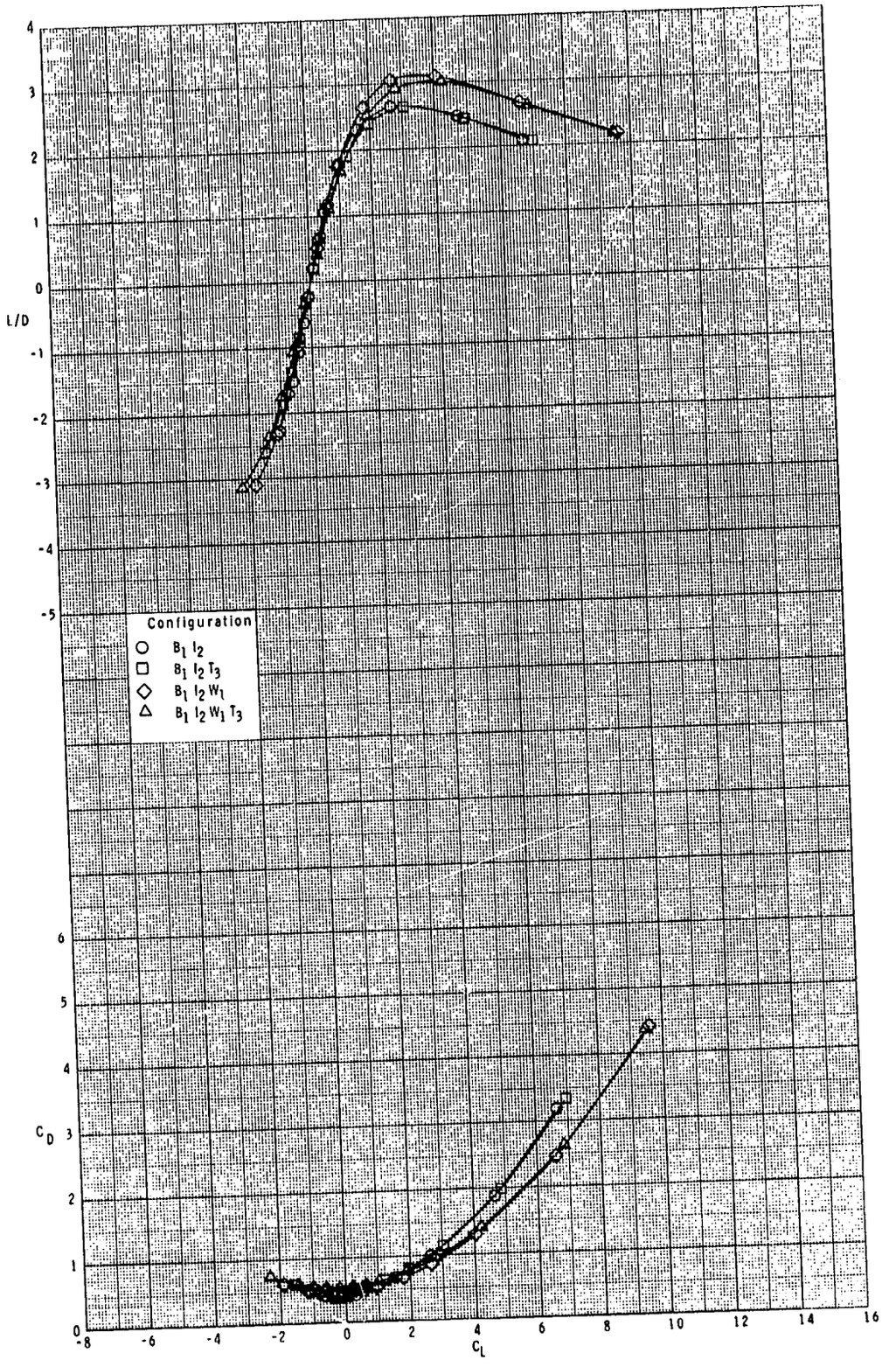

(b) Concluded.

Figure 10.- Continued.

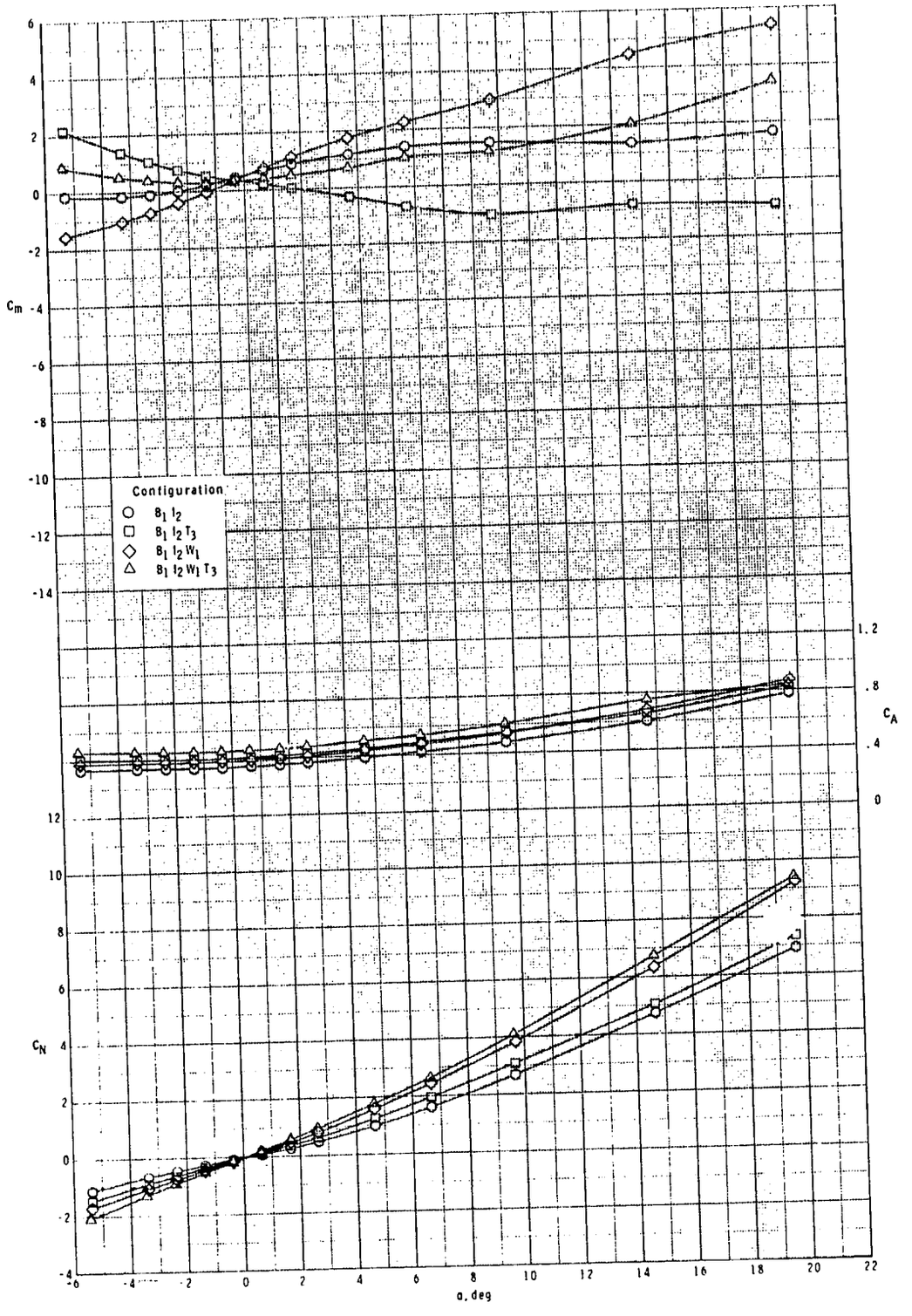

(c) M = 3.50.

Figure 10.- Continued.

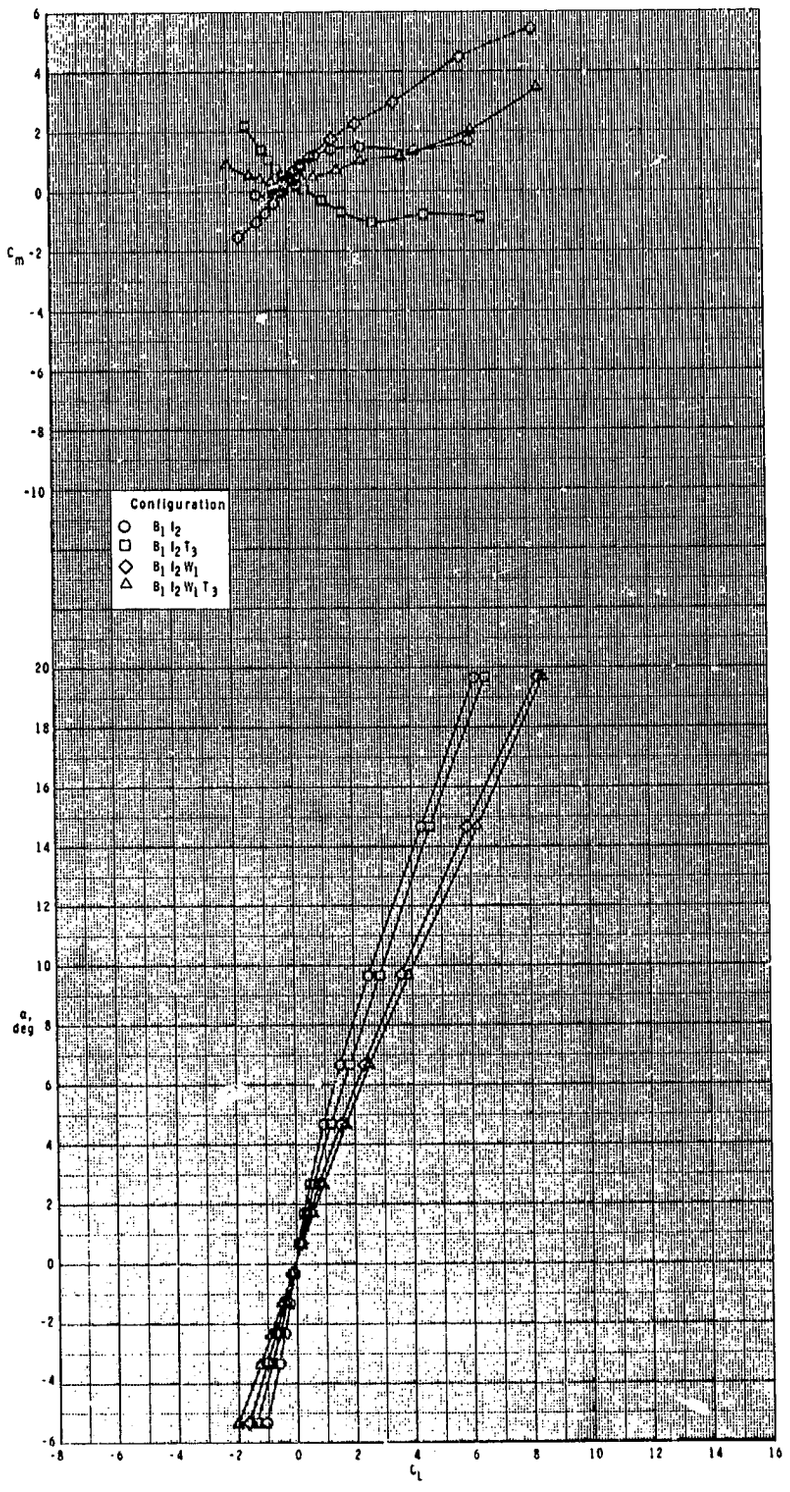

(c) Continued.

Figure 10.- Continued.

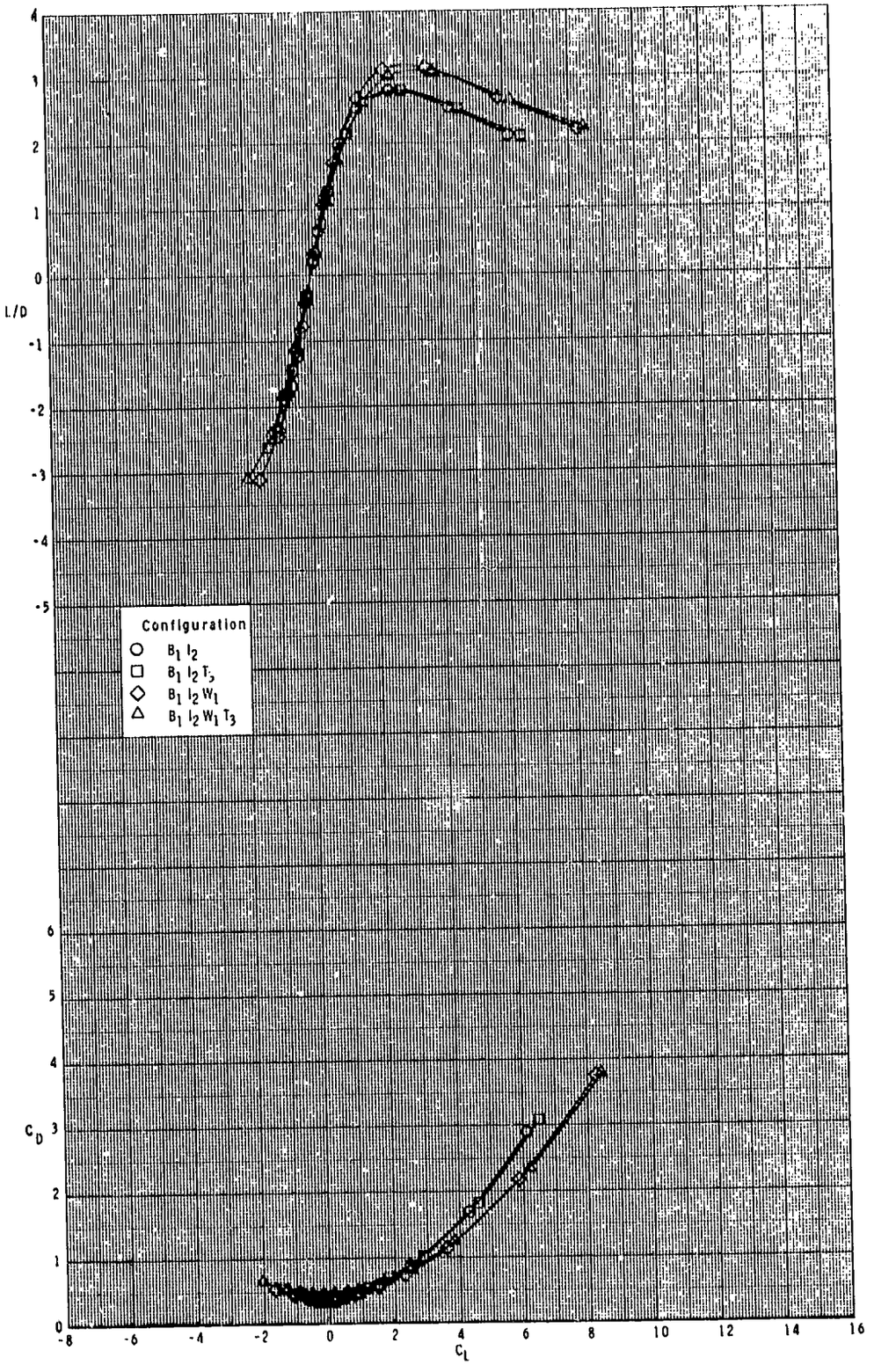

(c) Concluded.

Figure 10.- Continued.

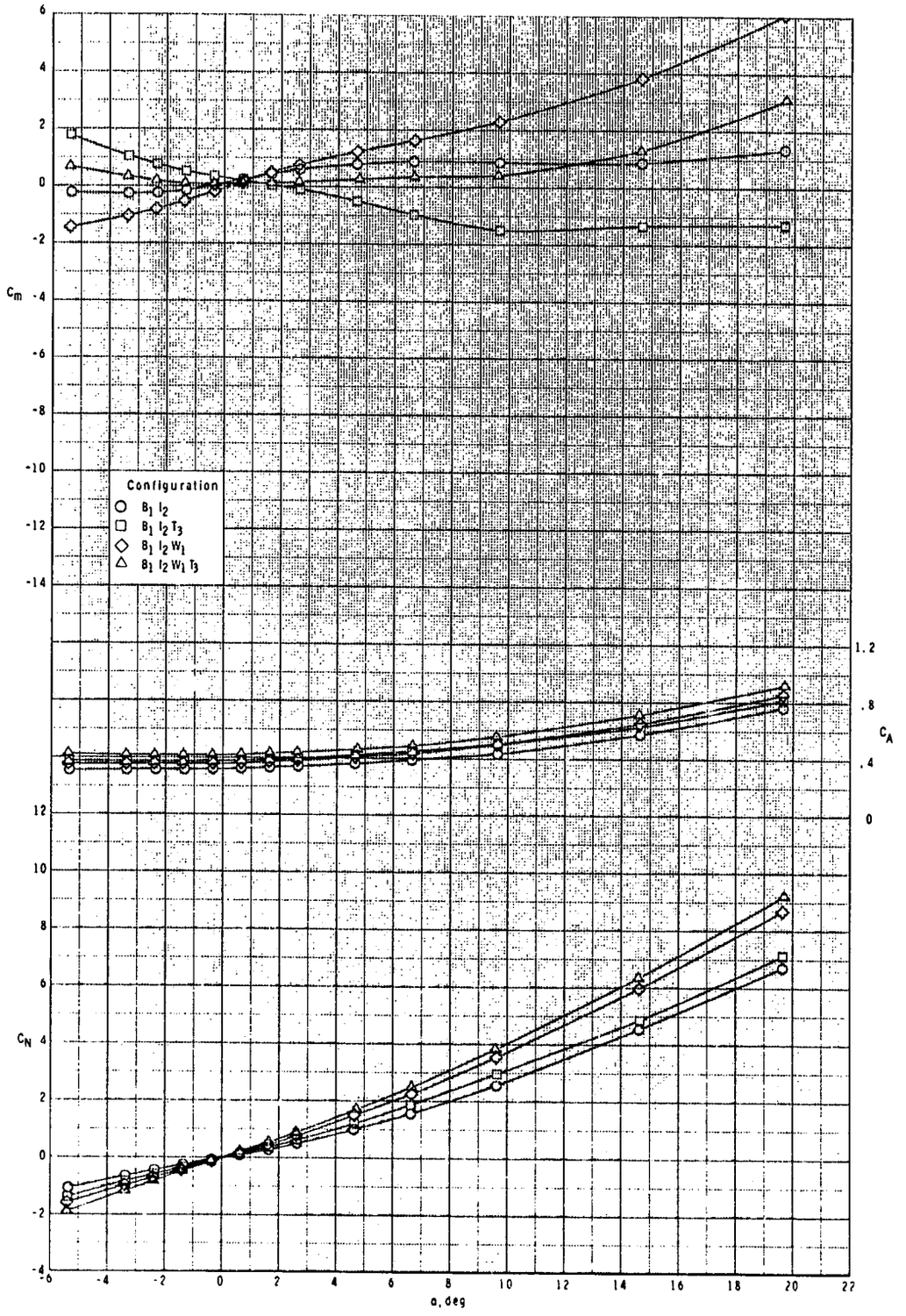

(d) M = 3.95.

Figure 10.- Continued.

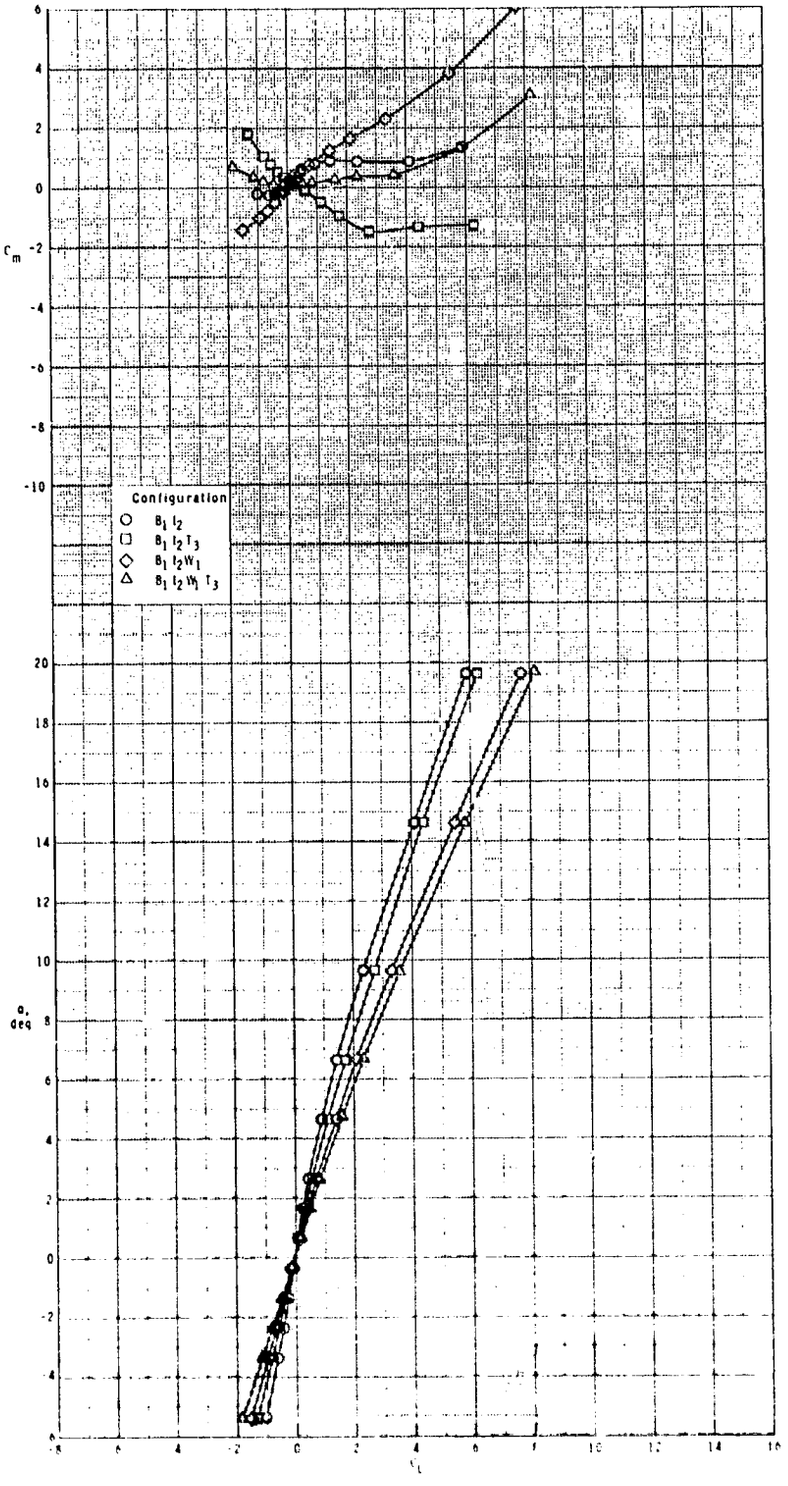

(d) Continued.

Figure 10.- Continued.

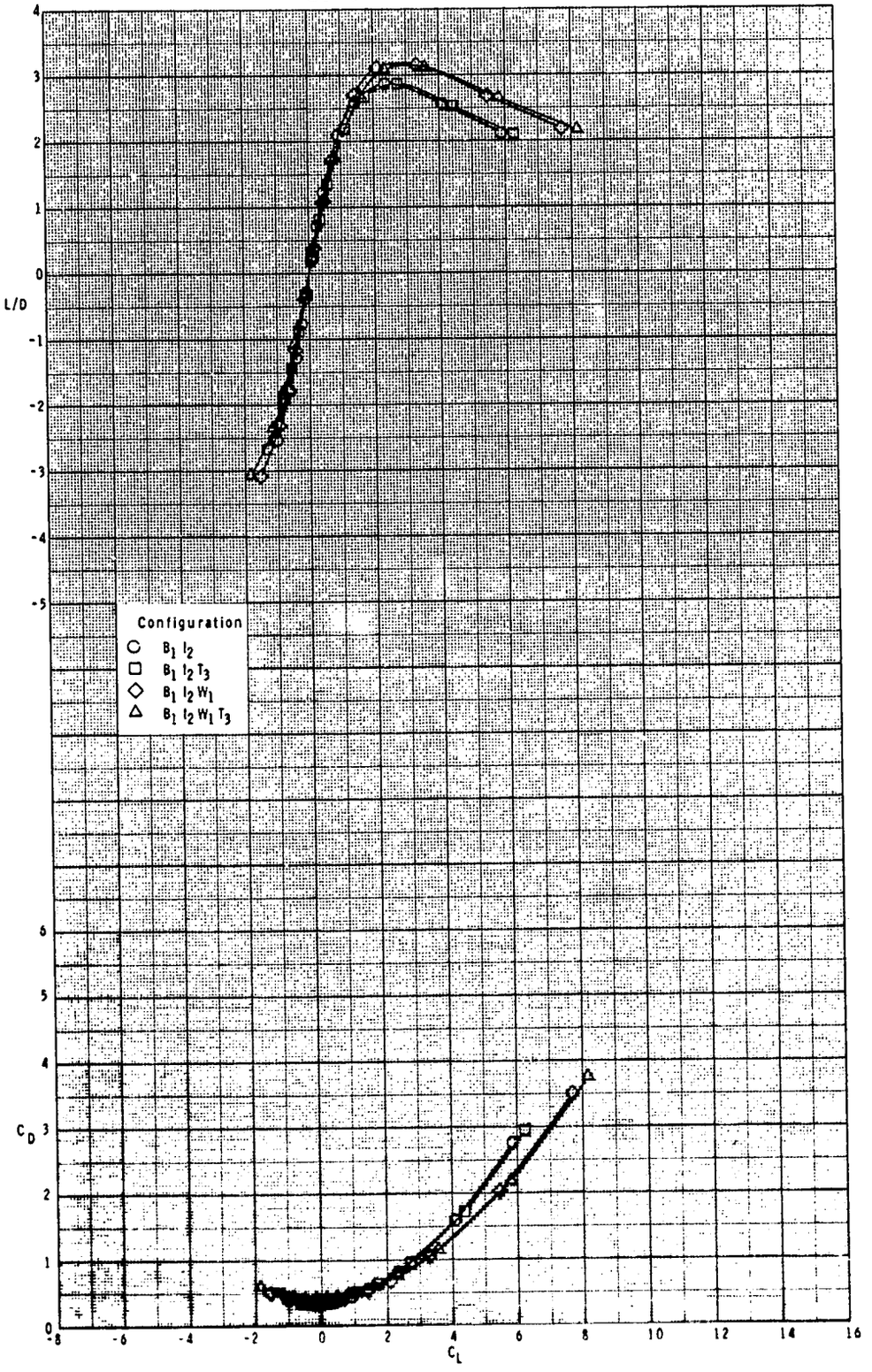

(d) Concluded.

Figure 10.- Concluded.

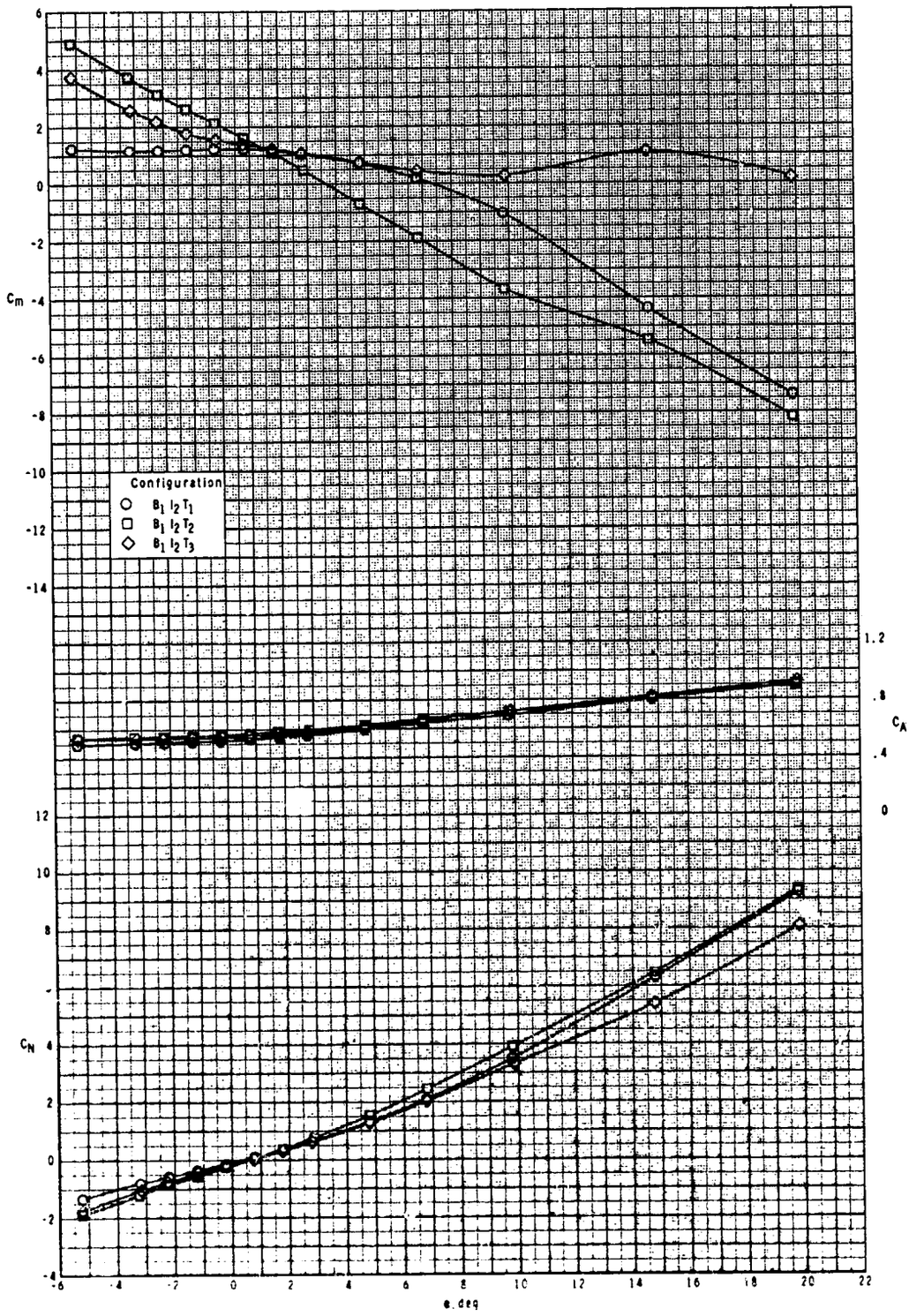

(a) M = 2.50.

Figure 11.- Effect of tail configuration on longitudinal aerodynamic characteristics of configuration $B_1 I_2 T$ with $\phi_I = 135°$ and $\delta_p = 0°$.

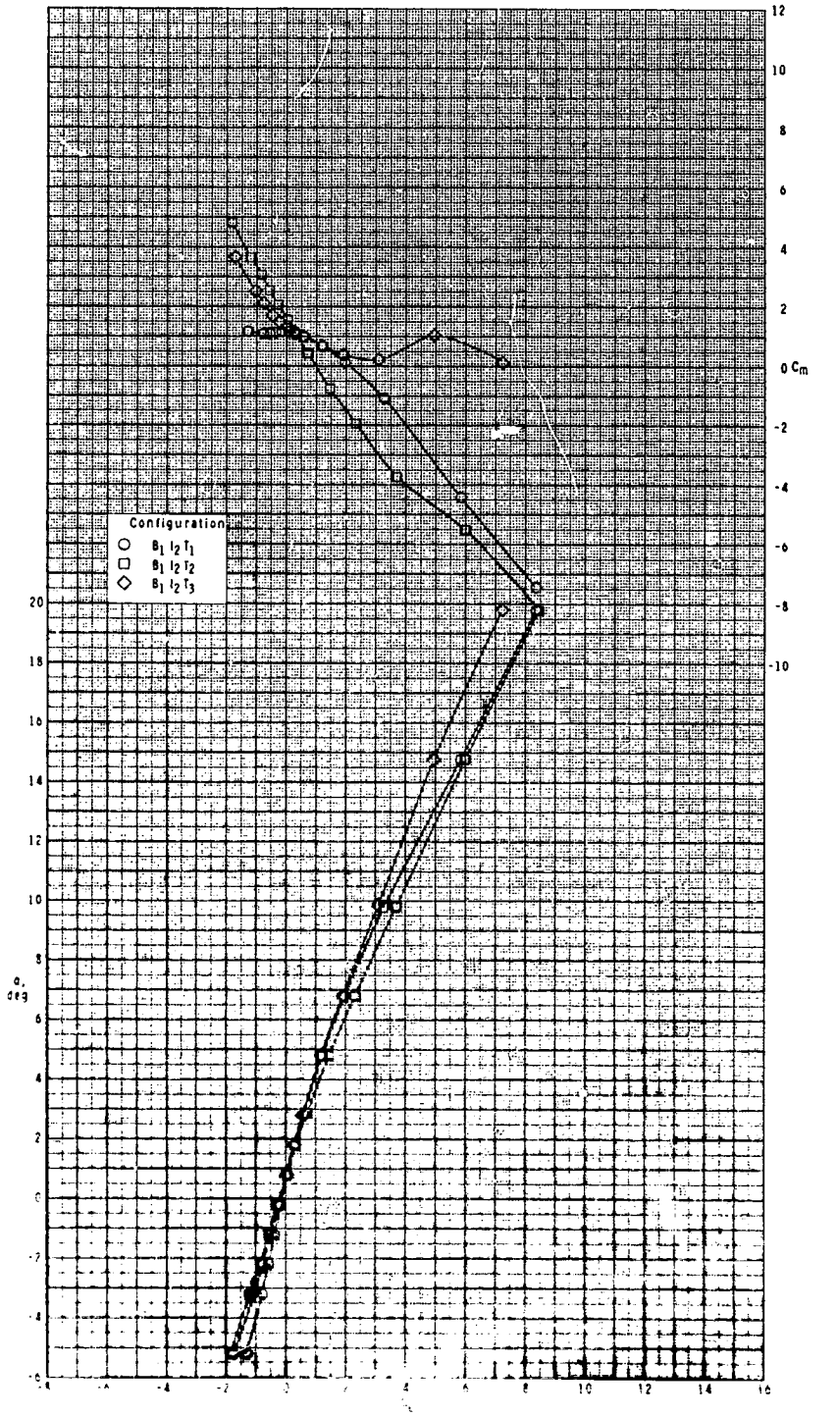

(a) Continued.

Figure 11.- Continued.

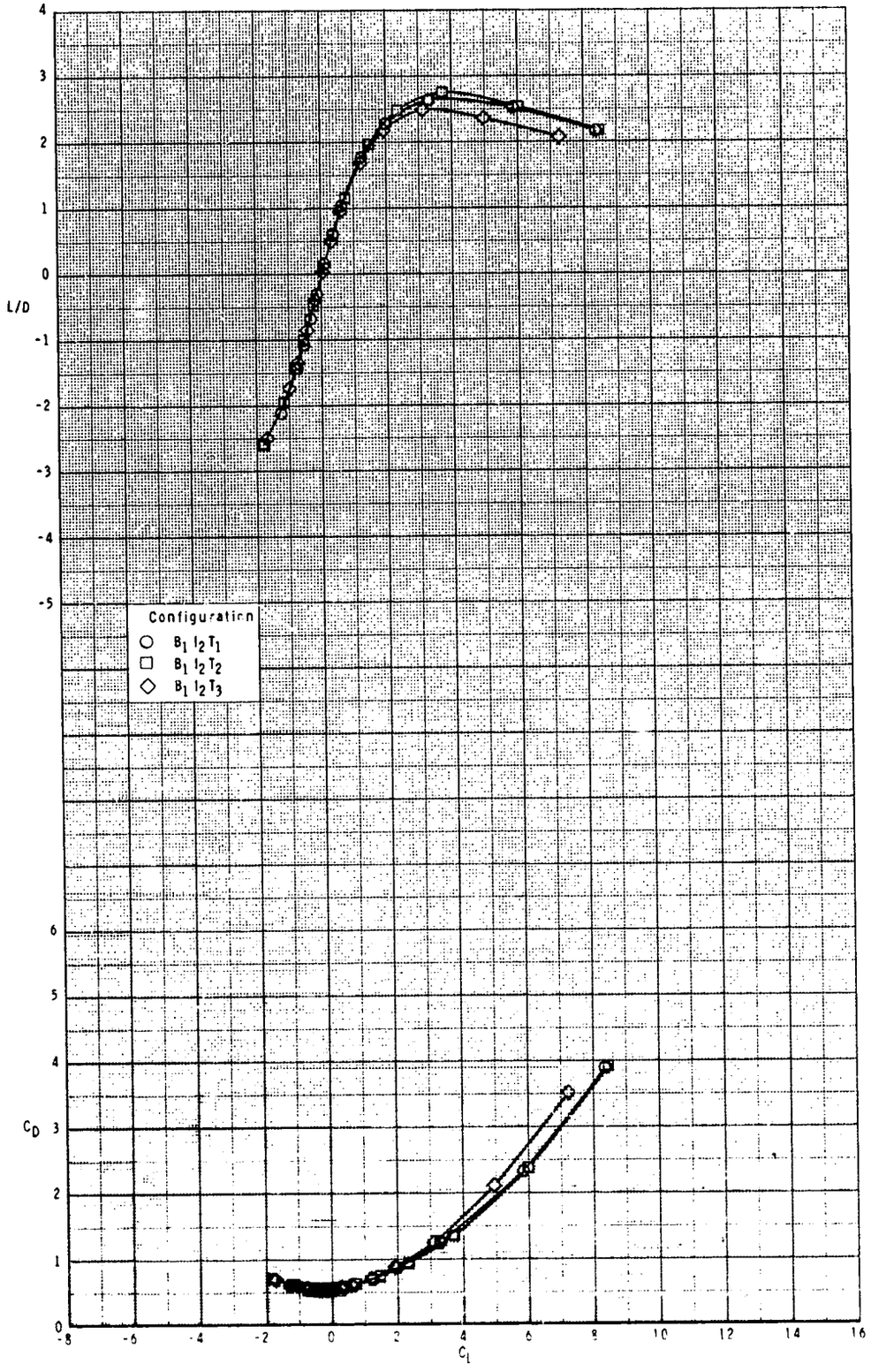

(a) Concluded.

Figure 11.- Continued.

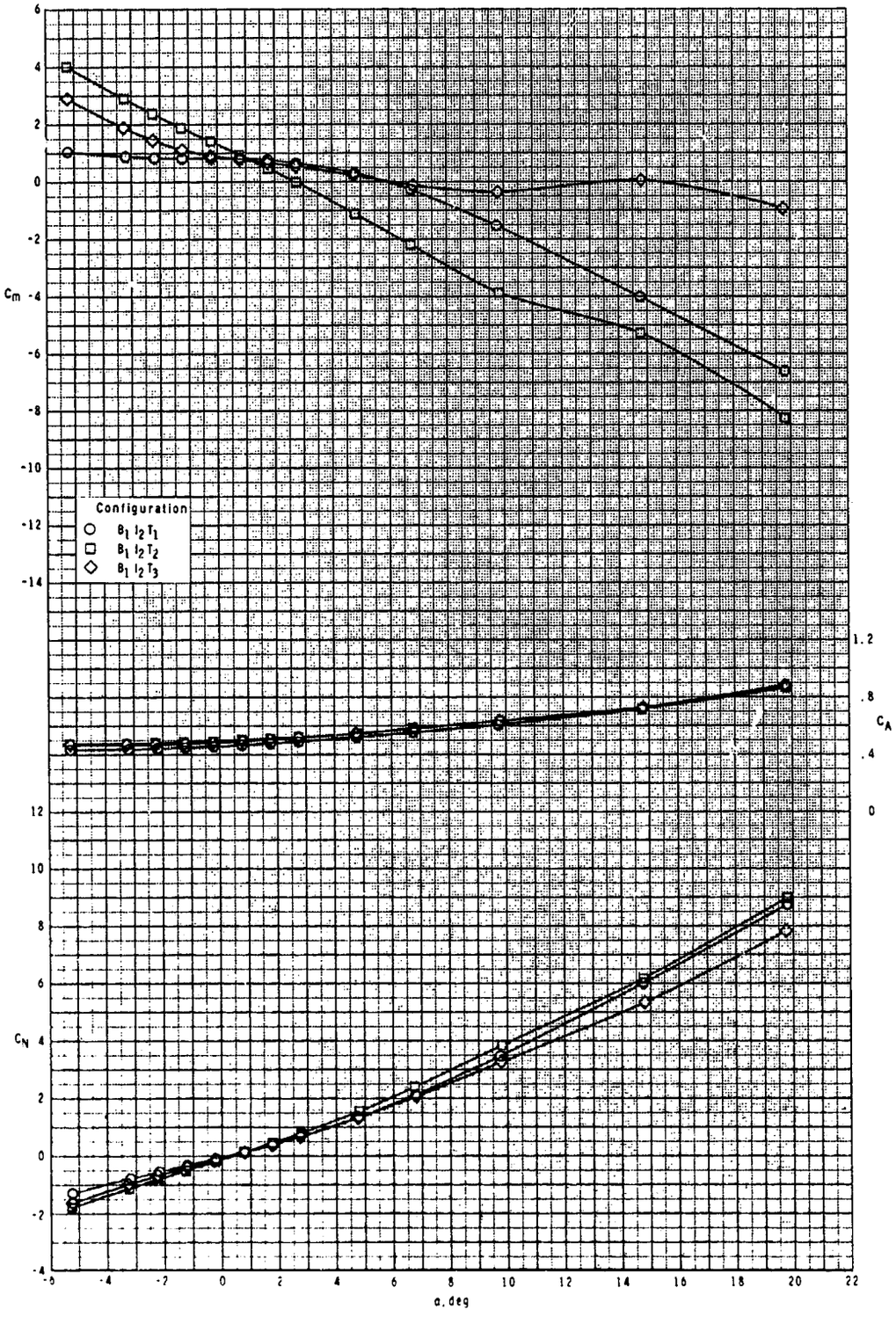

(b) M = 2.95.

Figure 11.- Continued.

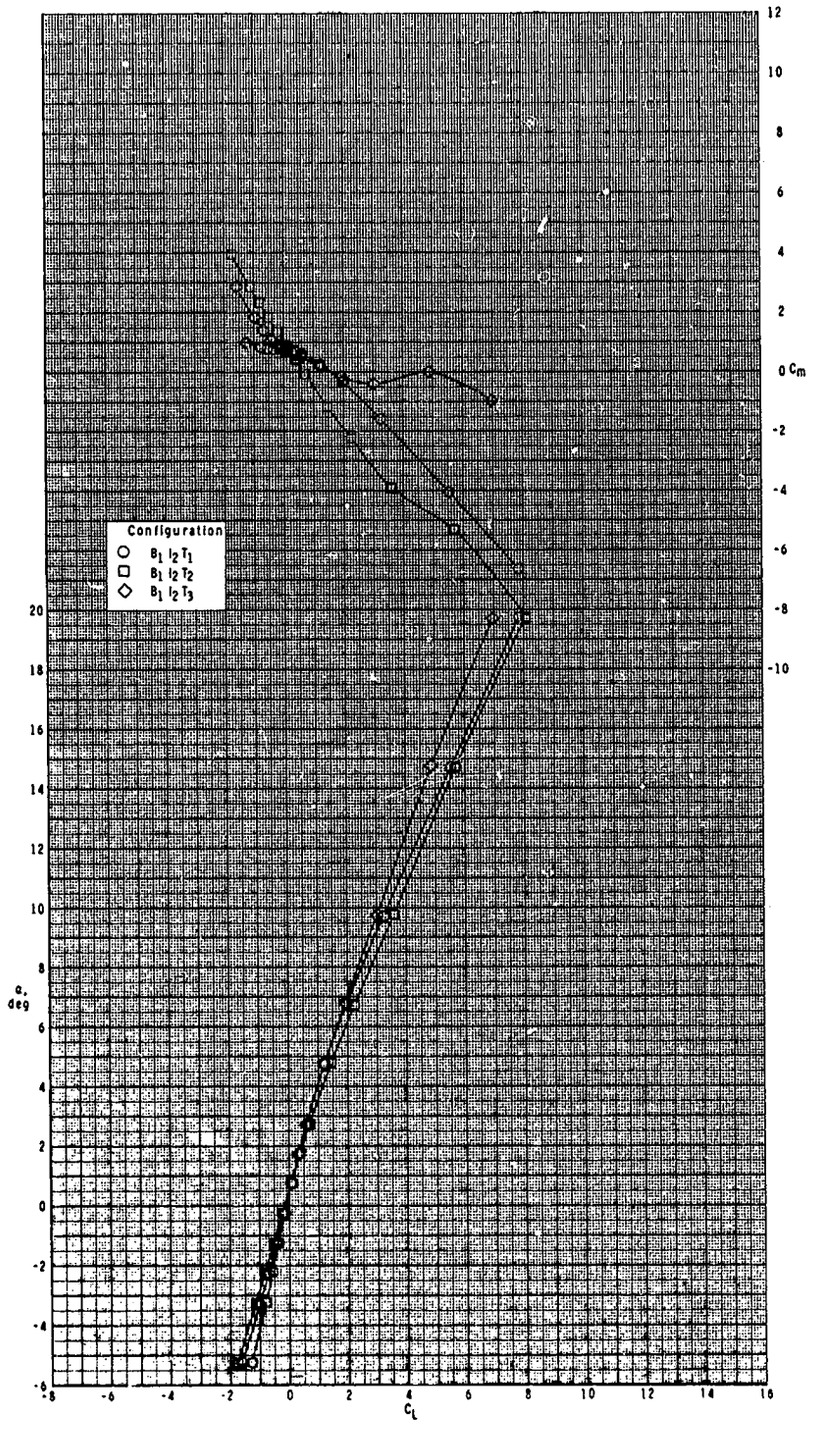

(b) Continued.

Figure 11.- Continued.

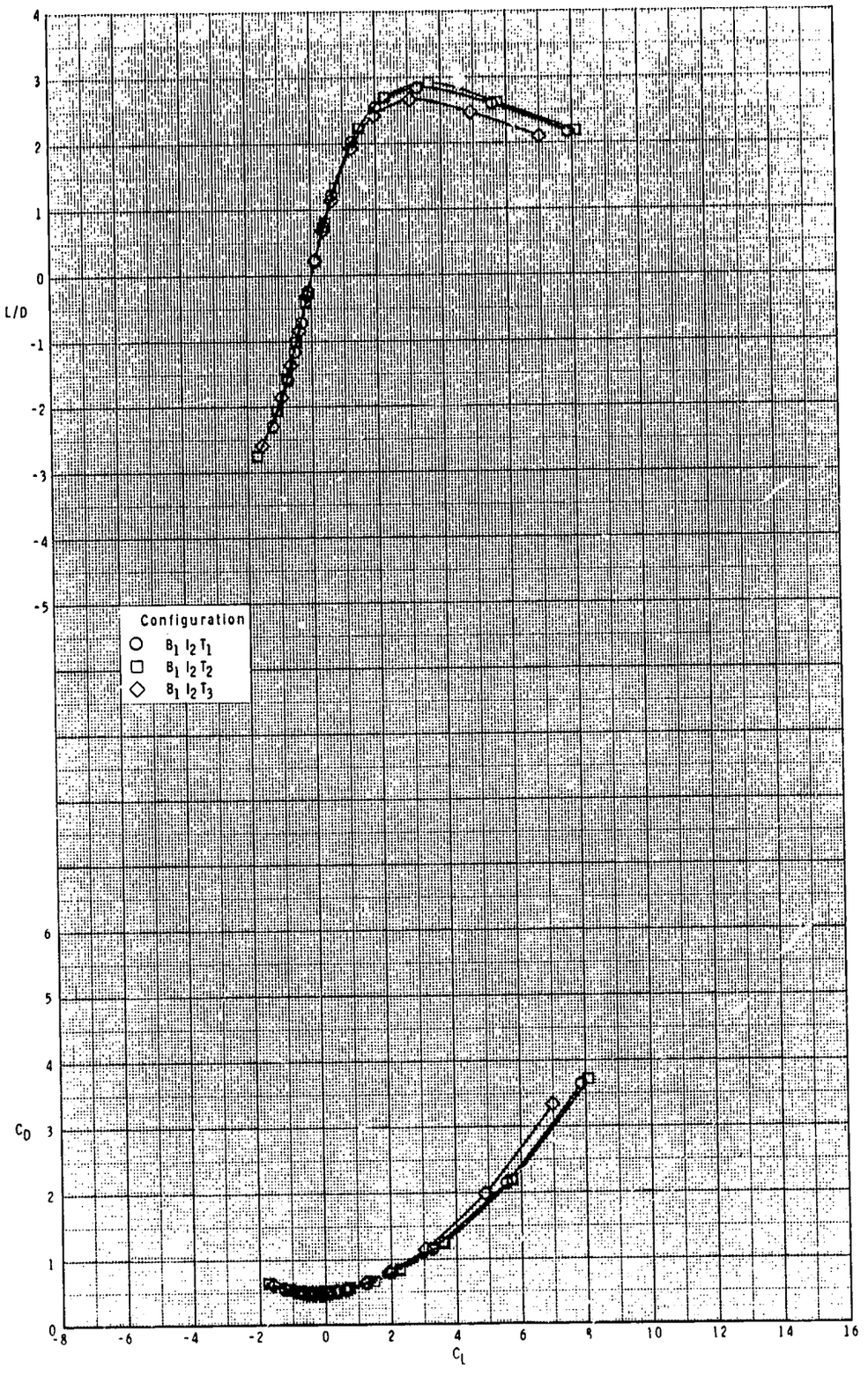

(b) Concluded.

Figure 11.- Continued.

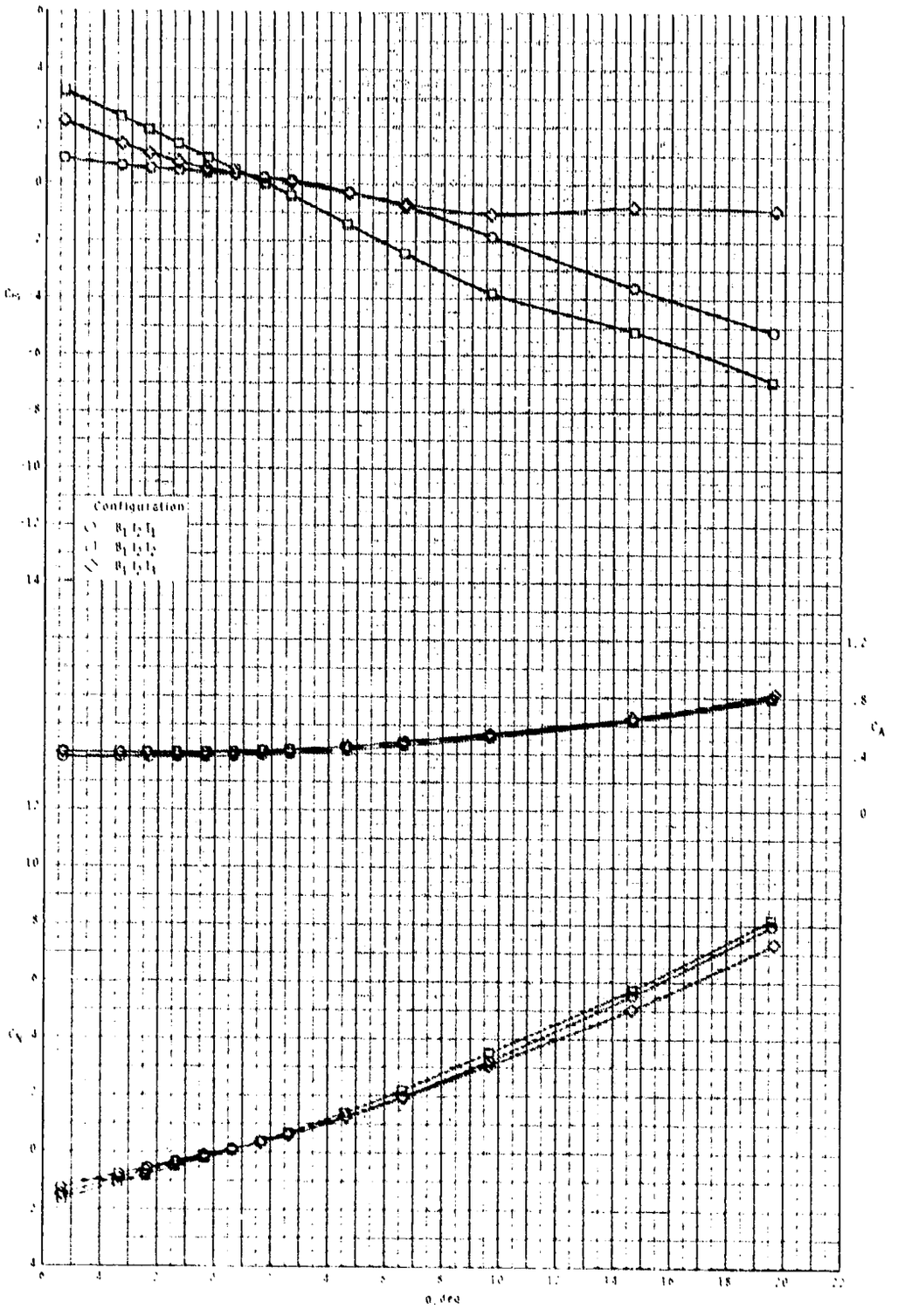

(c) M = 3.50.

Figure 11.- Continued.

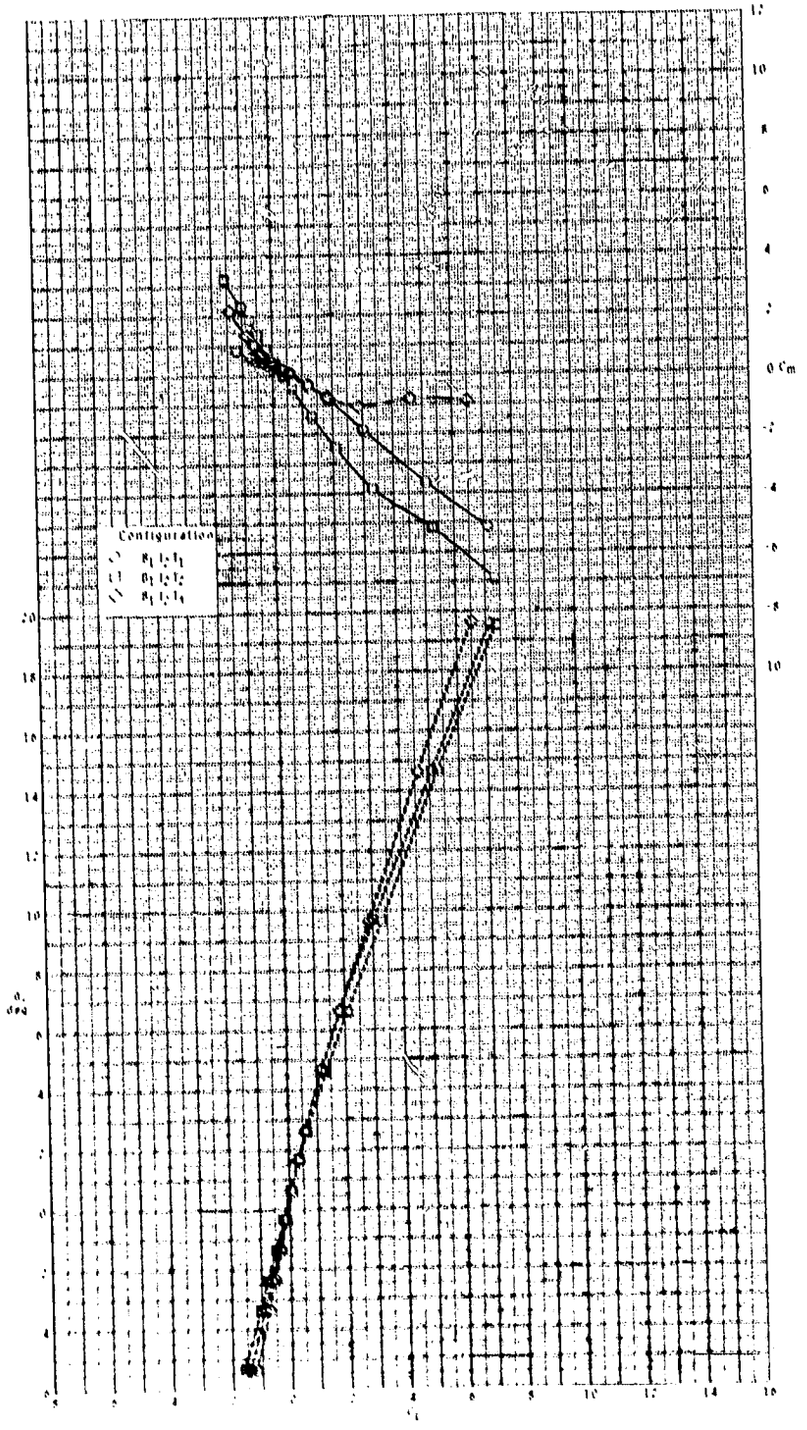

(c) Continued.

Figure 11.- Continued.

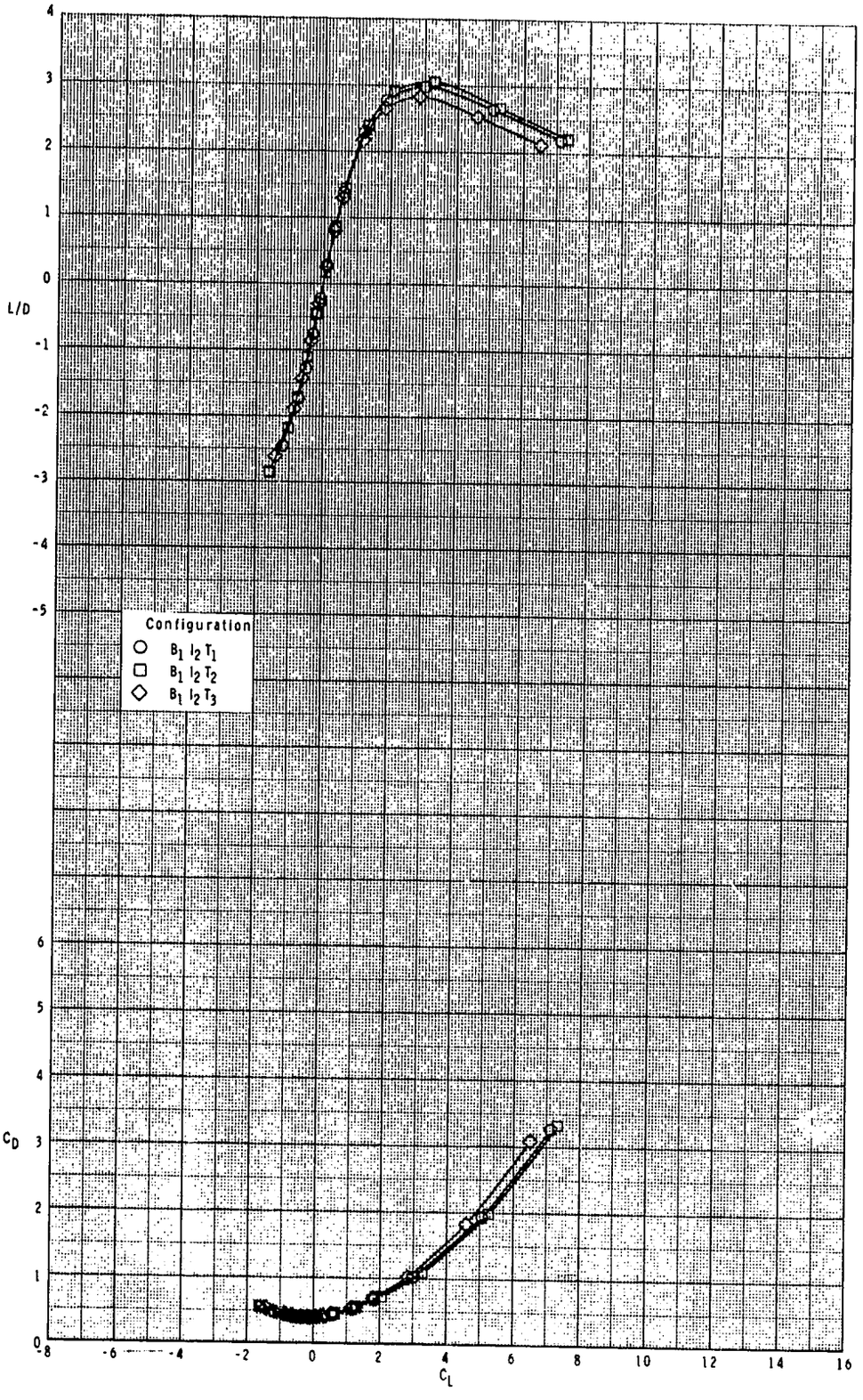

(c) Concluded.

Figure 11.- Continued.

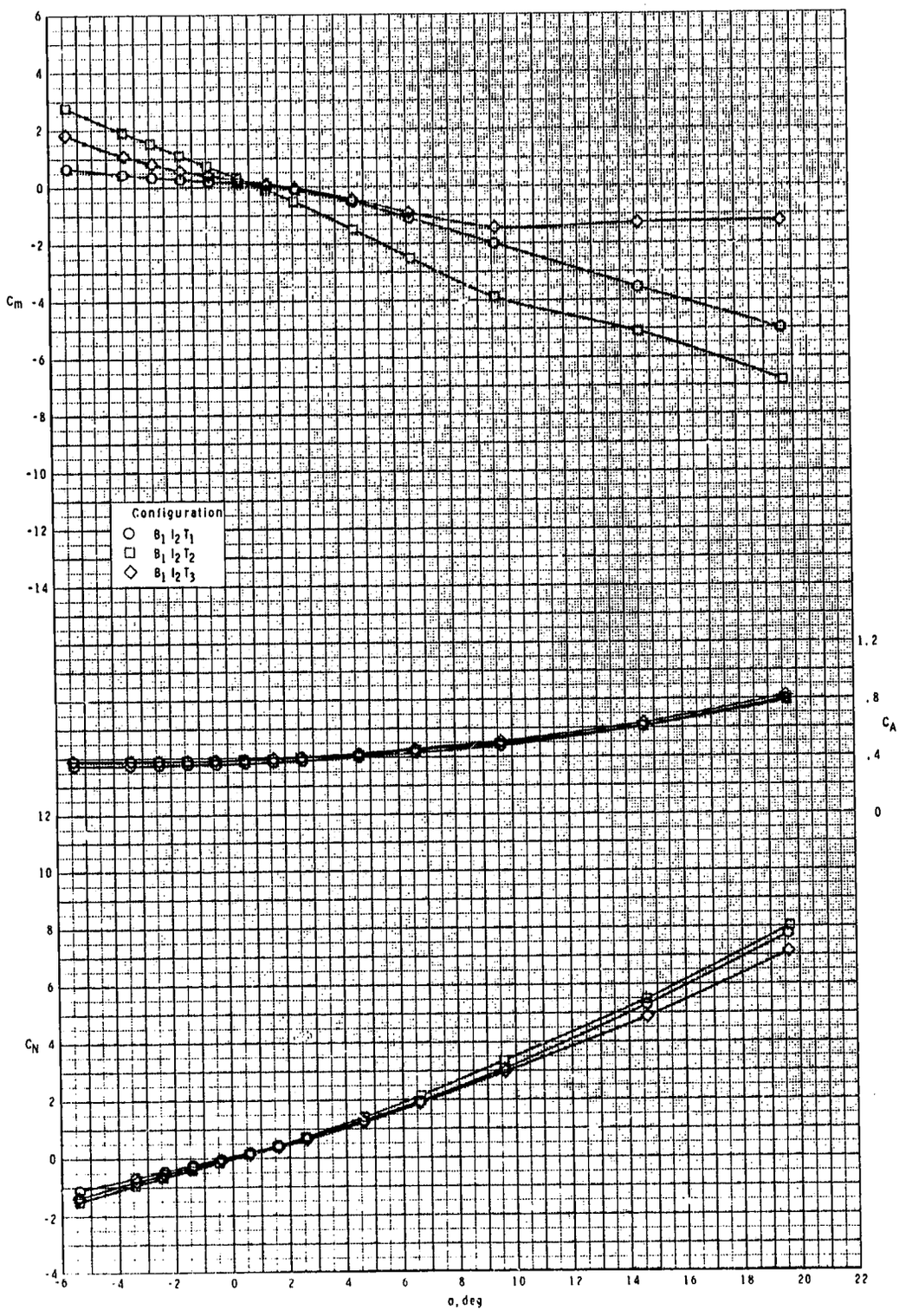

(d) M = 3.95.

Figure 11.- Continued.

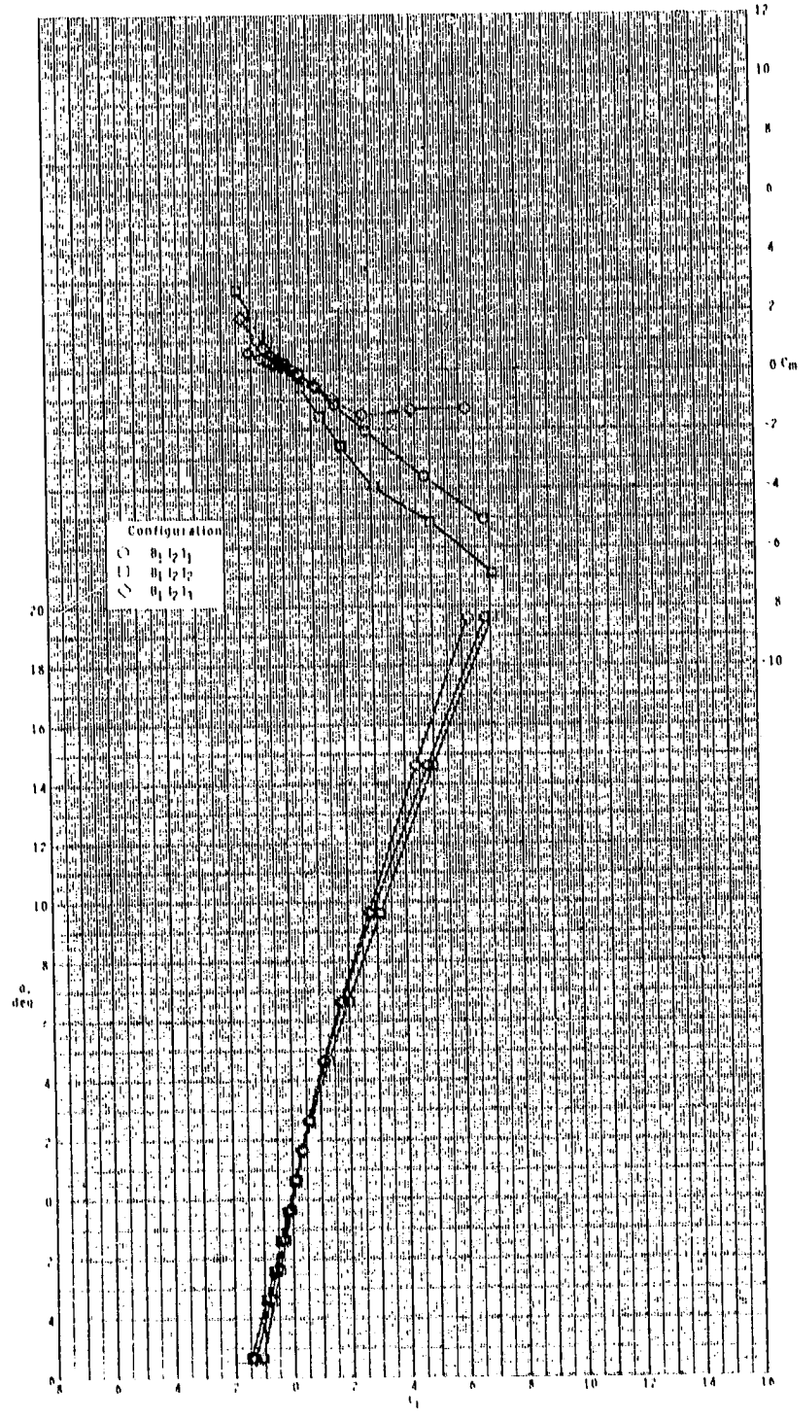

(d) Continued.

Figure 11.- Continued.

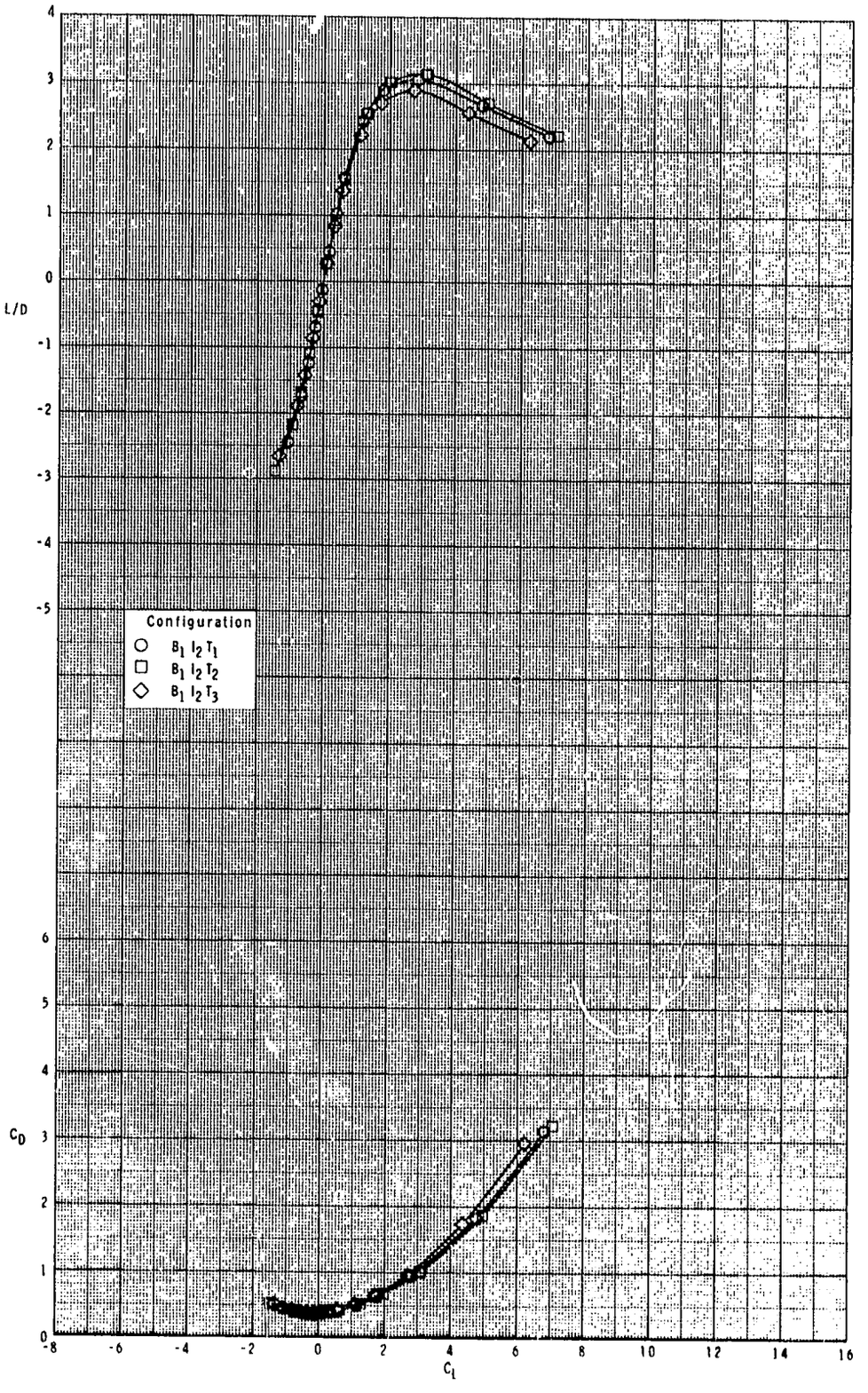

(d) Concluded.

Figure 11.- Concluded.

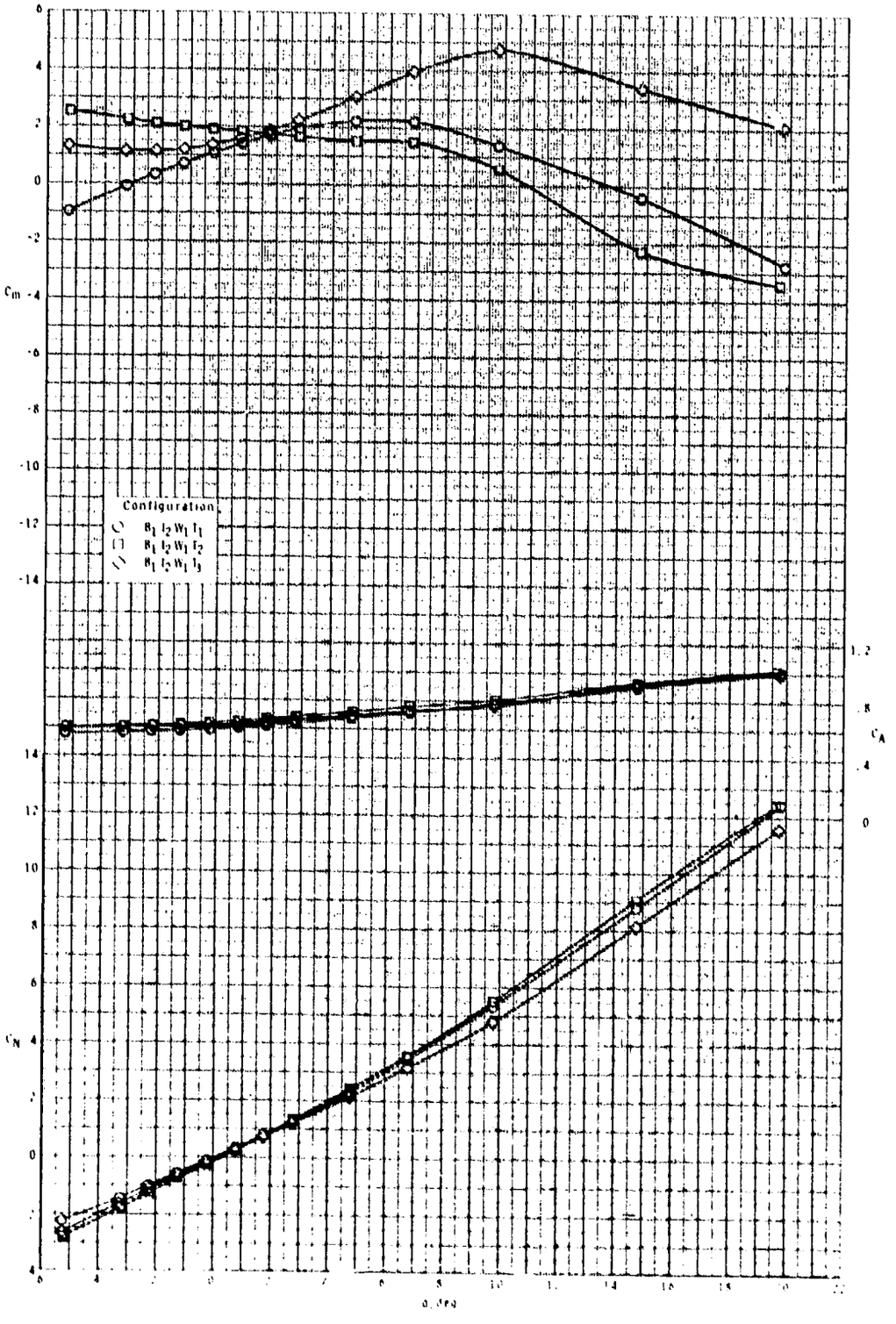

(a) M = 2.50.

Figure 12.- Effect of tail configuration on longitudinal aerodynamic characteristics of configuration $B_1 l_2 W_1 T$ with $\delta_1 = 135°$ and $\delta_p = 0°$.

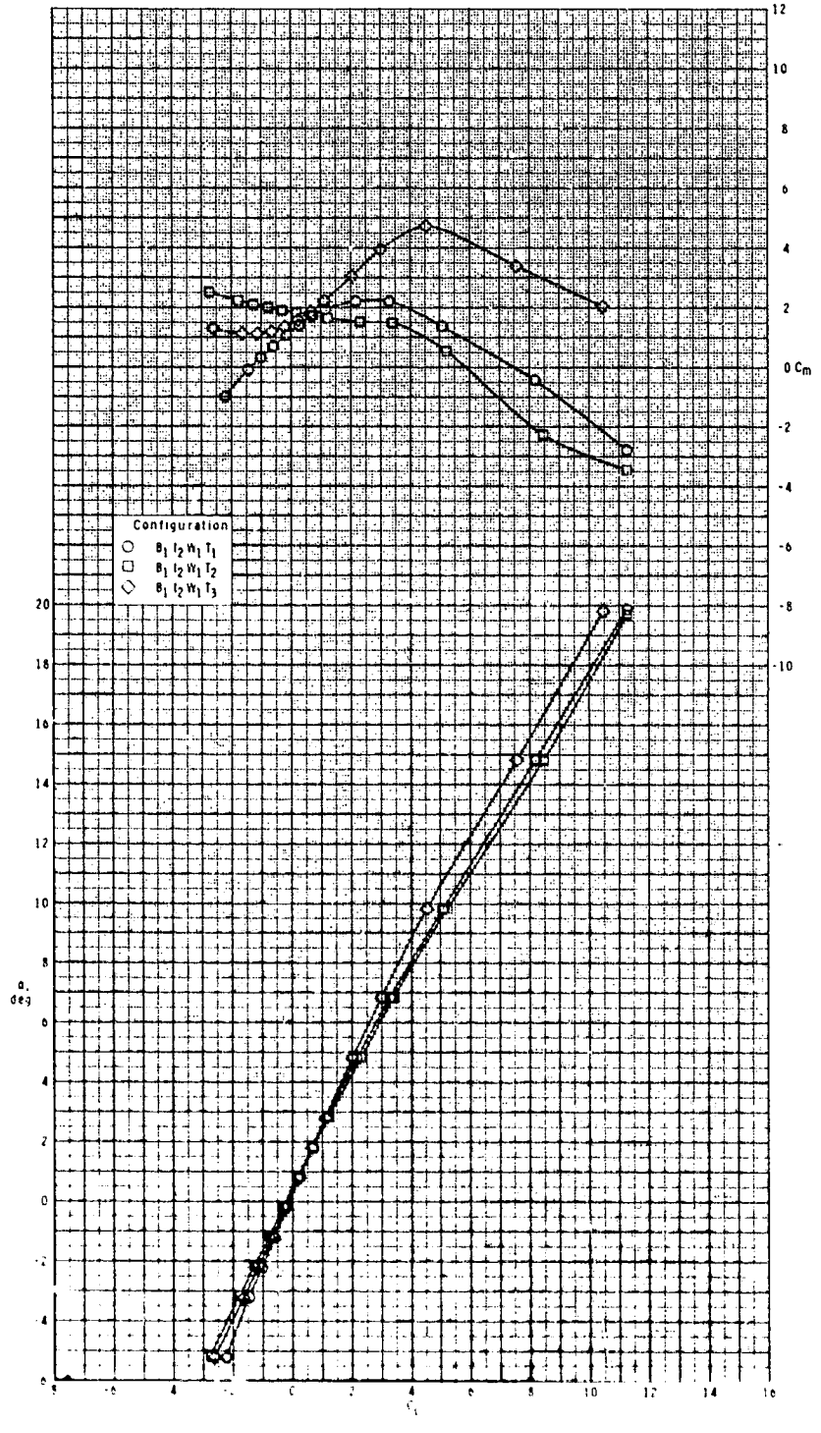

(a) Continued.

Figure 12.- Continued.

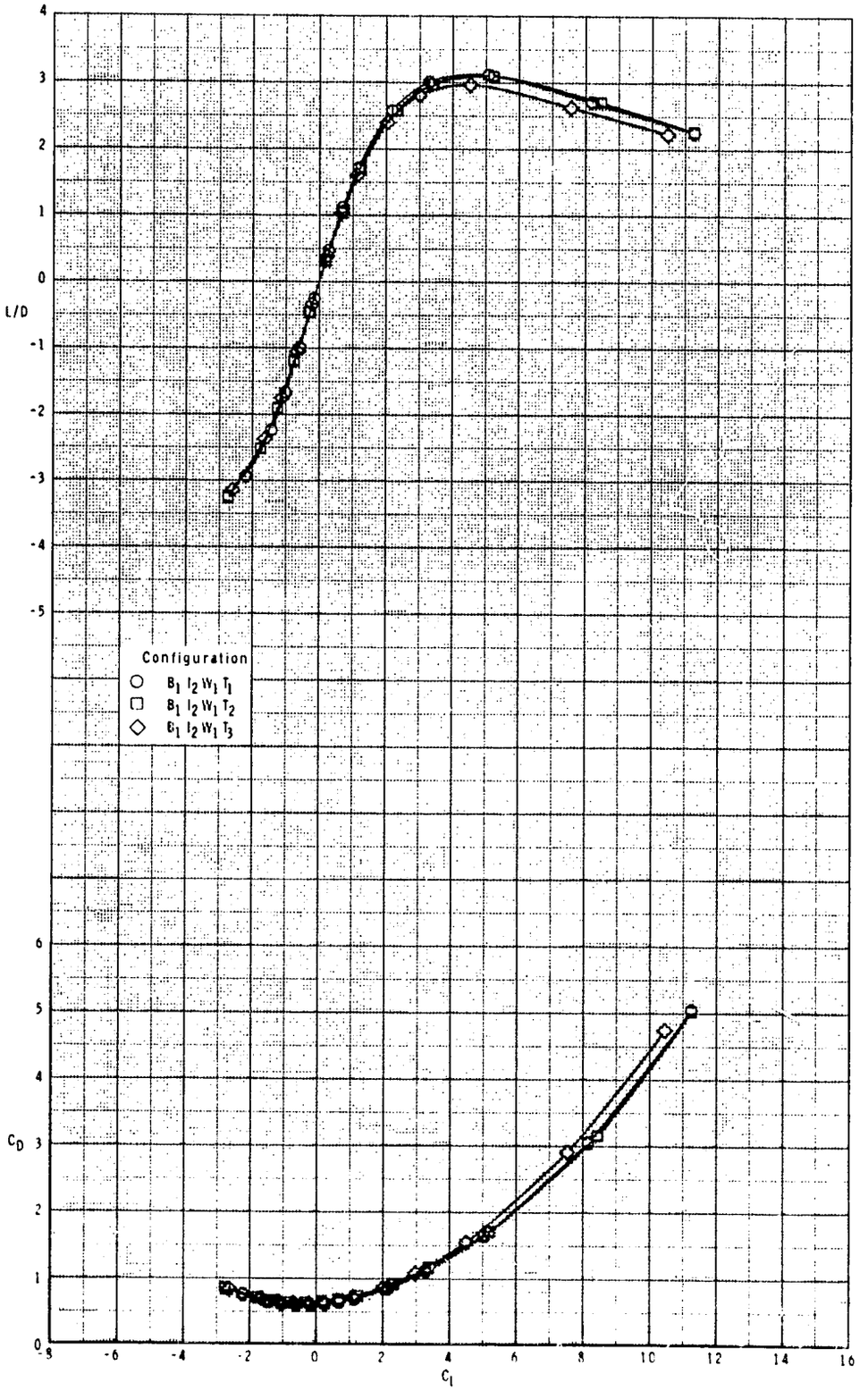

(a) Concluded.

Figure 12.- Continued.

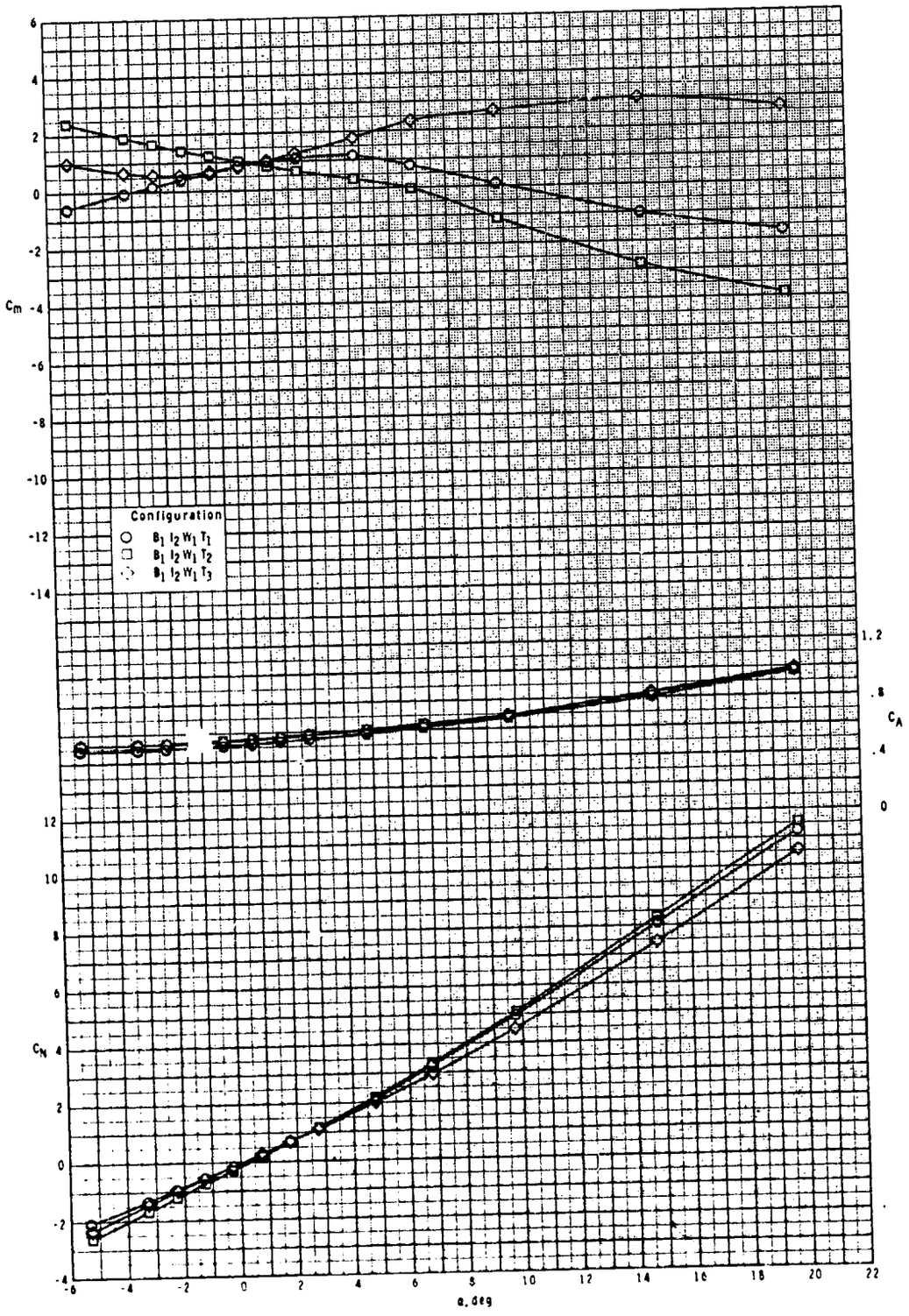

(b) M = 2.95.

Figure 12.- Continued.

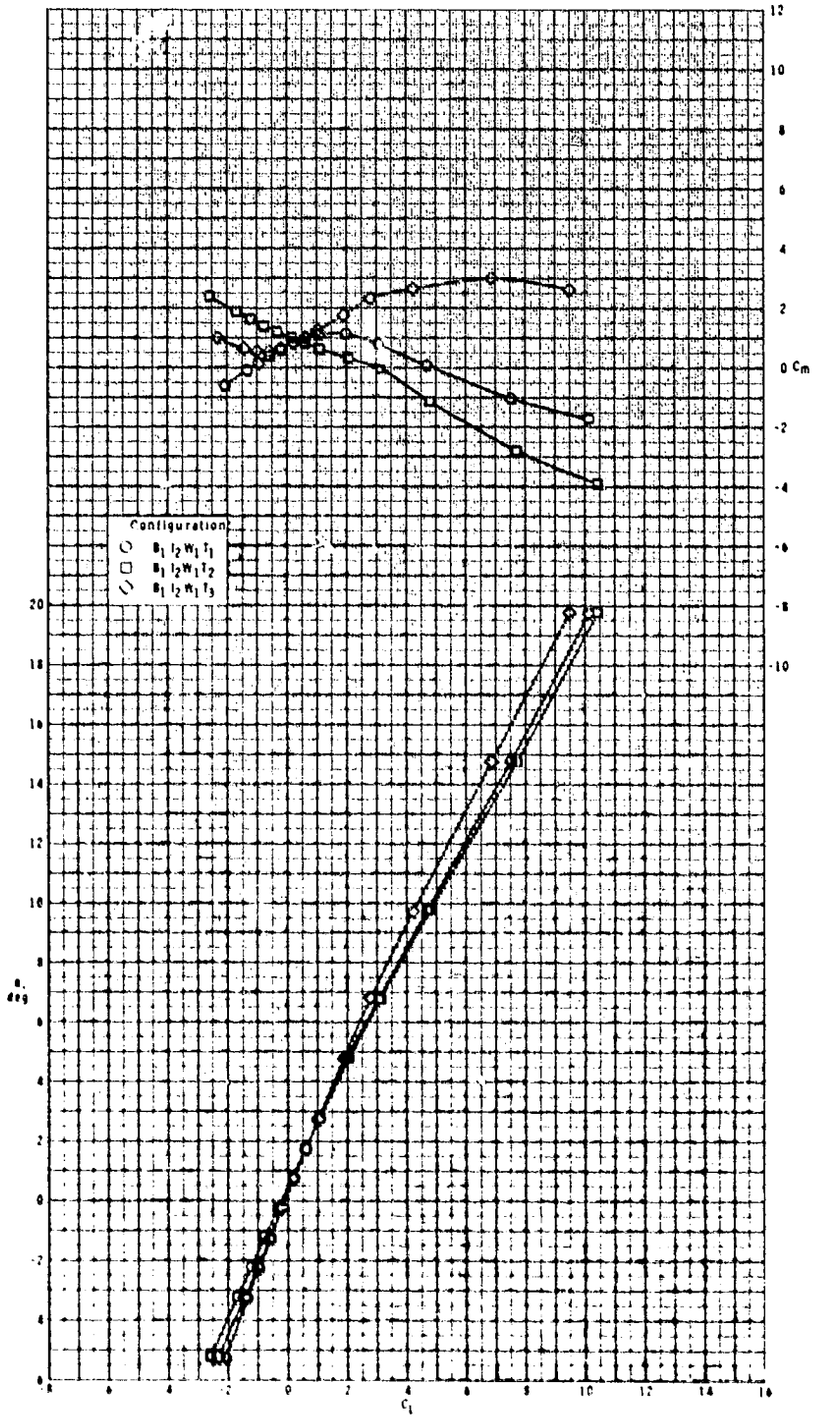

(b) Continued.

Figure 12.- Continued.

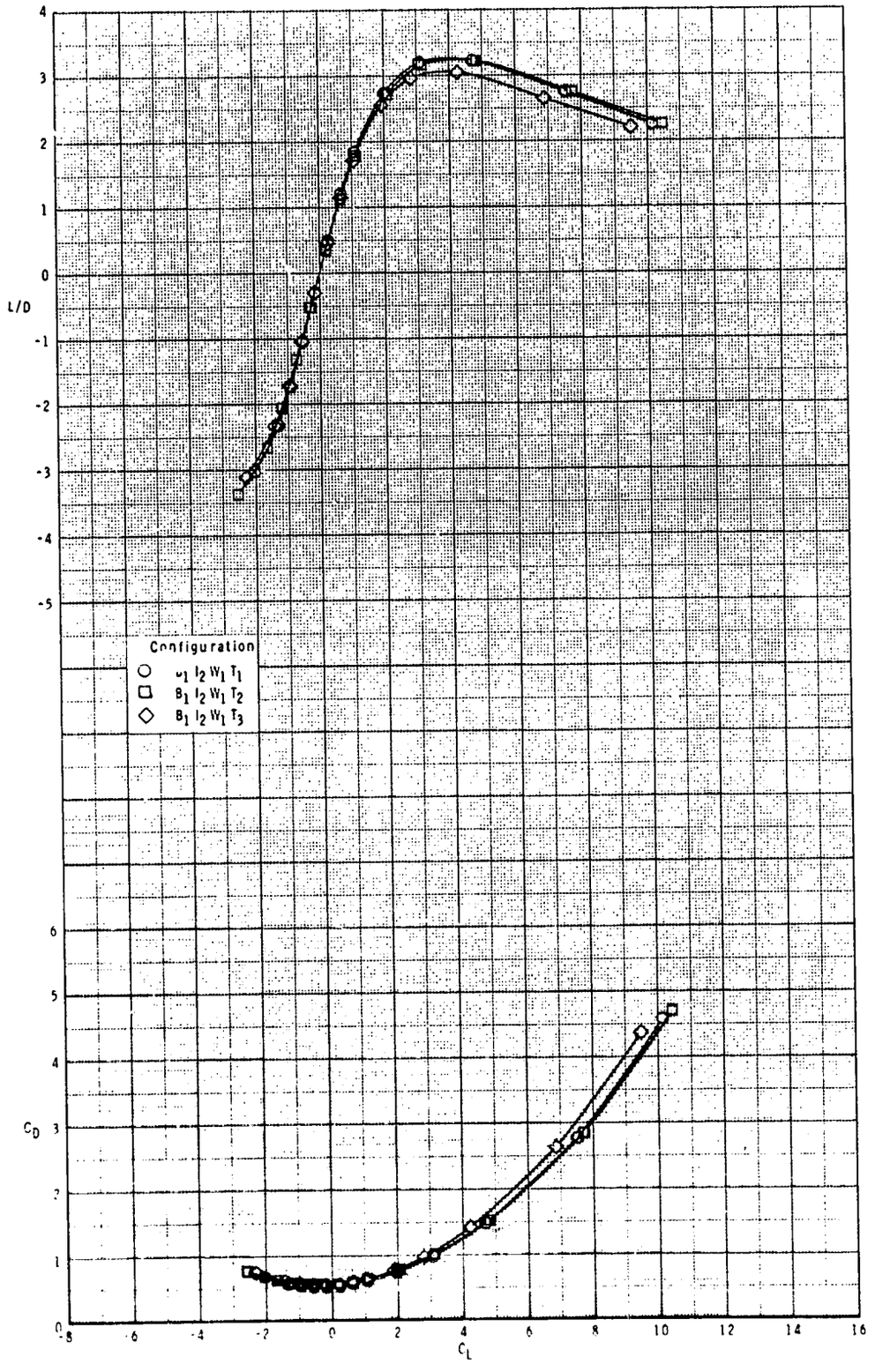

(b) Concluded.

Figure 12.- Continued.

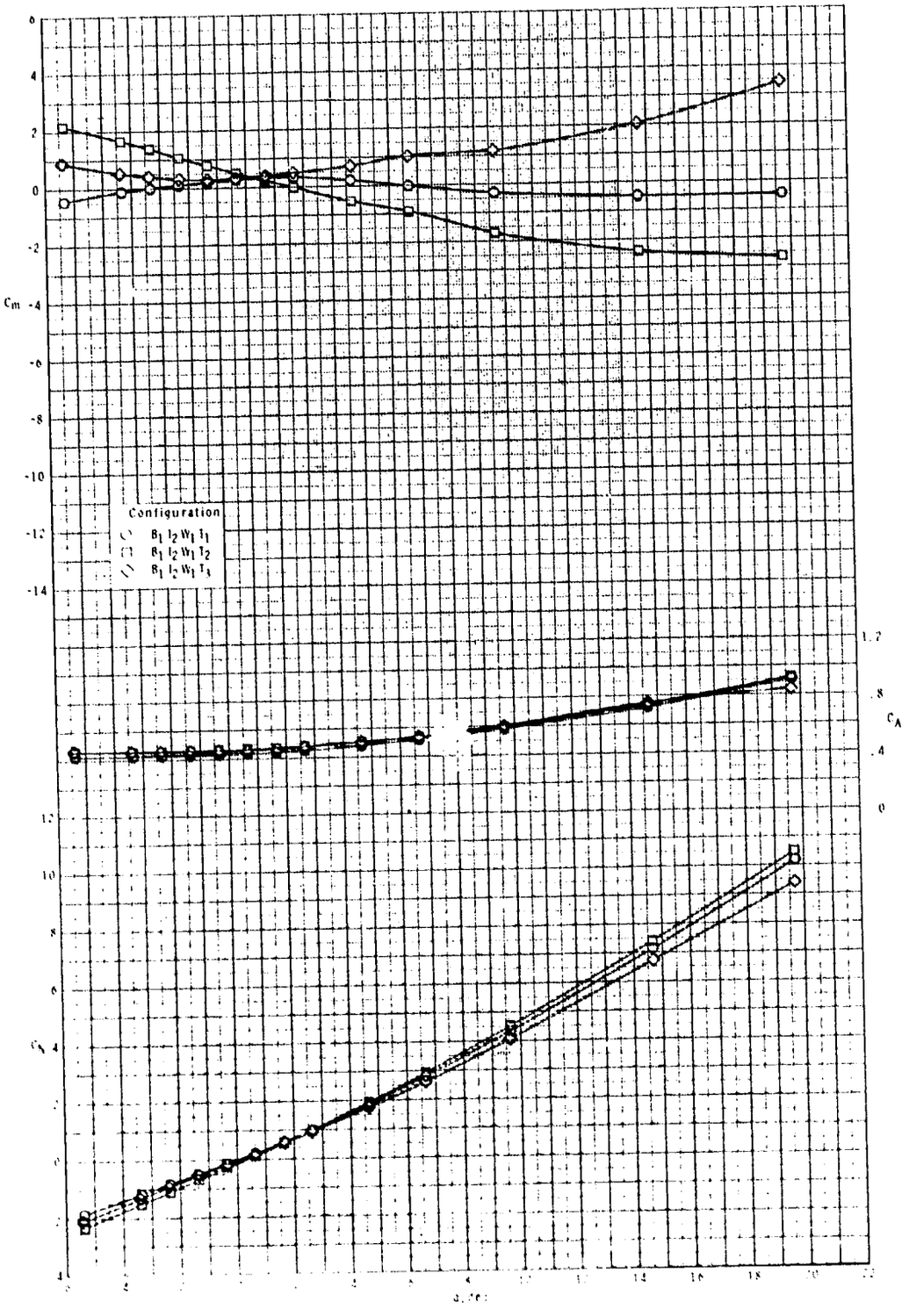

(c) M = 3.50.

Figure 12.- Continued.

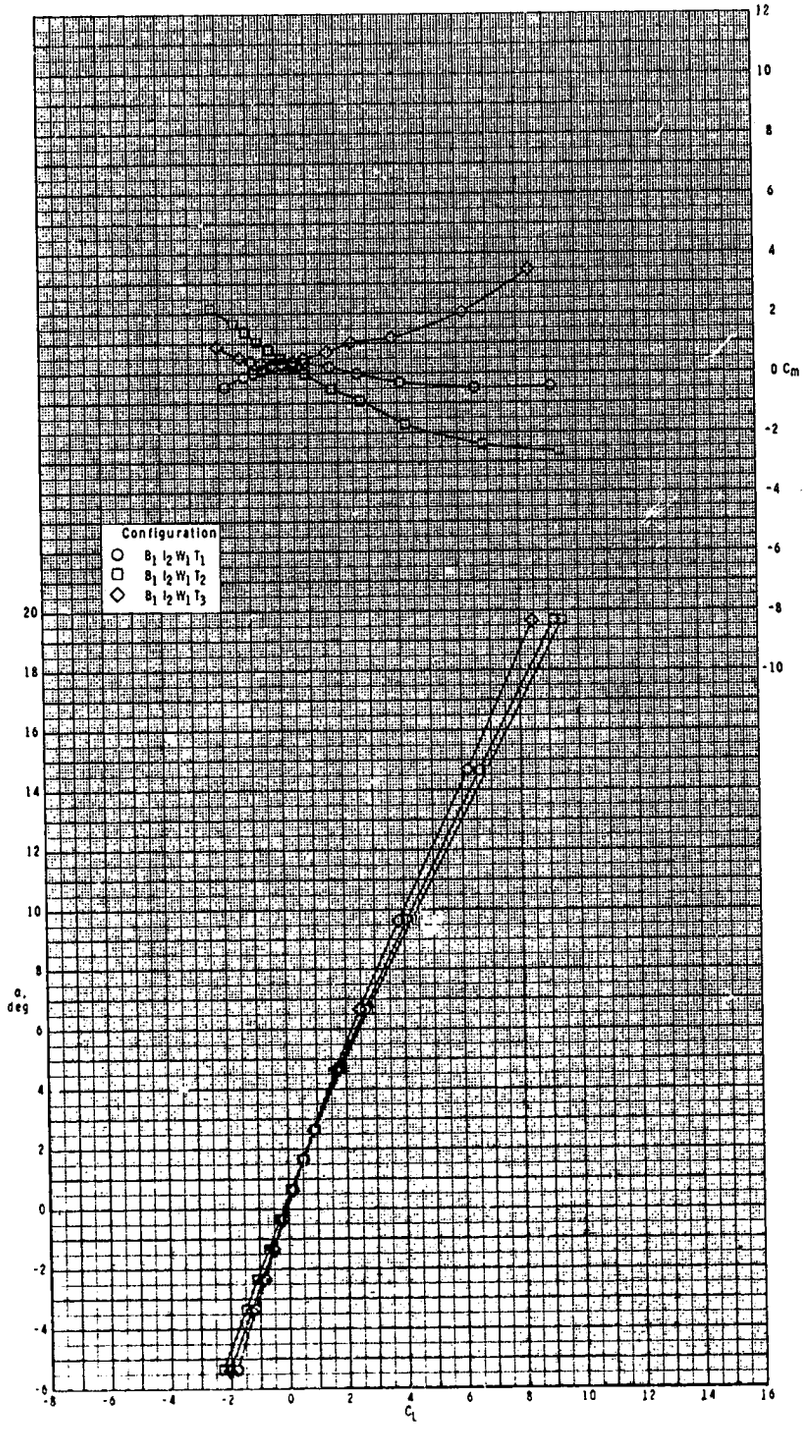

(c) Continued.

Figure 12.- Continued.

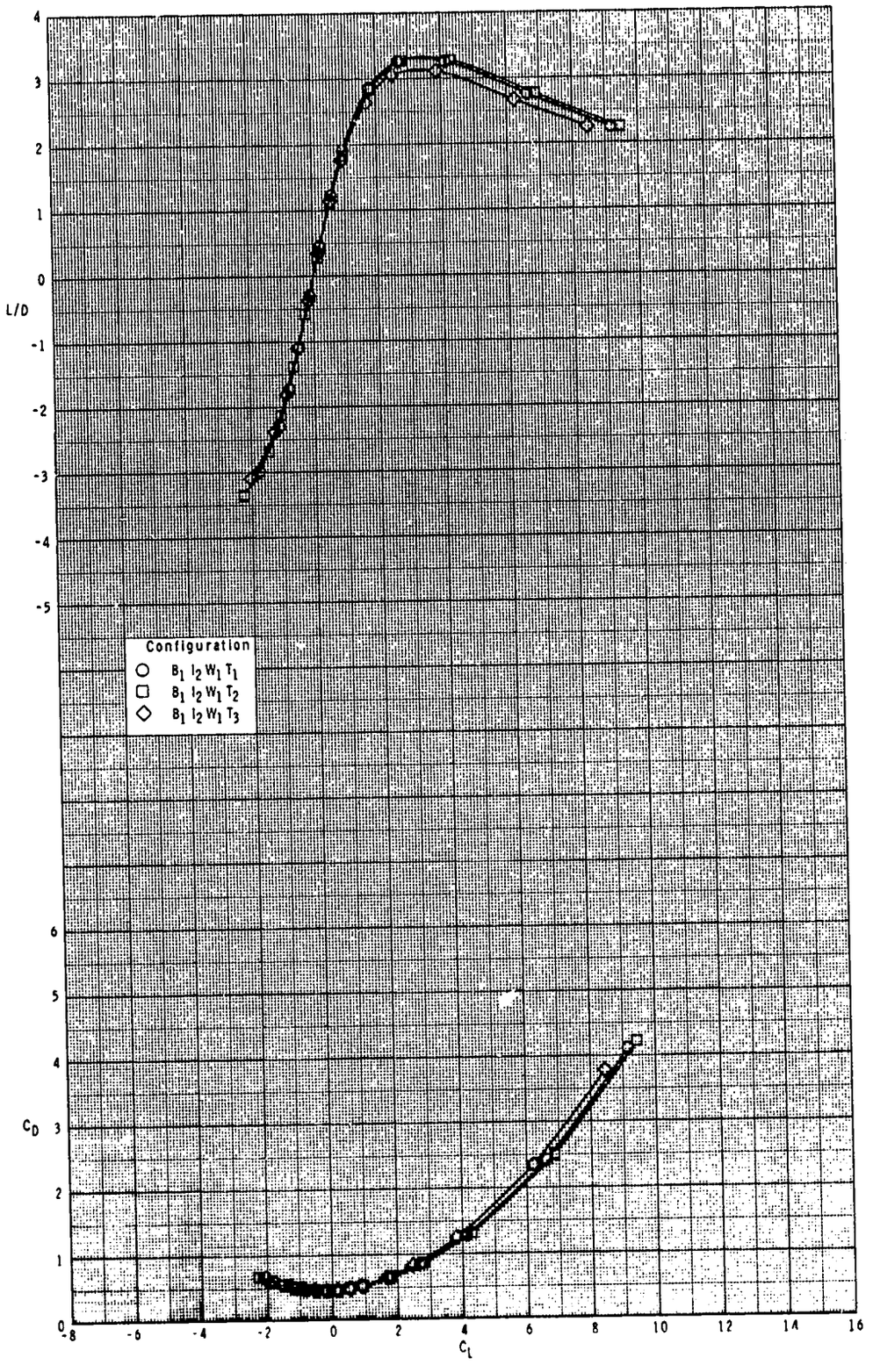

(c) Concluded.

Figure 12.- Continued.

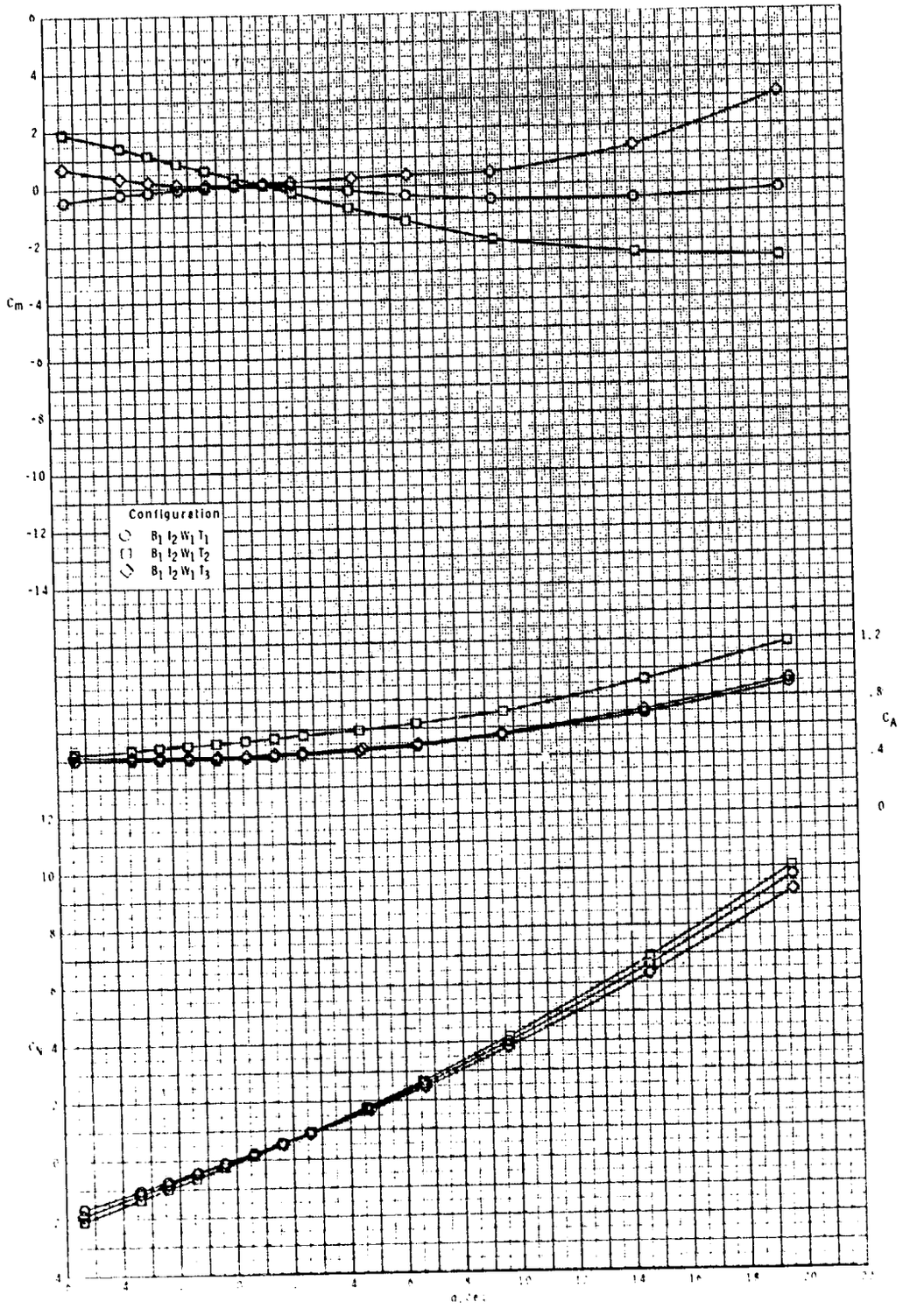

(d) M = 3.95.

Figure 12.- Continued.

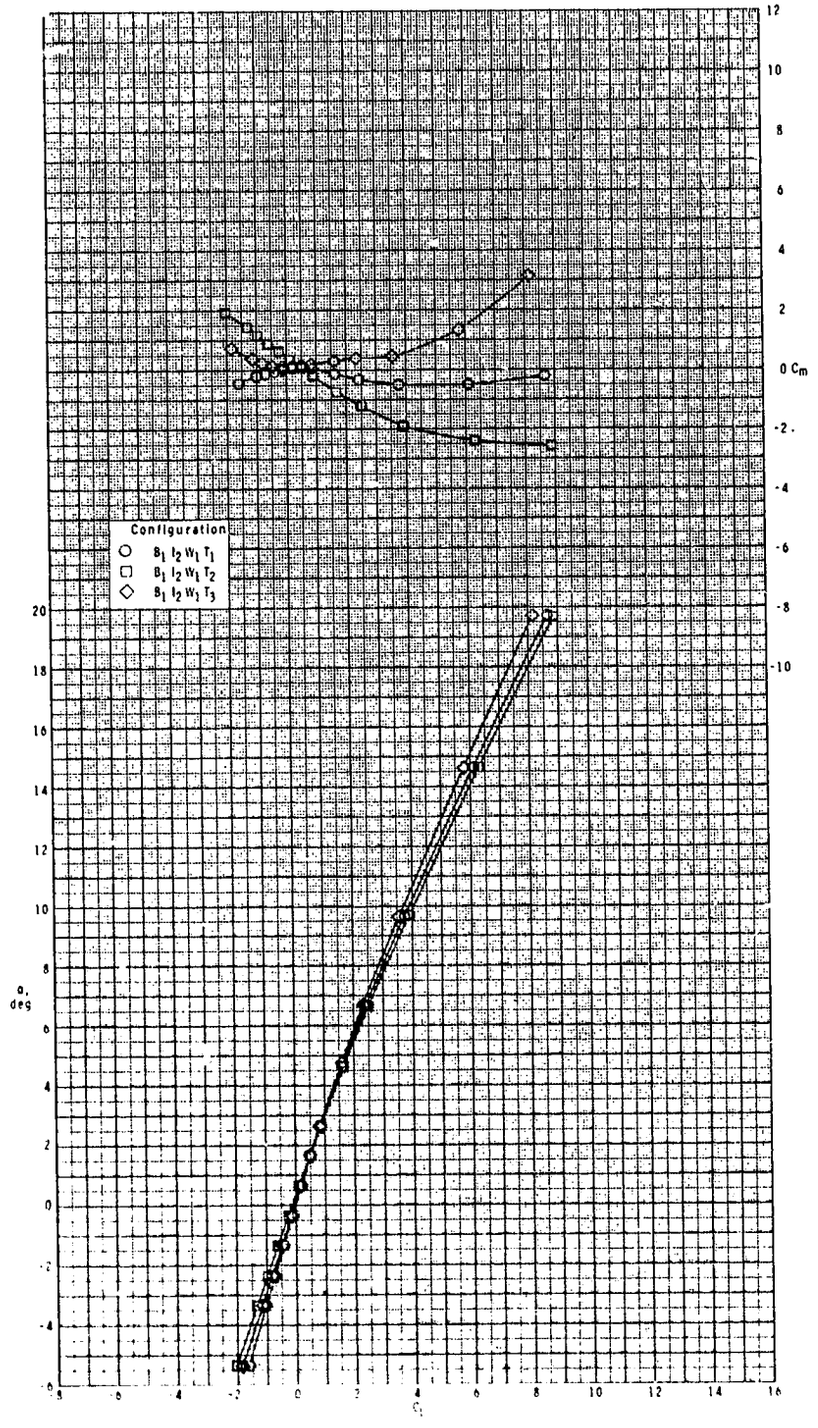

(d) Continued.

Figure 12.- Continued.

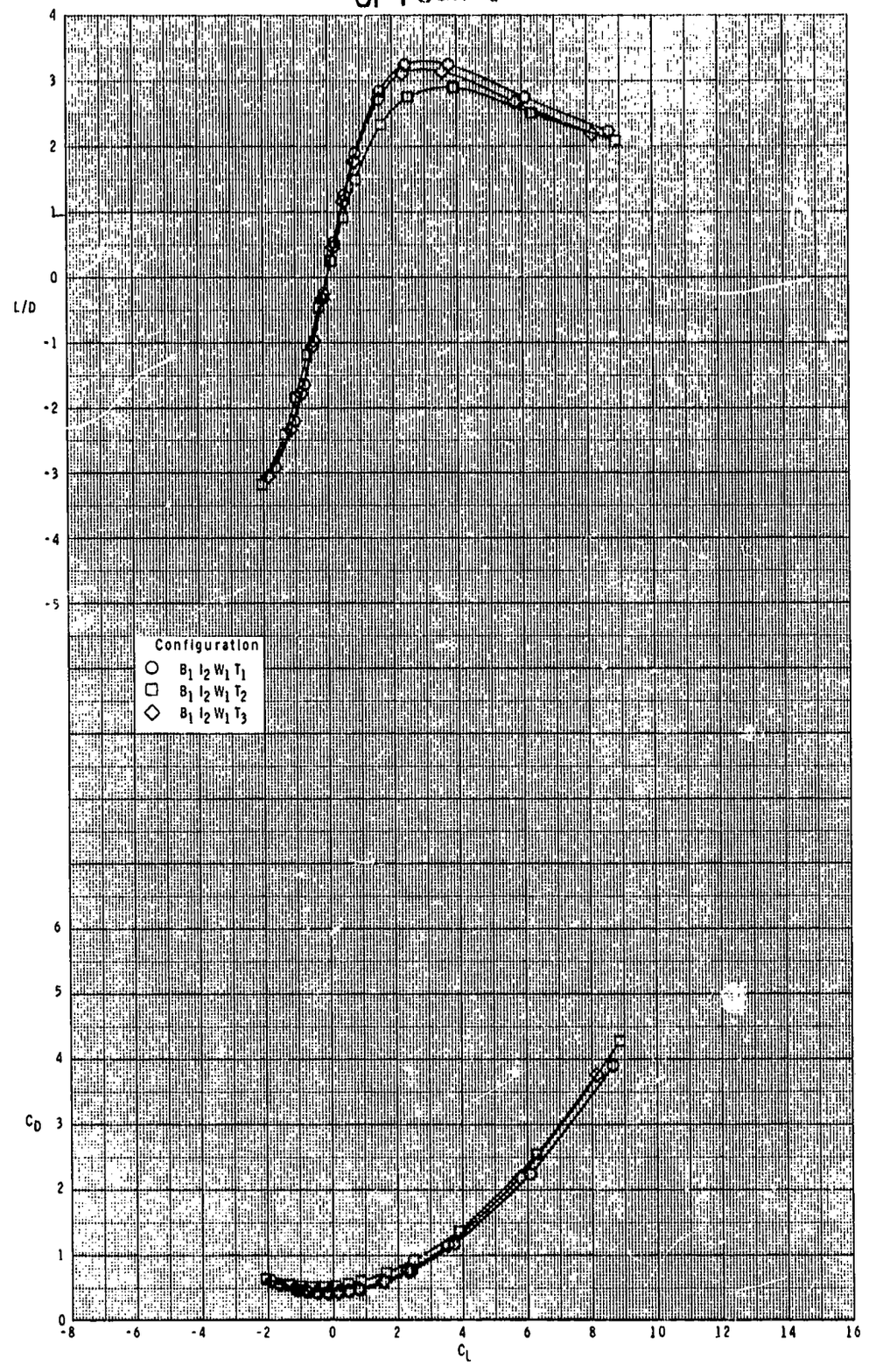

(d) Concluded.

Figure 12.- Concluded.

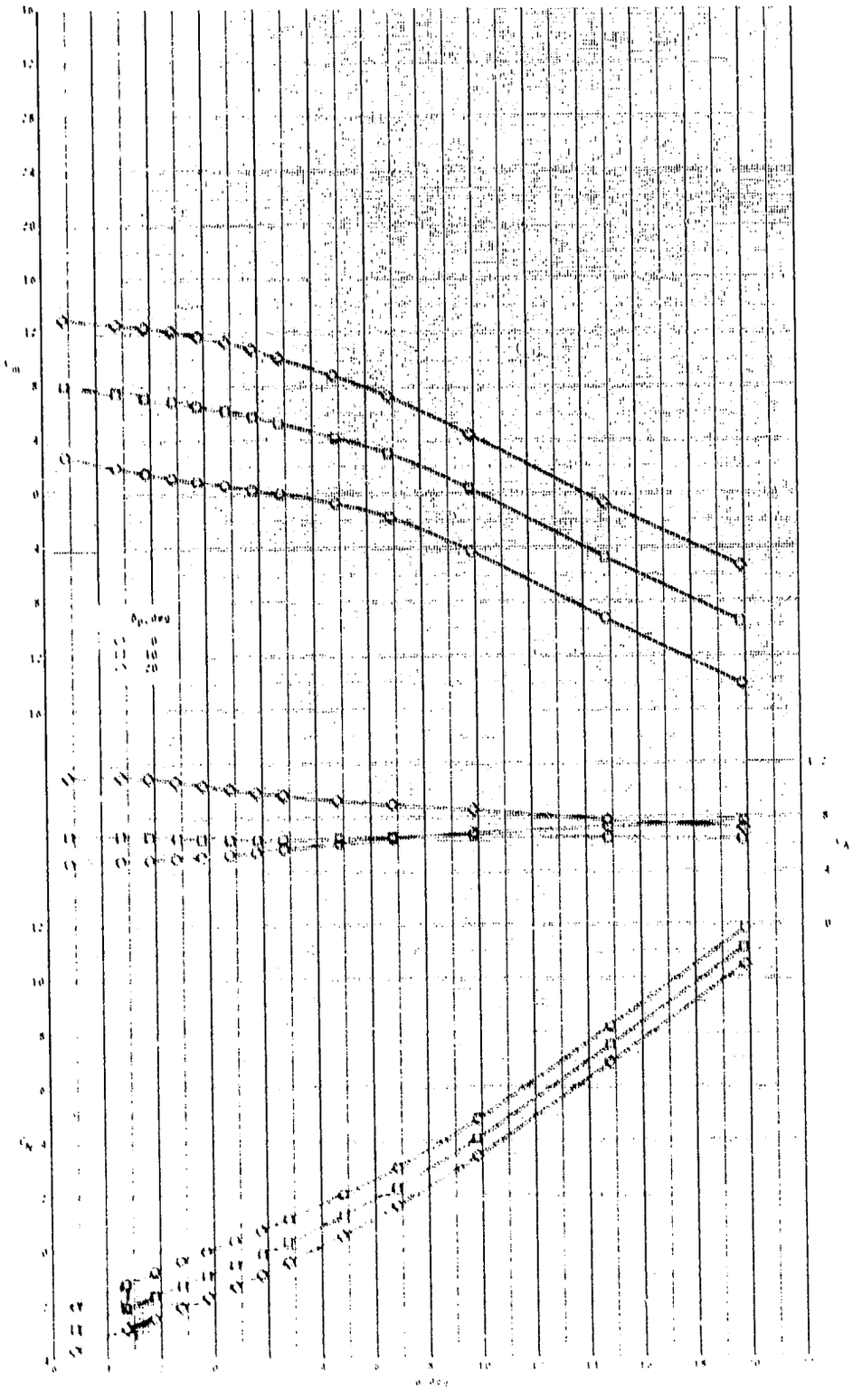

(a) M = 2.50.

Figure 13.- Pitch-control effectiveness of configuration $B_1L_1F_1$ with ϕ_1 = 90°.

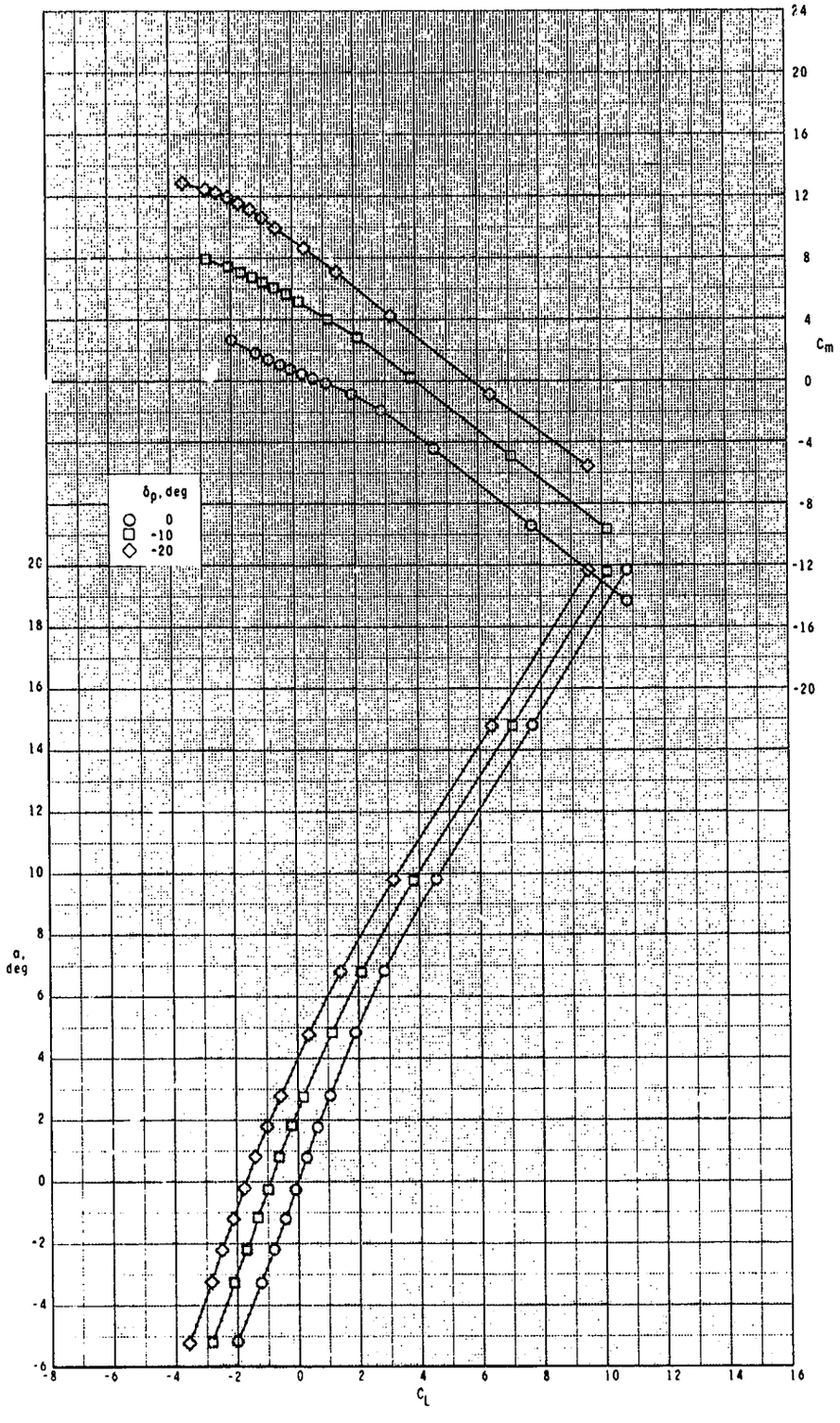

(a) Continued.

Figure 13.- Continued.

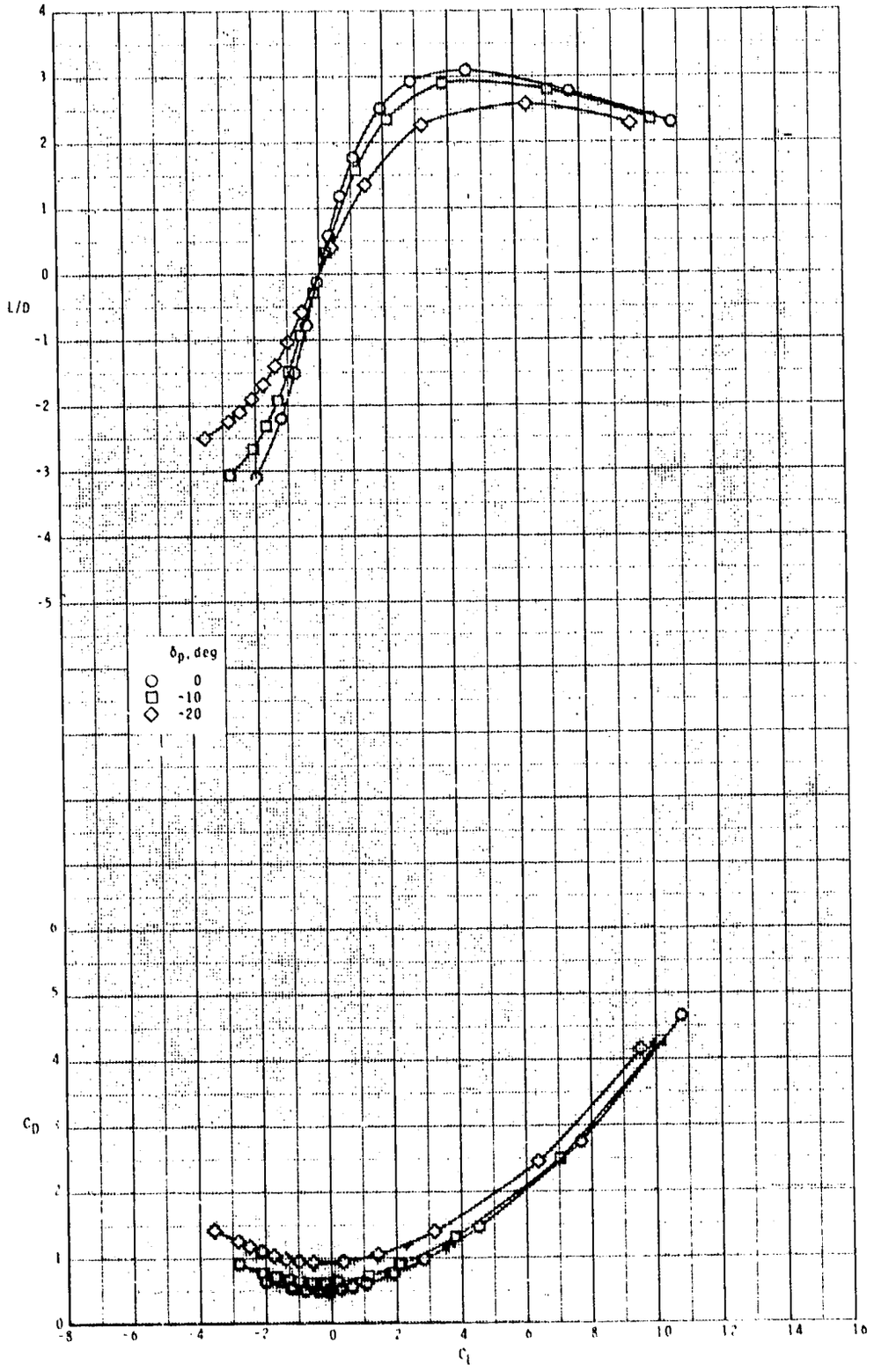

(a) Concluded.

Figure 13.- Continued.

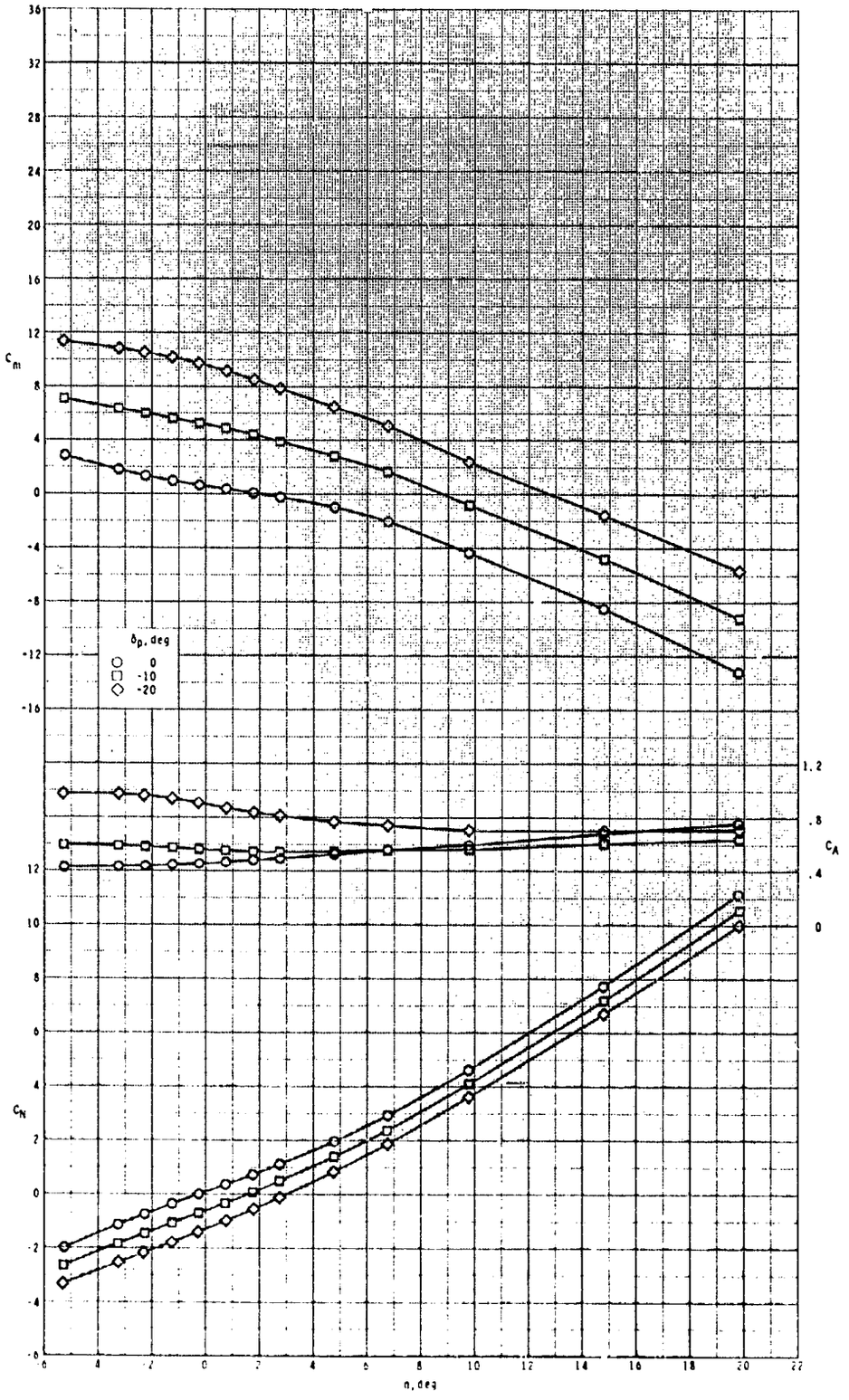

(b) M = 2.95.

Figure 13.- Continued.

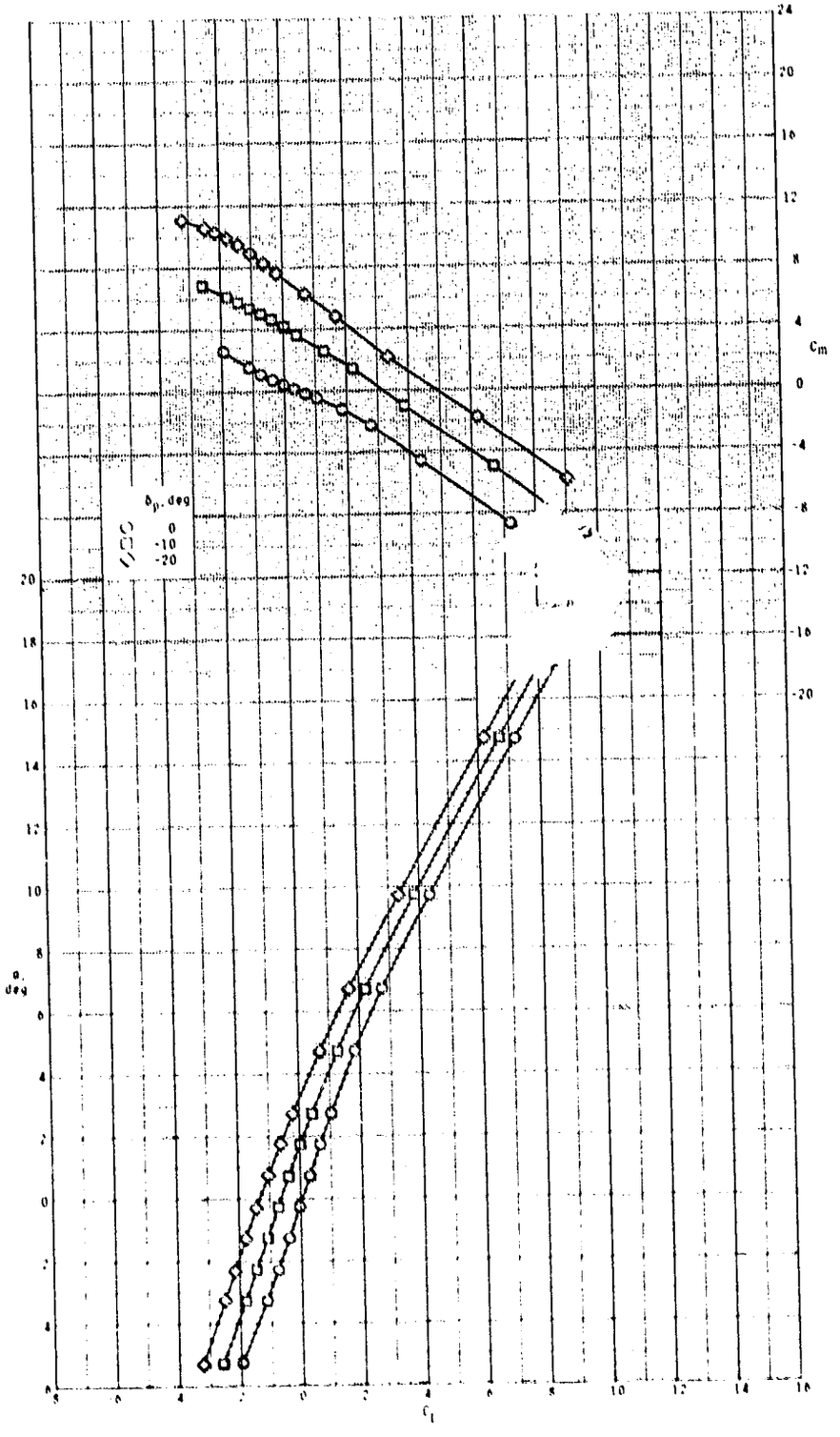

(b) Continued.

Figure 13.- Continued.

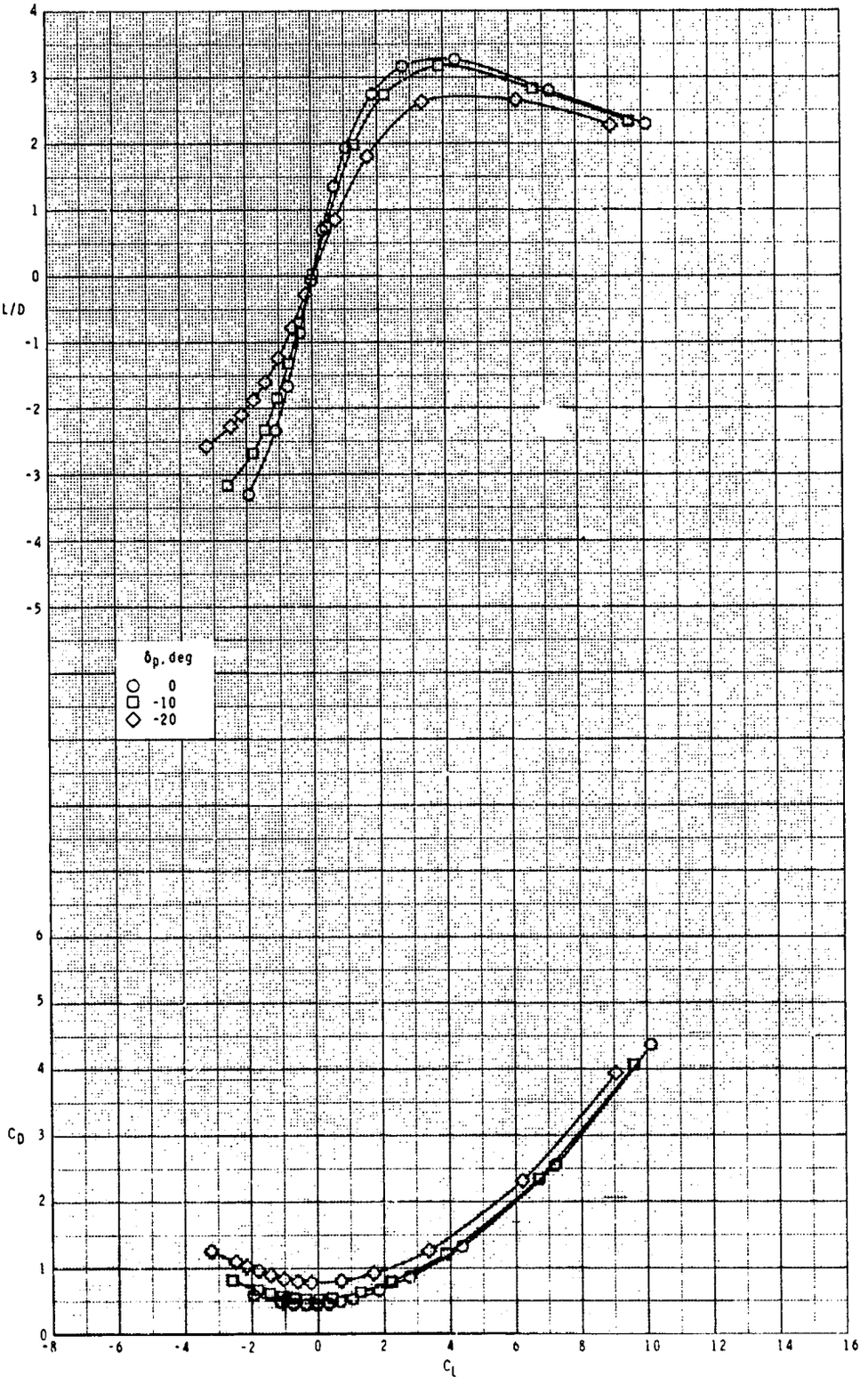

(b) Concluded.

Figure 13.- Continued.

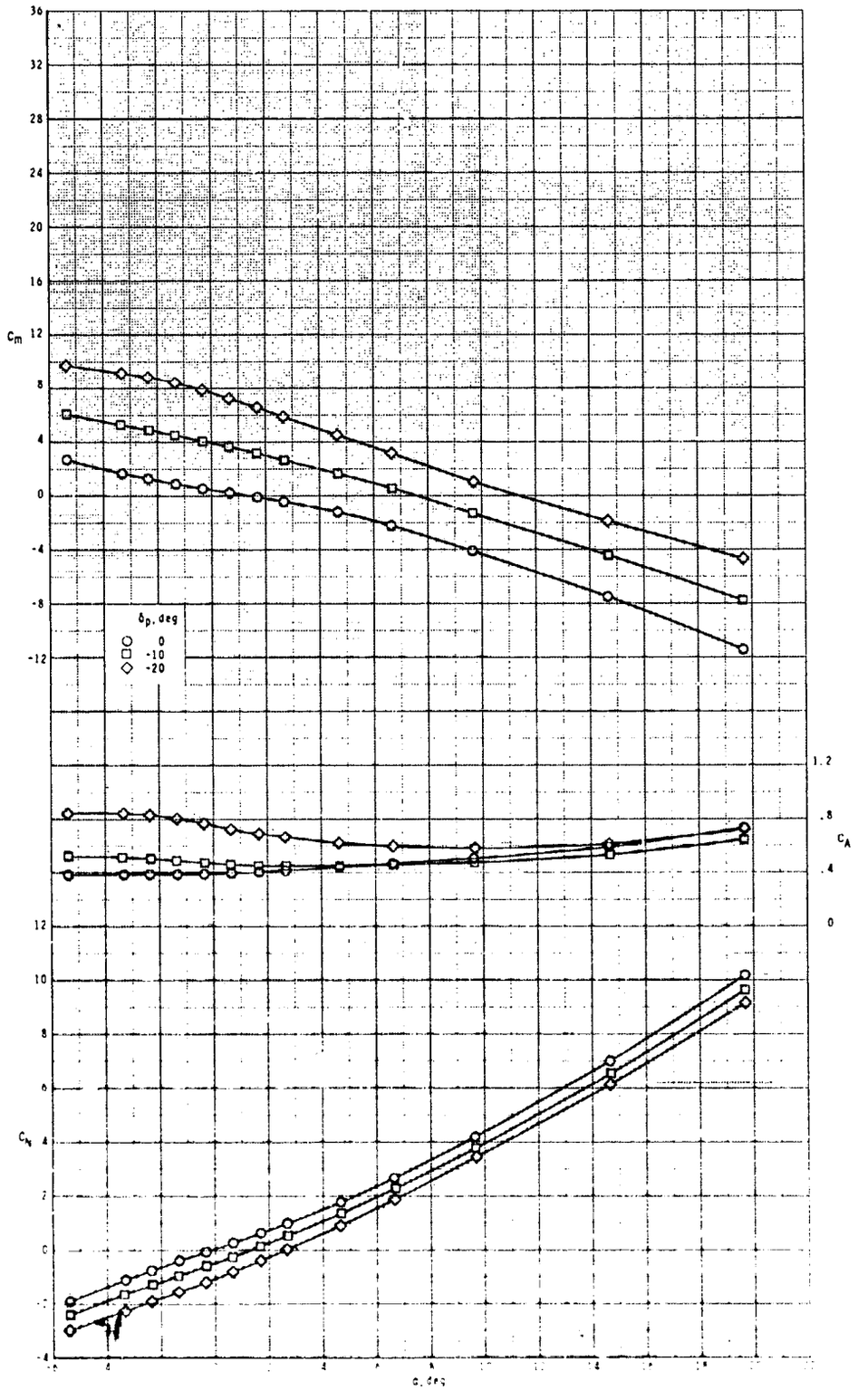

(c) M = 3.50.

Figure 13.- Continued.

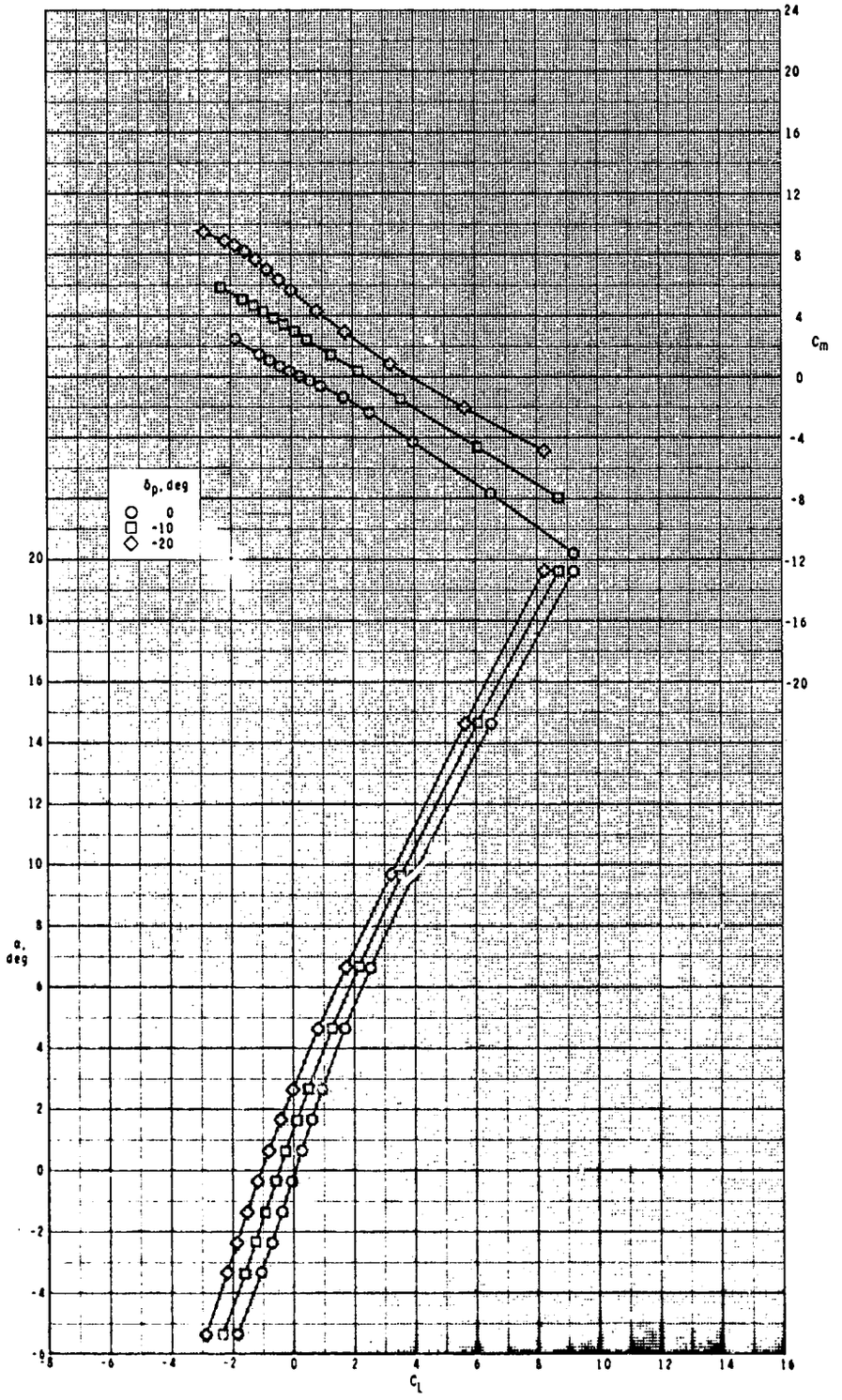

(c) Continued.

Figure 13.- Continued.

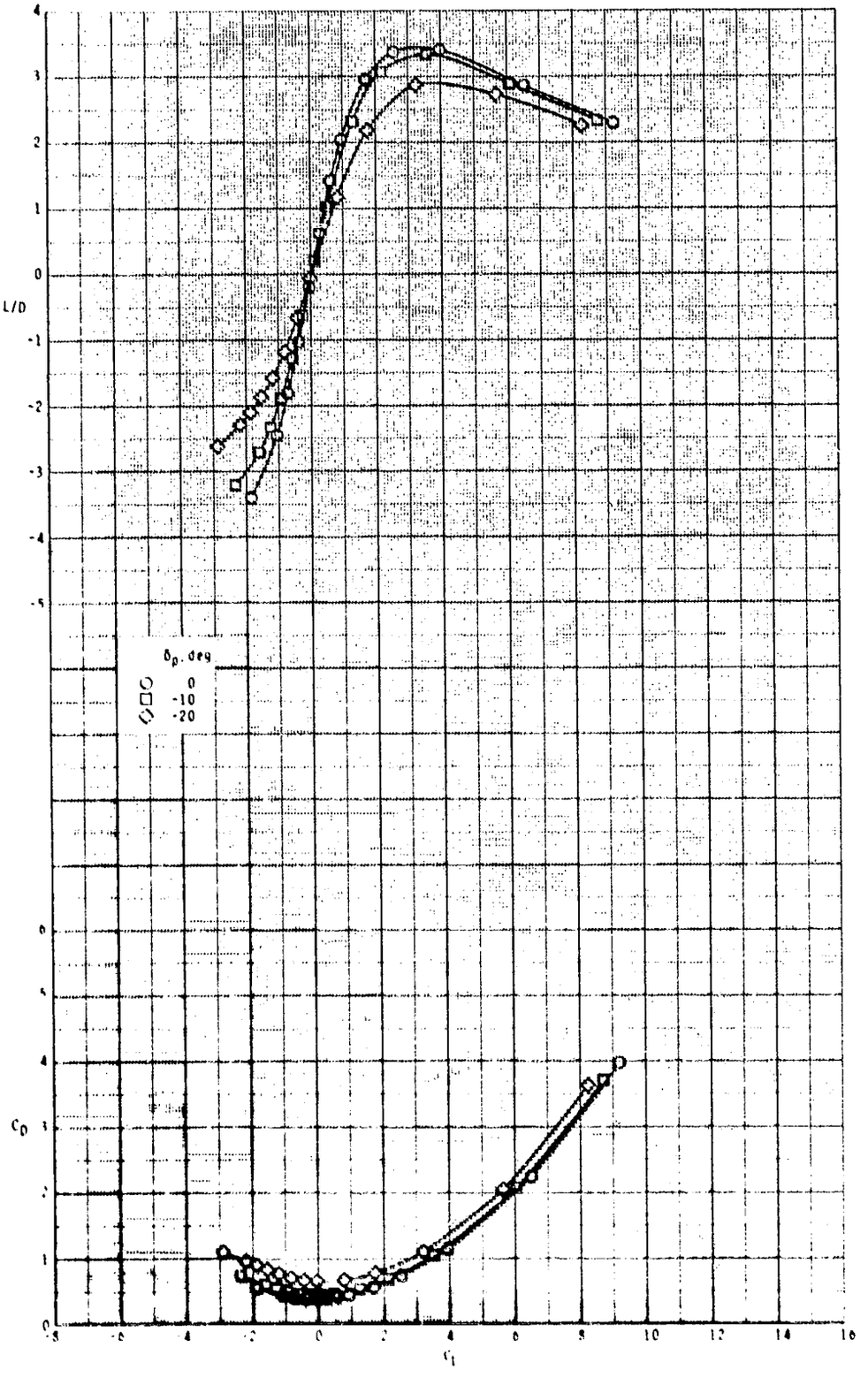

(c) Concluded.

Figure 13.- Continued.

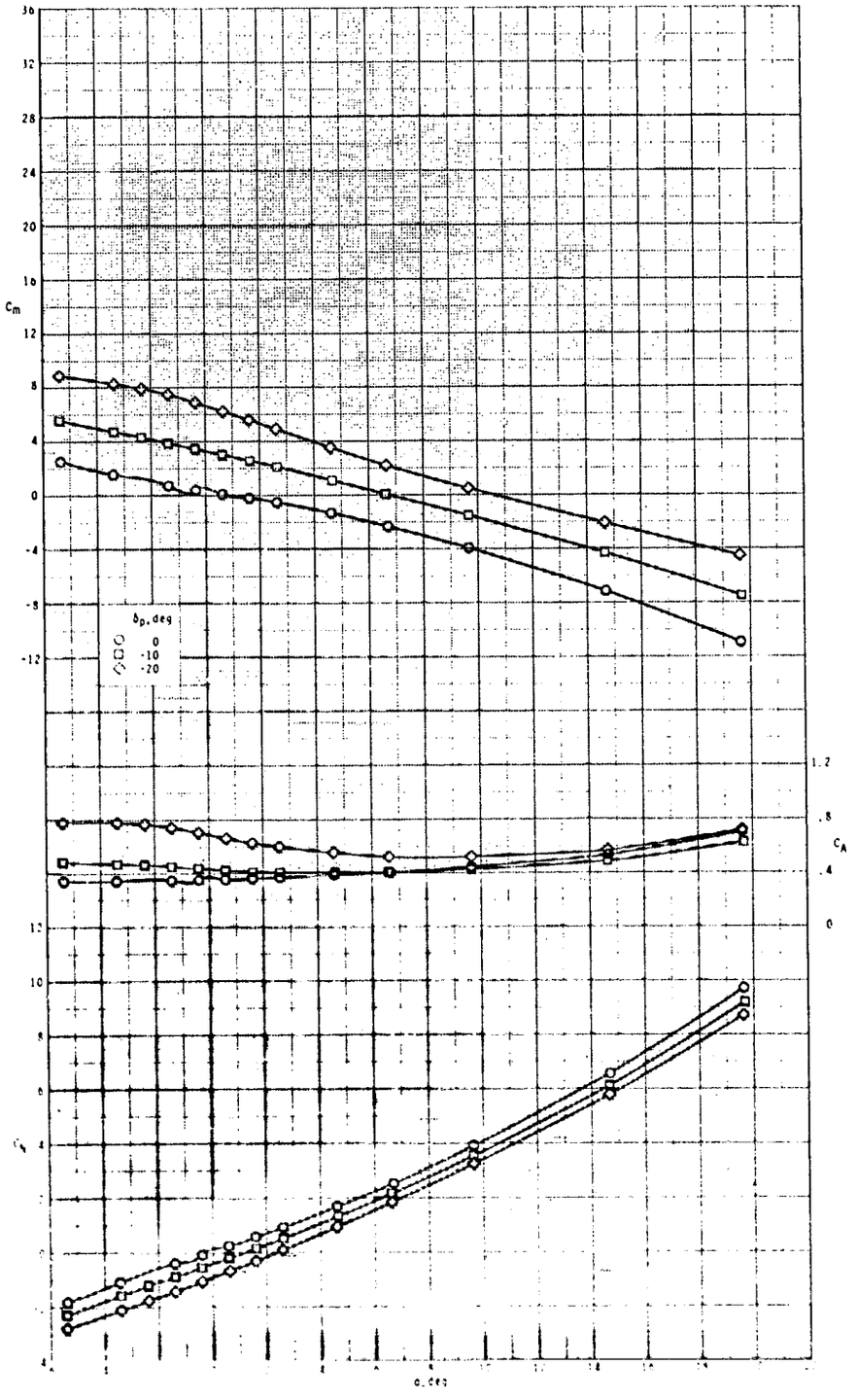

(d) M = 3.95.

Figure 13.- Continued.

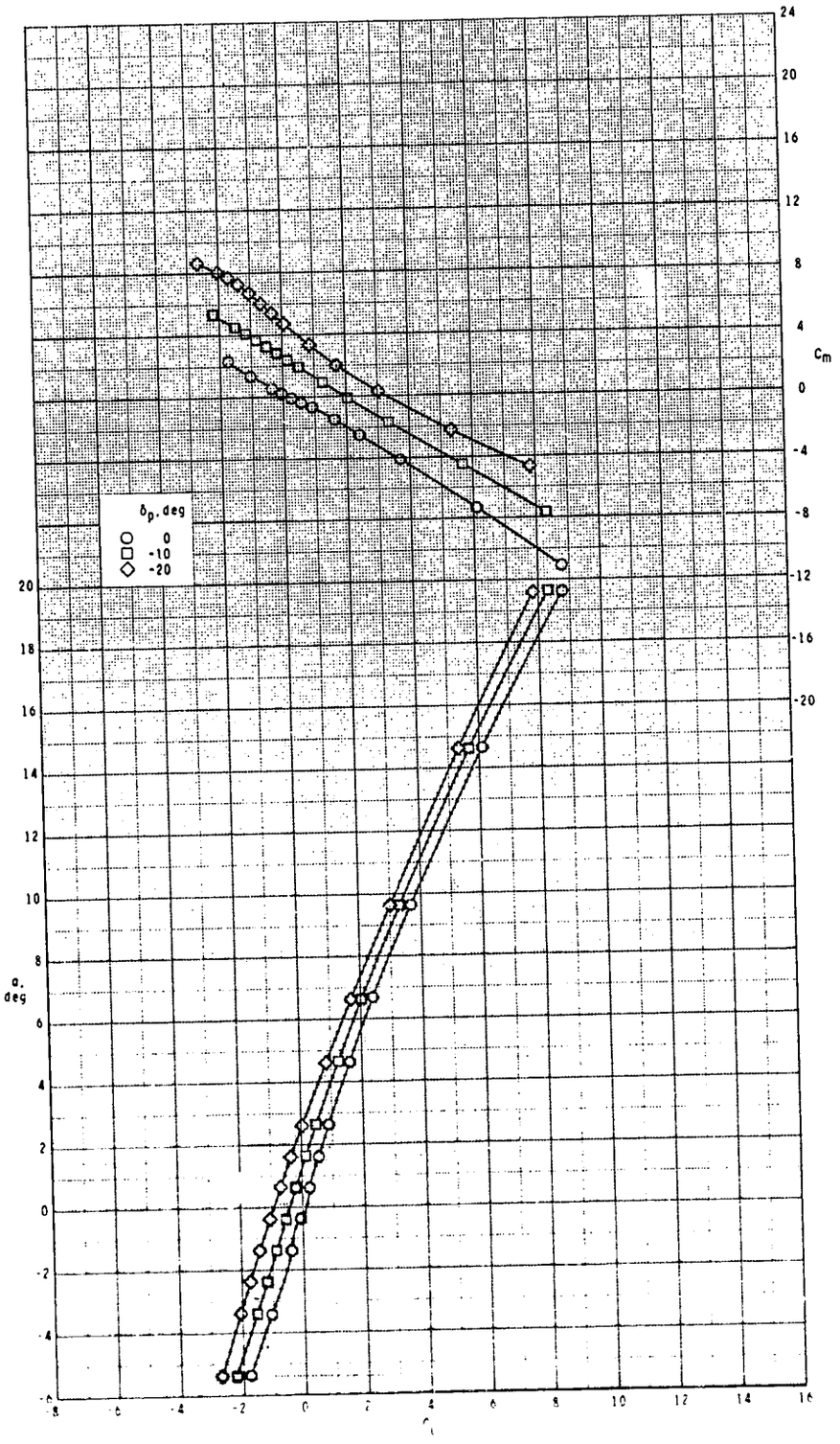

(d) Continued.

Figure 13.- Continued.

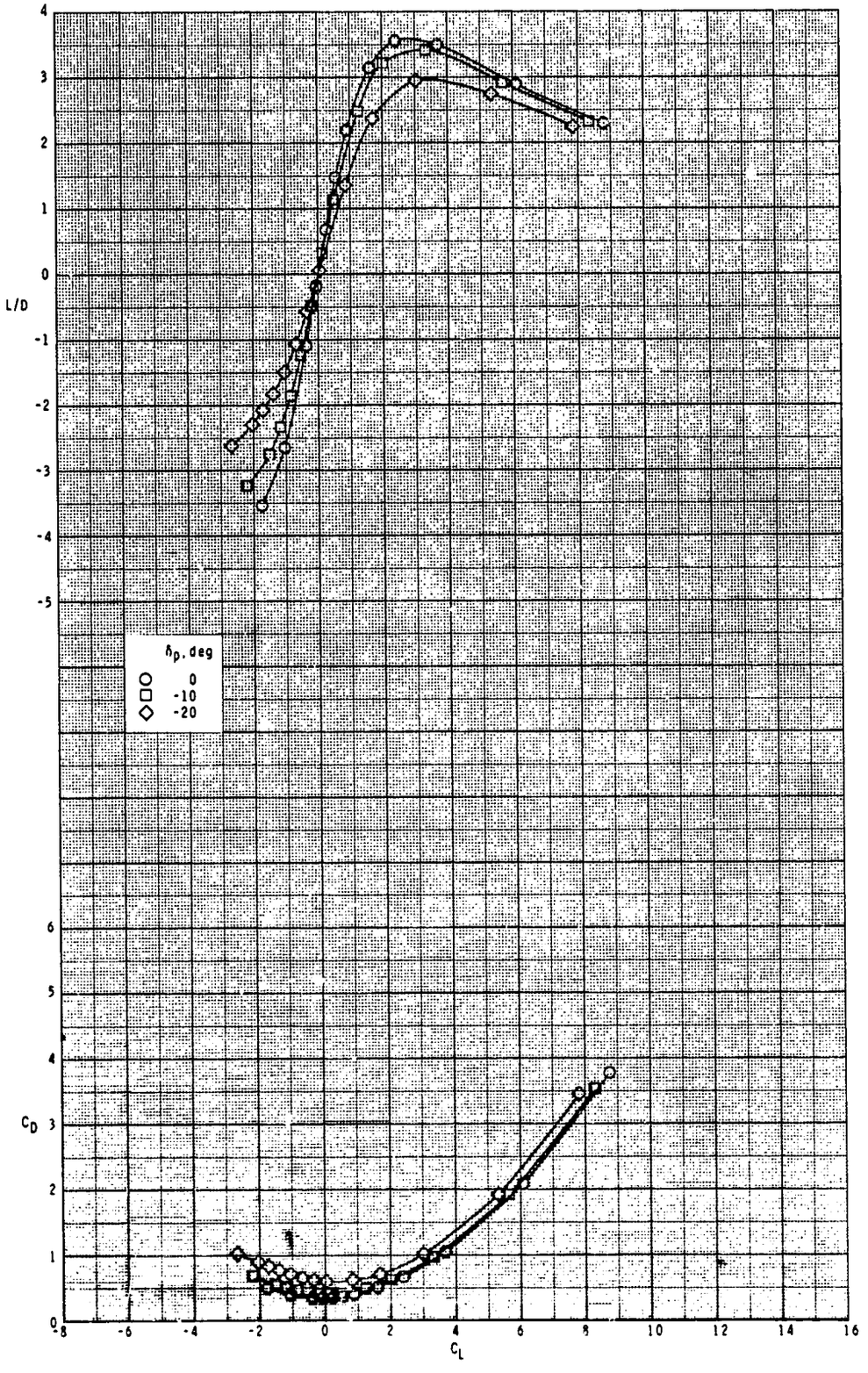

(d) Concluded.

Figure 13.- Concluded.

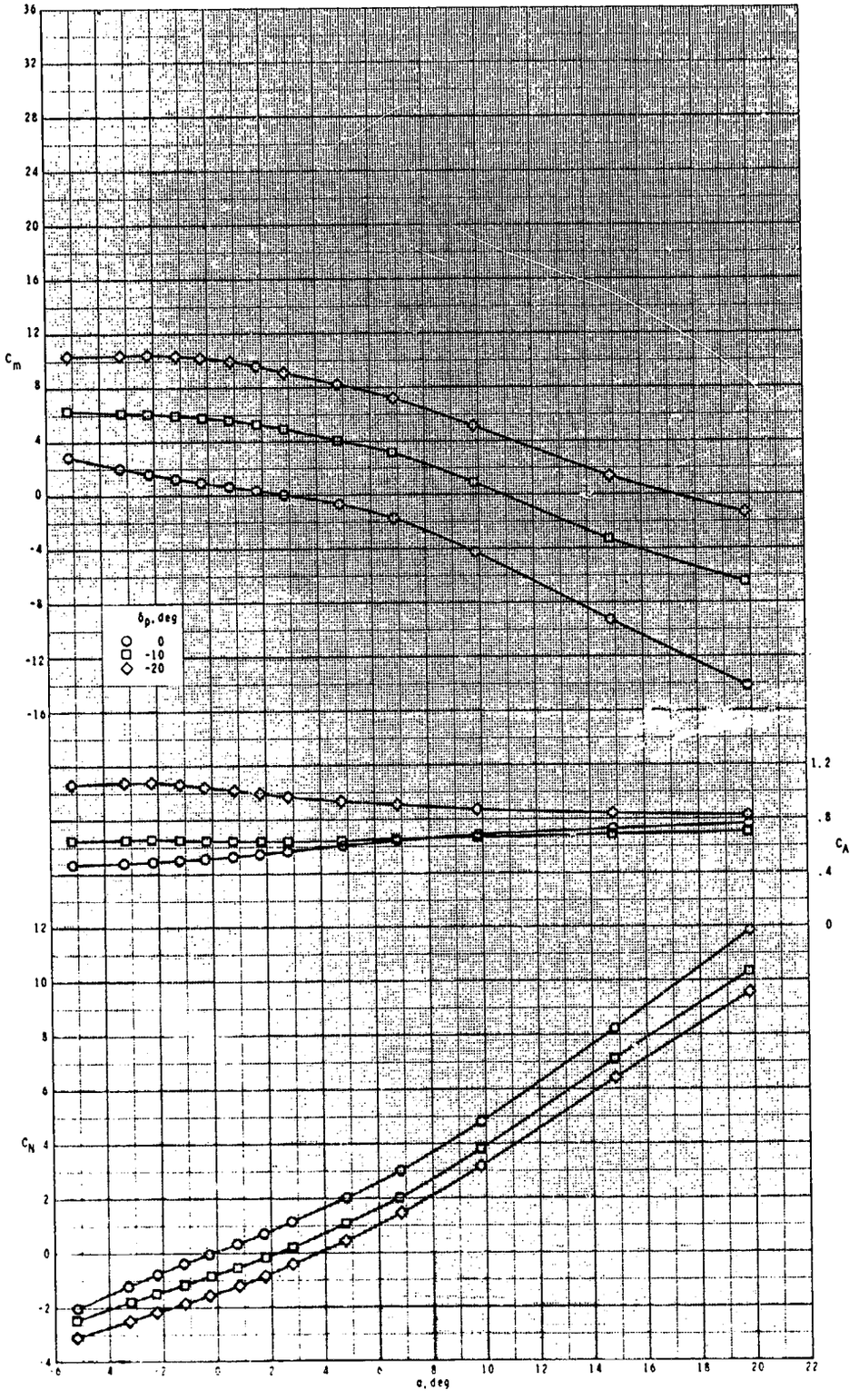

(a) M = 2.50.

Figure 14.- Pitch-control effectiveness of configuration $B_1 I_2 T_1$ with $\phi_I = 115°$.

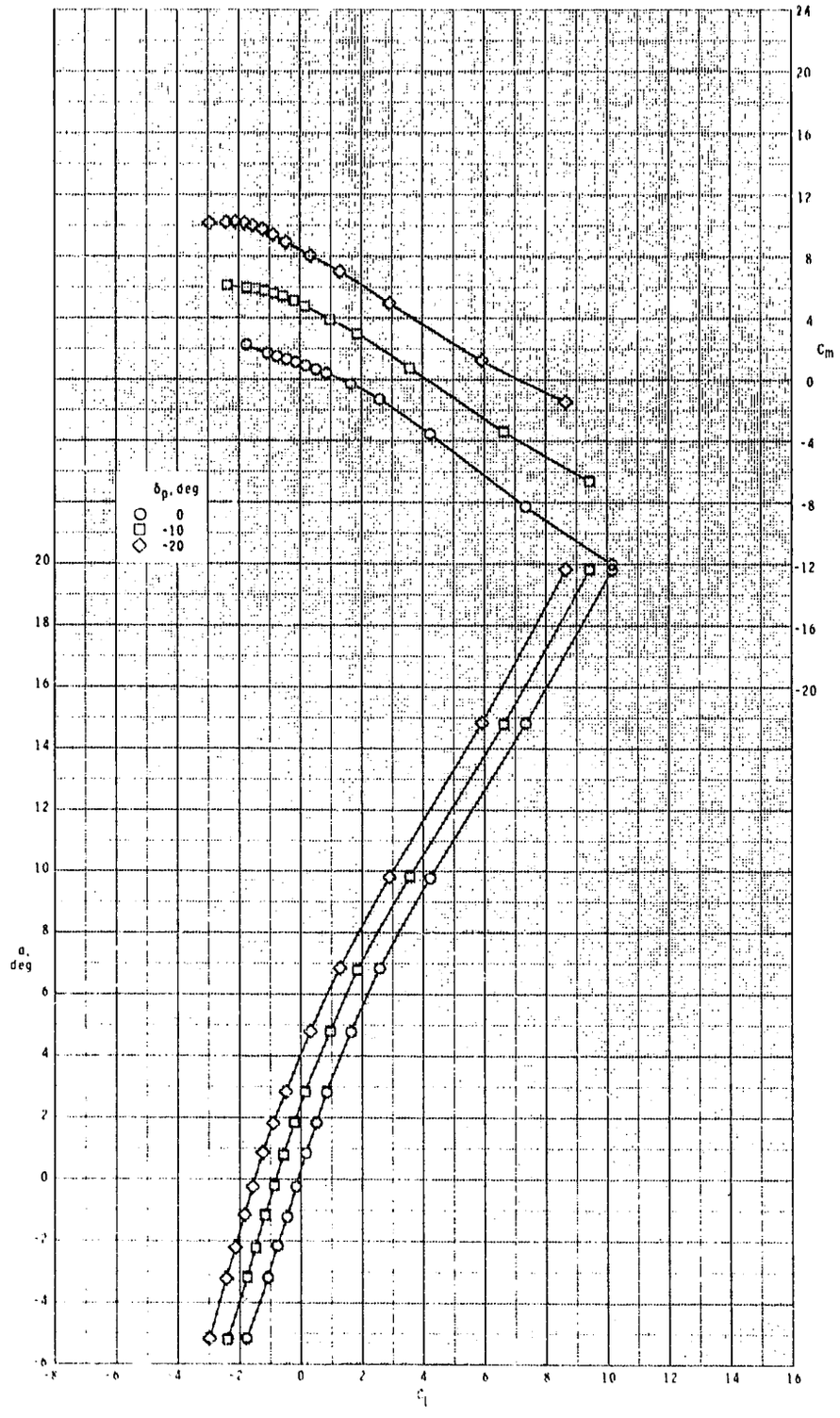

(a) Continued.

Figure 14.- Continued.

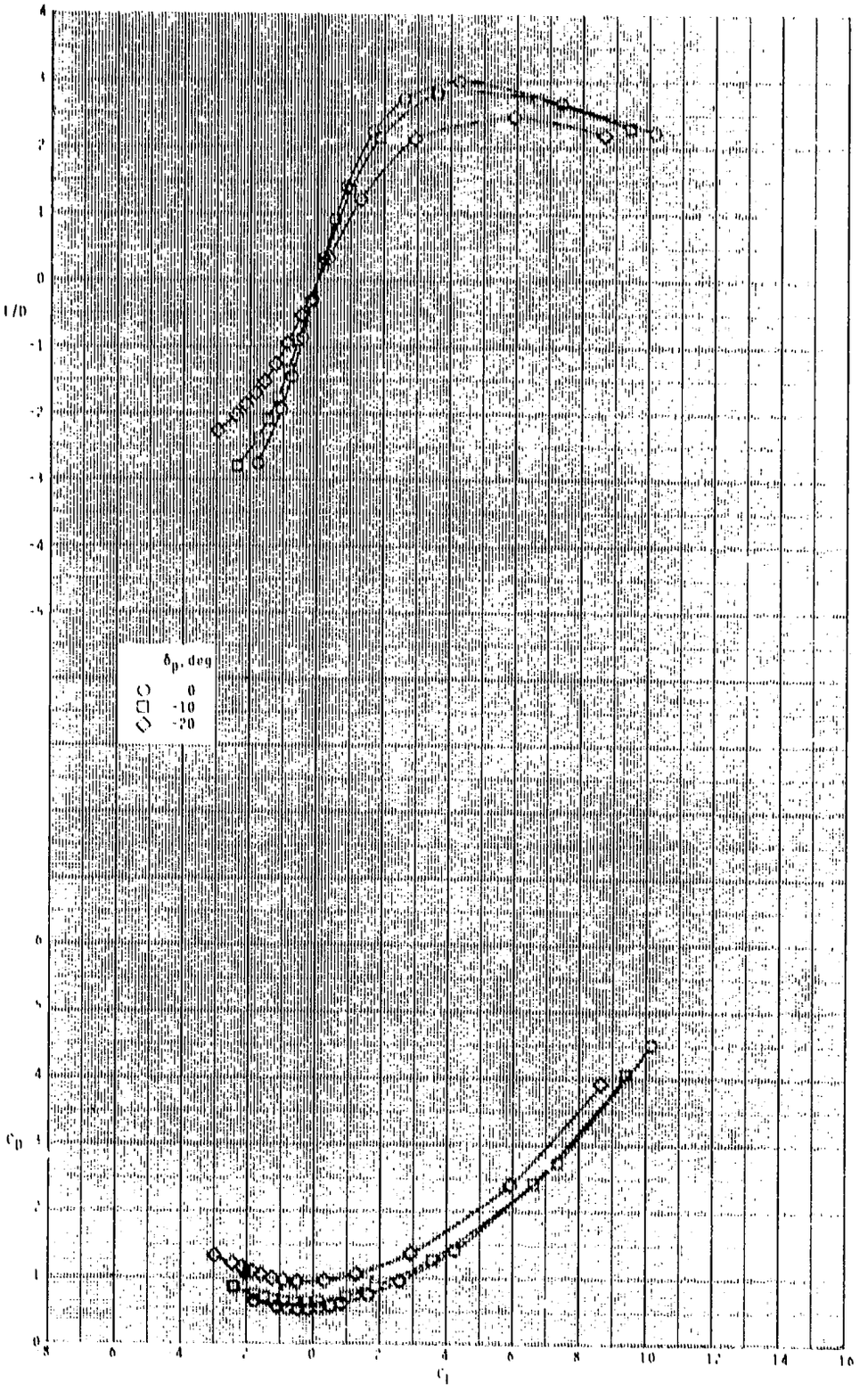

(a) Concluded.

Figure 14.- Continued.

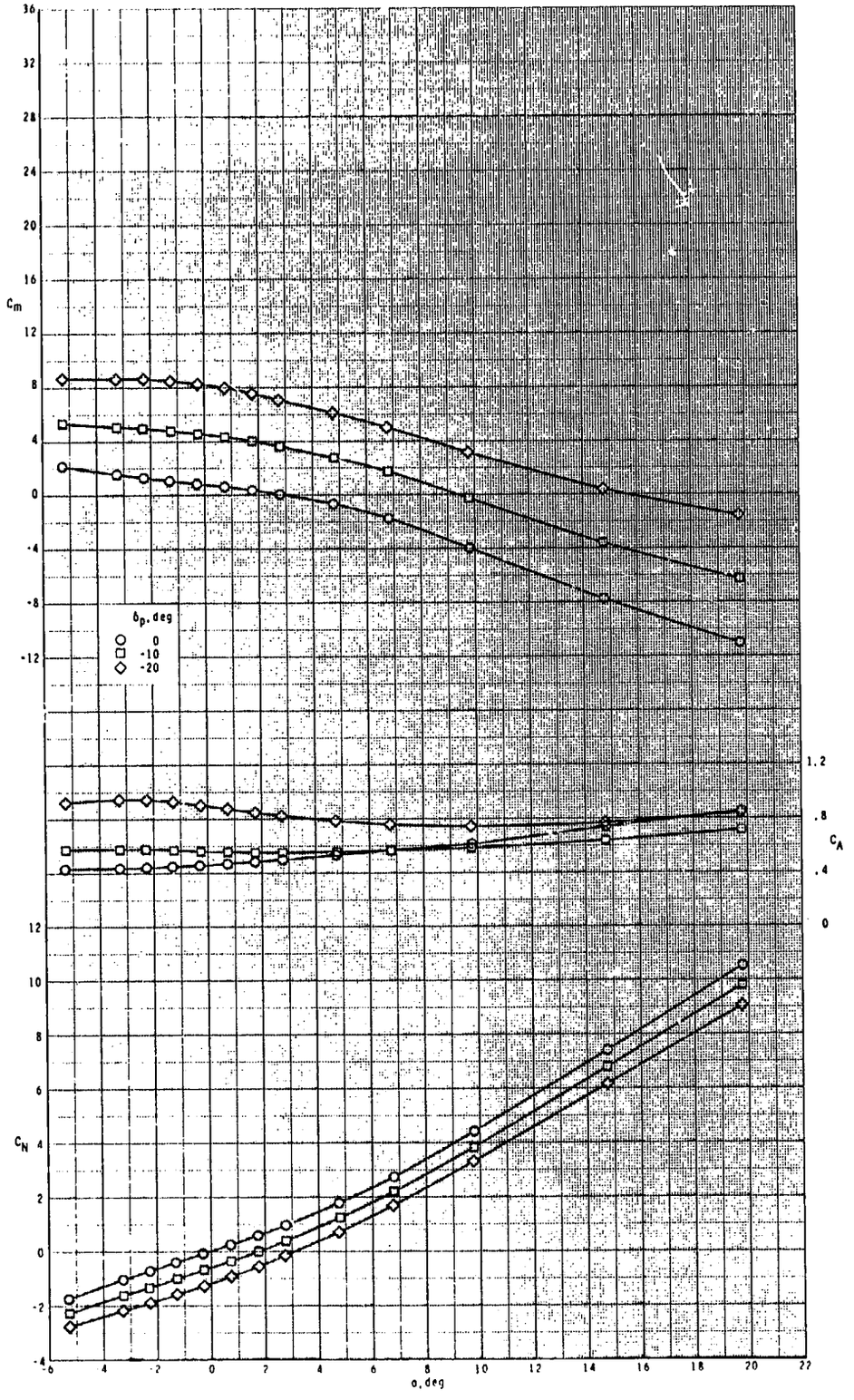

(b) M = 2.95.

Figure 14.- Continued.

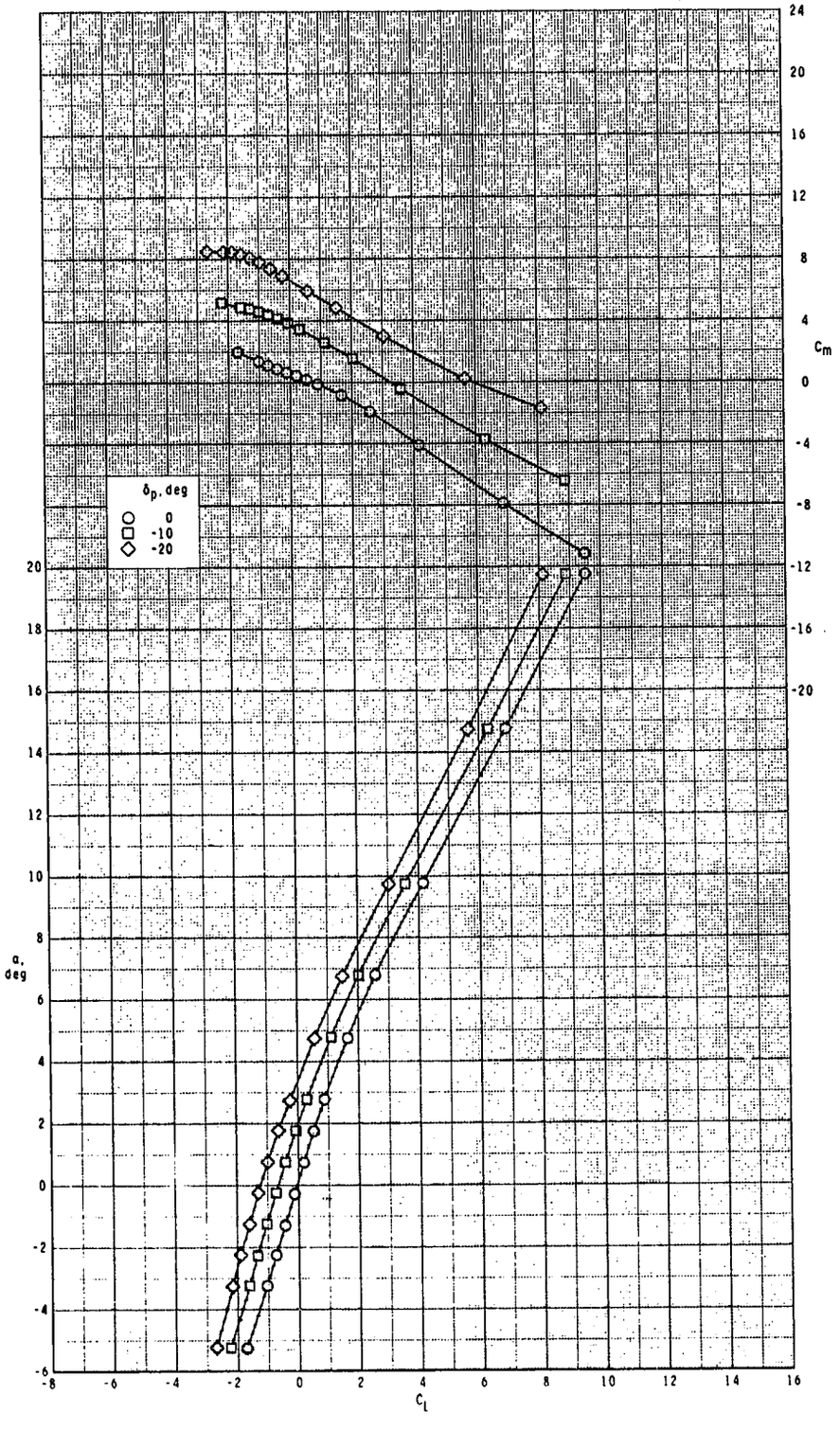

(b) Continued.

Figure 14.- Continued.

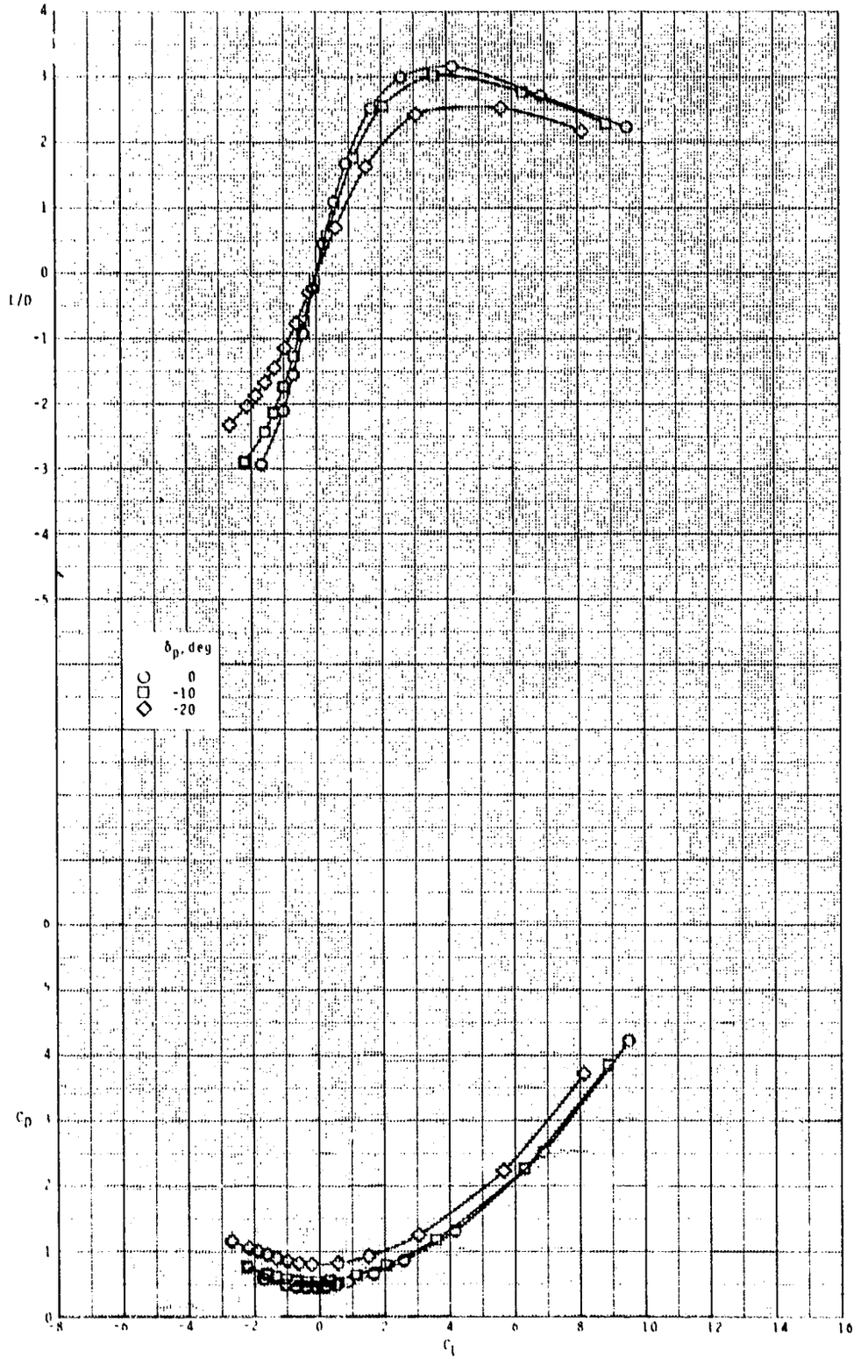

(b) Concluded.

Figure 14.- Continued.

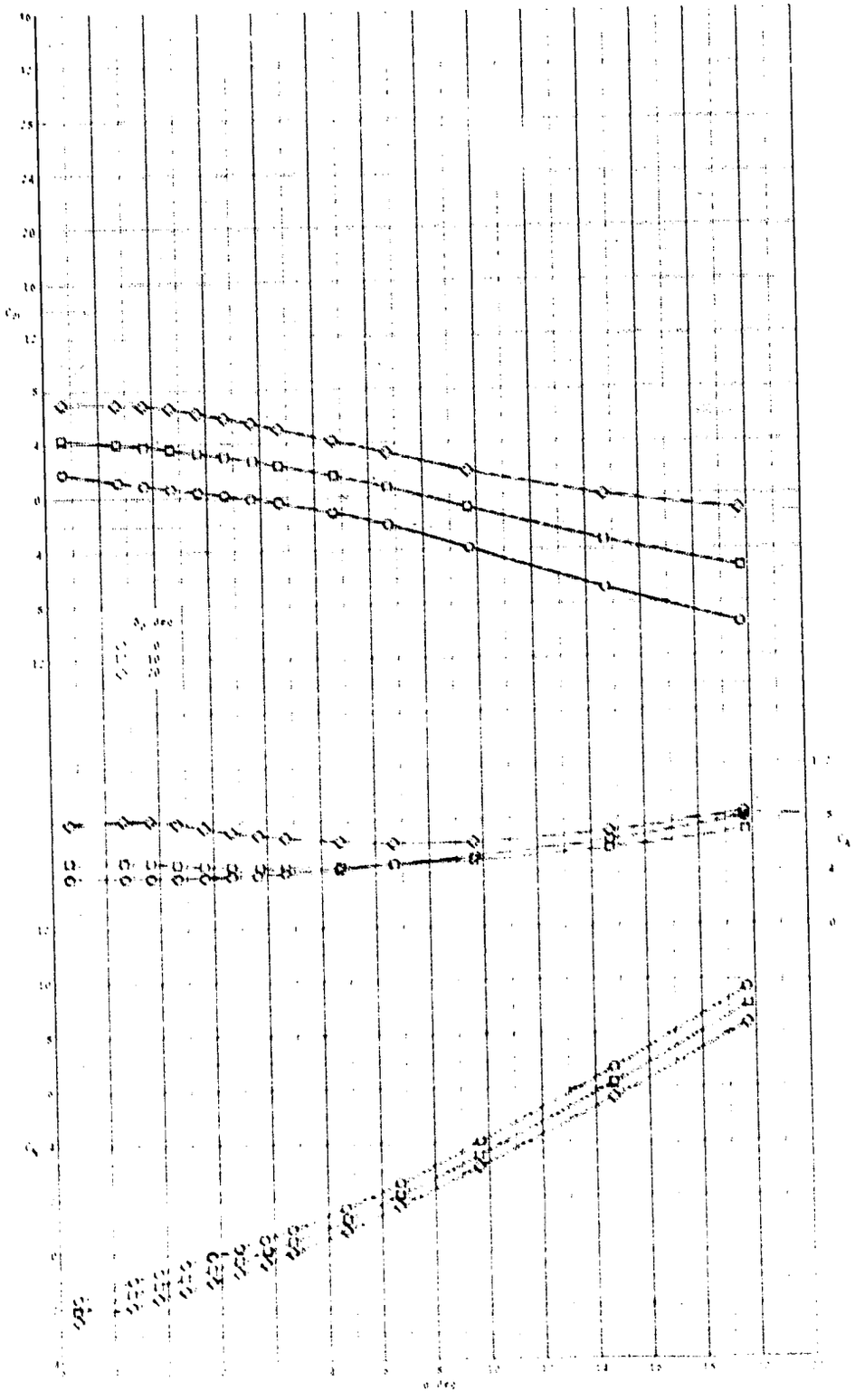

(c) M = 3.50.

Figure 14.- Continued.

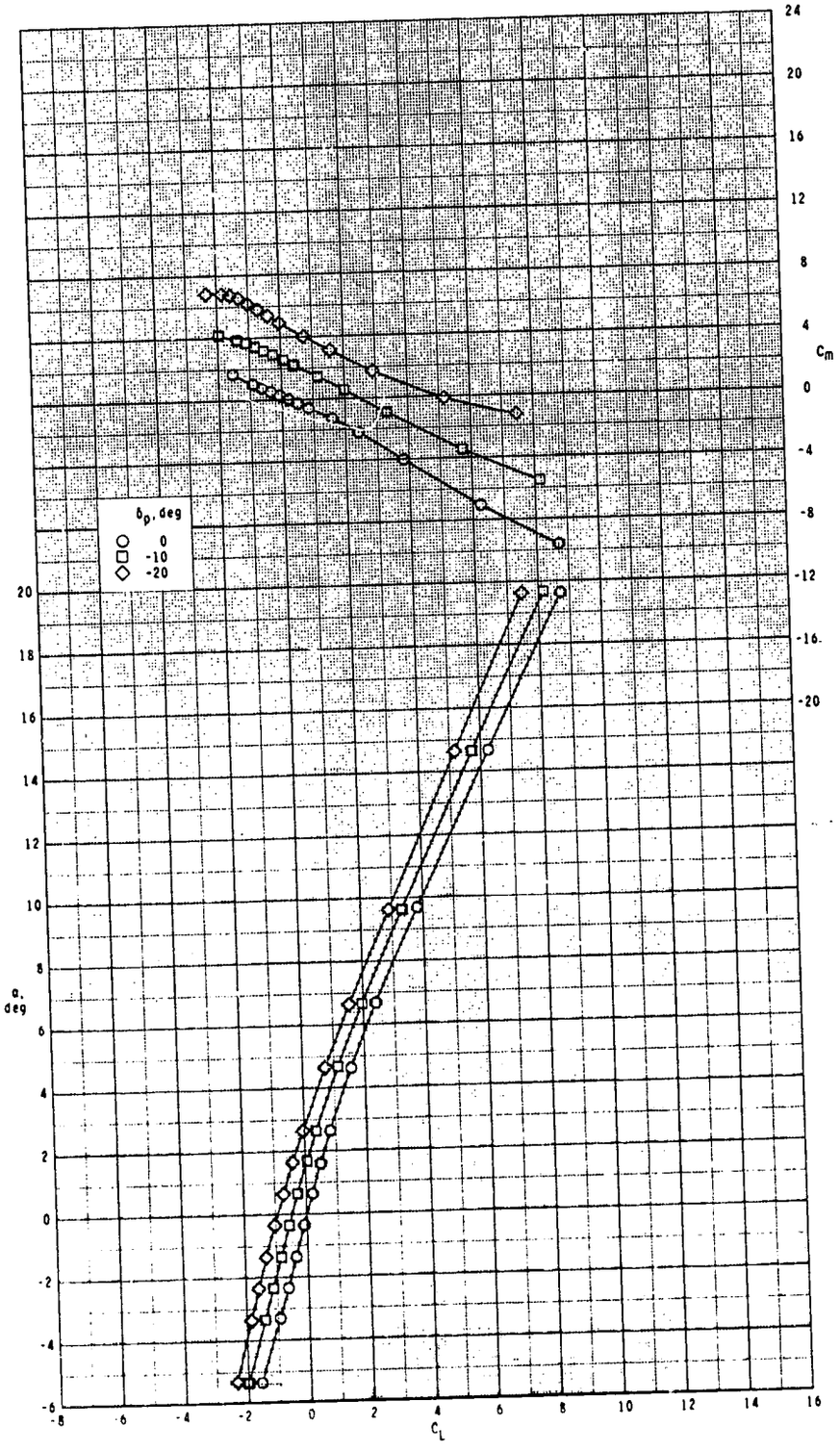

(c) Continued.

Figure 14.- Continued.

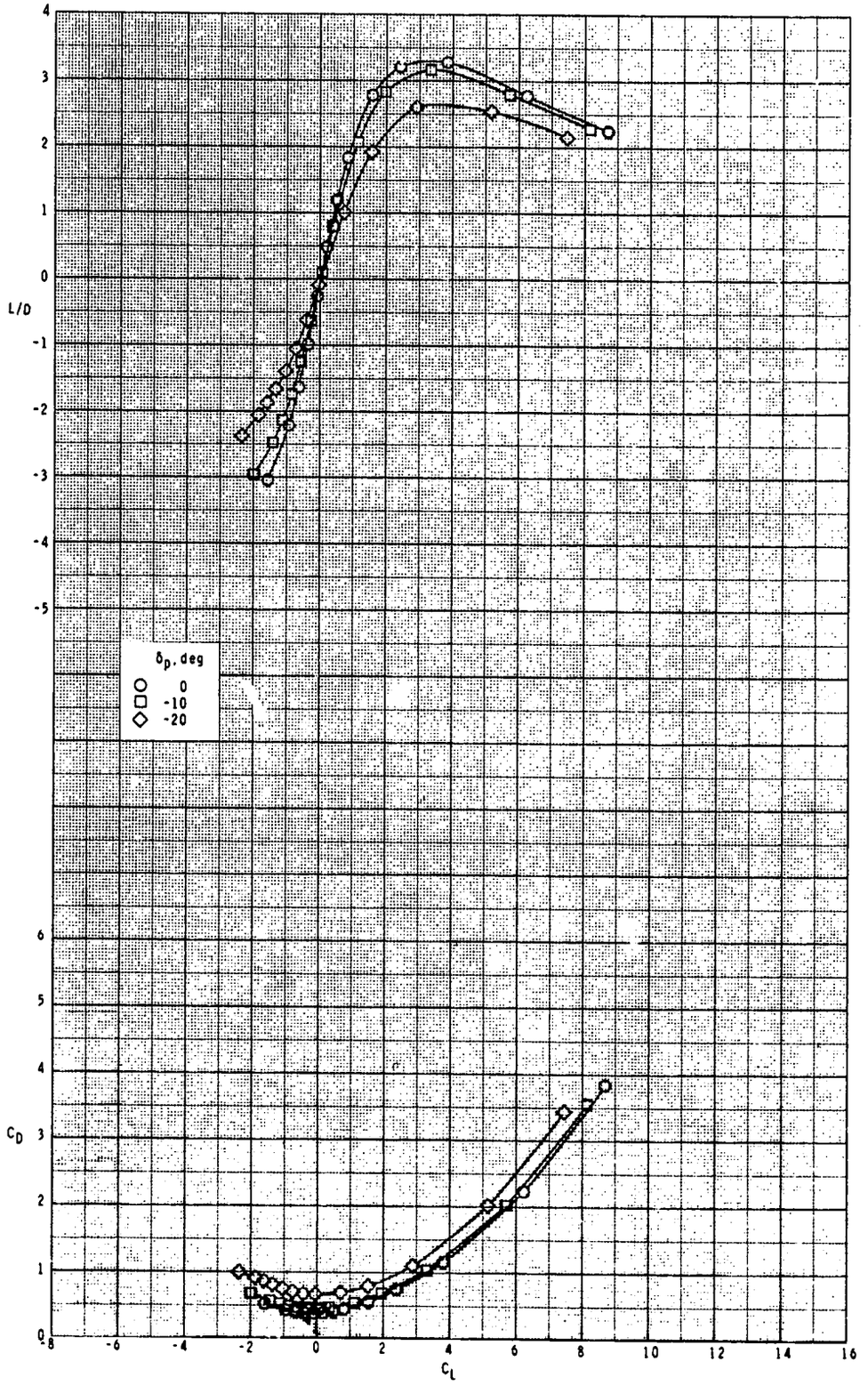

(c) Concluded.

Figure 14.- Continued.

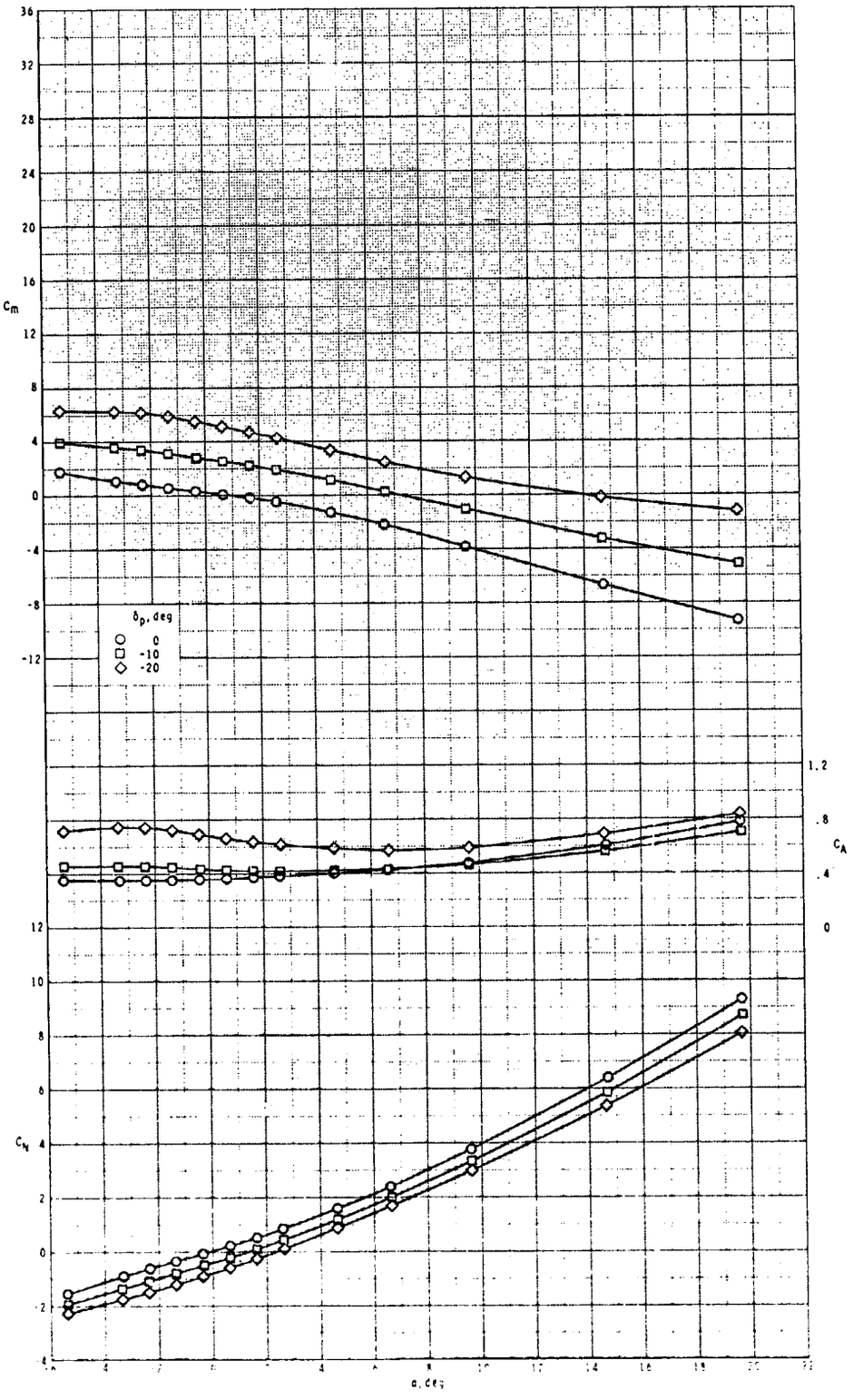

(d) M = 3.95.

Figure 14.- Continued.

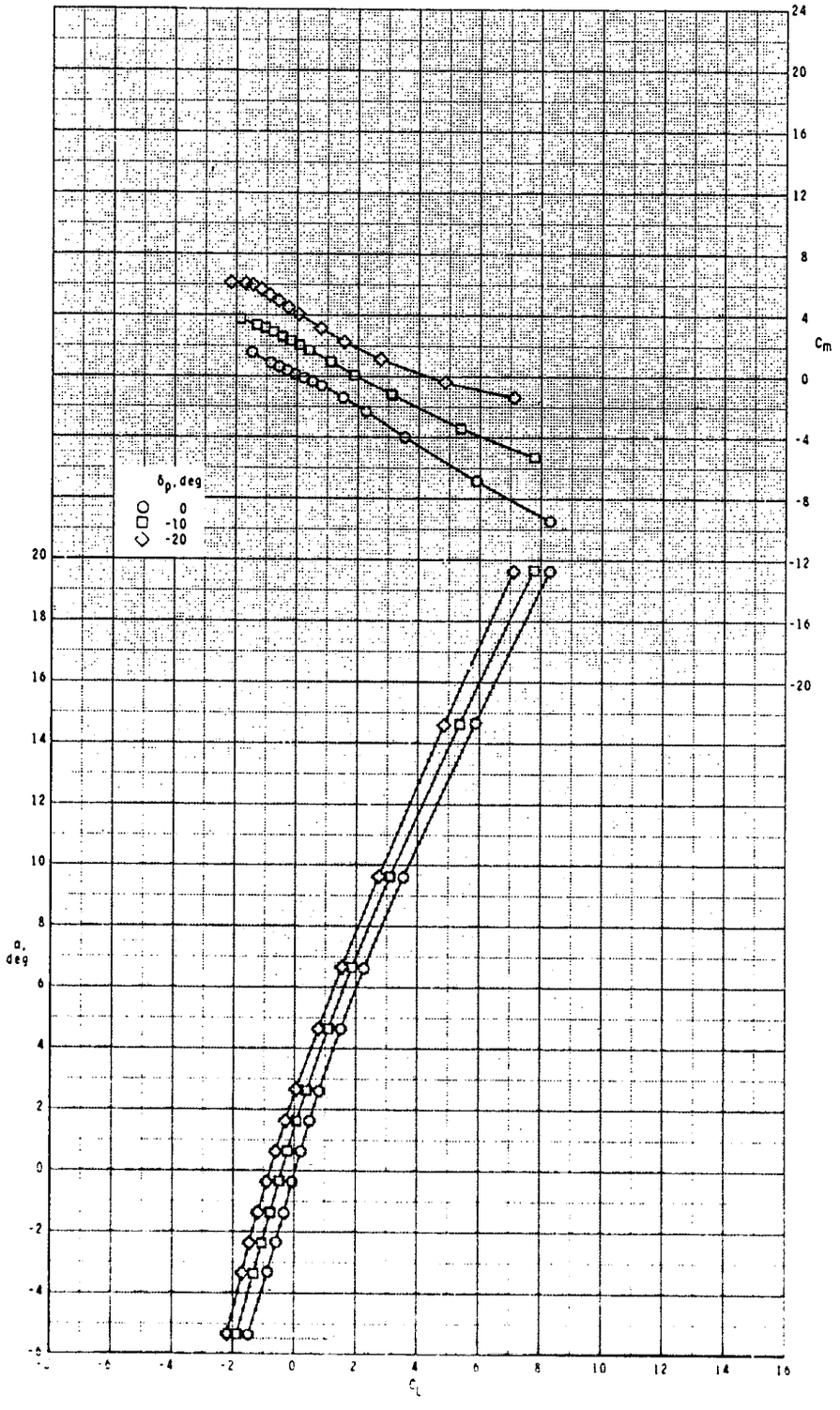

(d) Continued.

Figure 14.- Continued.

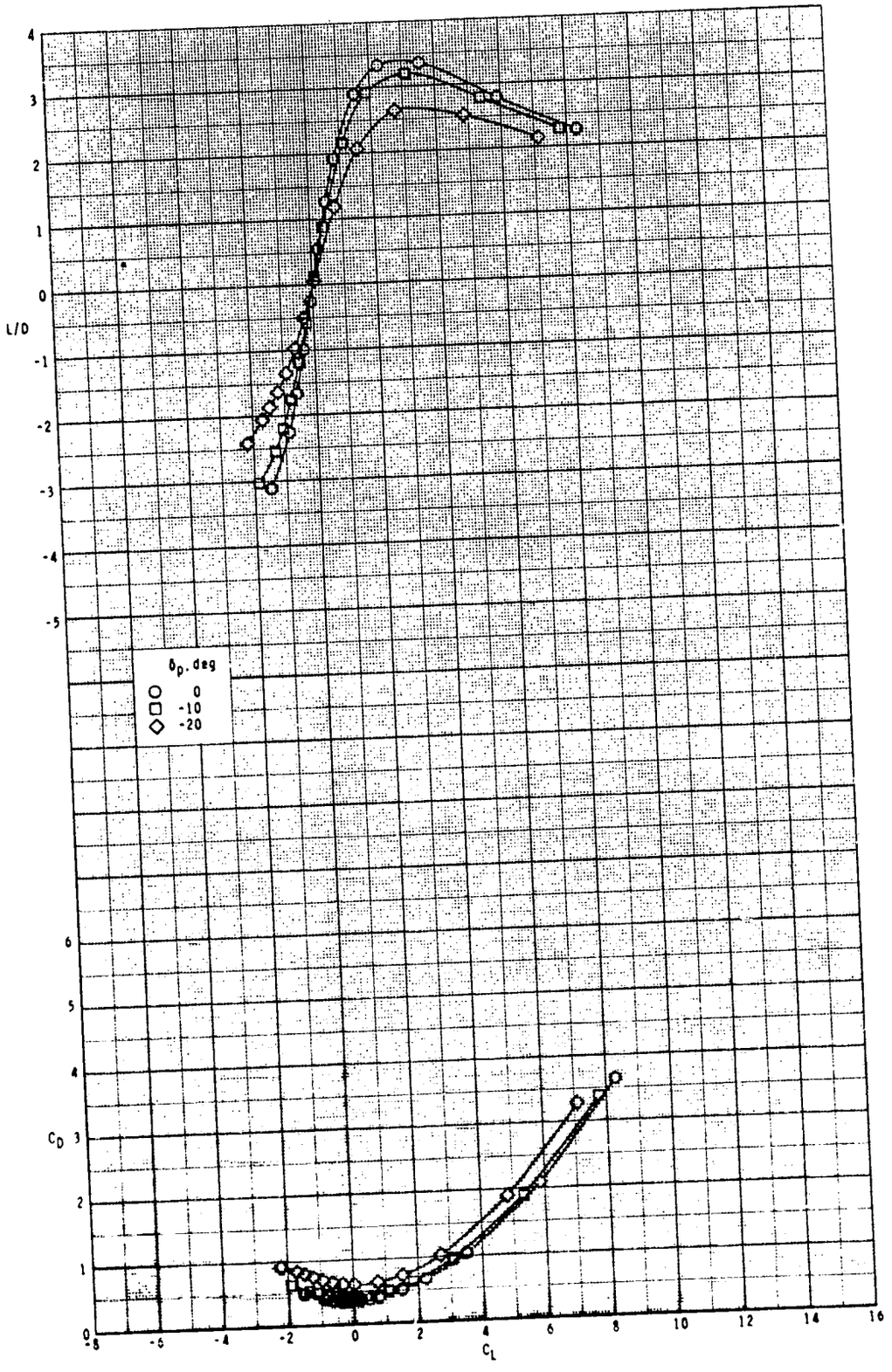

(d) Concluded.

Figure 14.- Concluded.

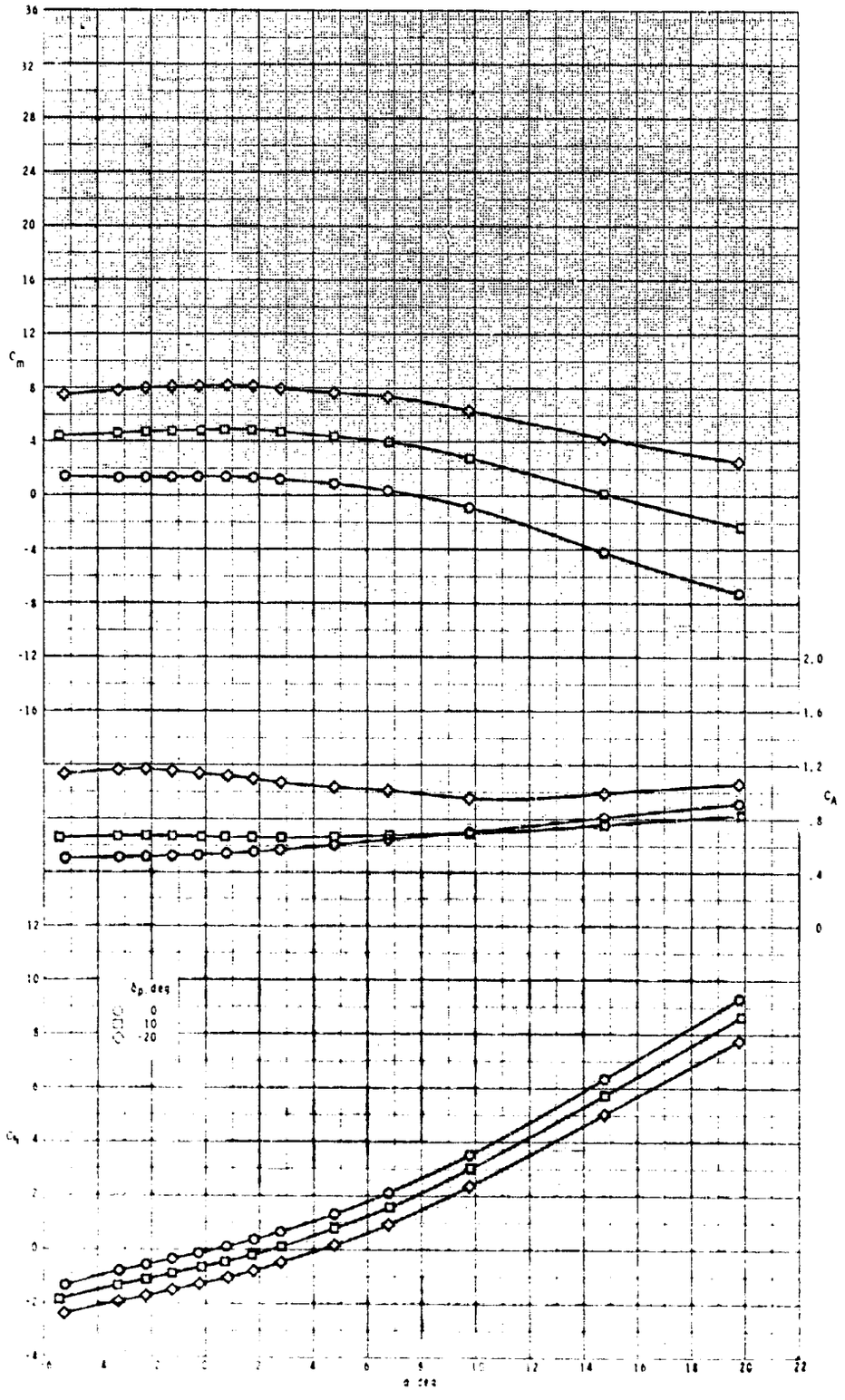

(a) M = 2.50.

Figure 15.- Pitch-control effectiveness of configuration $B_1I_2T_1$ with $\phi_I = 135°$.

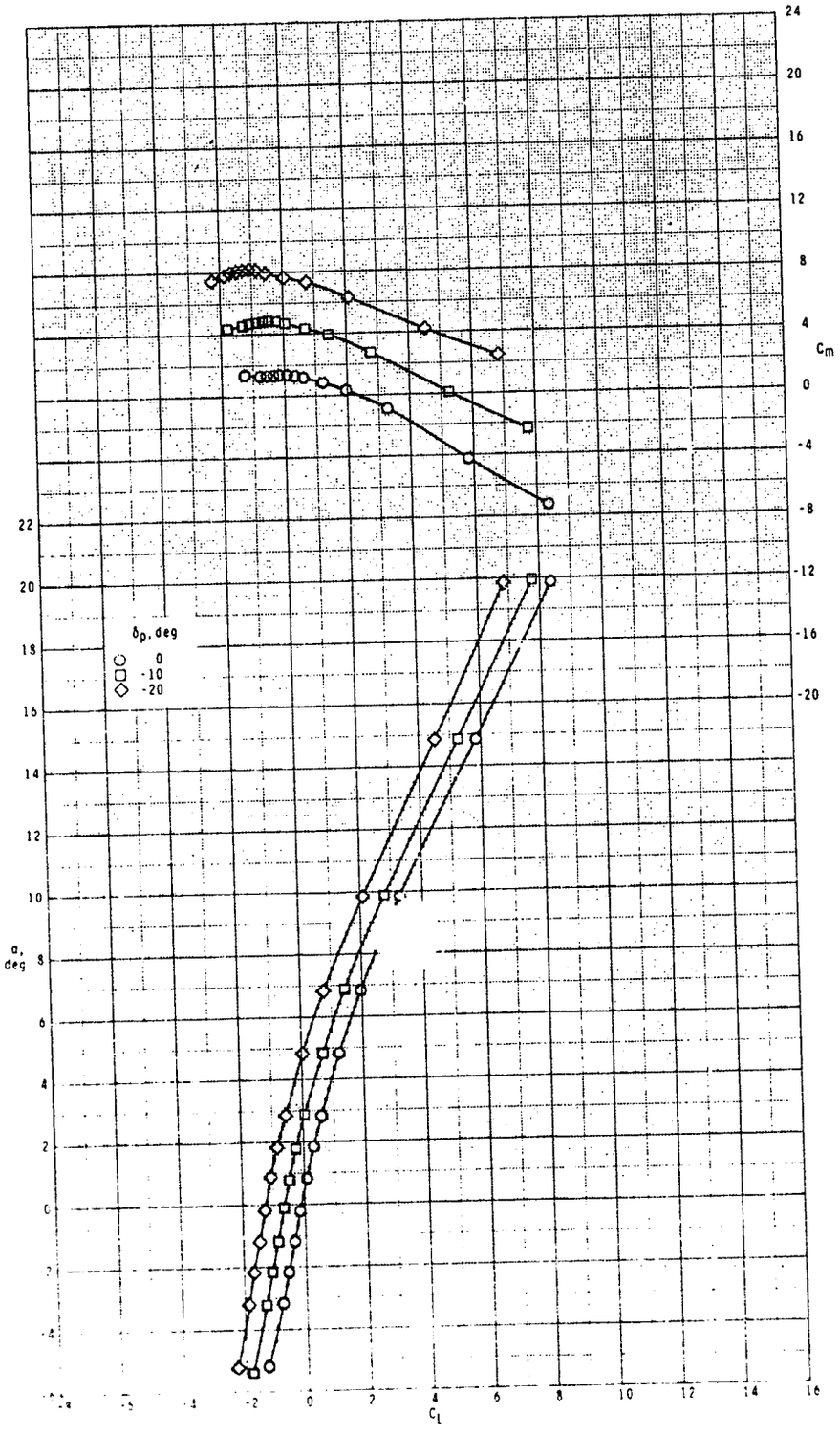

(a) Continued.

Figure 15.- Continued.

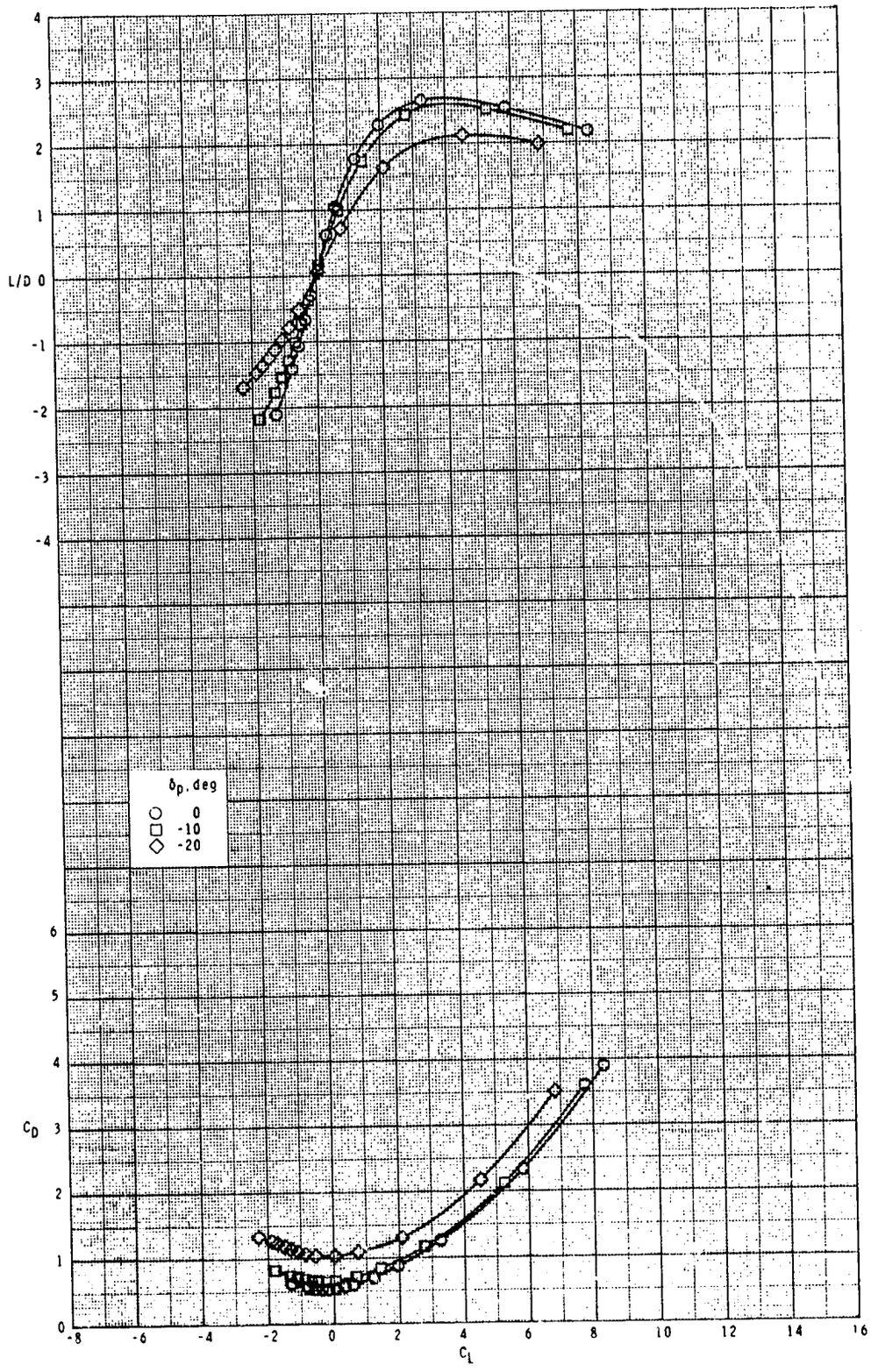

(a) Concluded.

Figure 15.- Continued.

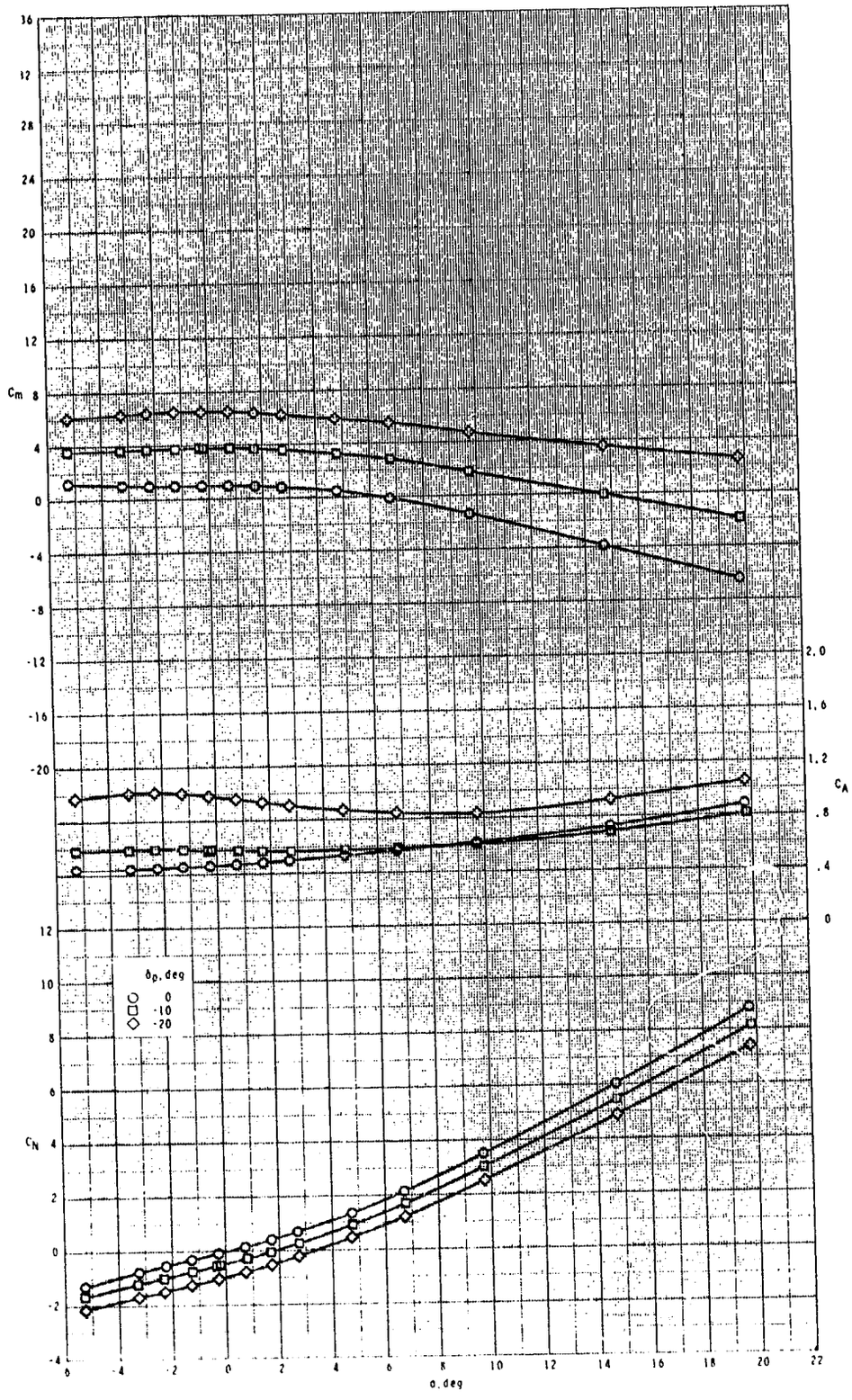

(b) M = 2.95.

Figure 15.- Continued.

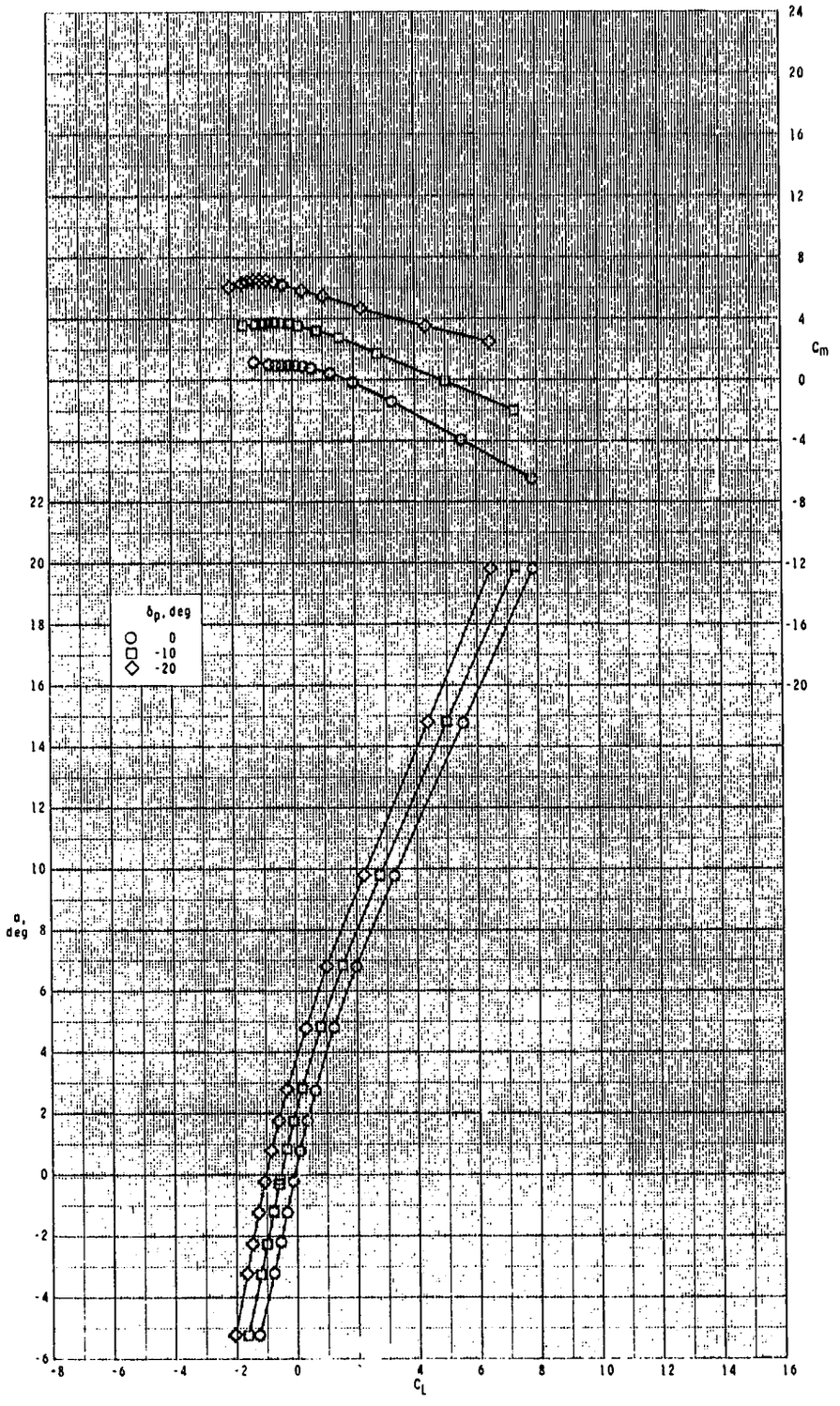

(b) Continued.

Figure 15.- Continued.

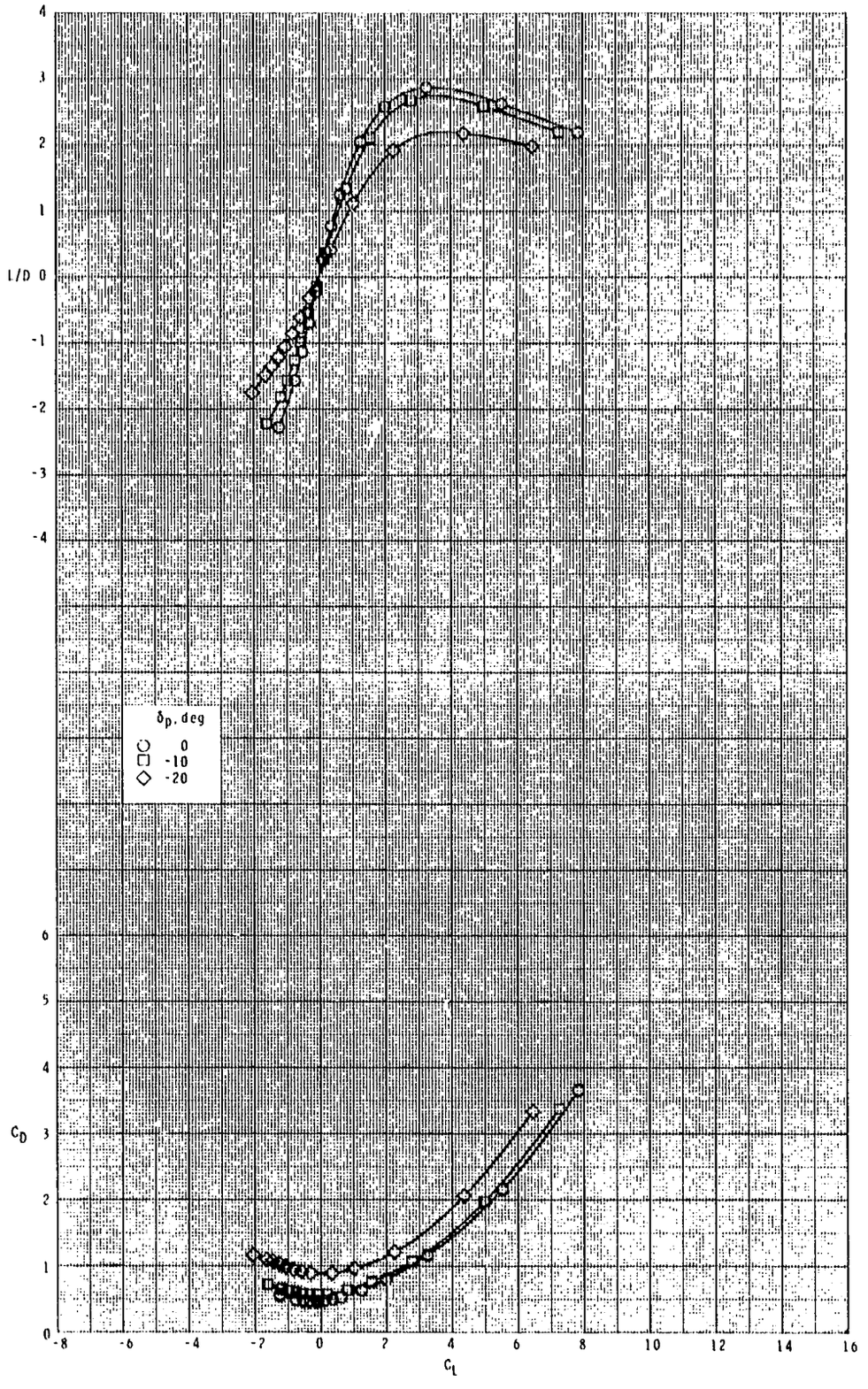

(b) Concluded.

Figure 15.- Continued.

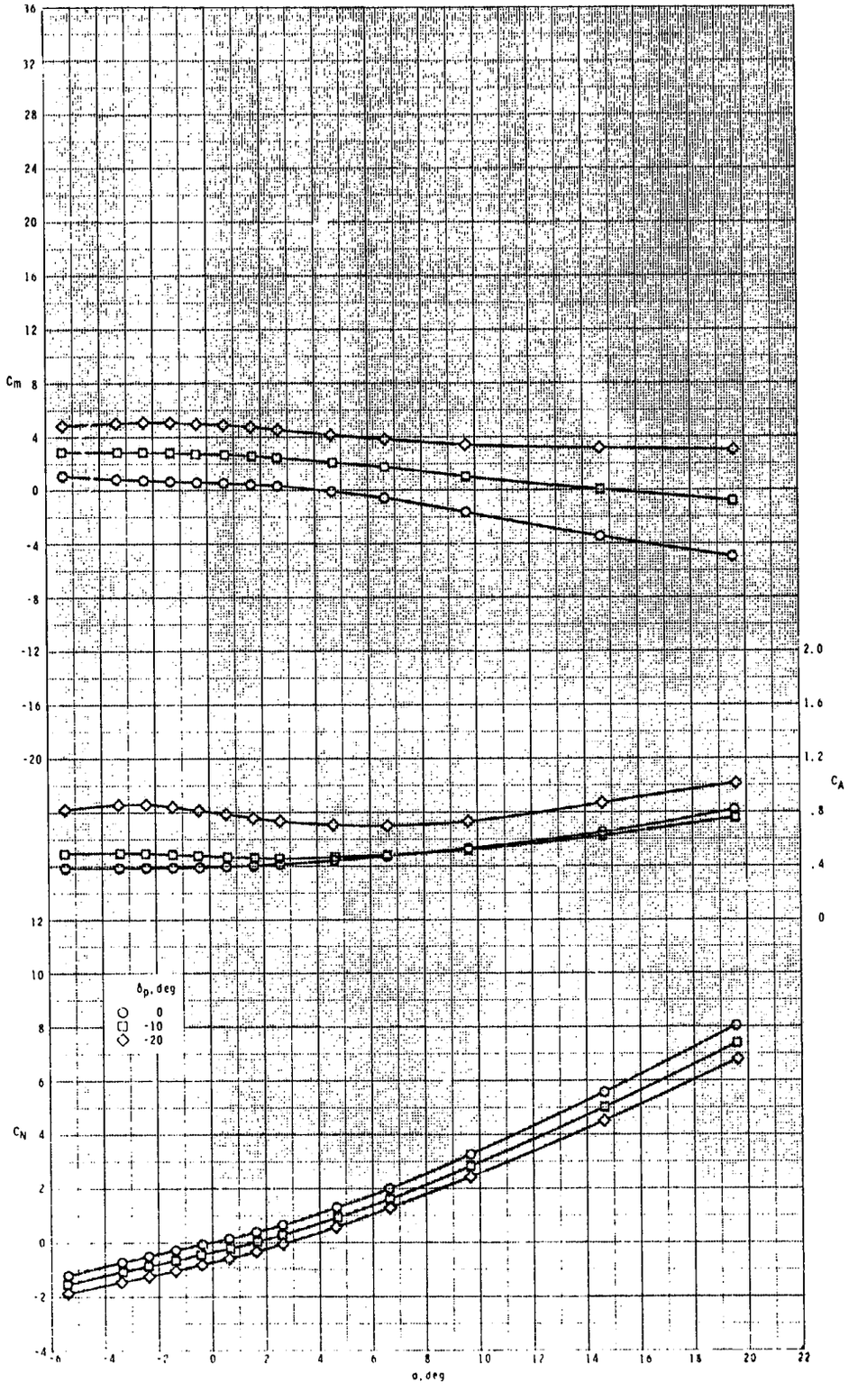

(c) M = 3.50.

Figure 15.- Continued.

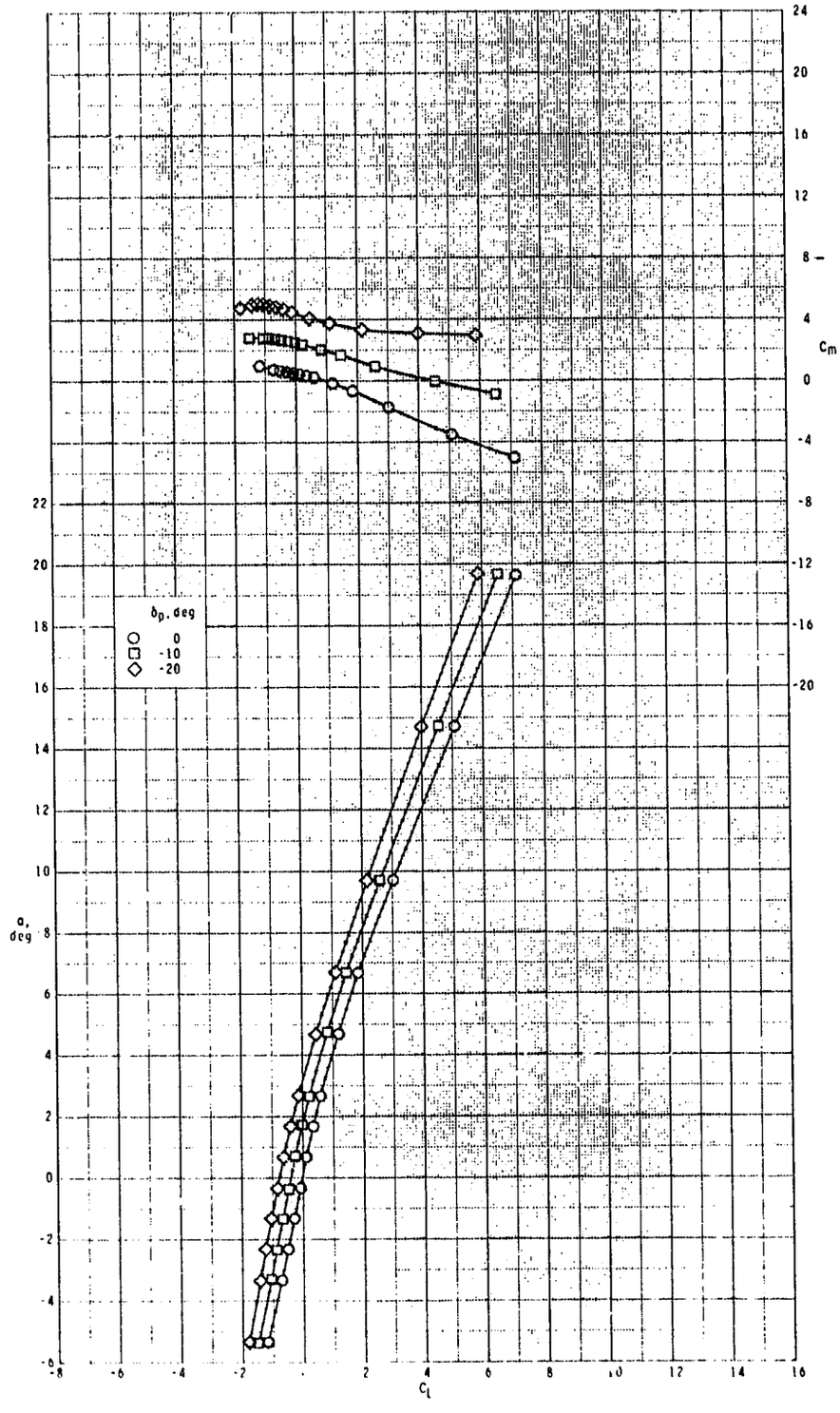

(c) Continued.

Figure 15.- Continued.

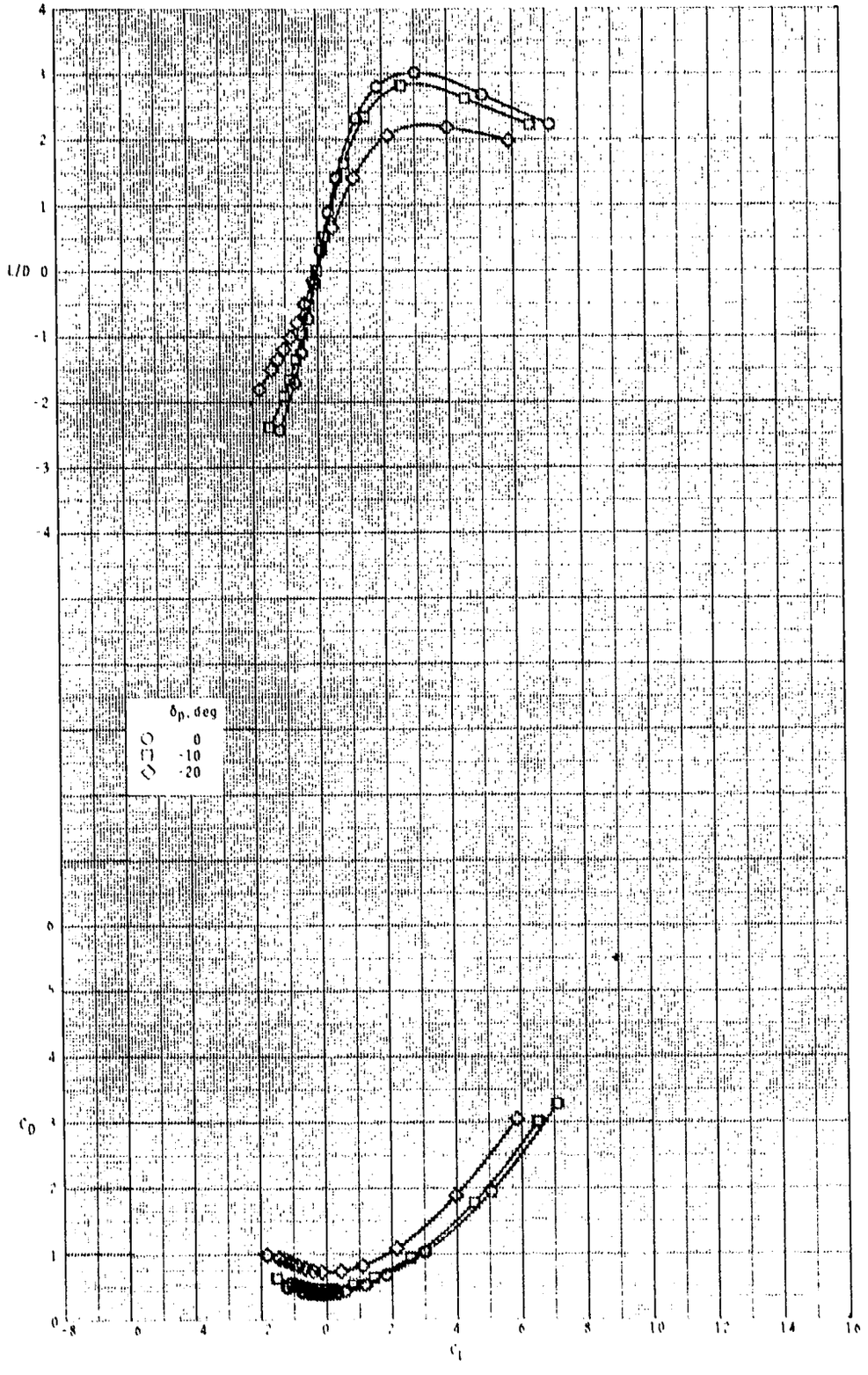

(c) Concluded.

Figure 15.- Continued.

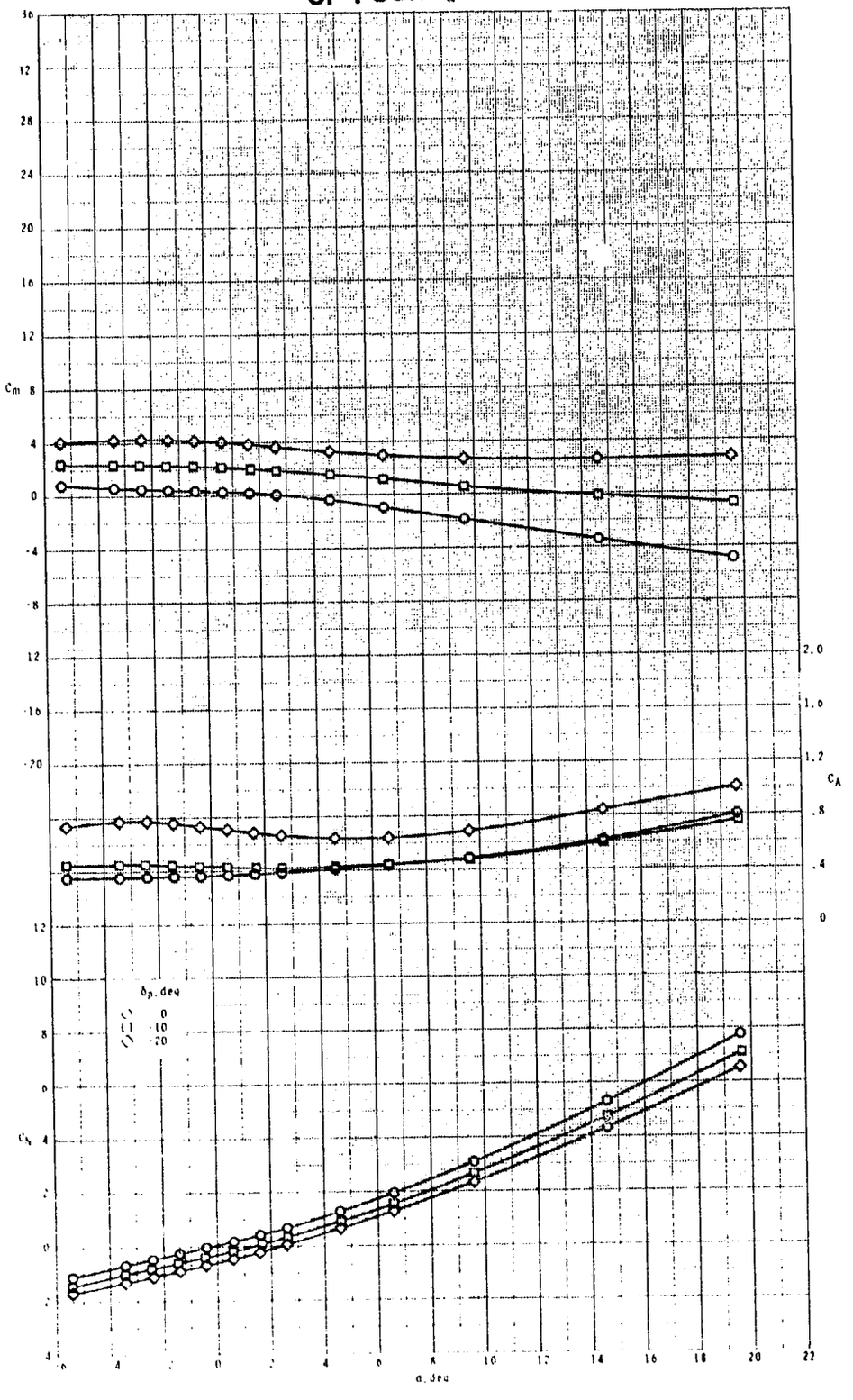

(d) M = 3.95.

Figure 15.- Continued.

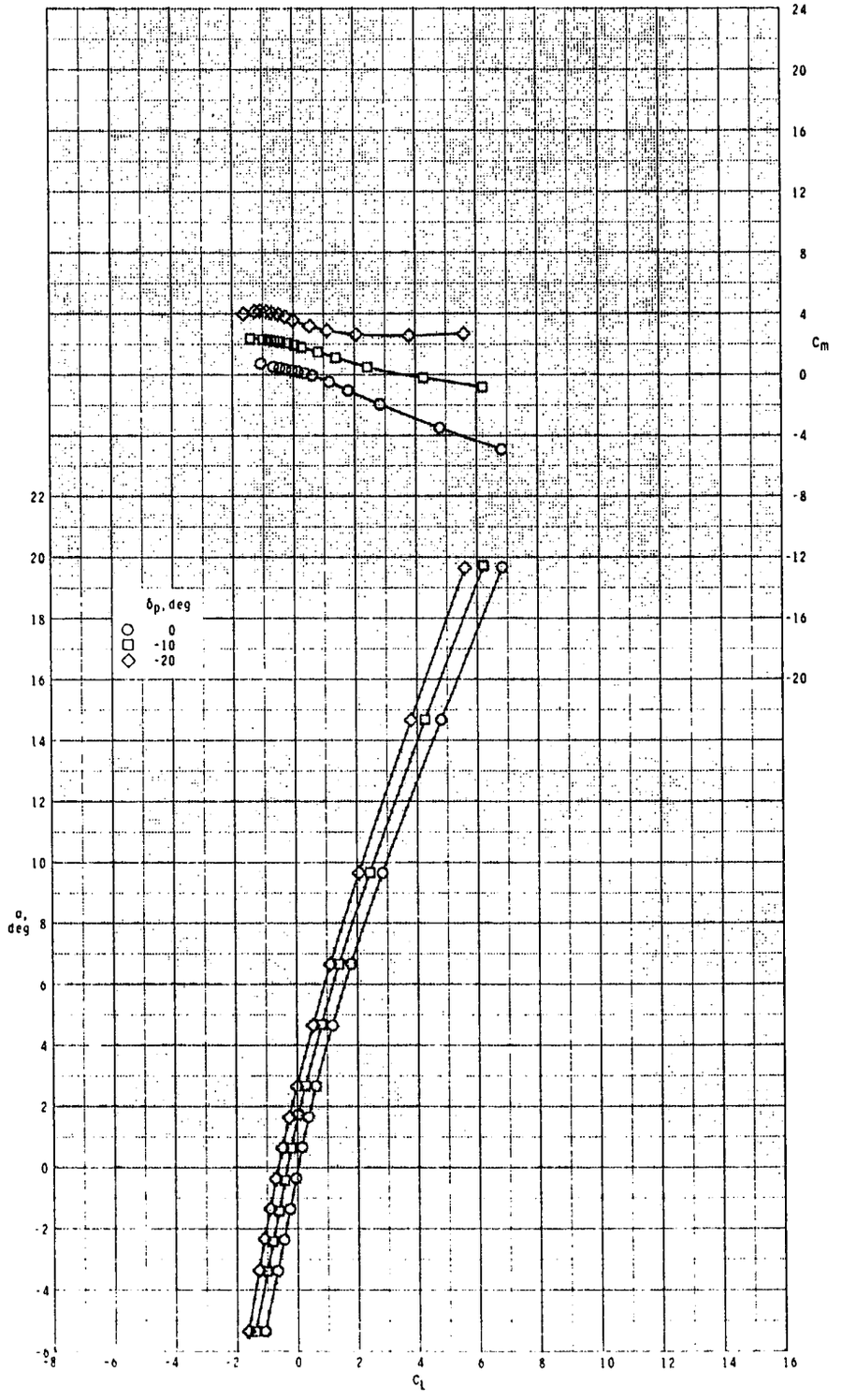

(d) Continued.

Figure 15.- Continued.

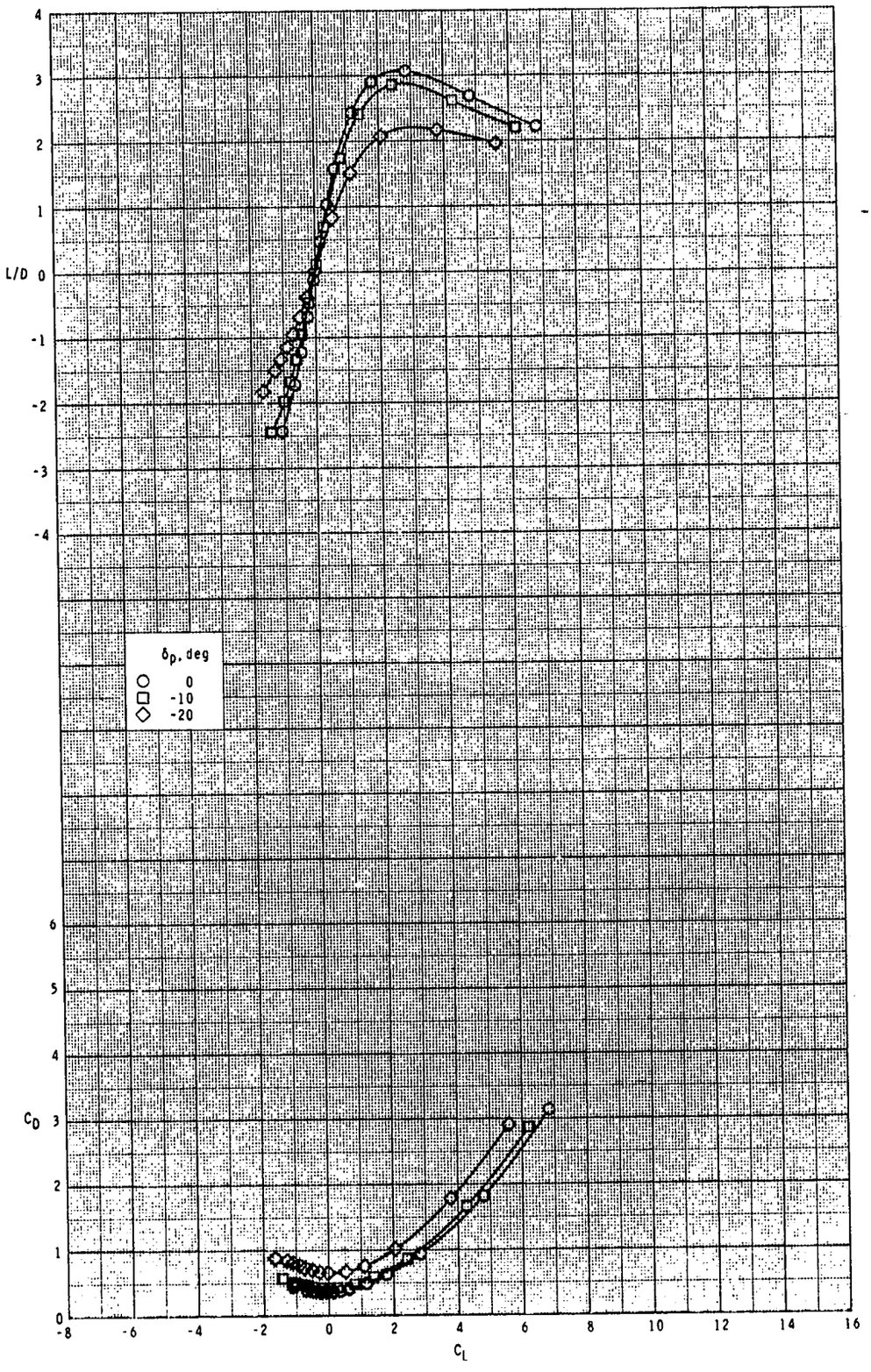

(d) Concluded.

Figure 15.- Concluded.

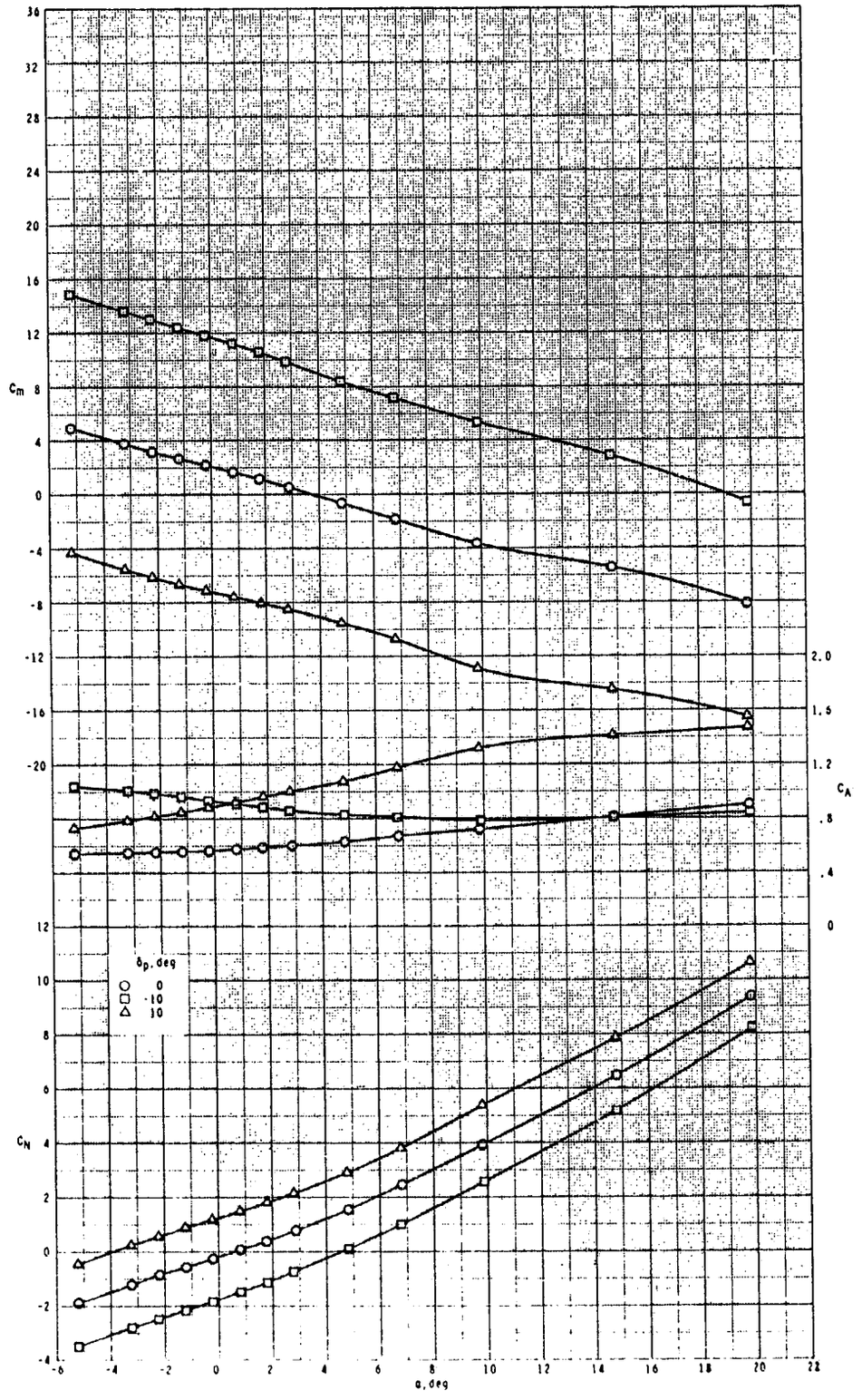

(a) M = 2.50.

Figure 16.- Pitch-control effectiveness of configuration $B_1I_2T_2$ with $\phi_I = 135°$.

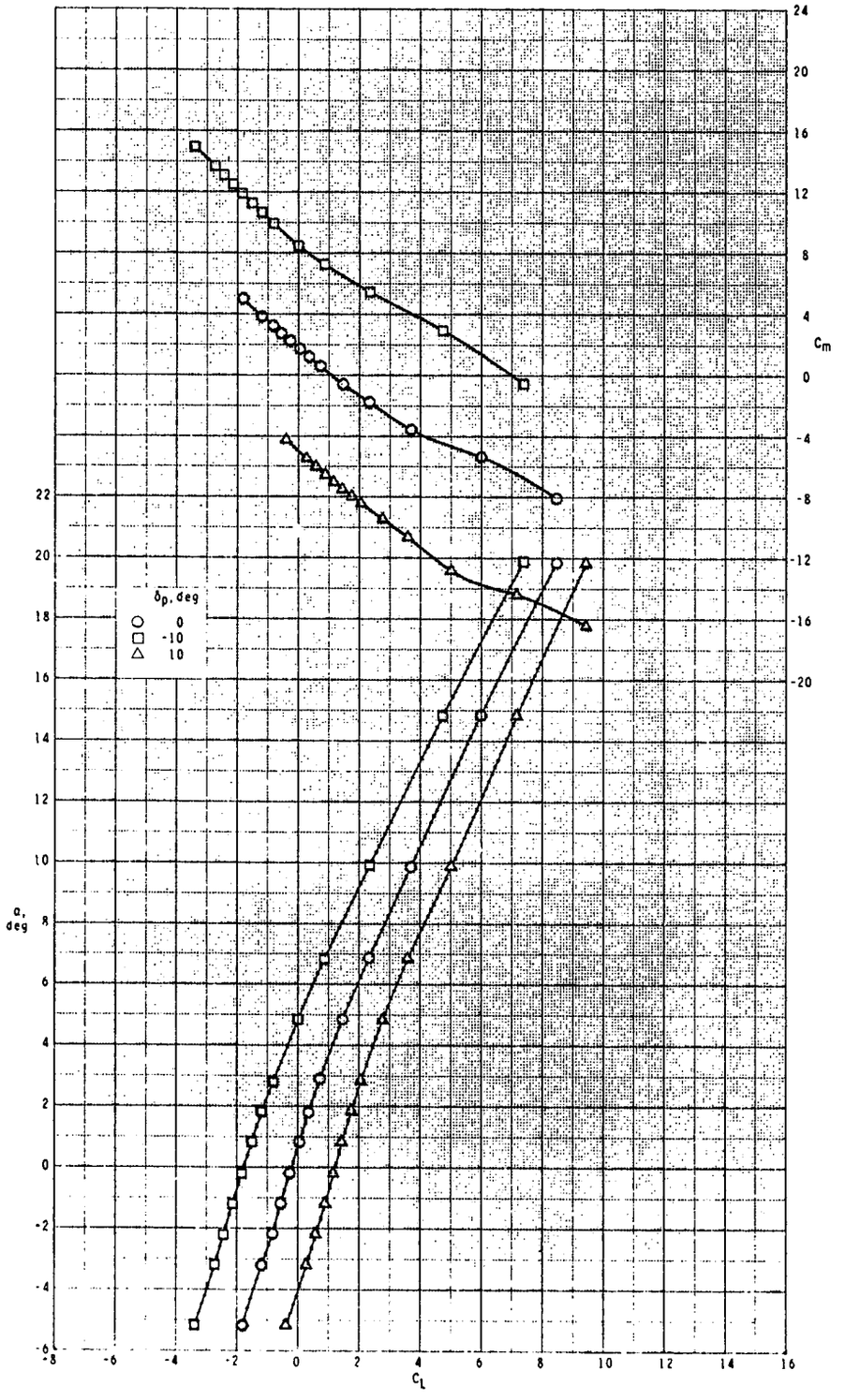

(a) Continued.

Figure 16.- Continued.

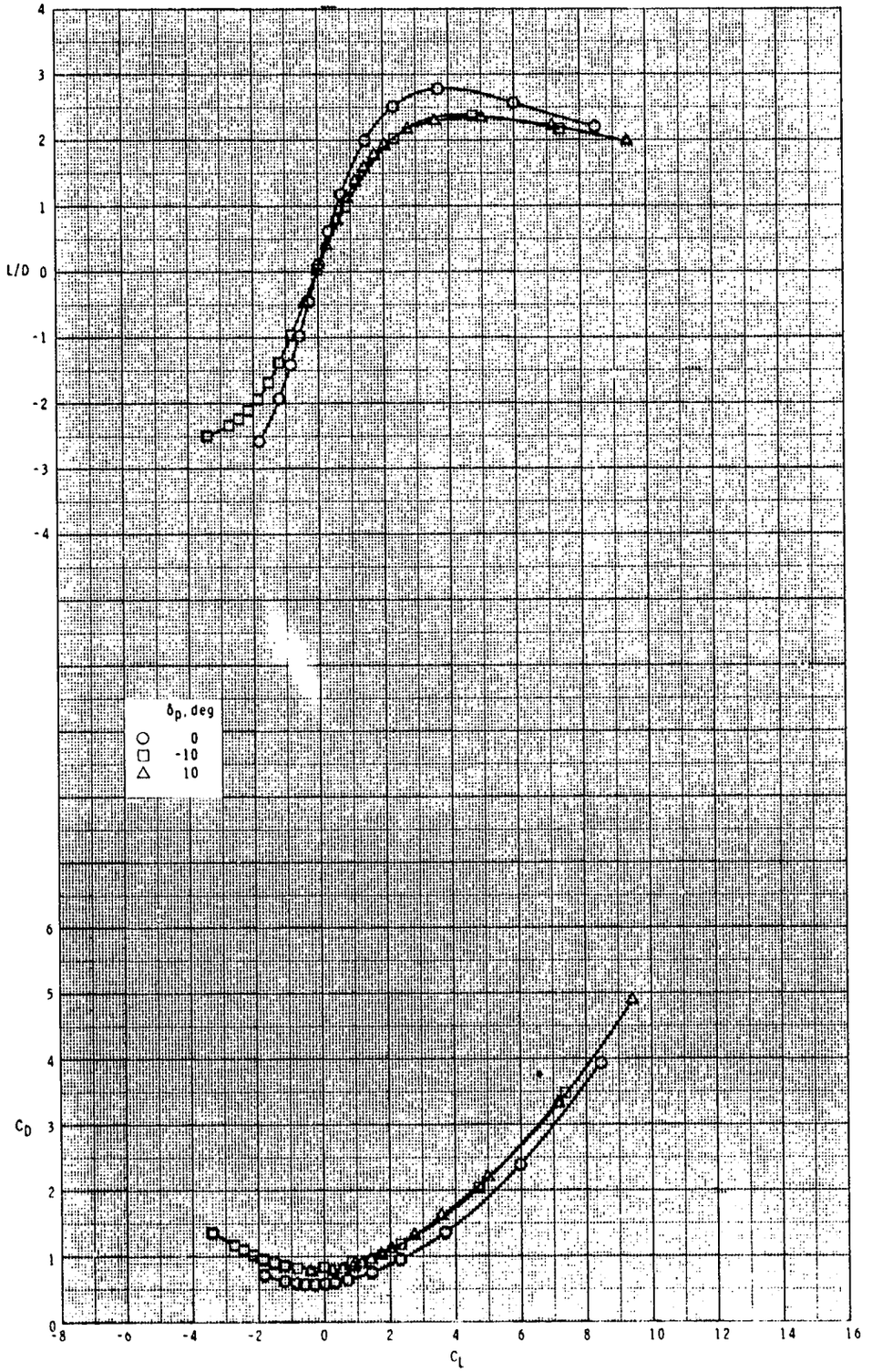

(a) Concluded.

Figure 16.- Continued.

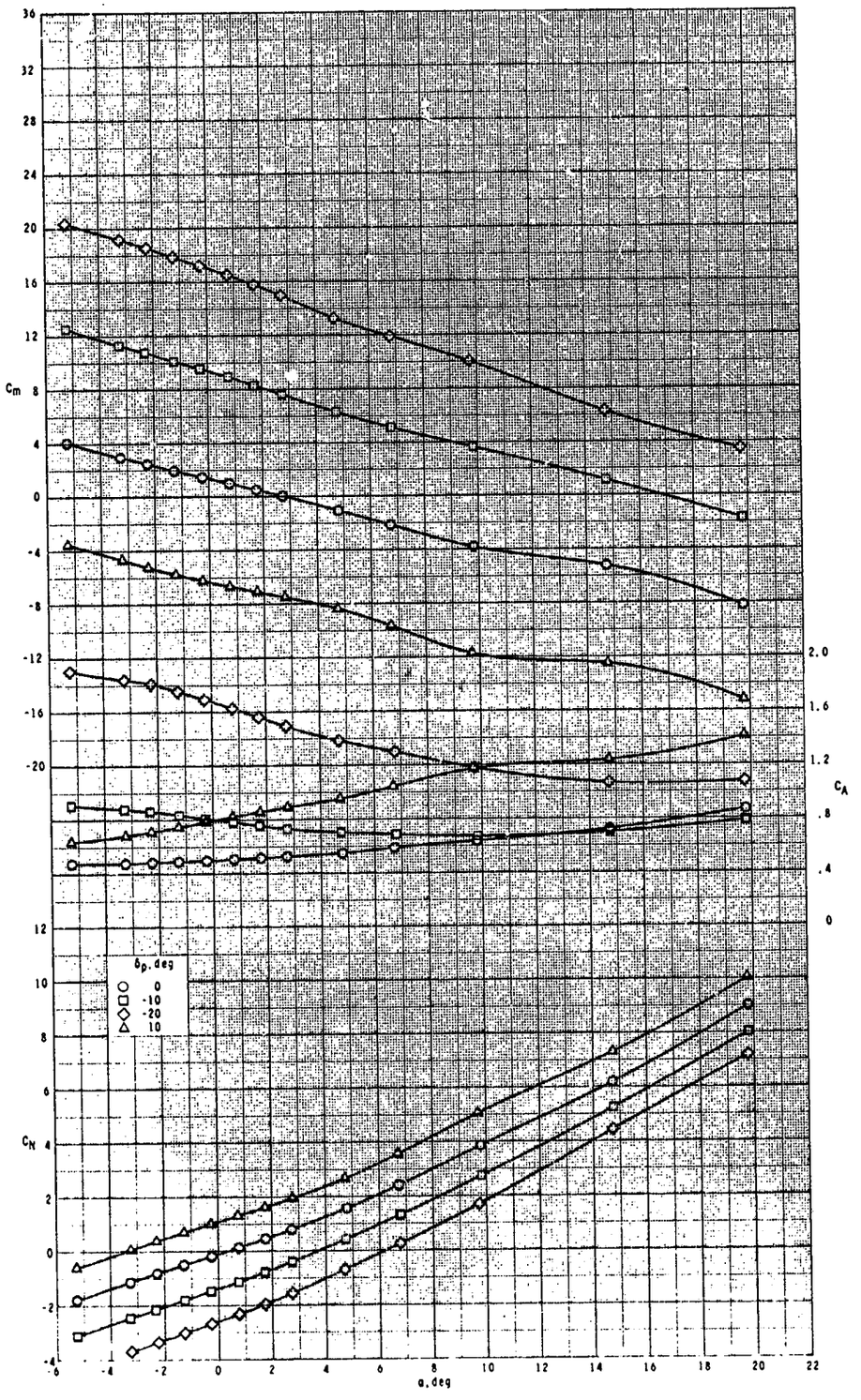

(b) M = 2.95.

Figure 16.- Continued.

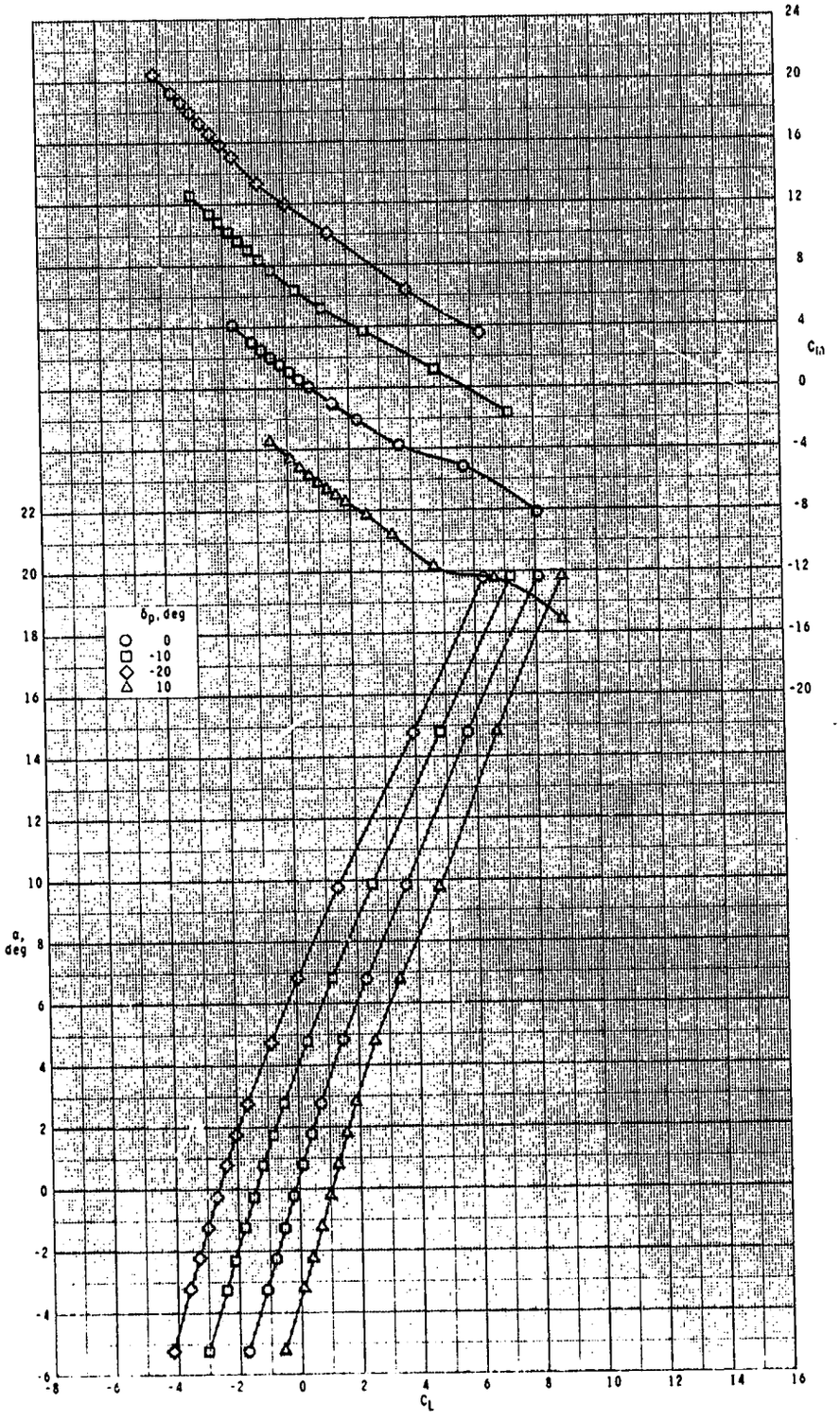

(b) Continued.

Figure 16.- Continued.

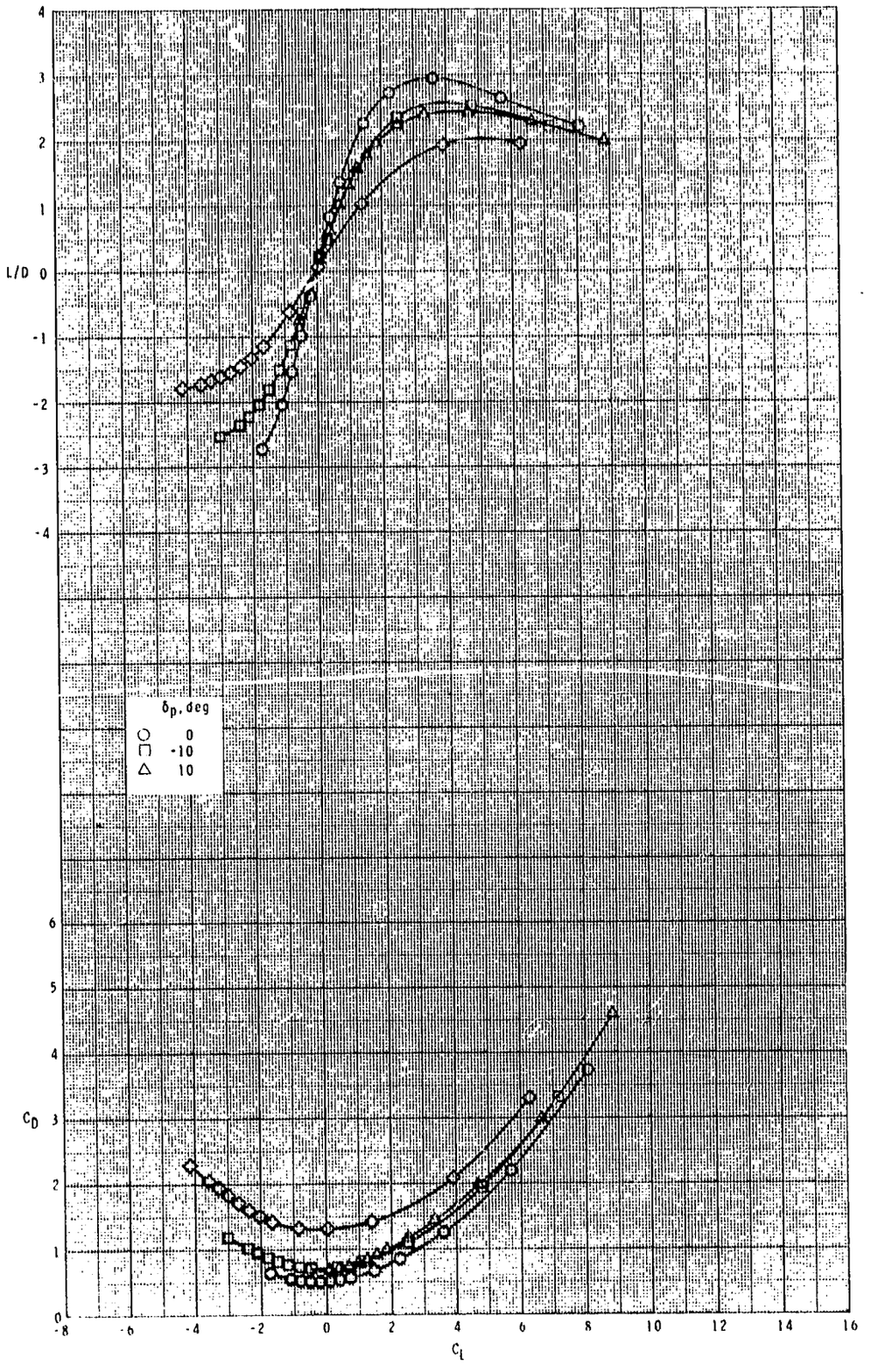

(b) Concluded.

Figure 16.- Continued.

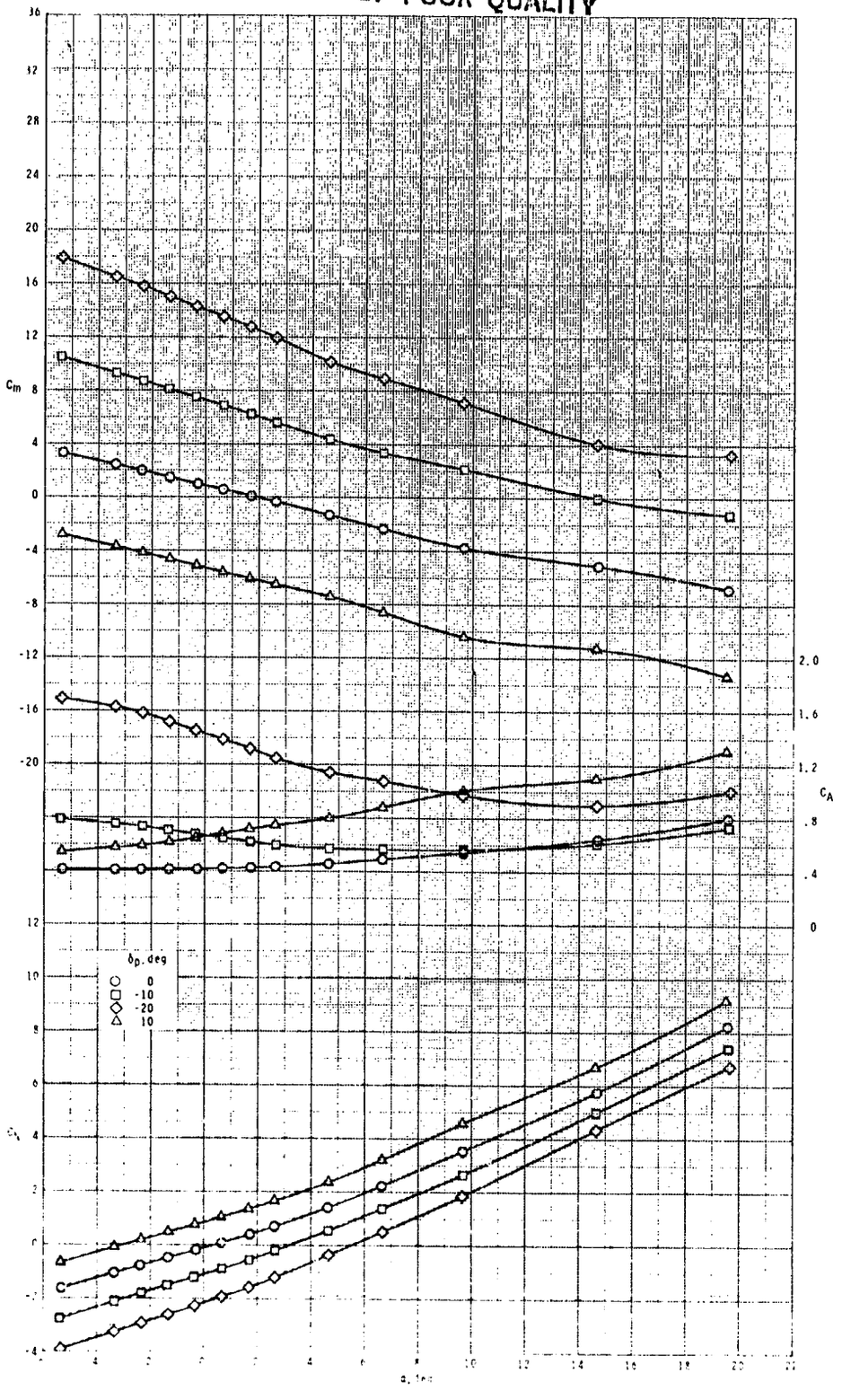

(c) M = 3.50.

Figure 16.- Continued.

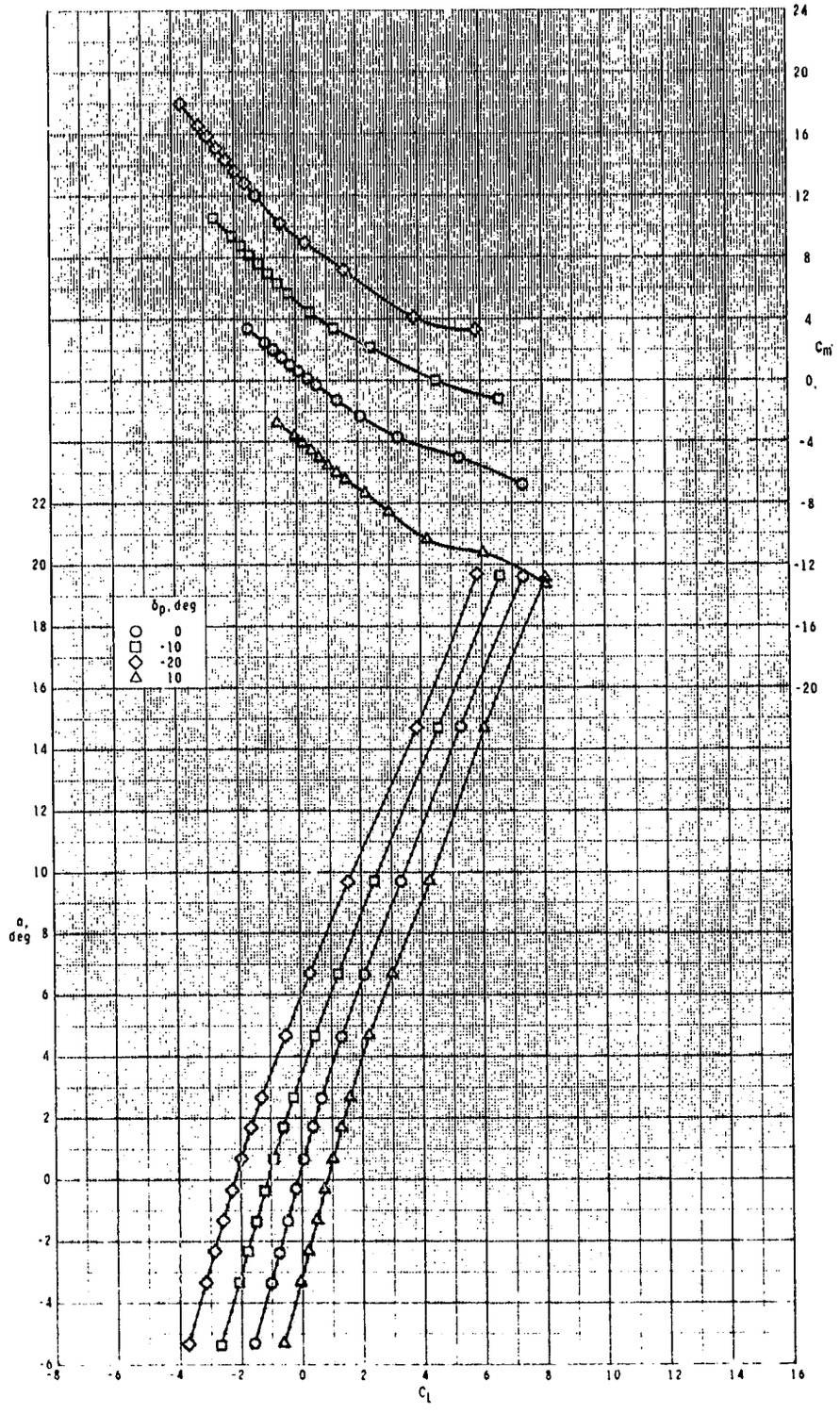

(c) Continued.

Figure 16.- Continued.

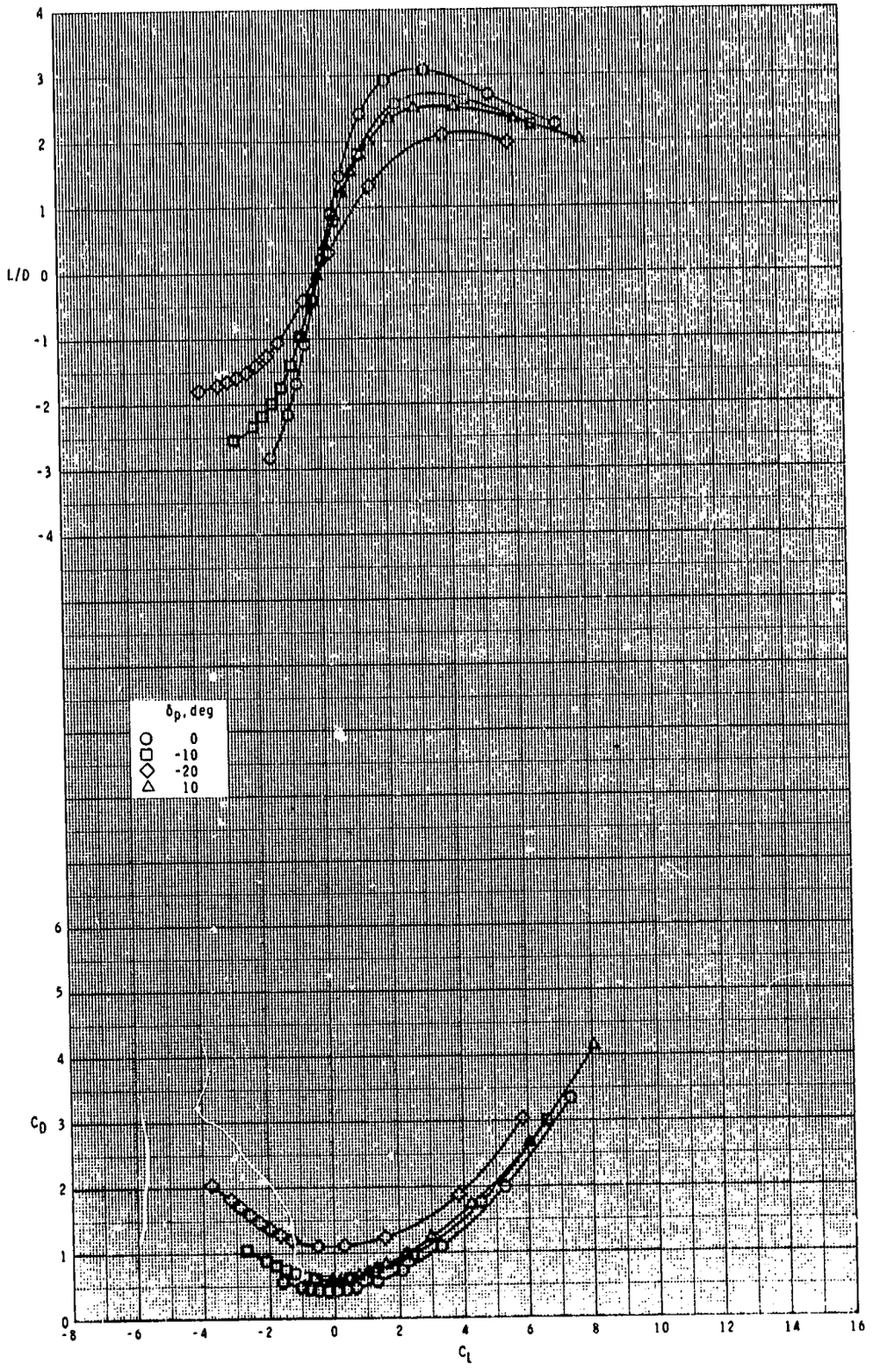

(c) Concluded.

Figure 16.- Continued.

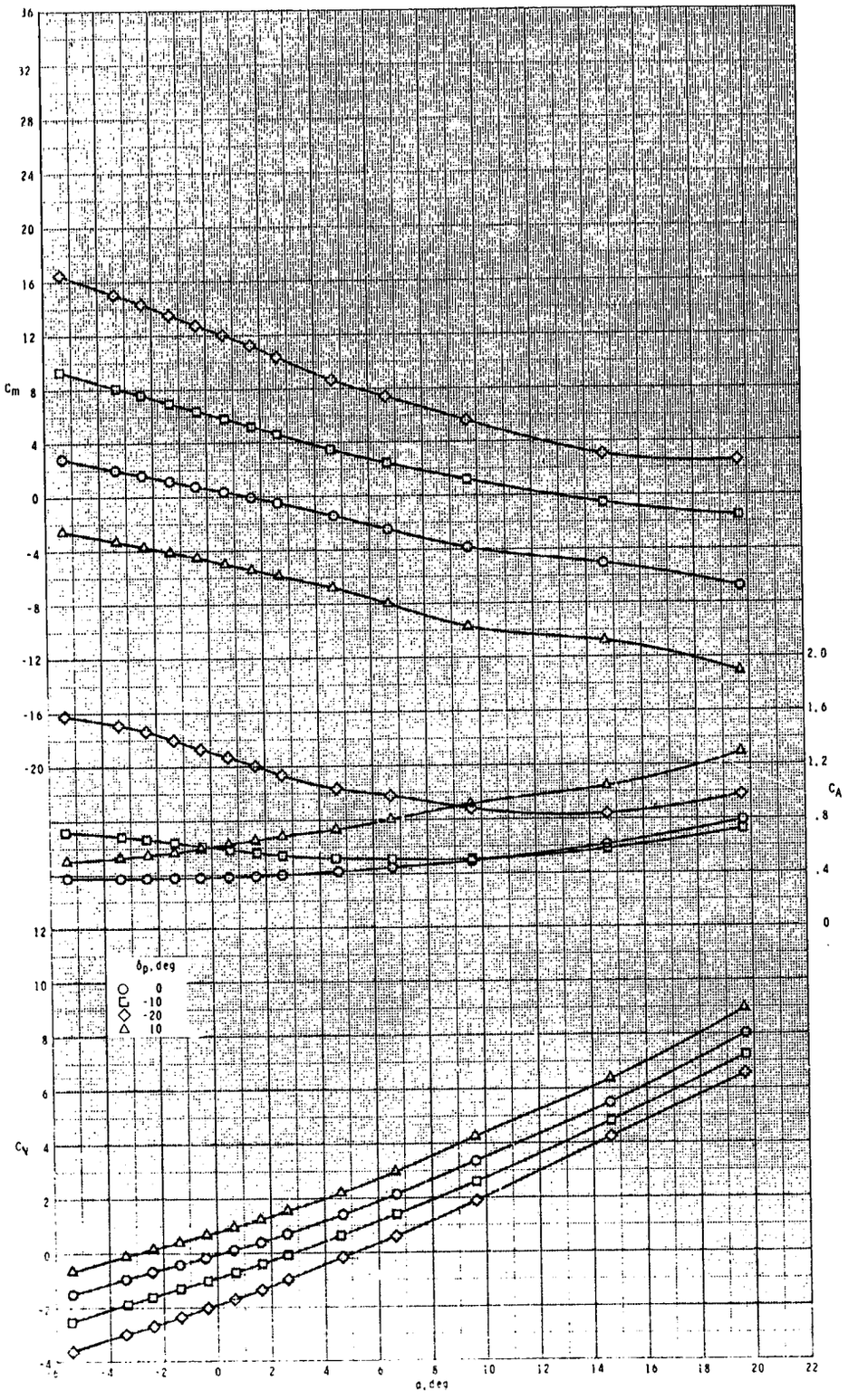

(d) M = 3.95.

Figure 16.- Continued.

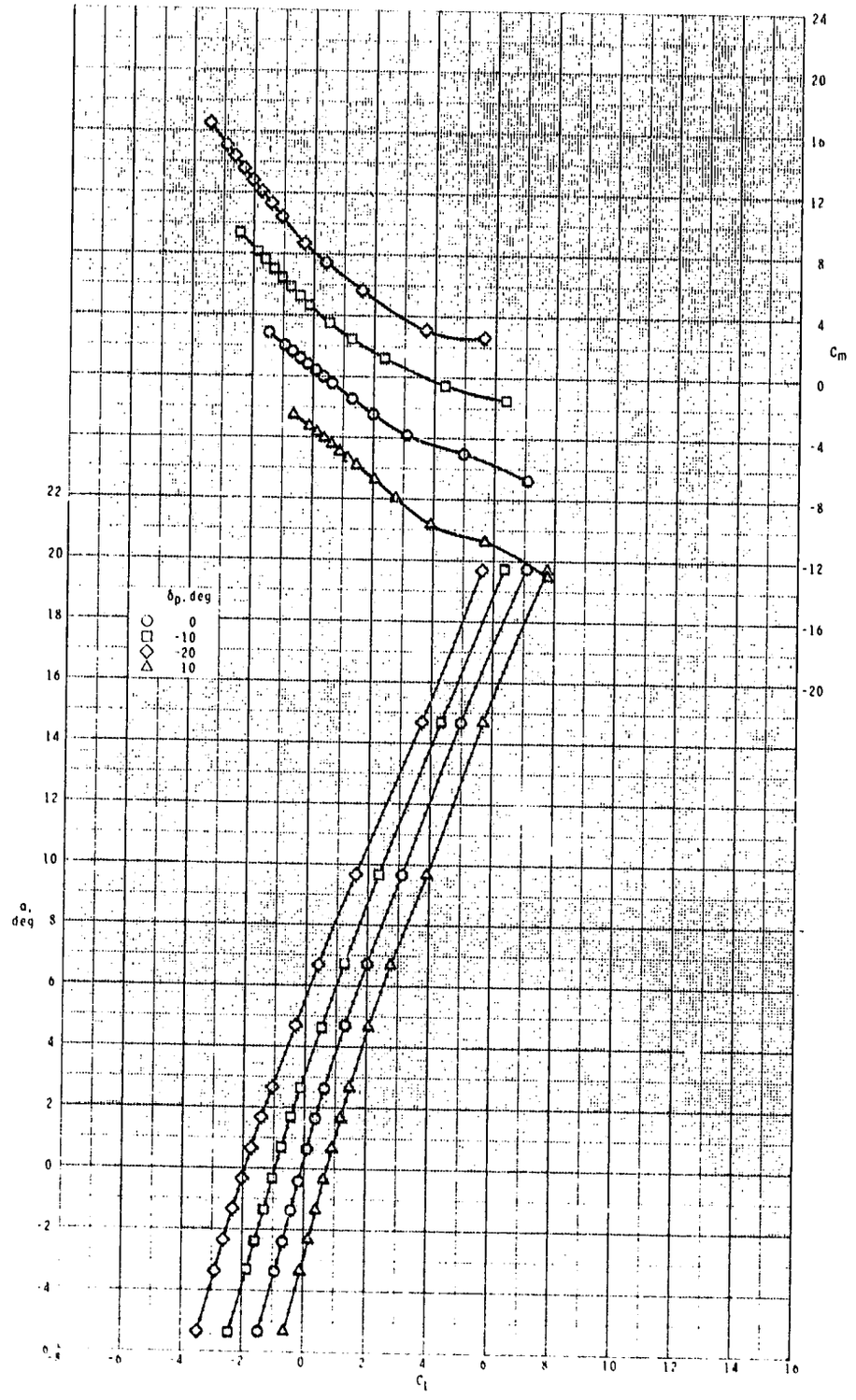

(d) Continued.

Figure 16.- Continued.

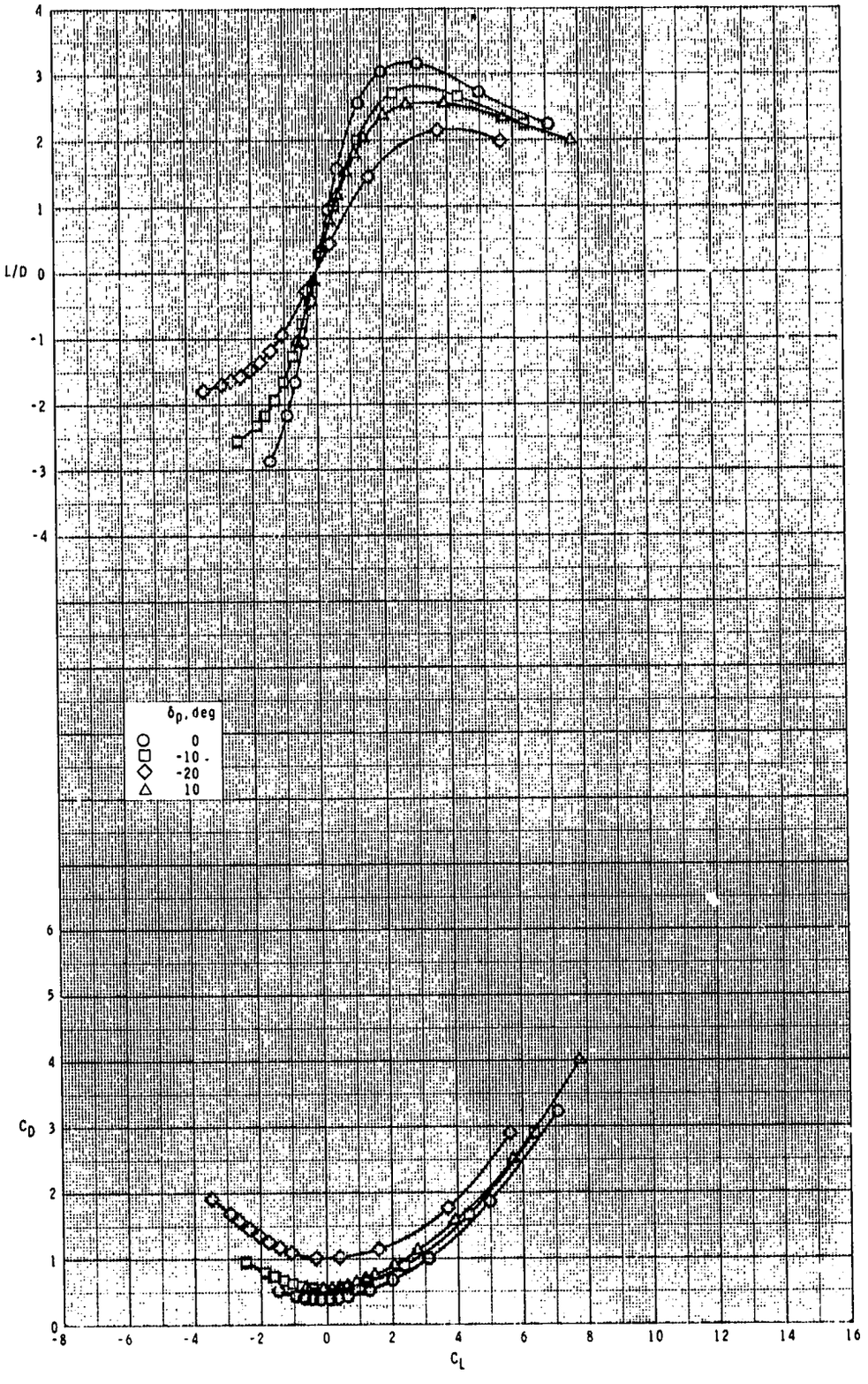

(d) Concluded.

Figure 16.- Concluded.

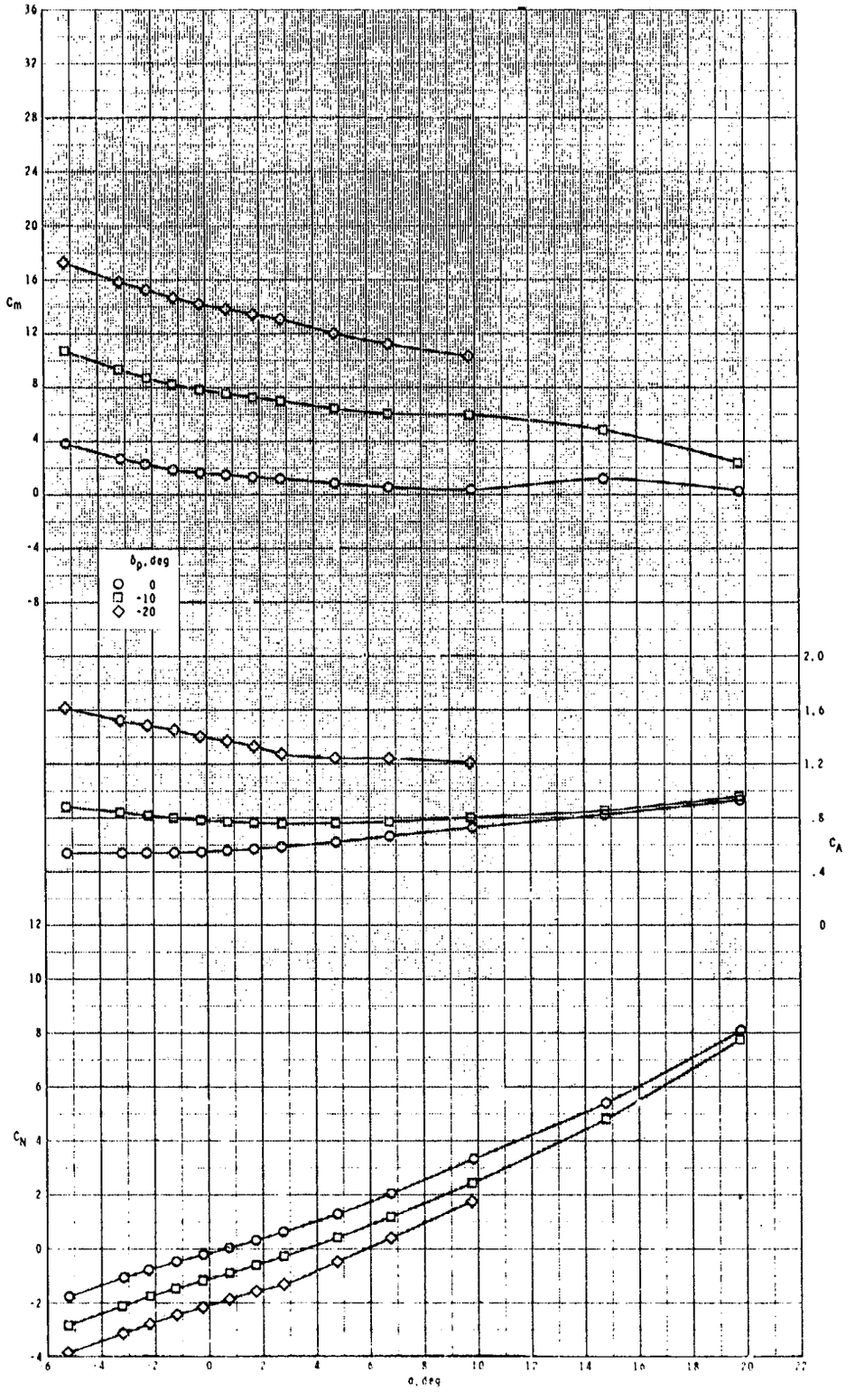

(a) M = 2.50.

Figure 17.- Pitch-control effectiveness of configuration $B_1I_2T_3$ with ϕ_I = 135°.

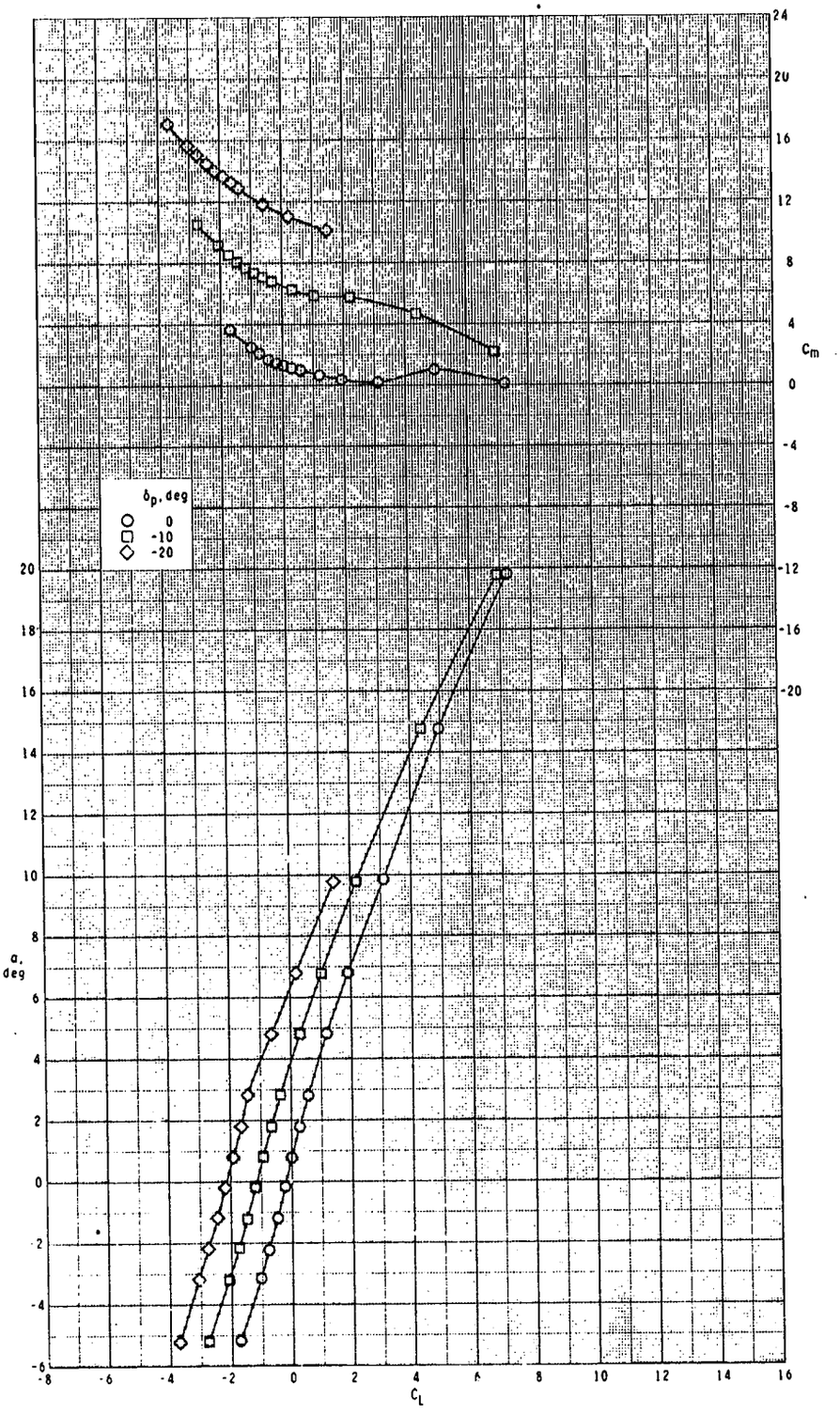

(a) Continued.

Figure 17.- Continued.

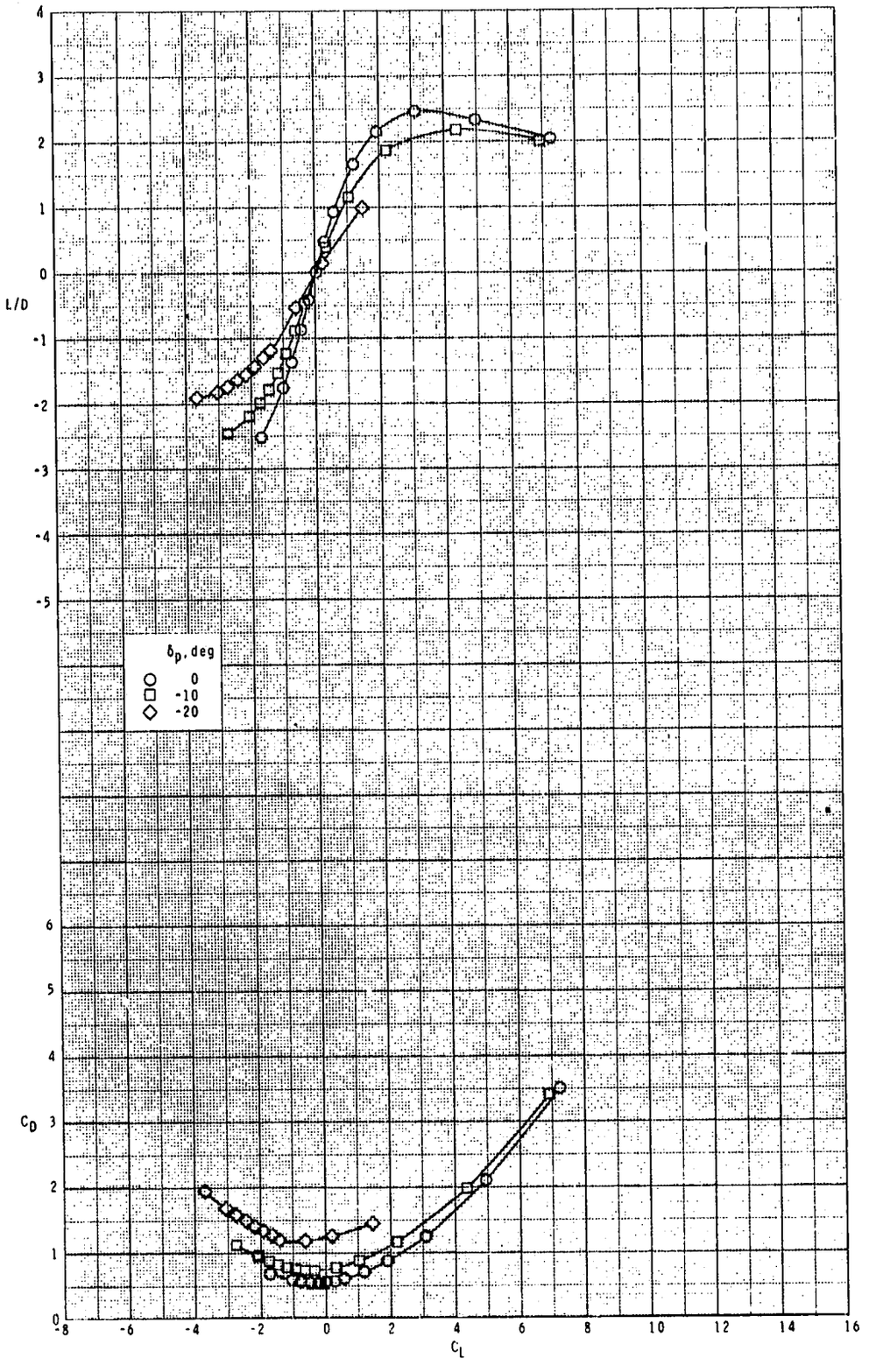

(a) Concluded.

Figure 17.- Continued.

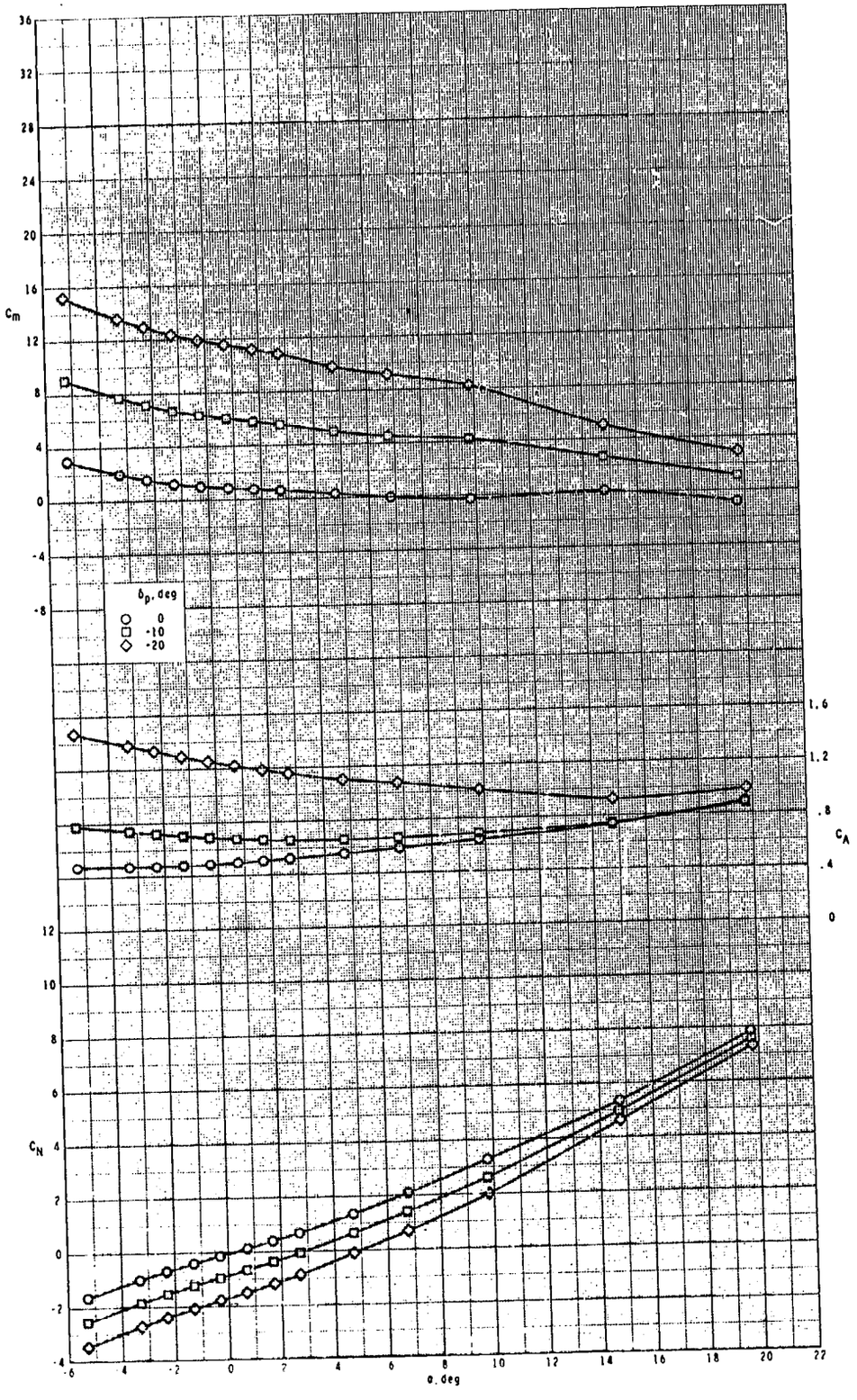

(b) M = 2.95.

Figure 17.- Continued.

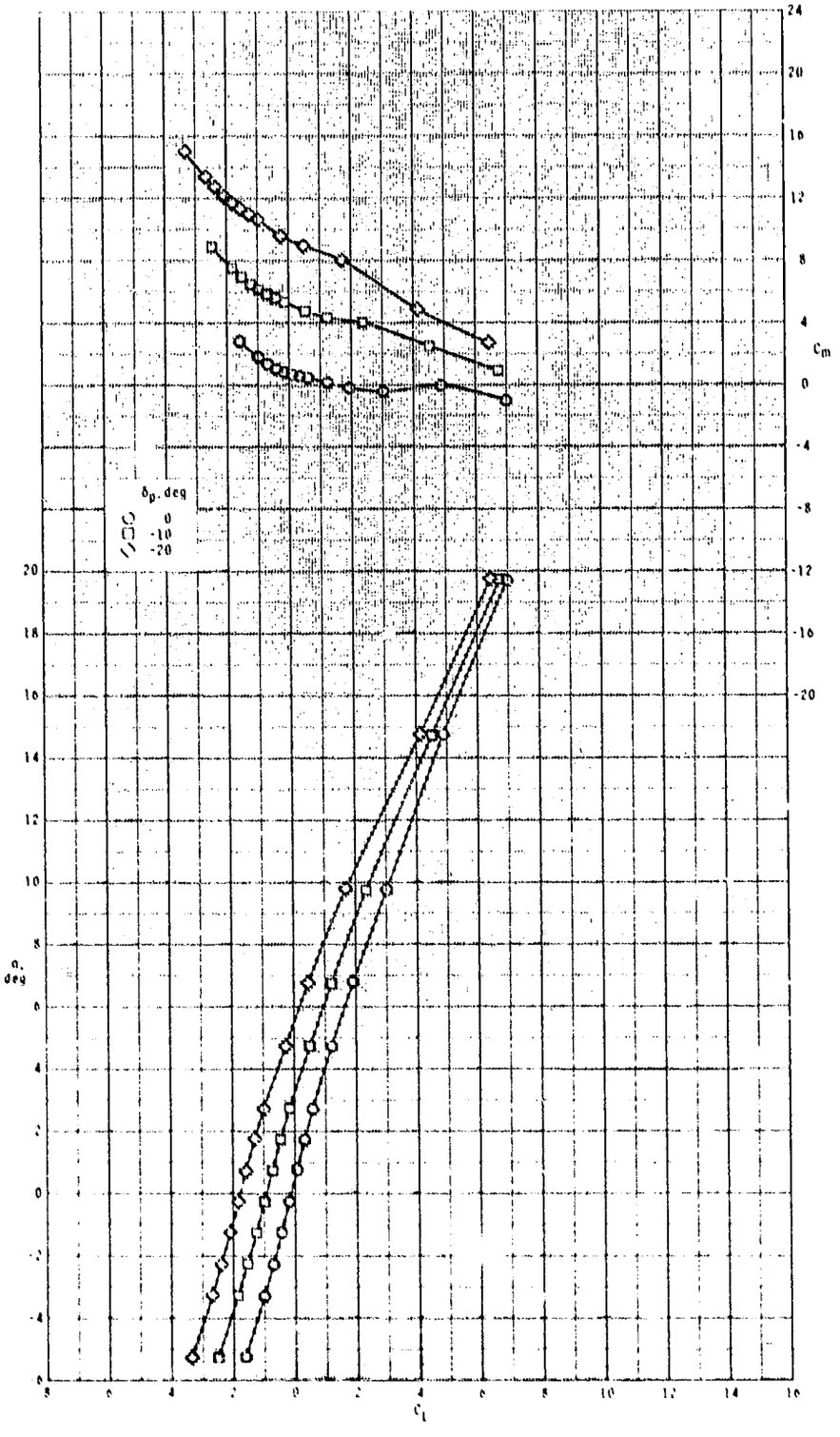

(b) Continued.

Figure 17.- Continued.

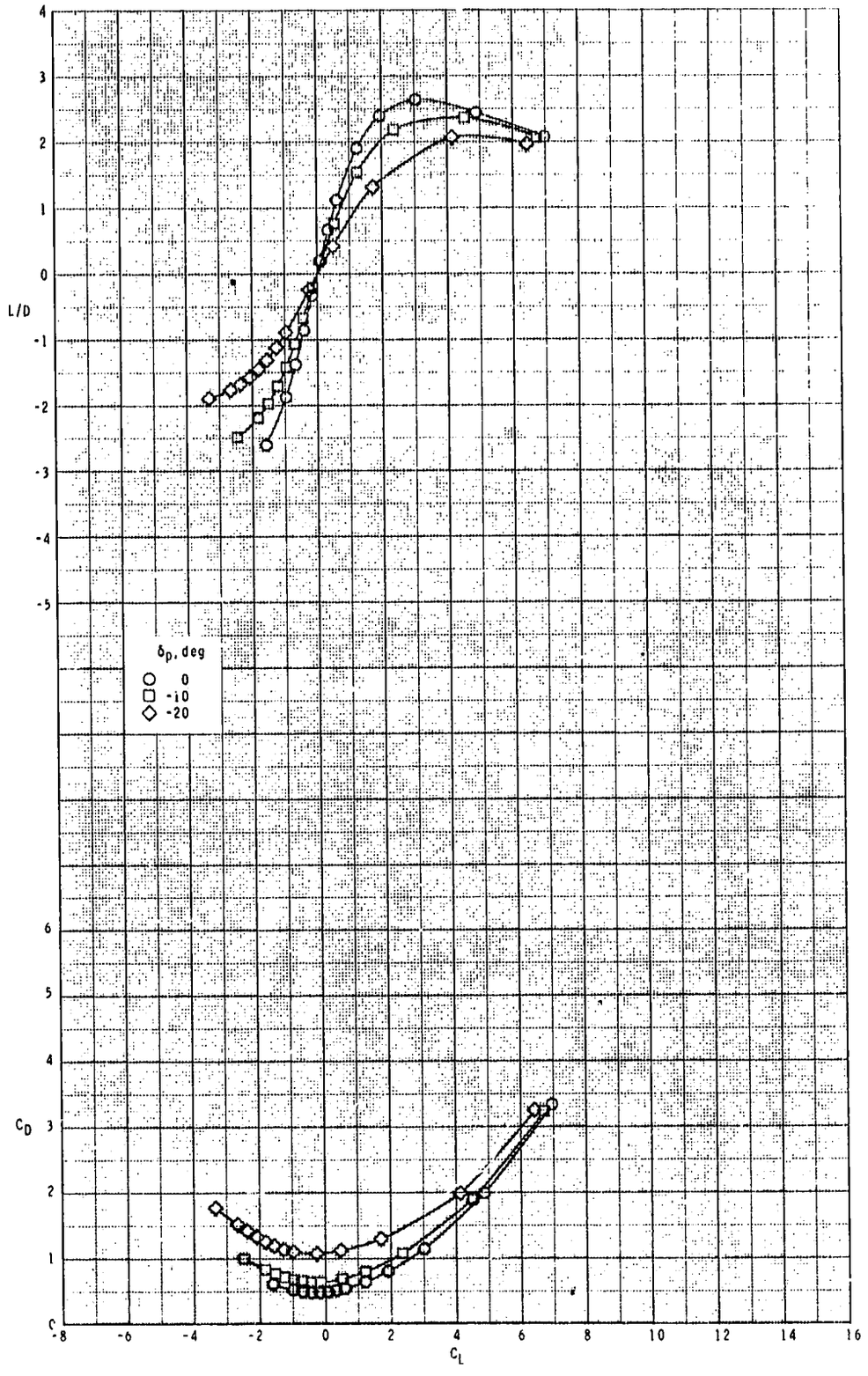

(b) Concluded.

Figure 17.- Continued.

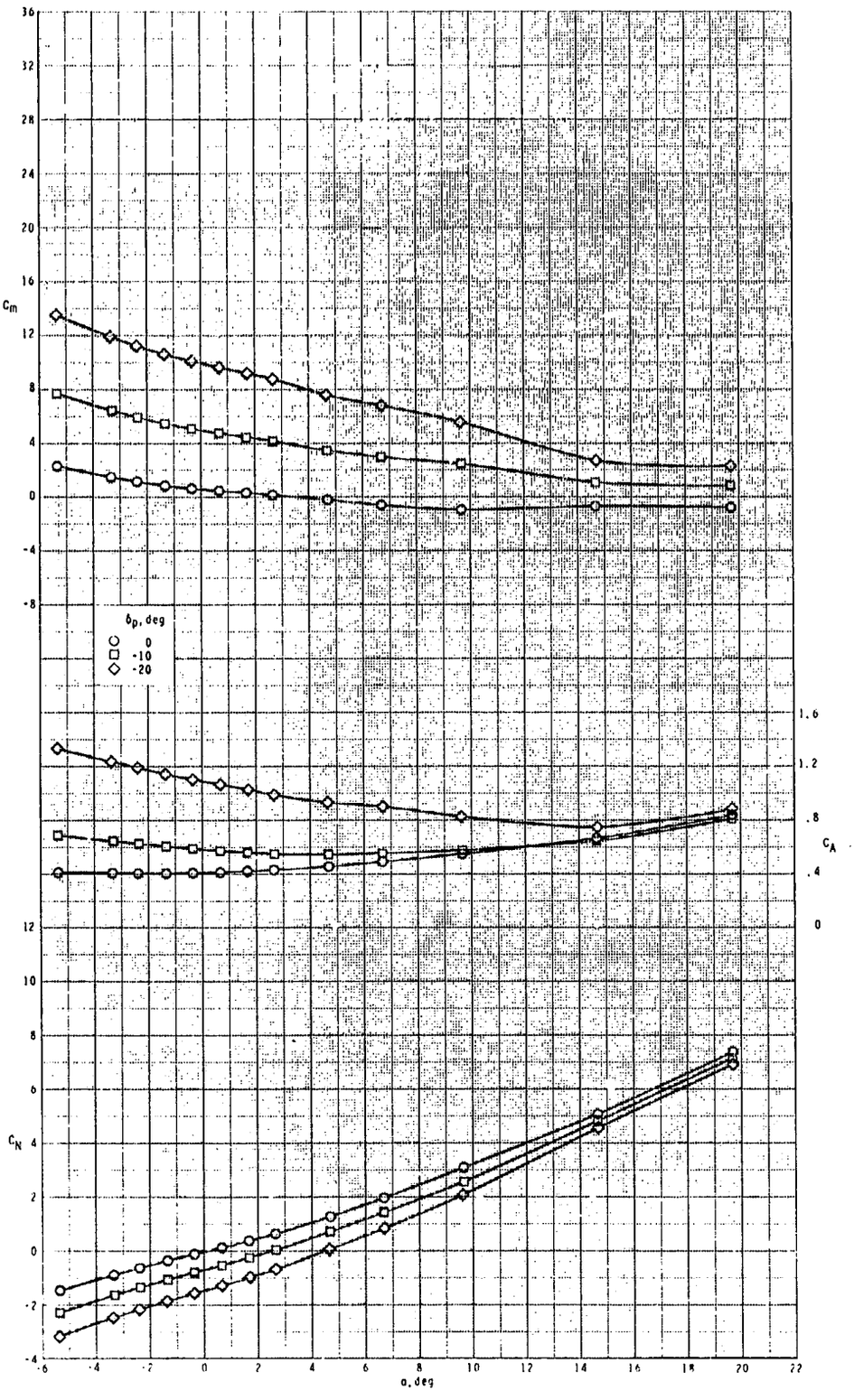

(c) M = 3.50.

Figure 17.- Continued.

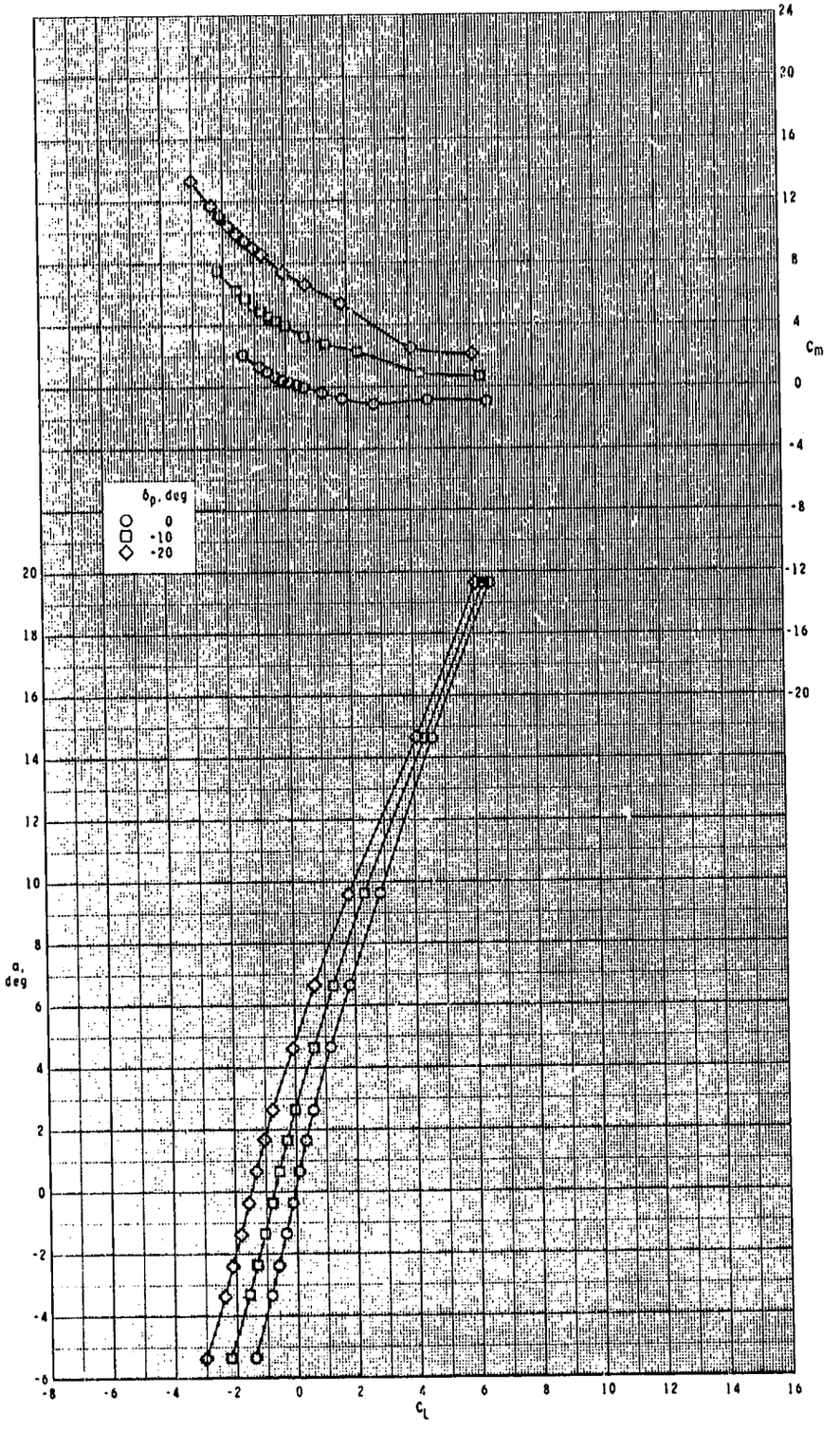

(c) Continued.

Figure 17.- Continued.

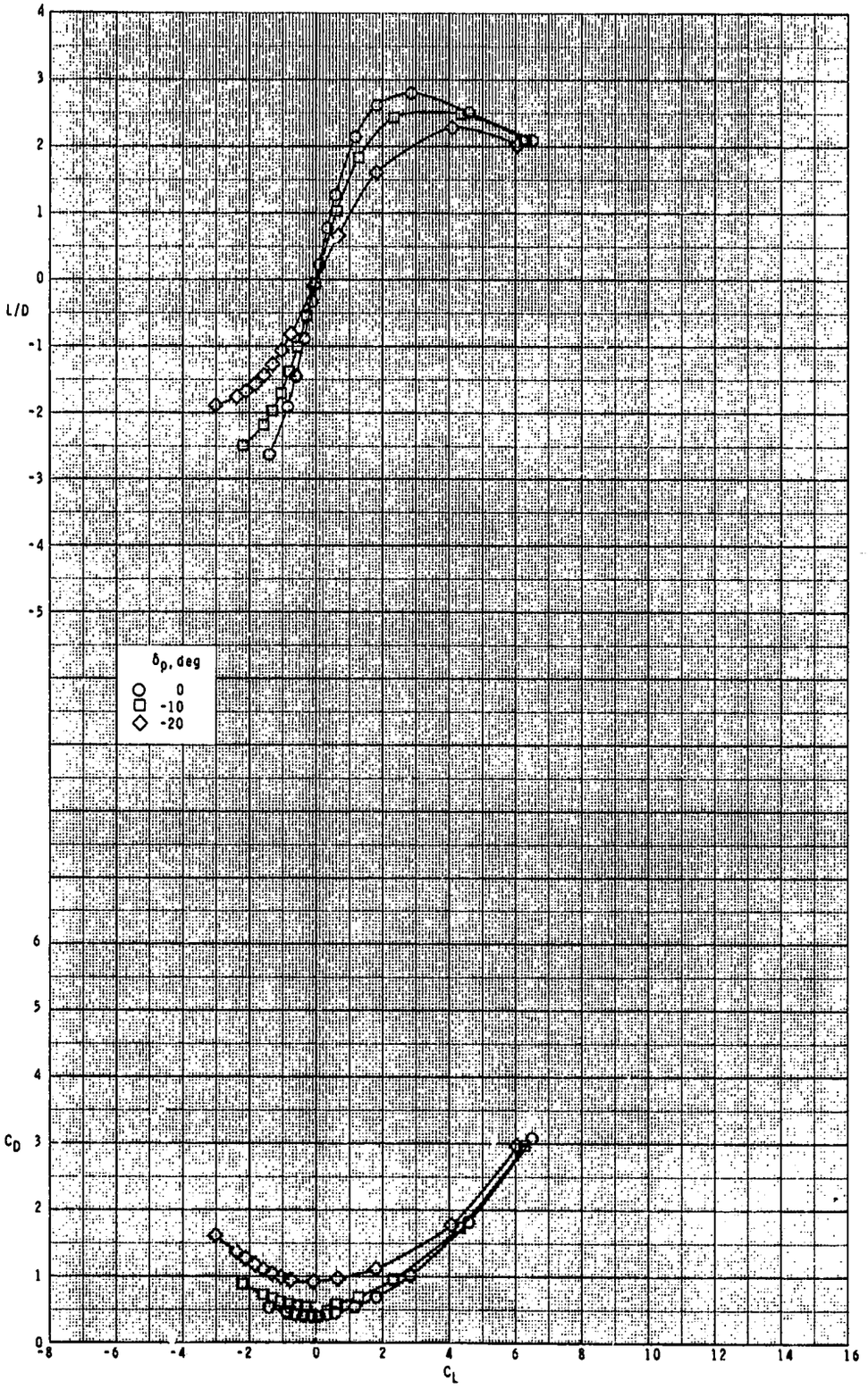

(c) Concluded.

Figure 17.- Continued.

C-3

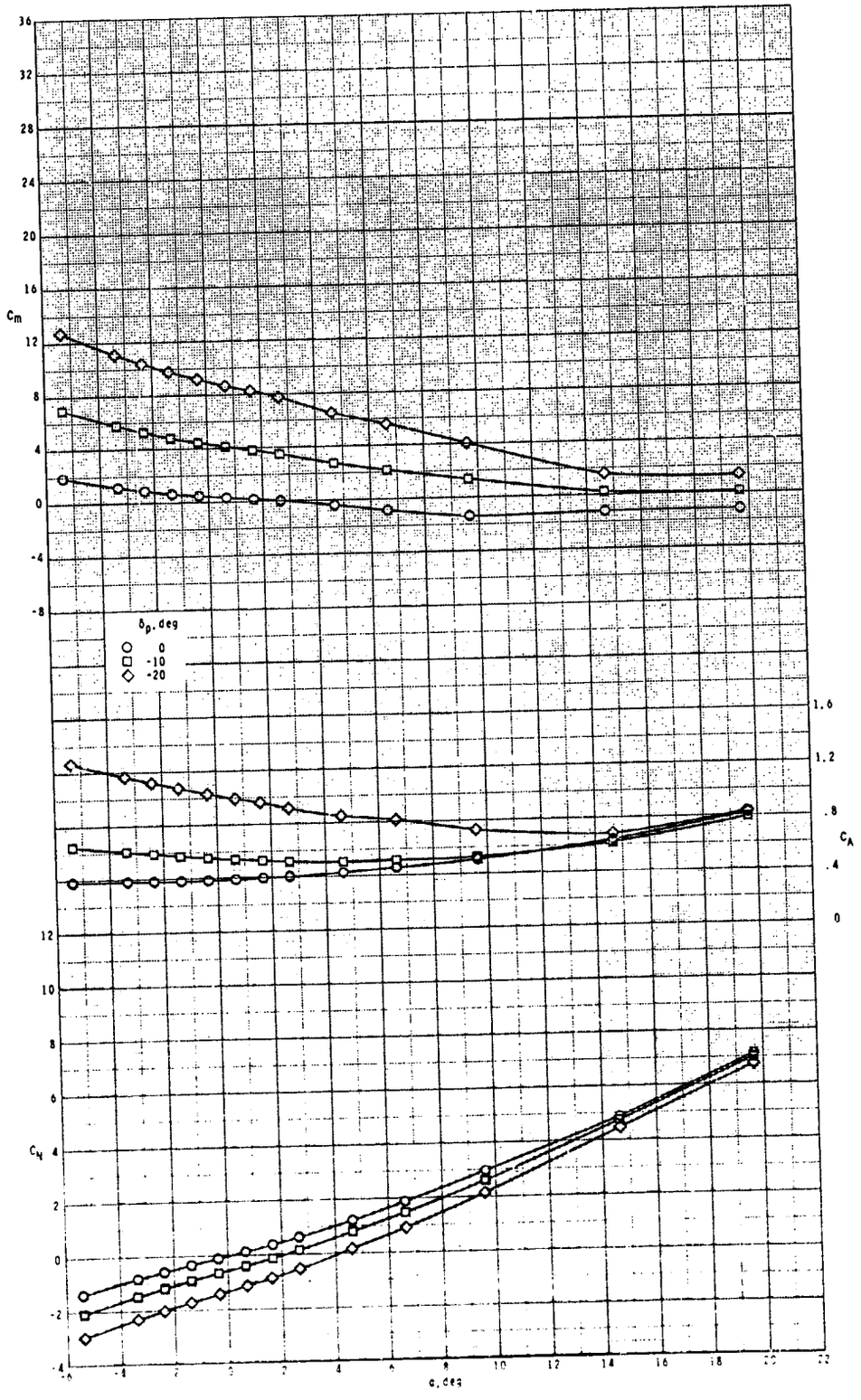

(d) M = 3.95.

Figure 17.- Continued.

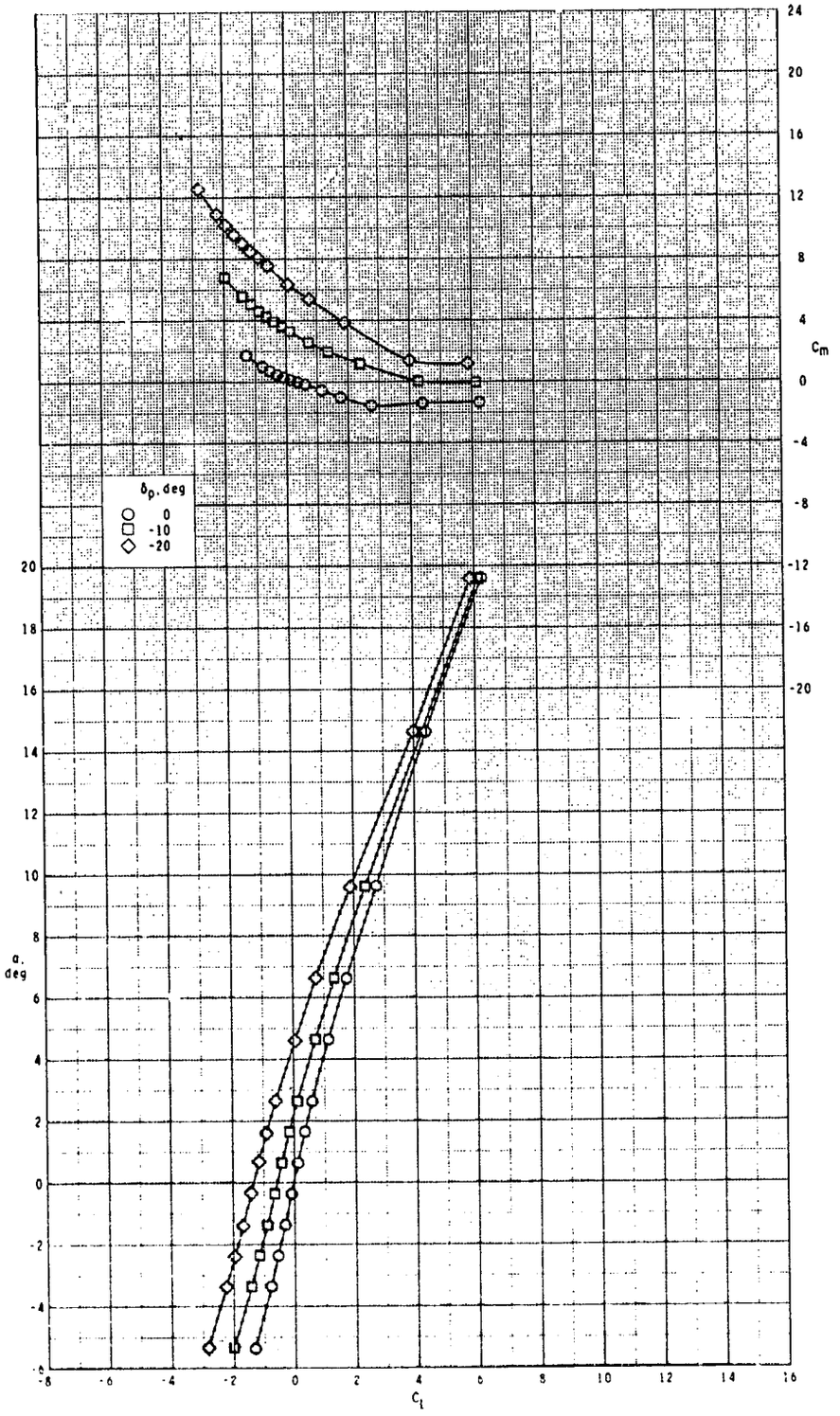

(d) Continued.

Figure 17.- Continued.

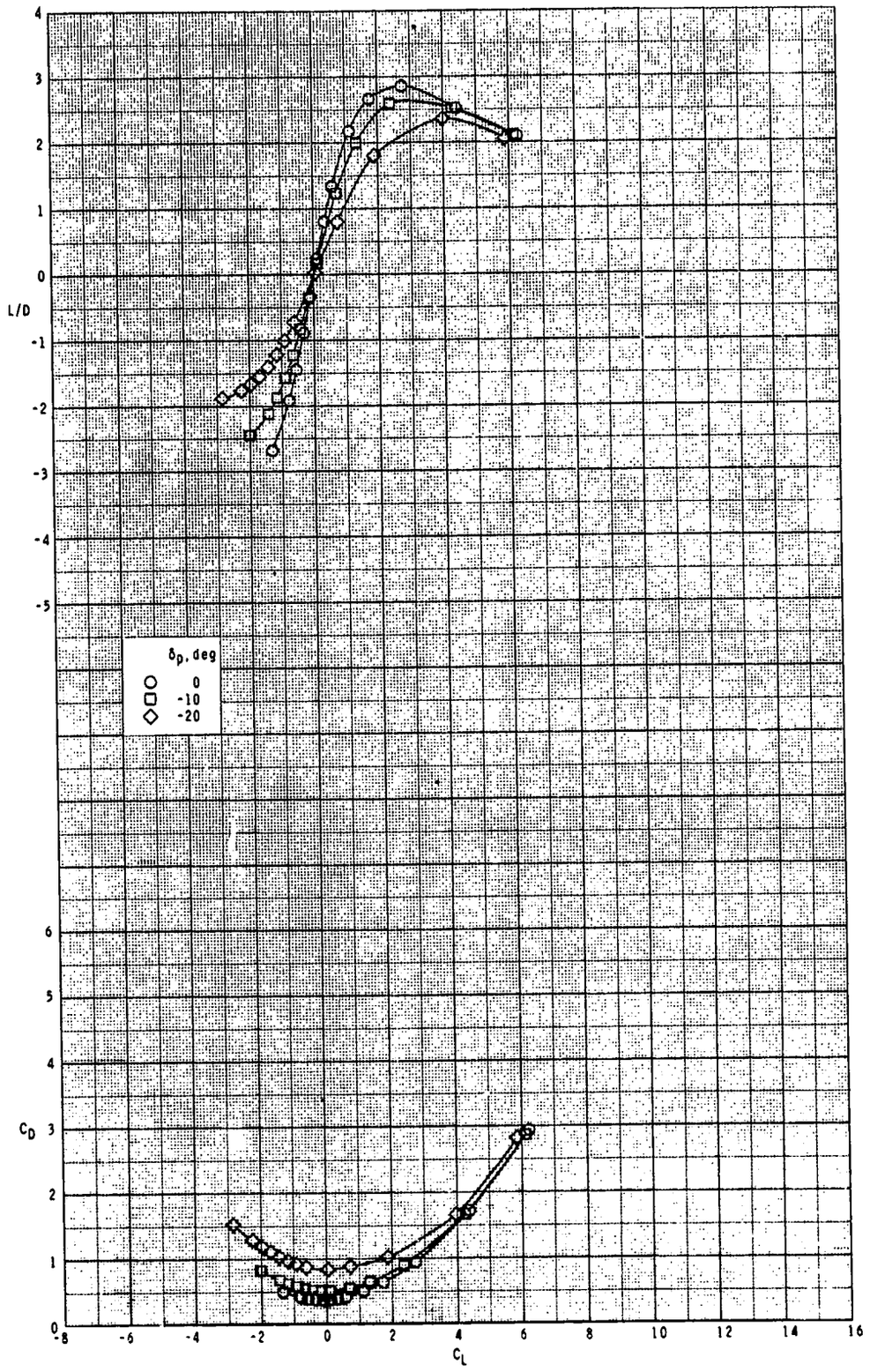

(d) Concluded.

Figure 17.- Concluded.

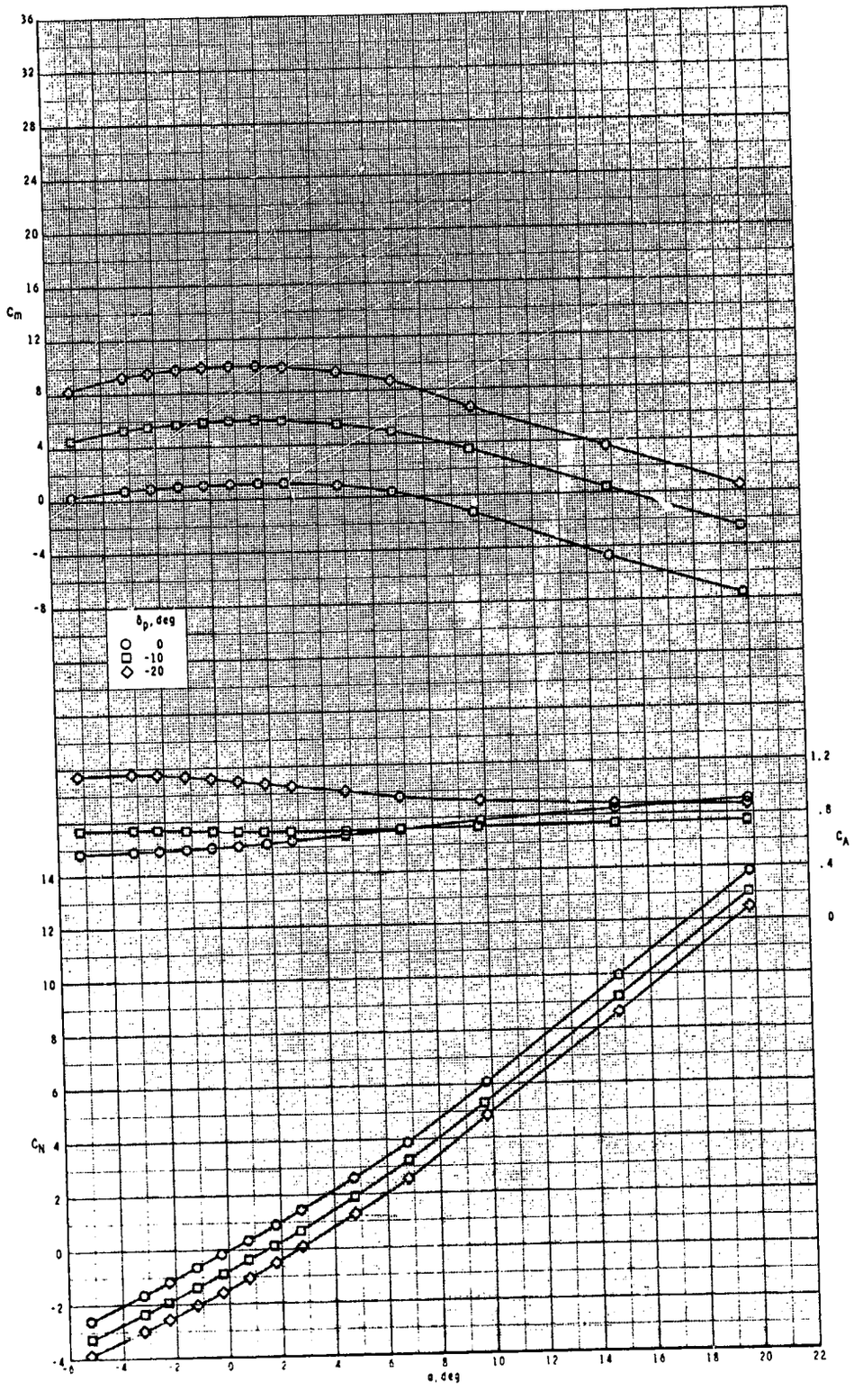

(a) M = 2.50.

Figure 18.- Pitch-control effectiveness of configuration $B_1I_2W_1T_1$ with $\phi_I = 115°$.

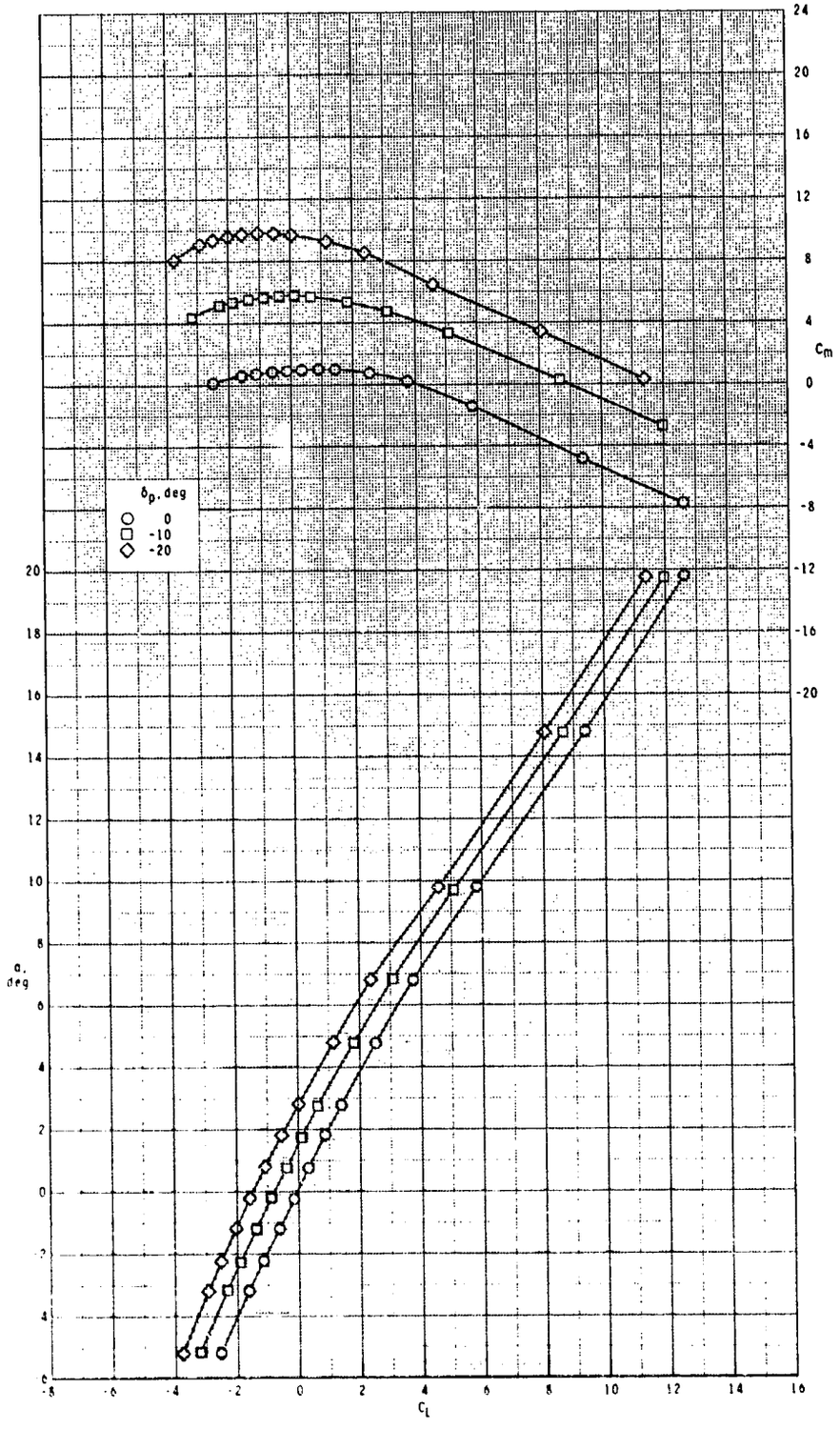

(a) Continued.

Figure 18.- Continued.

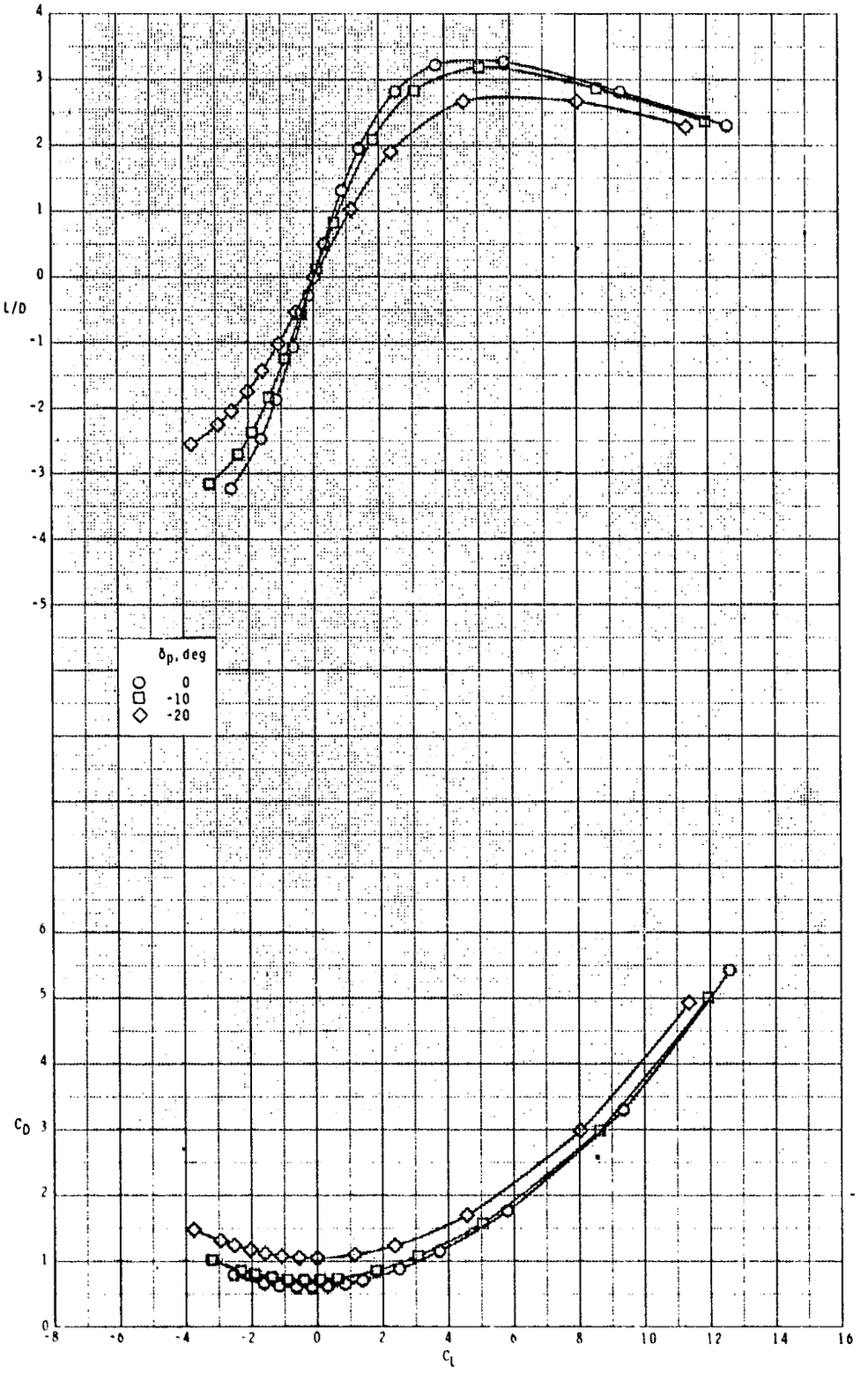

(a) Concluded.

Figure 18.- Continued.

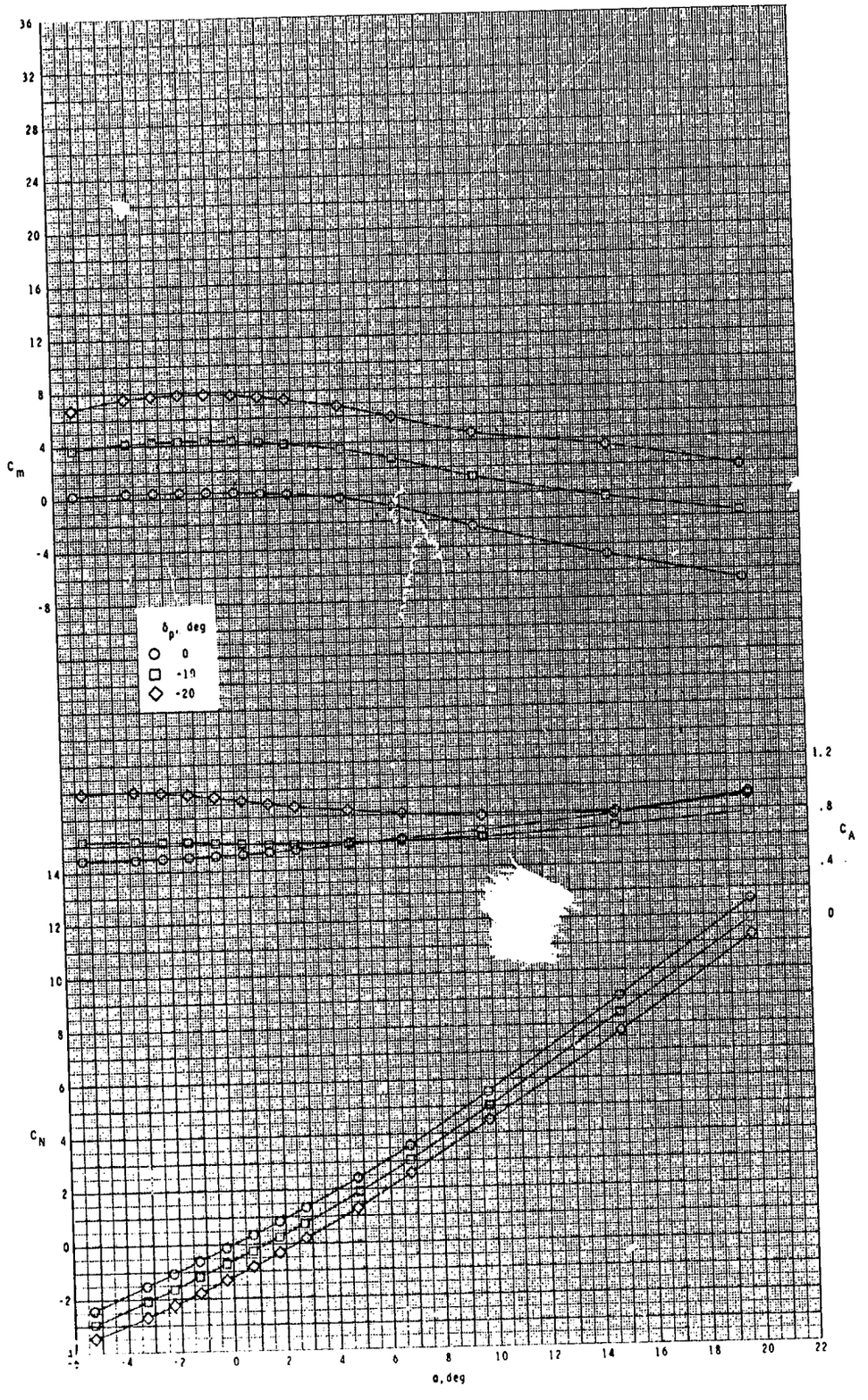

(b) M = 2.95.

Figure 18.- Continued.

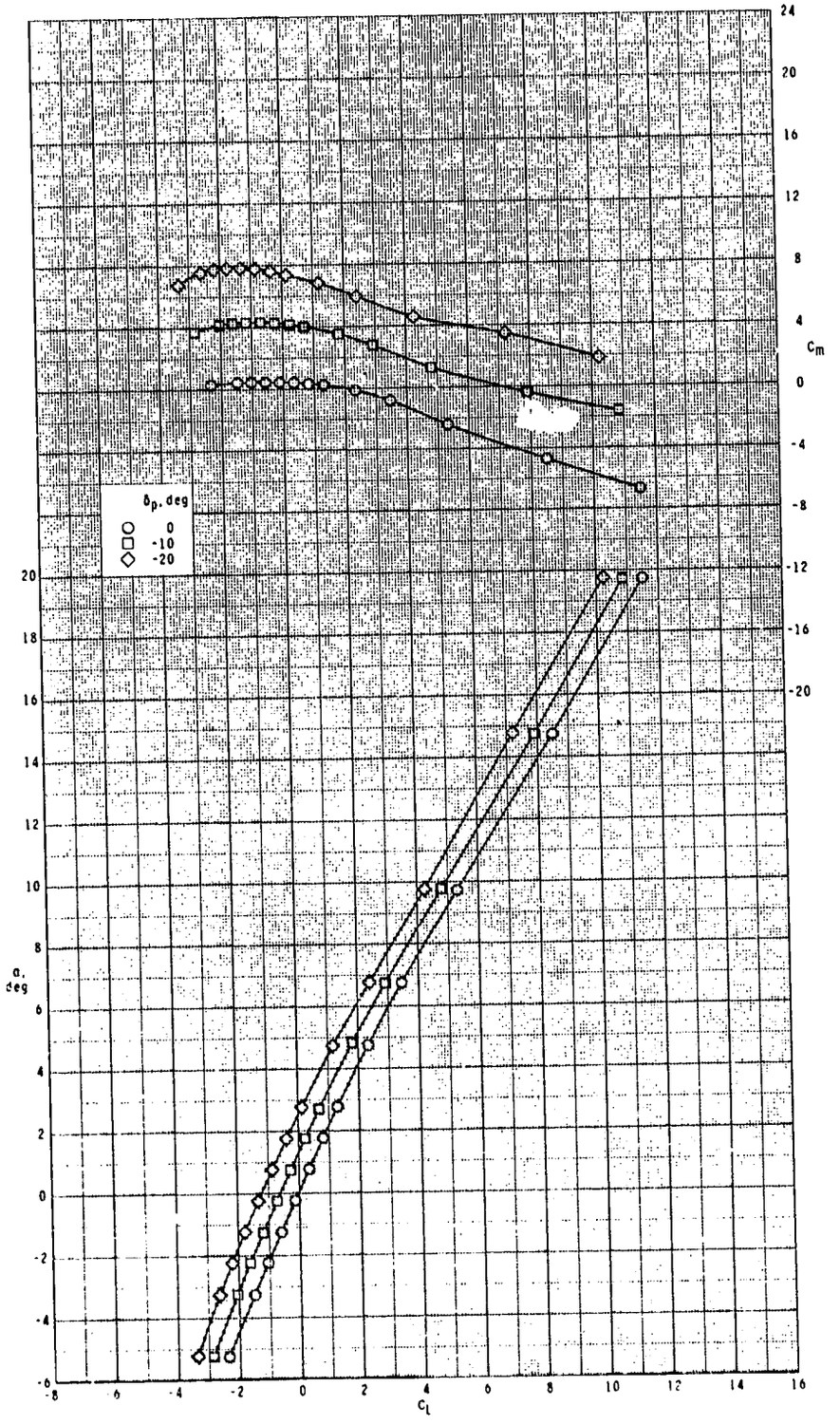

(b) Continued.

Figure 18.- Continued.

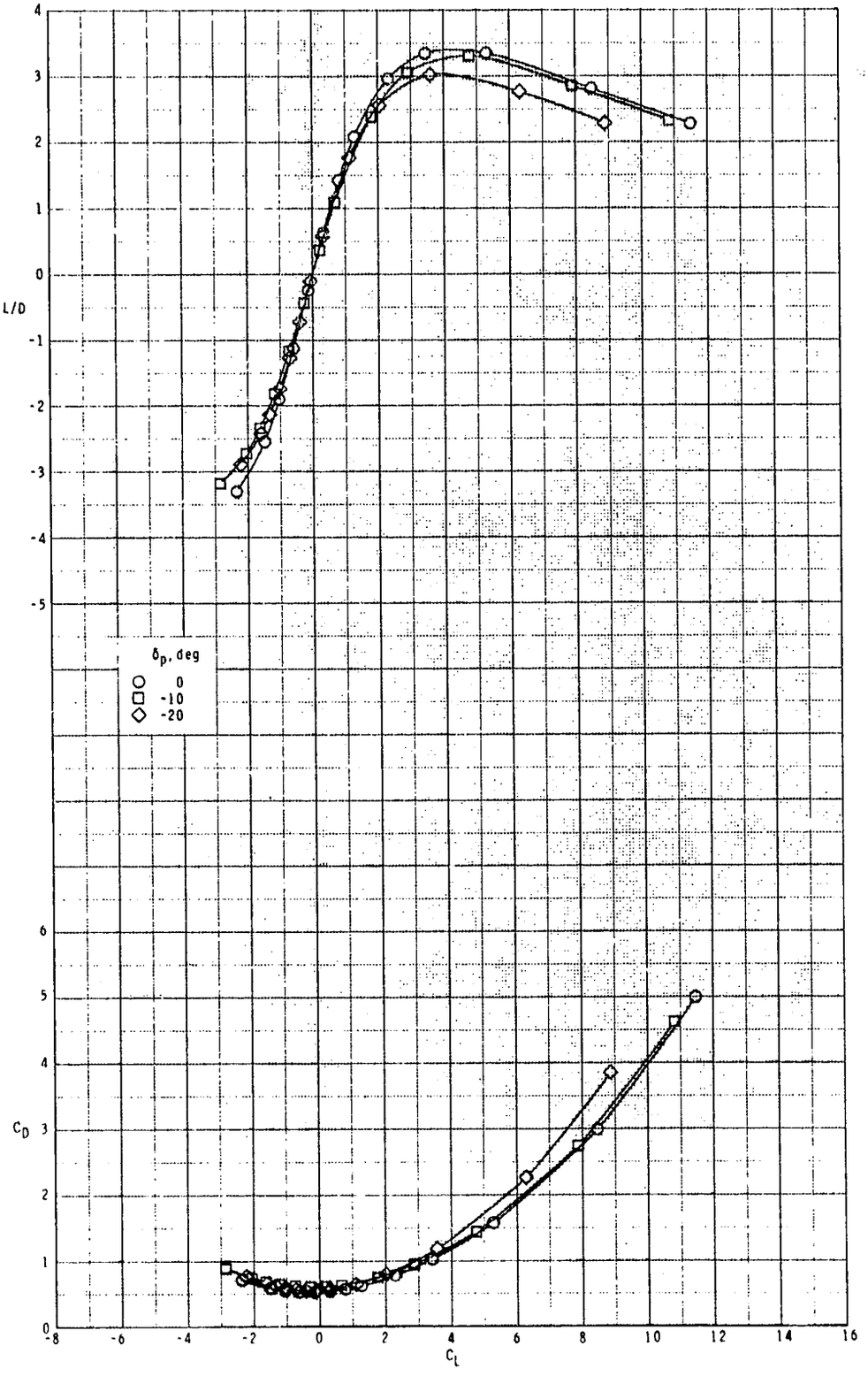

(b) Concluded.

Figure 18.- Continued.

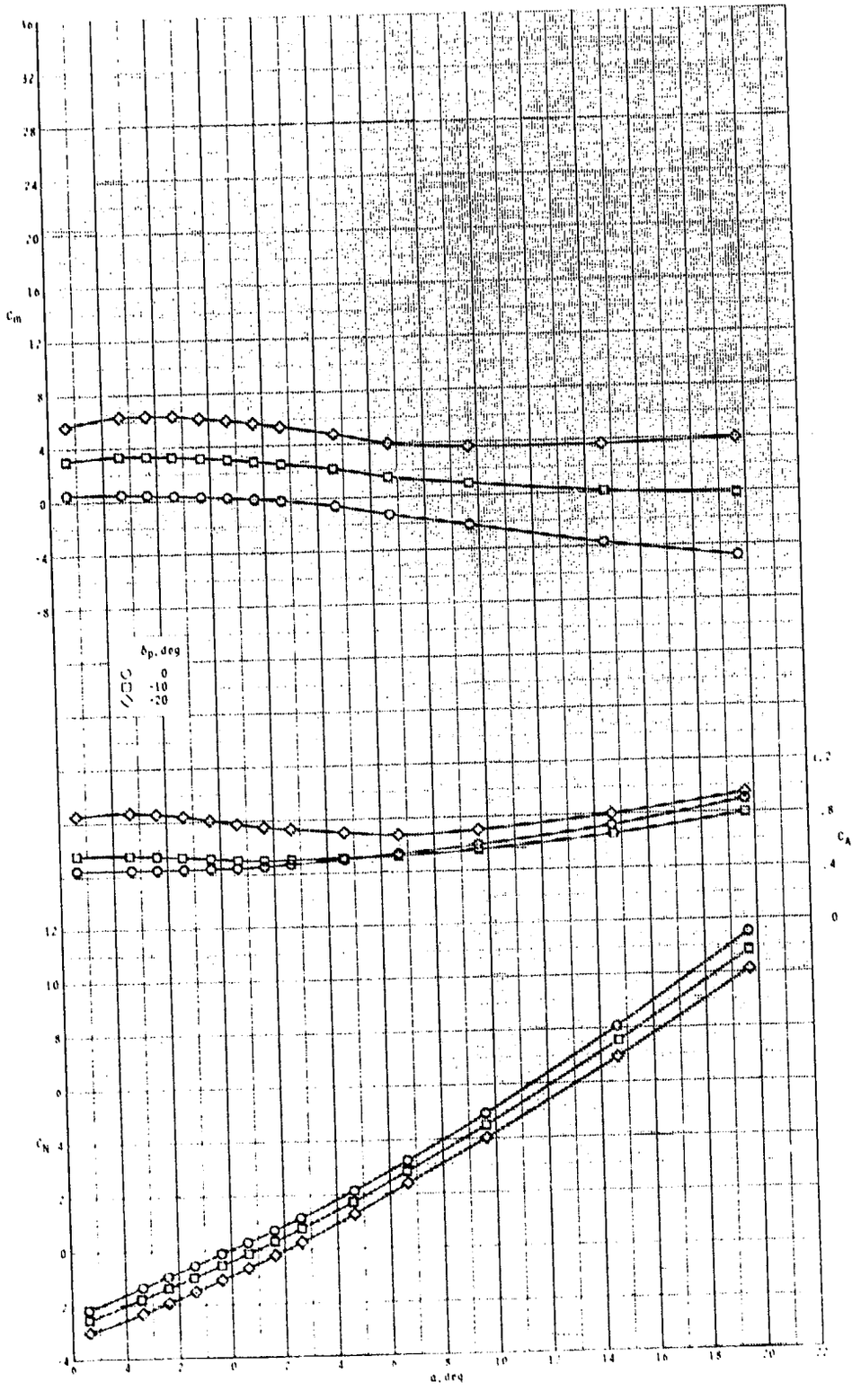

(c) M = 3.50.

Figure 18.- Continued.

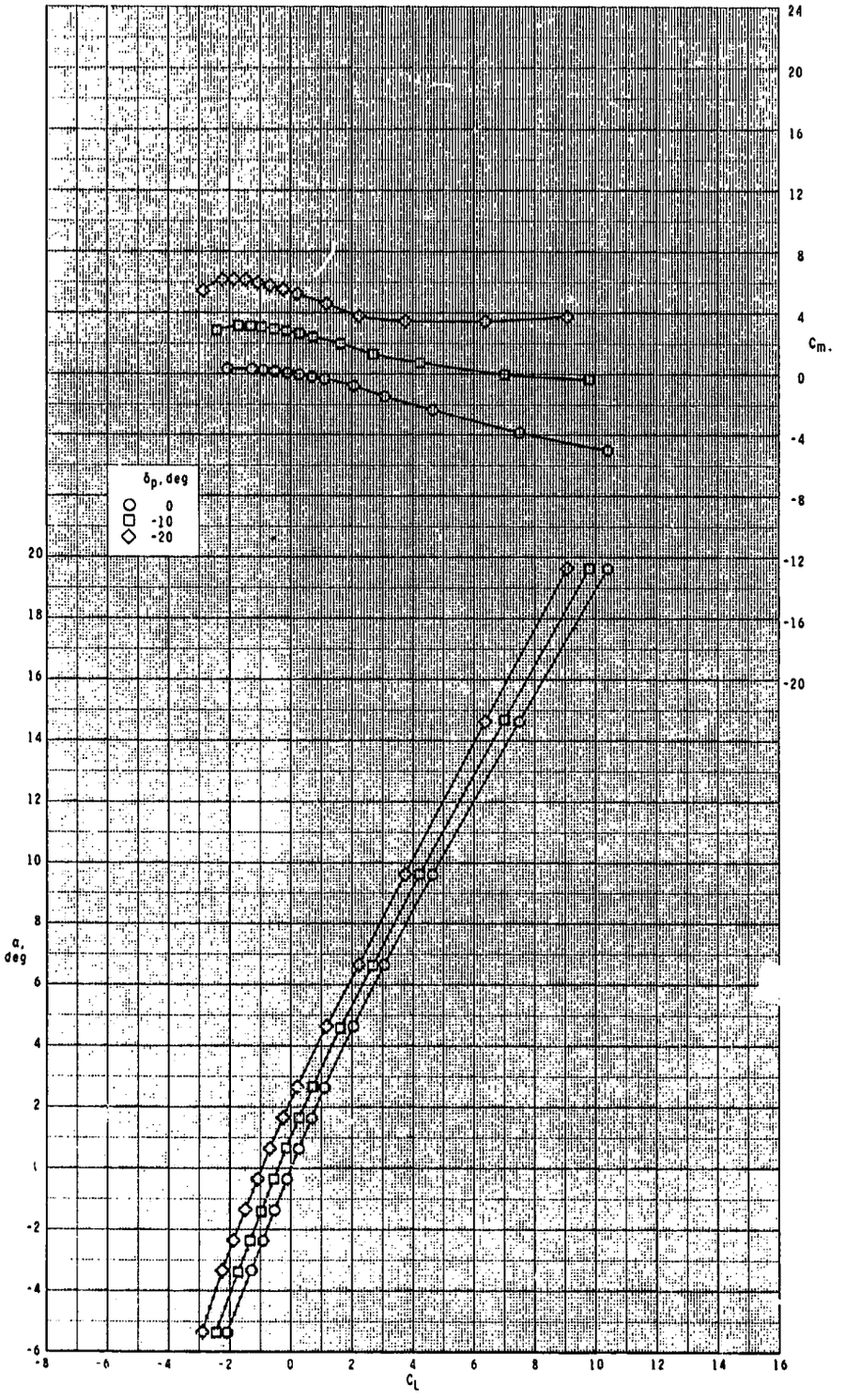

(c) Continued.

Figure 18.- Continued.

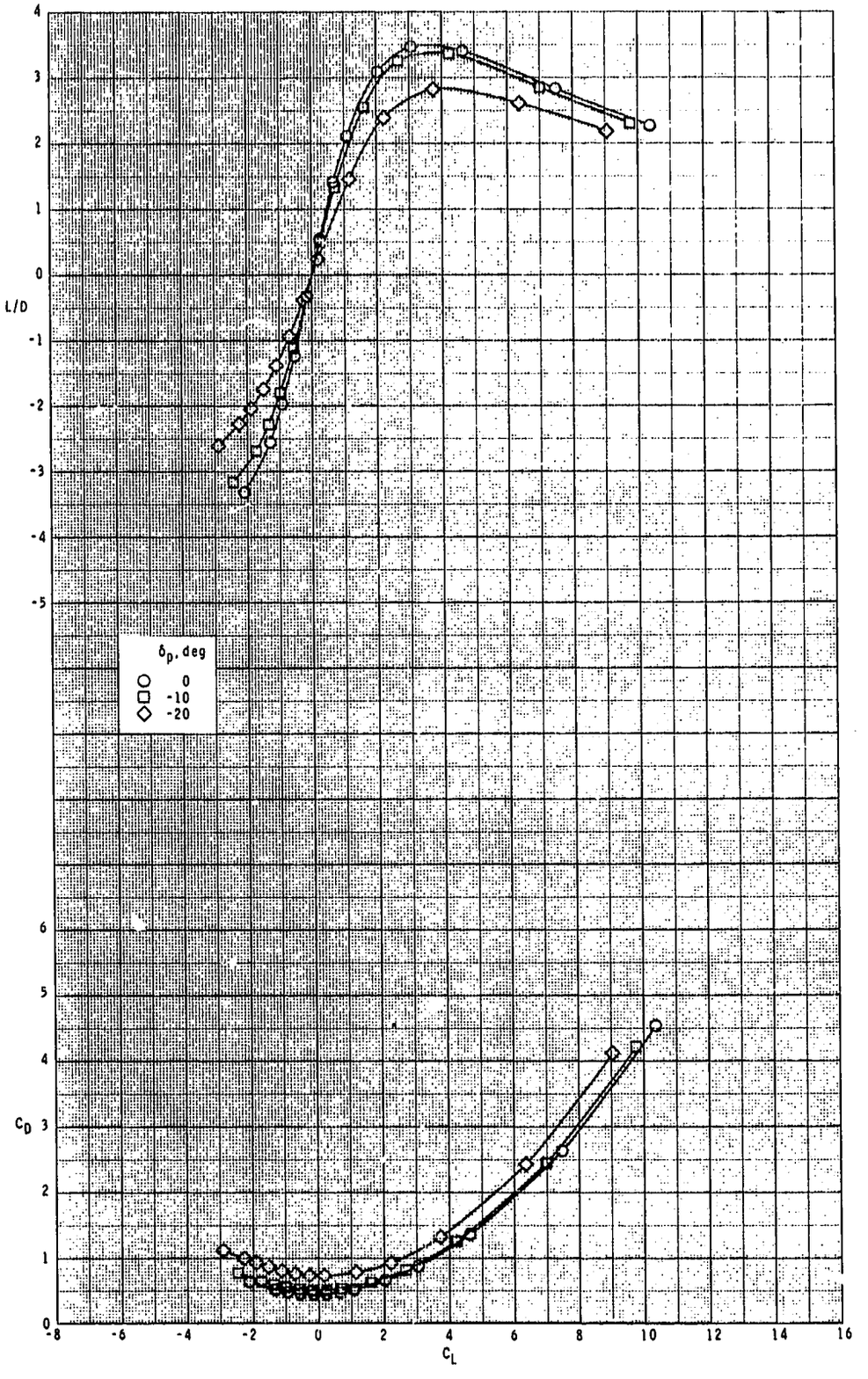

(c) Concluded.

Figure 18.- Continued.

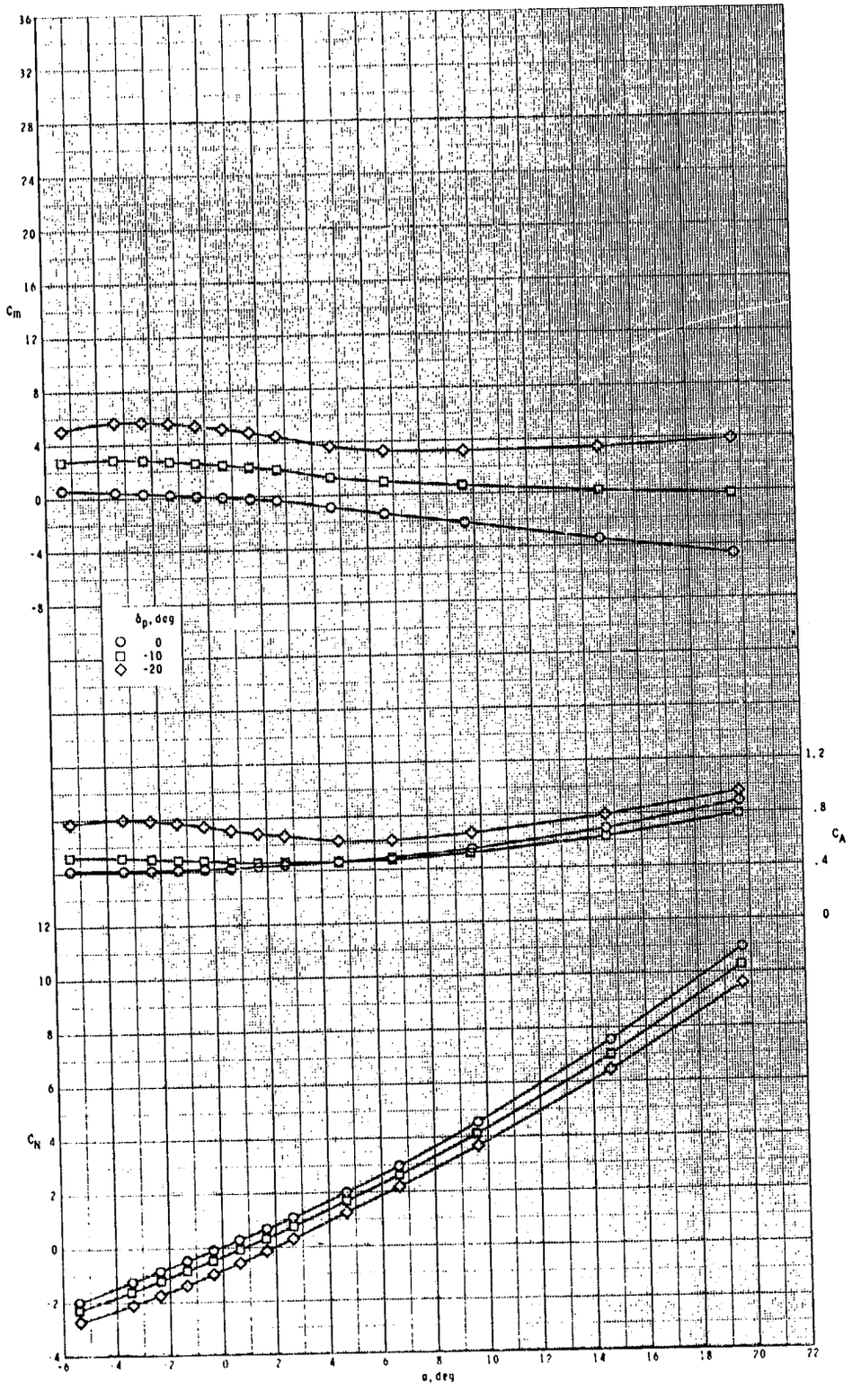

(d) M = 3.95.

Figure 18.- Continued.

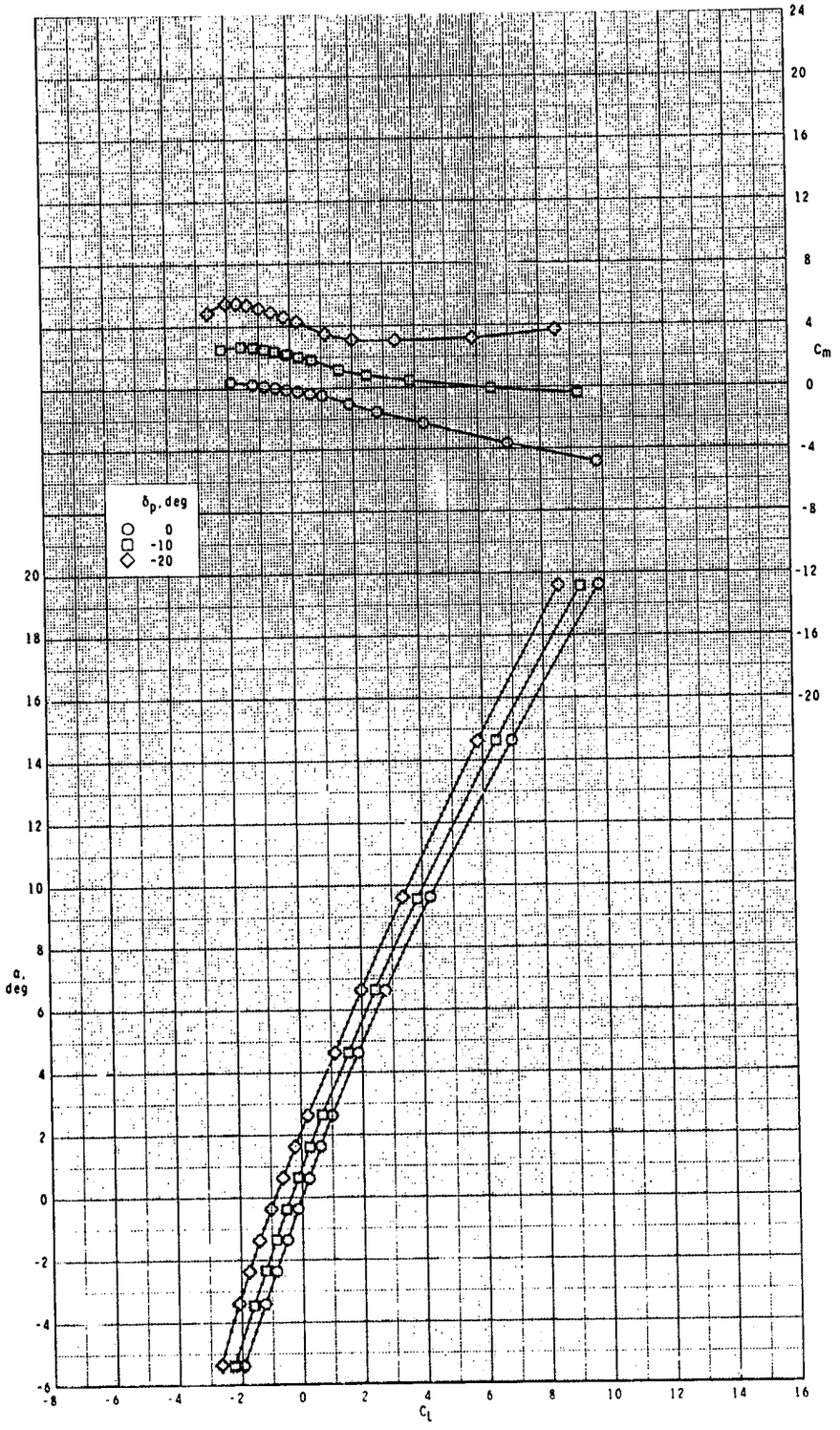

(d) Continued.

Figure 18.- Continued.

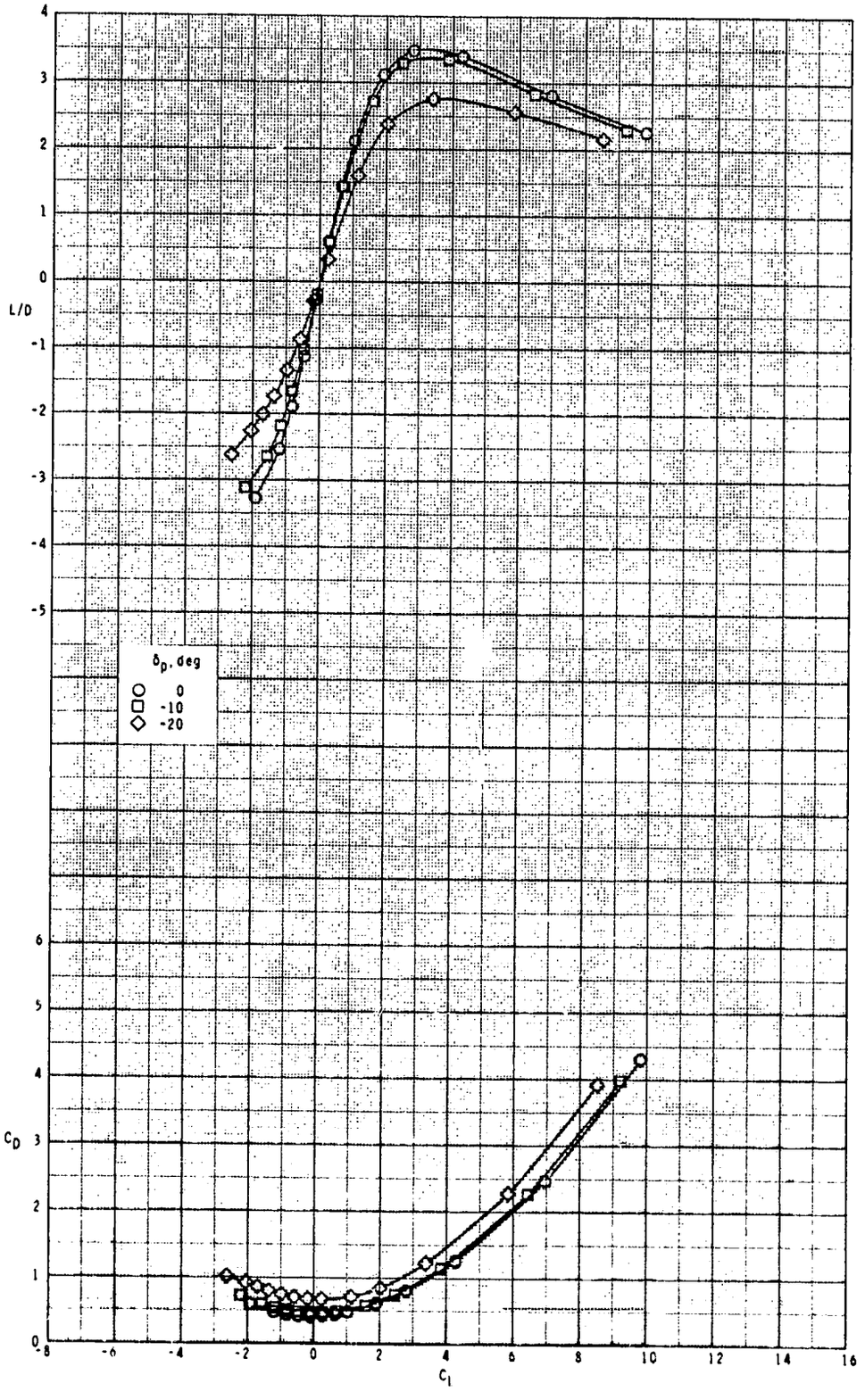

(d) Concluded.

Figure 18.- Concluded.

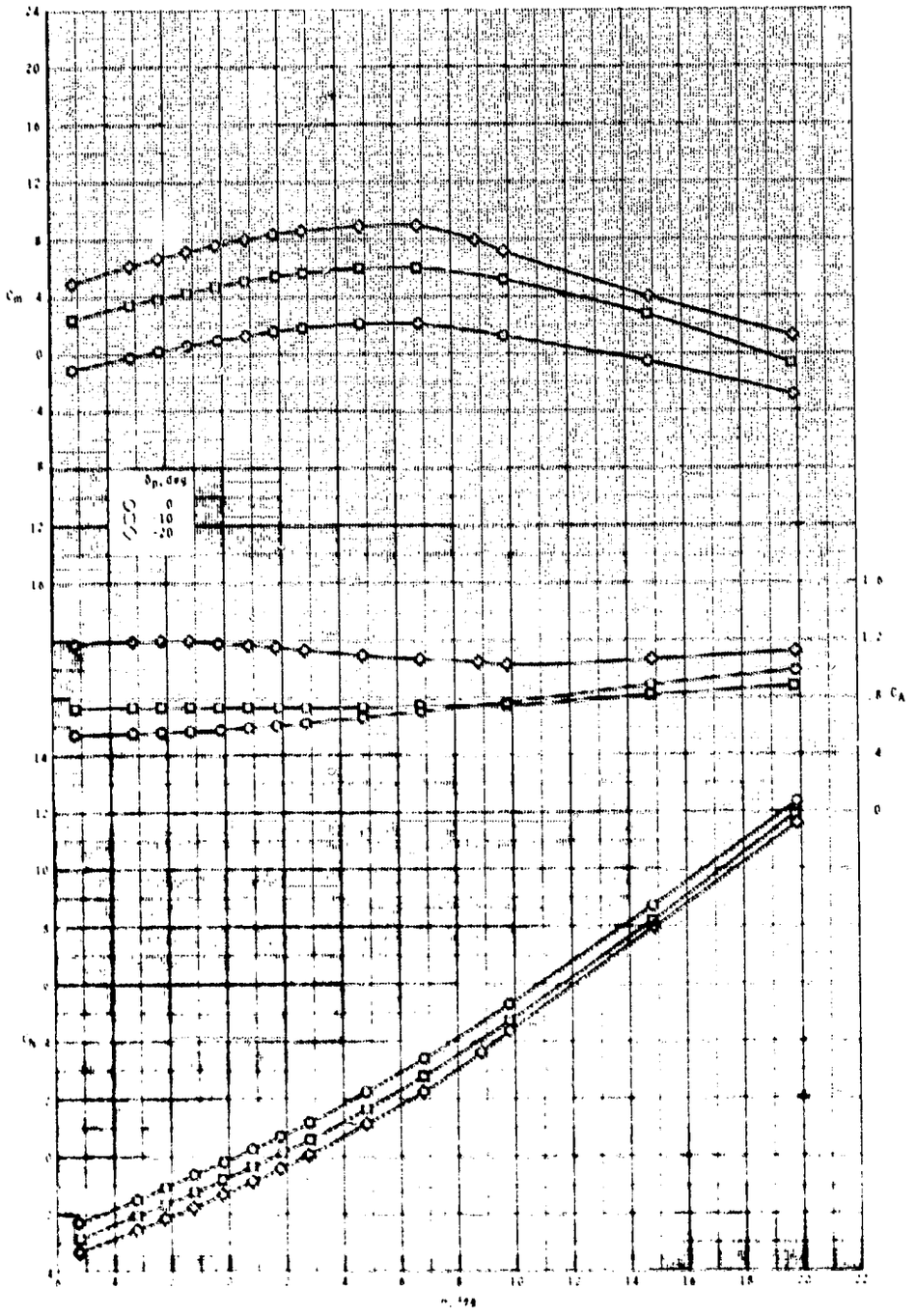

(a) M = 2.50.

Figure 19.- Pitch-control effectiveness of configuration $B_1T_2W_1T_1$ with $\Phi_I = 135°$.

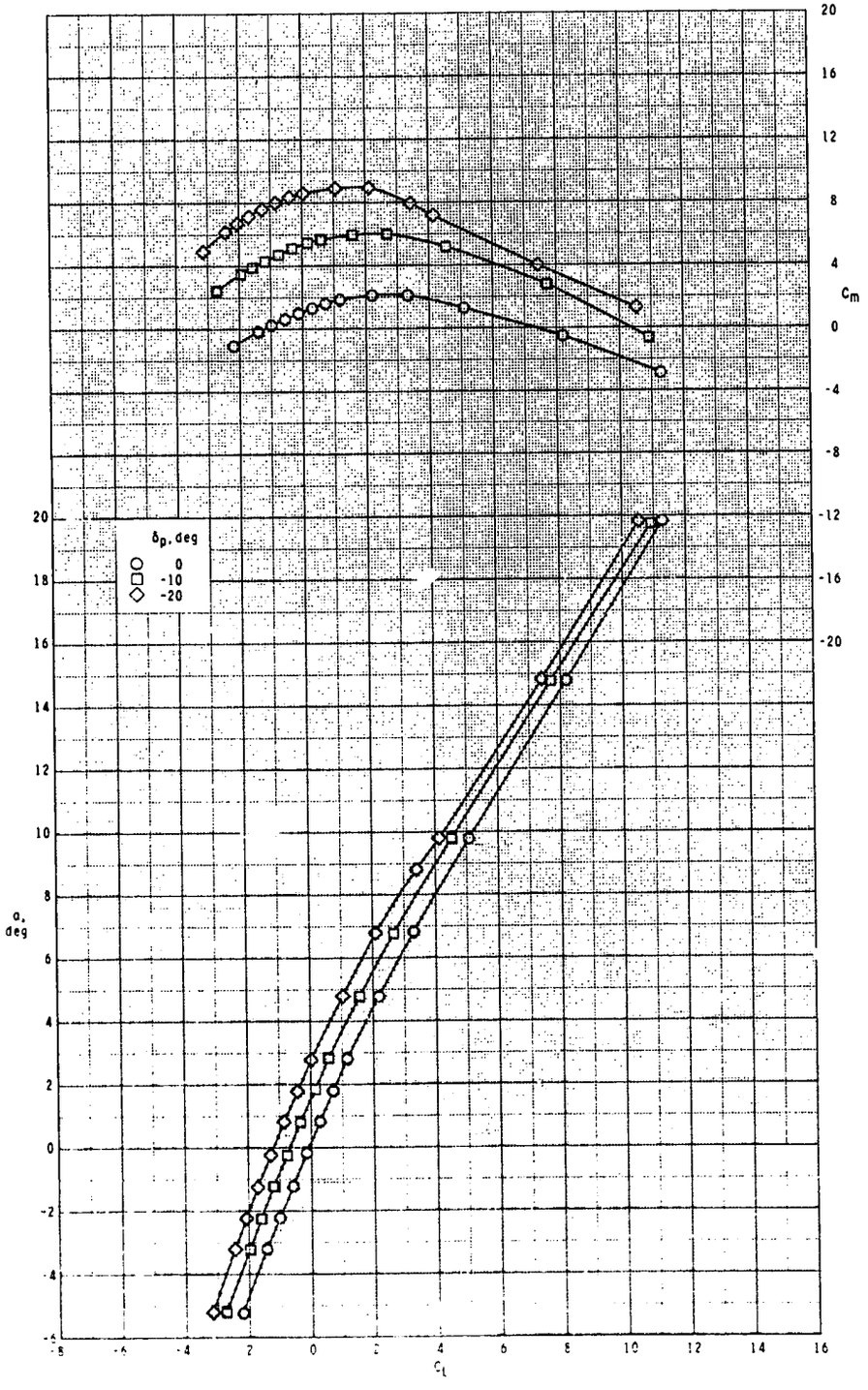

(a) Continued.

Figure 19.- Continued.

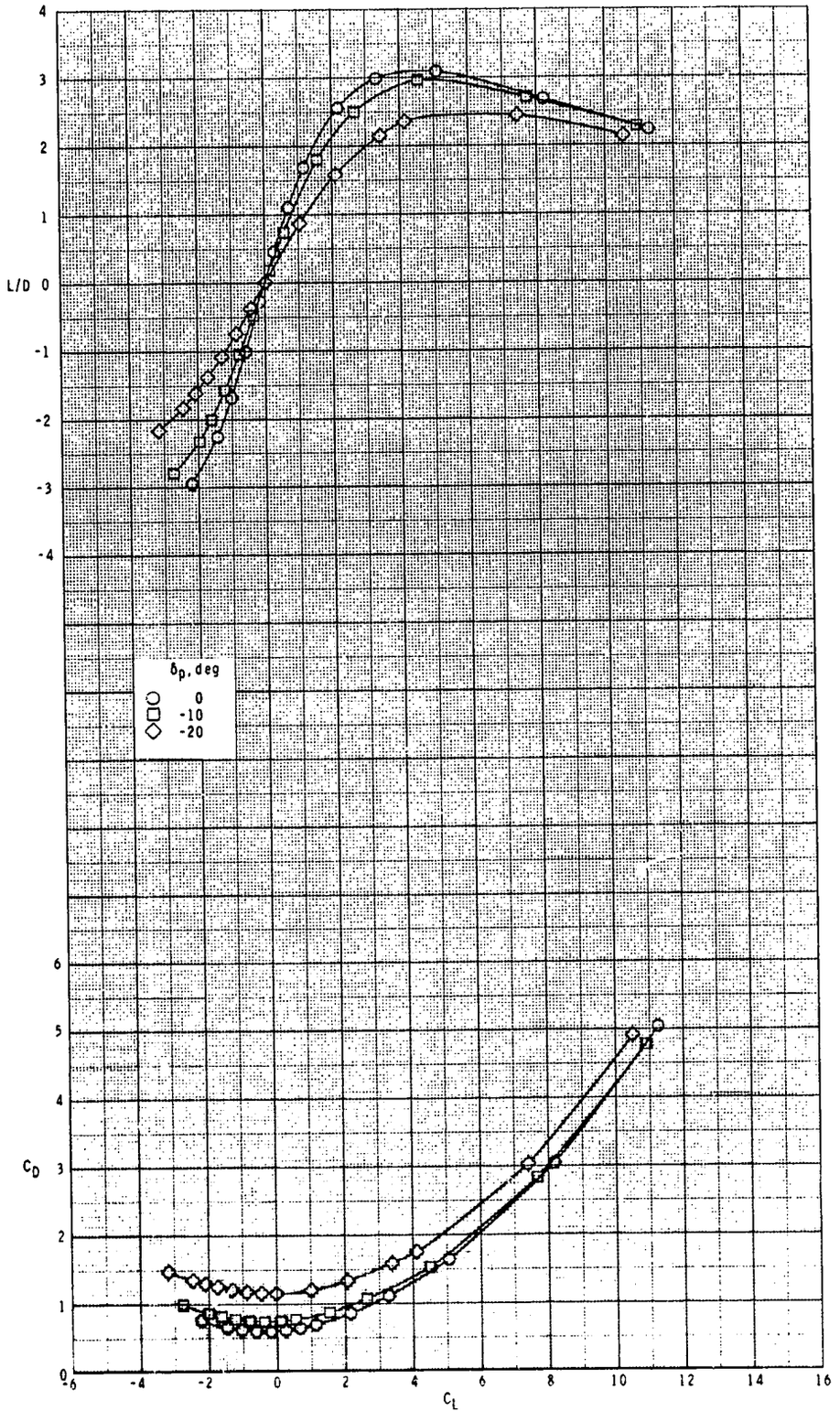

(a) Concluded.

Figure 19.- Continued.

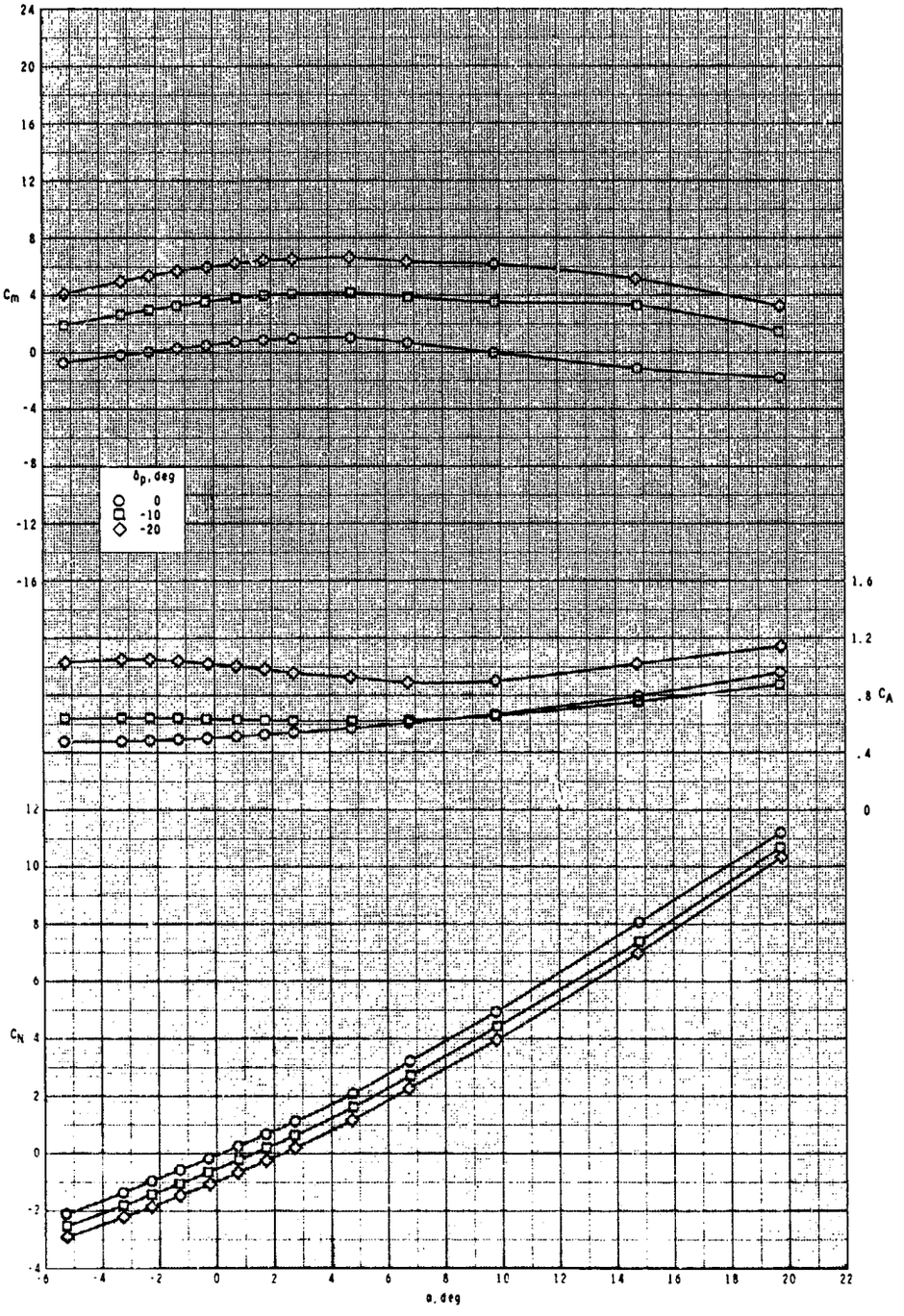

(b) M = 2.95.

Figure 19.- Continued.

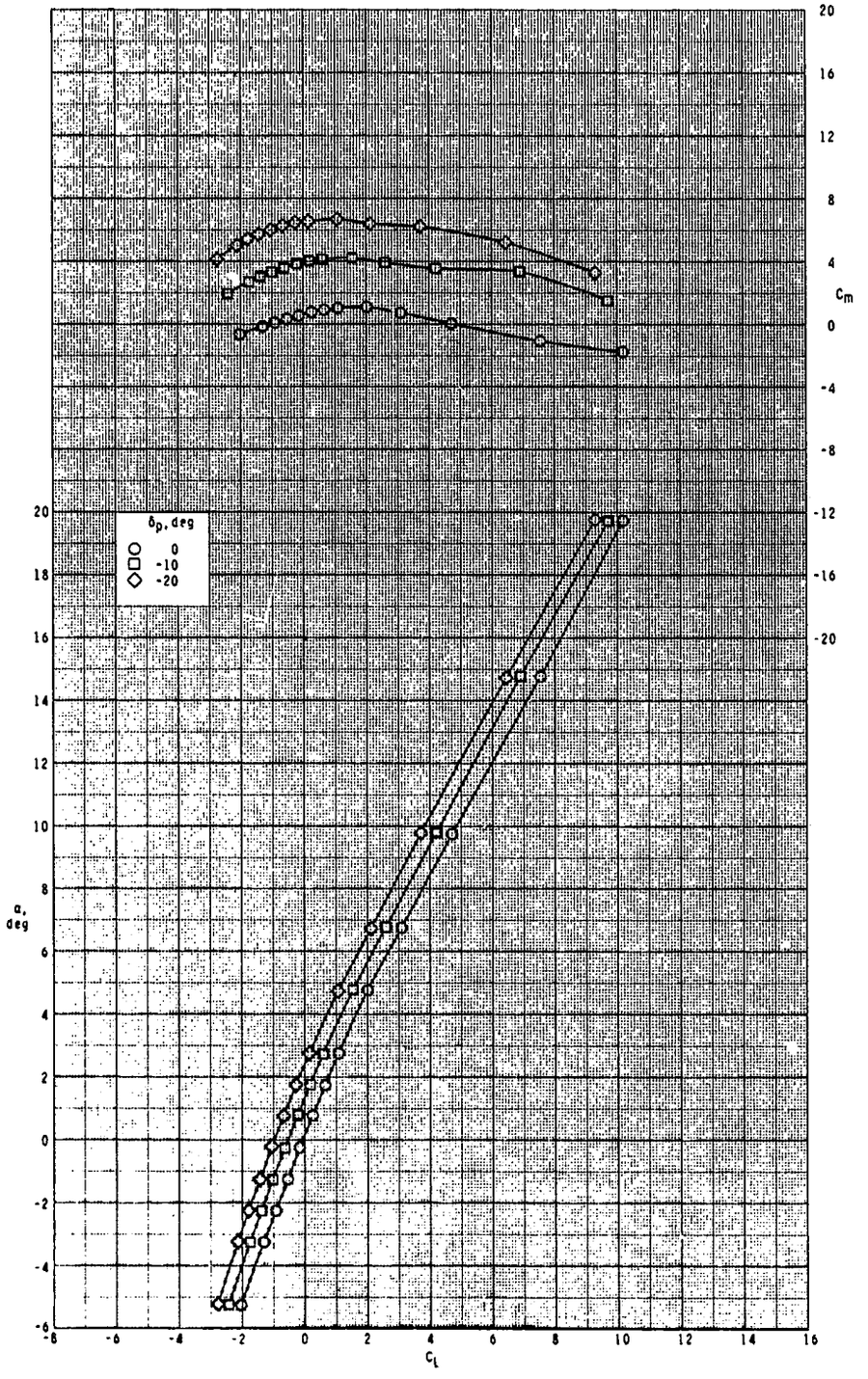

(b) Continued.

Figure 19.- Continued.

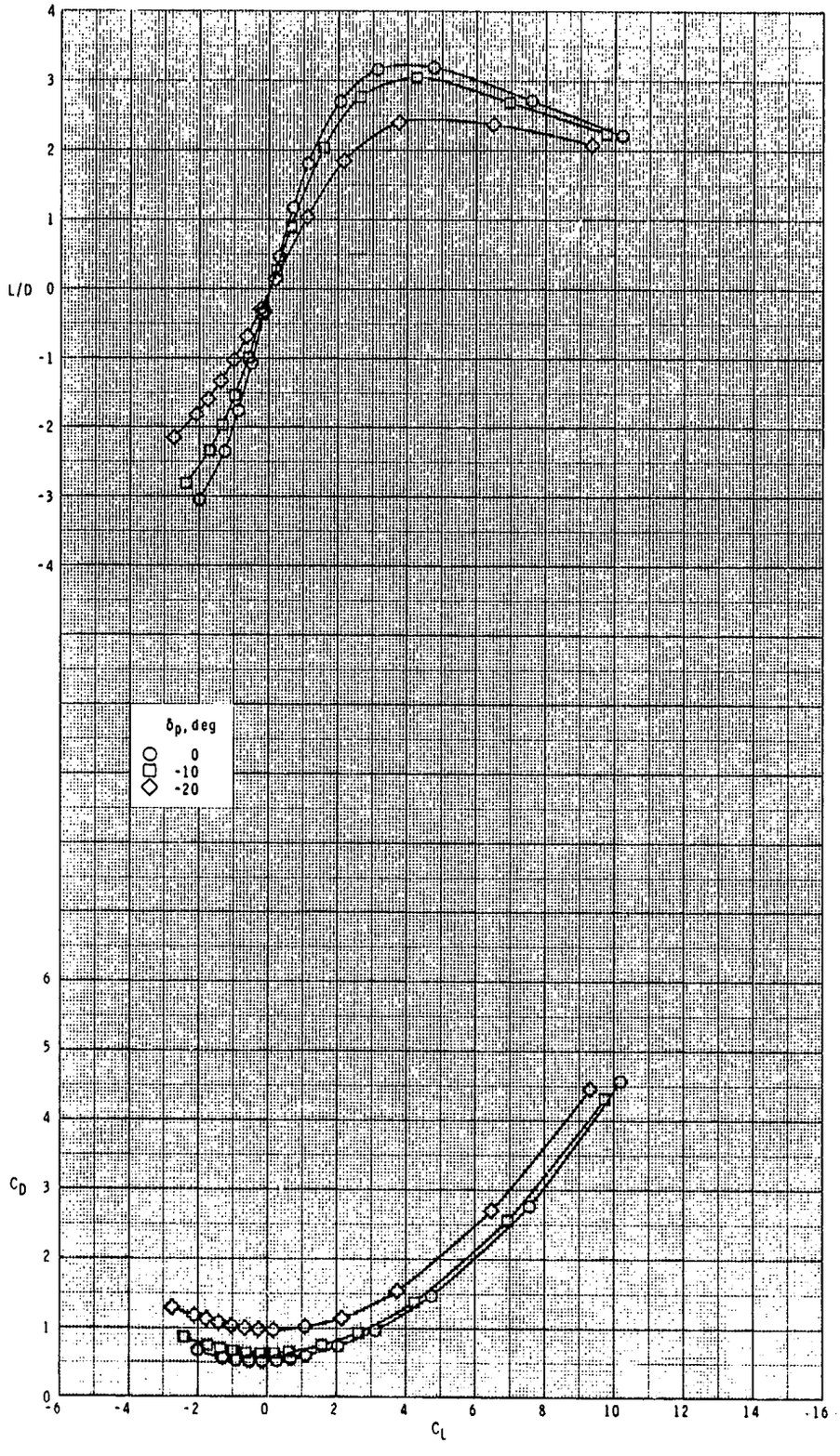

(b) Concluded.

Figure 19.- Continued.

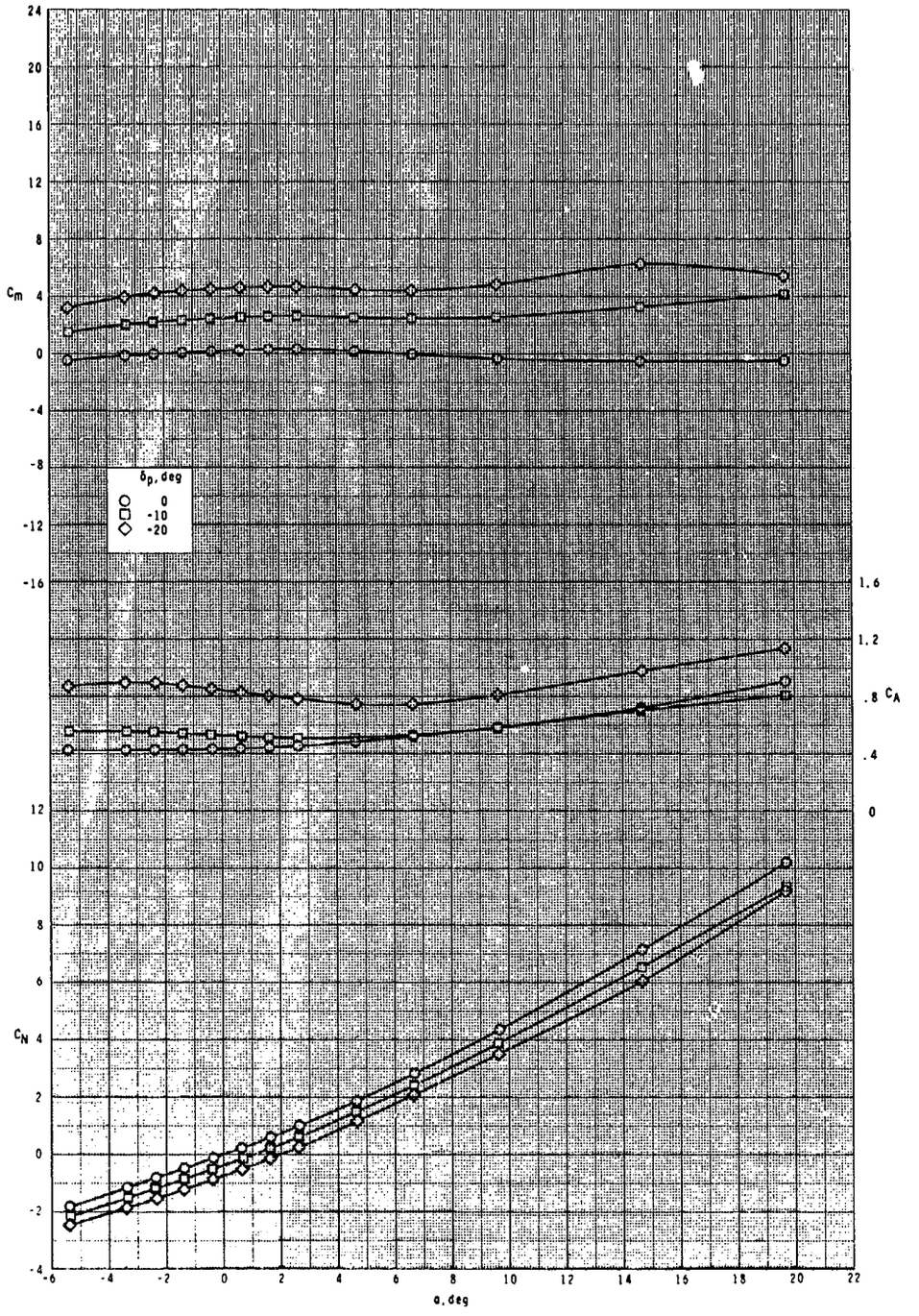

(c) M = 3.50.

Figure 19.- Continued.

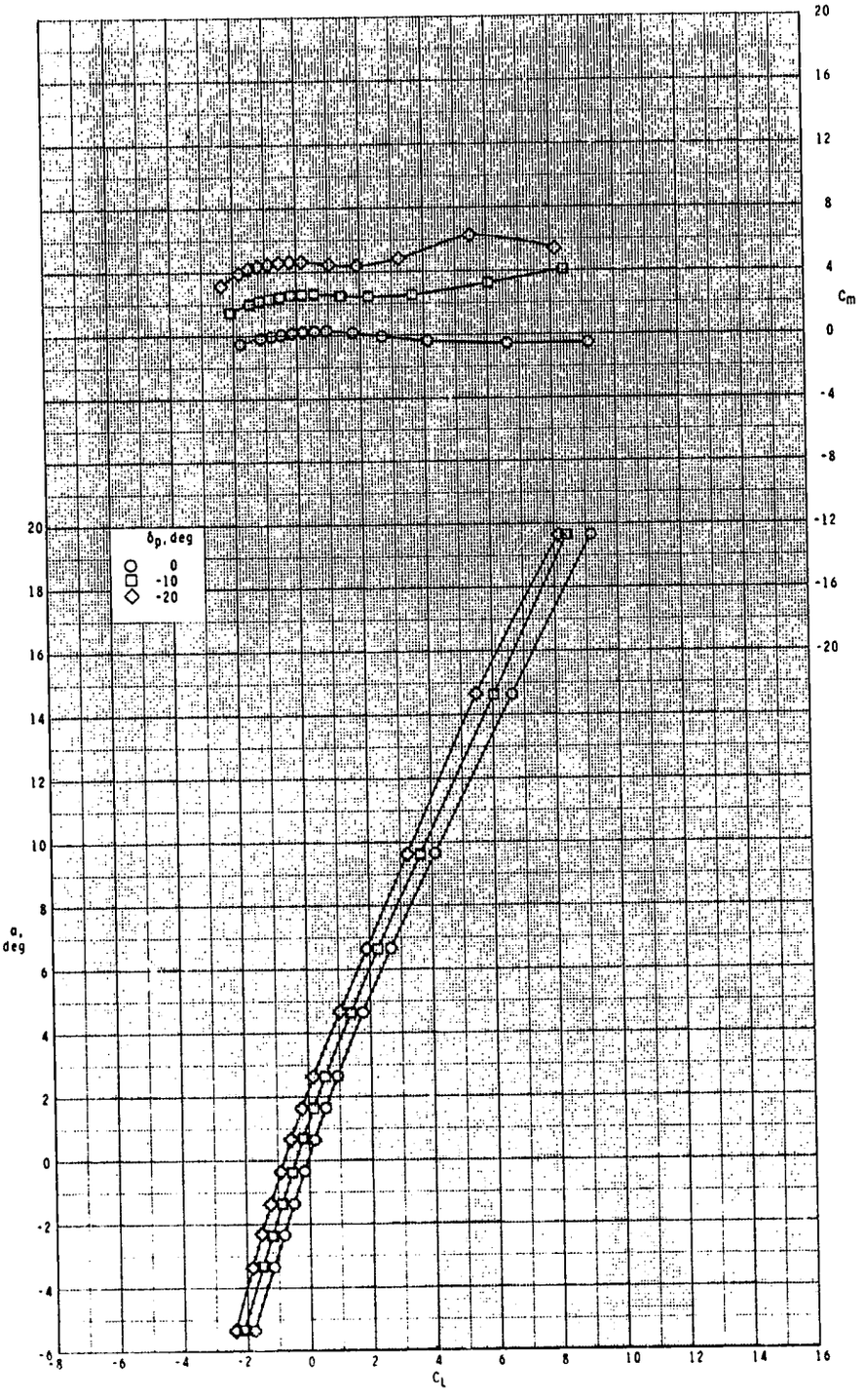

(c) Continued.

Figure 19.- Continued.

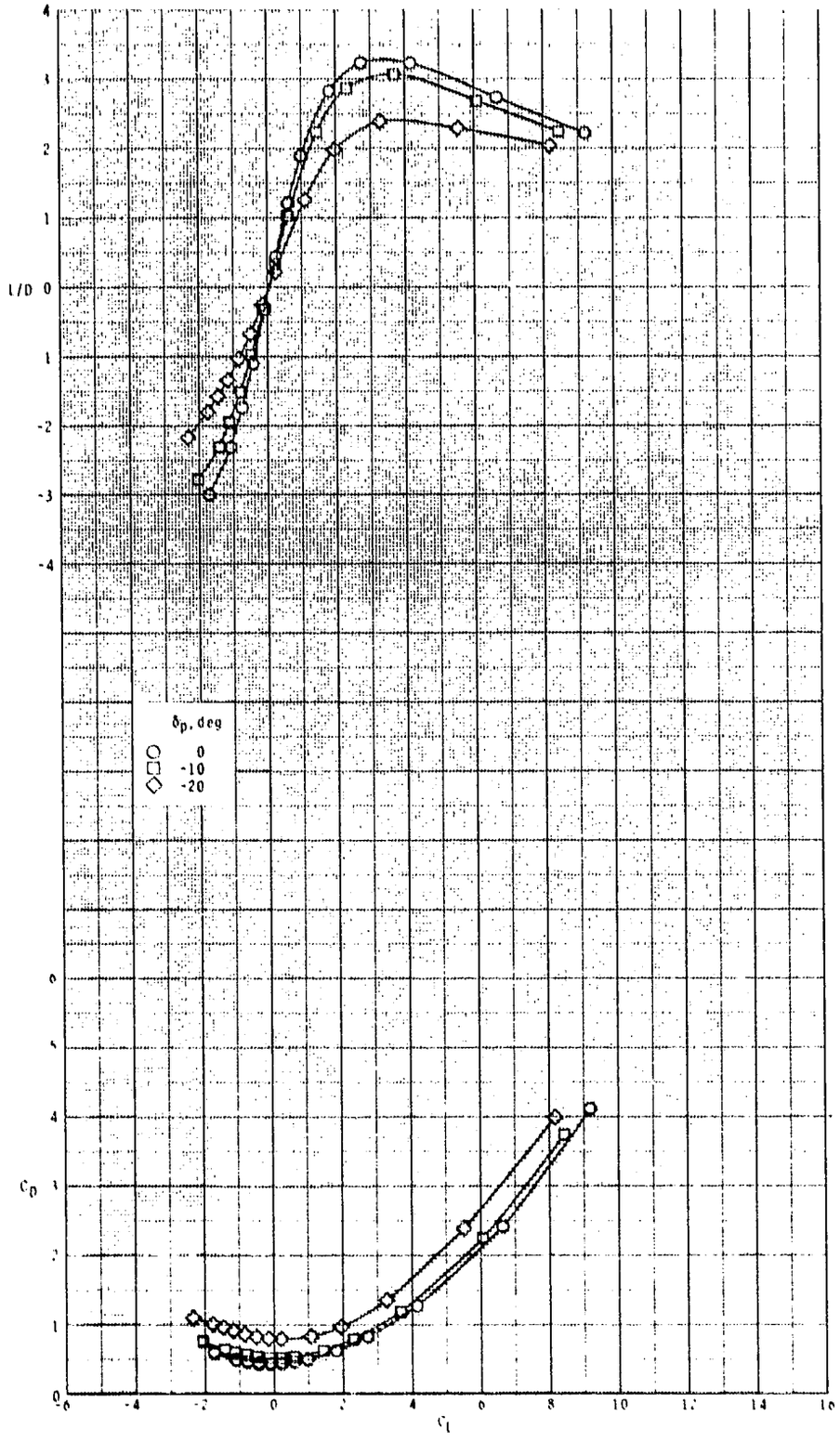

(c) Concluded.

Figure 19.- Continued.

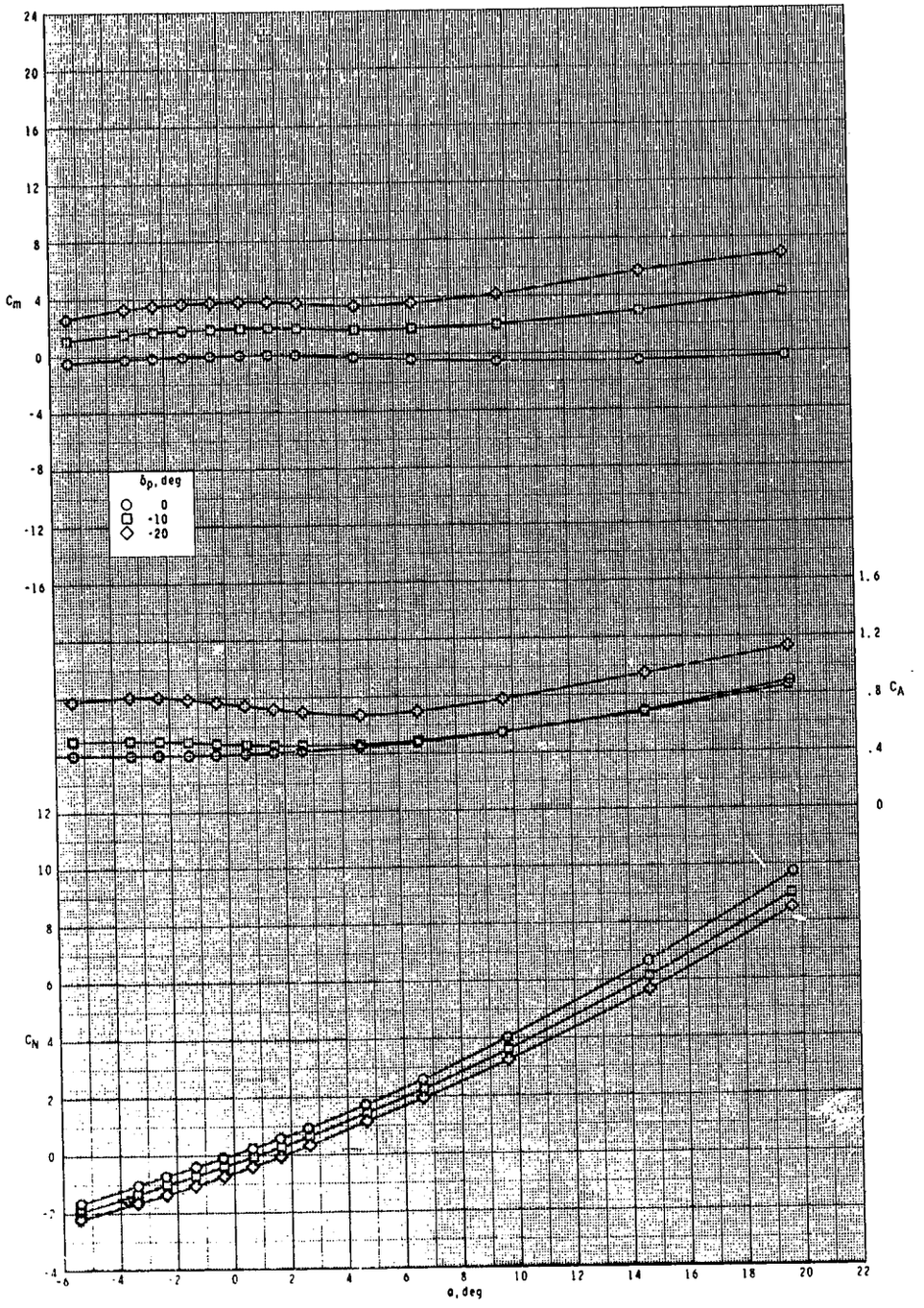

(d) M = 3.95.

Figure 19.- Continued.

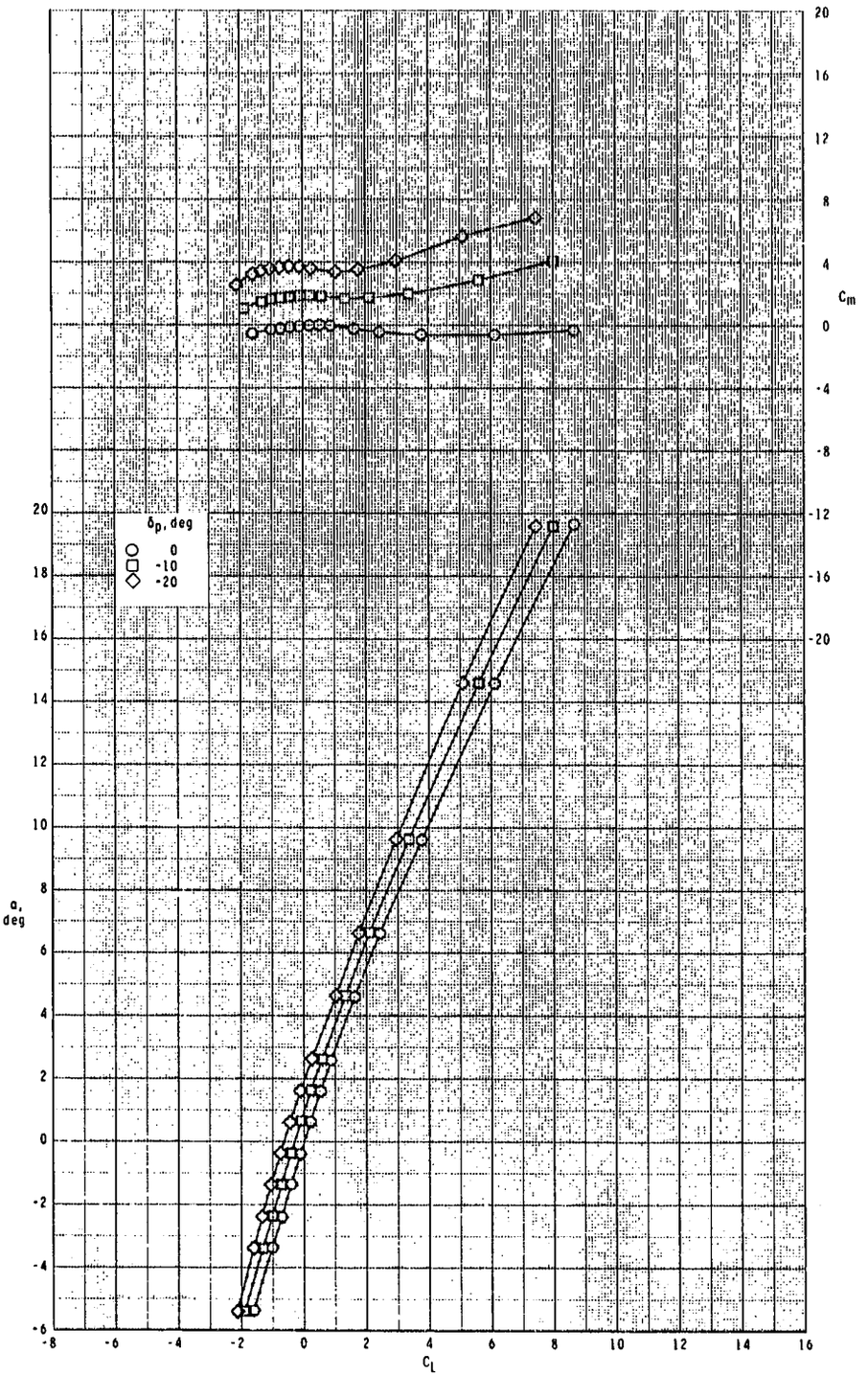

(d) Continued.

Figure 19.- Continued.

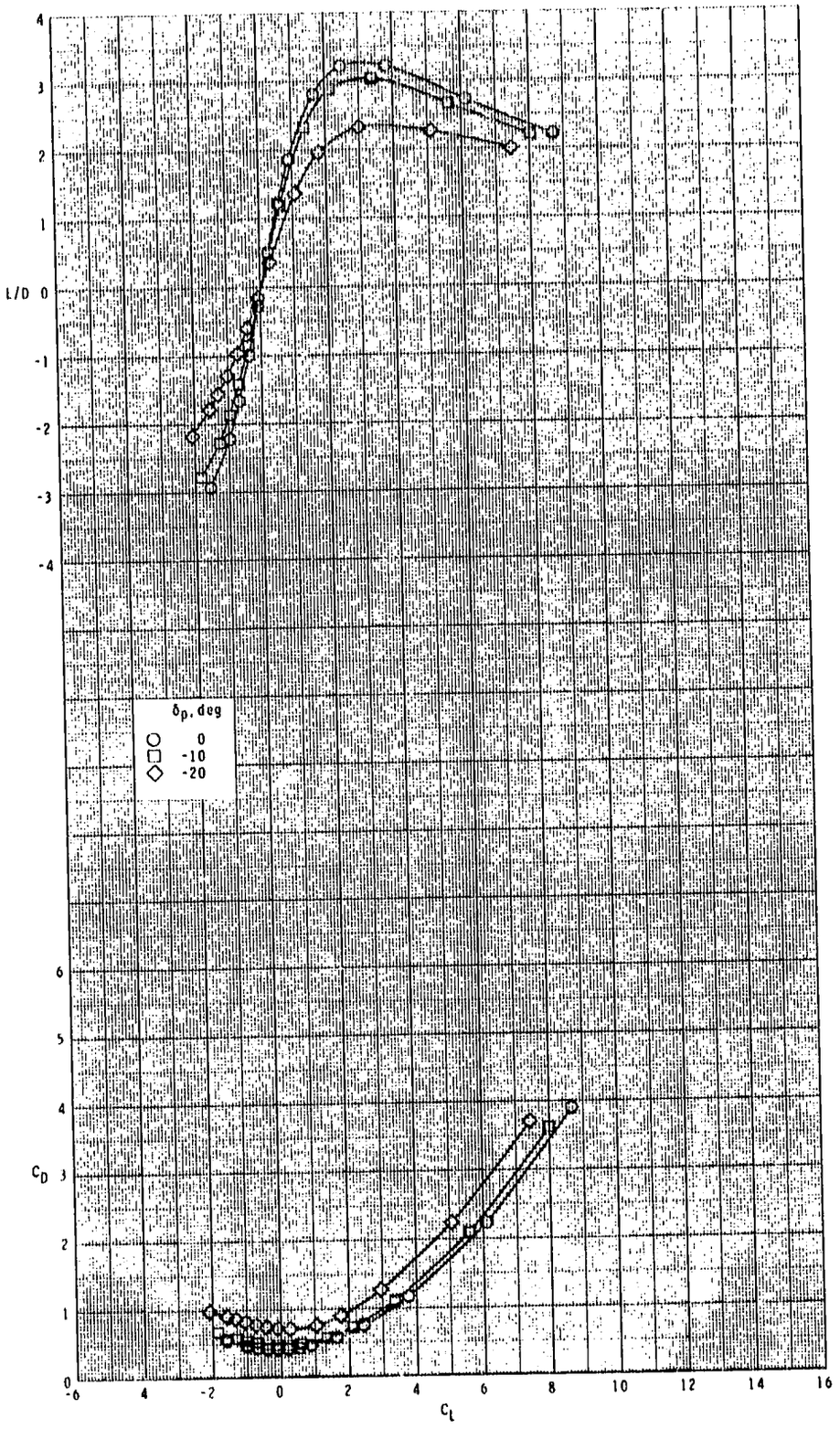

(d) Concluded.

Figure 19.- Concluded.

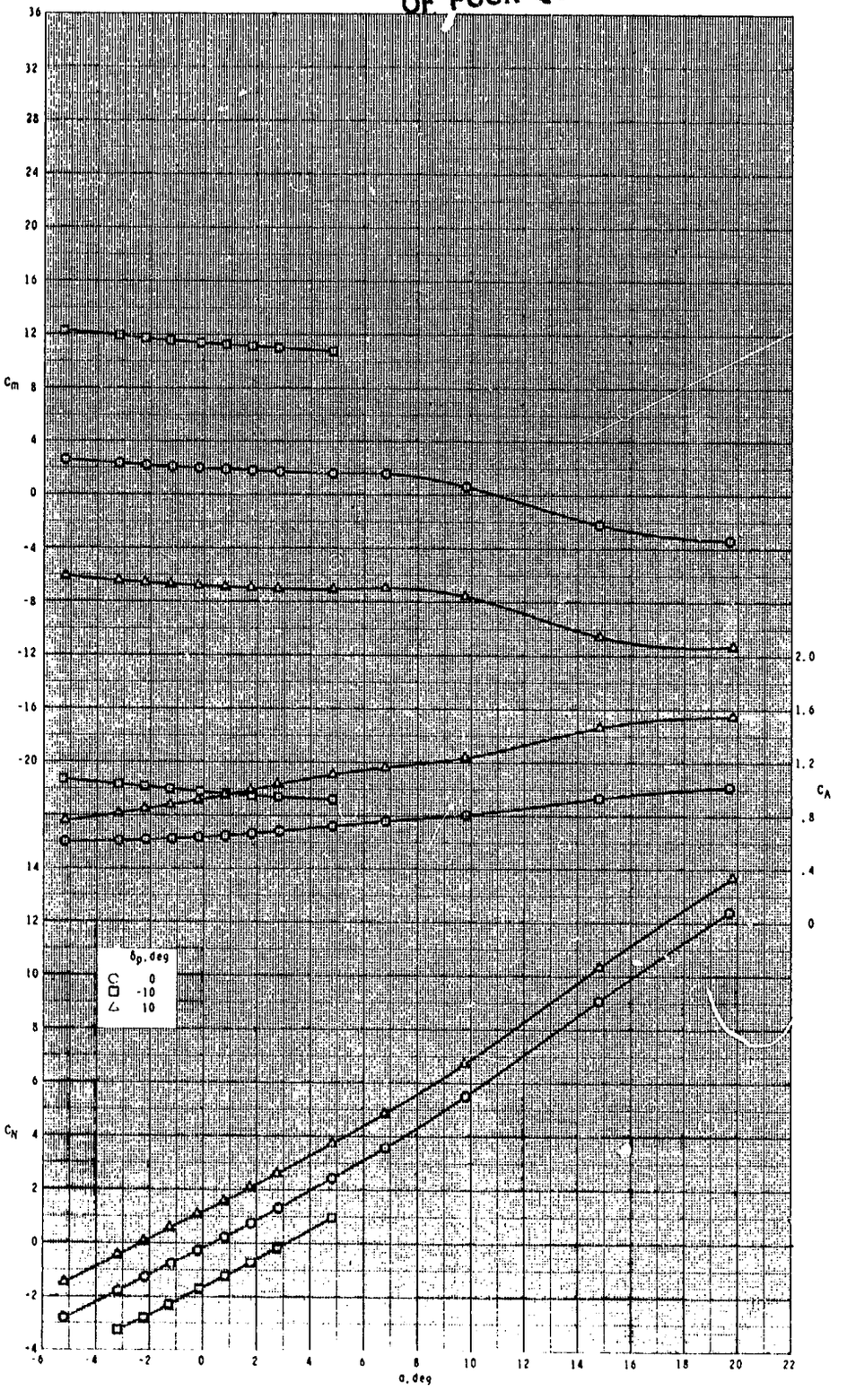

(a) M = 2.50.

Figure 20.- Pitch-control effectiveness of configuration $B_1I_2W_1T_2$ with $\phi_I = 135°$.

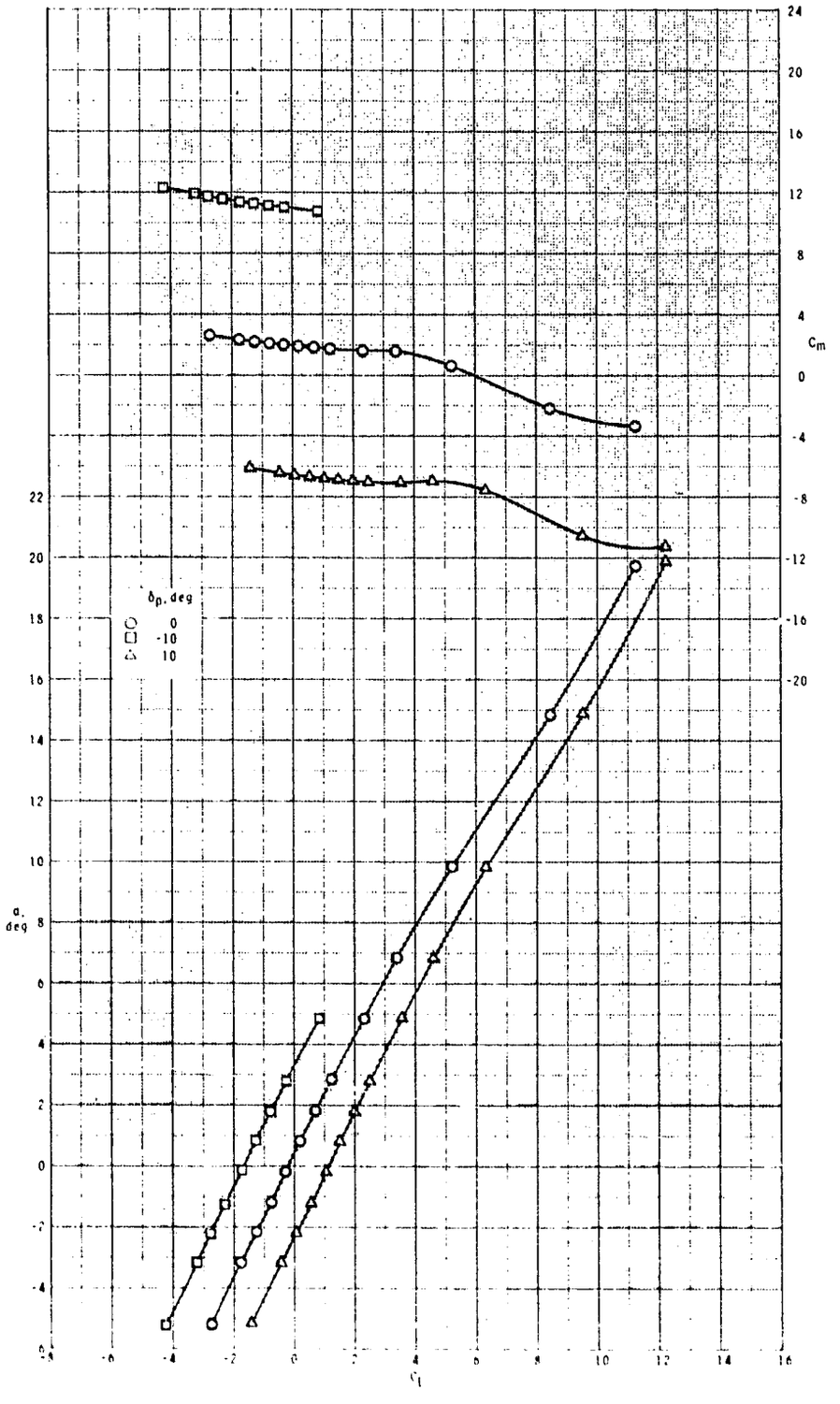

(a) Continued.

Figure 20.- Continued.

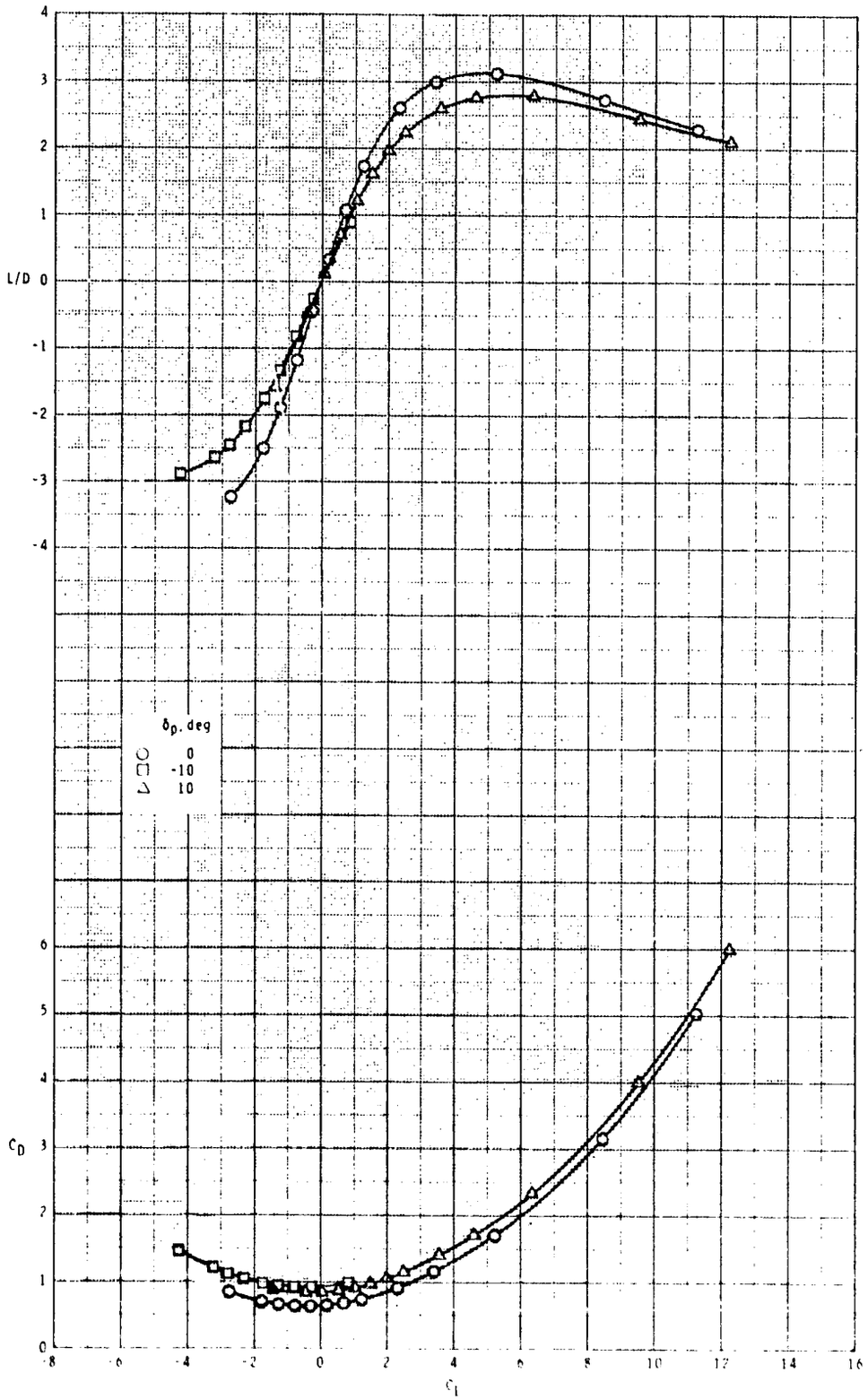

(a) Concluded.

Figure 20.- Continued.

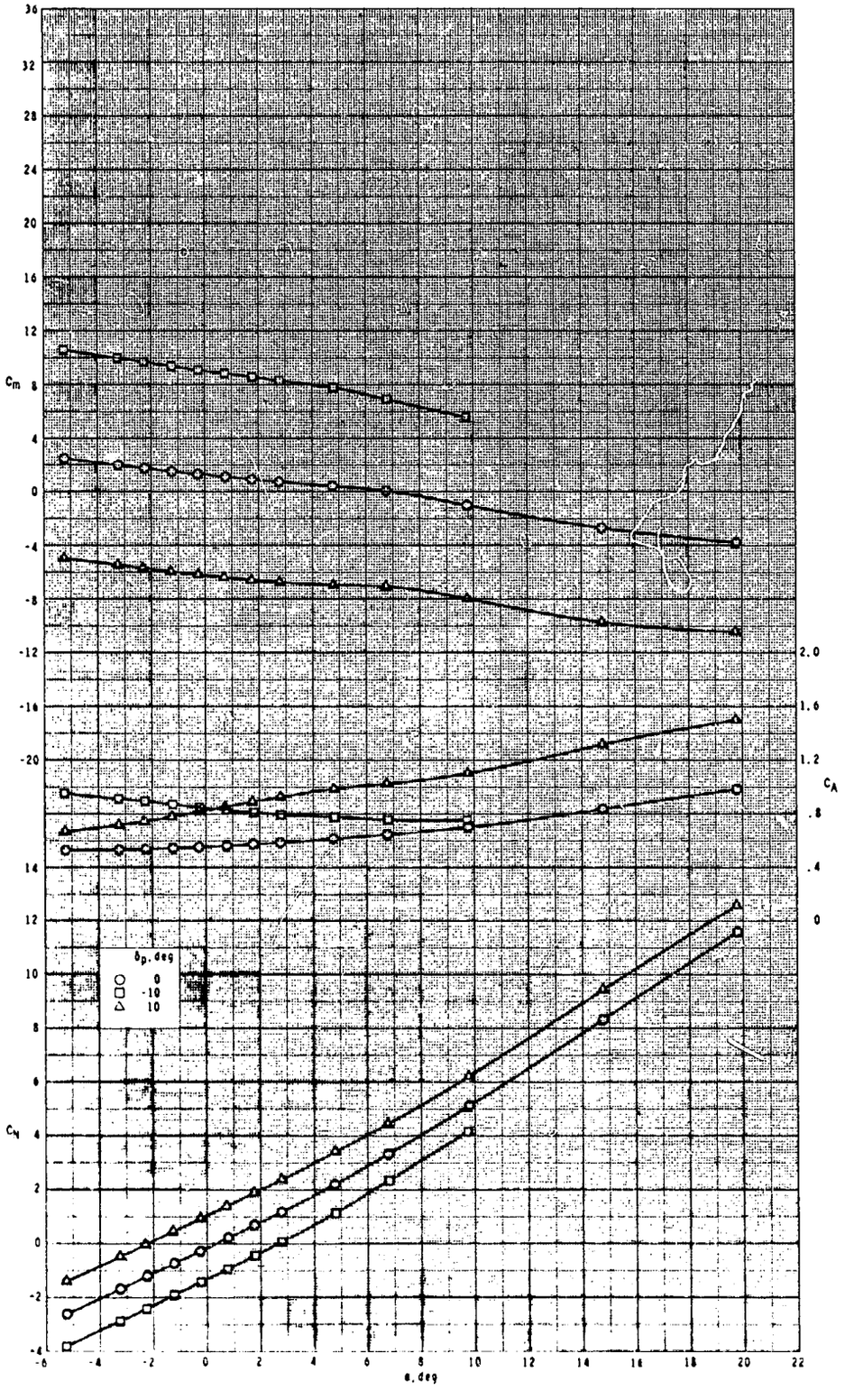

(b) M = 2.95.

Figure 20.- Continued.

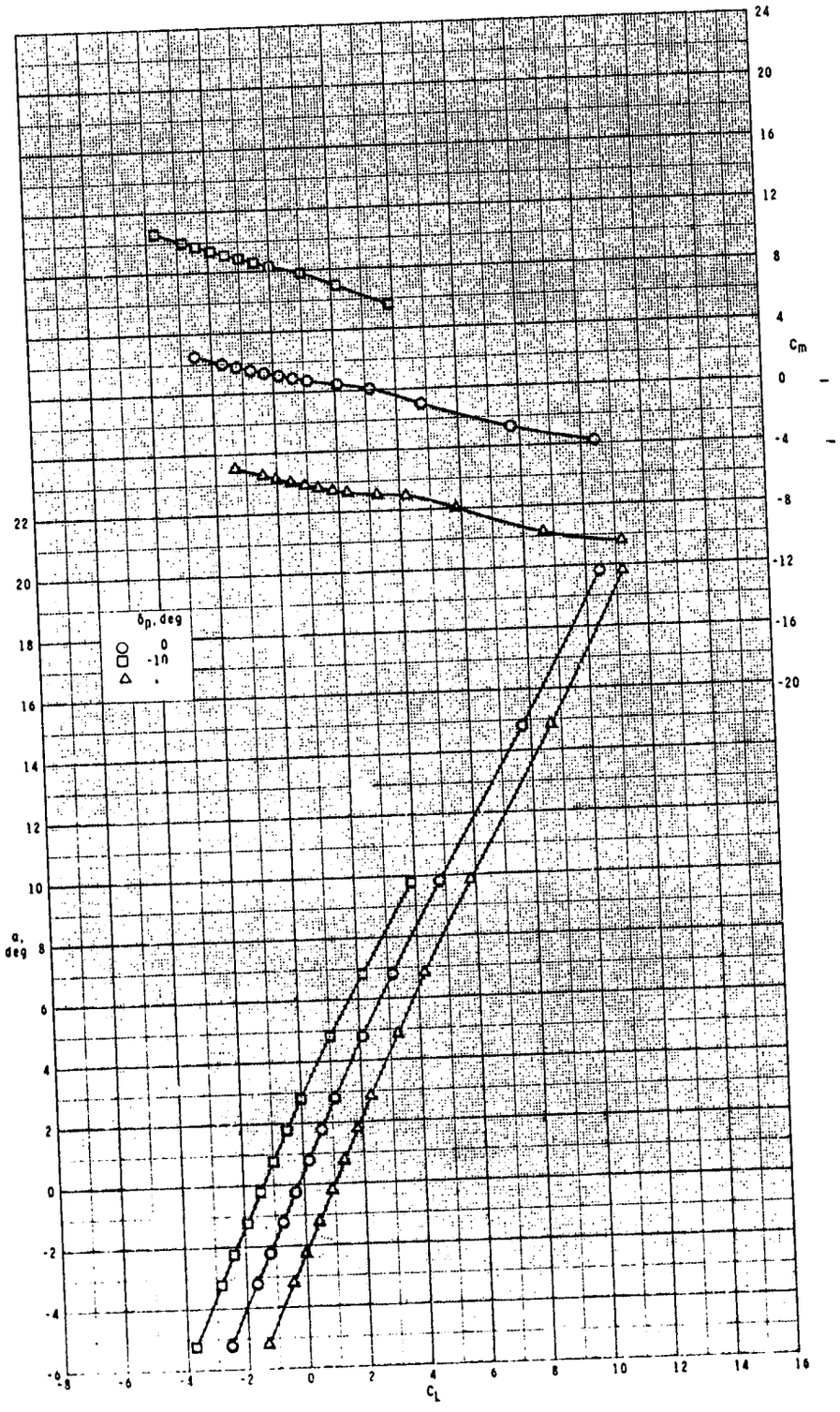

(b) Continued.

Figure 20.- Continued.

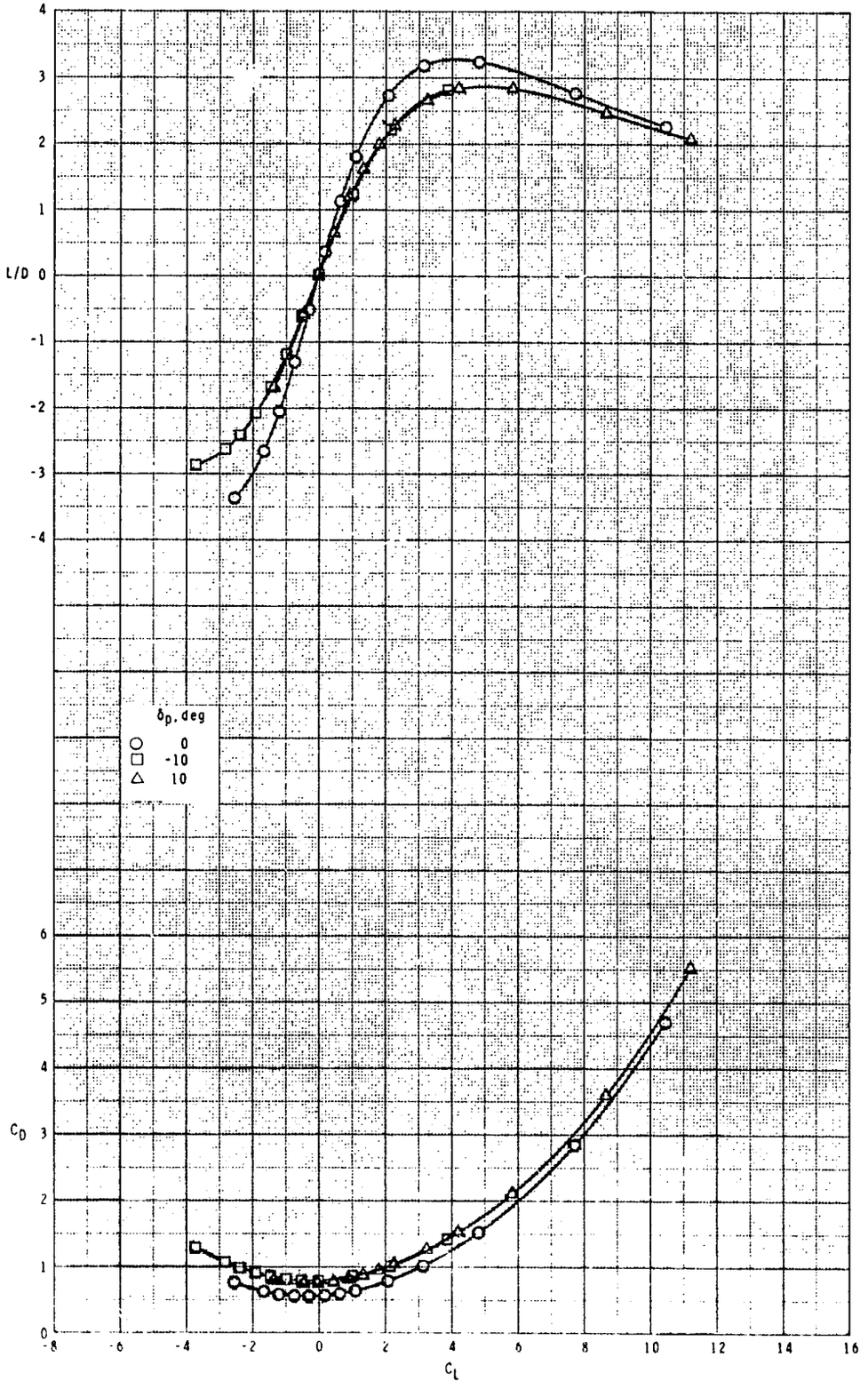

(b) Concluded.

Figure 20.- Continued.

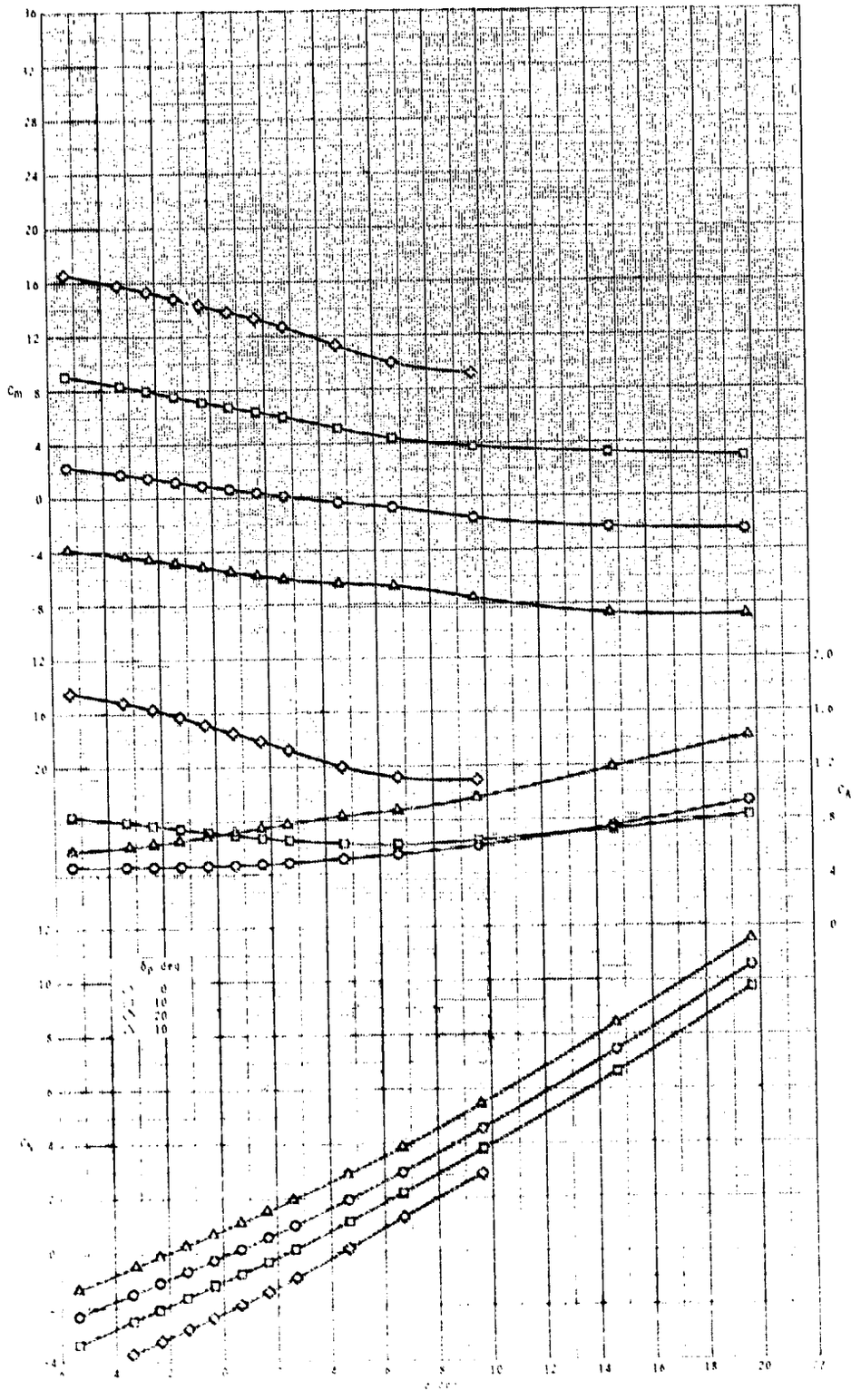

(c) M = 3.50.

Figure 20.- Continued.

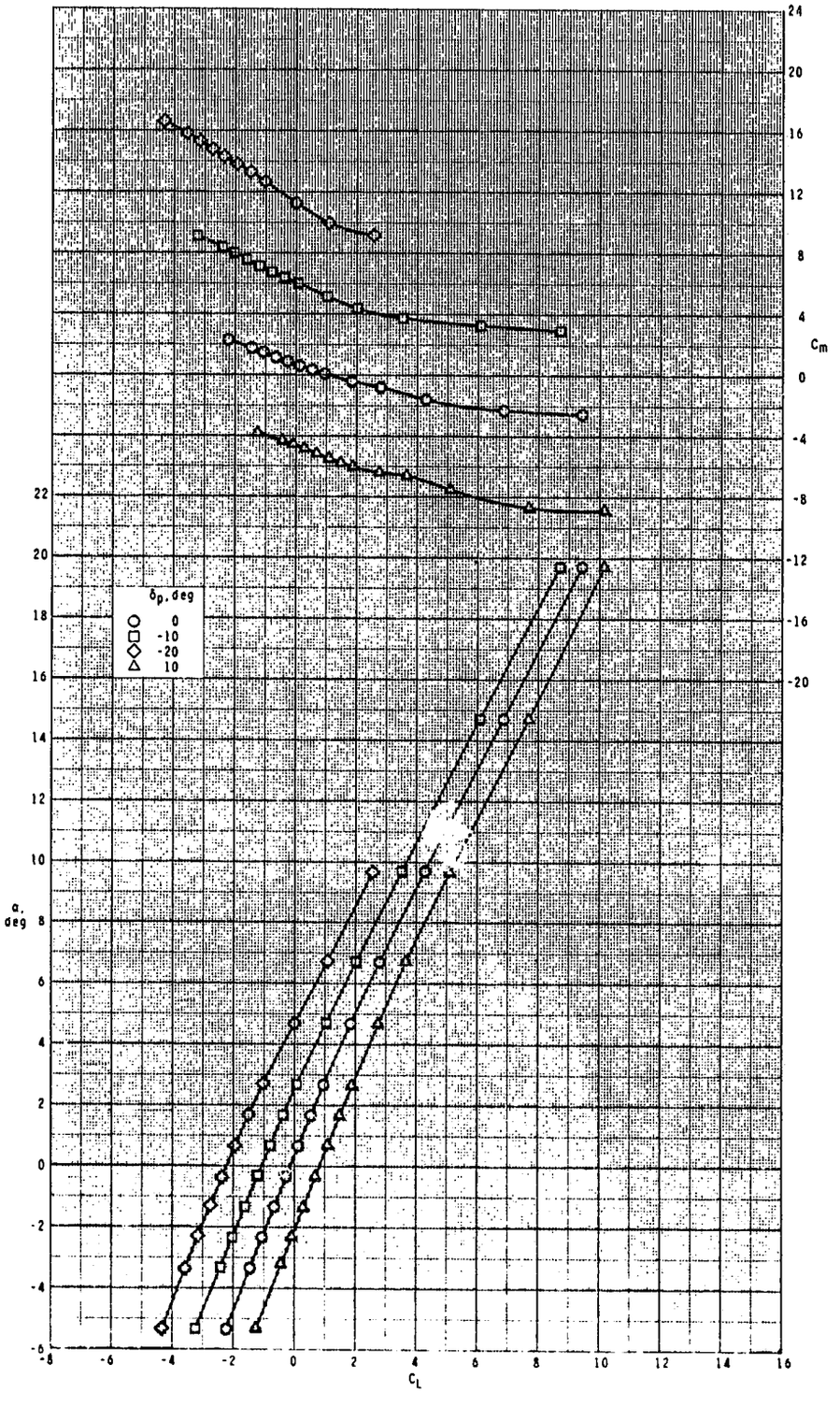

(c) Continued.

Figure 20.- Continued.

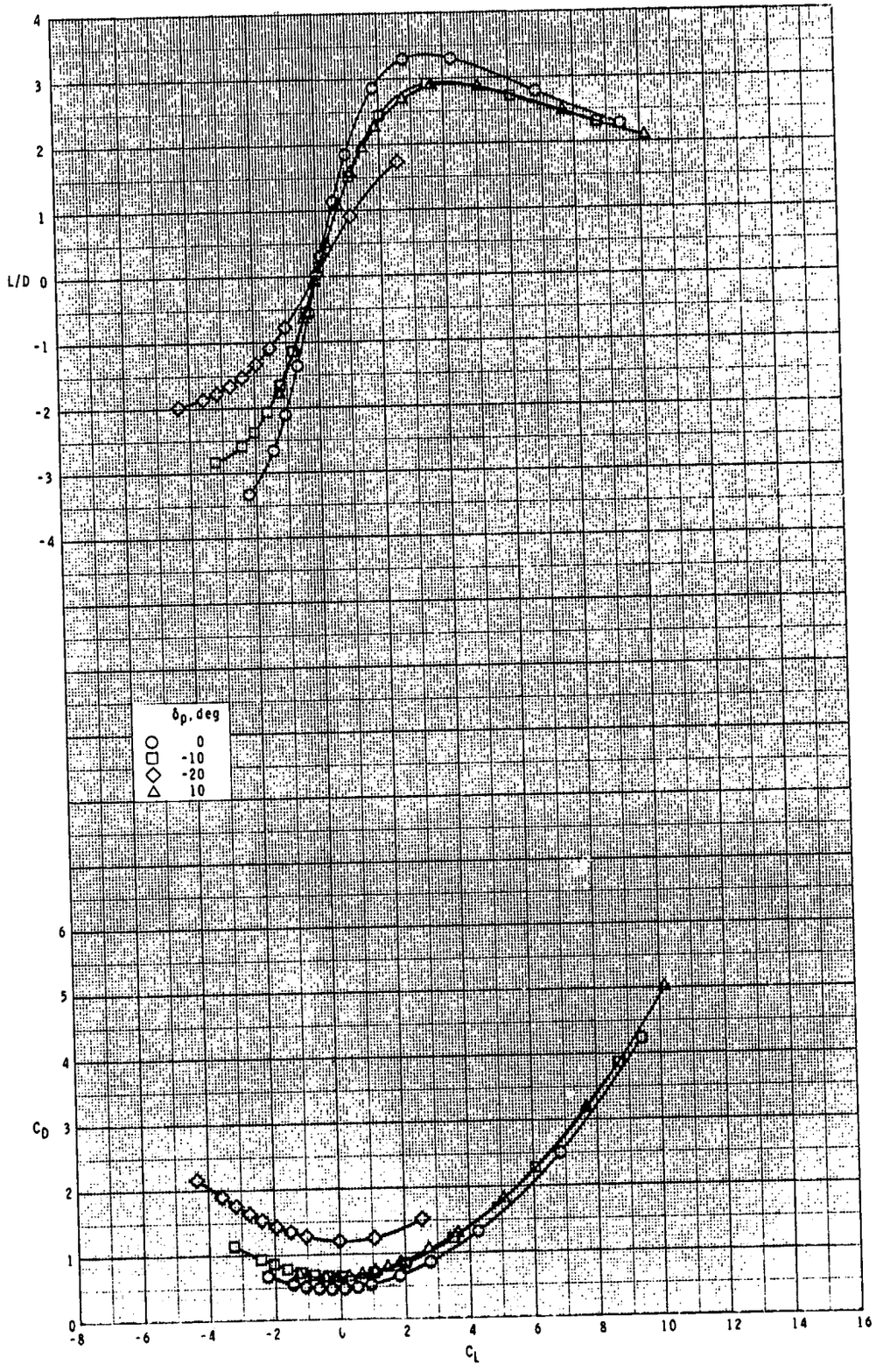

(c) Concluded.

Figure 20.- Continued.

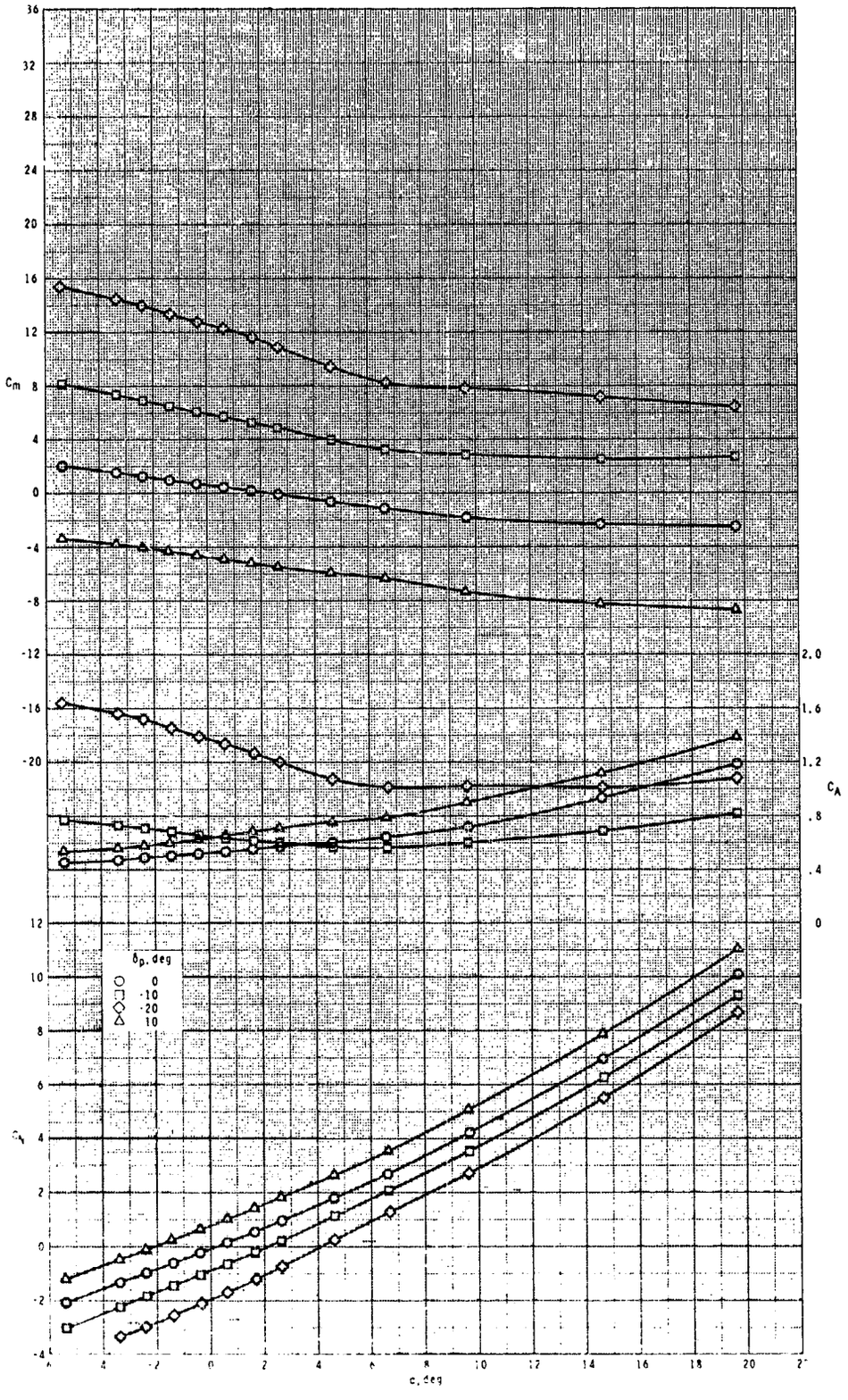

(d) M = 3.95.

Figure 20.- Continued.

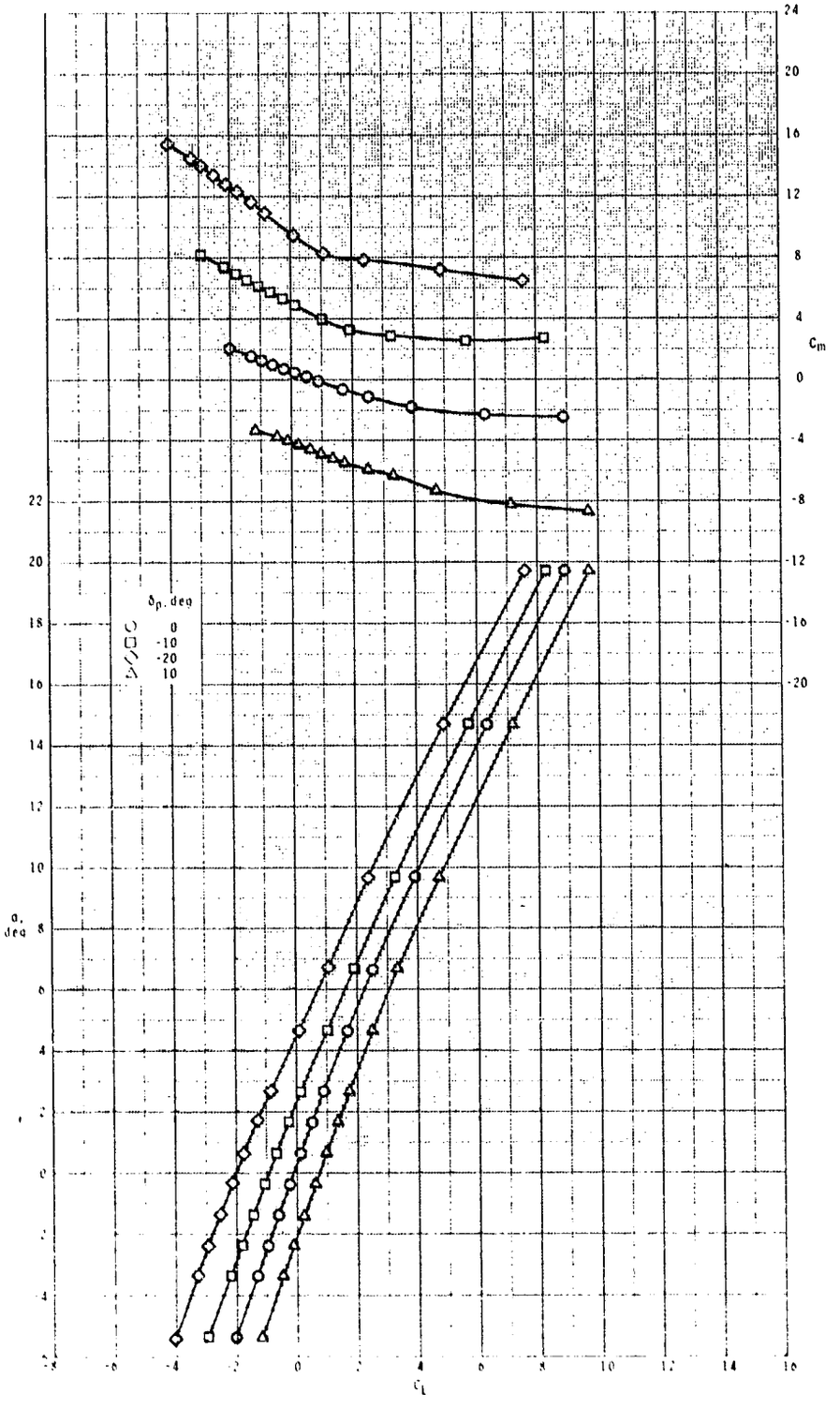

(d) Continued.

Figure 20.- Continued.

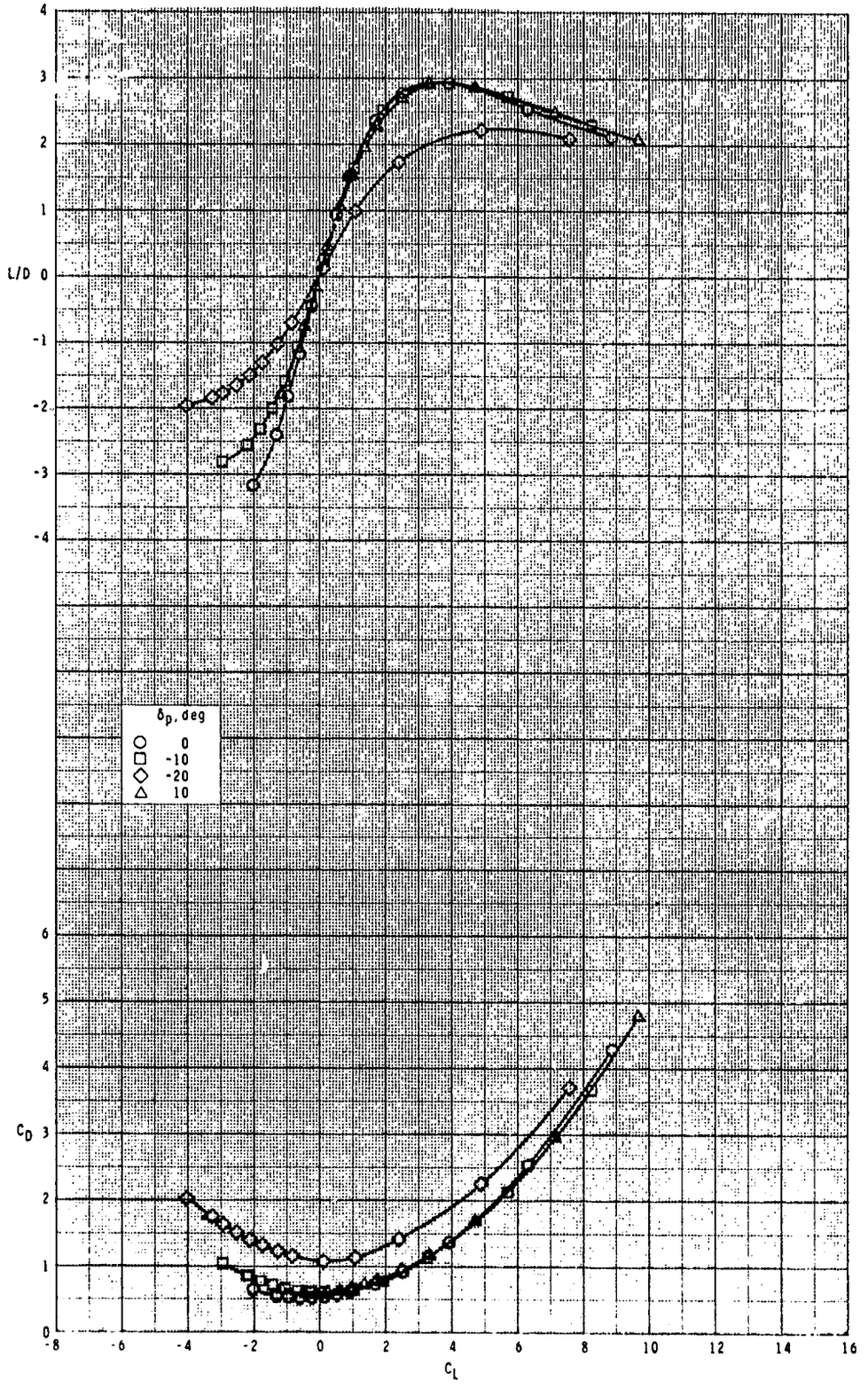

(d) Concluded.

Figure 20.- Concluded.

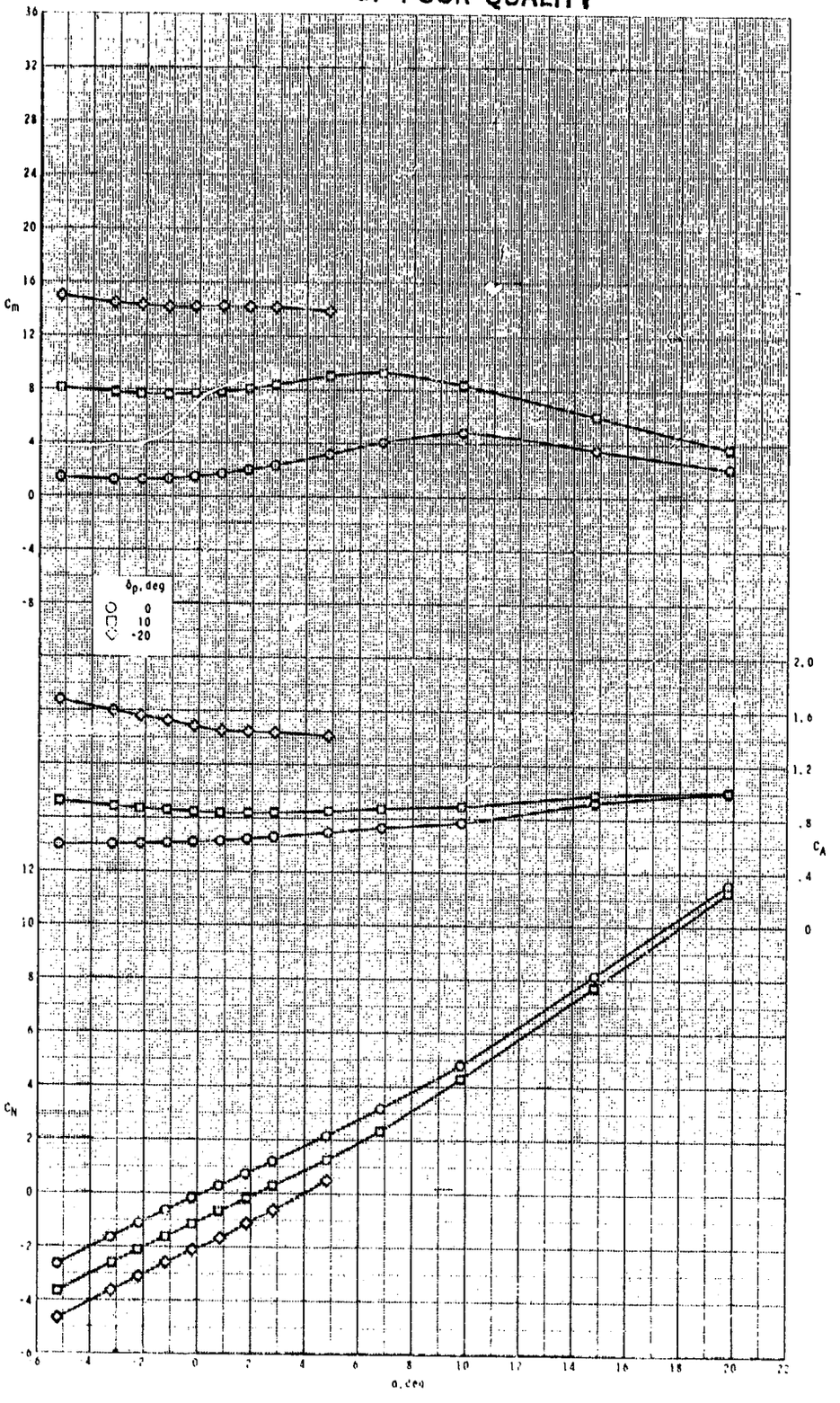

(a) M = 2.50.

Figure 21.- Pitch-control effectiveness of configuration $B_1I_2W_1T_3$ with $\phi_I = 135°$.

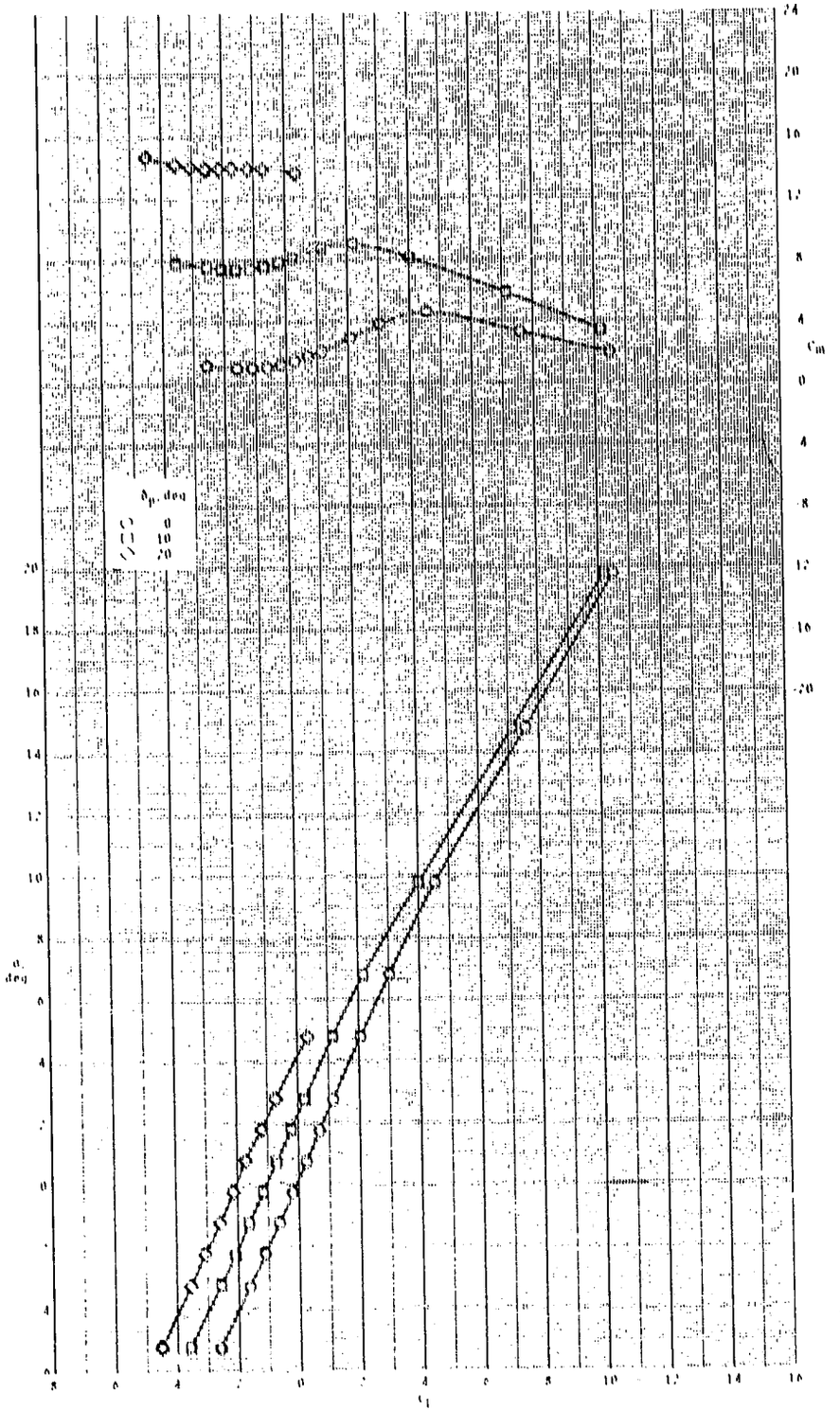

(a) Continued.

Figure 21.- Continued.

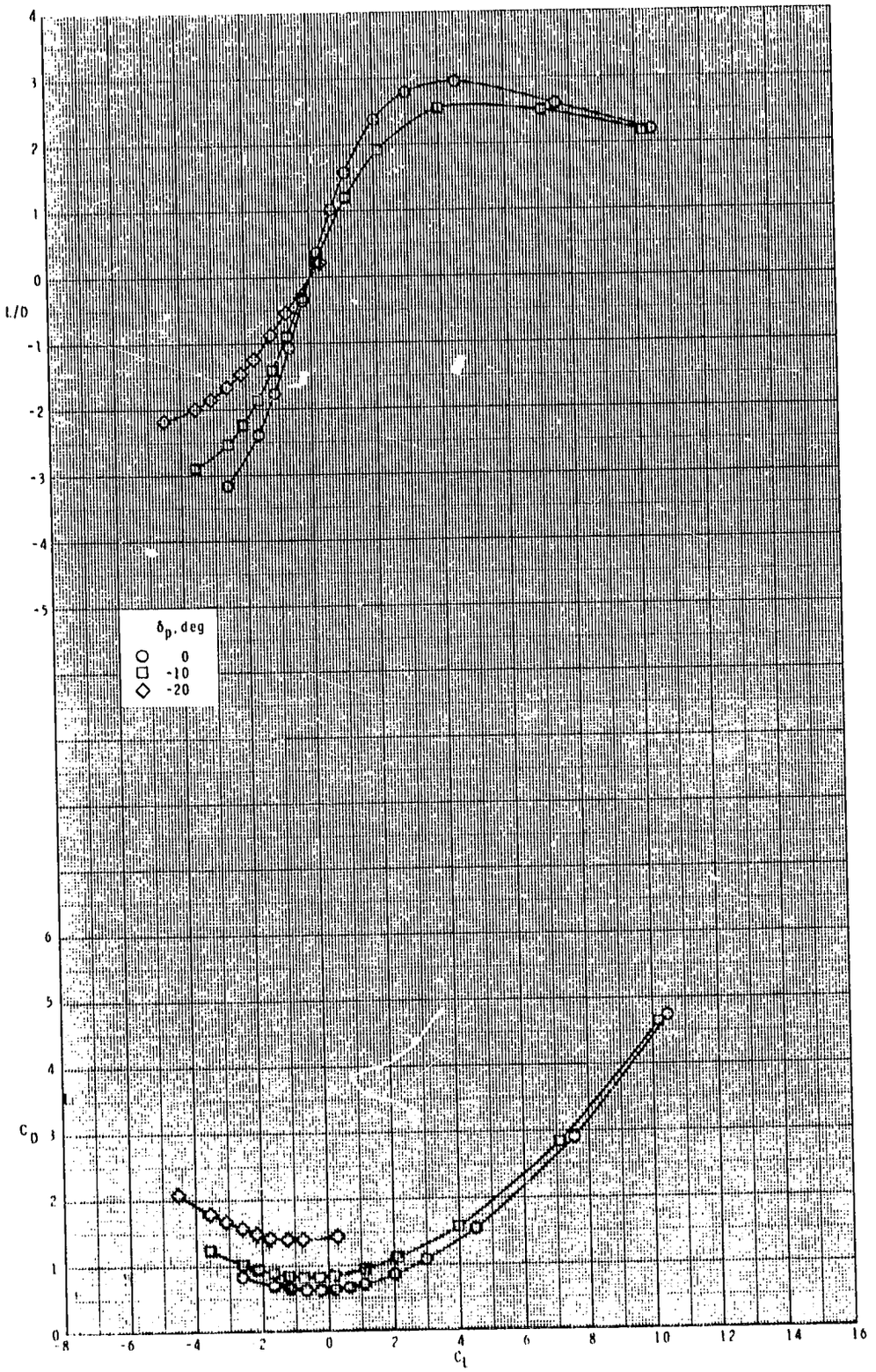

(a) Concluded.

Figure 21.- Continued.

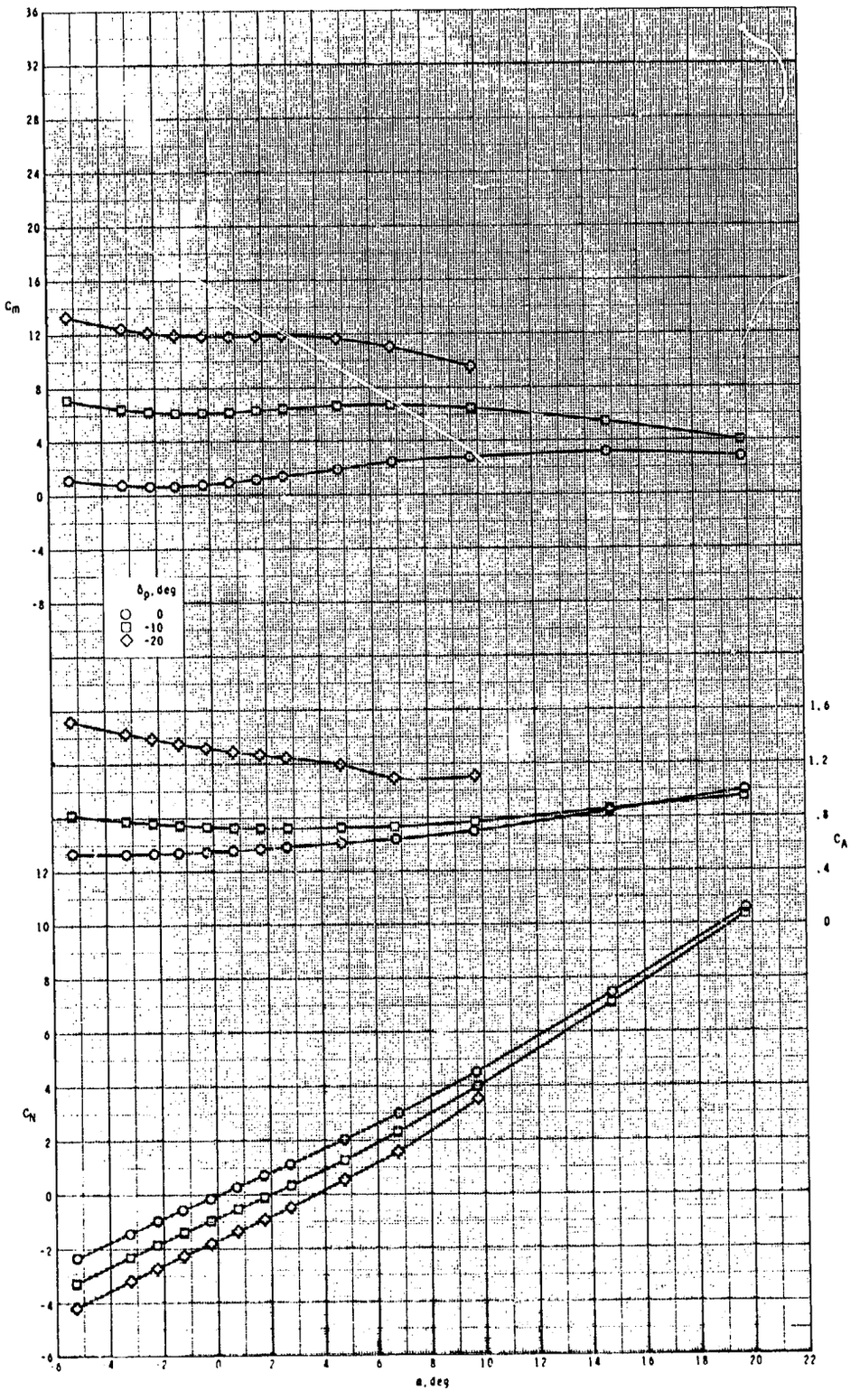

(b) M = 2.95.

Figure 21.- Continued.

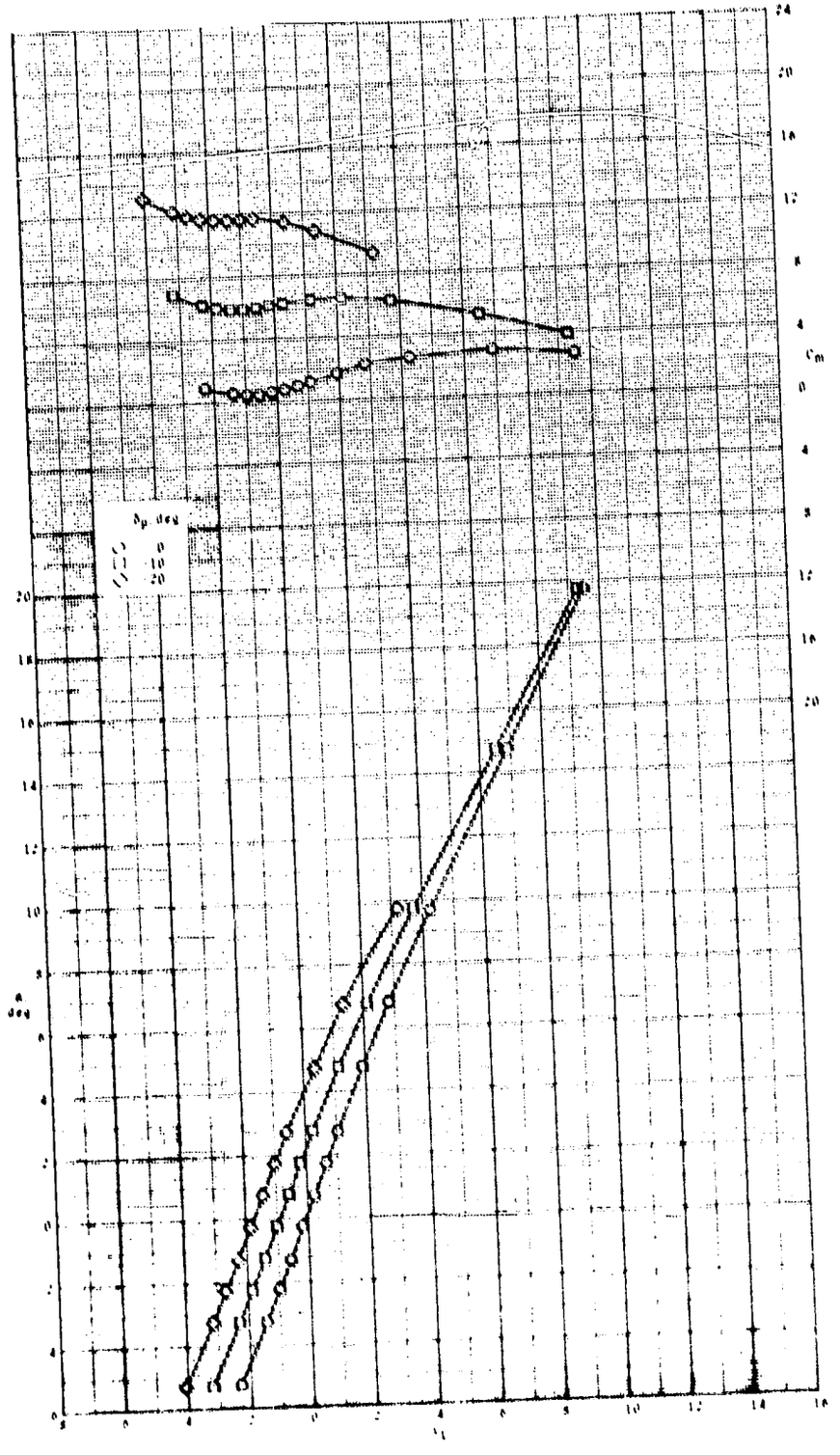

(b) Continued.

Figure 21.- Continued.

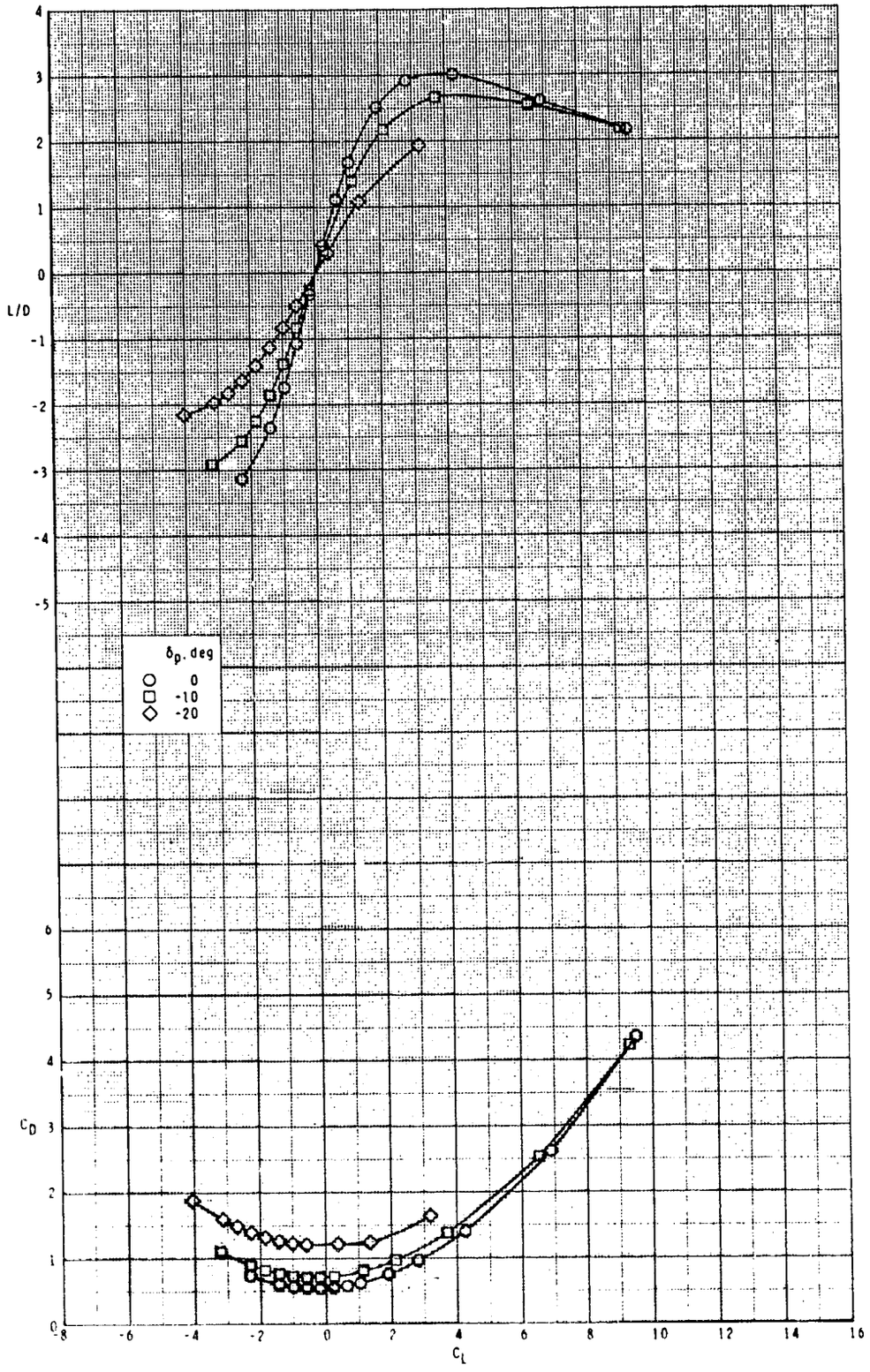

(b) Concluded.

Figure 21.- Continued.

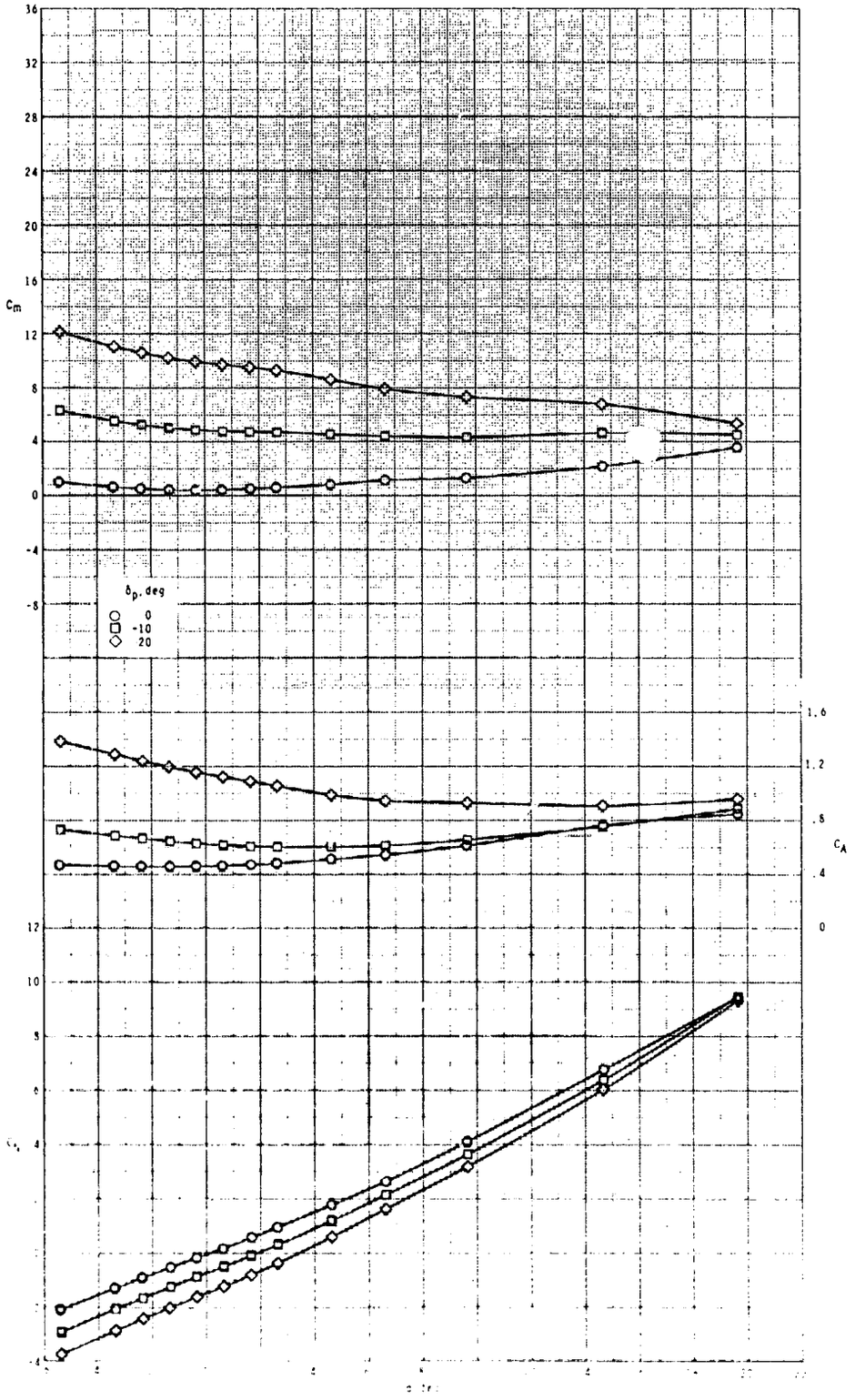

(c) M = 3.50.

Figure 21.- Continued.

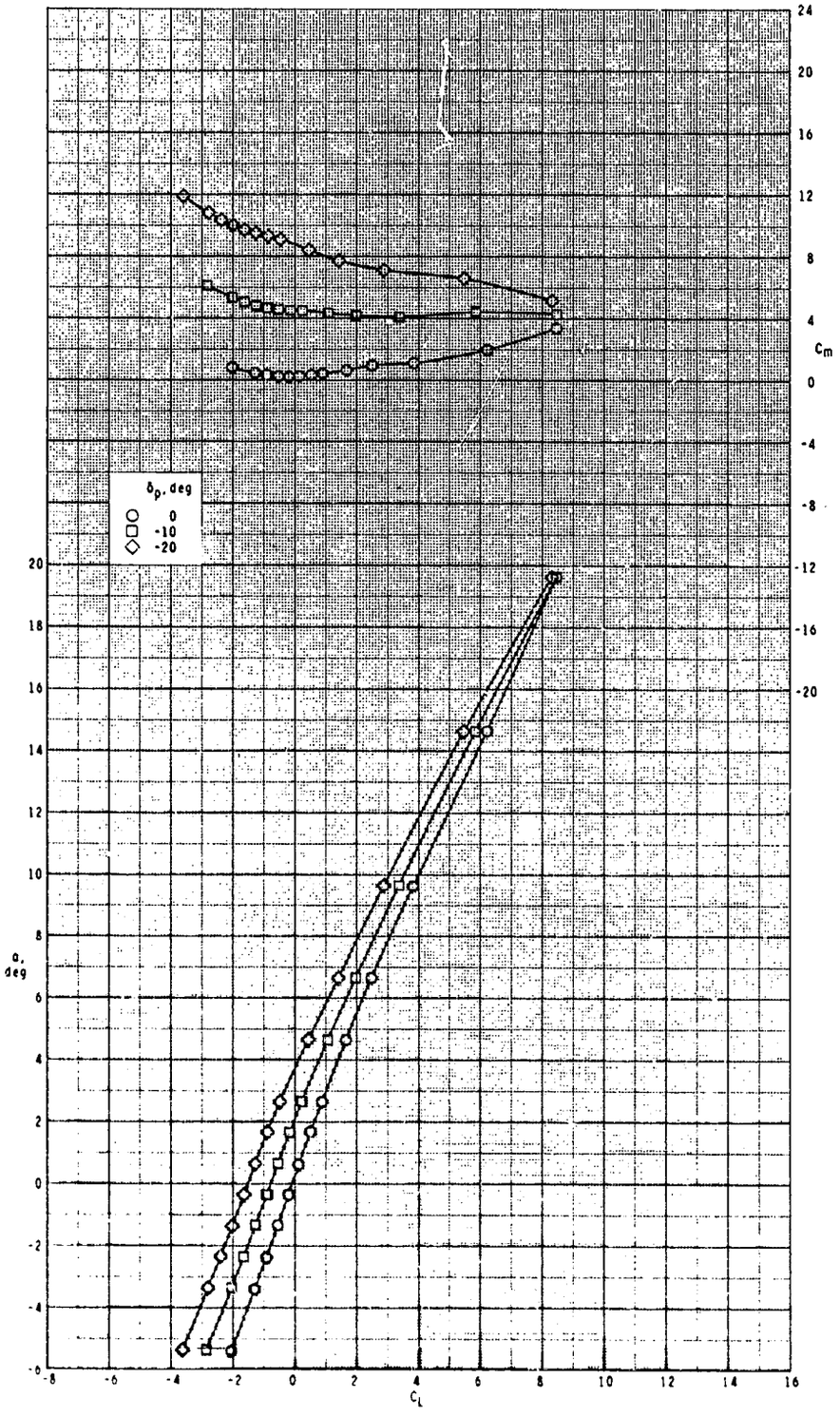

(c) Continued.

Figure 21.- Continued.

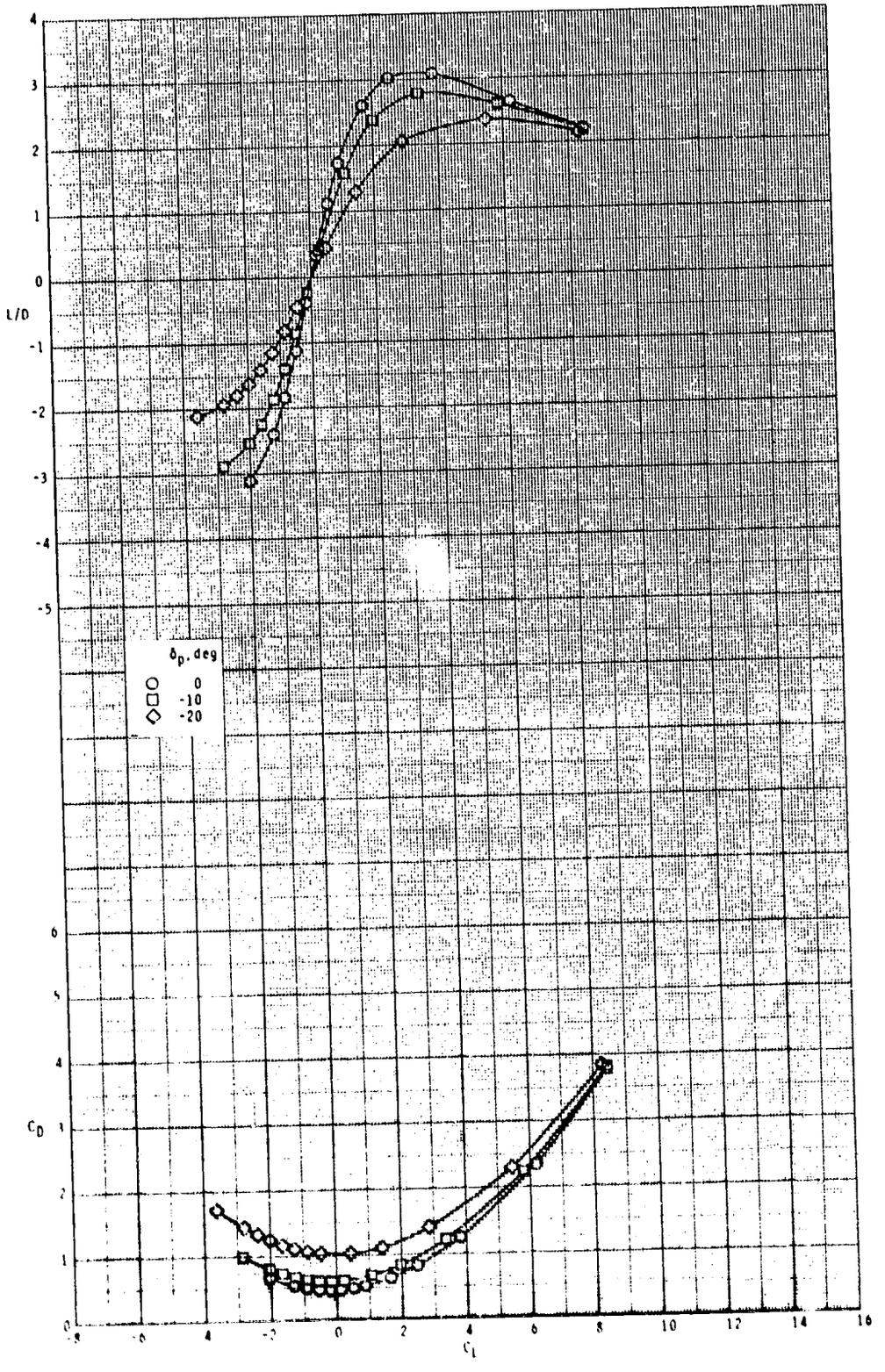

(c) Concluded.

Figure 21.- Continued.

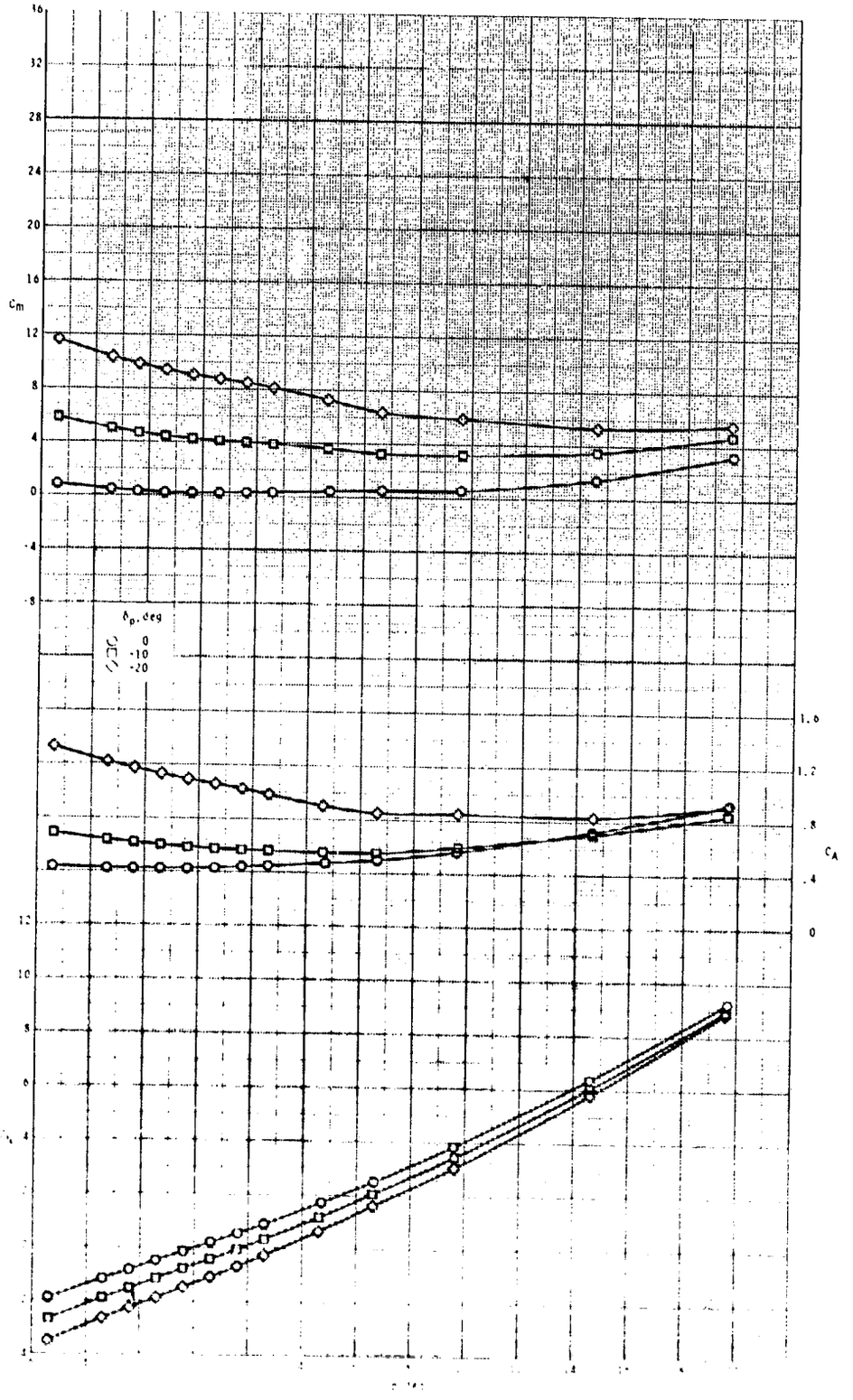

(d) M = 3.95.

Figure 21.- Continued.

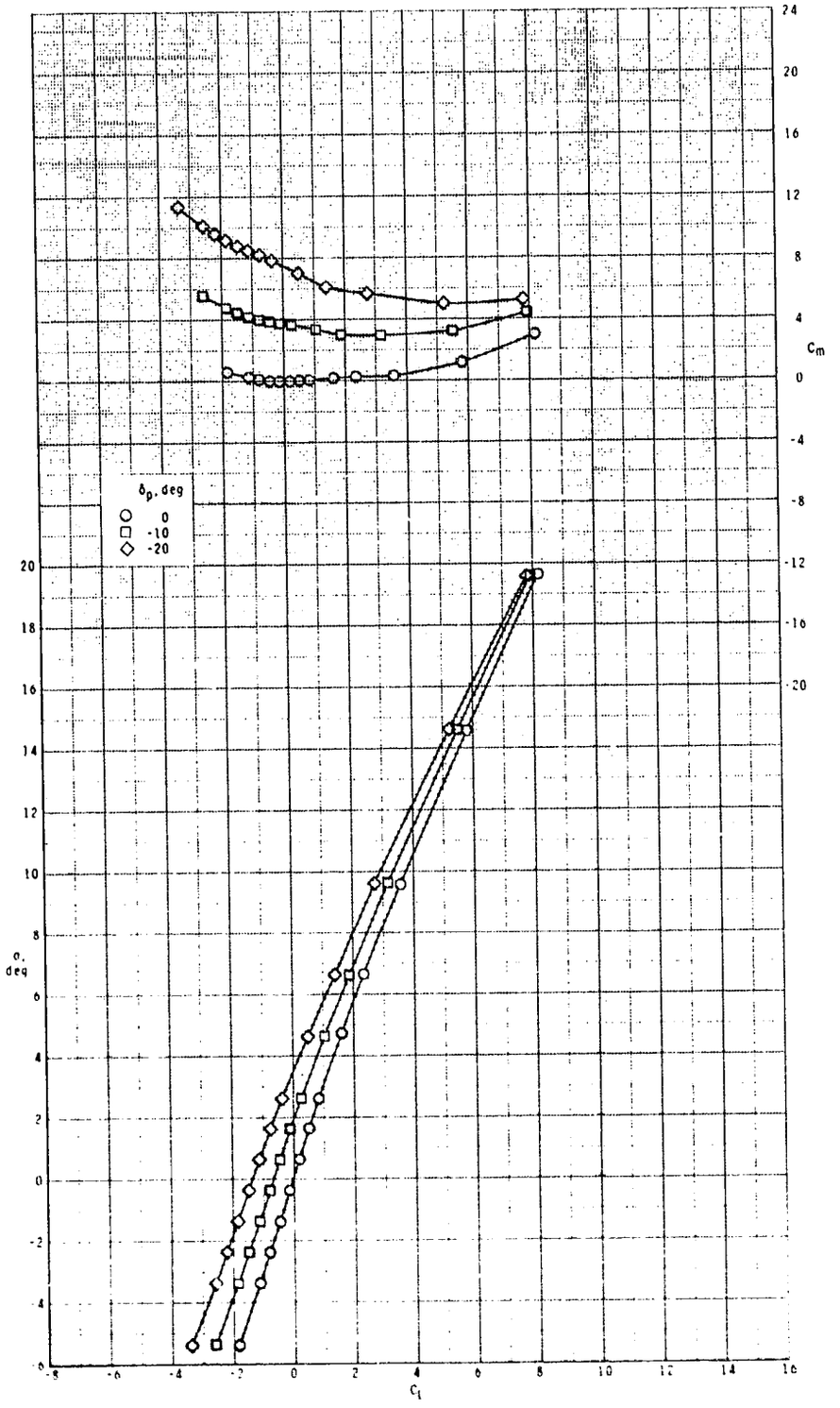

(d) Continued.

Figure 21.- Continued.

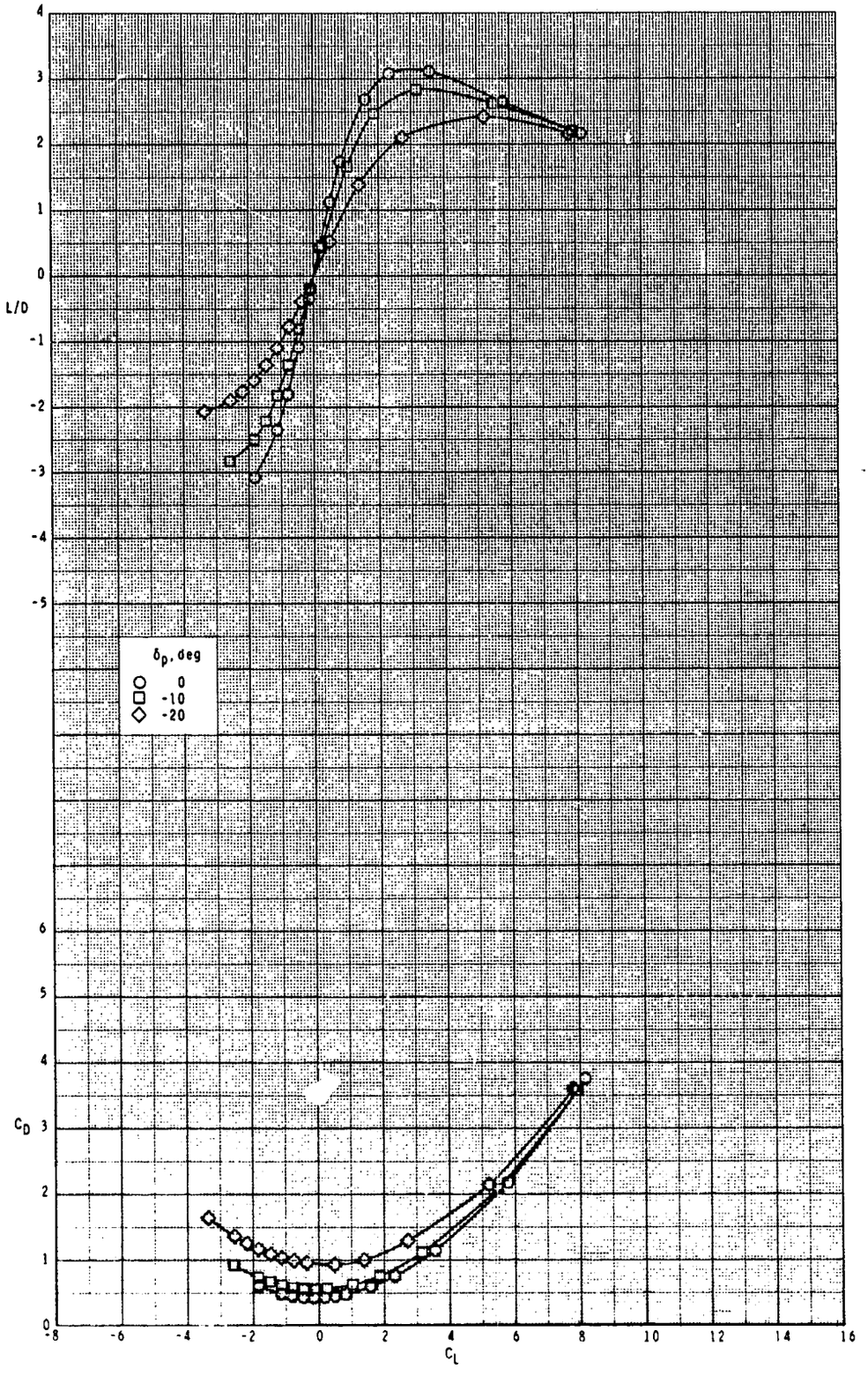

(d) Concluded.

Figure 21.- Concluded.

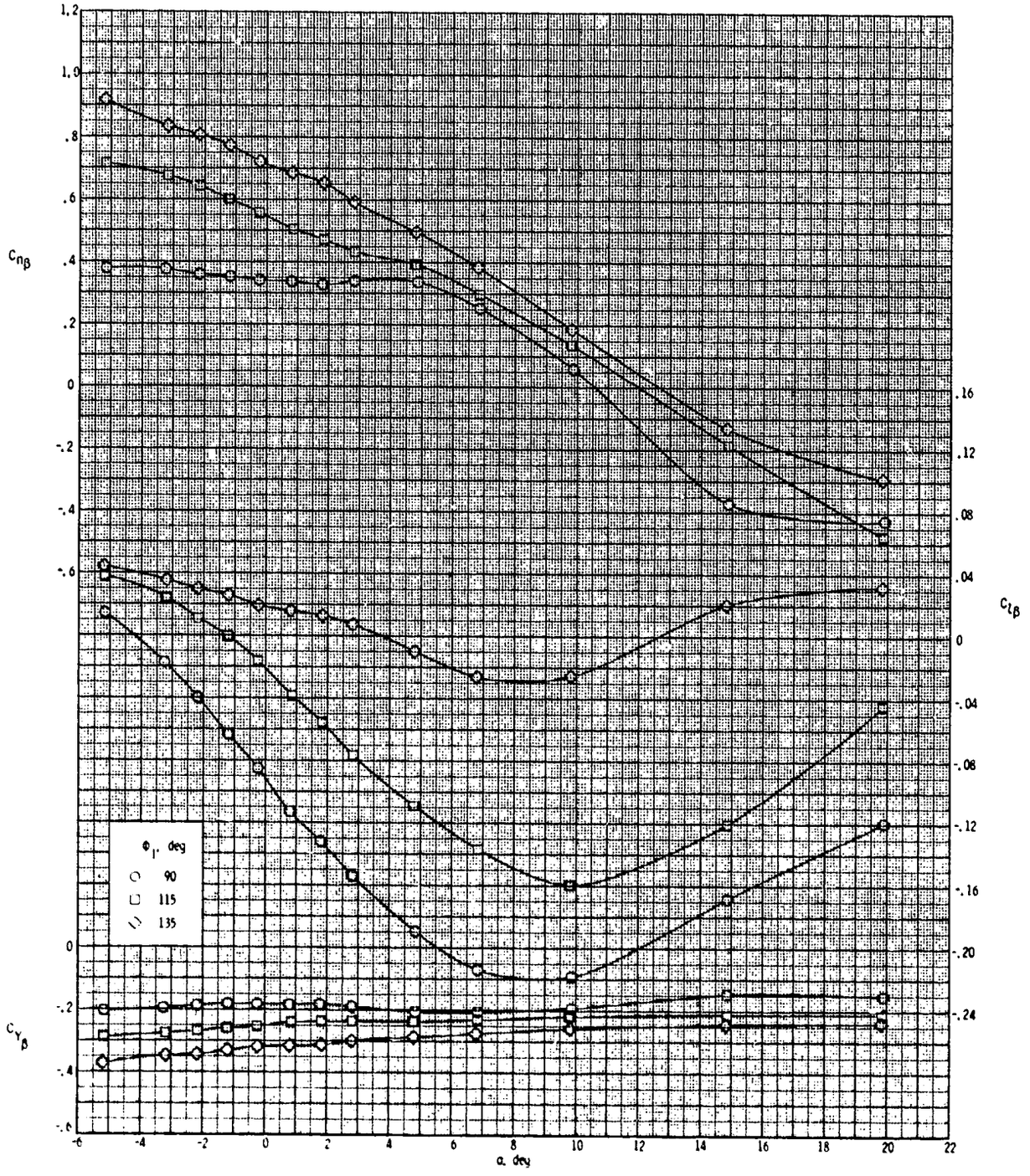

(a) M = 2.50.

Figure 22.- Effect of inlet orientation angle ϕ_I on lateral-directional stability of configuration $B_1I_2T_1$ with $\delta_p = 0°$.

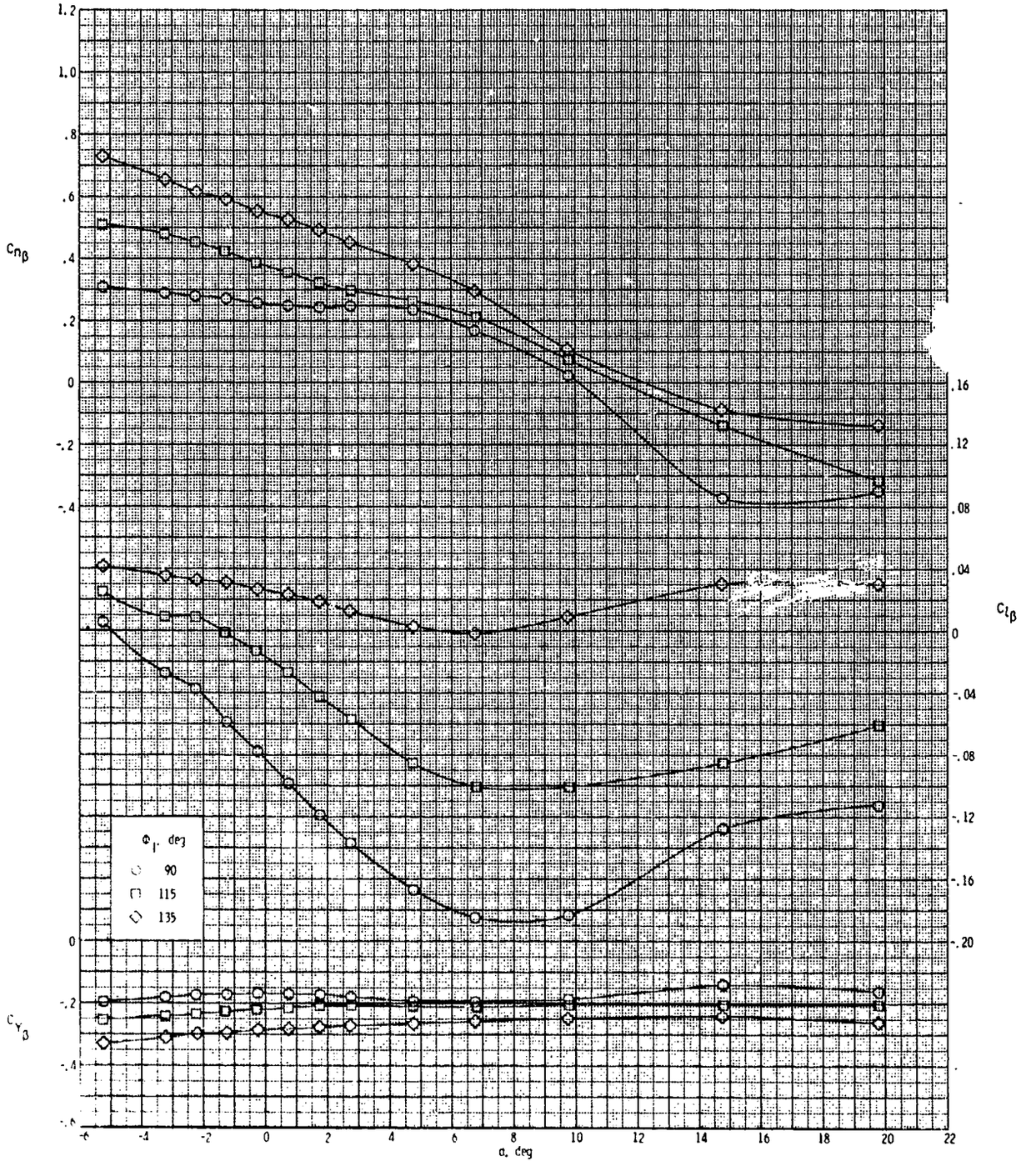

(b) M = 2.95.

Figure 22.- Continued.

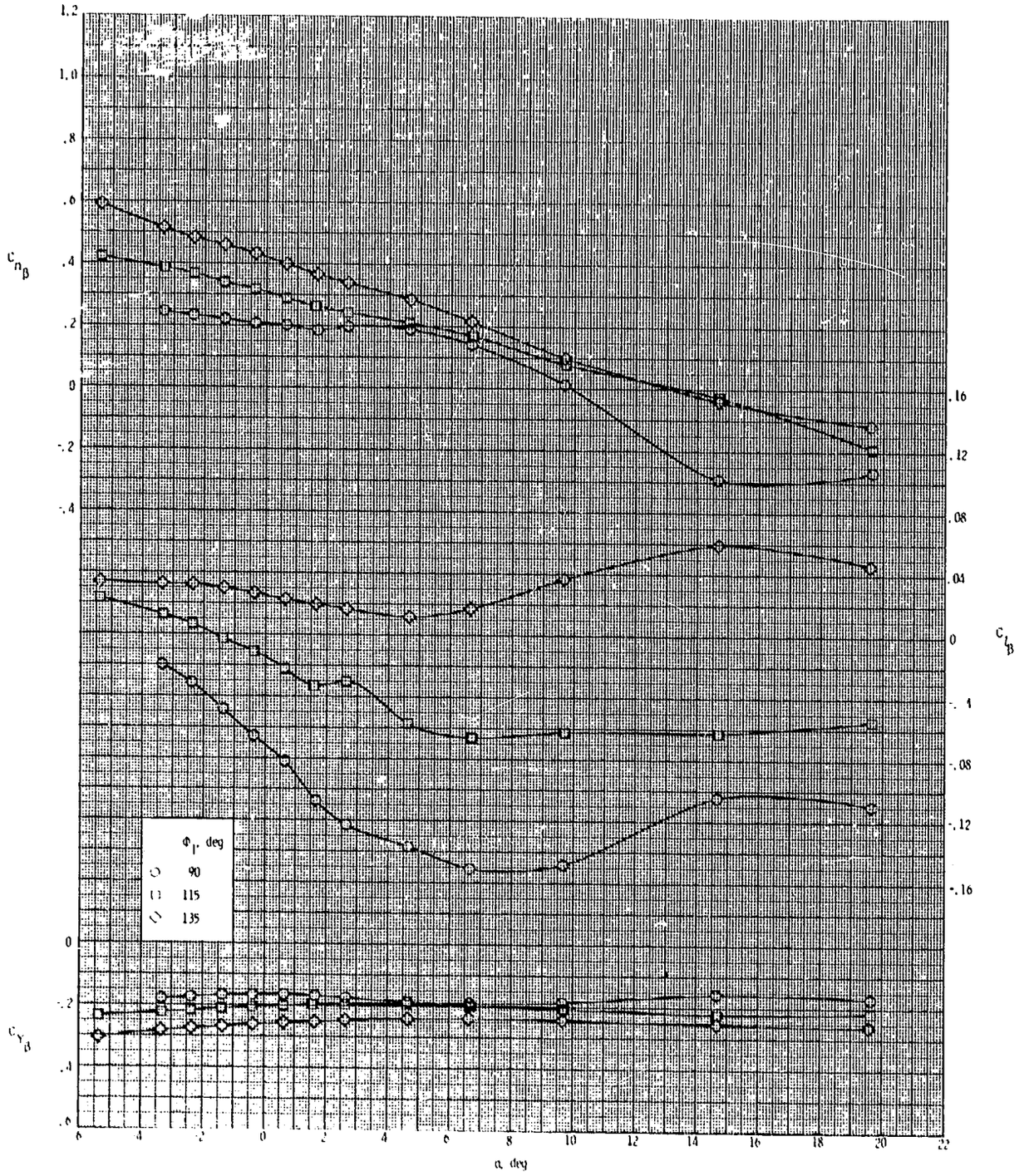

(c) M = 3.50.

Figure 22.- Continued.

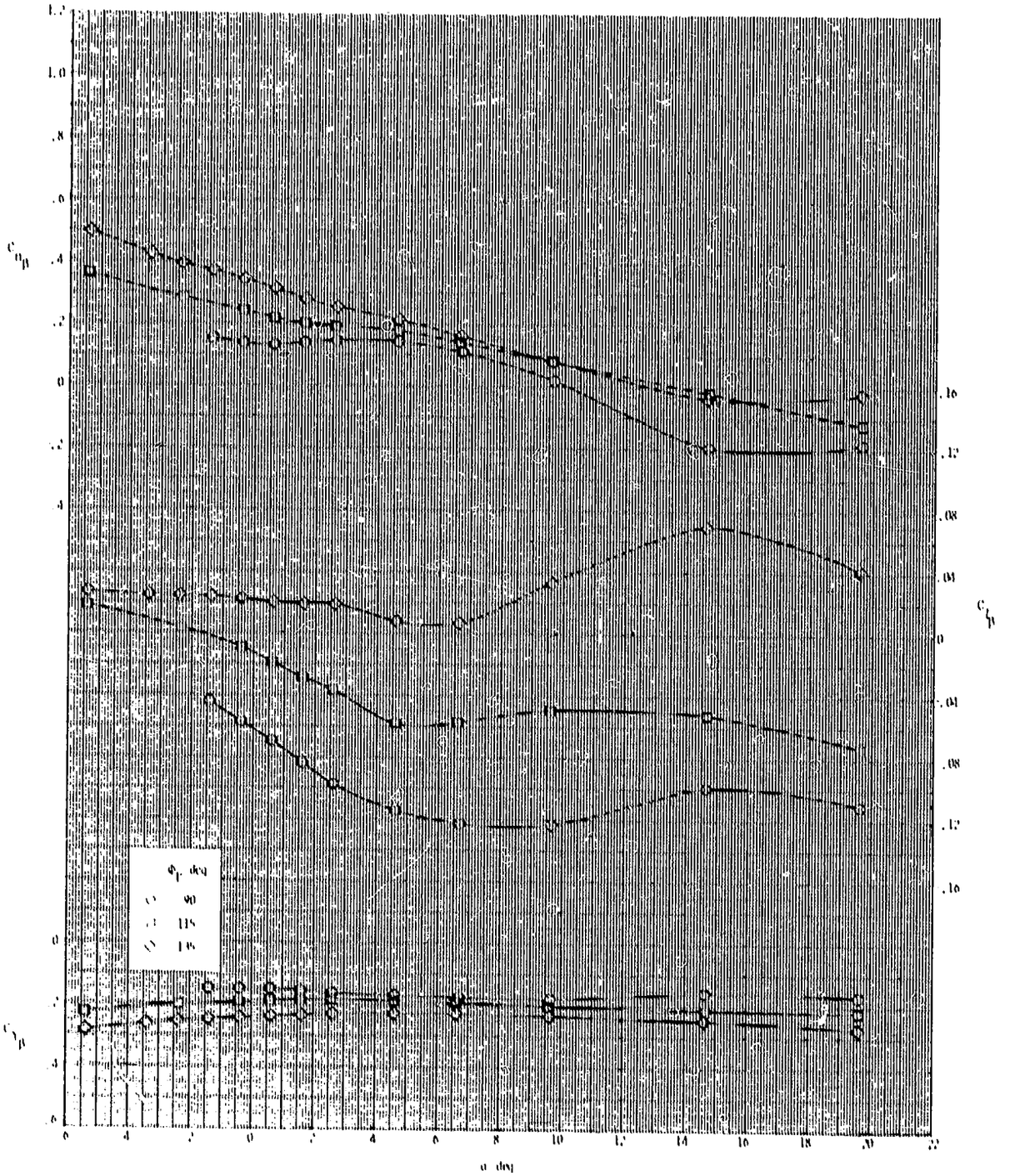

(d) M = 3.05.

Figure 22.- Concluded.

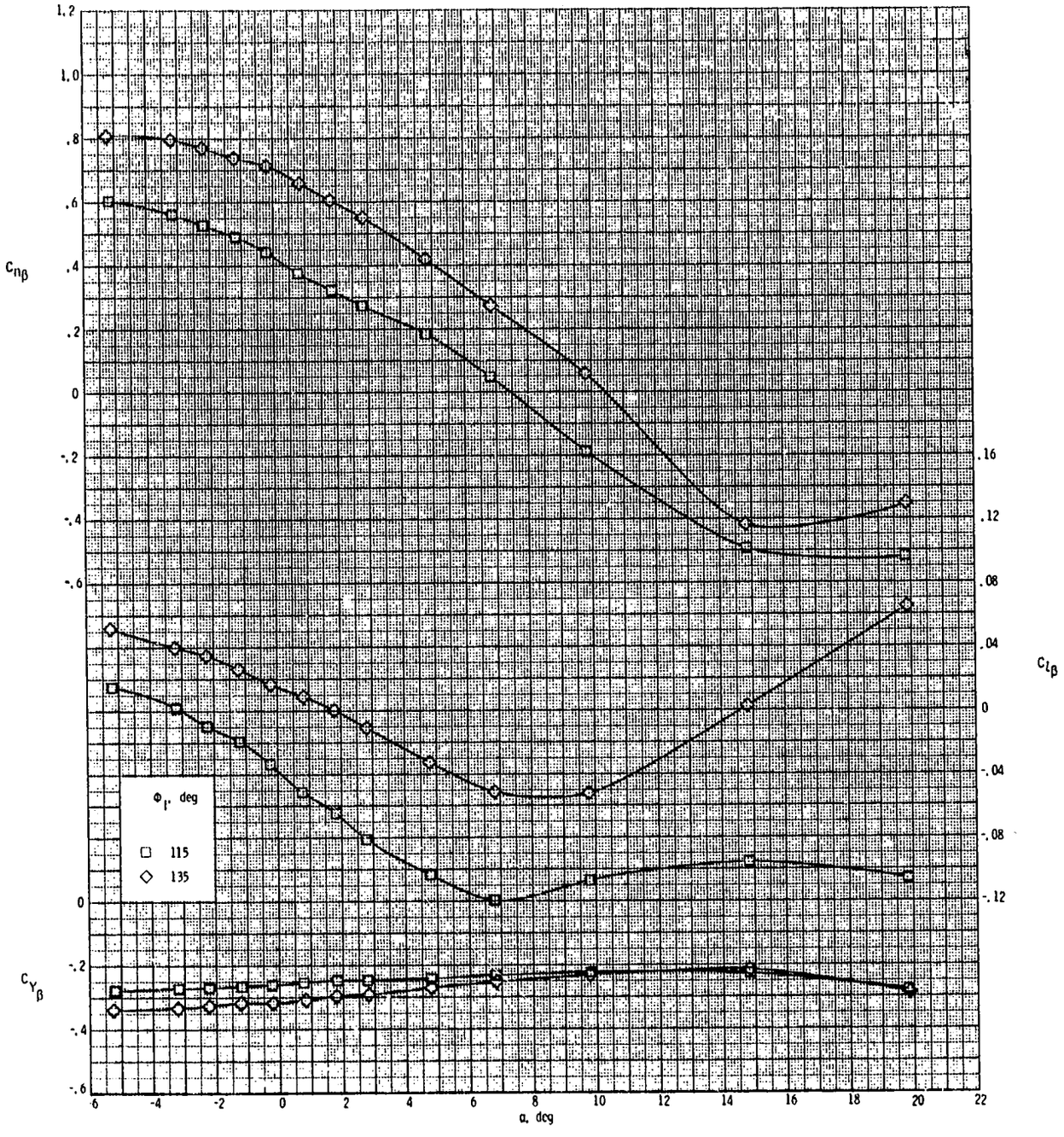

(a) M = 2.50.

Figure 23.- Effect of inlet orientation angle ϕ_I on lateral-directional stability of configuration $B_1I_2W_1T_1$ with $\delta_p = 0°$.

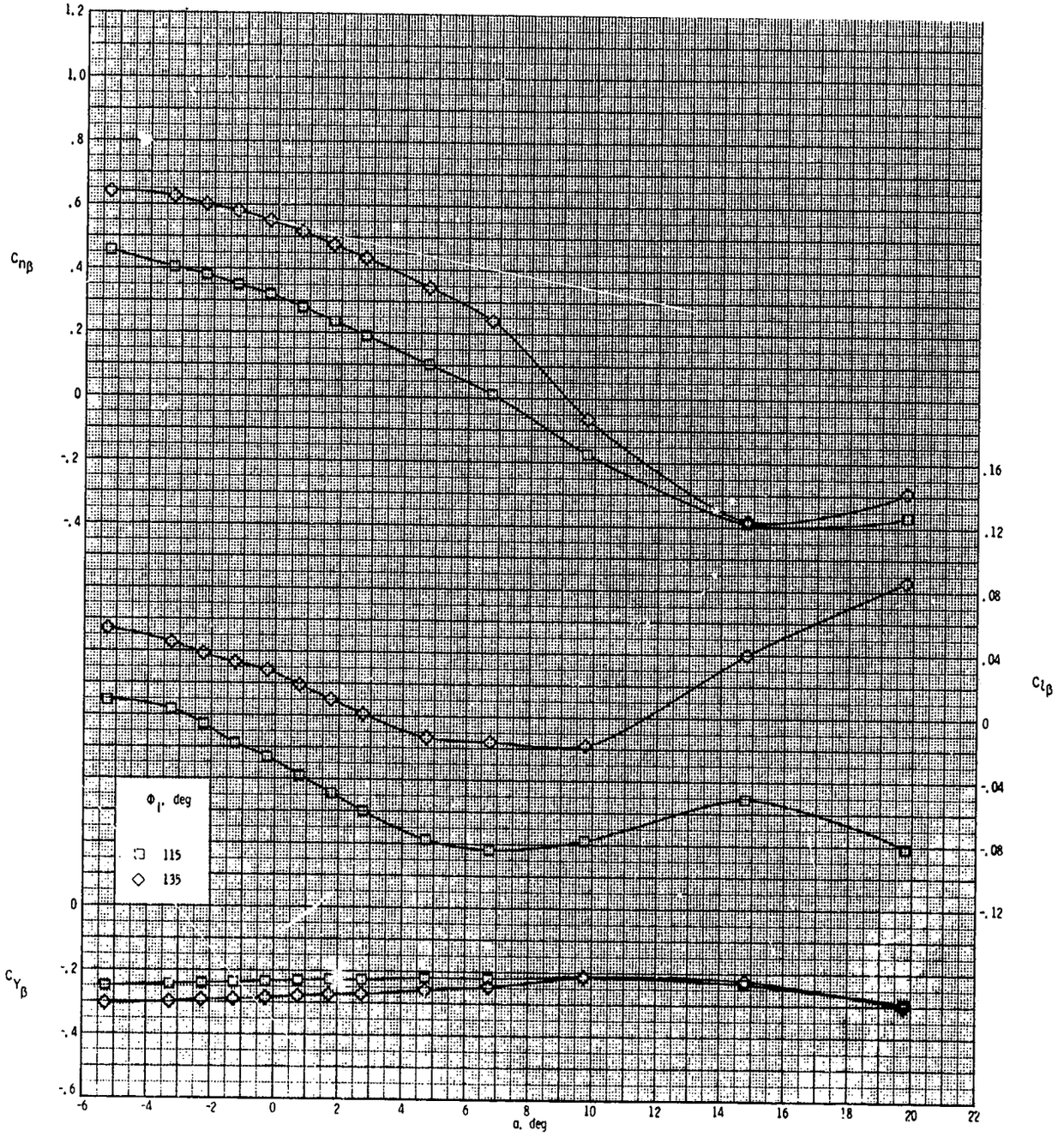

(b) M = 2.95.

Figure 23.- Continued.

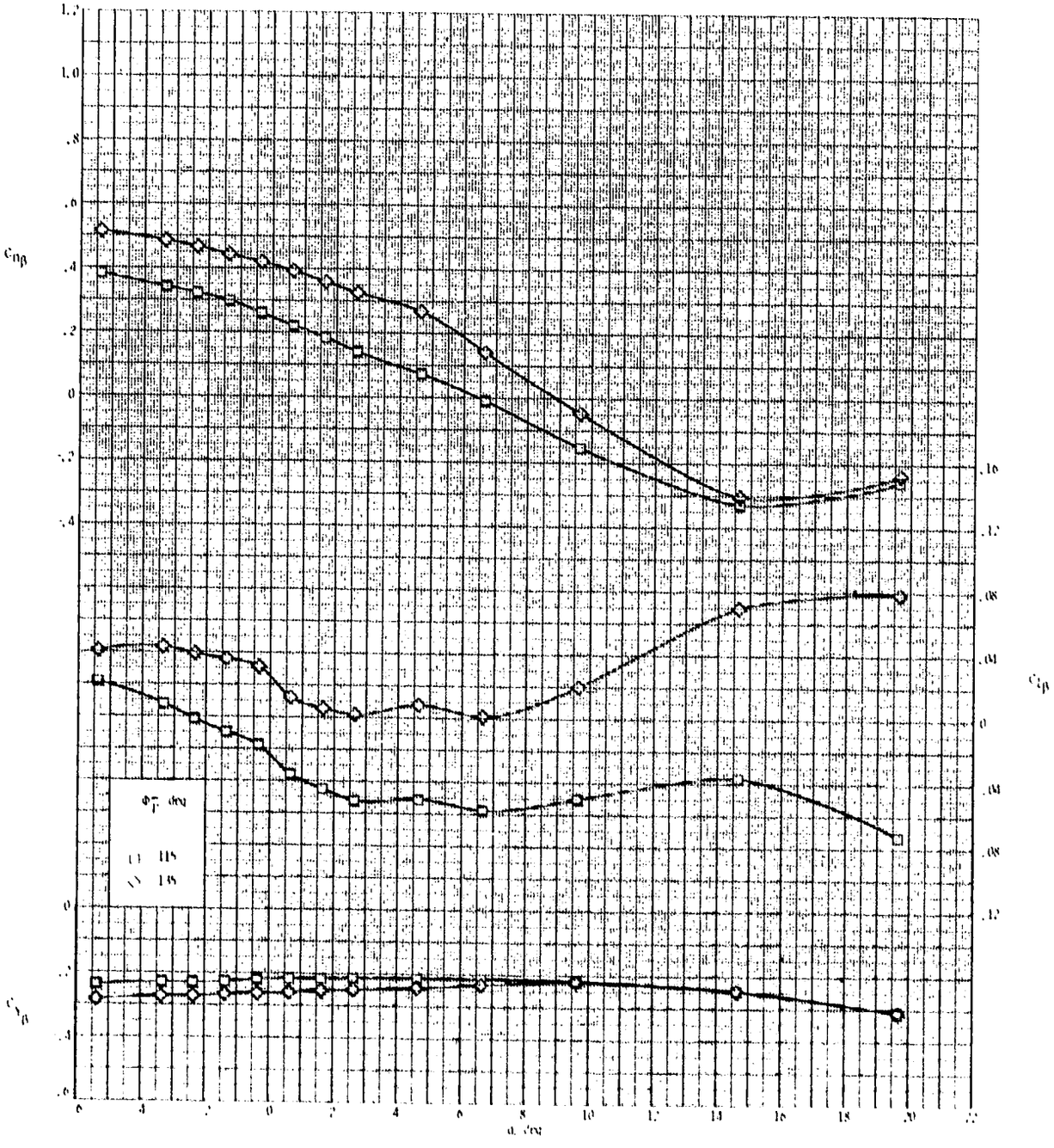

(c) M = 3.50.

Figure 23.- Continued.

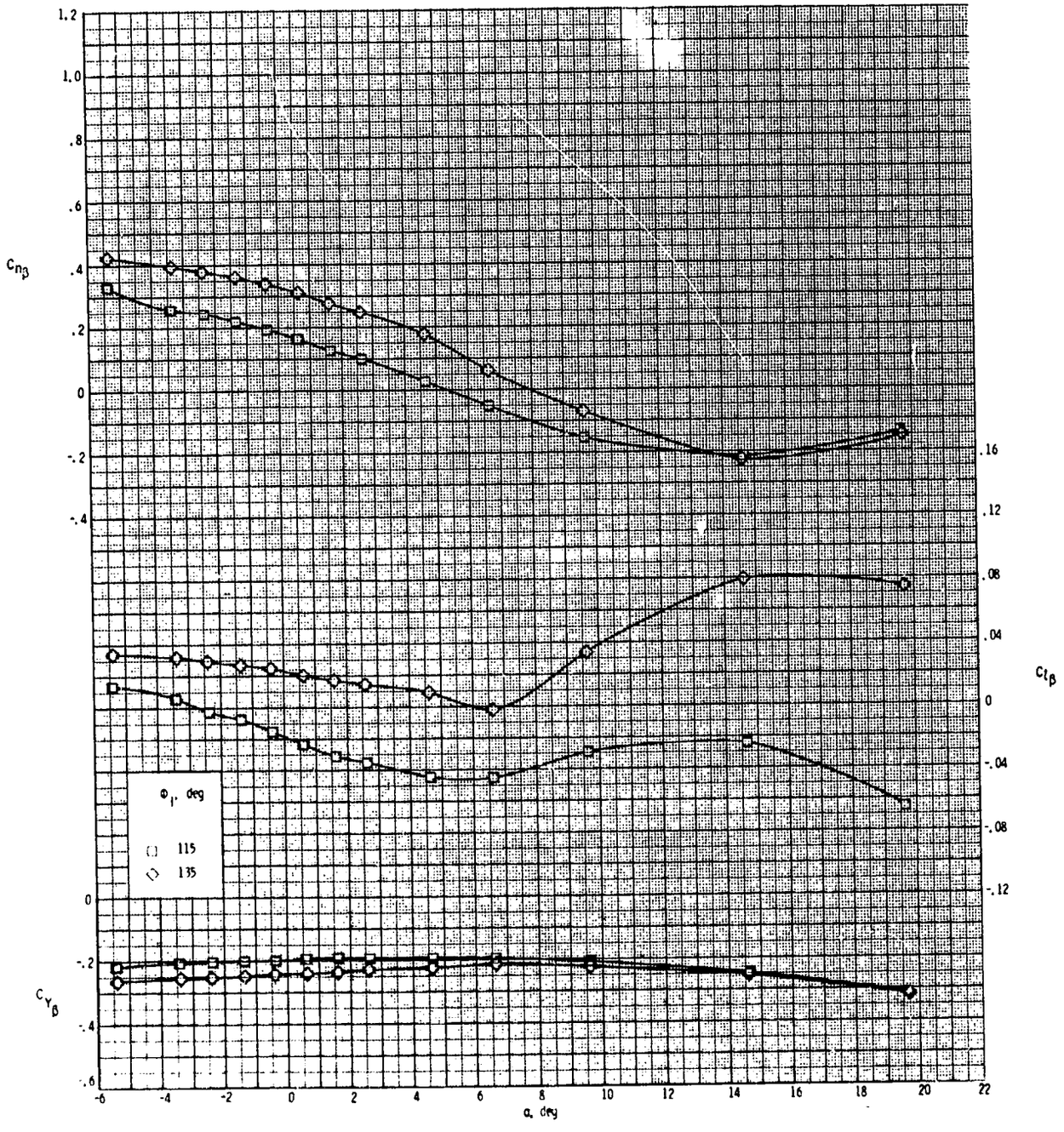

(d) M = 3.95.

Figure 23.- Concluded.

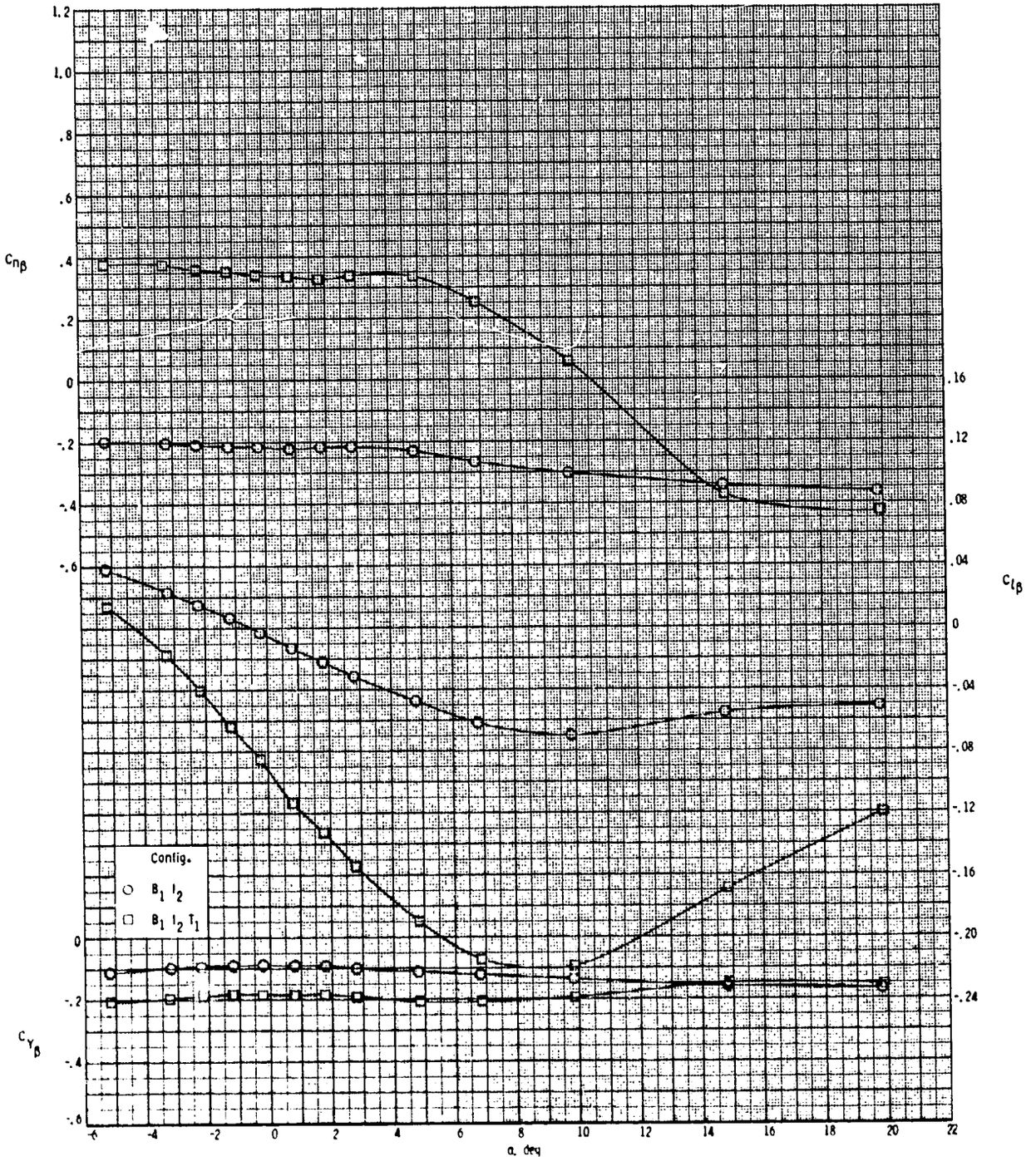

(a) M = 2.50.

Figure 24.- Effect of various model components on lateral-directional stability for two-dimensional inlets with $\phi_I = 90°$ and $\delta_p = 0°$.

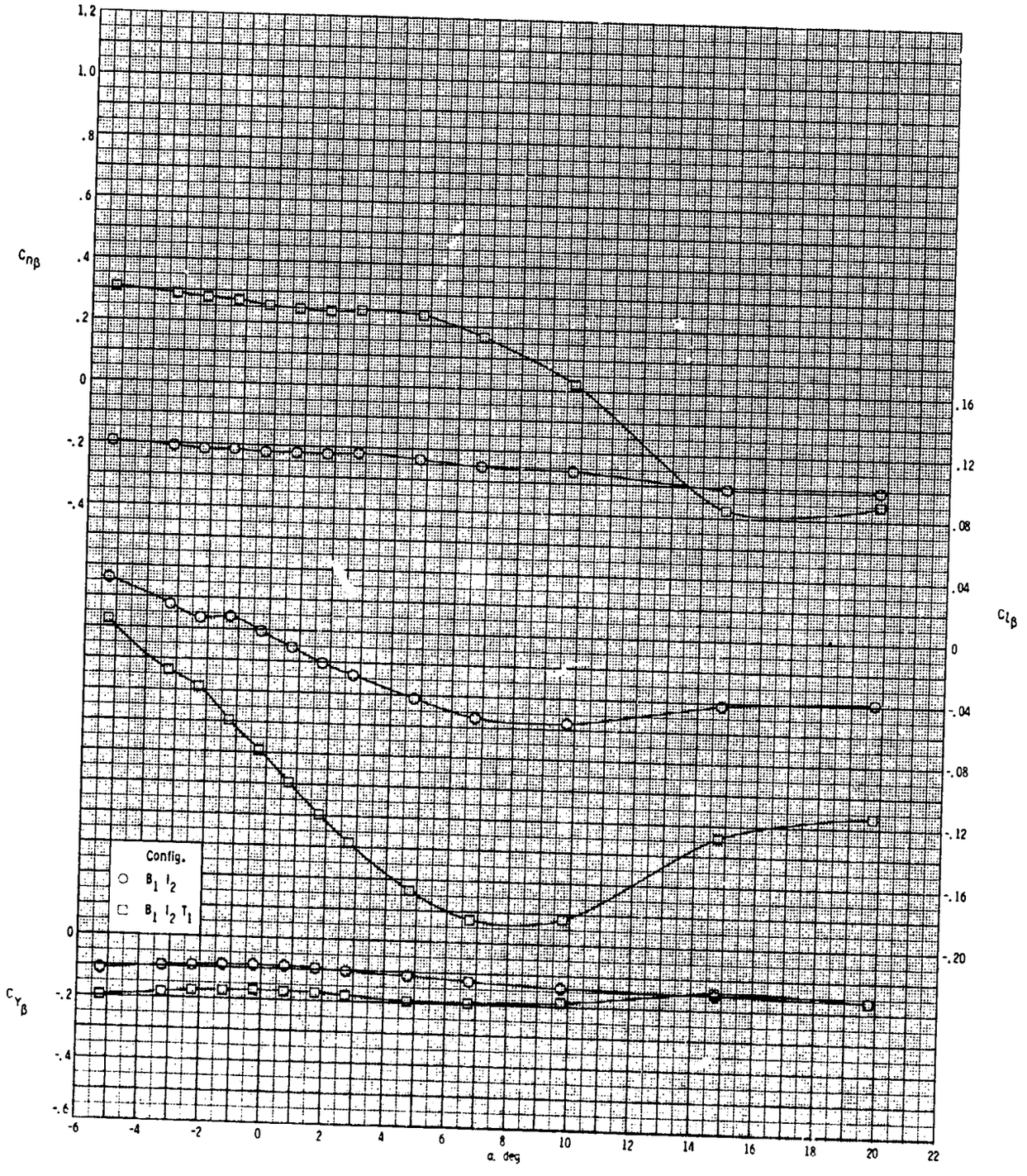

(b) M = 2.95.

Figure 24.- Continued.

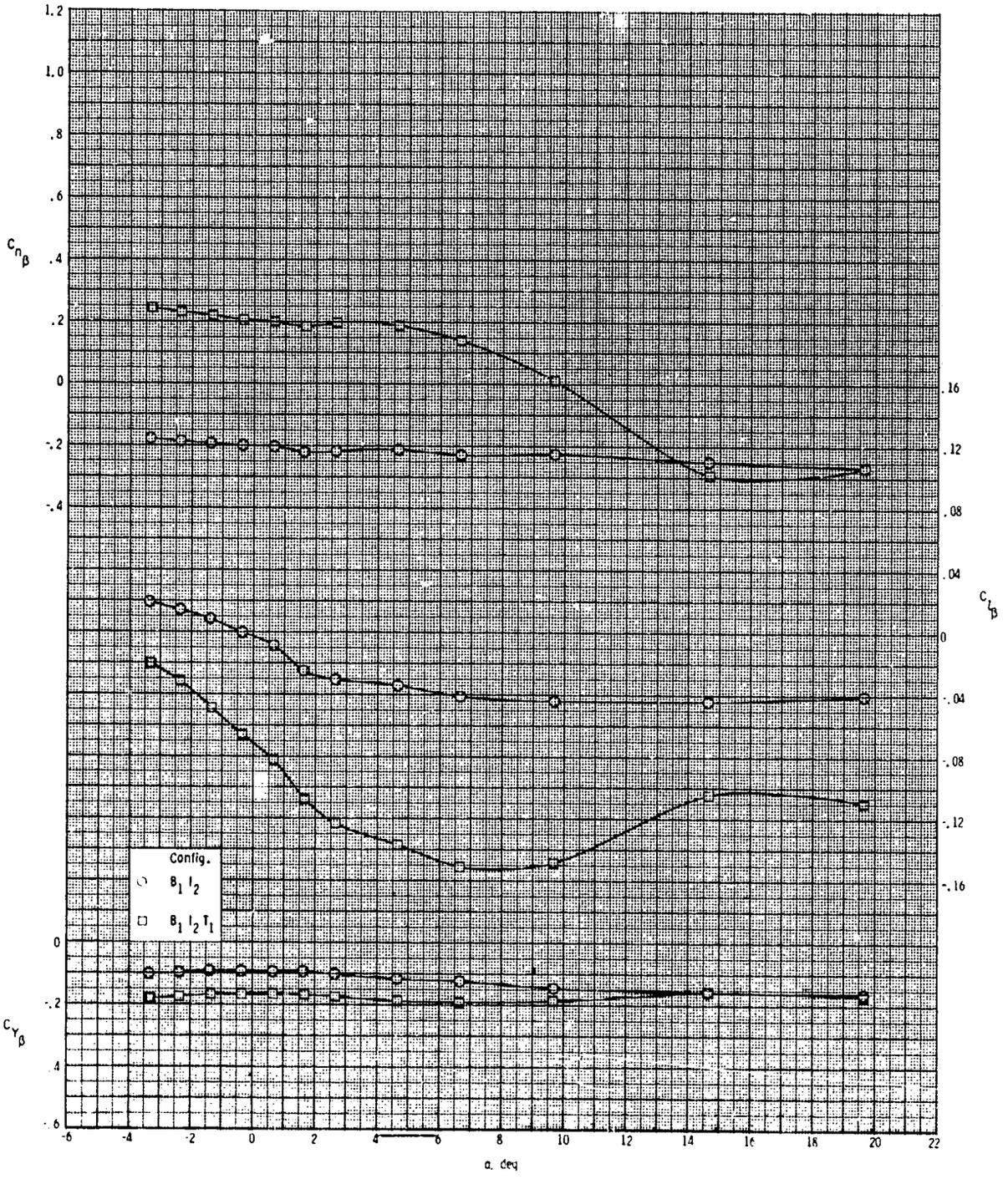

(c) M = 3.50.

Figure 24.- Continued.

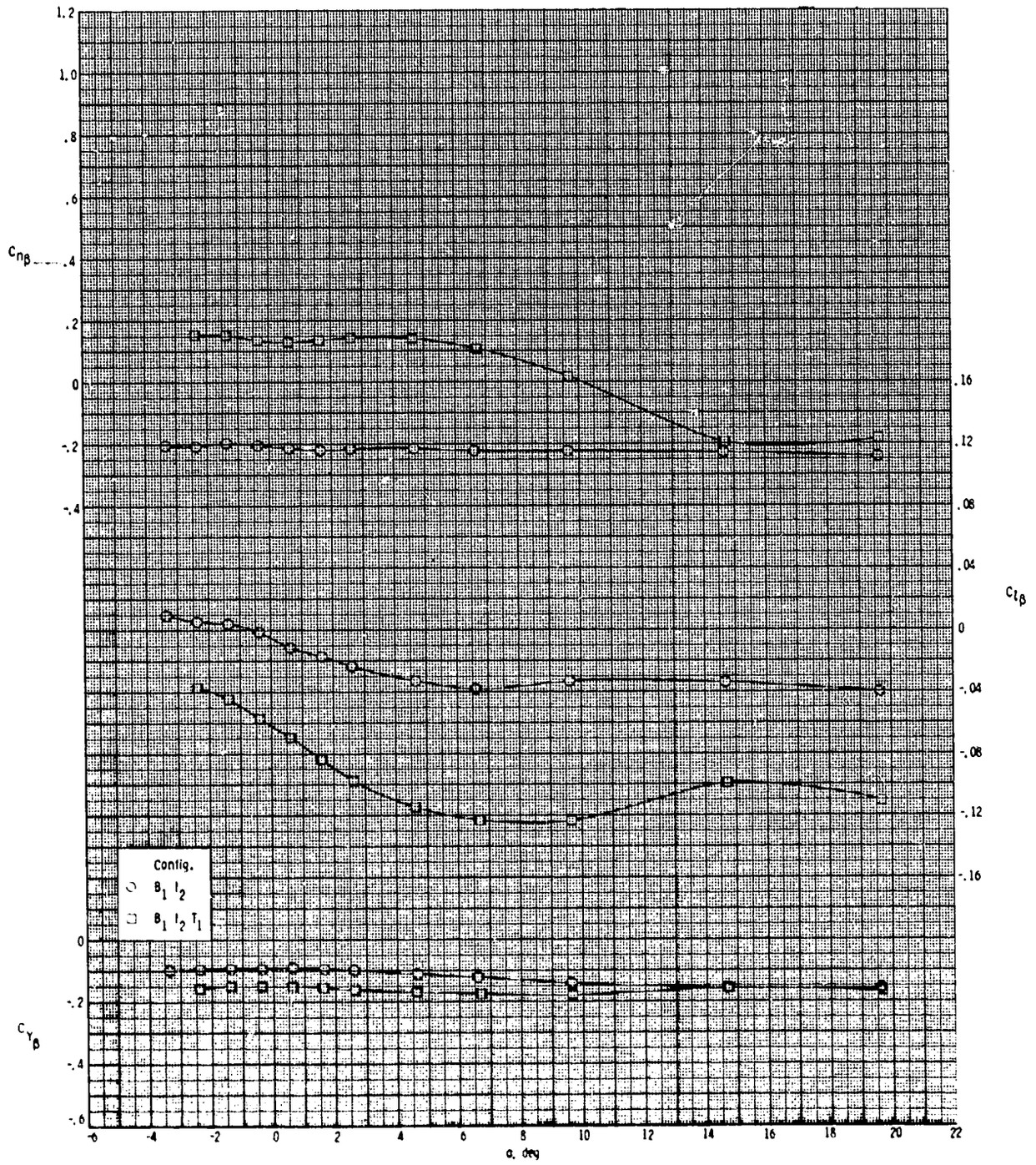

(d) M = 3.95.

Figure 24.- Concluded.

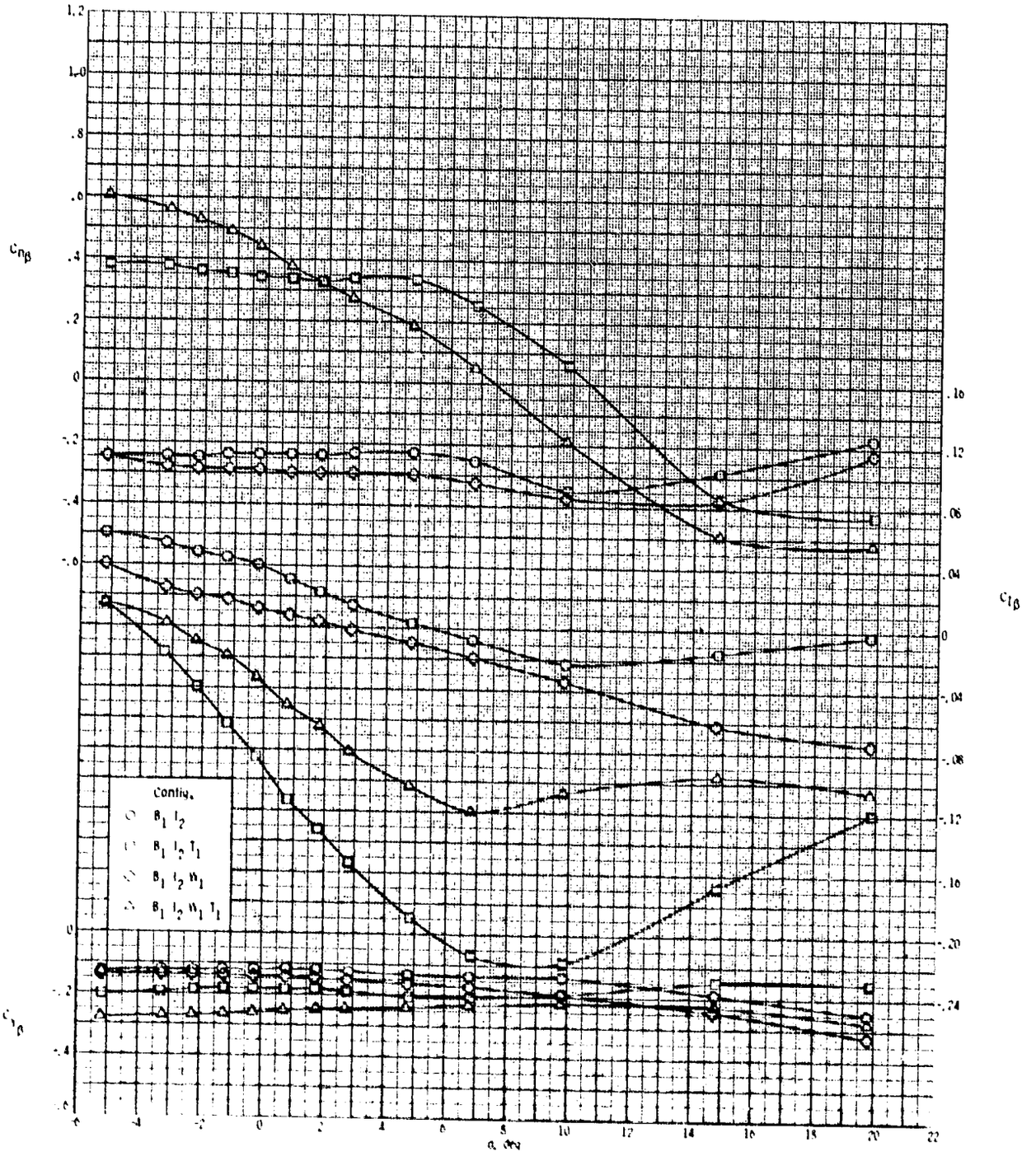

(a) M = 2.50.

Figure 25.- Effect of various model components on lateral-directional stability for two-dimensional inlets with $\phi_I = 115°$ and $\delta_p = 0°$.

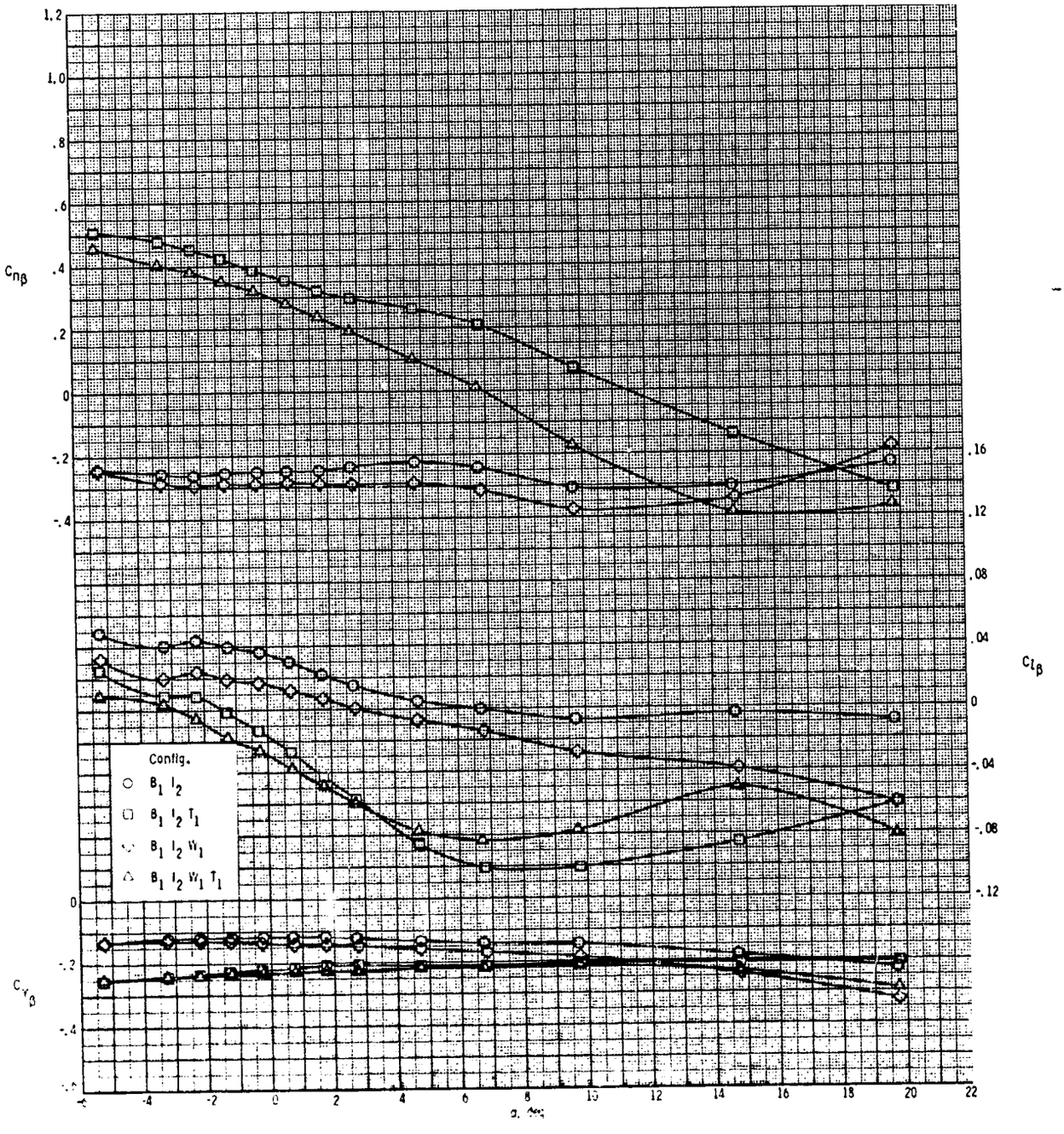

(b) M = 2.95.

Figure 25.- Continued.

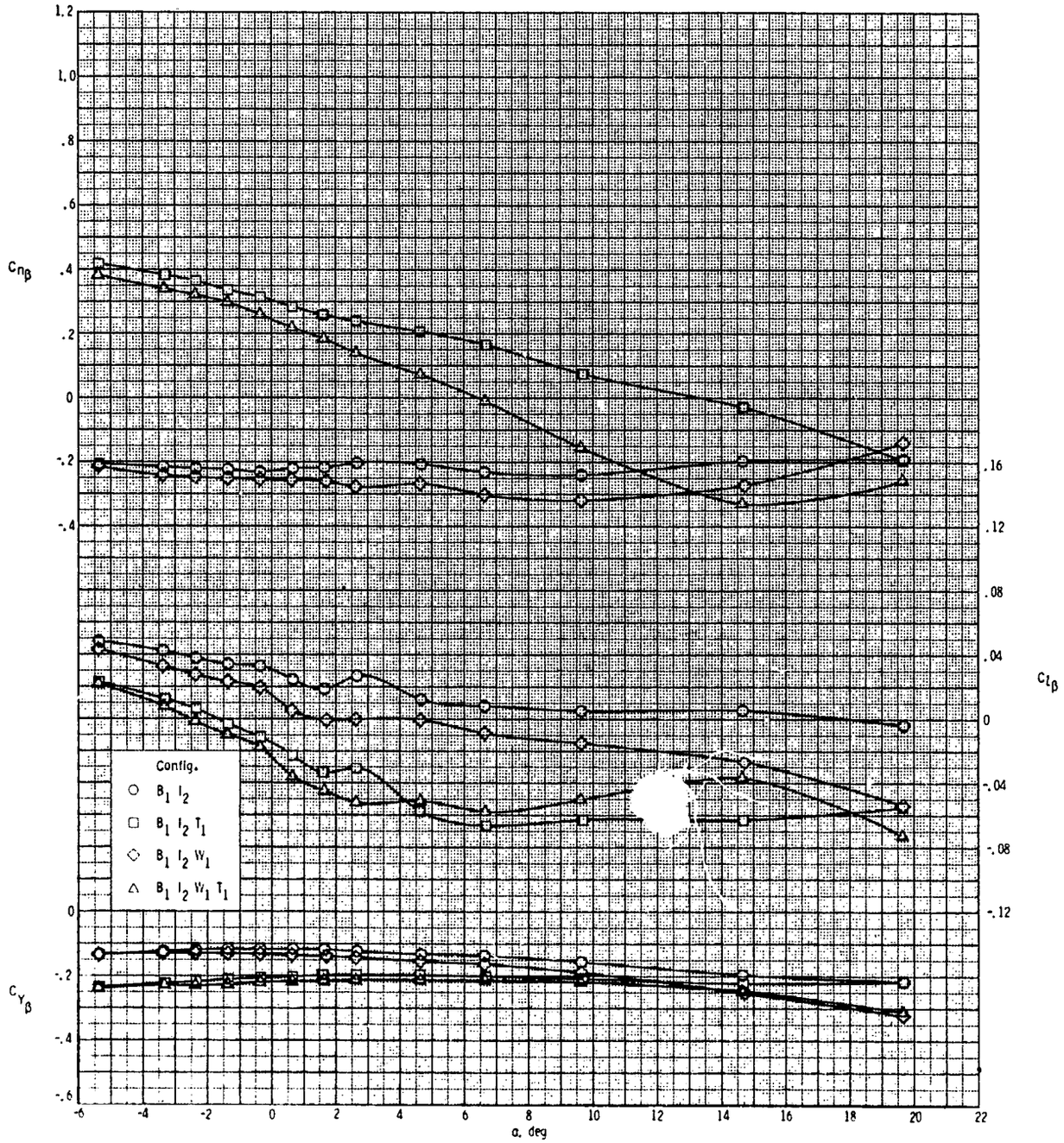

(c) M = 3.50.

Figure 25.- Continued.

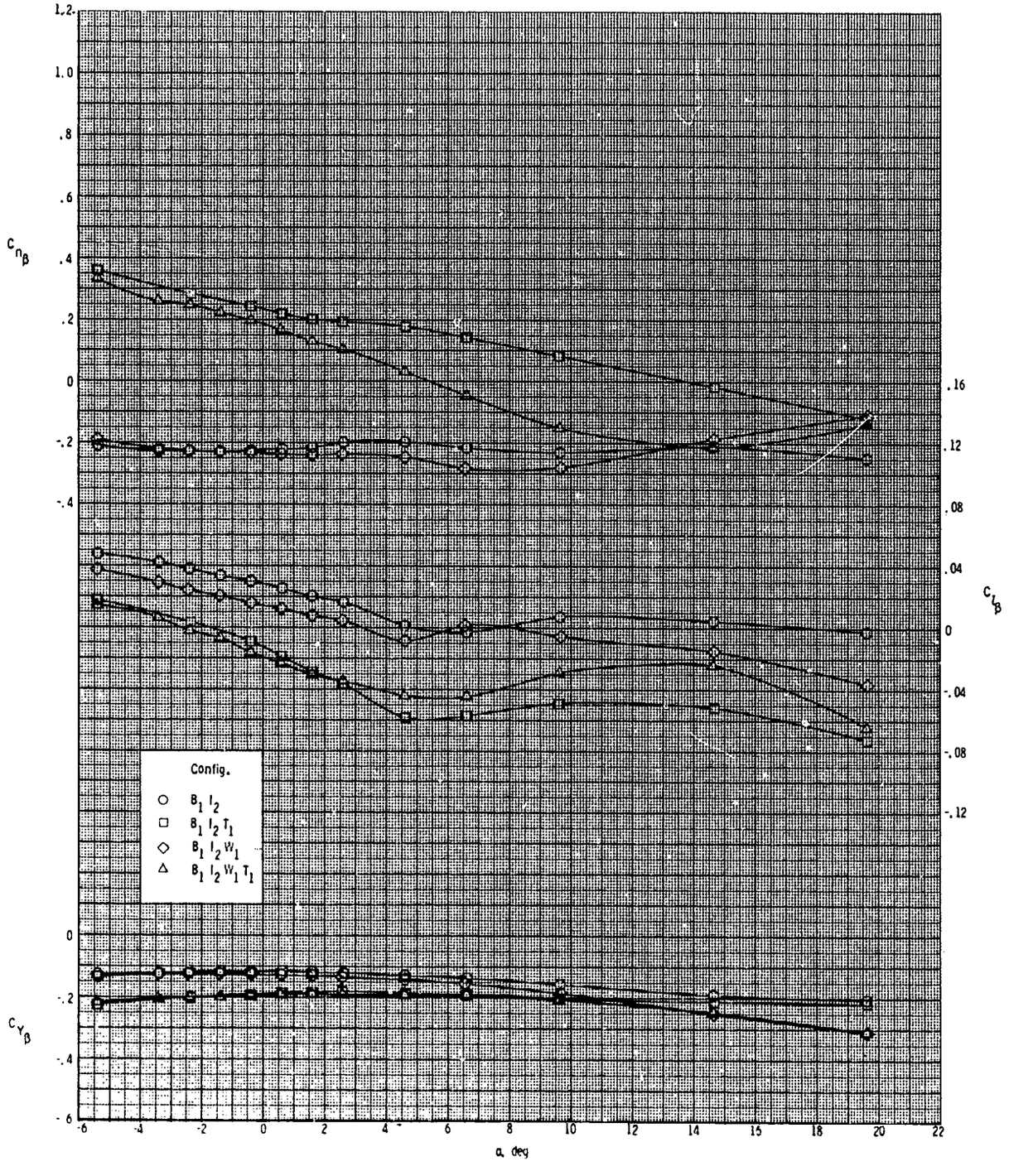

(d) M = 3.95.

Figure 25.- Concluded.

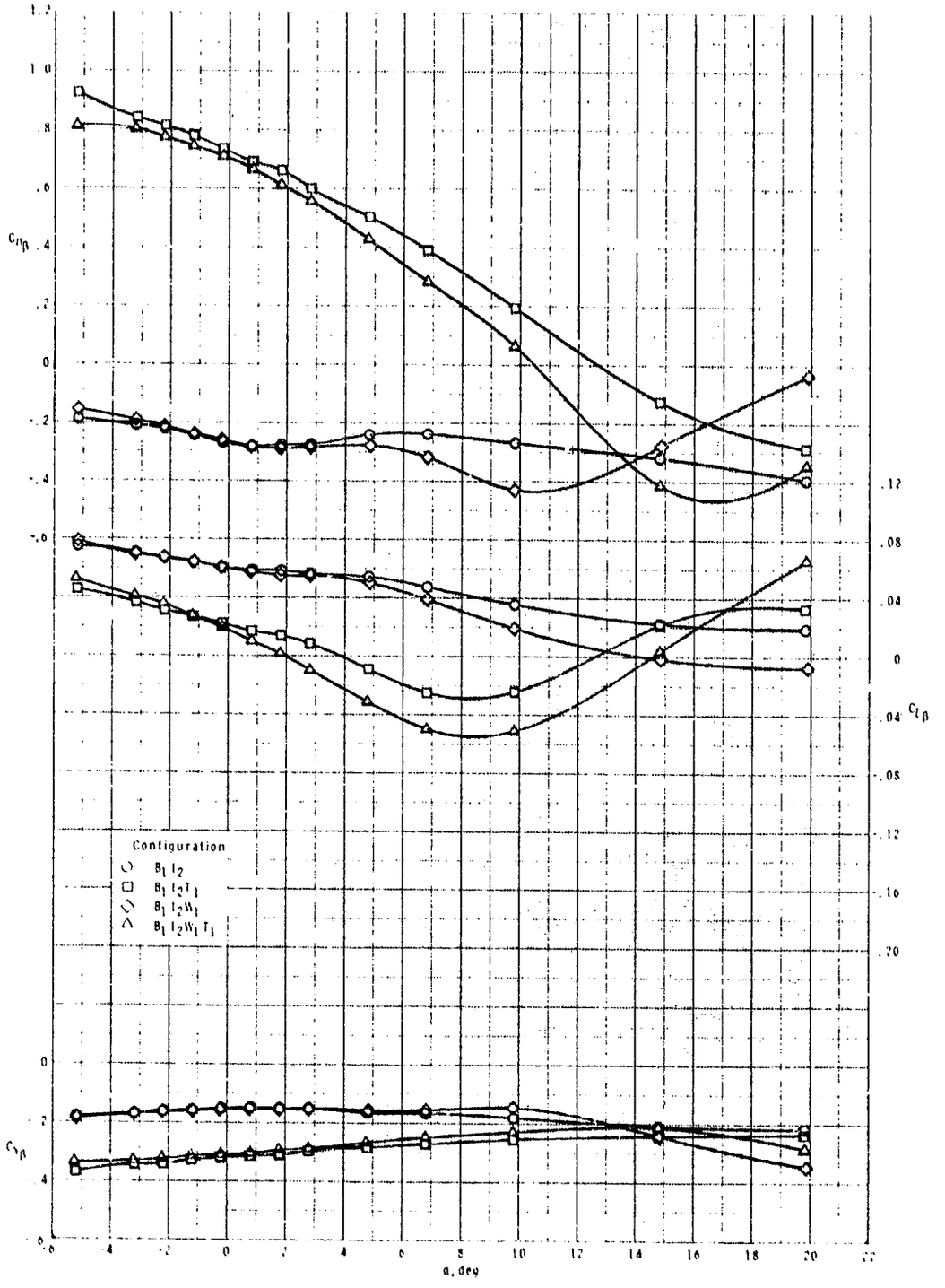

(a) M = 2.50.

Figure 26.- Effect of various model components on lateral-directional stability for two-dimensional inlets with T_1, $\phi_I = 135°$, and $\delta_p = 0°$.

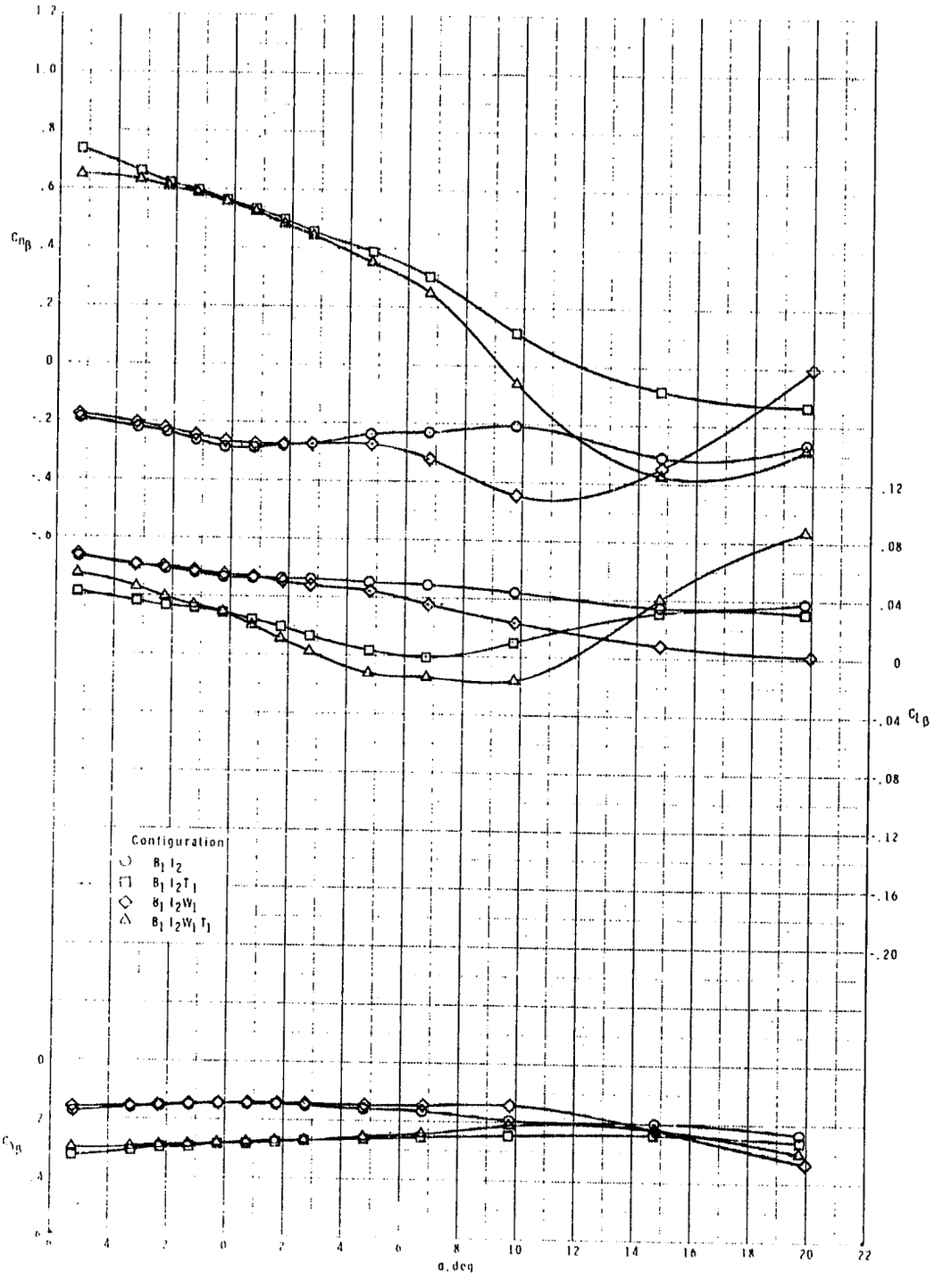

(b) M = 2.95.

Figure 26.- Continued.

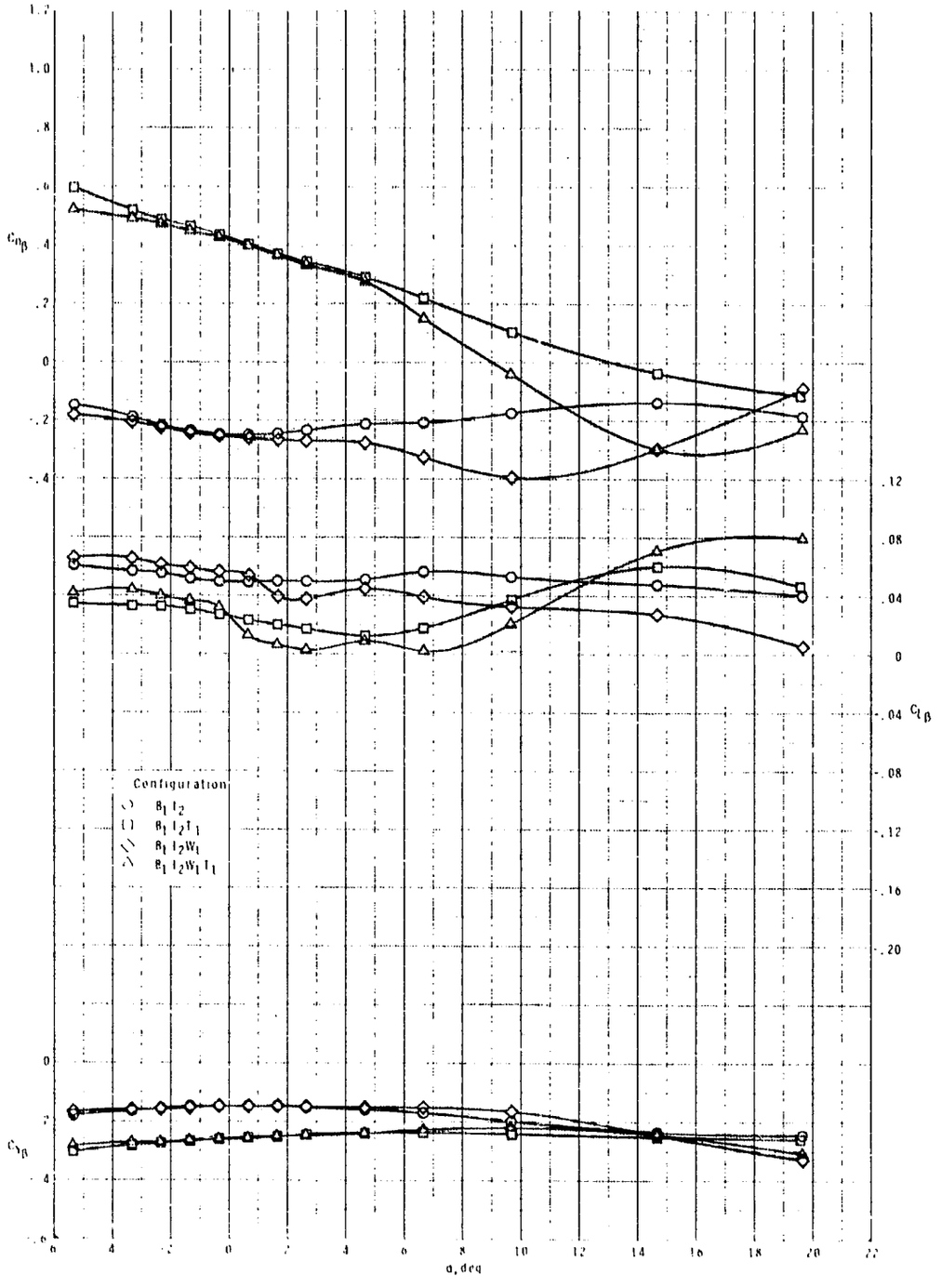

(c) M = 3.50.

Figure 26.- Continued.

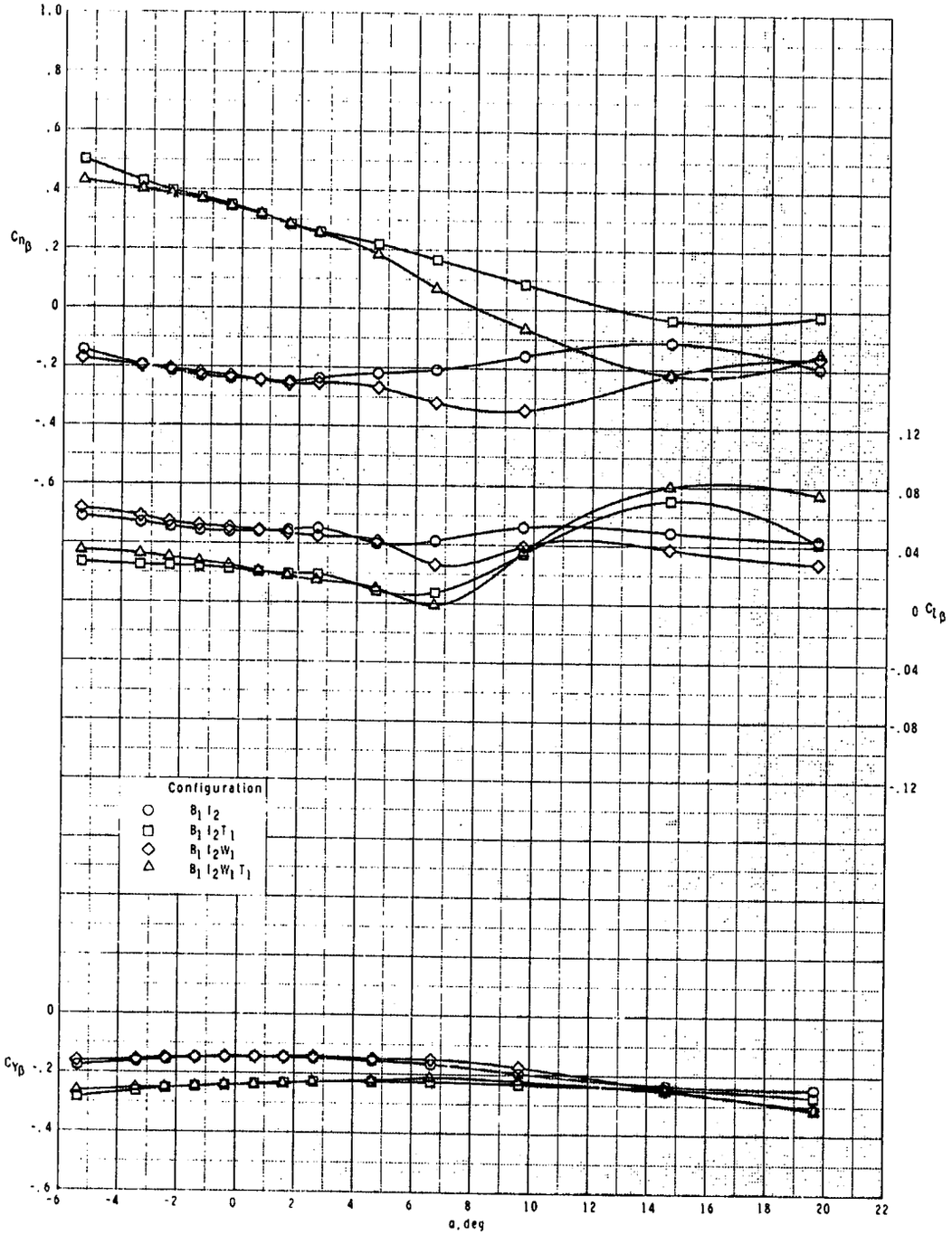

(d) M = 3.95.

Figure 26.- Concluded.

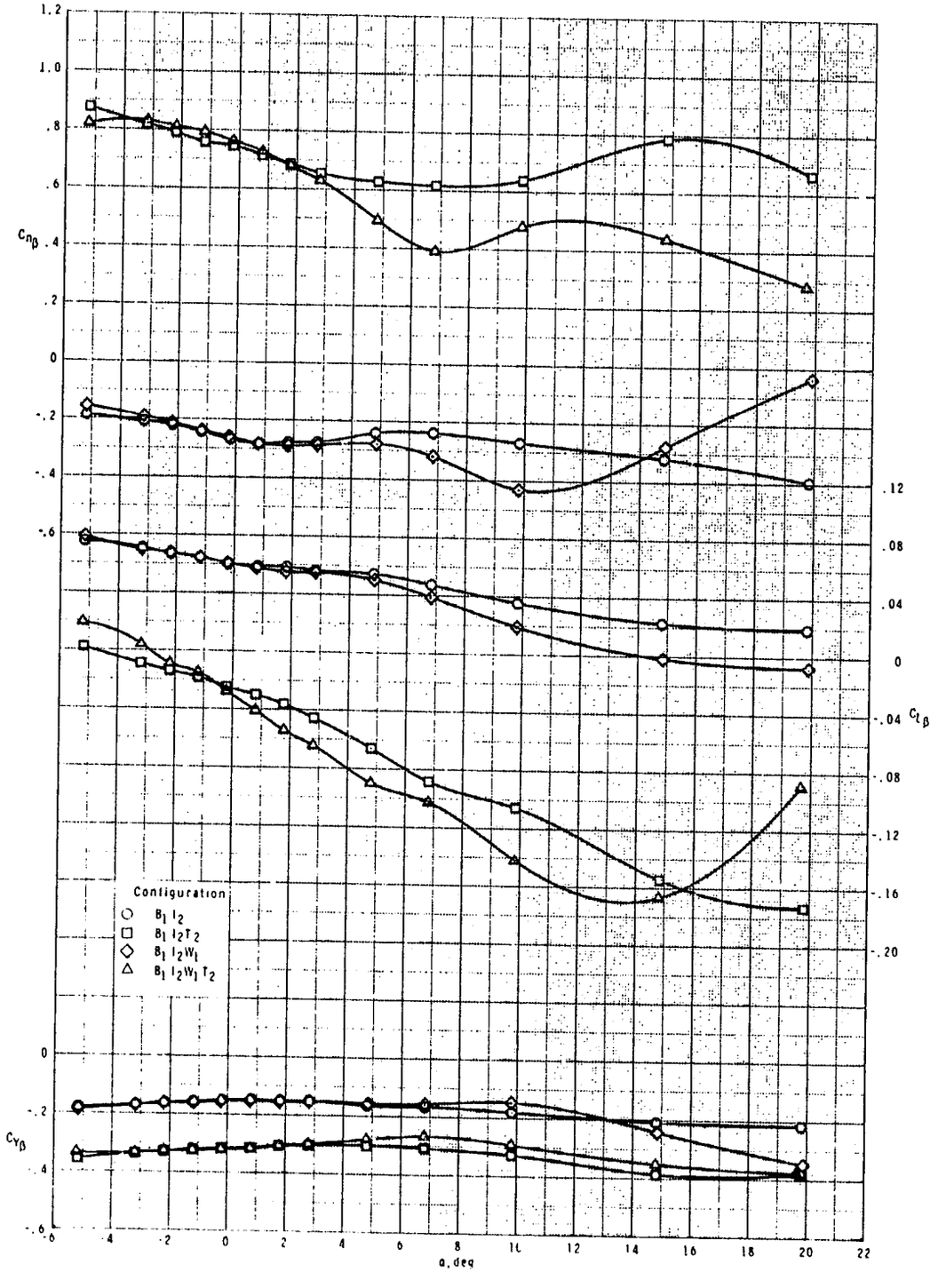

(a) M = 2.50.

Figure 27.- Effect of various model components on lateral-directional stability for two-dimensional inlets with T_2, ϕ_I = 135°, and δ_p = 0°.

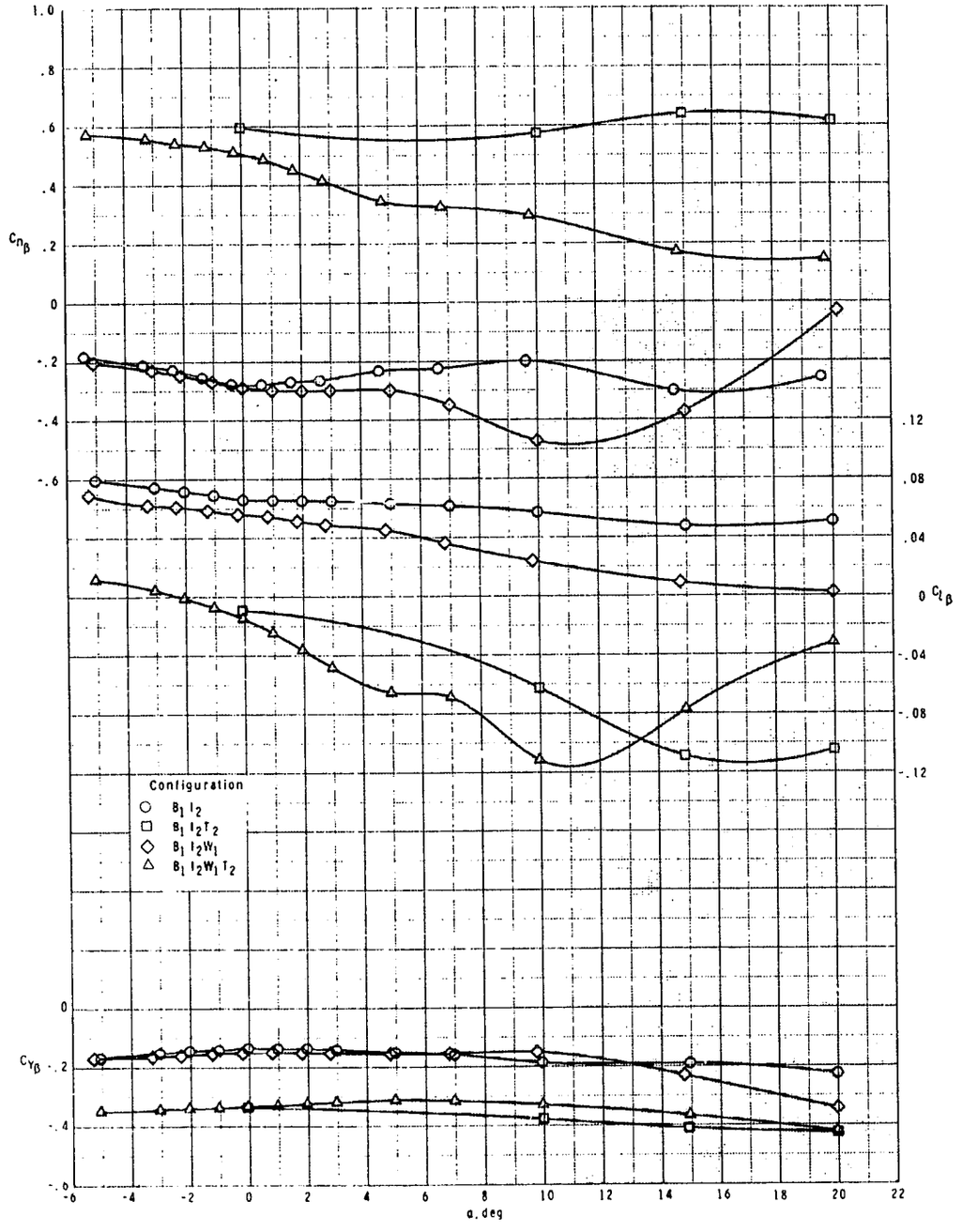

(b) M = 2.95.

Figure 27.- Continued.

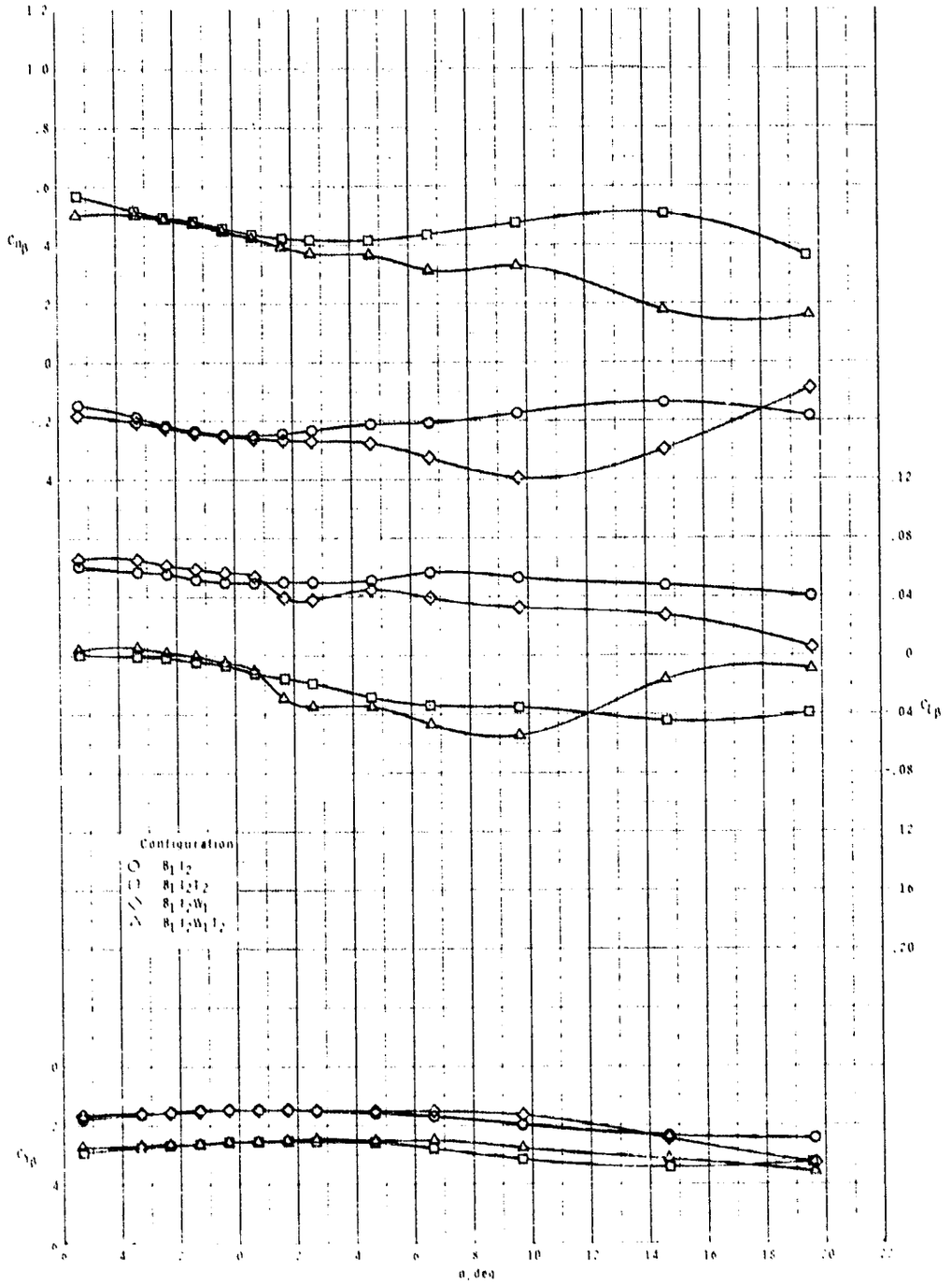

(c) M = 3.50.

Figure 27.- Continued.

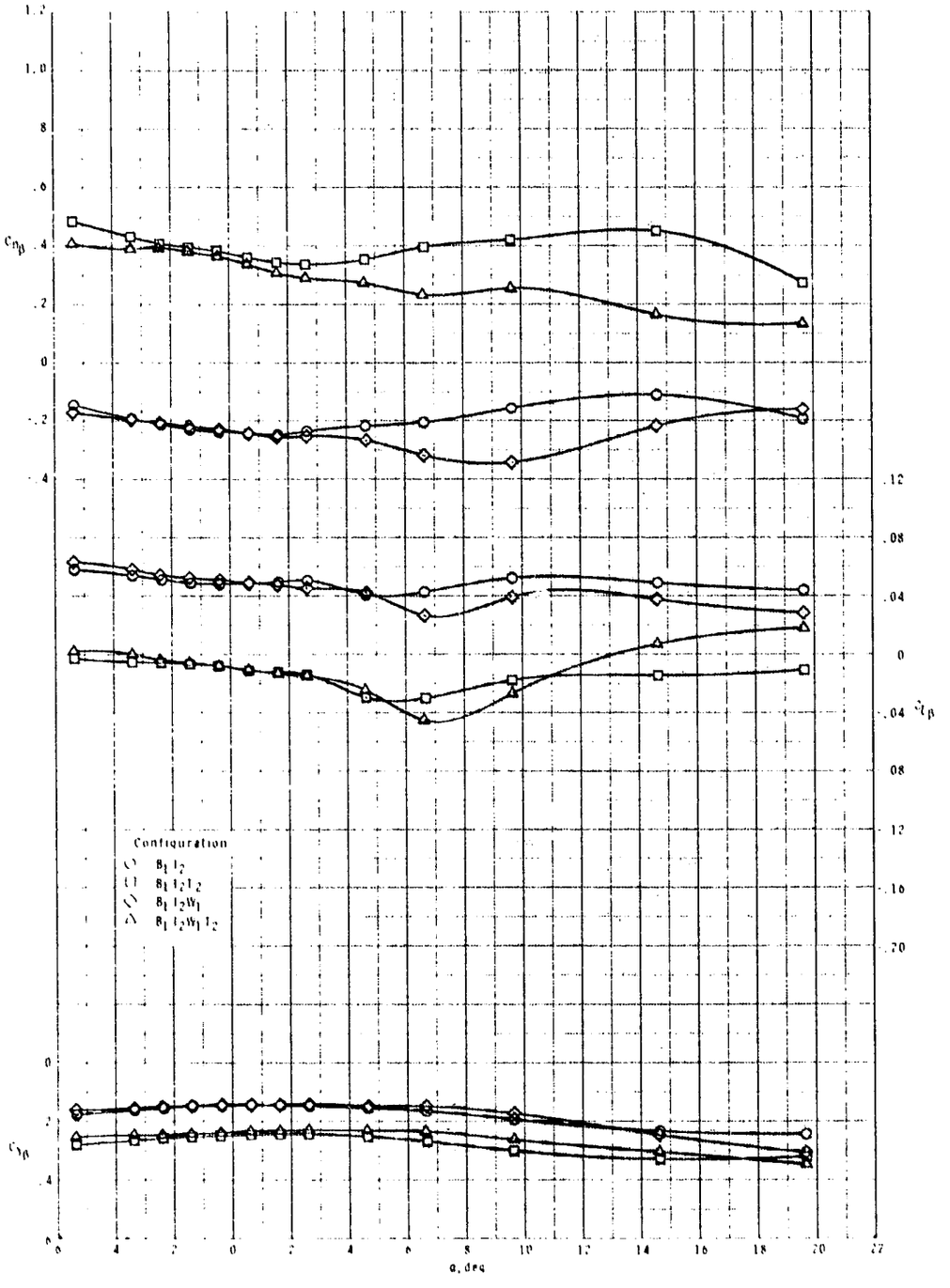

(d) M = 3.95.

Figure 27.- Concluded.

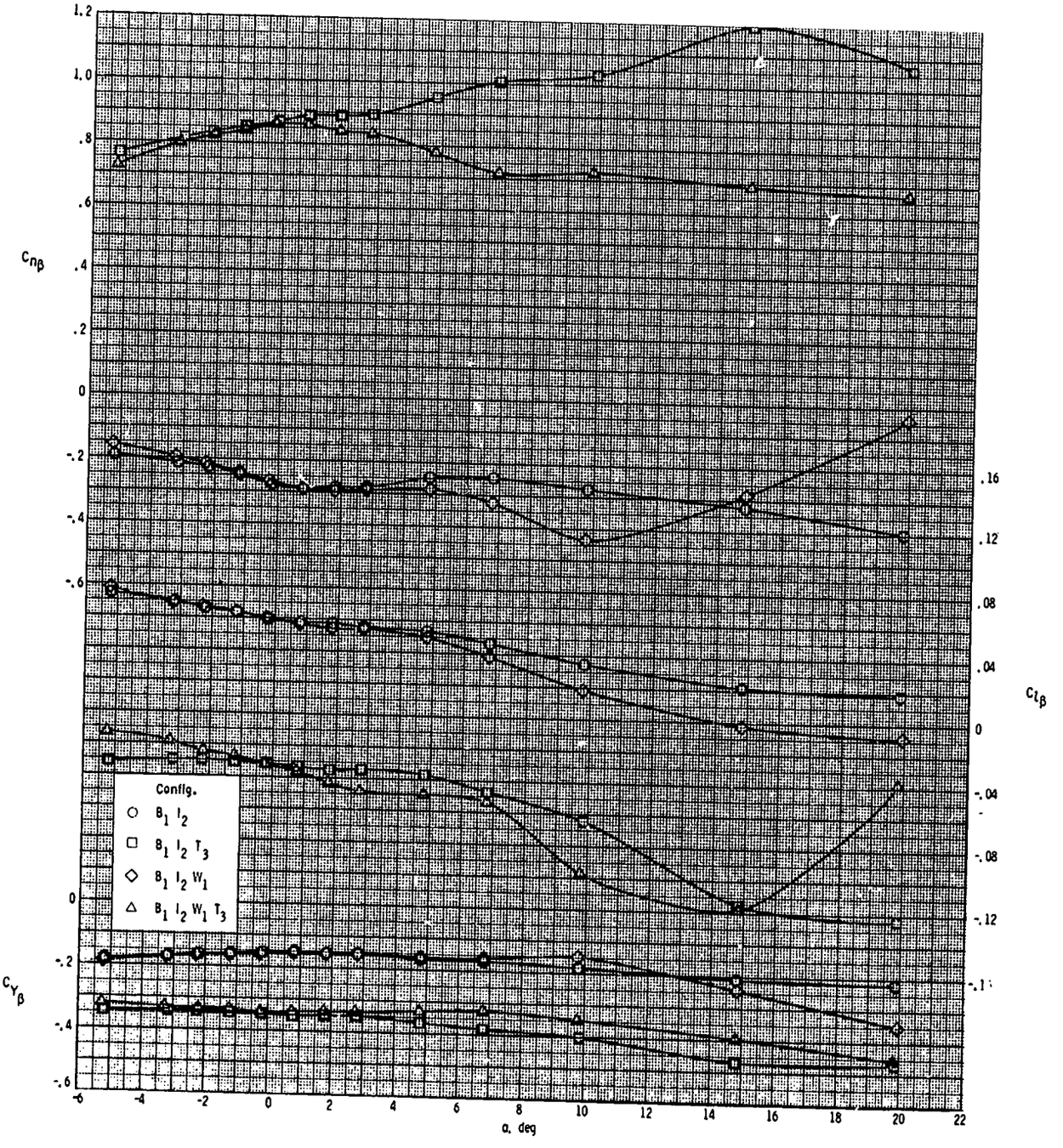

(a) M = 2.50.

Figure 28.- Effect of various model components on lateral-directional stability for two-dimensional inlets with T_3, $\phi_I = 135°$, and $\delta_p = 0°$.

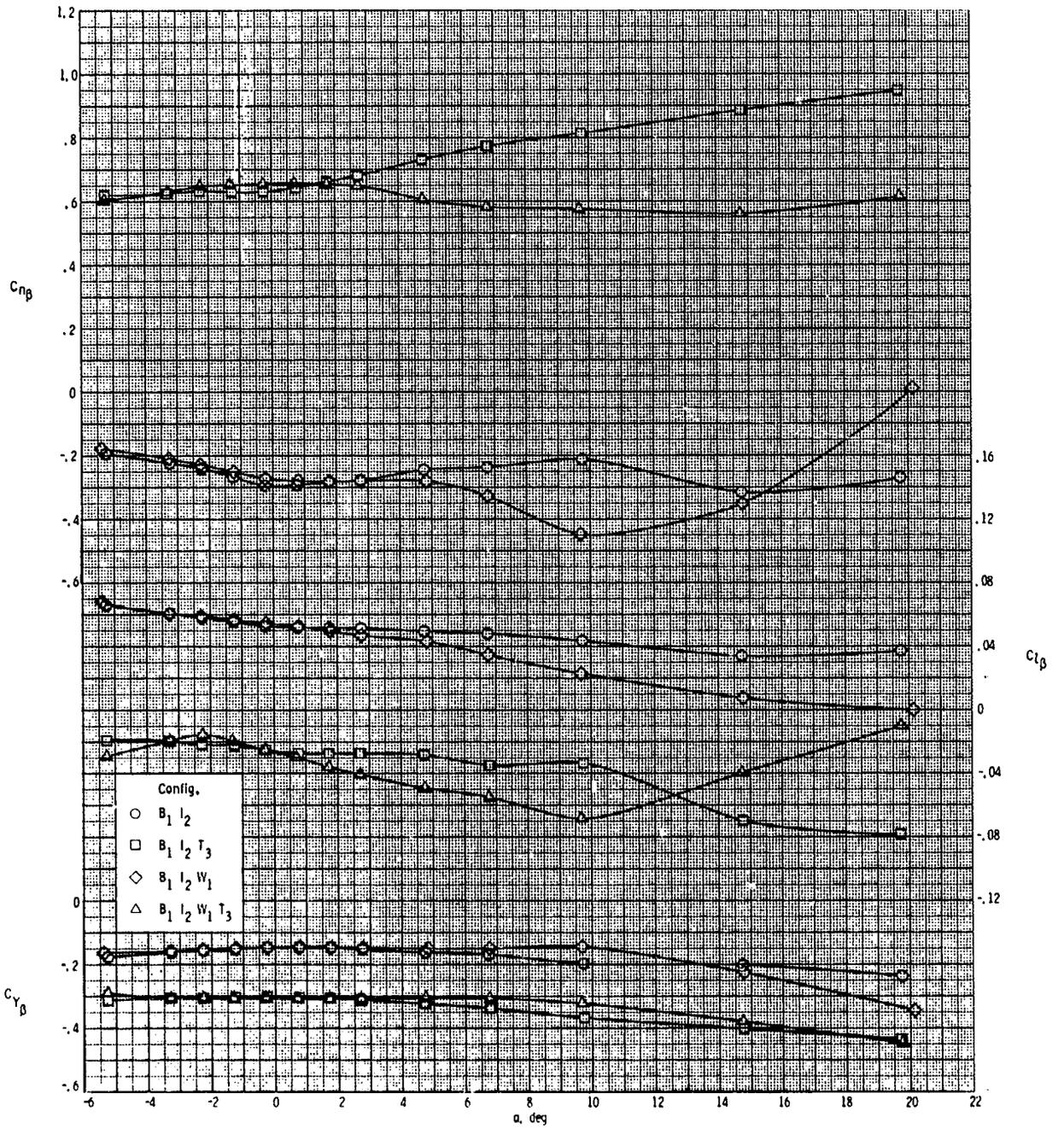

(b) M = 2.95.

Figure 28.- Continued.

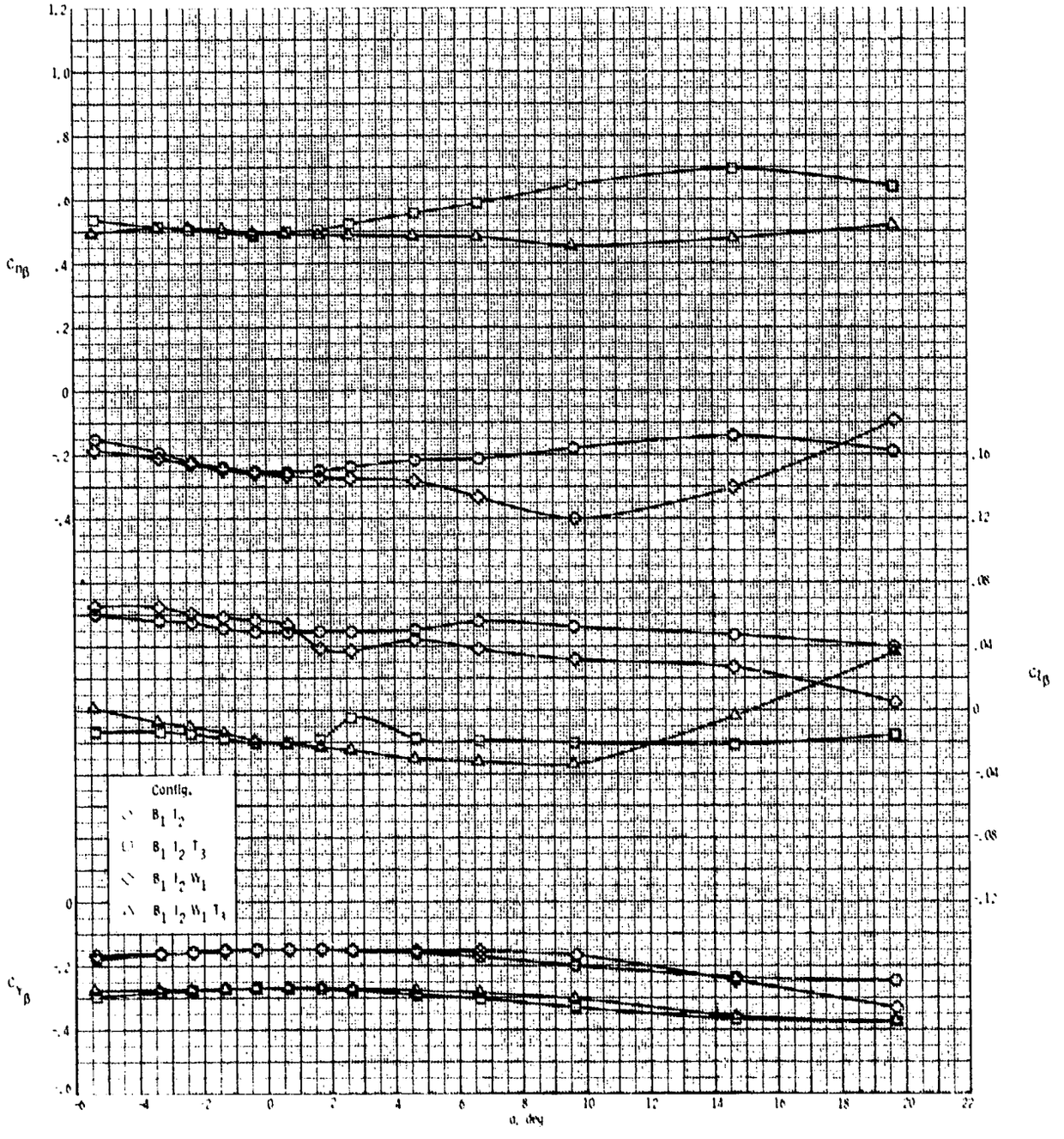

(c) M = 3.50.

Figure 28.- Continued.

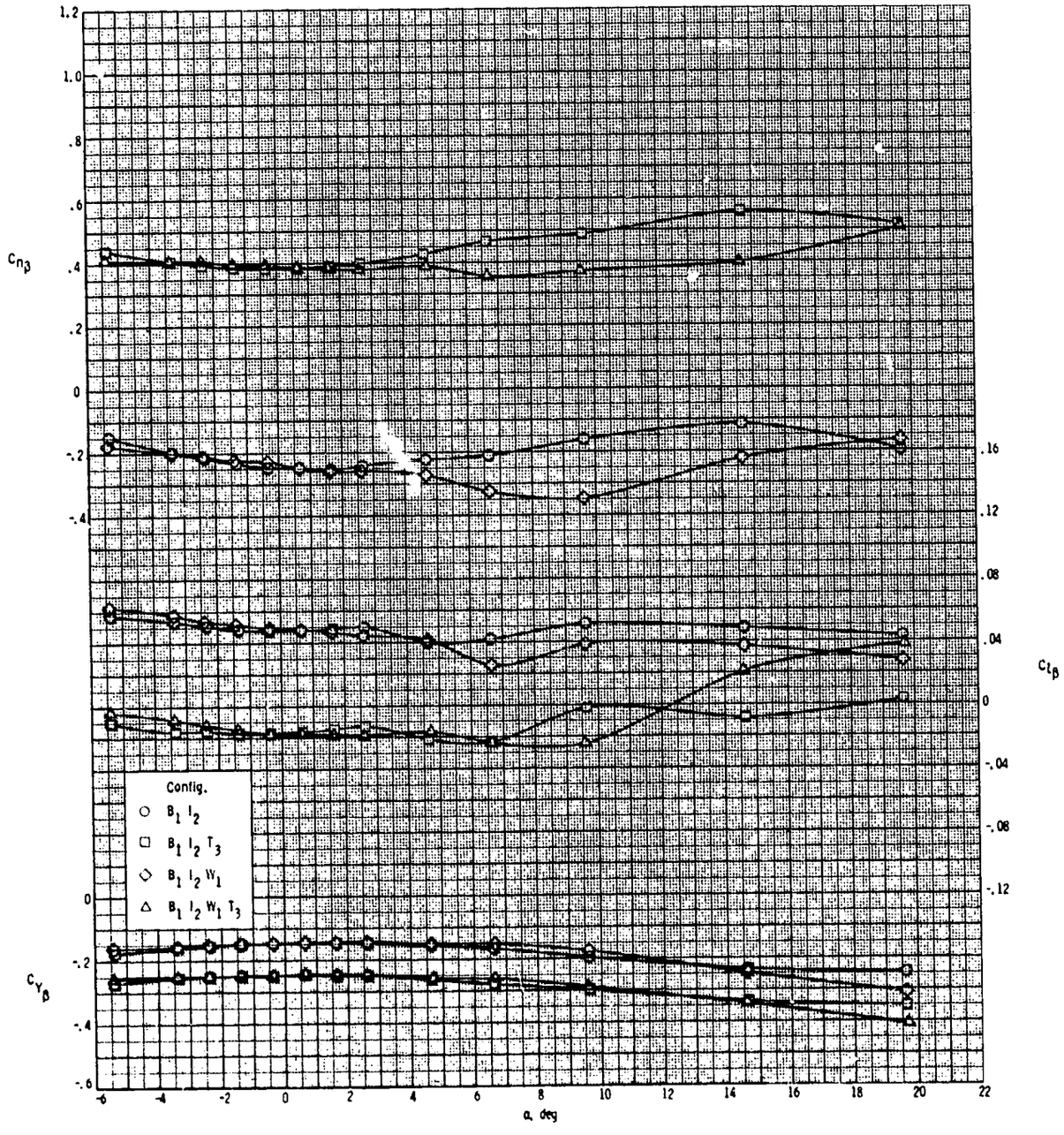

(d) M = 3.95.

Figure 28.- Concluded.

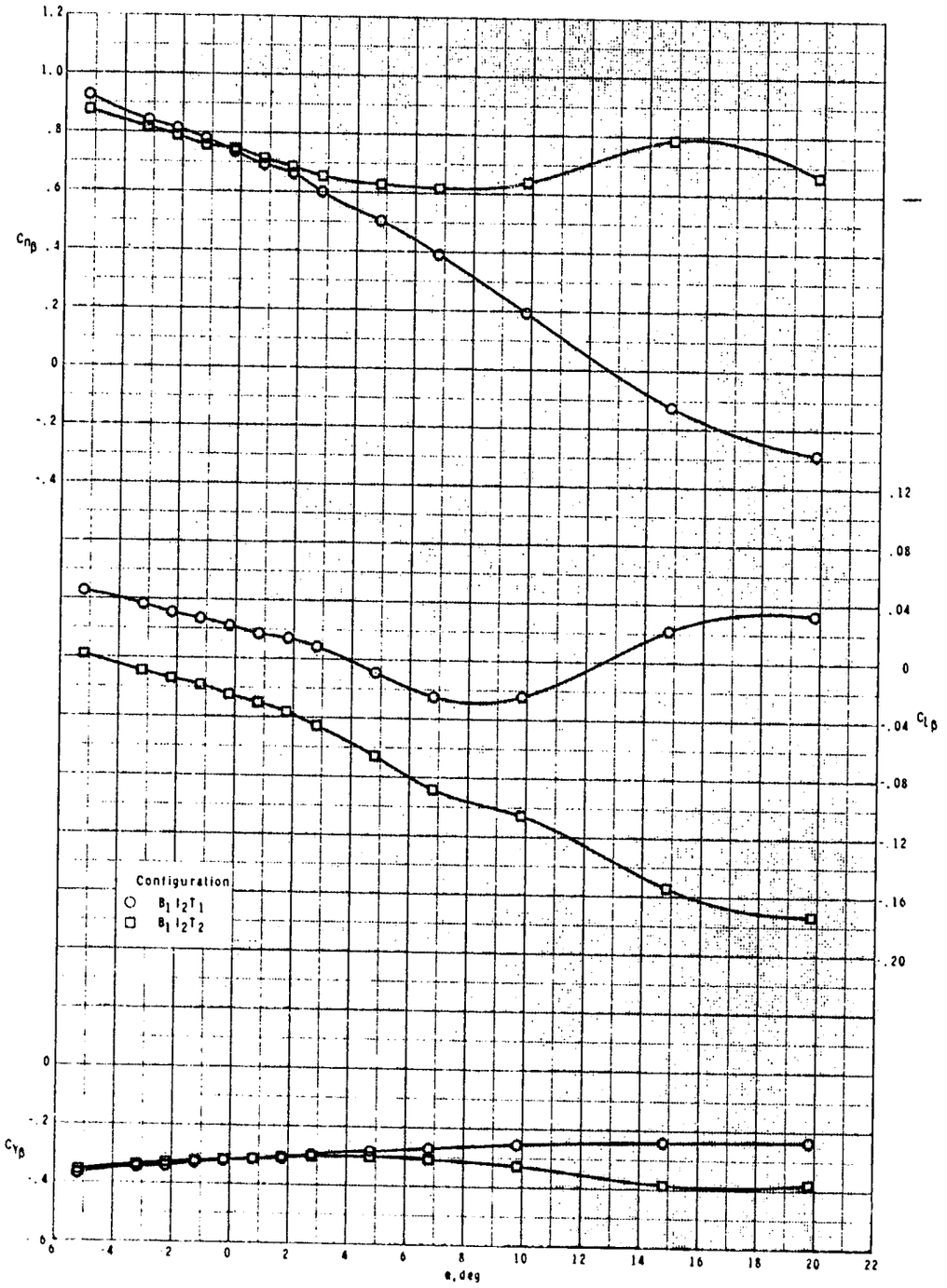

(a) M = 2.50.

Figure 29.- Effect of tail configuration on lateral-directional stability for configuration B_1I_2T with $\phi_I = 135°$ and $\delta_p = 0°$.

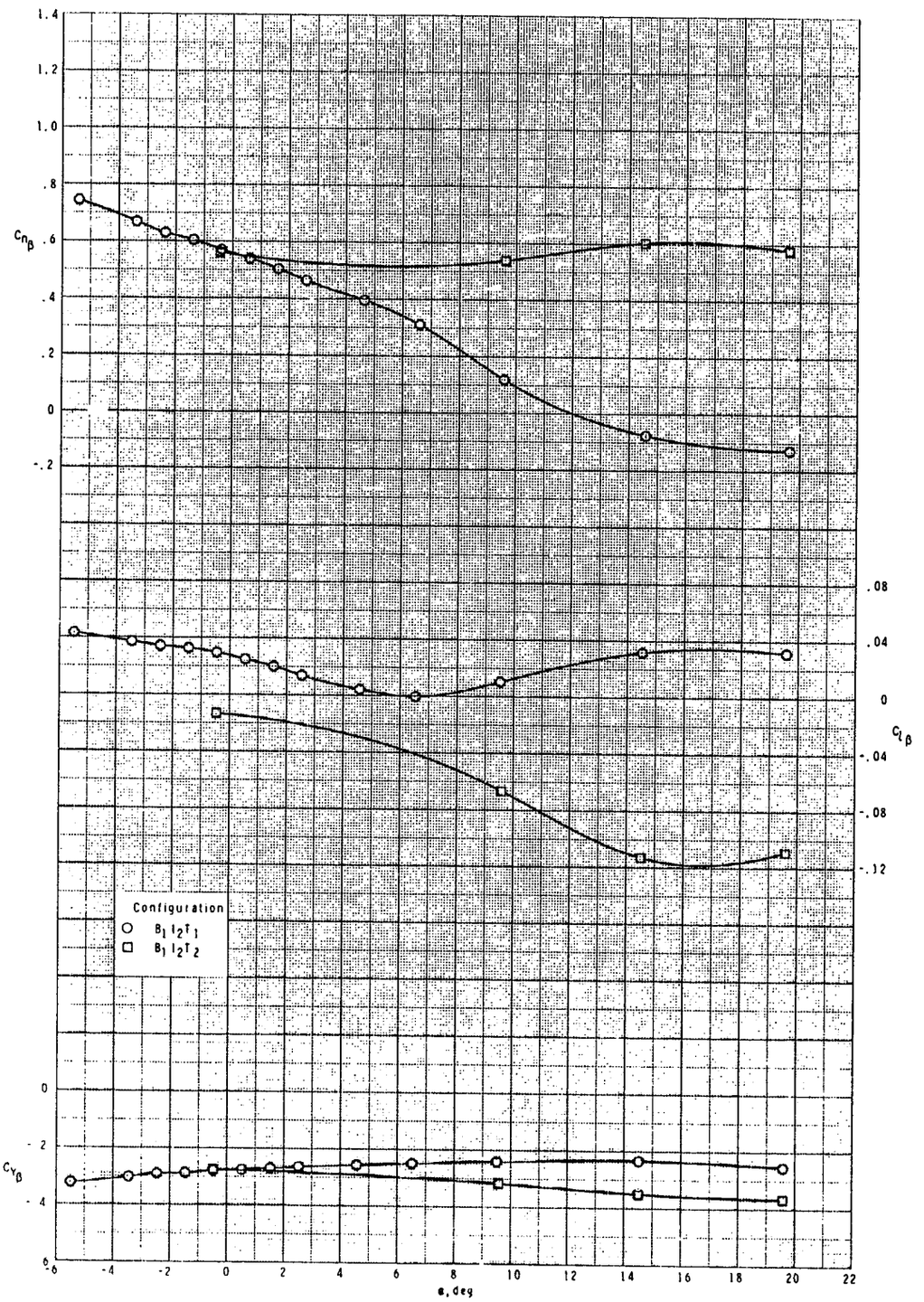

(b) M = 2.95.

Figure 29.- Continued.

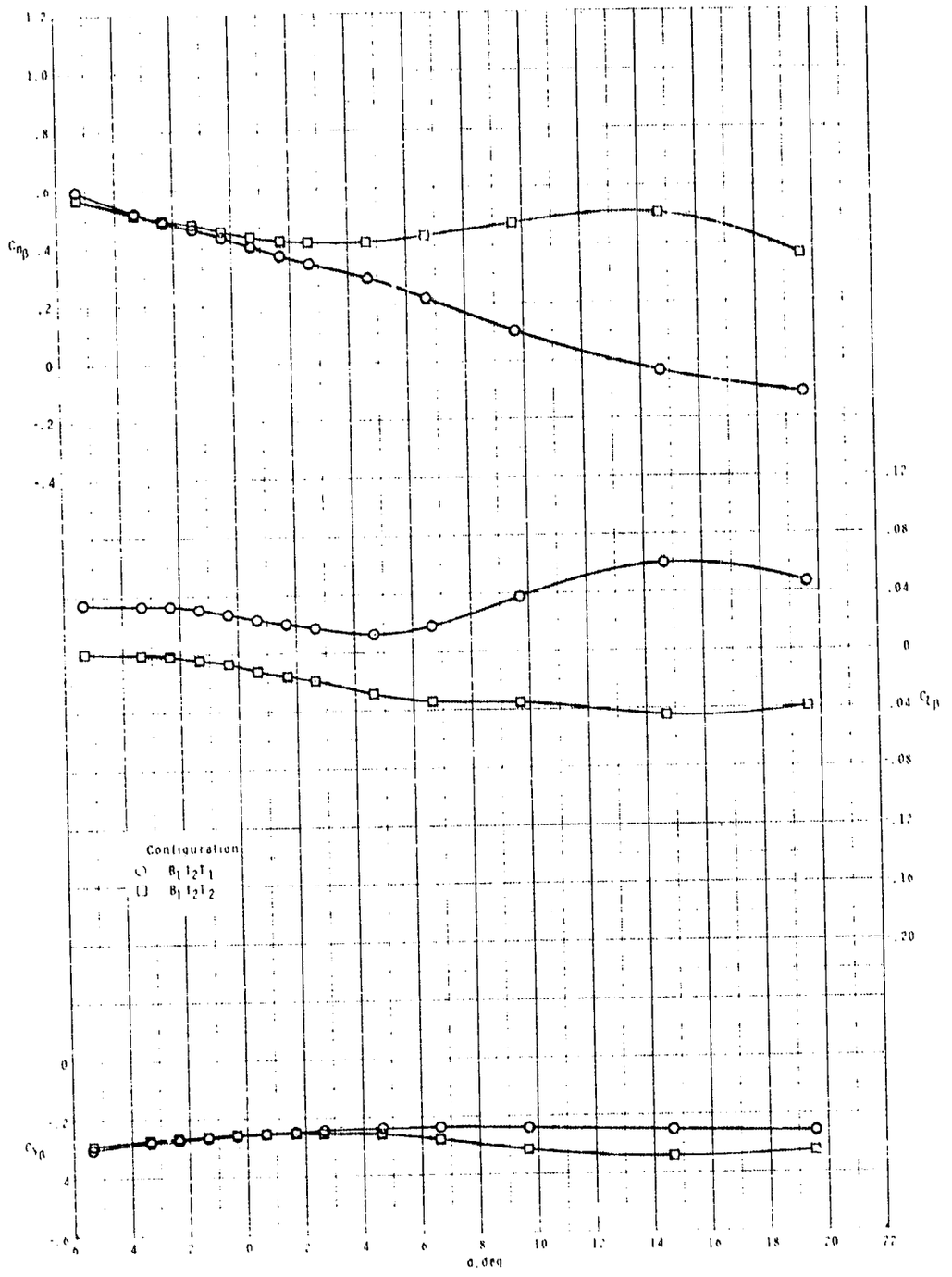

(c) M = 3.50.

Figure 29.- Continued.

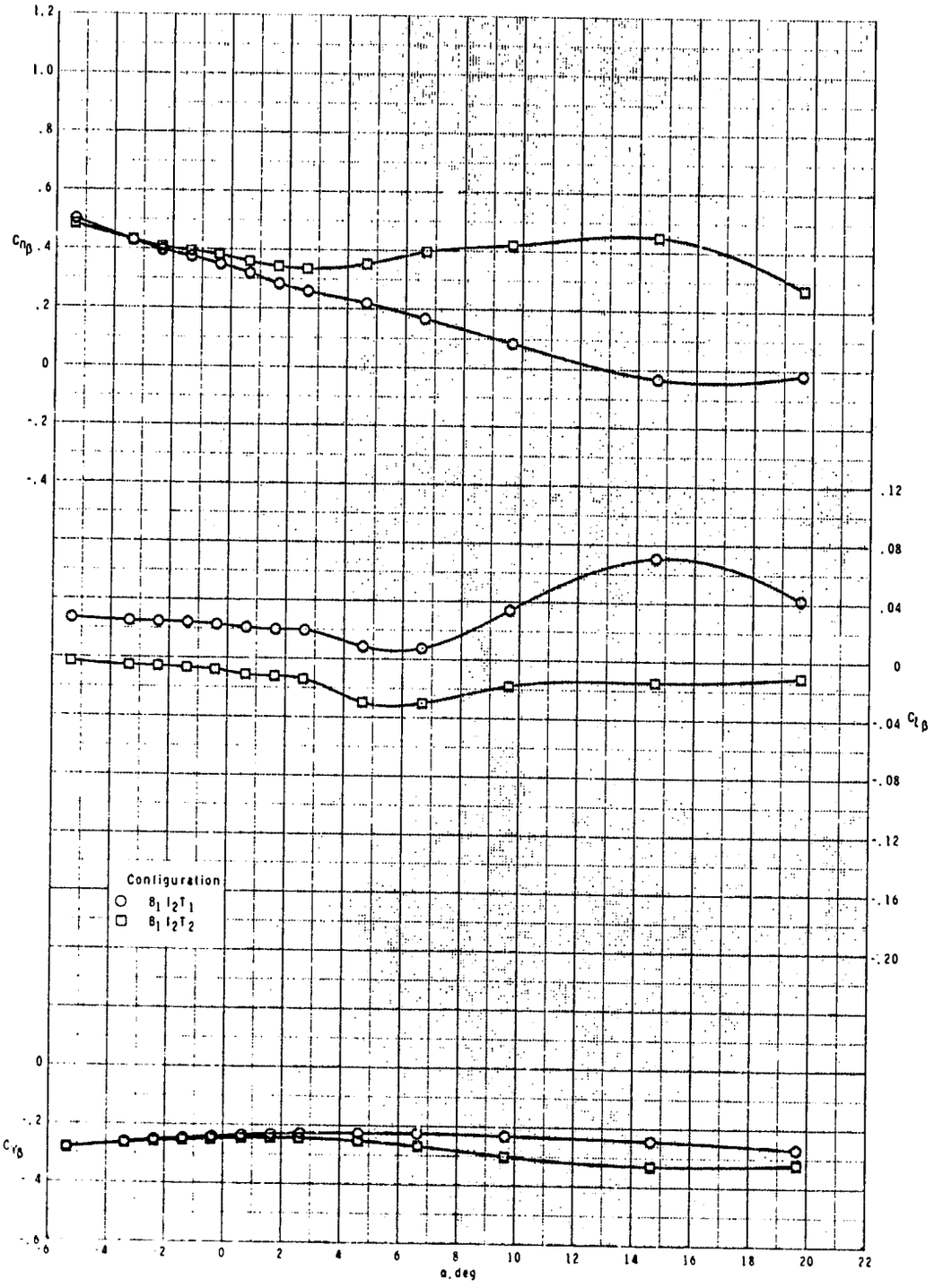

(d) M = 3.95.

Figure 29.- Concluded.

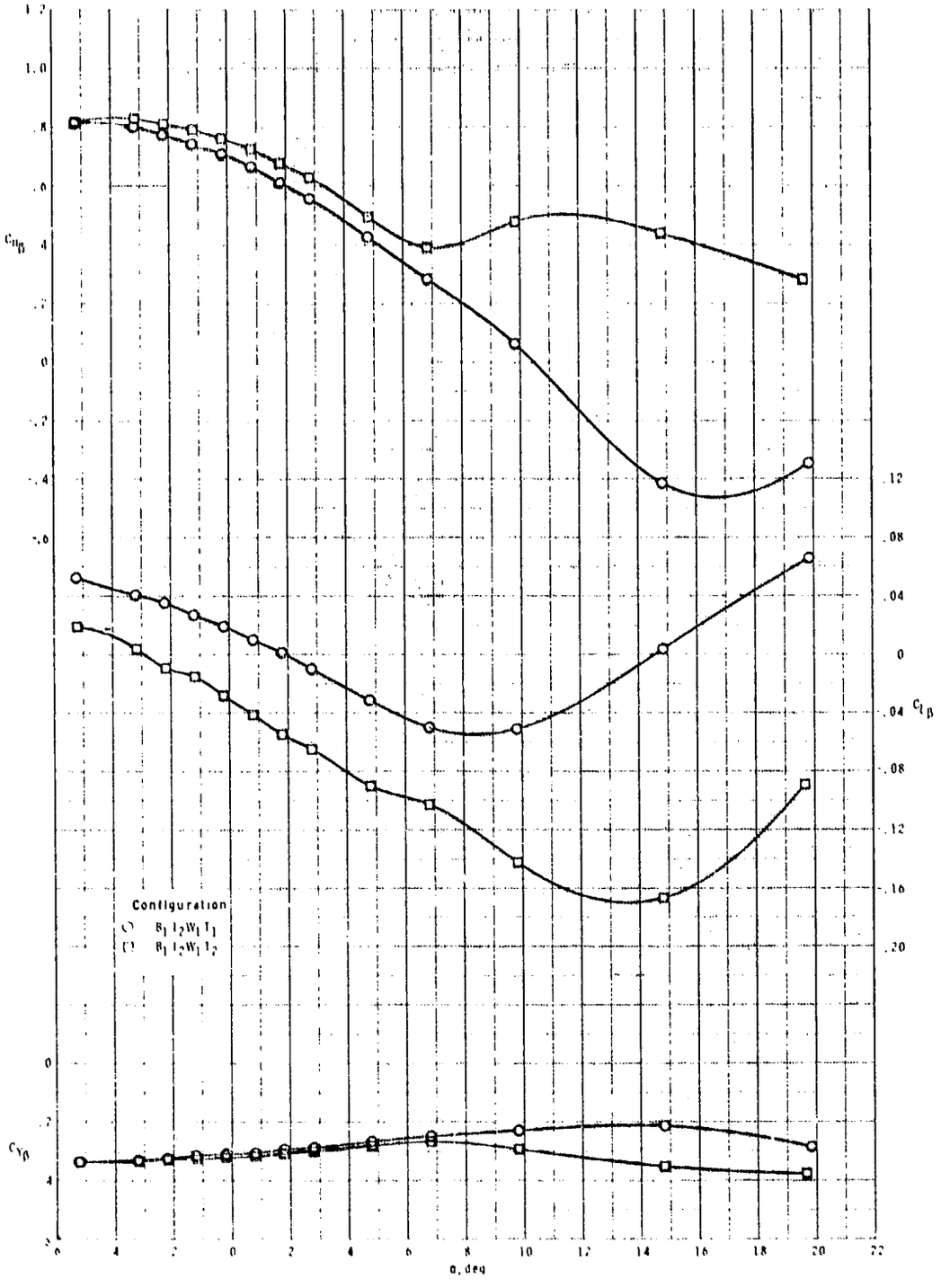

(a) M = 2.50.

Figure 30.- Effect of tail configuration on lateral-directional stability for configuration $B_1I_2W_1T$ with $\phi_I = 135°$ and $\delta_p = 0°$.

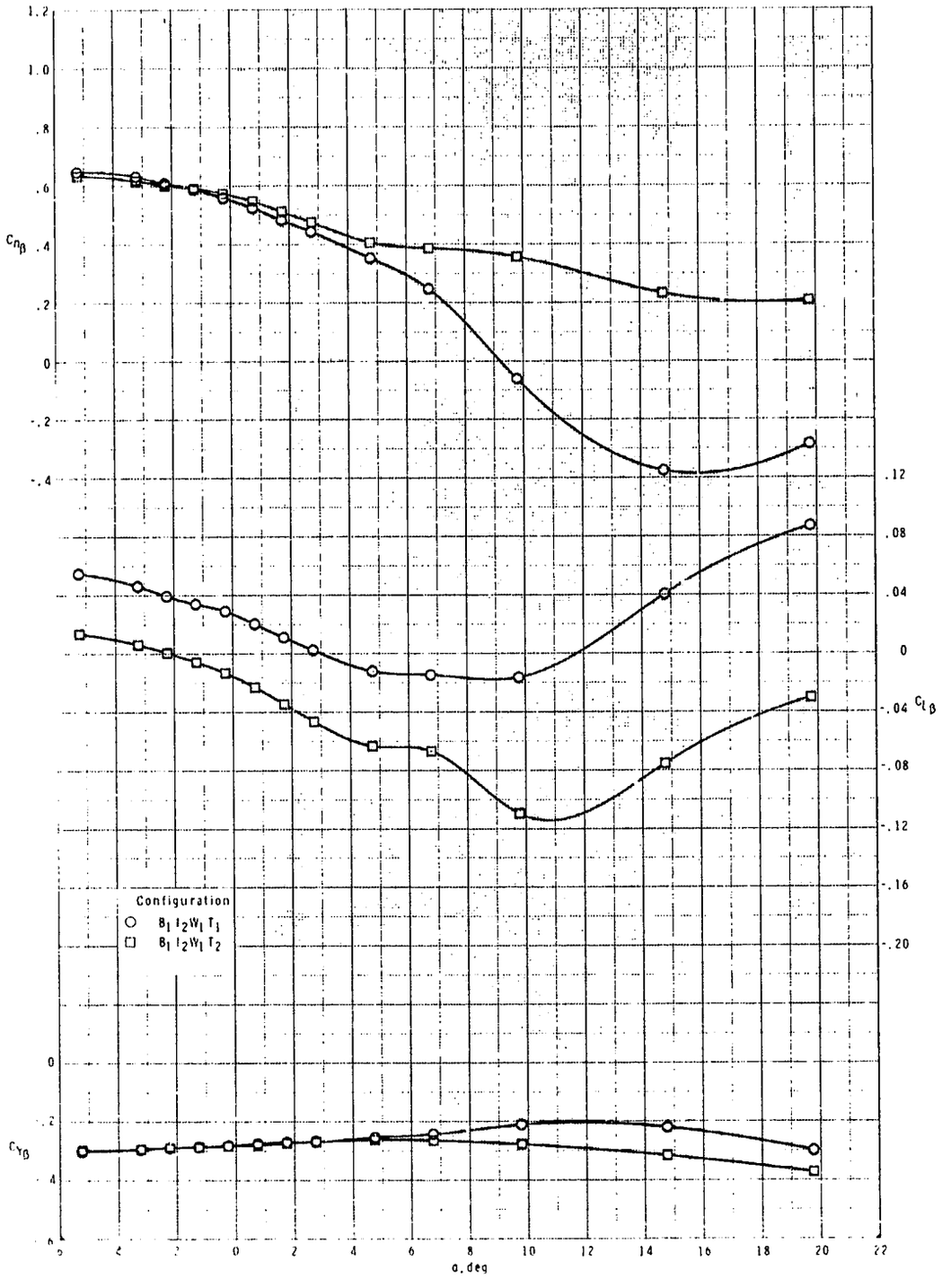

(b) M = 2.95.

Figure 30.- Continued.

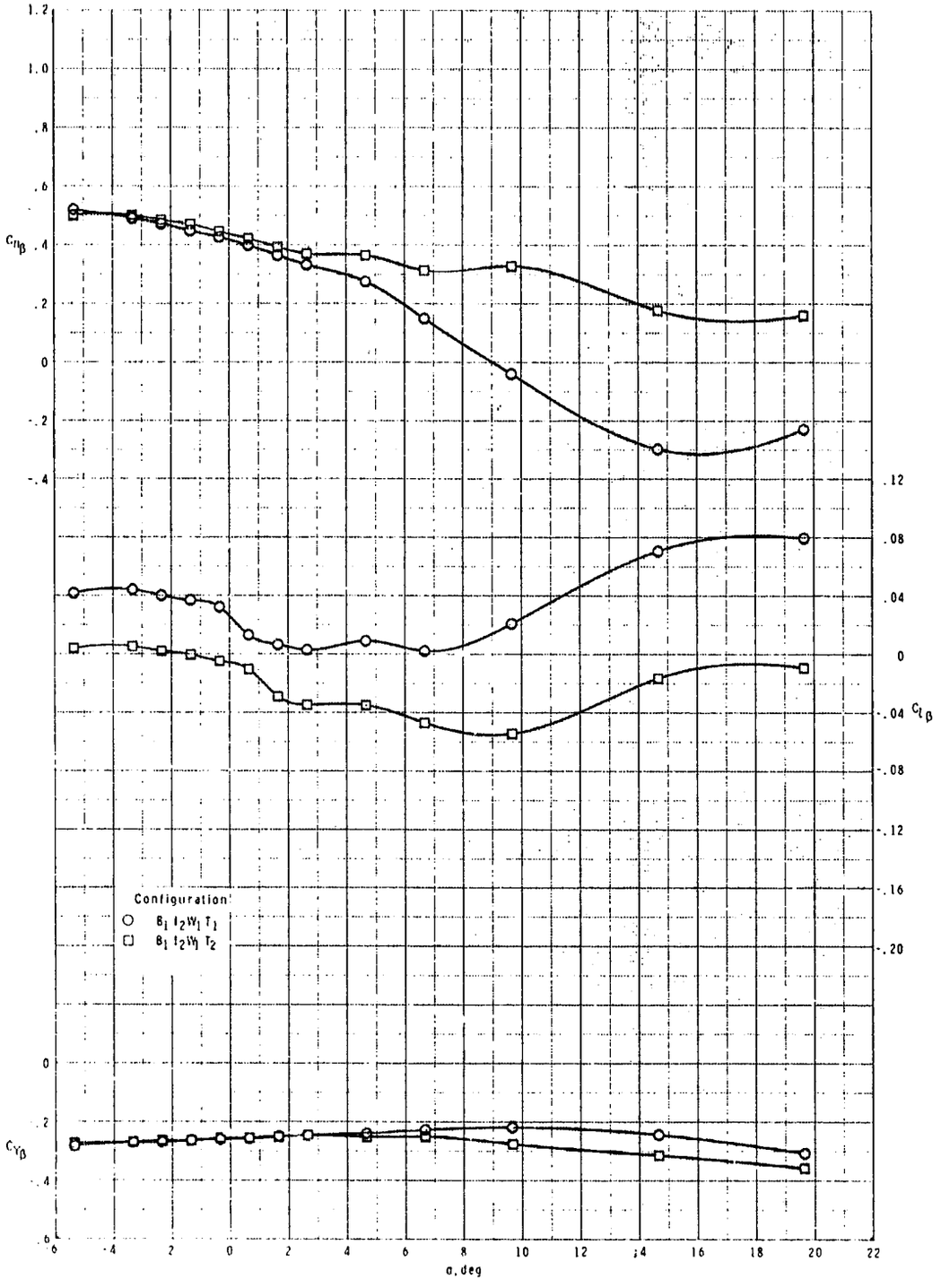

(c) M = 3.50.

Figure 30.- Continued.

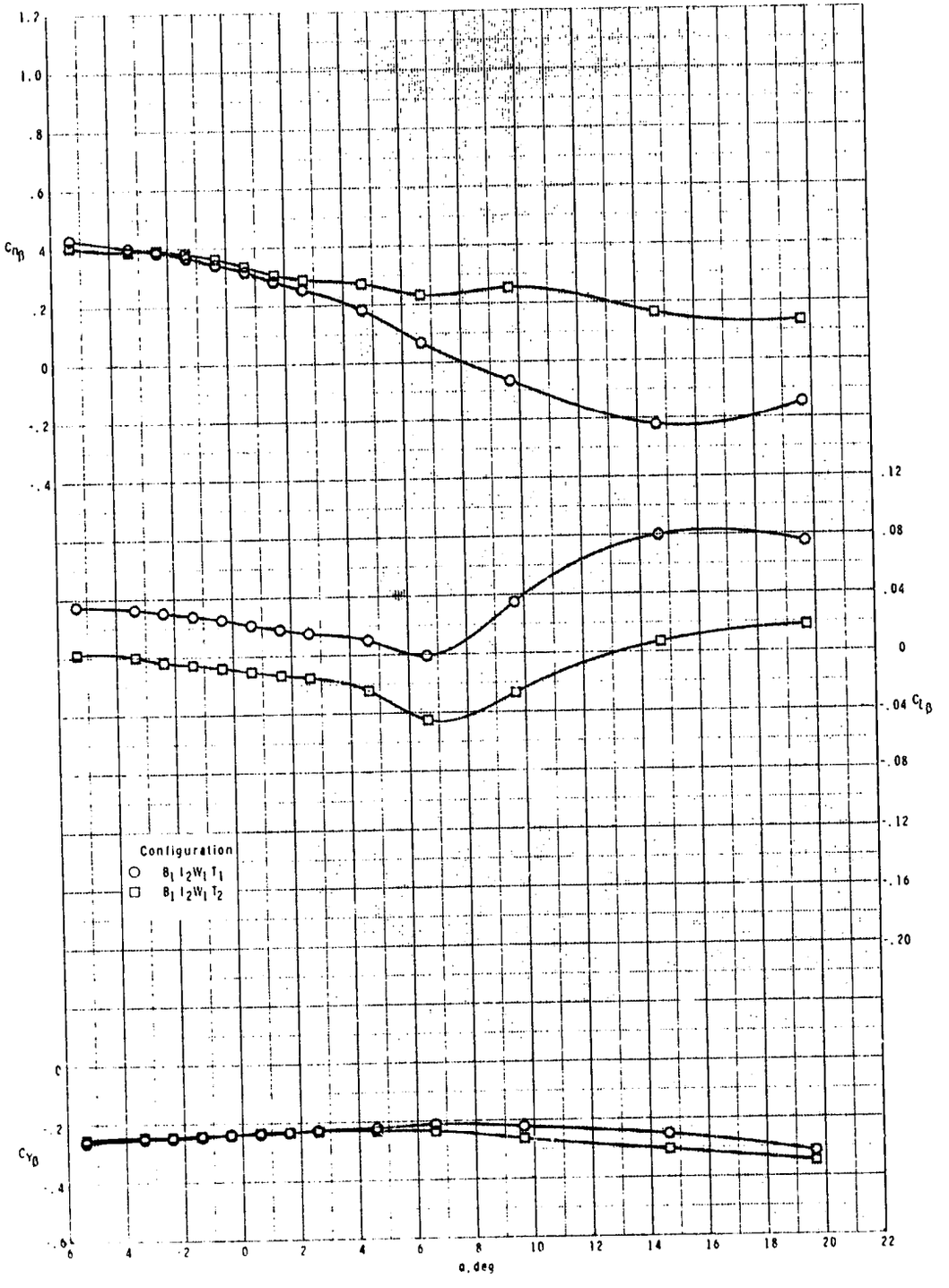

(d) M = 3.95.

Figure 30.- Concluded.

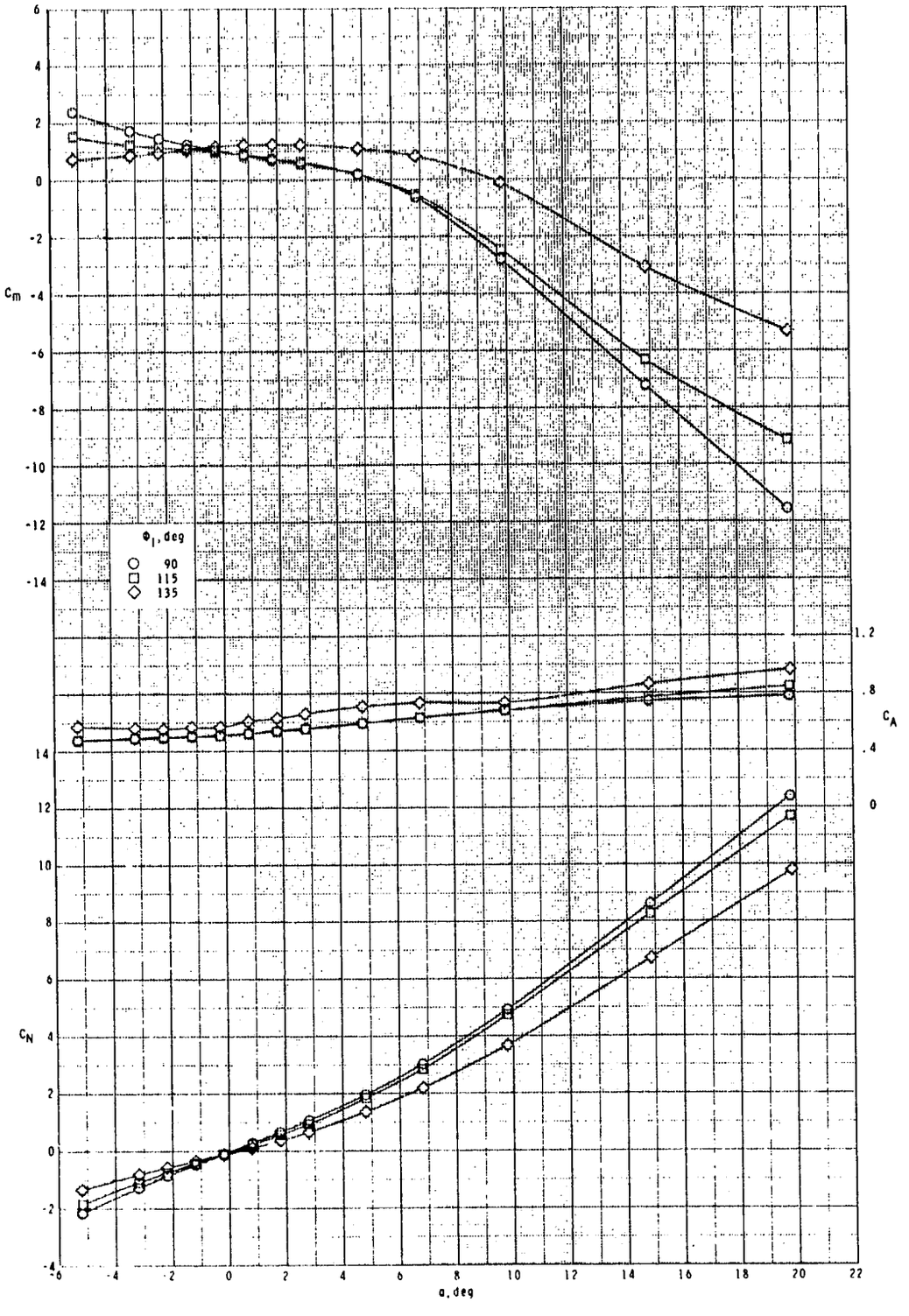

(a) M = 2.50.

Figure 31.- Effect of inlet orientation angle ϕ_I on longitudinal aerodynamic characteristics of configuration $B_1I_3T_1$ with $\delta_p = 0°$.

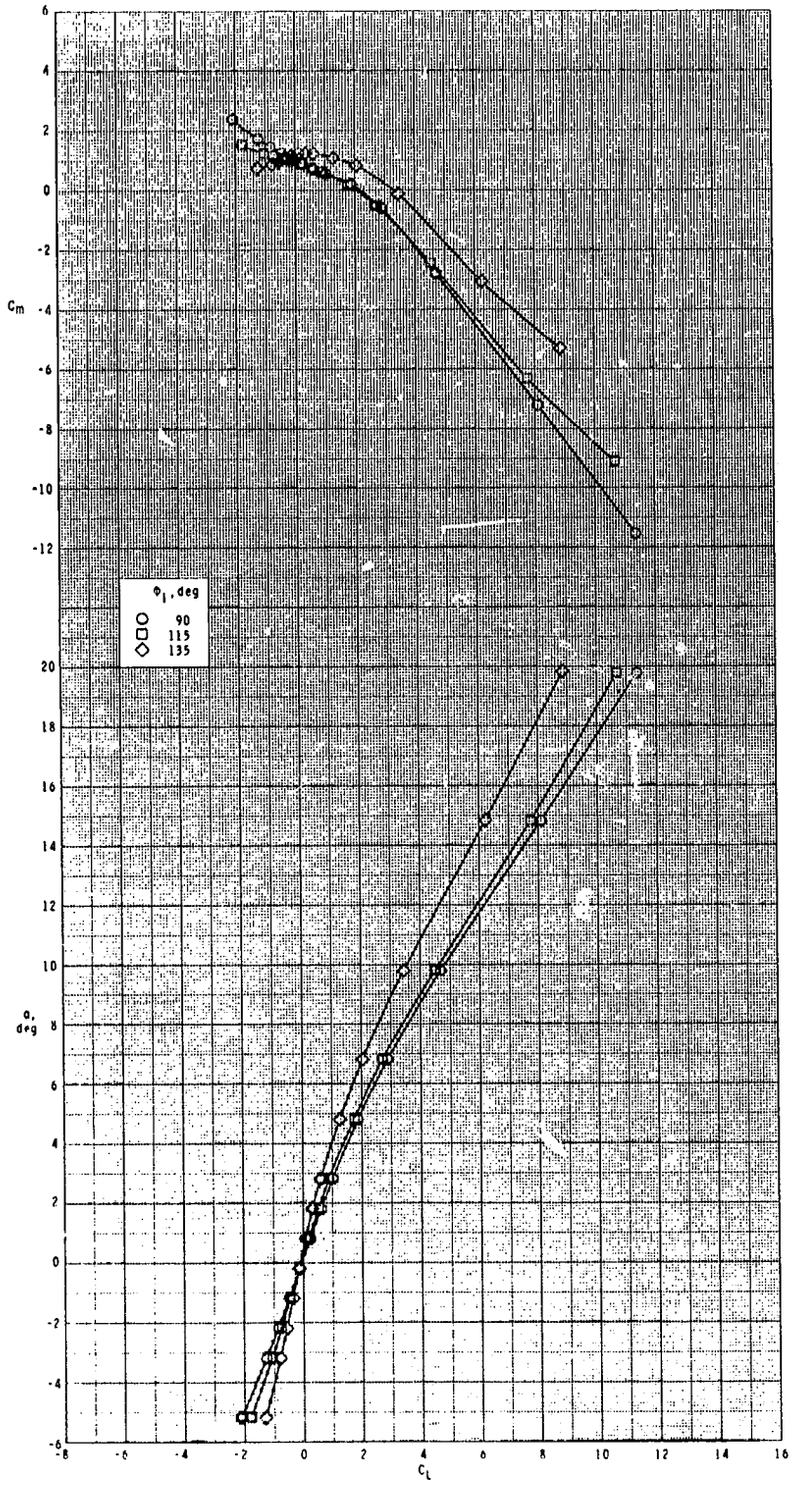

(a) Continued.

Figure 31.- Continued.

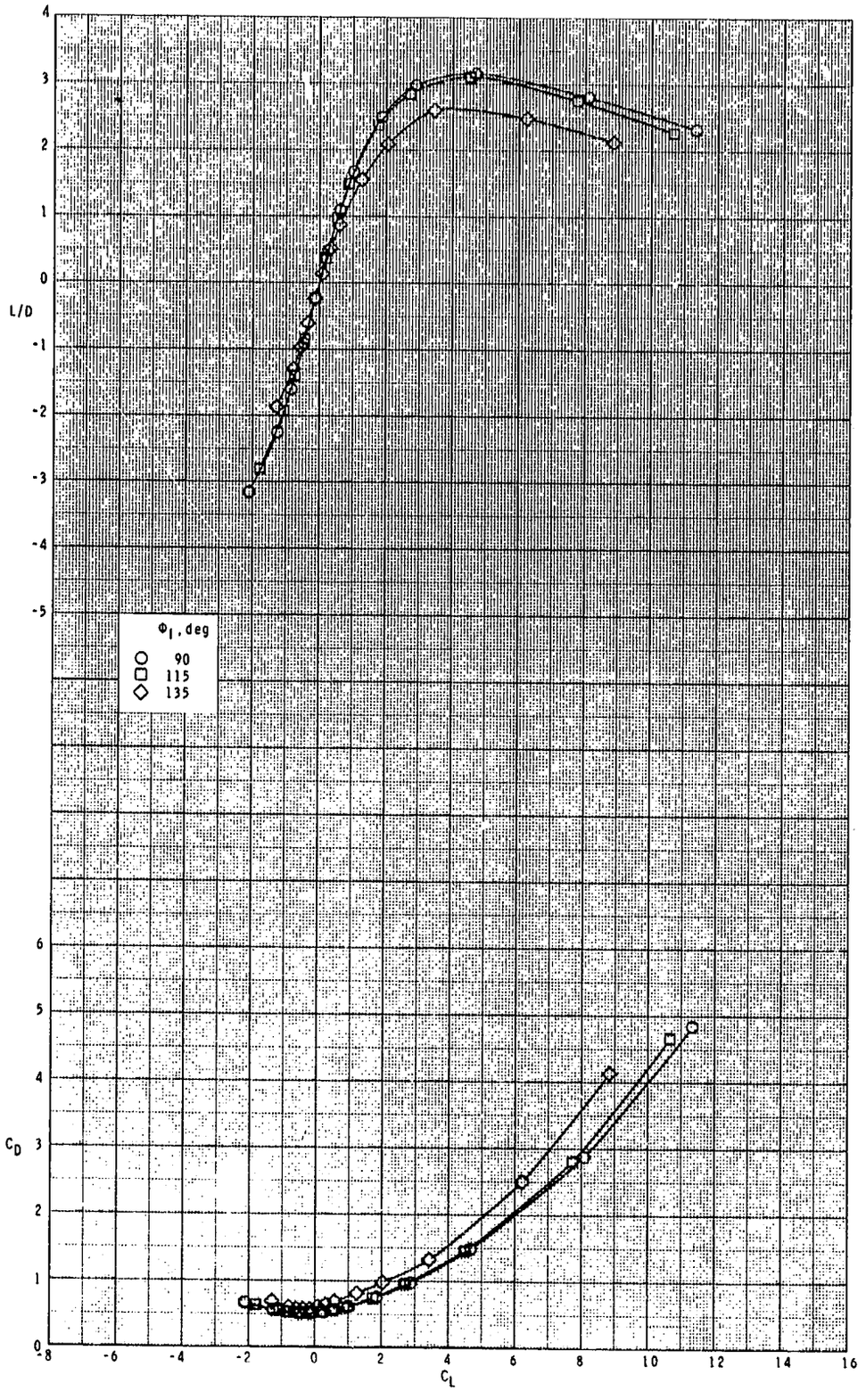

(a) Concluded.

Figure 31.- Continued.

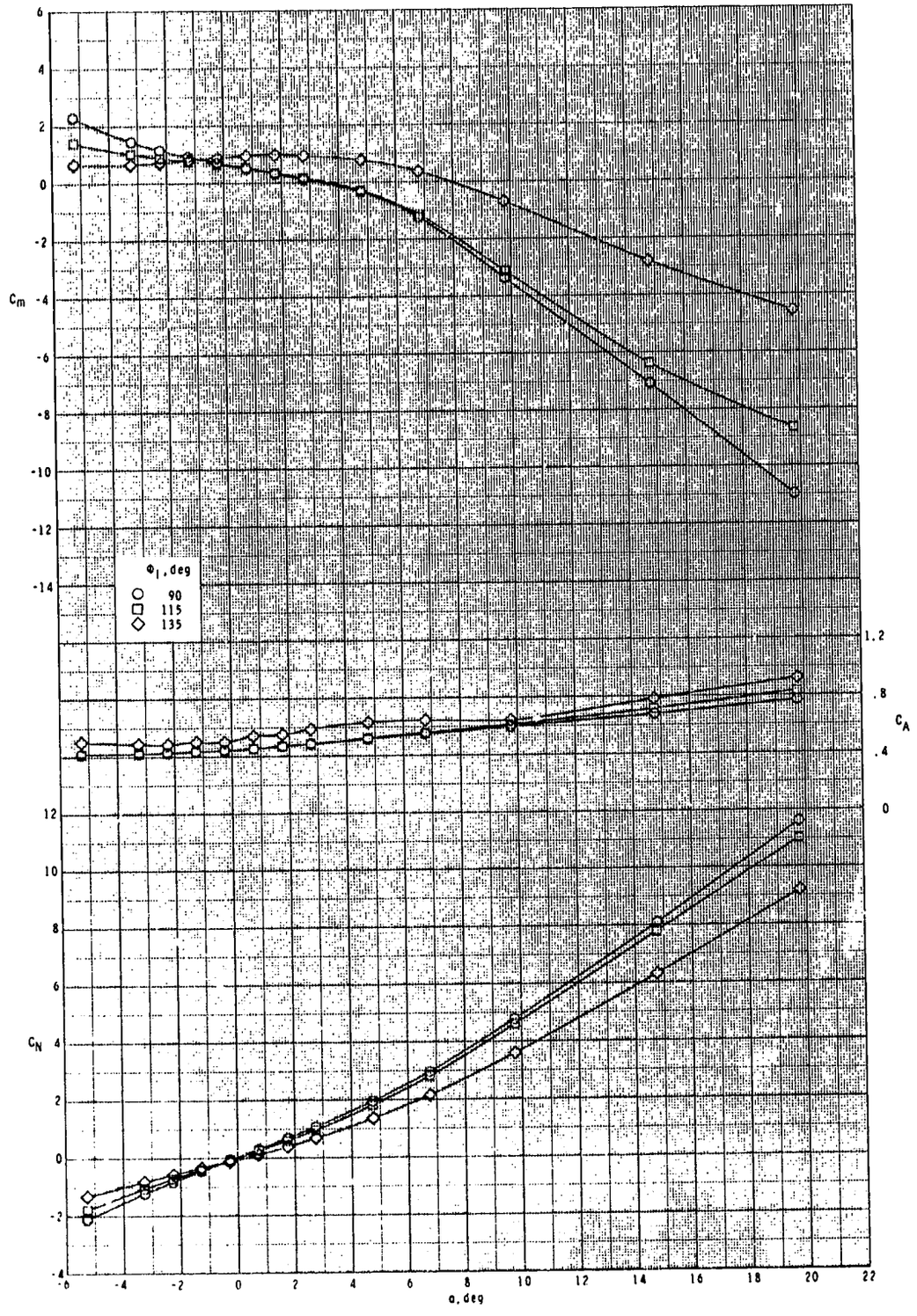

(b) M = 2.95.

Figure 31.- Continued.

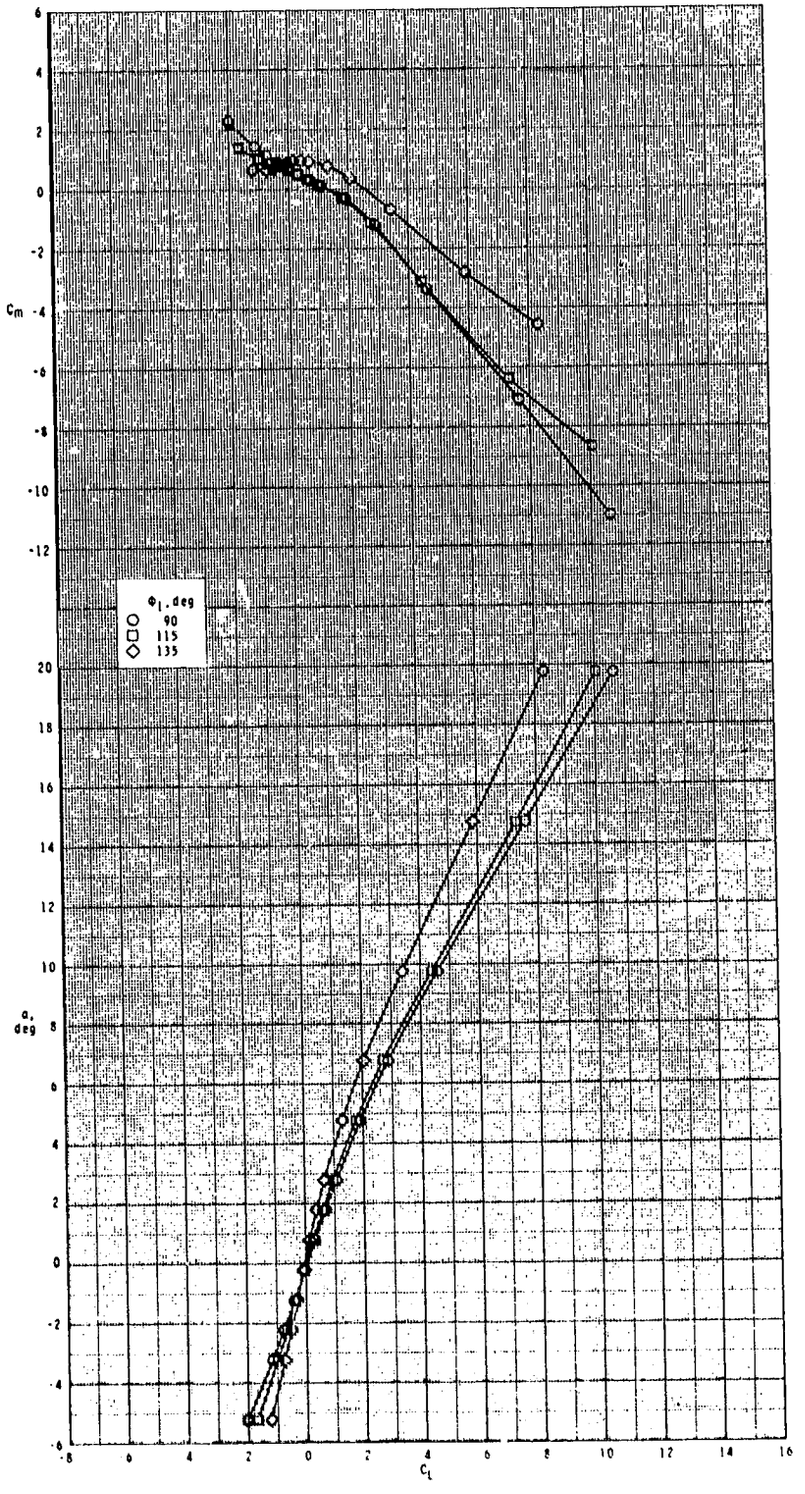

(b) Continued.

Figure 31.- Continued.

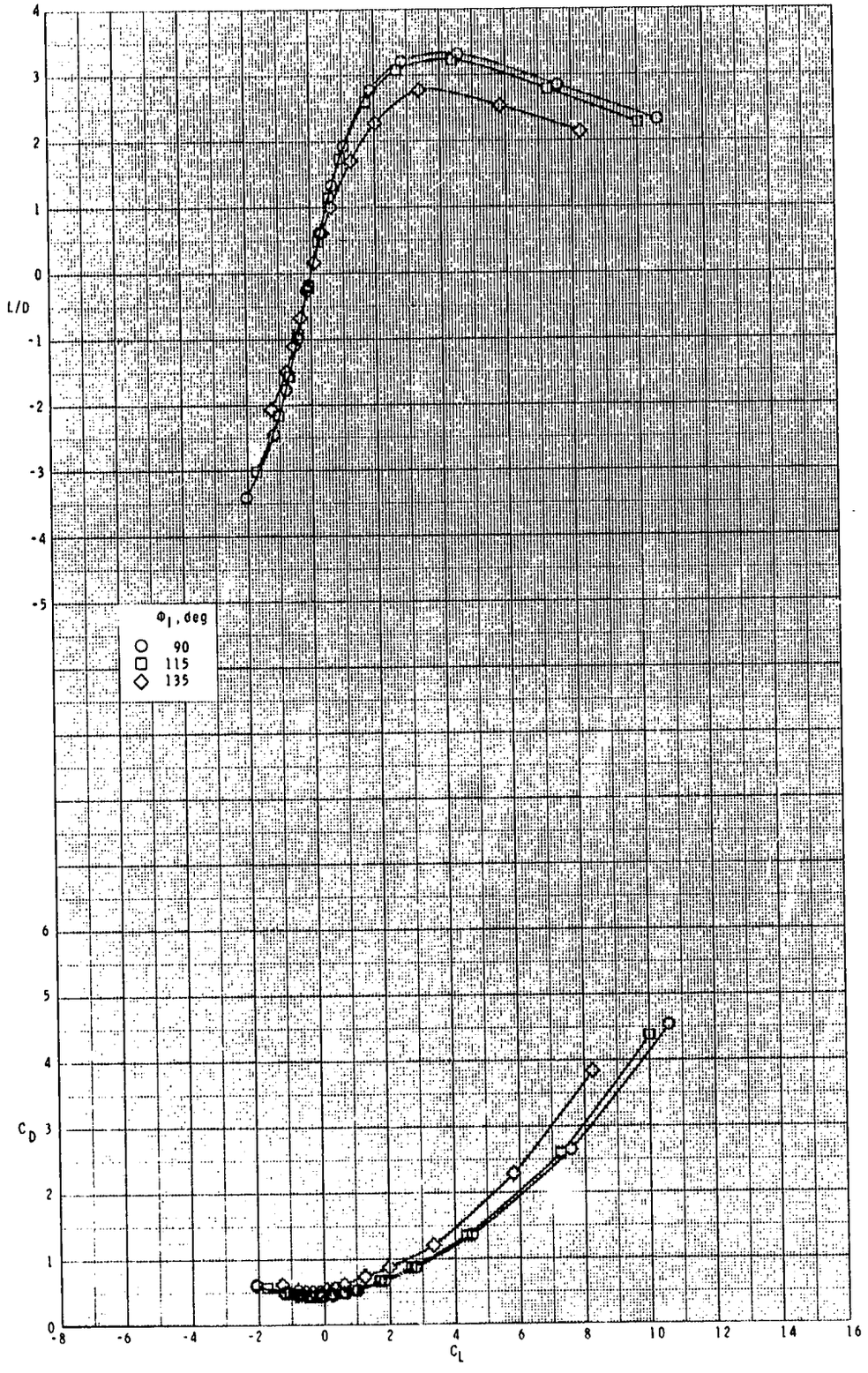

(b) Concluded.

Figure 31.- Continued.

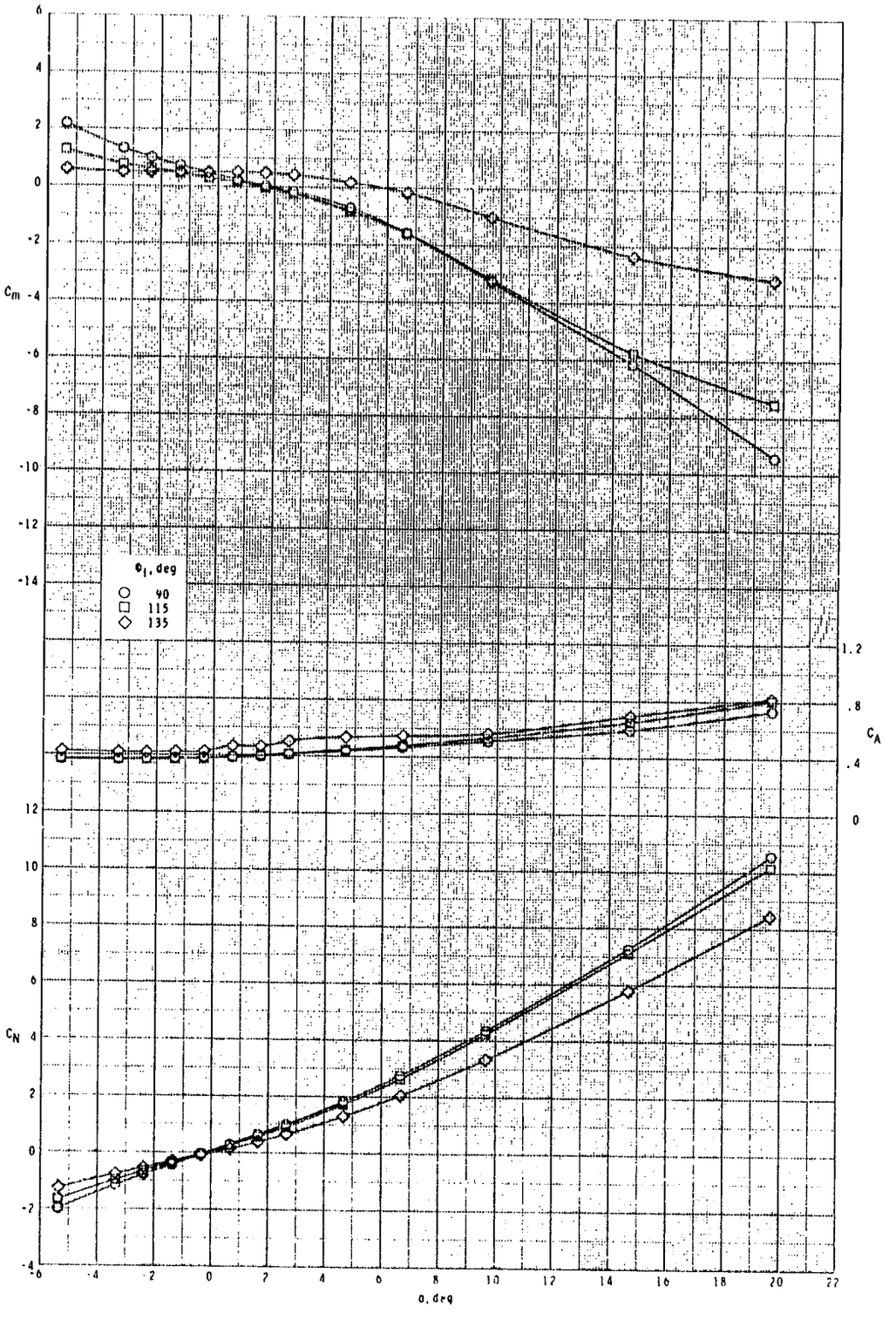

(c) M = 3.50.

Figure 31.- Continued.

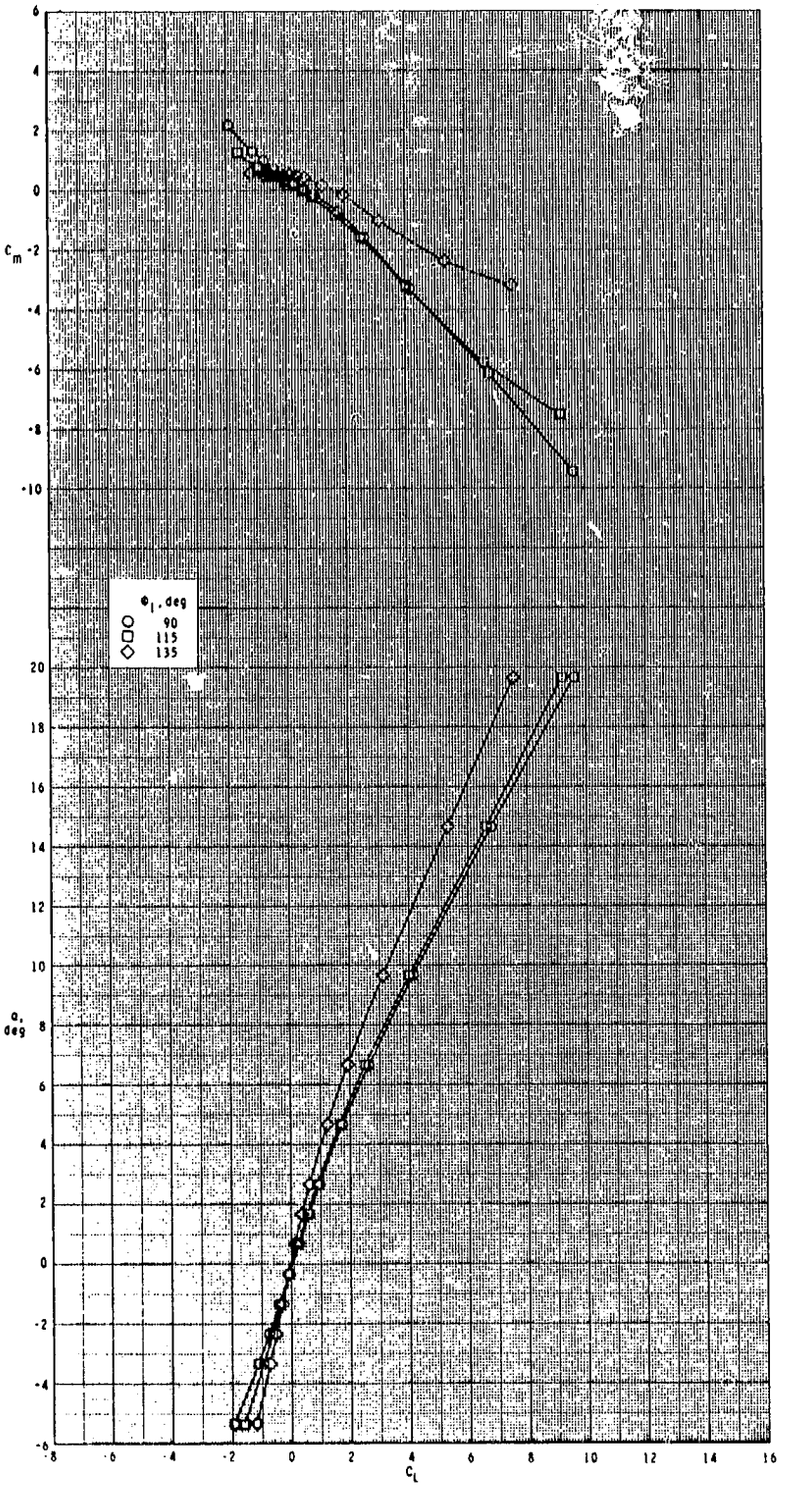

(c) Continued.

Figure 31.- Continued.

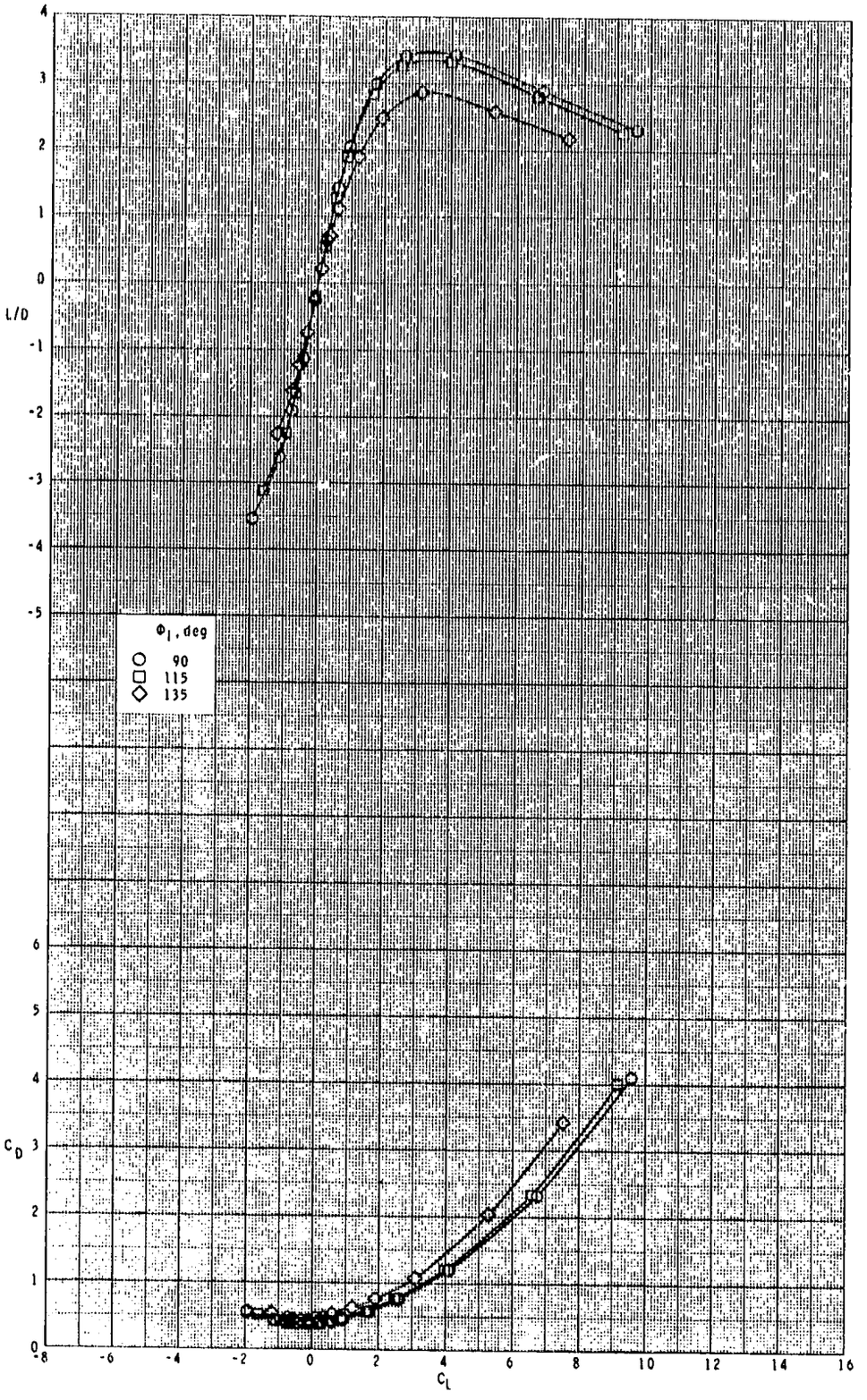

(c) Concluded.

Figure 31.- Continued.

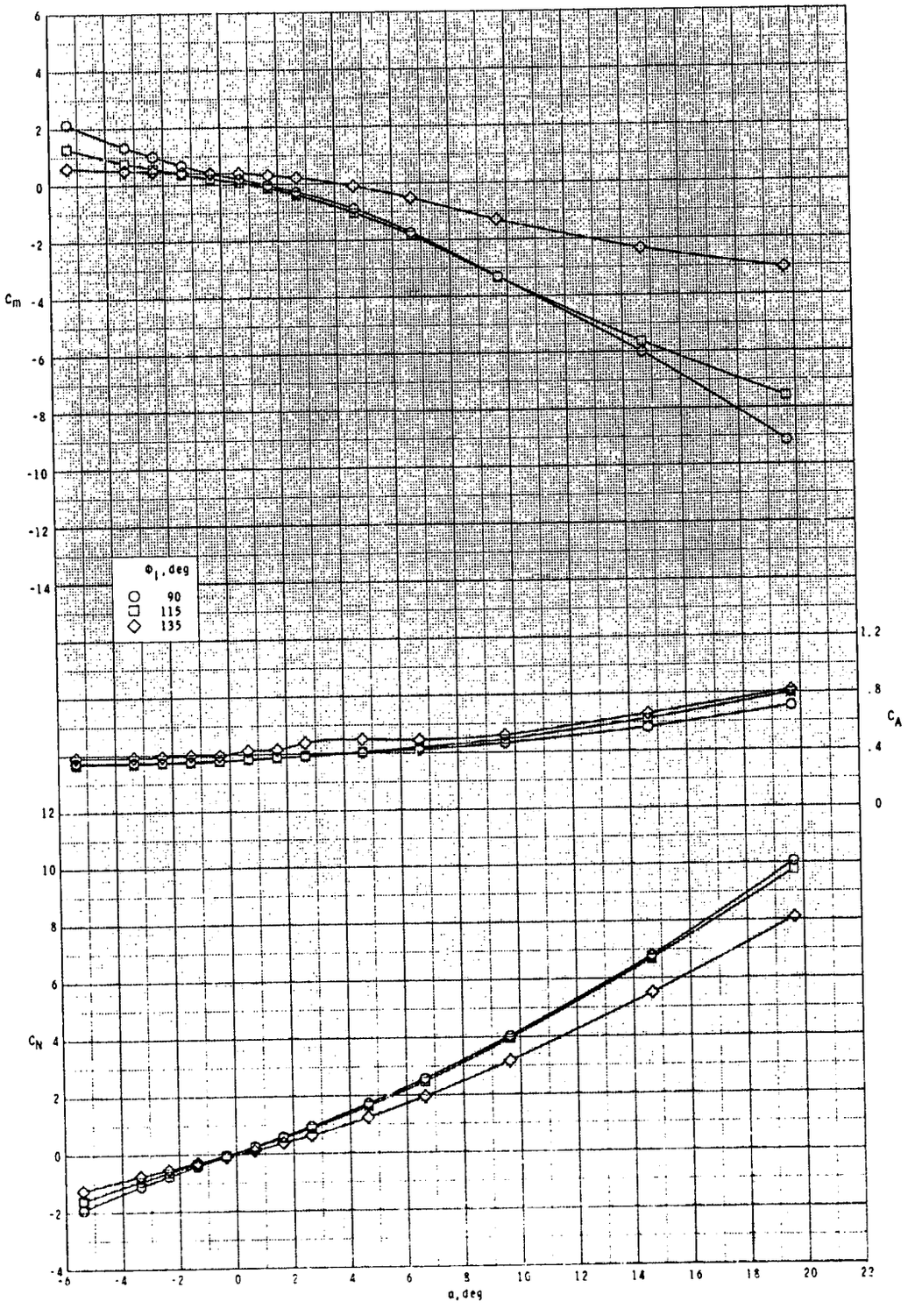

(d) M = 3.95.

Figure 31.- Continued.

C-4

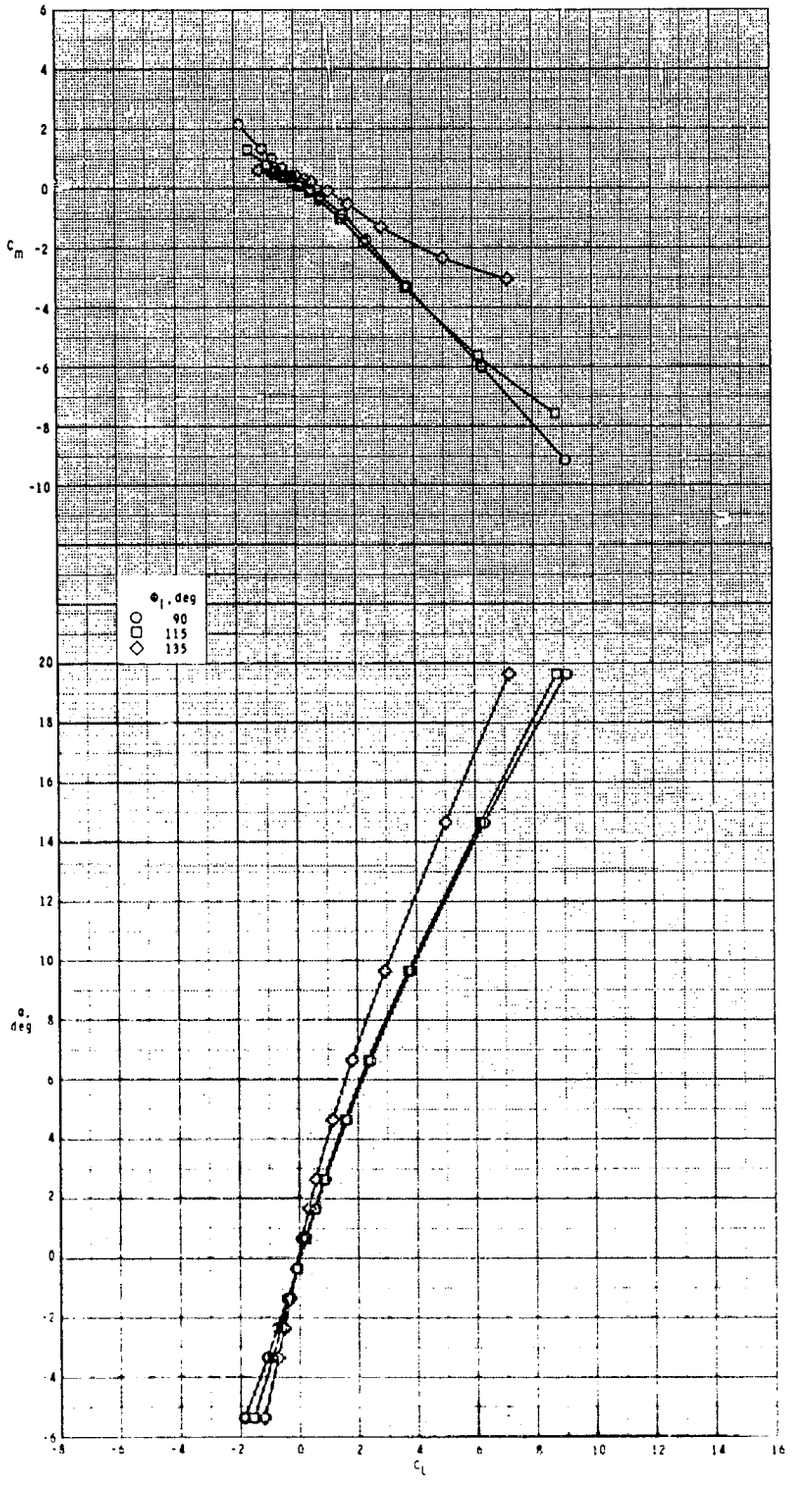

(d) Continued.

Figure 31.- Continued.

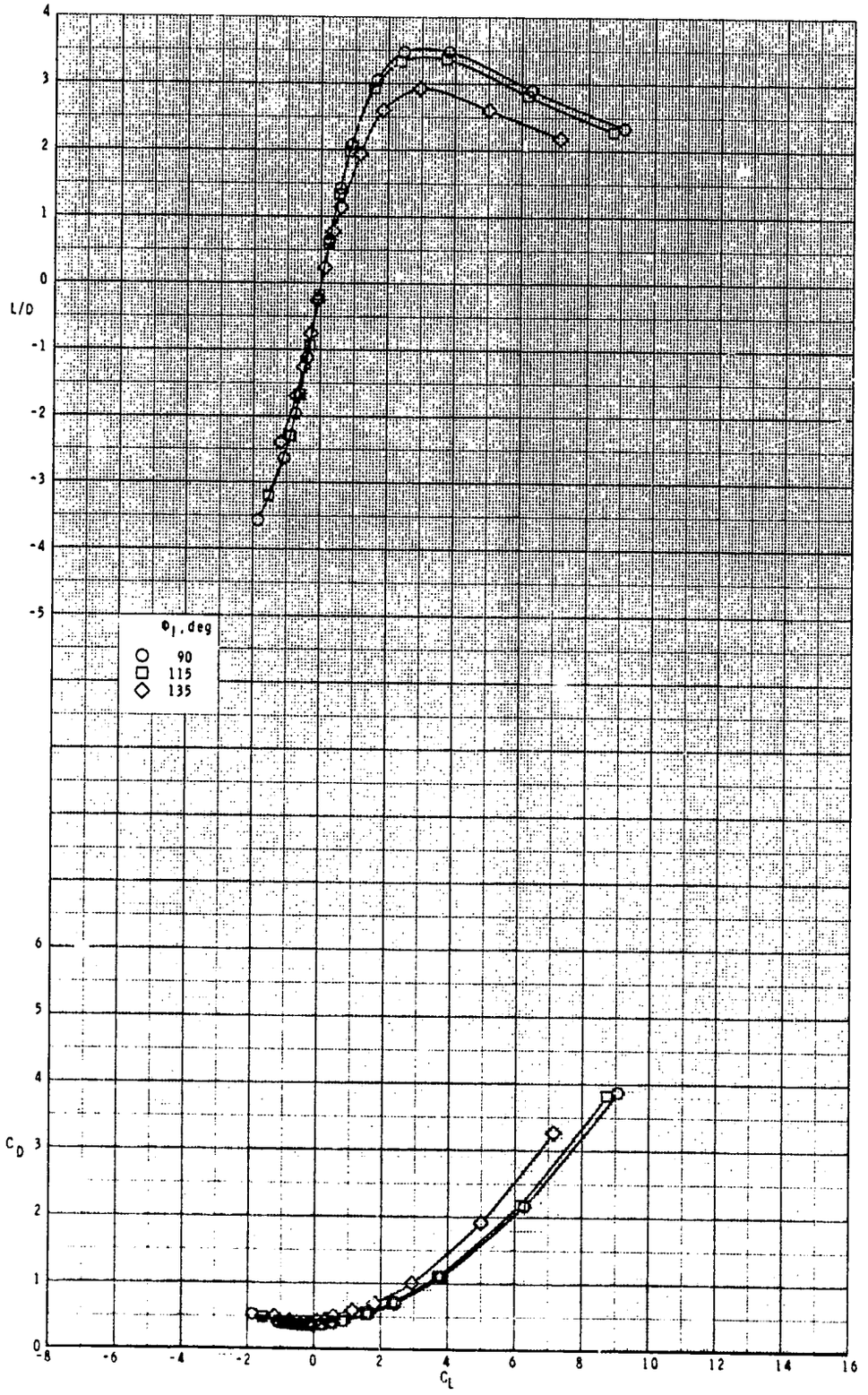

(d) Concluded.

Figure 31.- Concluded.

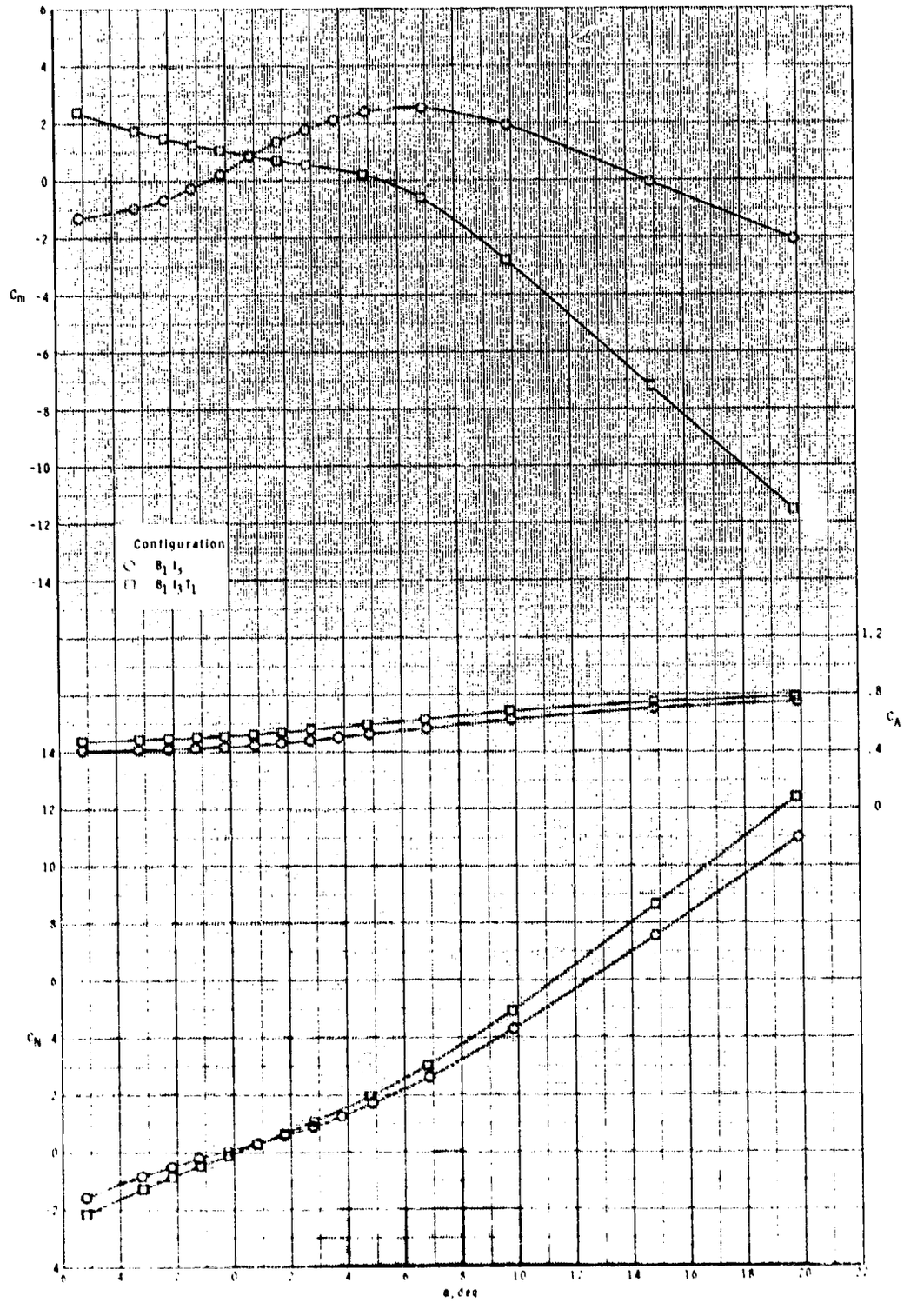

(a) M = 2.50.

Figure 32.- Effect of various model components on longitudinal aerodynamic characteristics for two-dimensional extended inlets with $\phi_I = 90°$ and $\delta_p = 0°$.

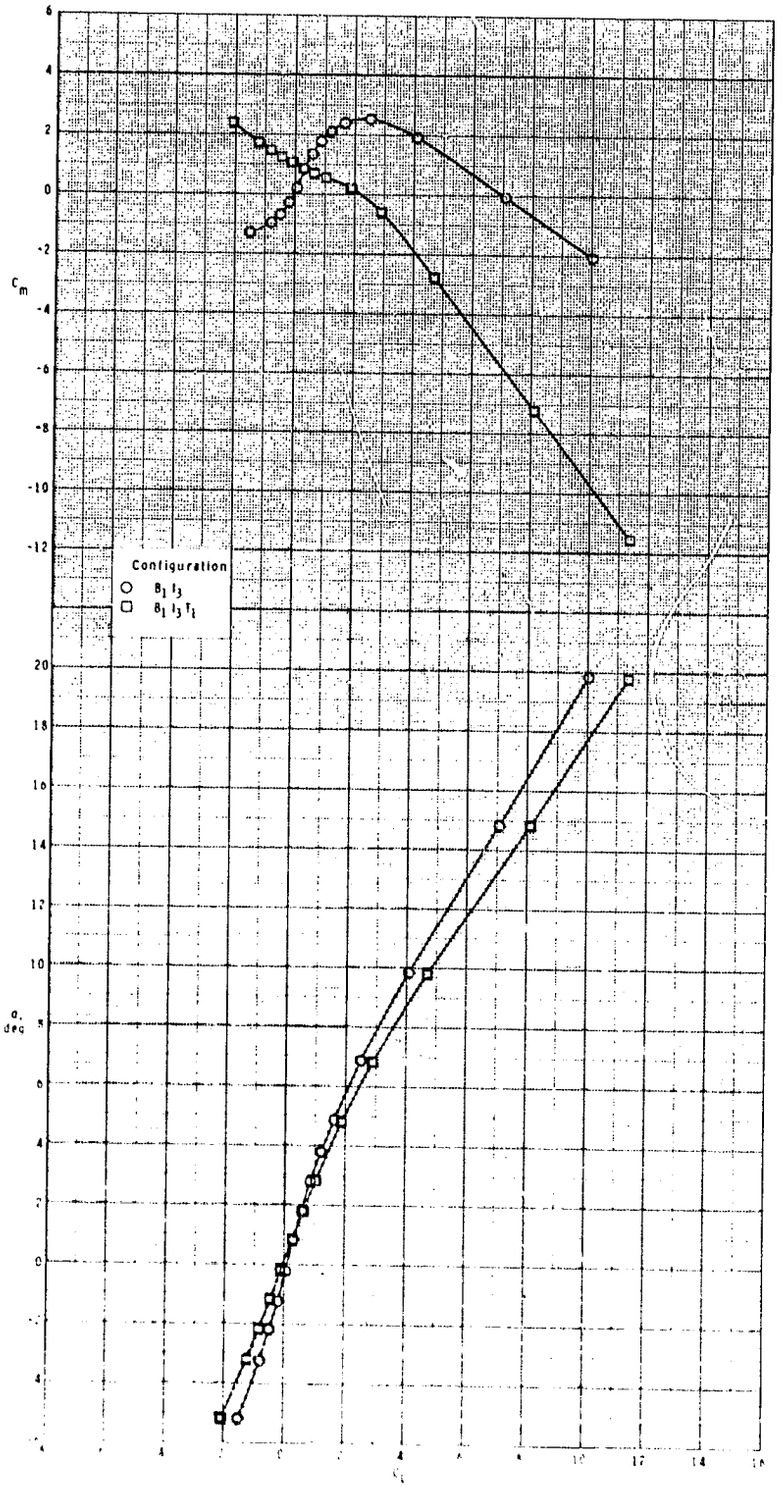

(a) Continued.

Figure 32.- Continued.

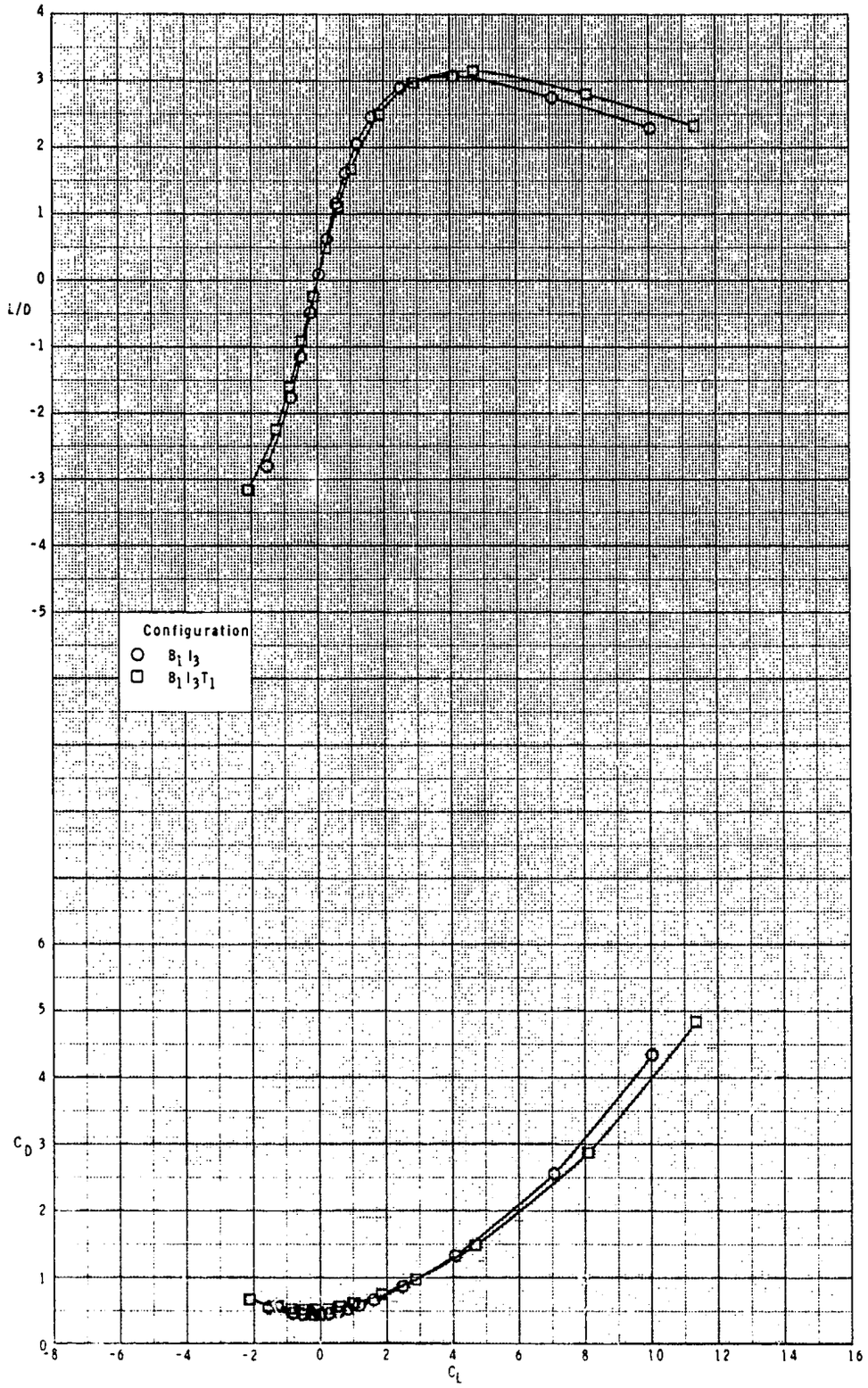

(a) Concluded.

Figure 32.- Continued.

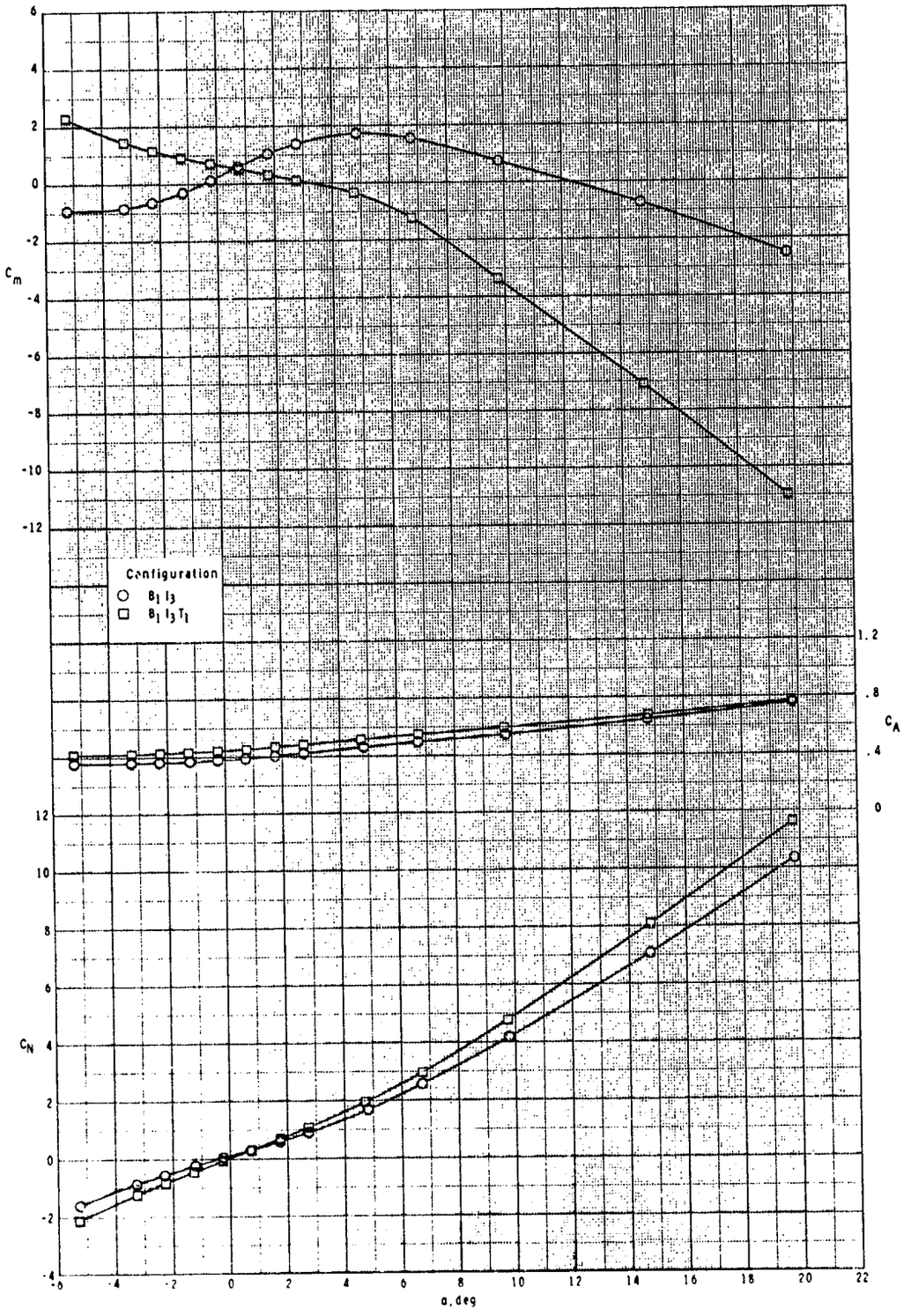

(b) M = 2.95.

Figure 32.- Continued.

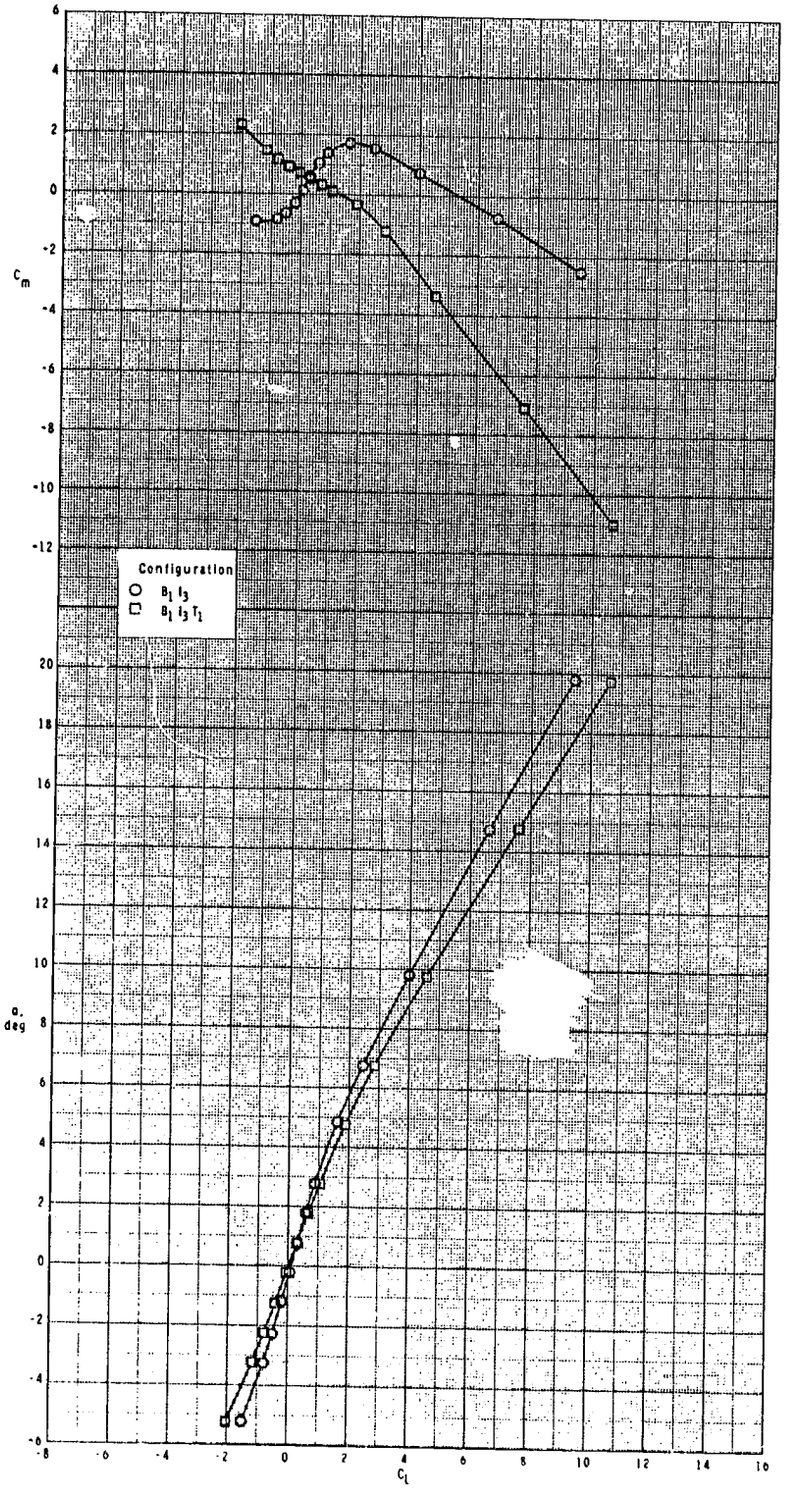

(b) Continued.

Figure 32.- Continued.

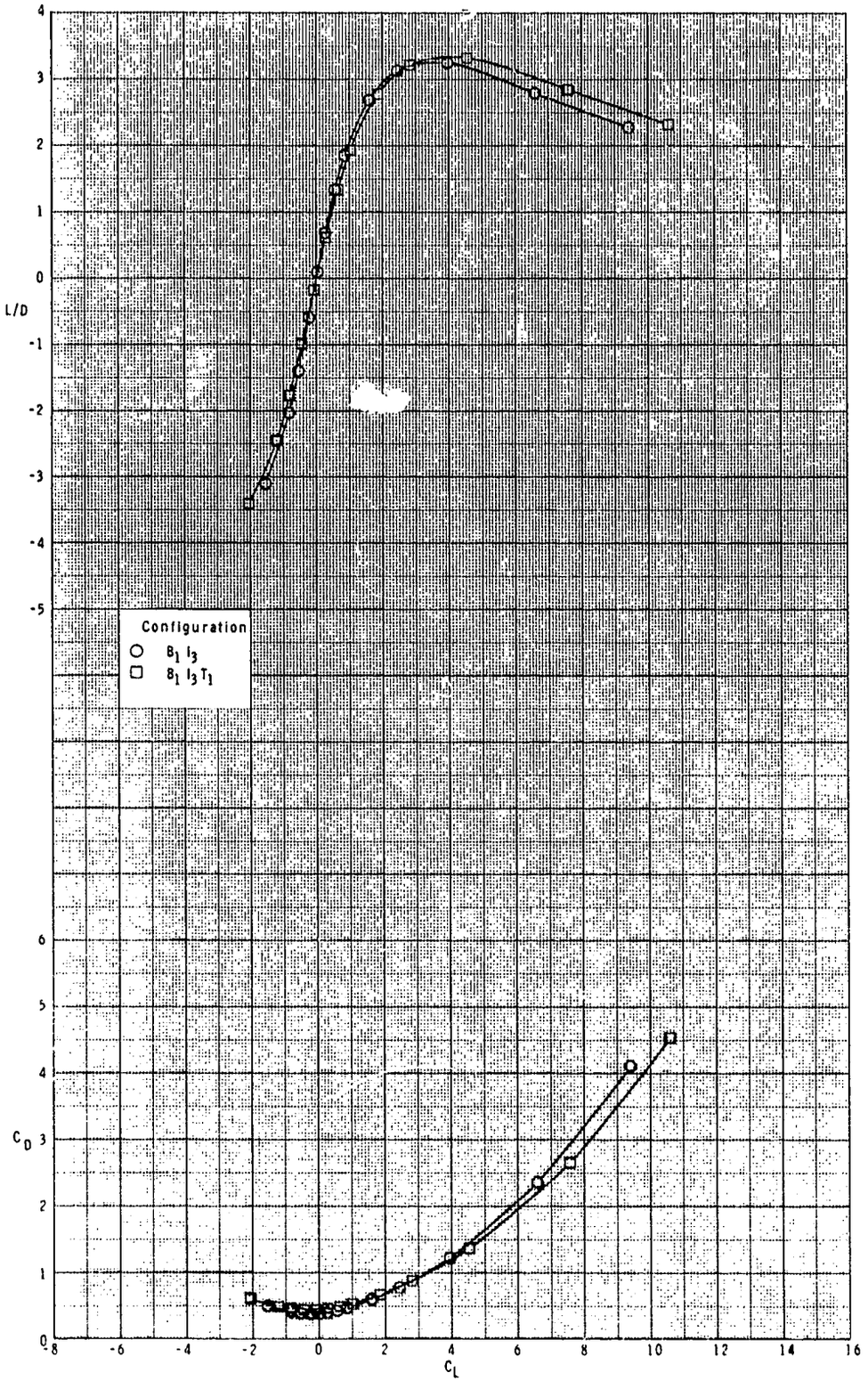

(b) Concluded.

Figure 32.- Continued.

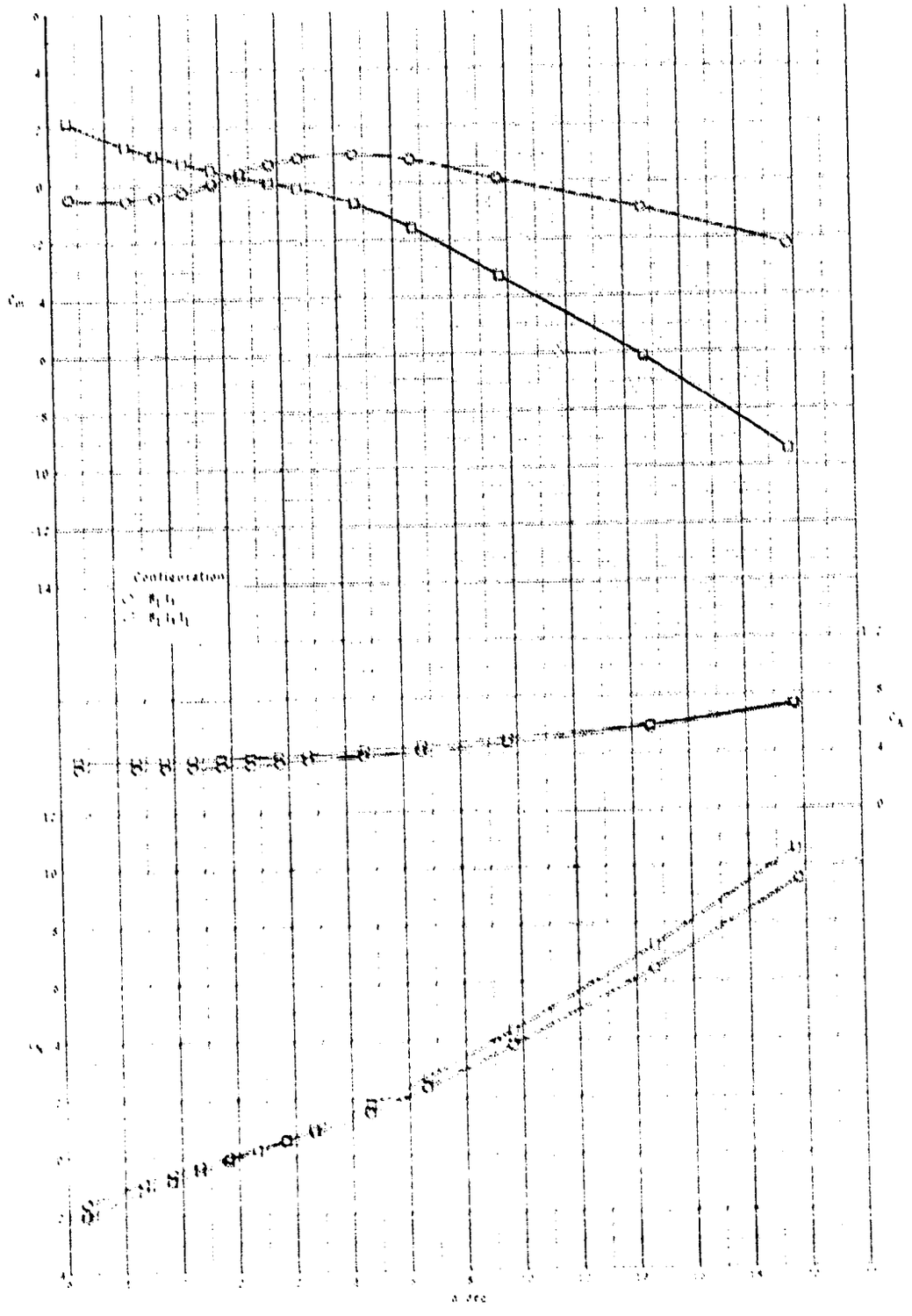

(c) M = 3.50.

Figure 37.- Continued.

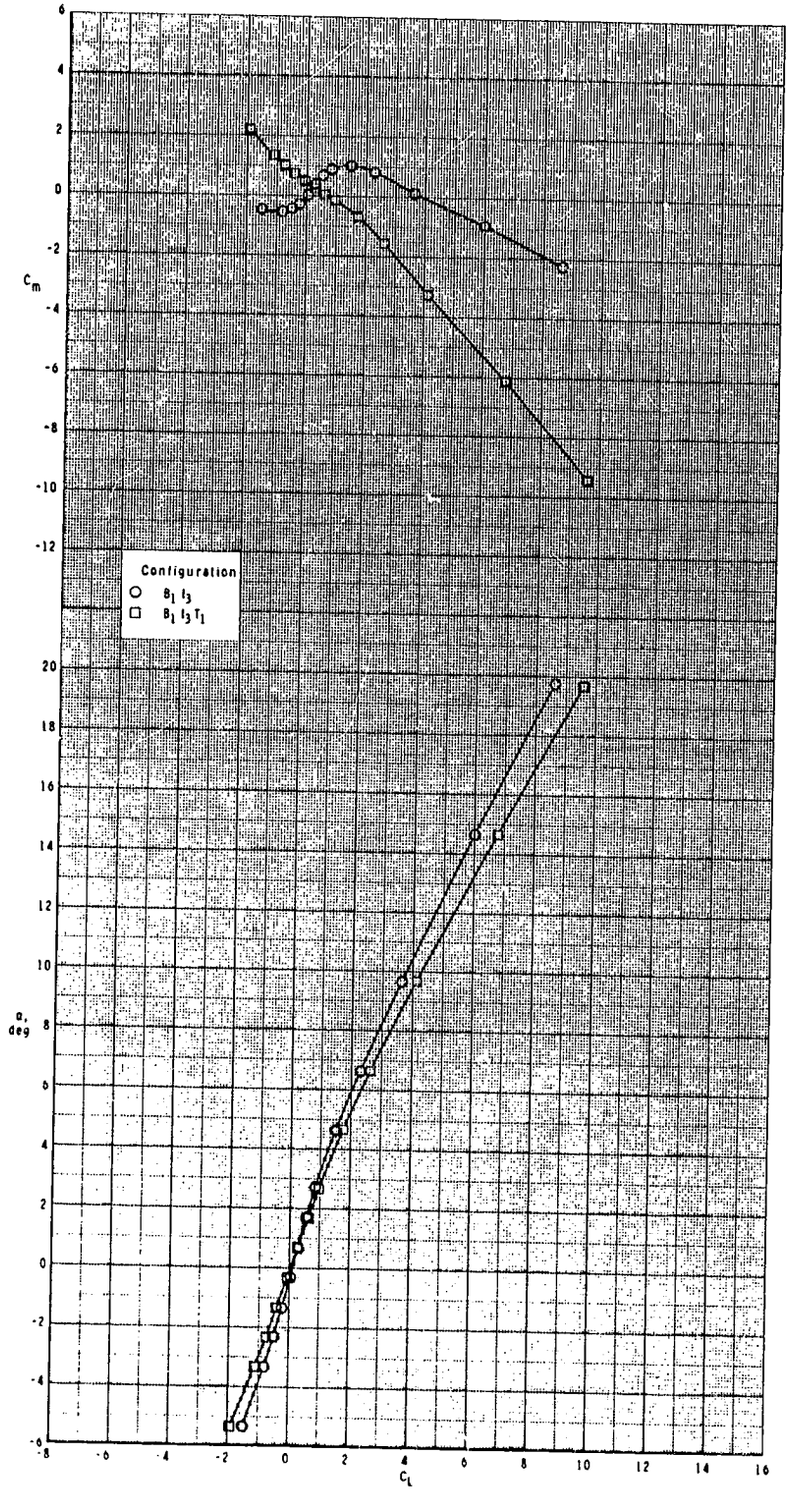

(c) Continued.

Figure 32.- Continued.

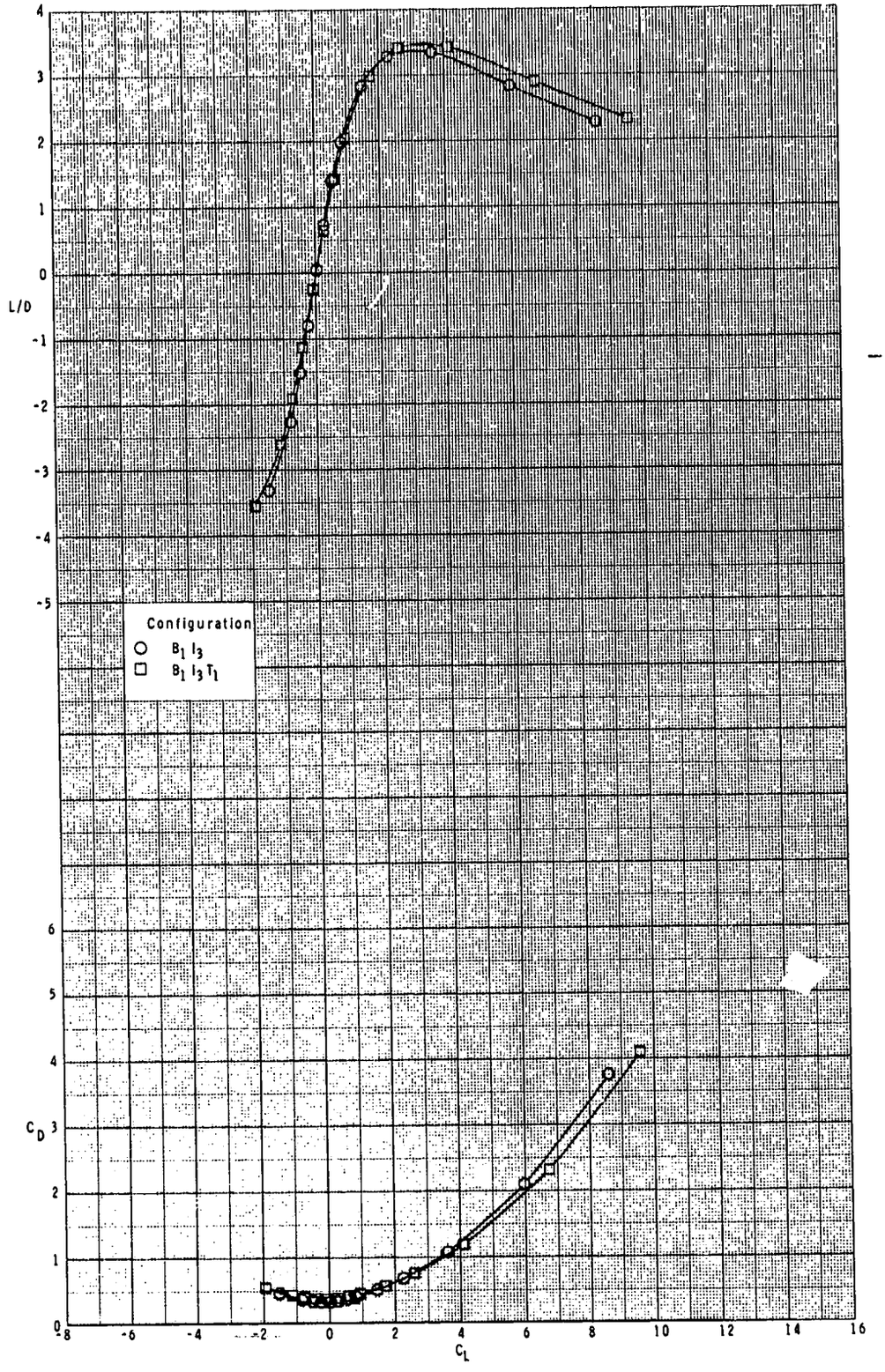

(c) Concluded.

Figure 32.- Continued.

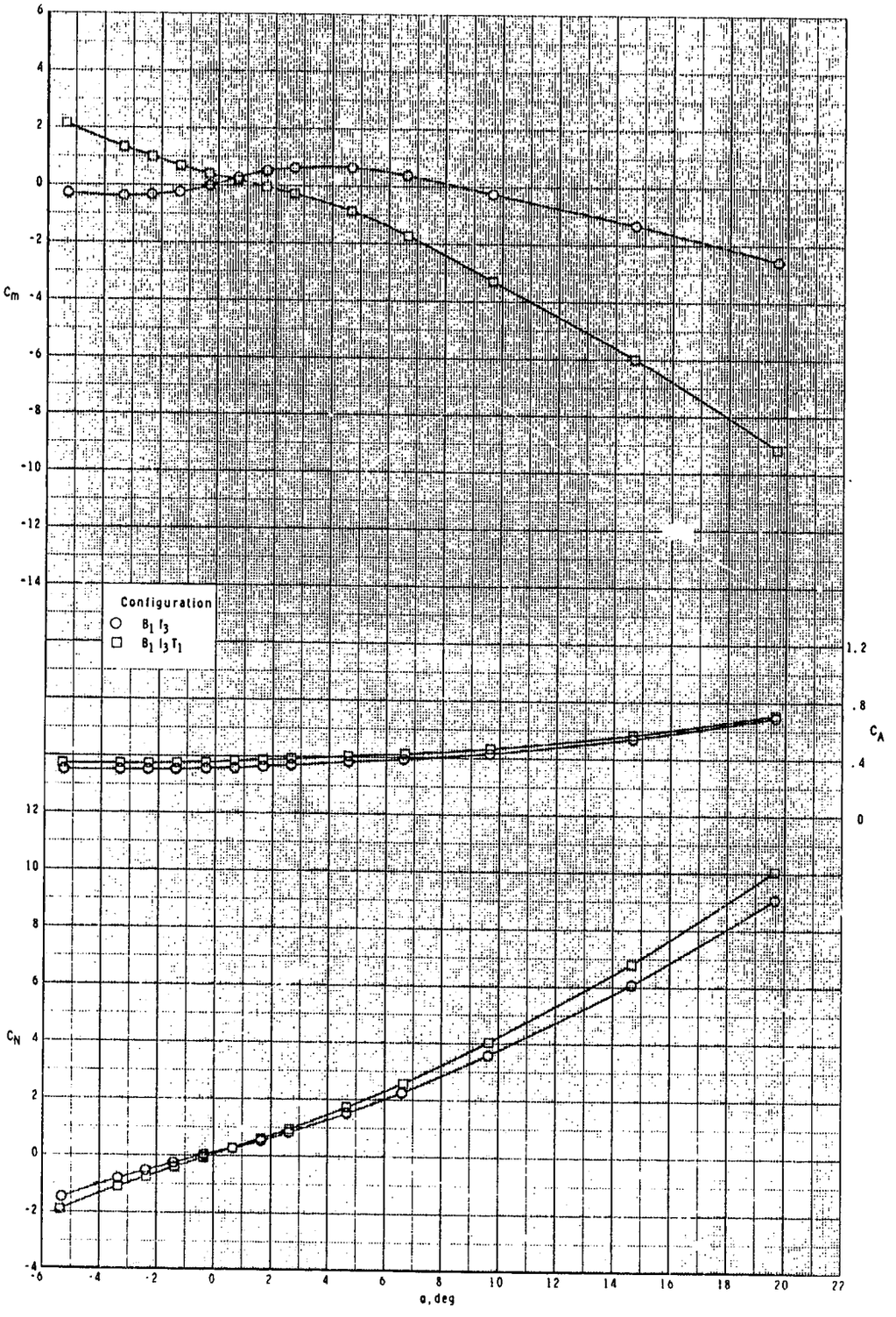

(d) M = 3.95.

Figure 32.- Continued.

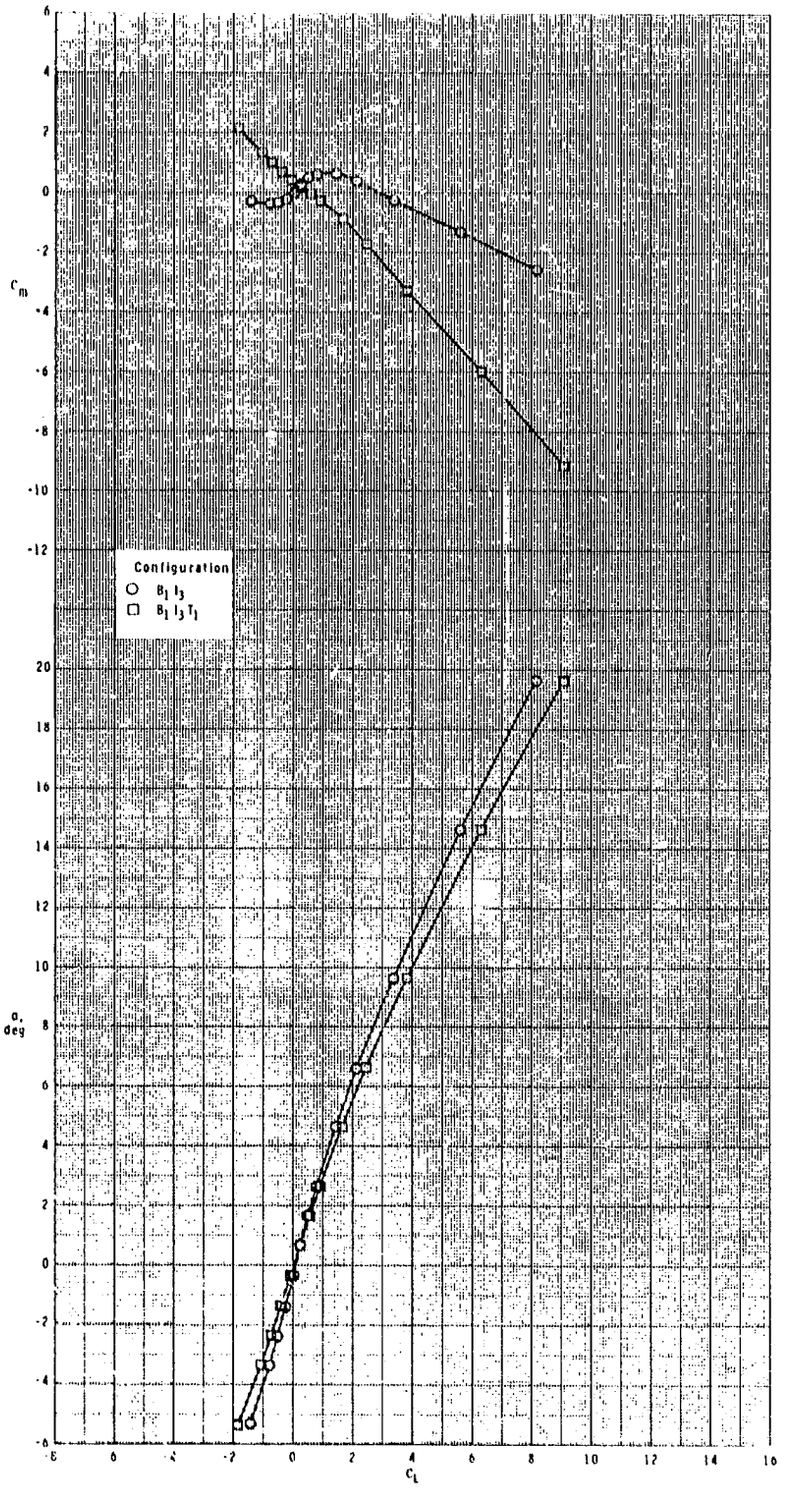

(d) Continued.

Figure 32.- Continued.

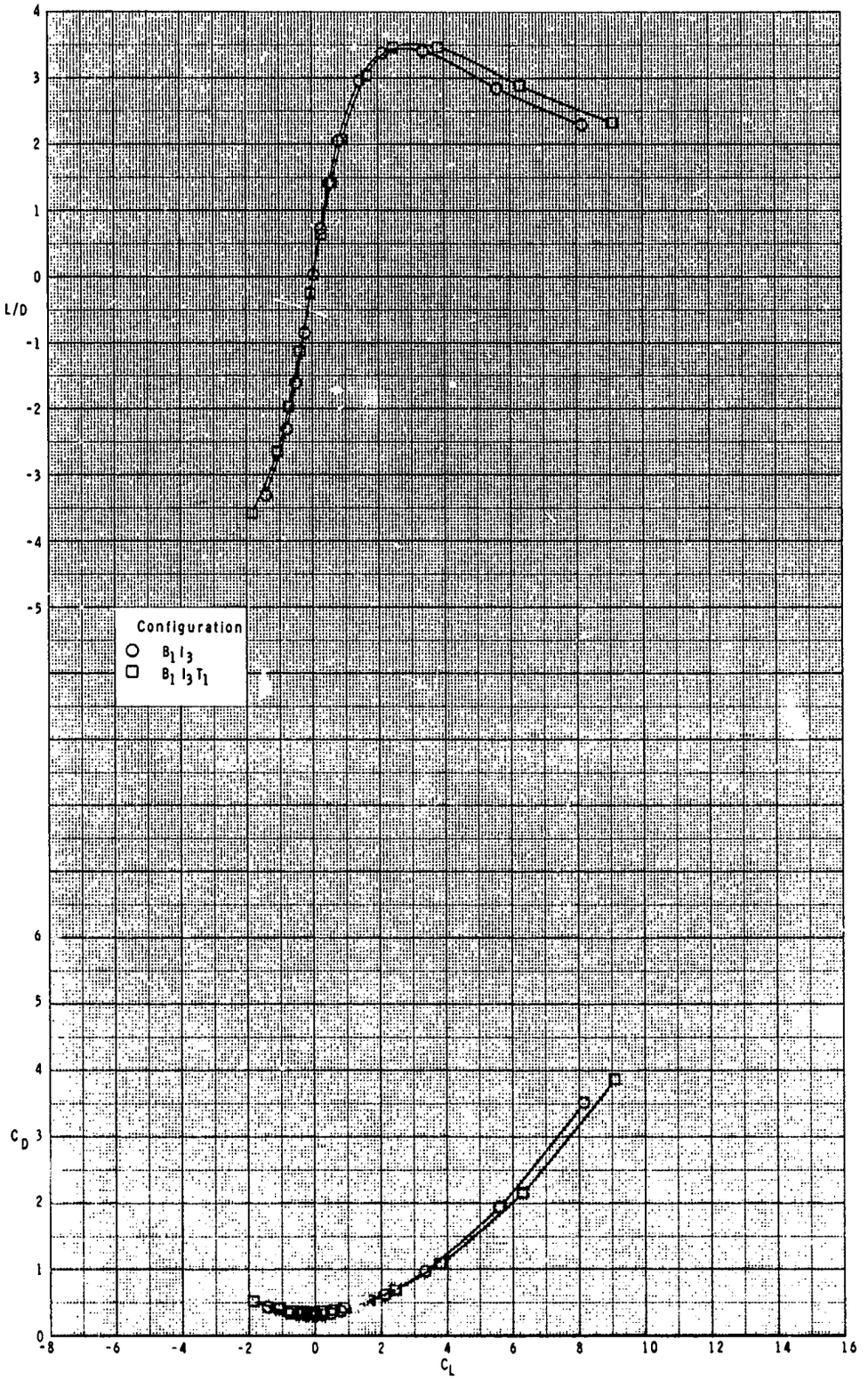

(d) Concluded.

Figure 32. Concluded.

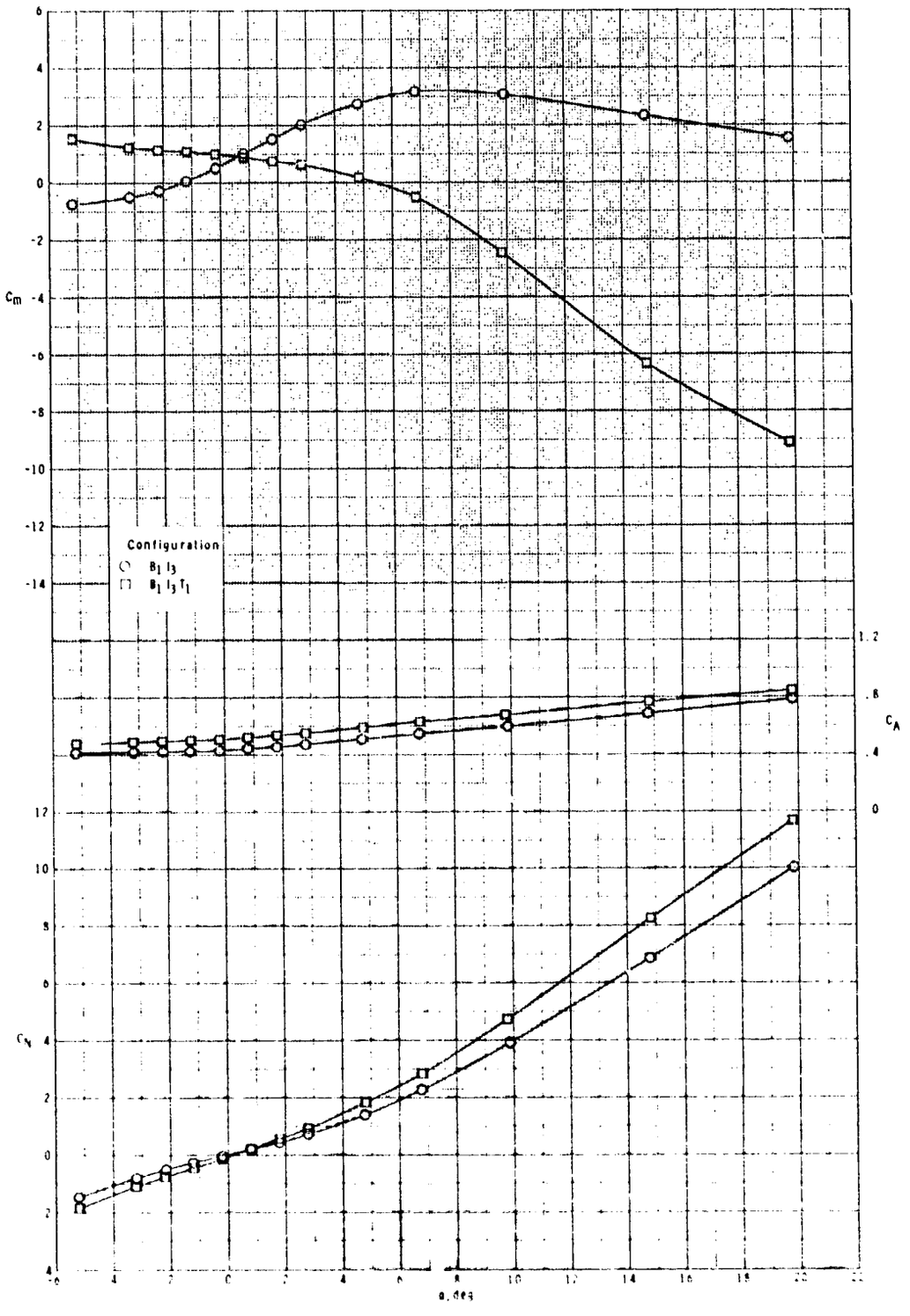

(a) M = 2.50.

Figure 33.- Effect of various model components on longitudinal aerodynamic characteristics for two-dimensional extended inlets with ϕ_I = 115° and δ_p = 0°.

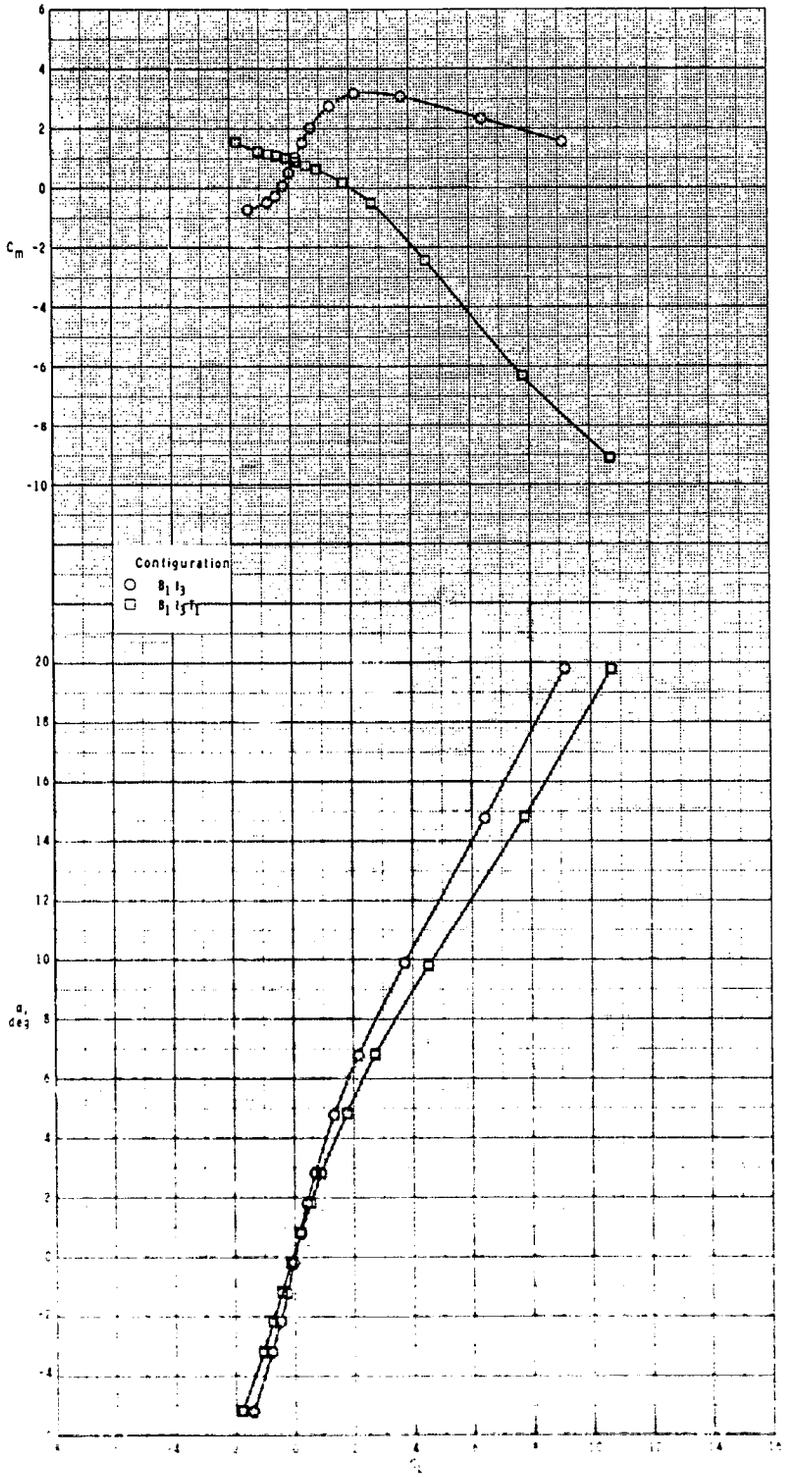

(a) Continued.

Figure 33.- Continued.

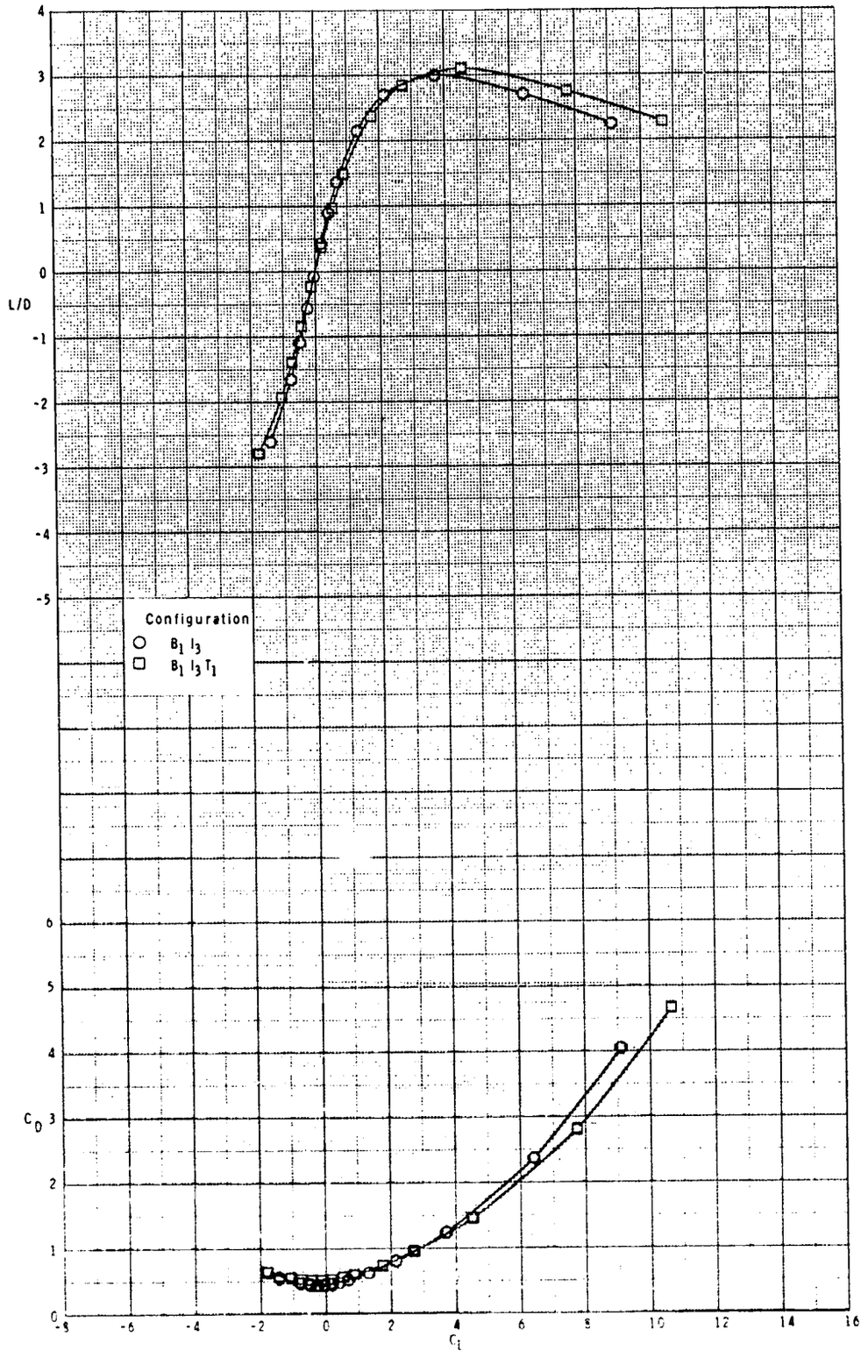

(a) Concluded.

Figure 33.- Continued.

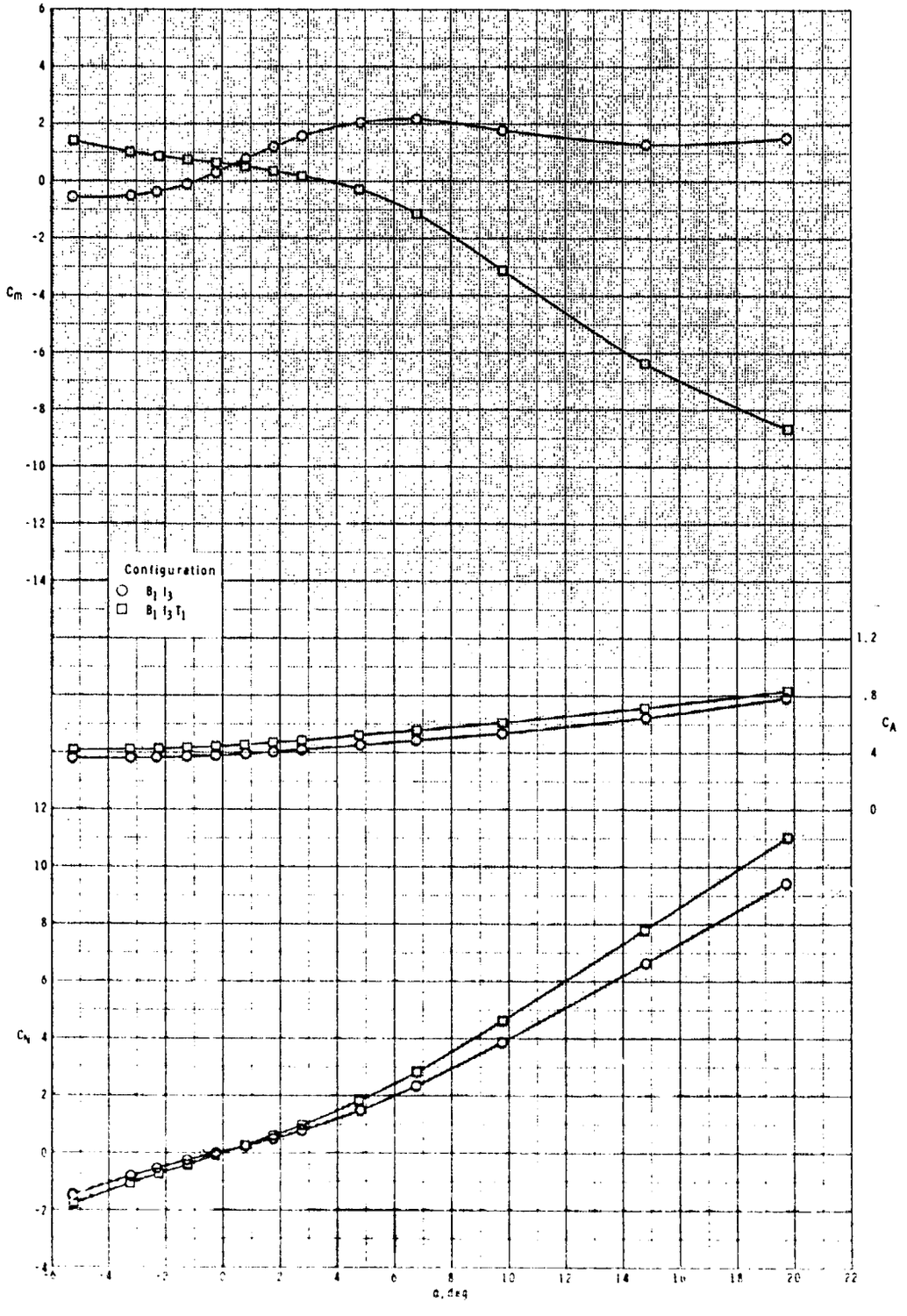

(b) M = 2.95.

Figure 33.- Continued.

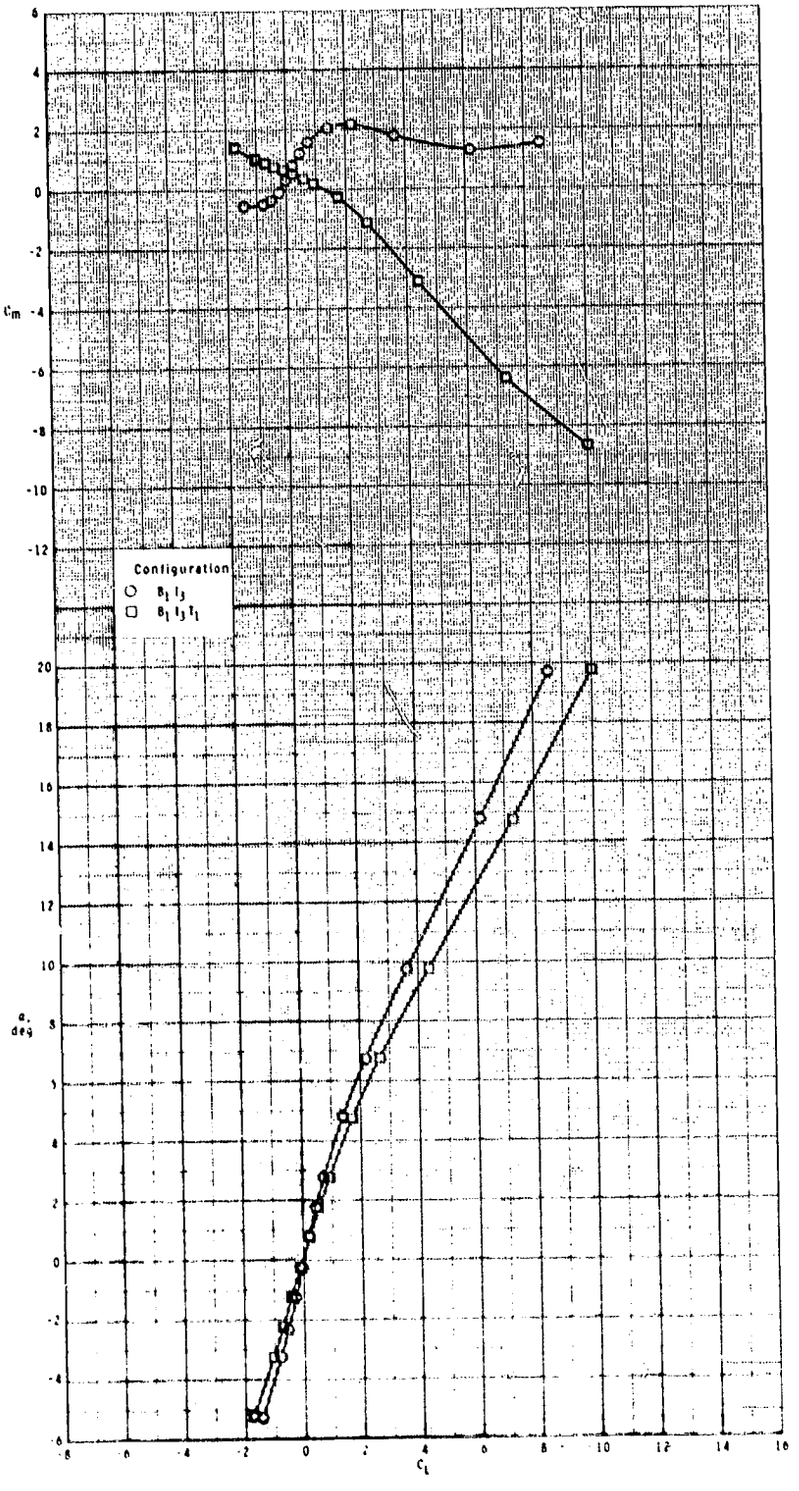

(b) Continued.

Figure 33.- Continued.

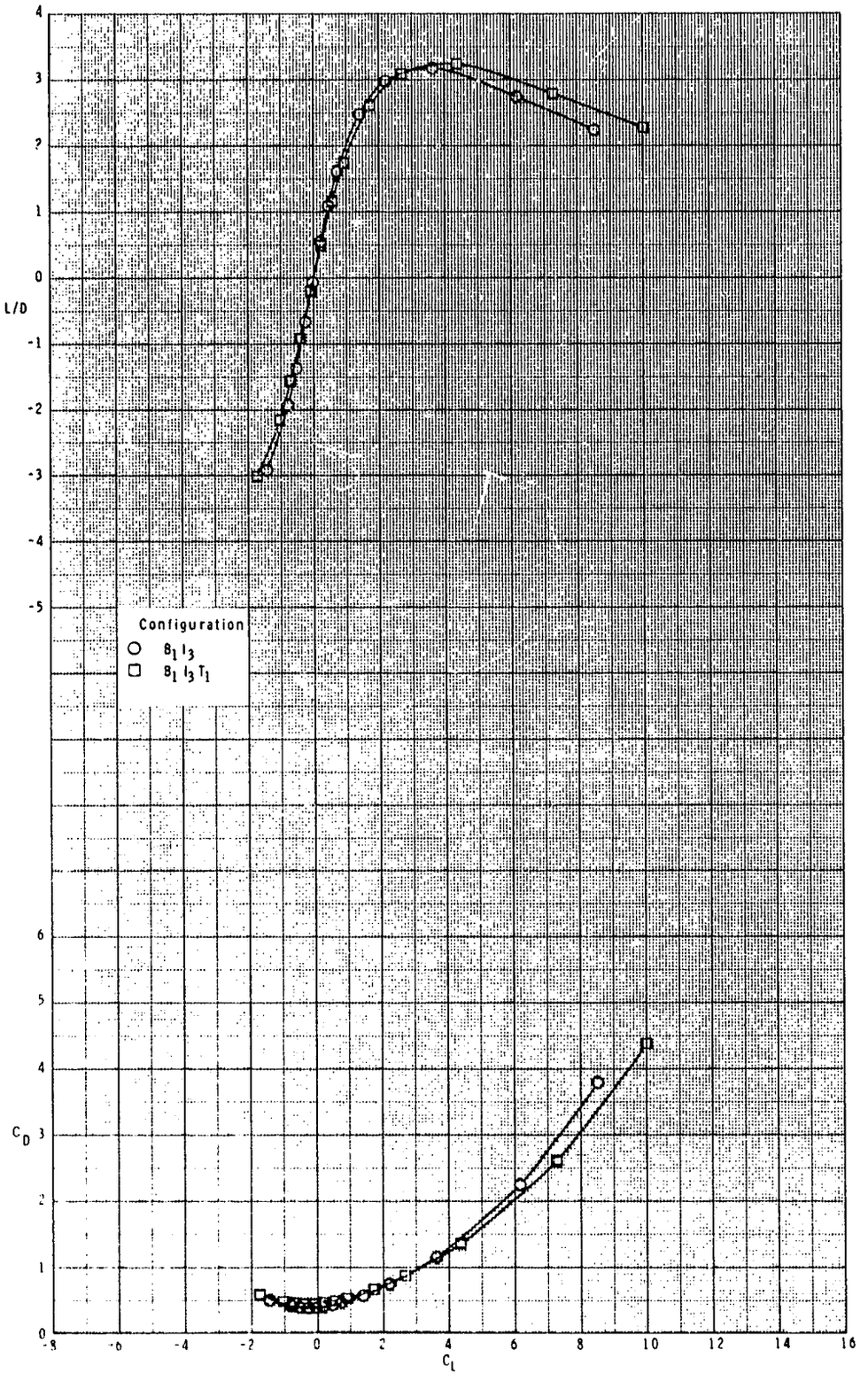

(b) Concluded.

Figure 33.- Continued.

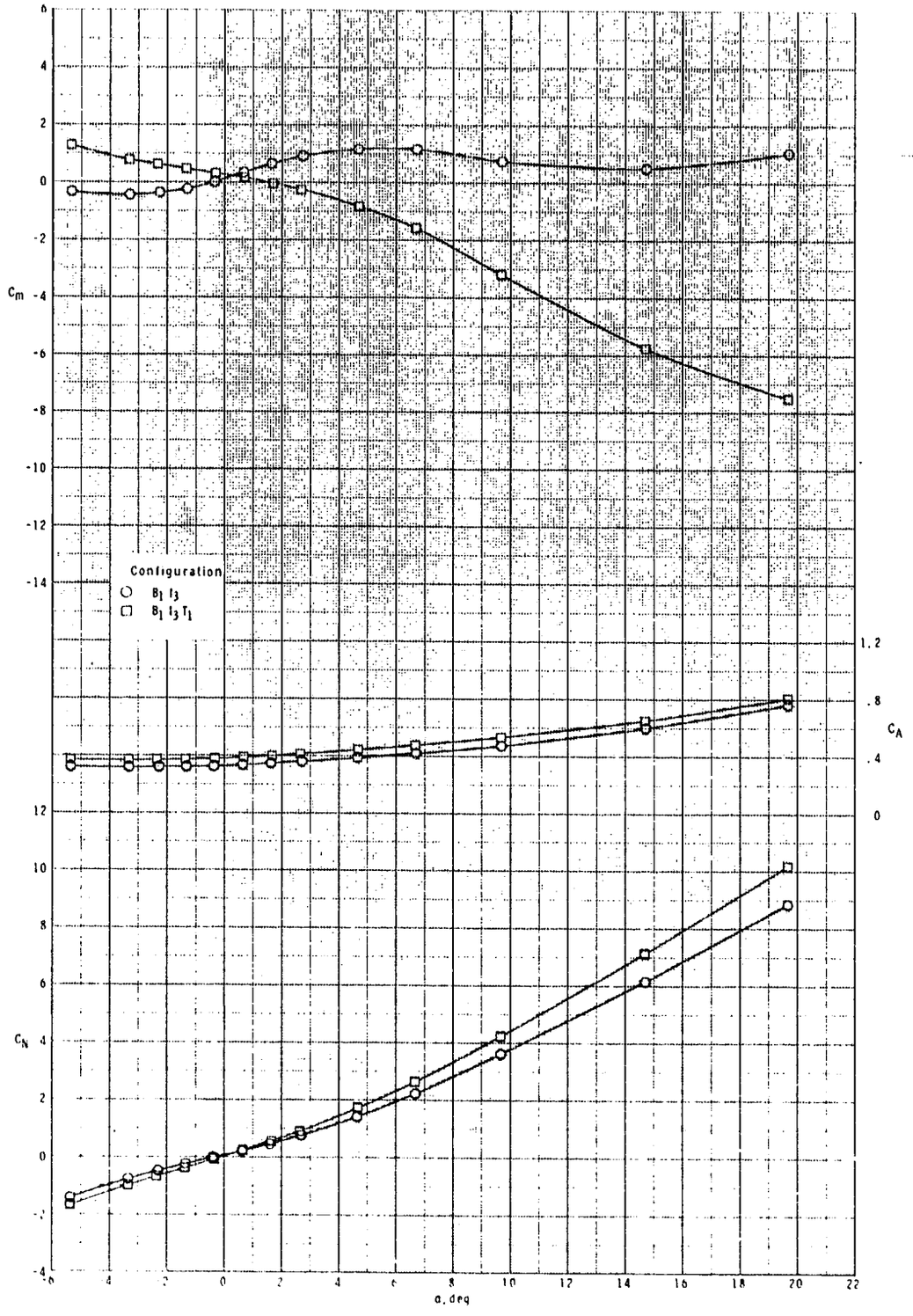

(c) M = 3.50.

Figure 33.- Continued.

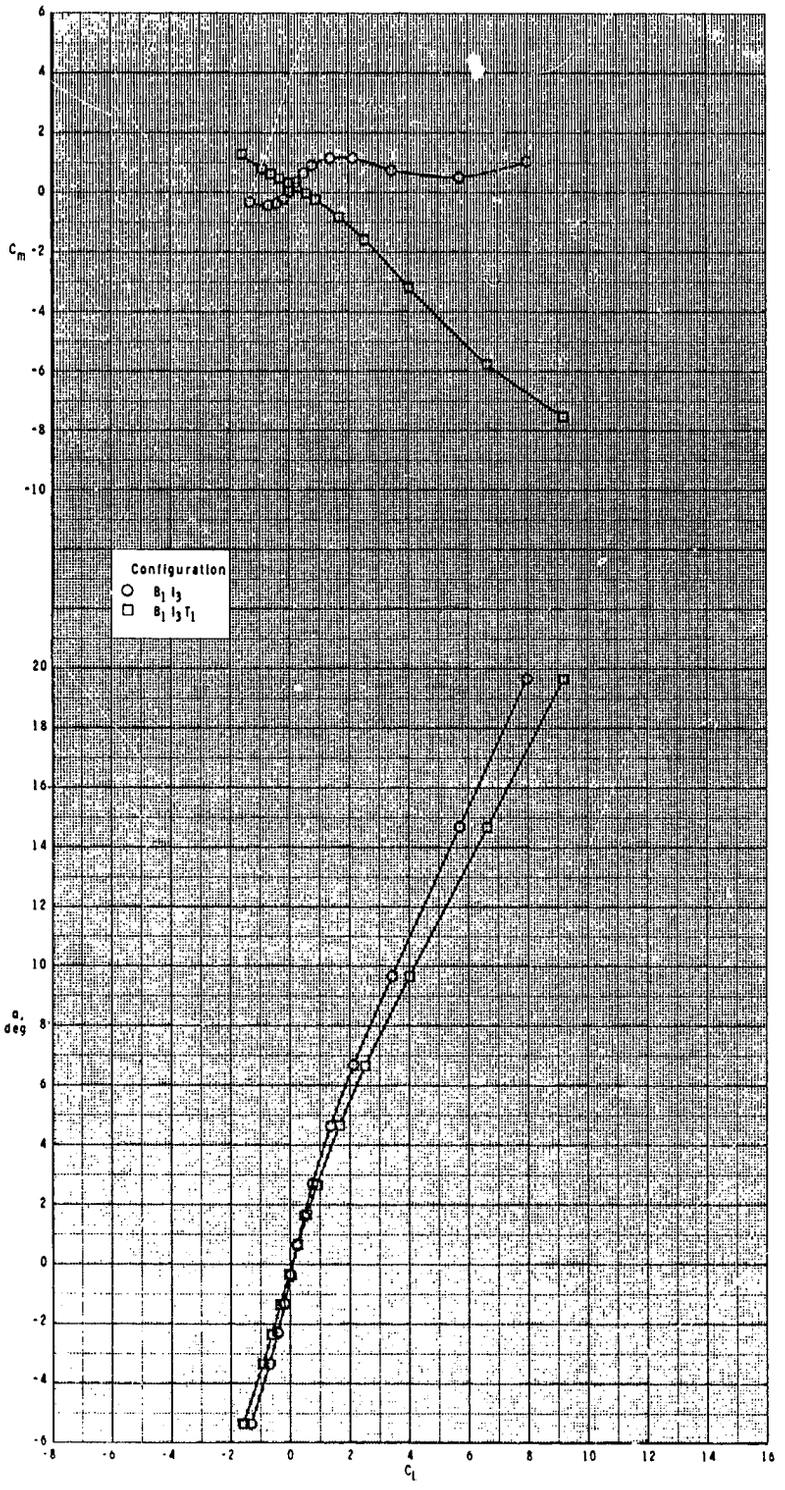

(c) Continued.

Figure 33.- Continued.

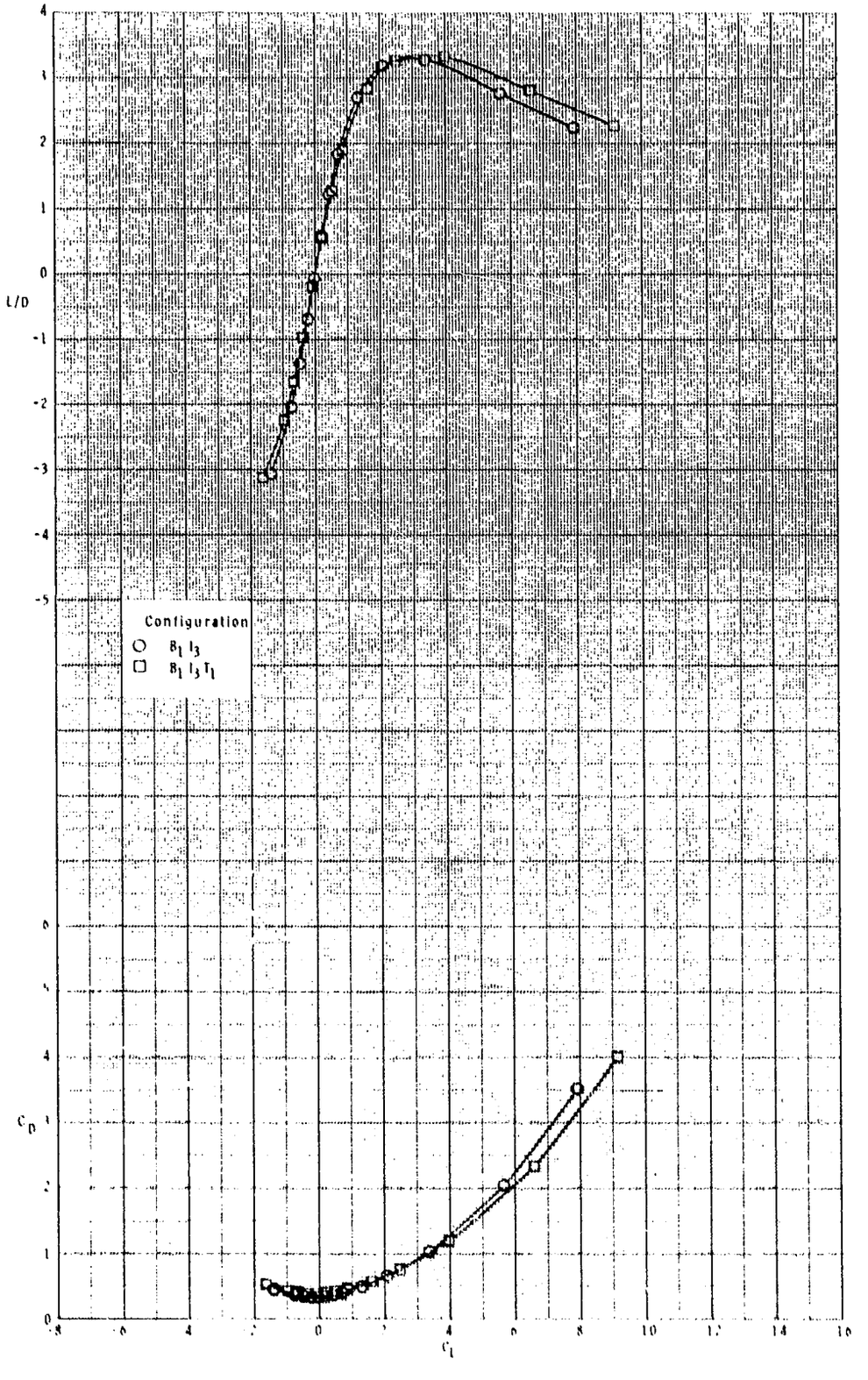

(c) Concluded.

Figure 33.- Continued.

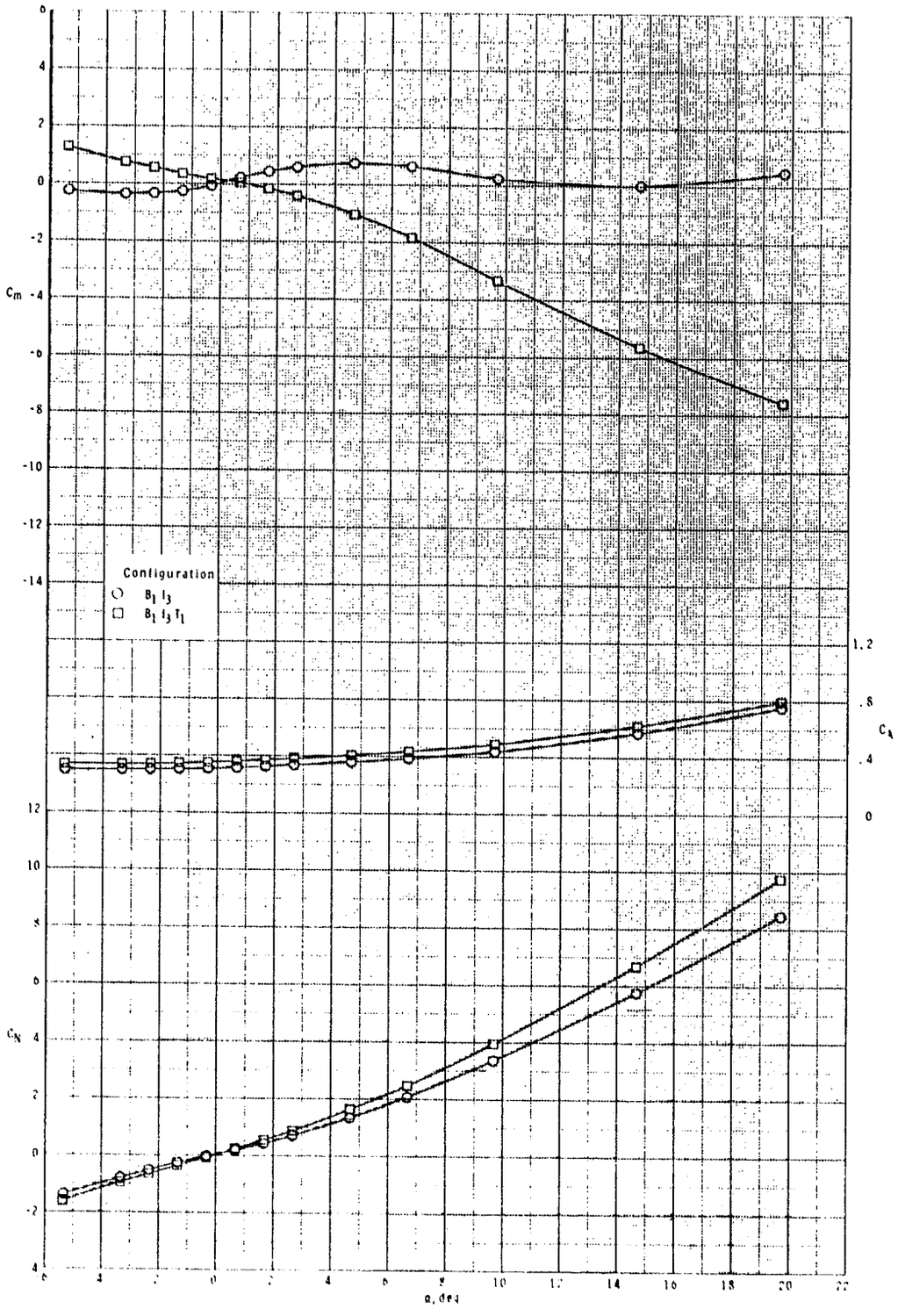

(d) M = 3.95.

Figure 33.- Continued.

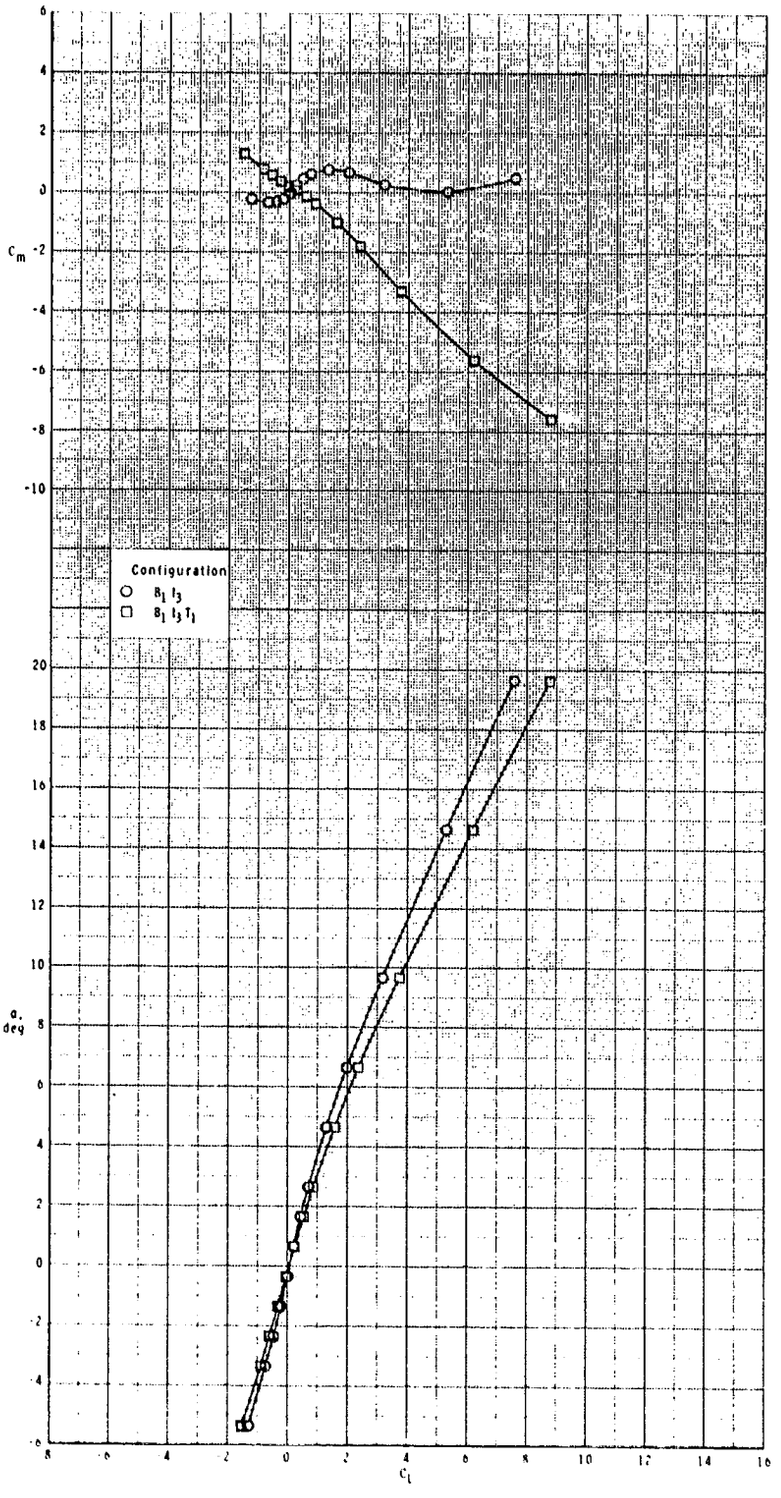

(d) Continued.

Figure 33.- Continued.

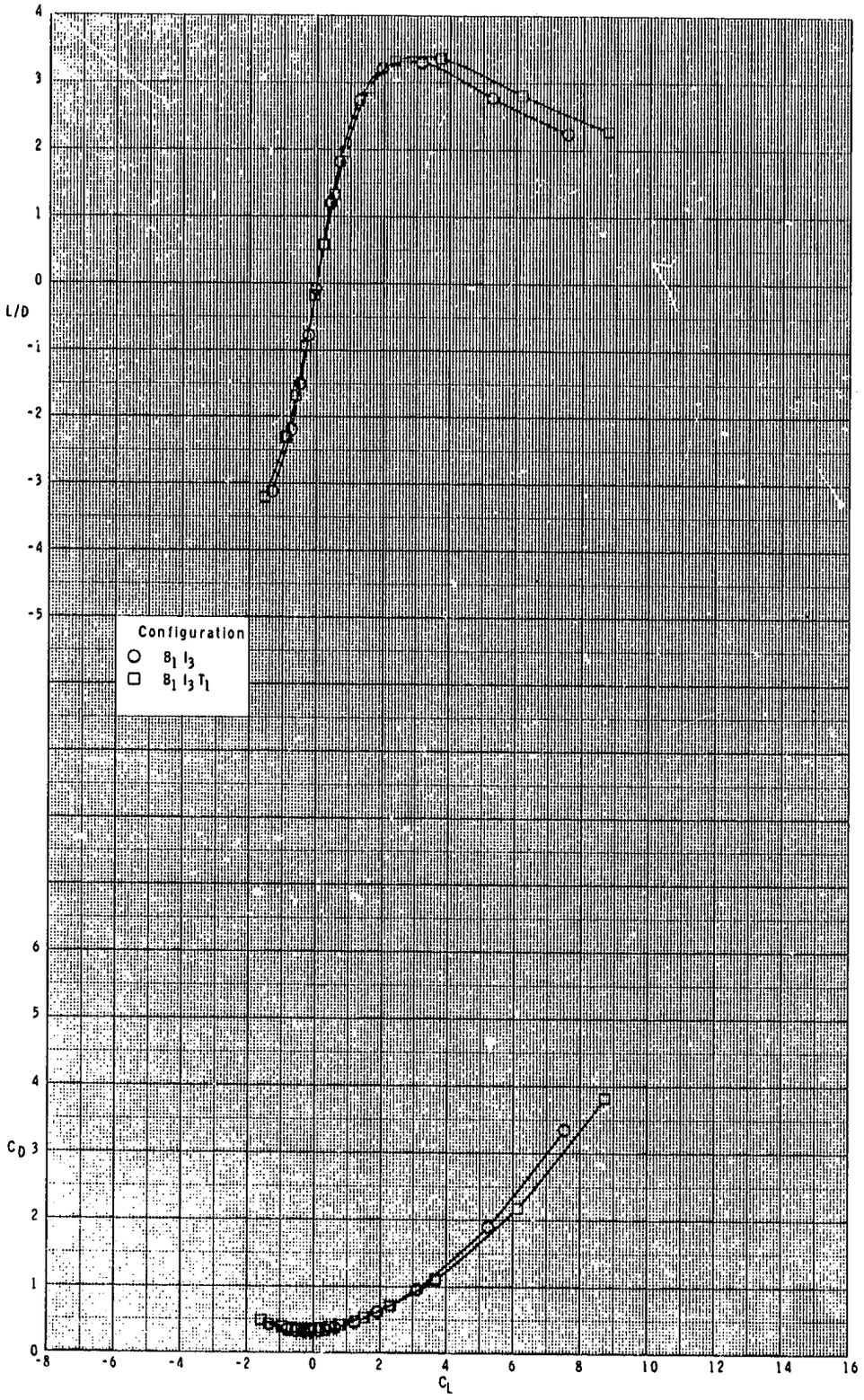

(d) Concluded.

Figure 33.- Concluded.

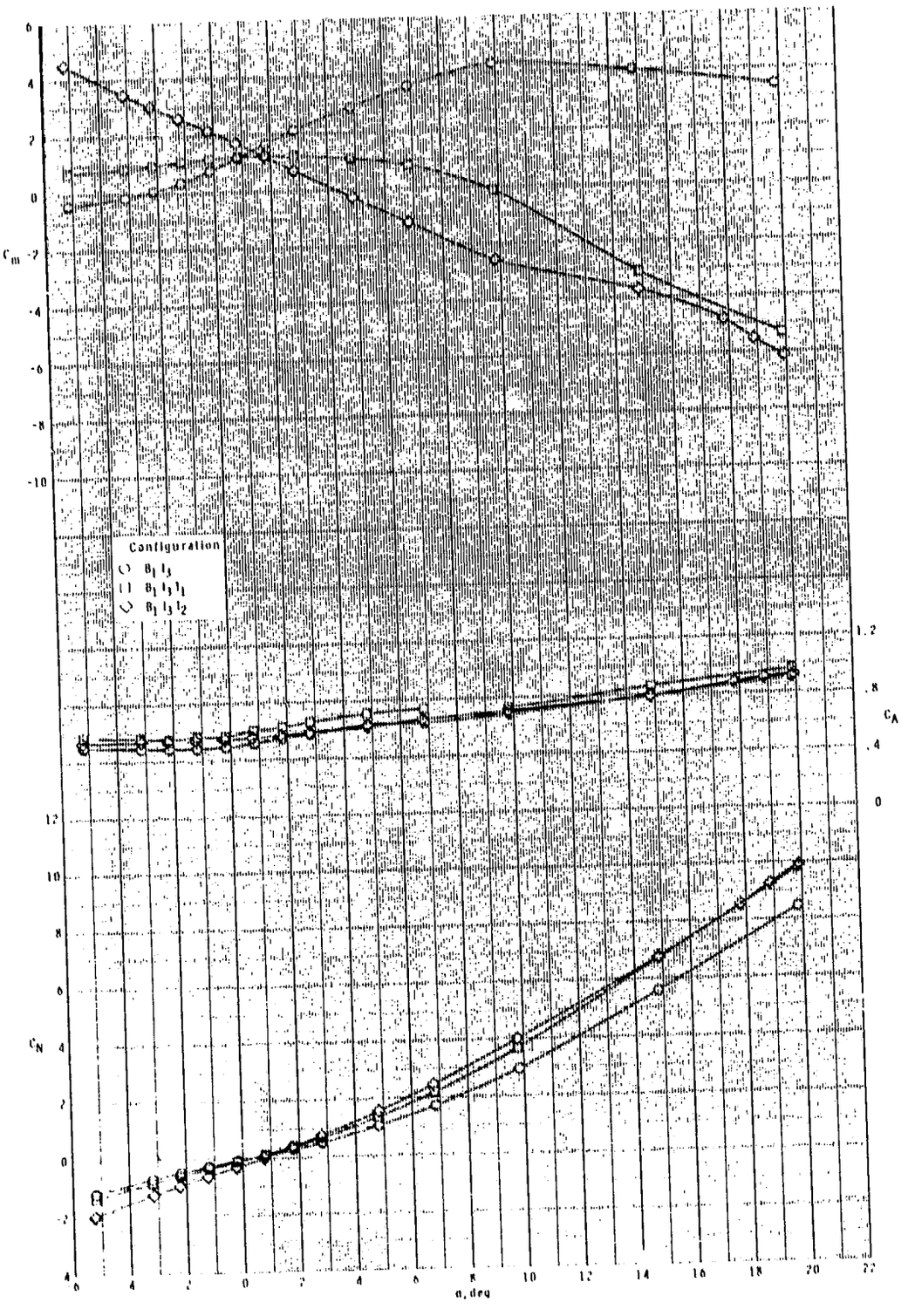

(a) M = 2.50.

Figure 34.- Effect of various model components on longitudinal aerodynamic characteristics for two-dimensional extended inlets with $\phi_I = 135°$ and $\delta_p = 0°$.

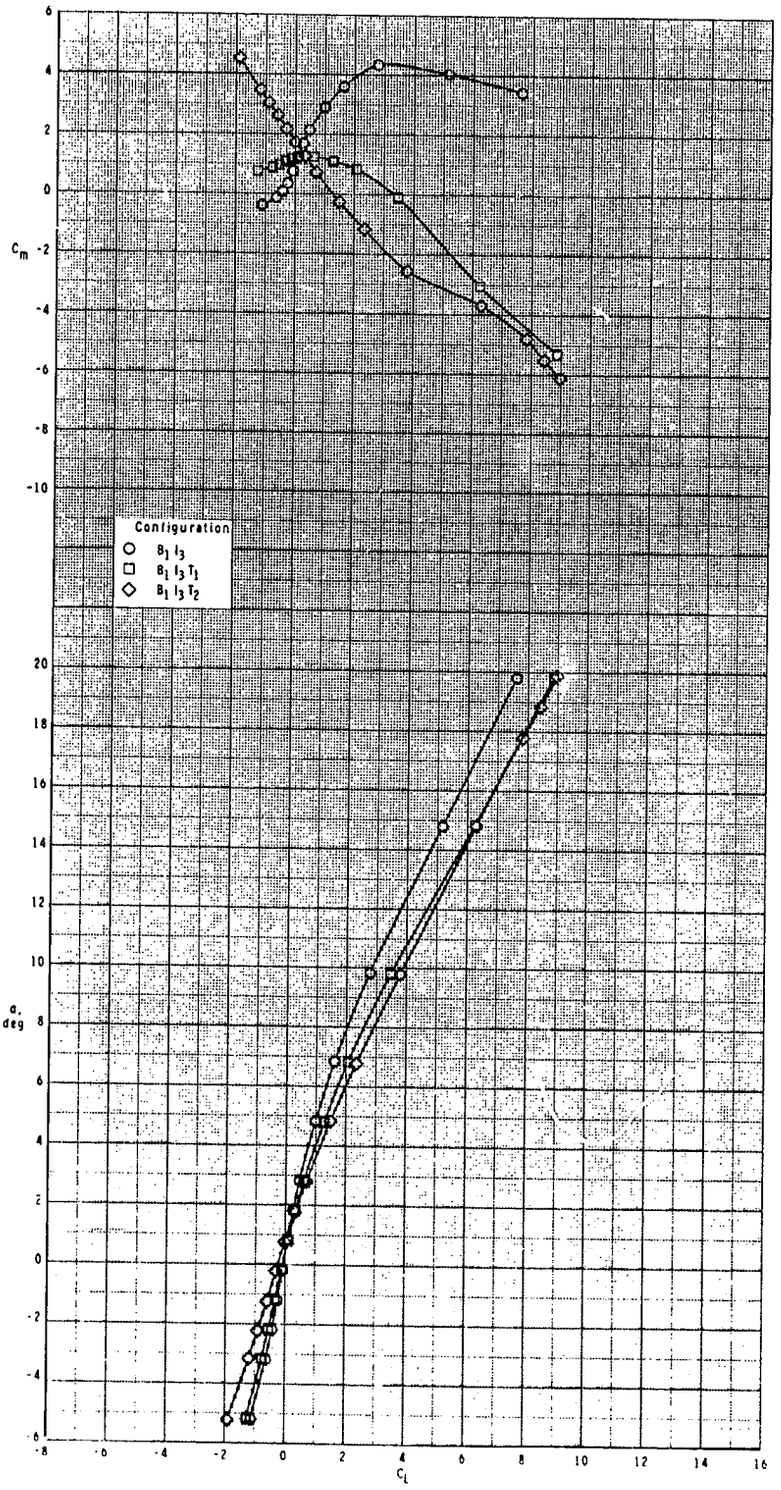

(a) Continued.

Figure 34.- Continued.

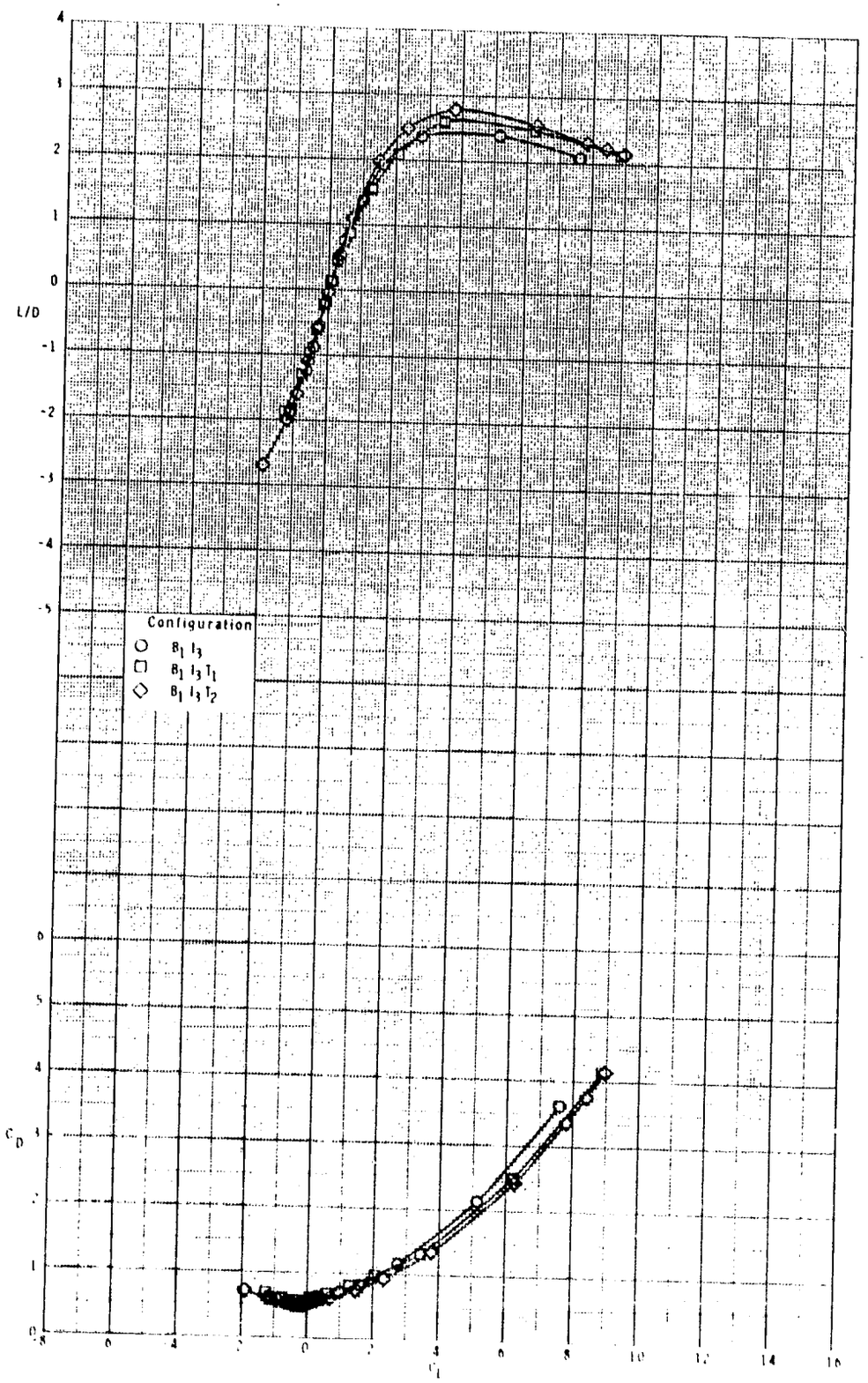

(a) Concluded.

Figure 34.- Continued.

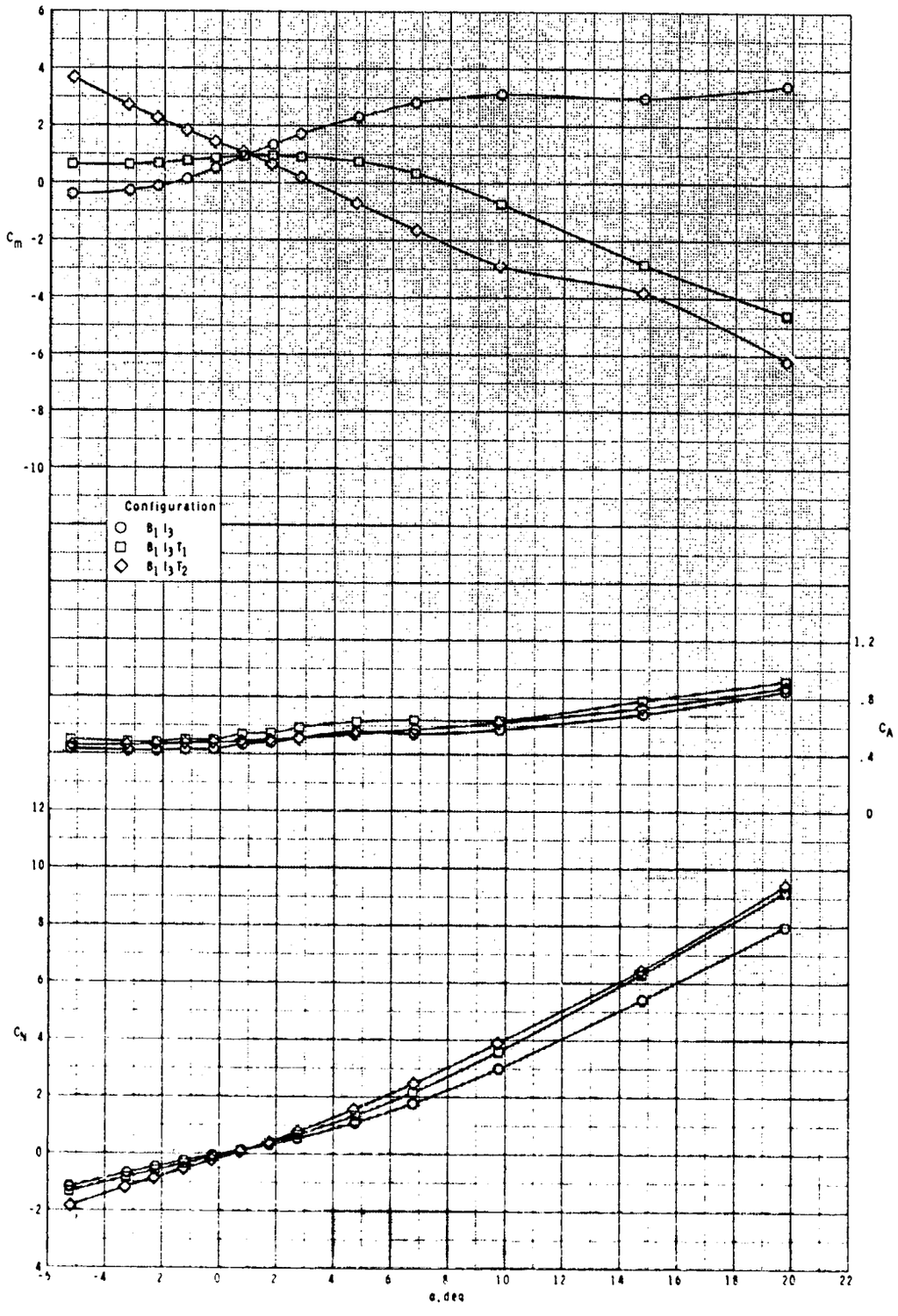

(b) M = 2.95.

Figure 34.- Continued.

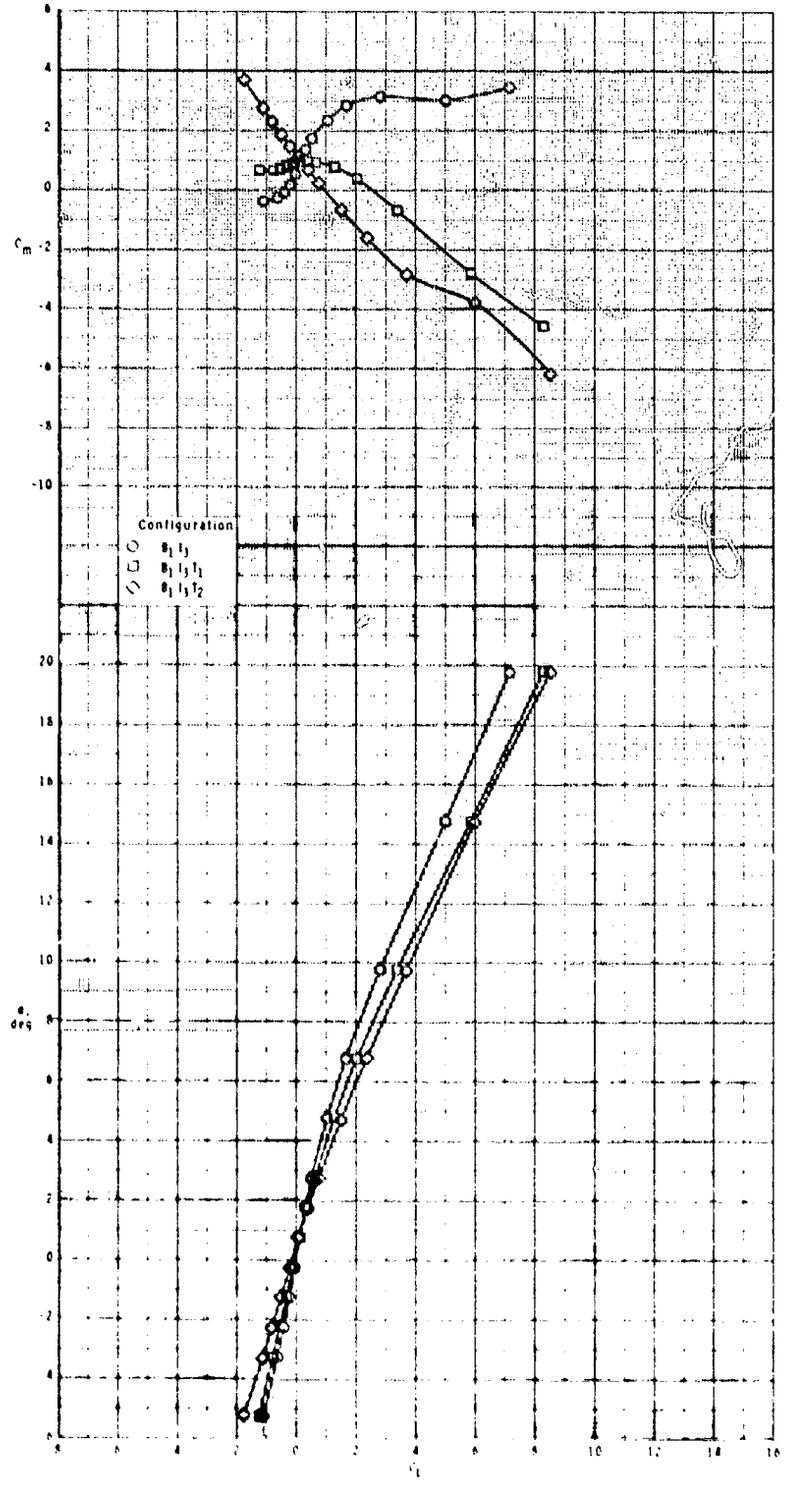

(b) Continued.

Figure 34.- Continued.

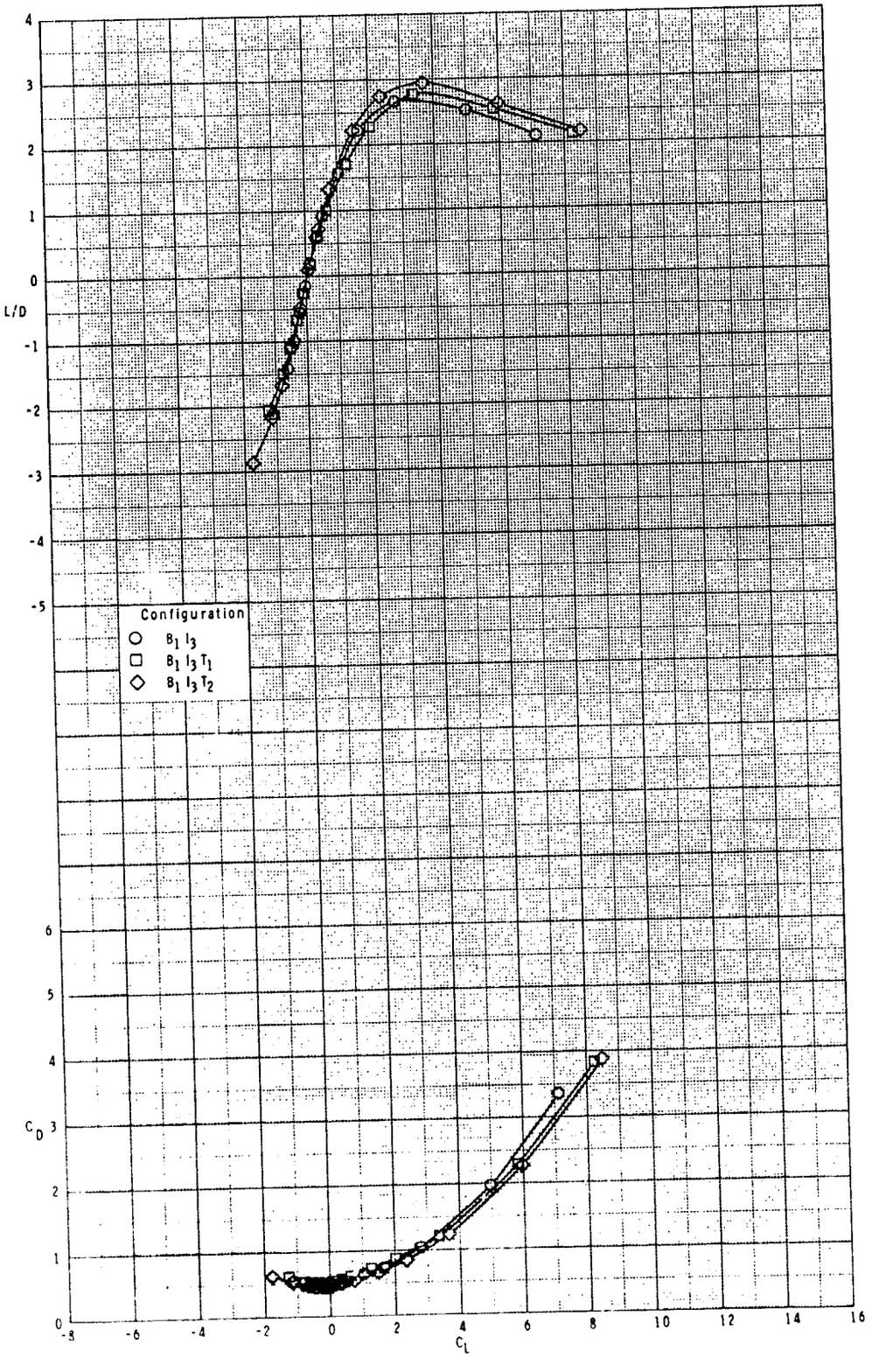

(b) Concluded.

Figure 34.- Continued.

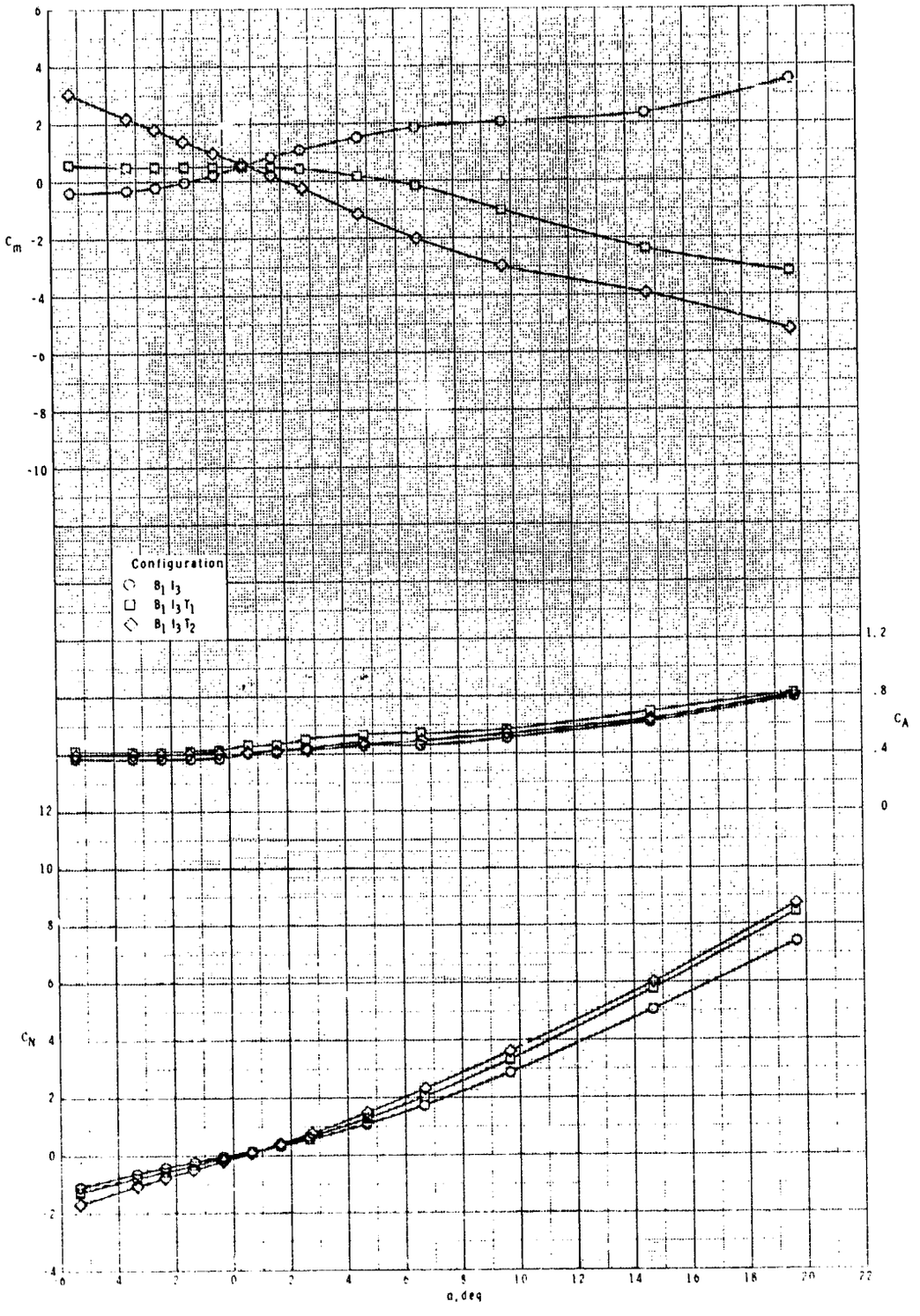

(c) M = 3.50.

Figure 34.- Continued.

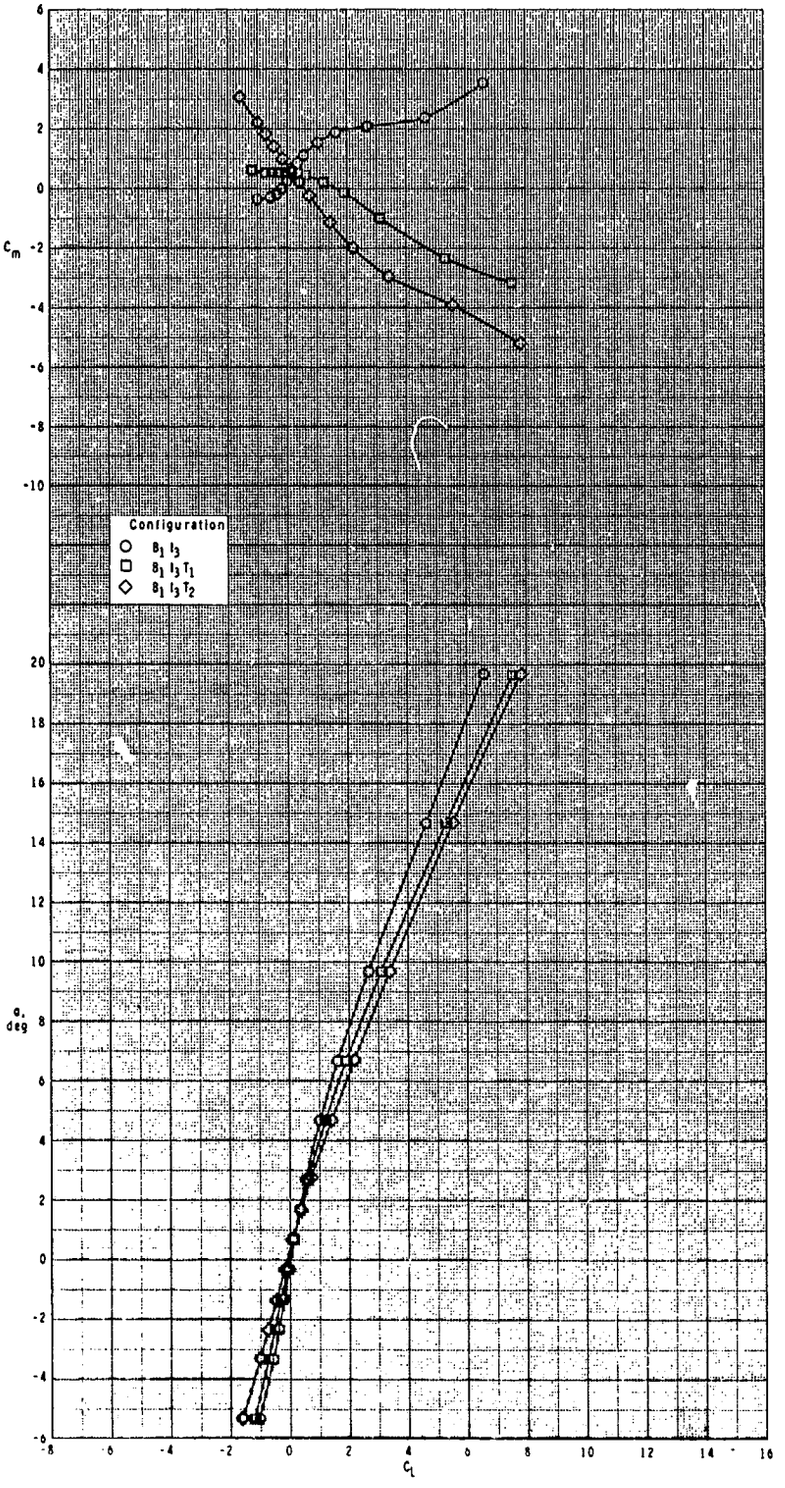

(c) Continued.

Figure 34.- Continued.

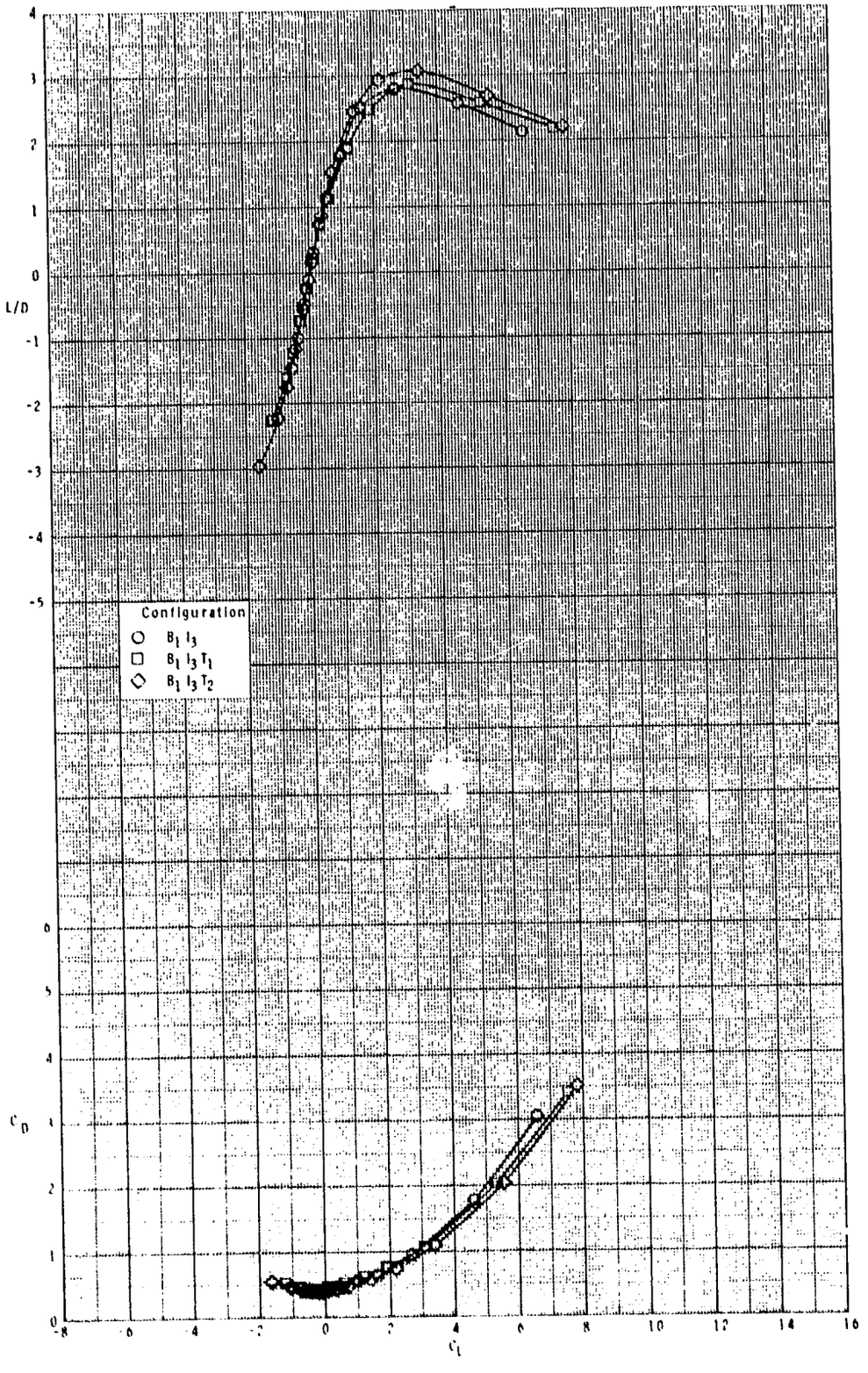

(c) Concluded.

Figure 34.- Continued.

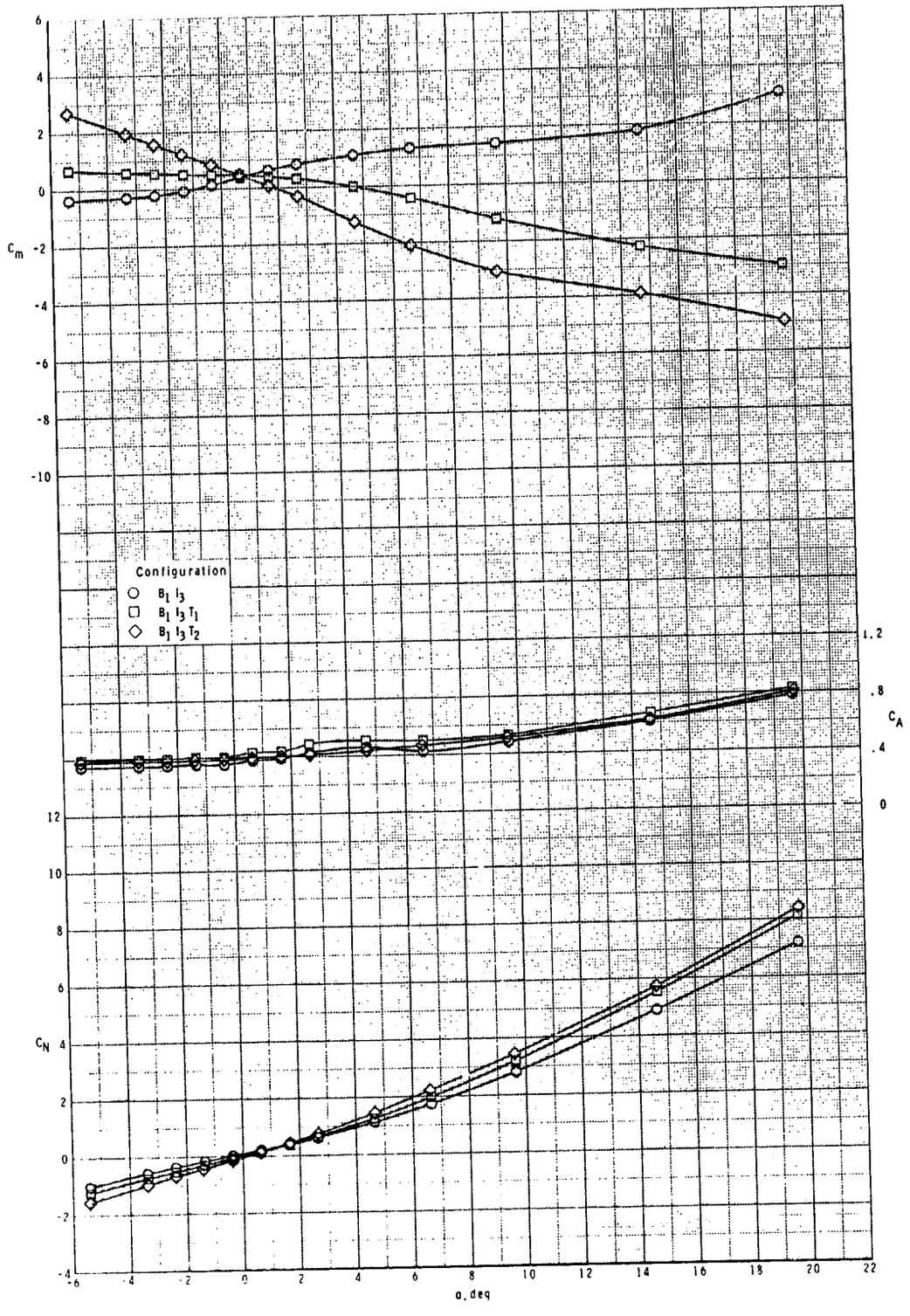

(d) M = 3.95.

Figure 34.- Continued.

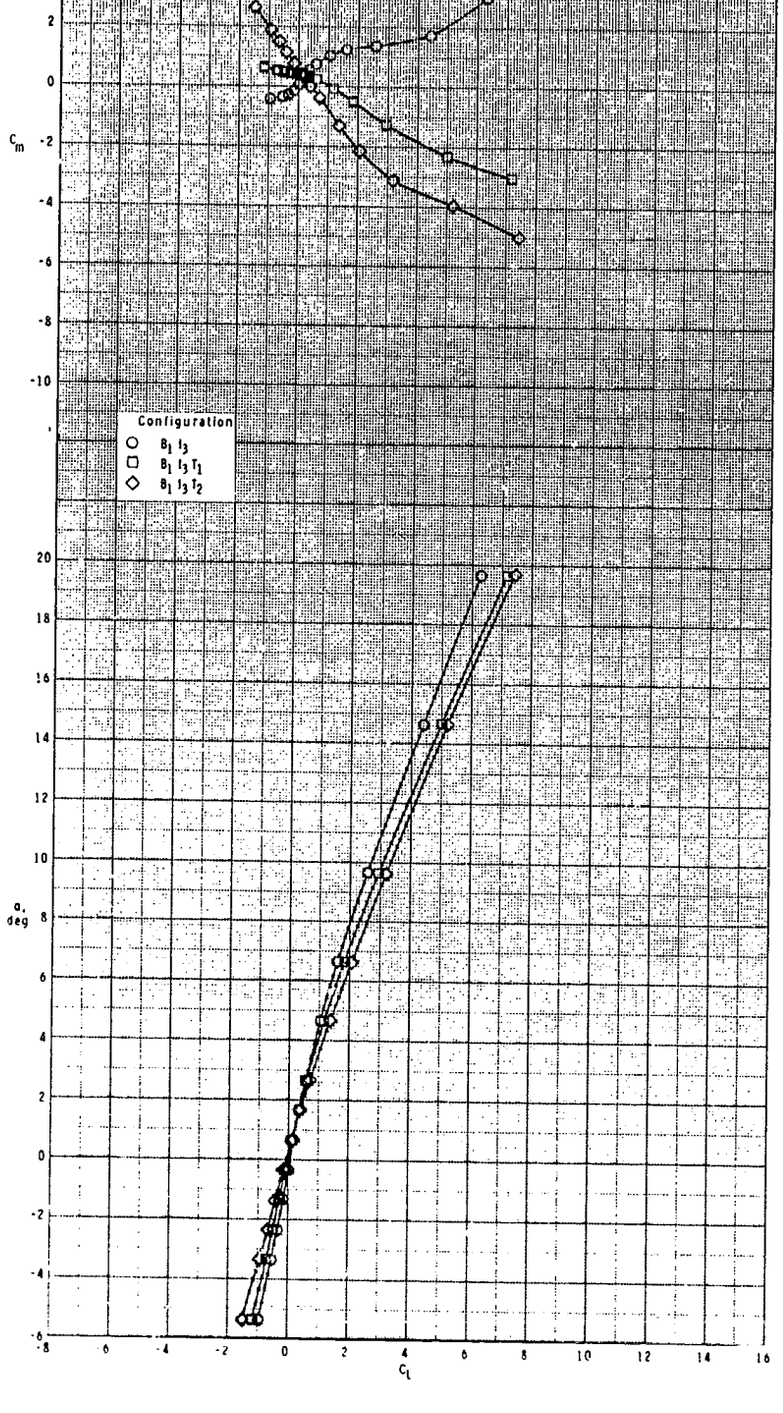

(d) Continued.

Figure 34.- Continued.

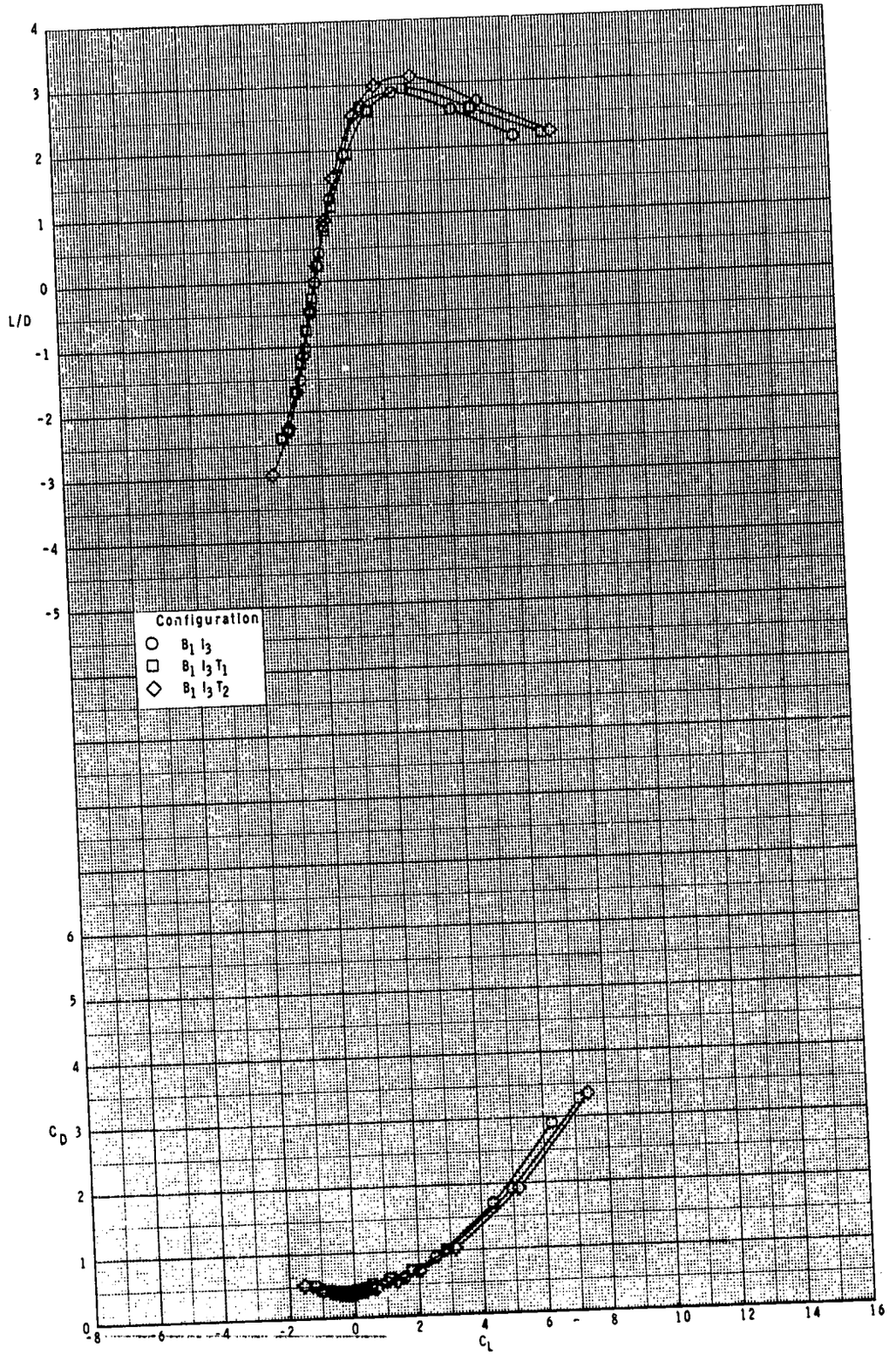

(d) Concluded.

Figure 34.- Concluded.

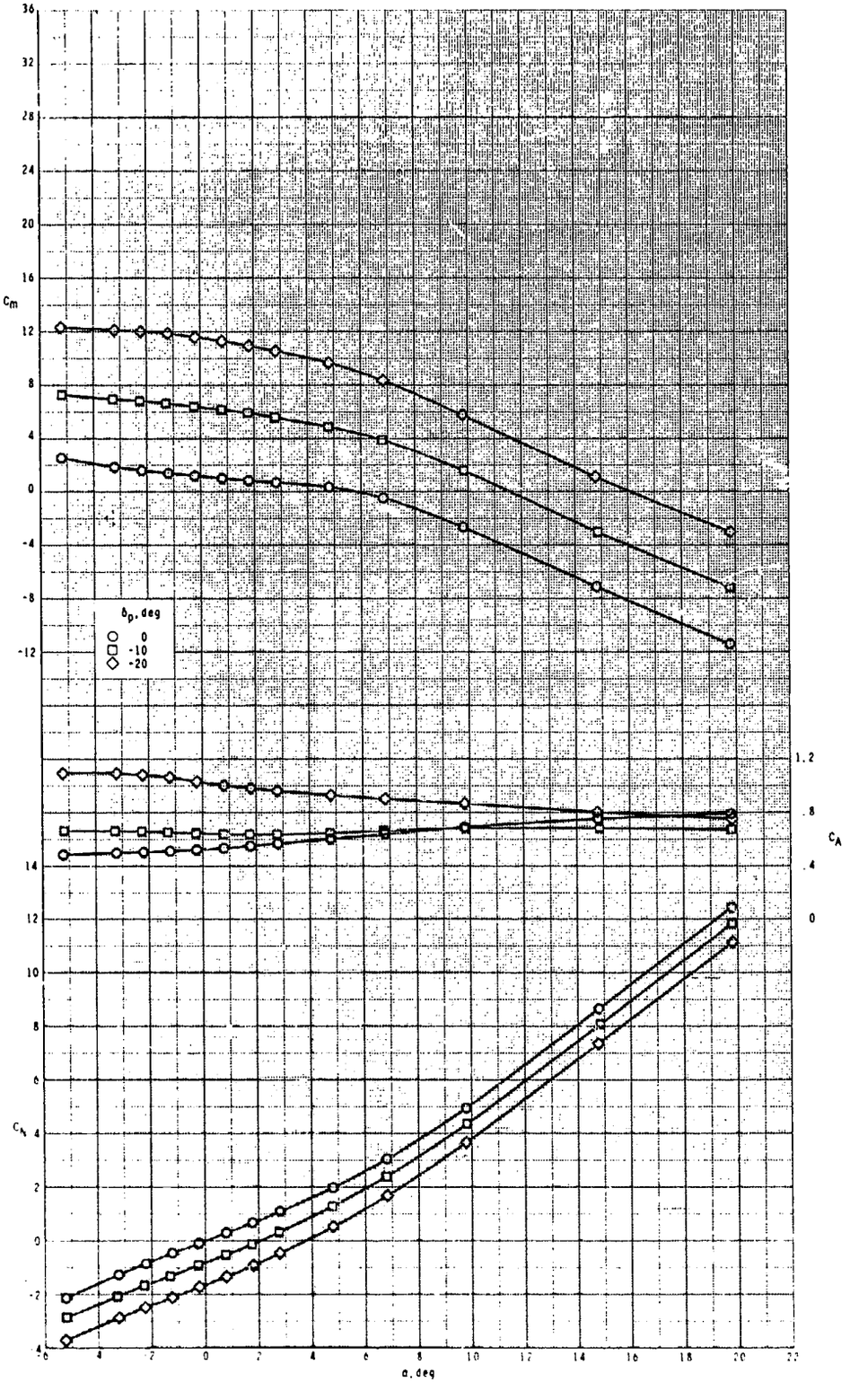

(a) M = 2.50.

Figure 35.- Pitch-control effectiveness of configuration $B_1 I_3 T_1$ with $\phi_I = 90°$.

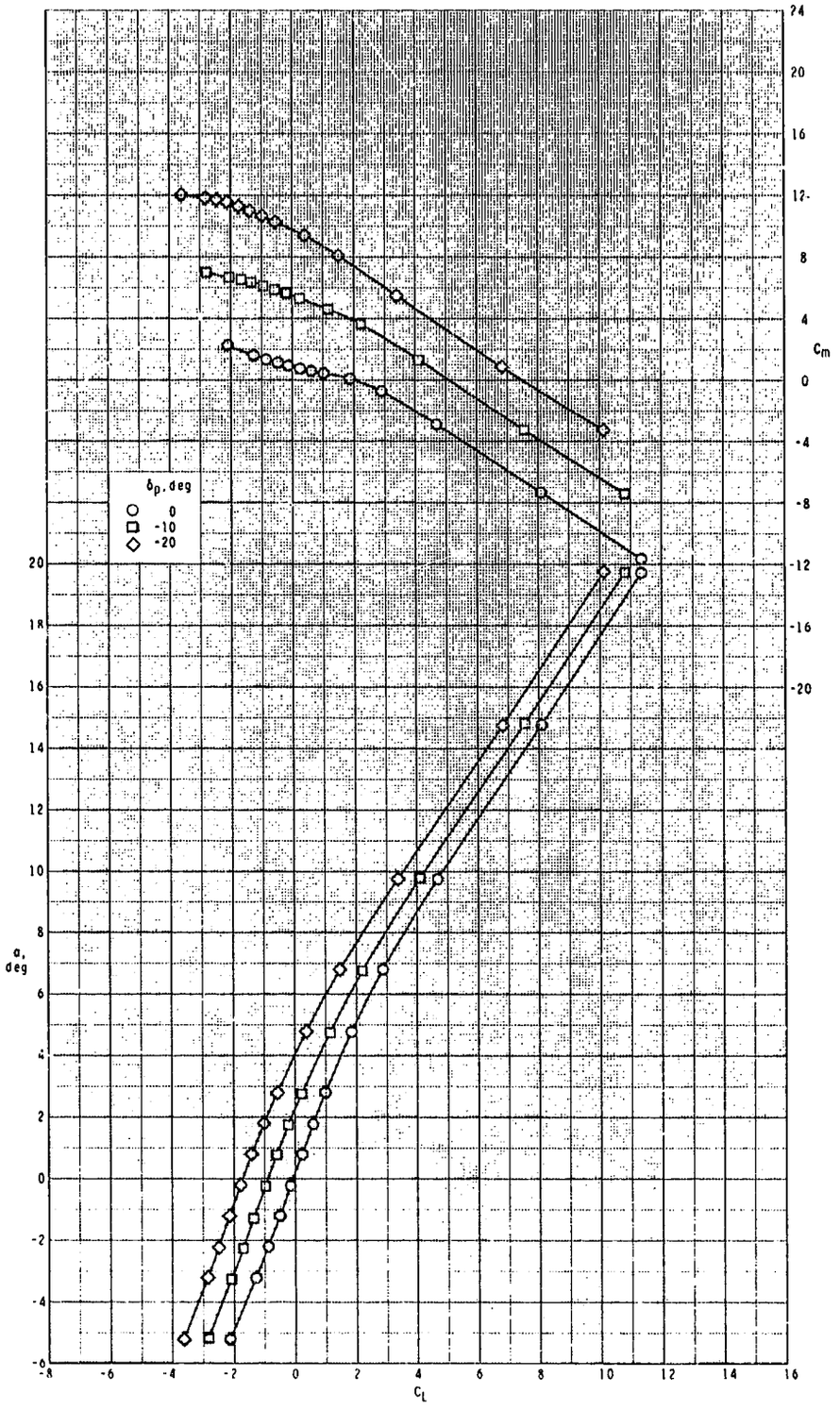

(a) Continued.

Figure 35.- Continued.

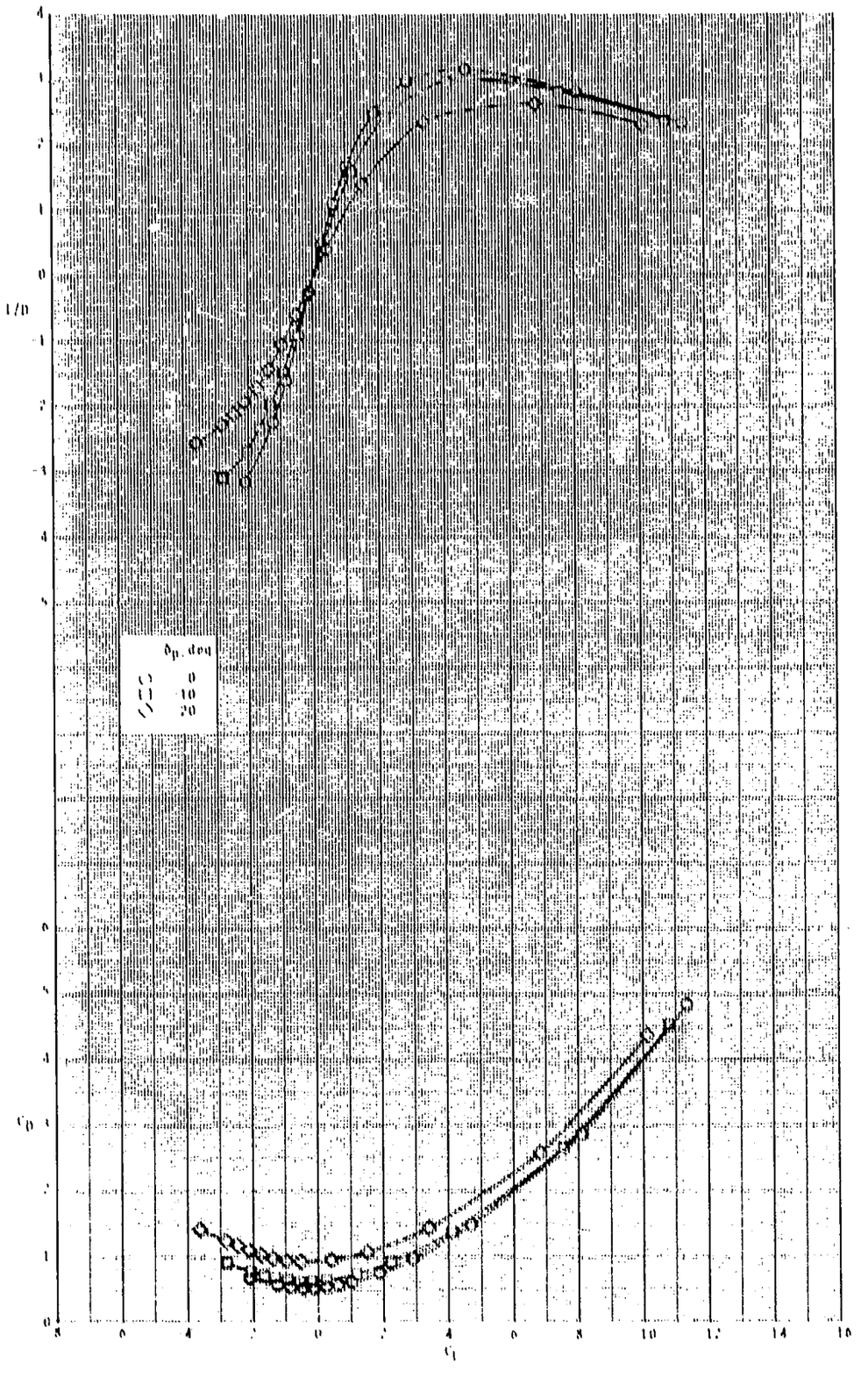

(a) Concluded.

Figure 9. Continued.

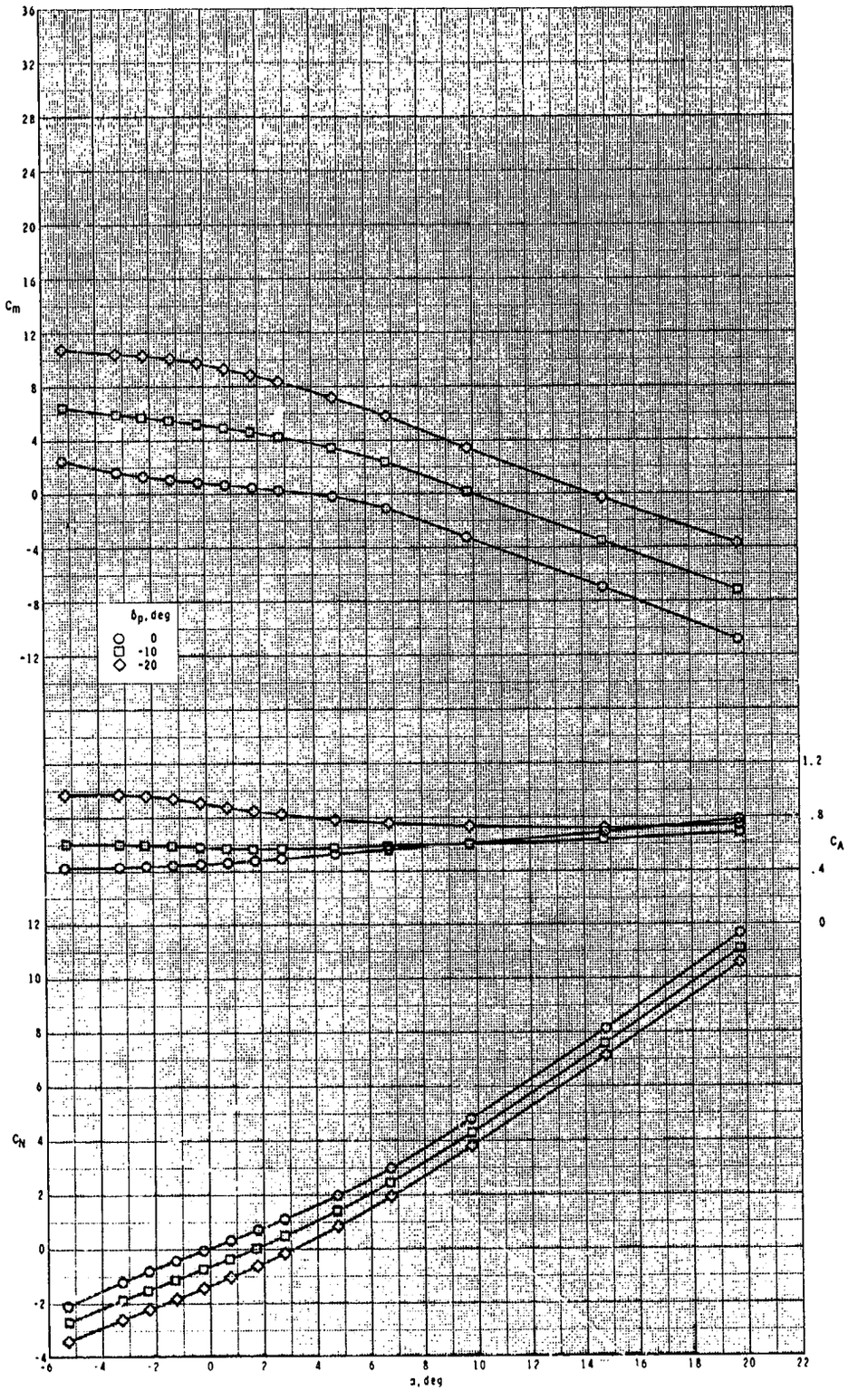

(b) M = 2.95.

Figure 35.- Continued.

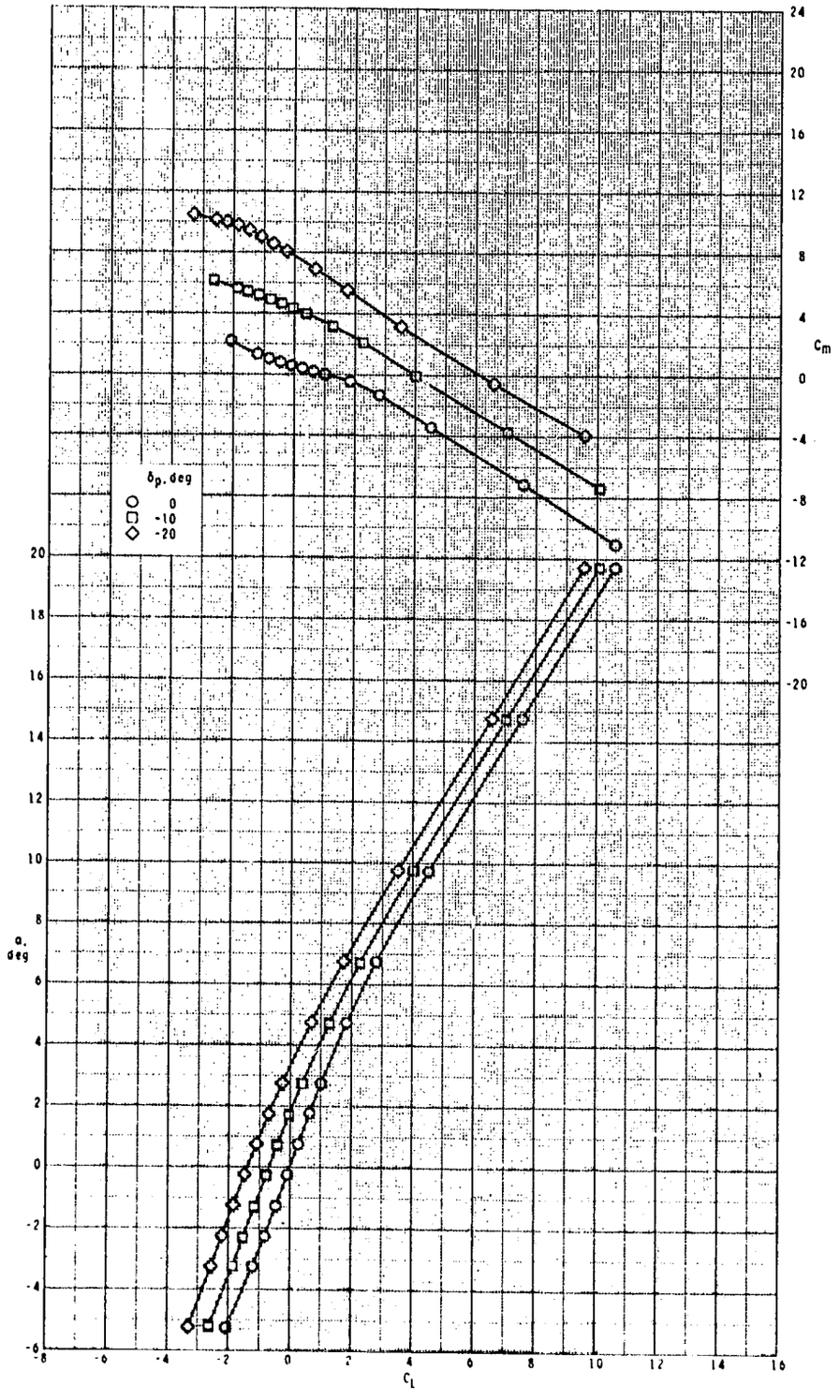

(b) Continued.

Figure 35.- Continued.

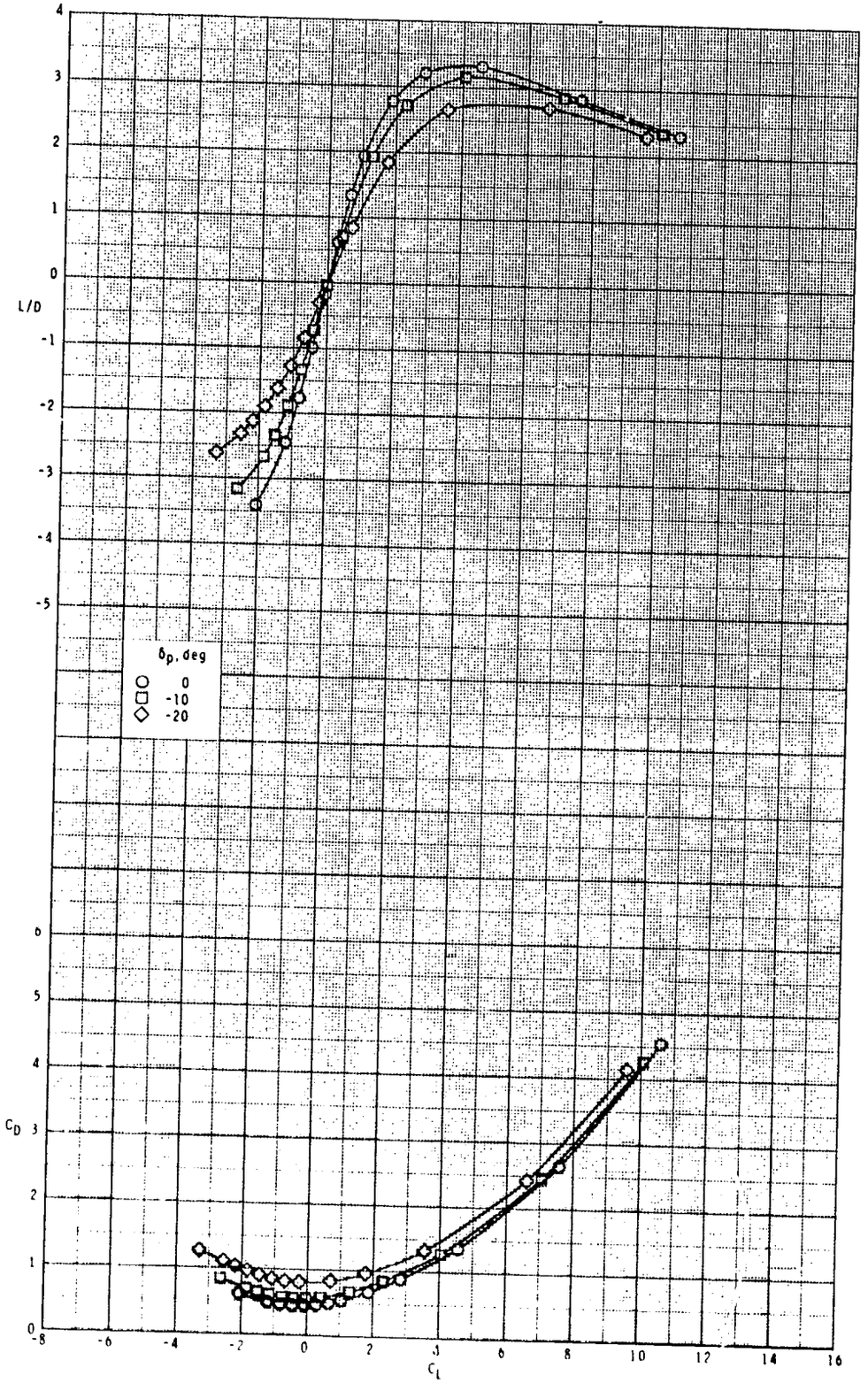

(b) Concluded.

Figure 35.- Continued.

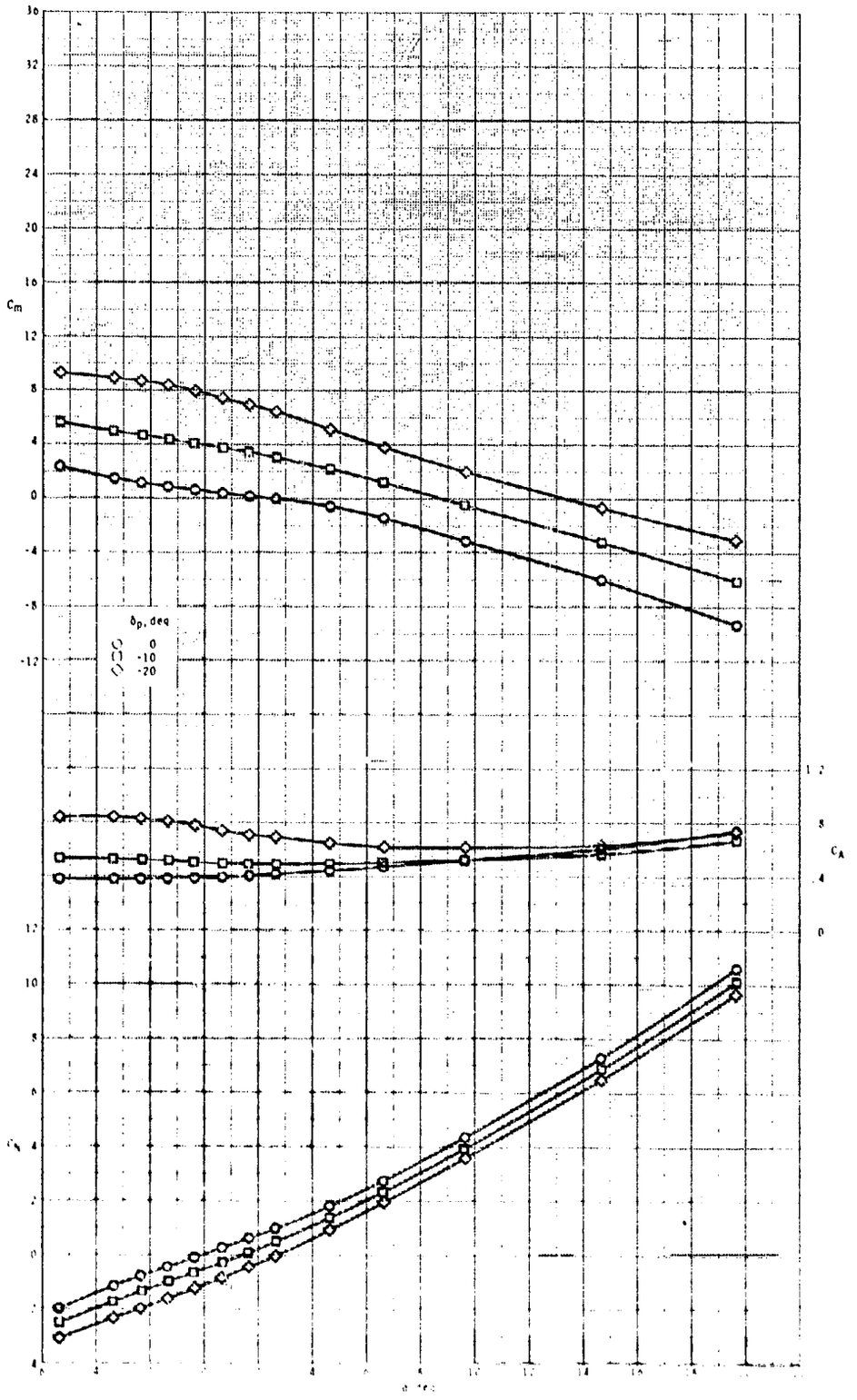

(c) M = 3.50.

Figure 35.- Continued.

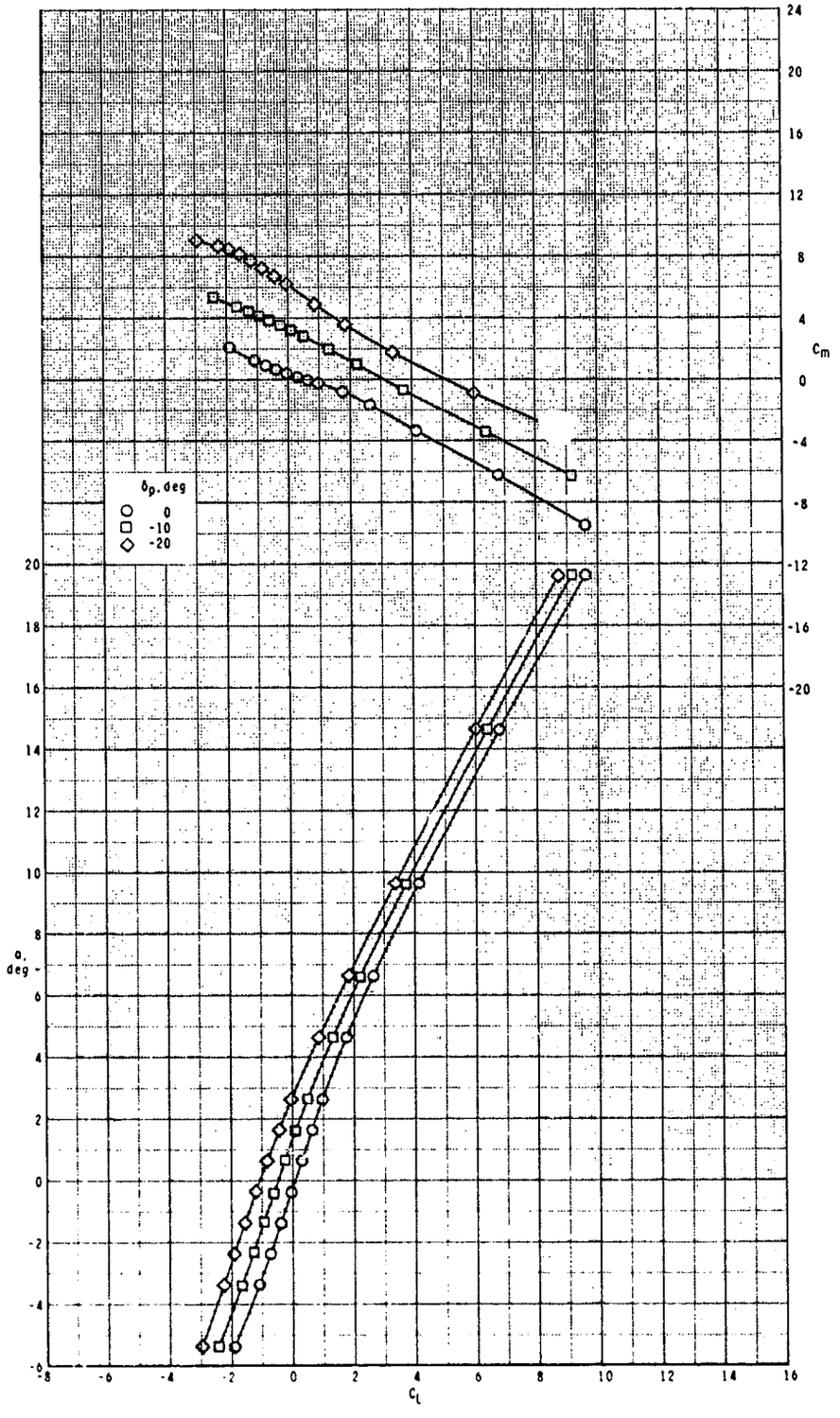

(c) Continued.

Figure 35.- Continued.

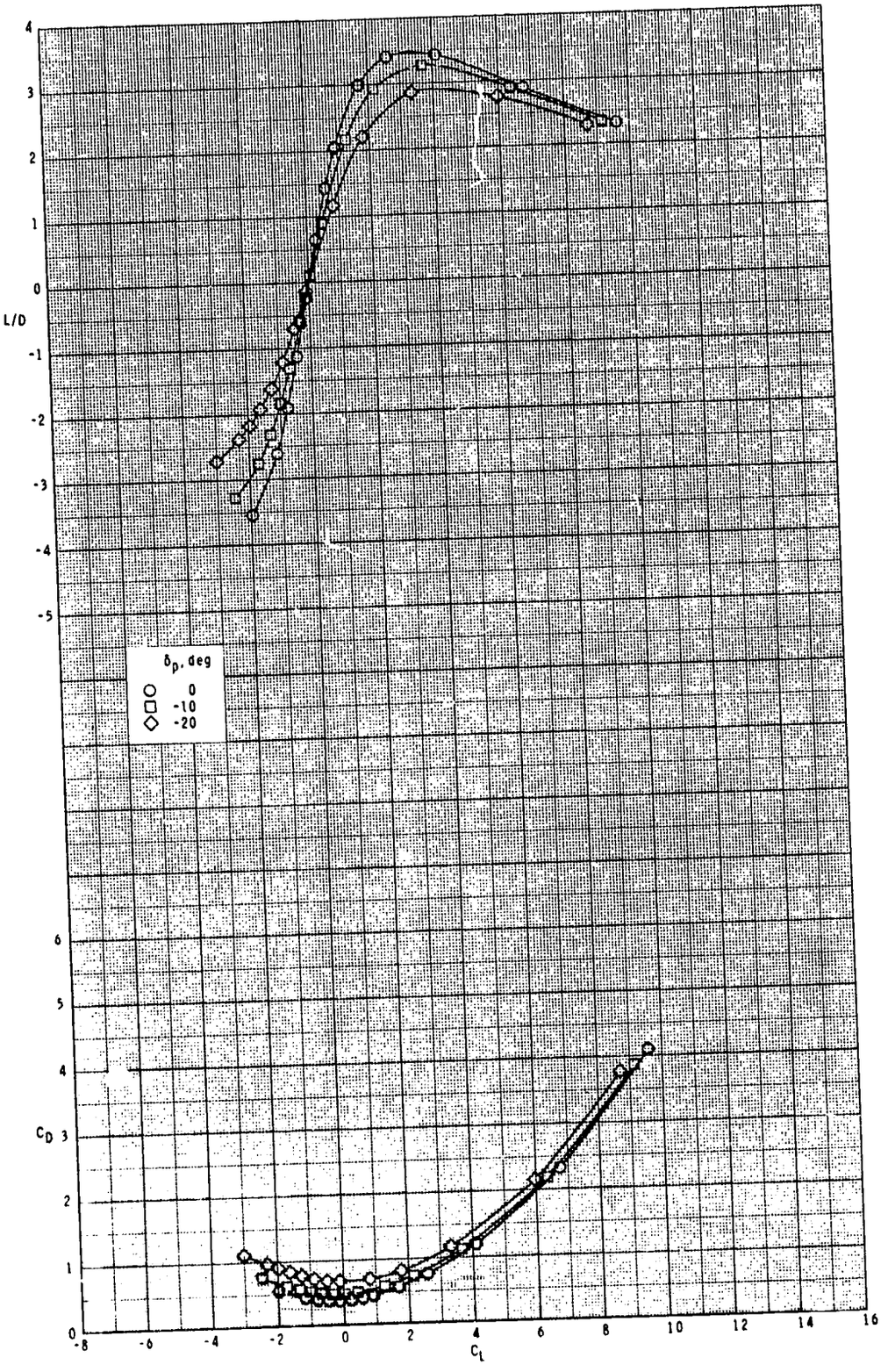

(c) Concluded.

Figure 35.- Continued.

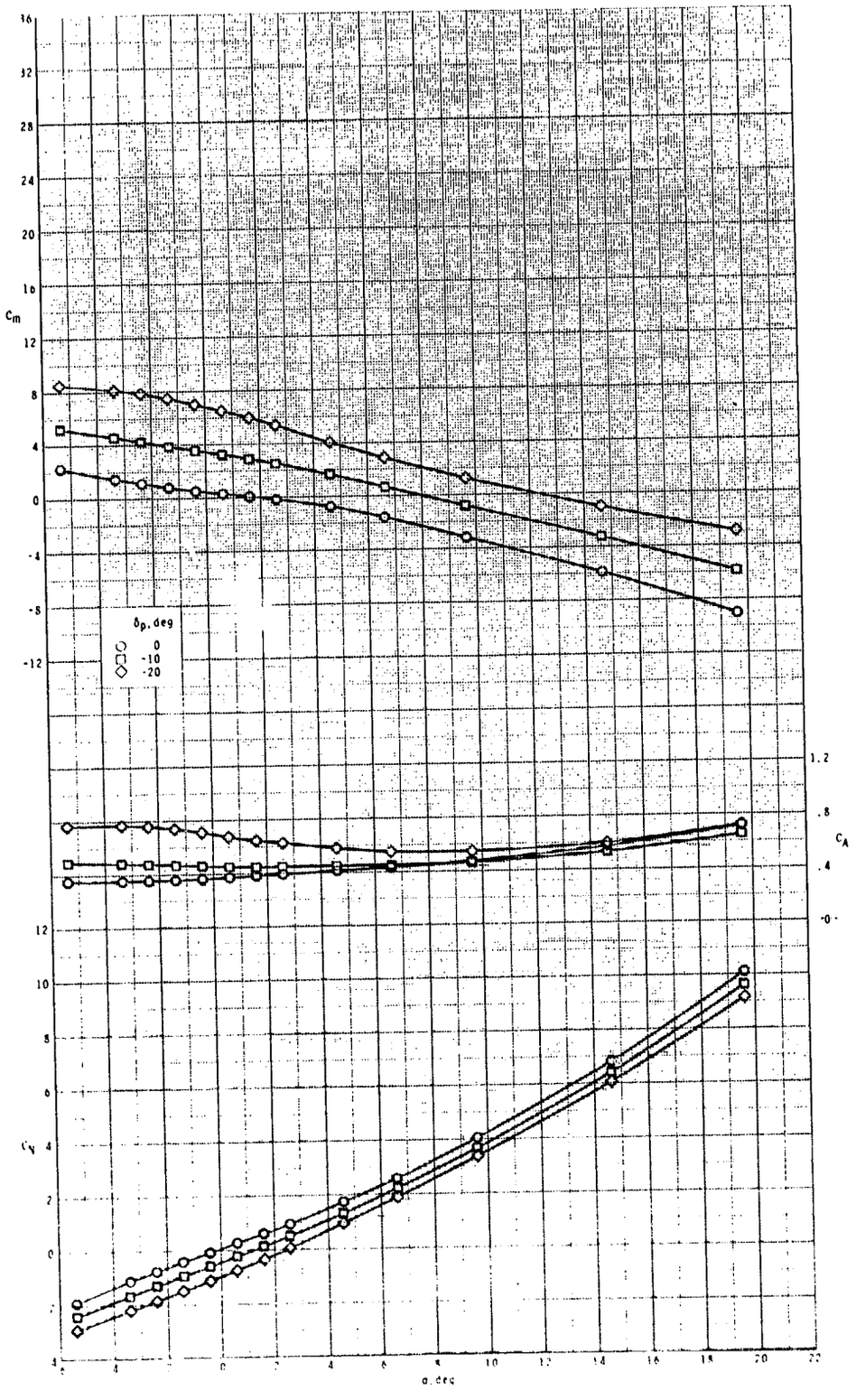

(d) M = 3.95.

Figure 35.- Continued.

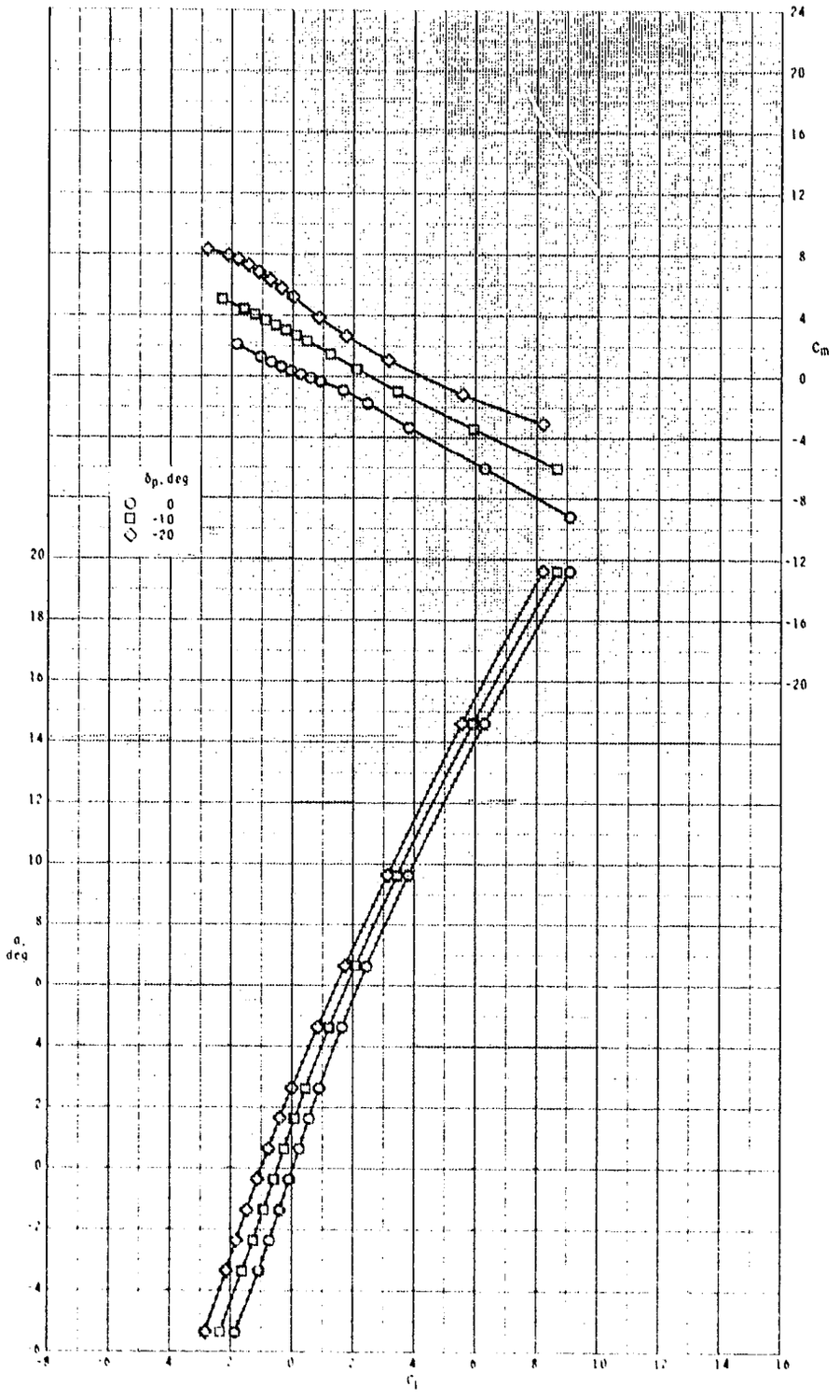

(d) Continued.

Figure 35.- Continued.

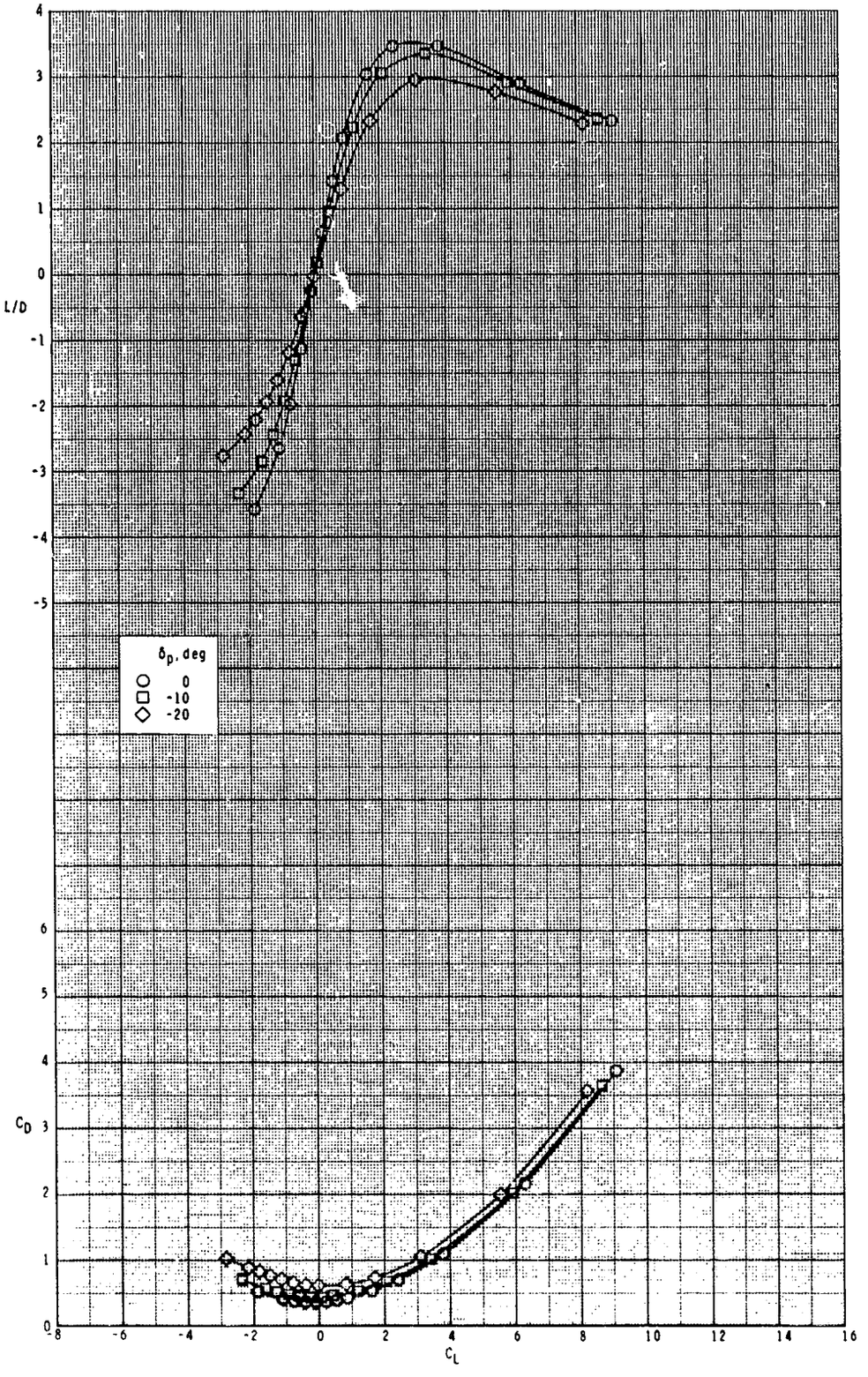

(d) Concluded.

Figure 35.- Concluded.

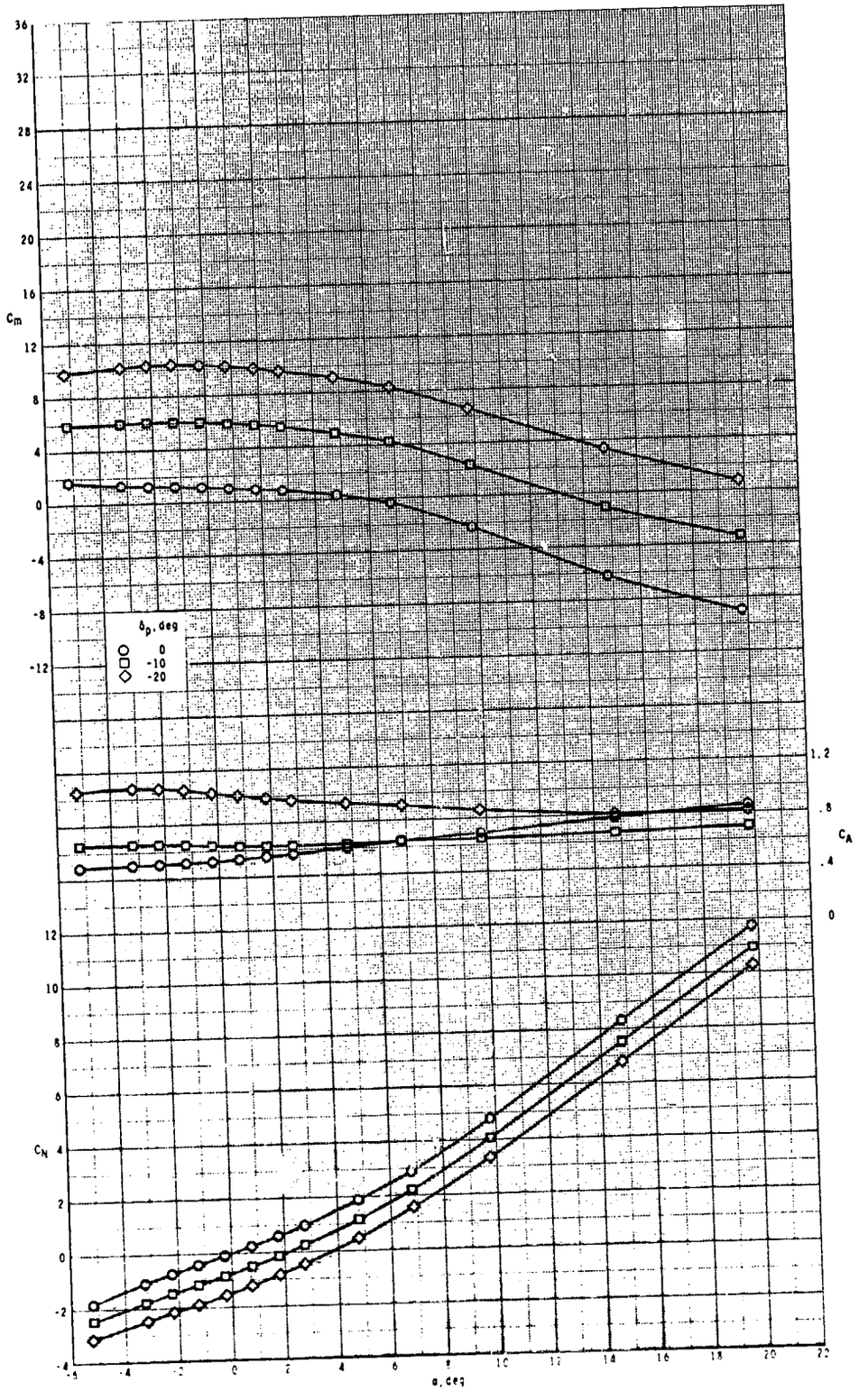

(a) M = 2.50.

Figure 36.- Pitch-control effectiveness of configuration $B_1I_3T_1$ with $\phi_I = 115°$.

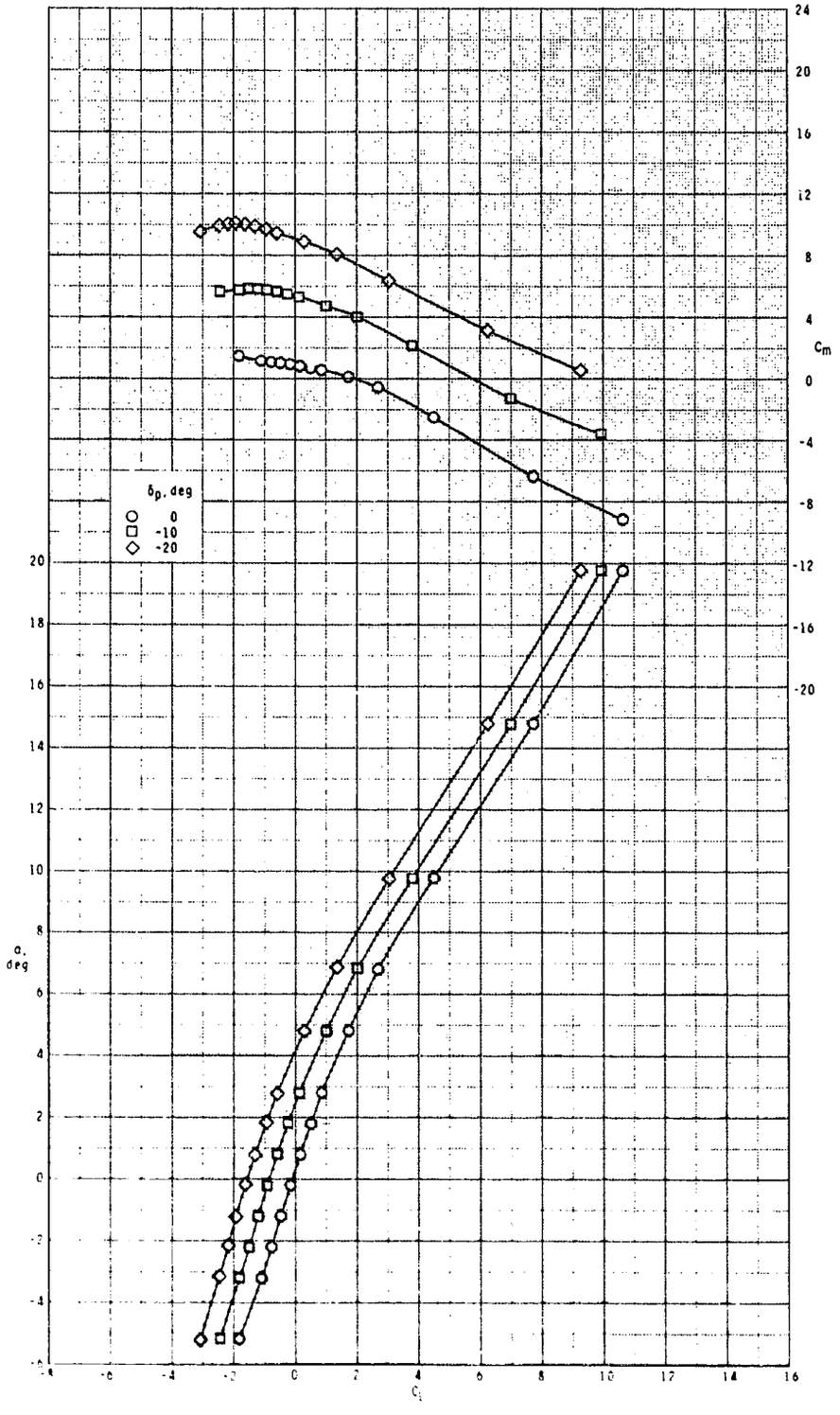

(a) Continued.

Figure 36.- Continued.

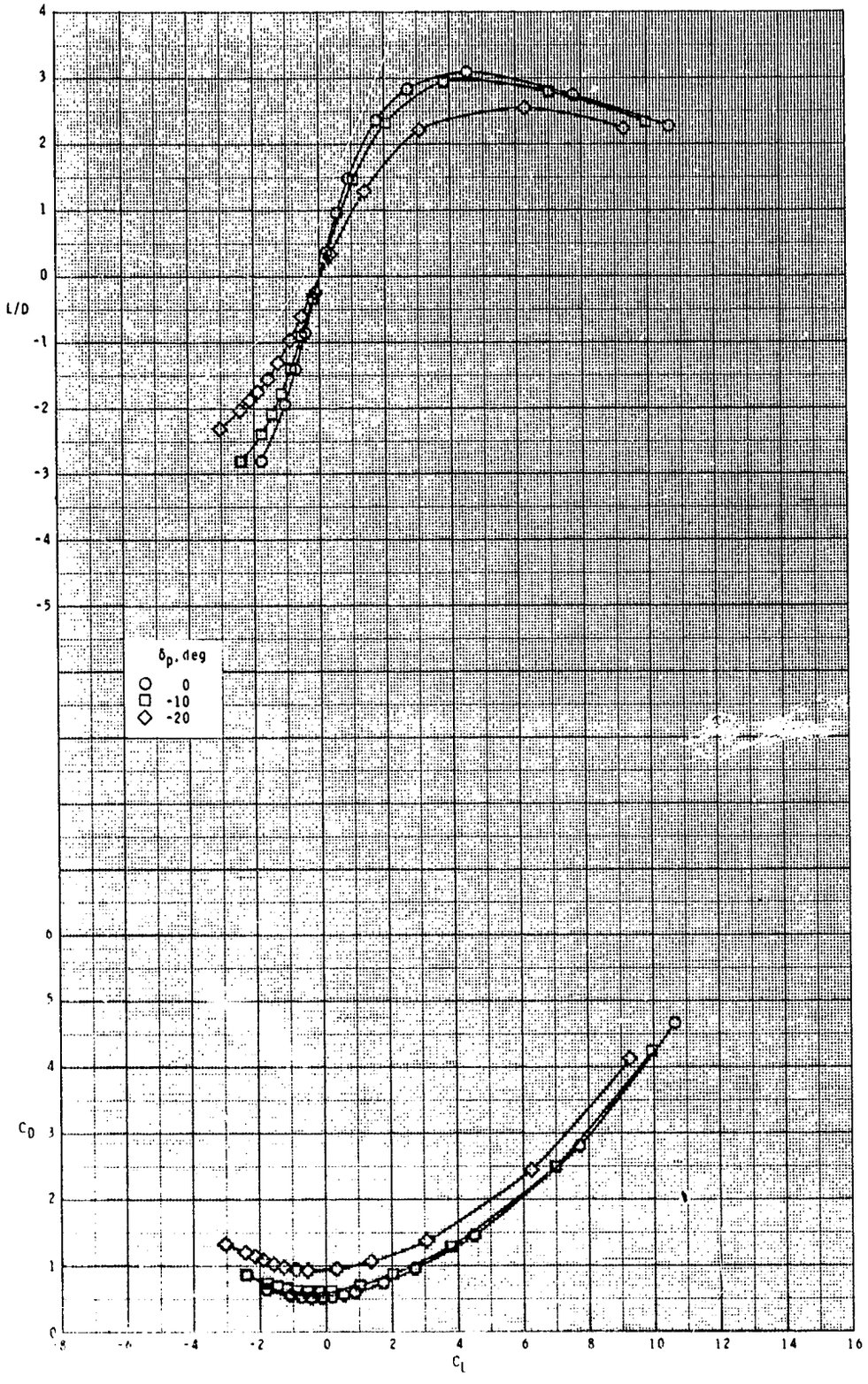

(a) Concluded.

Figure 36.- Continued.

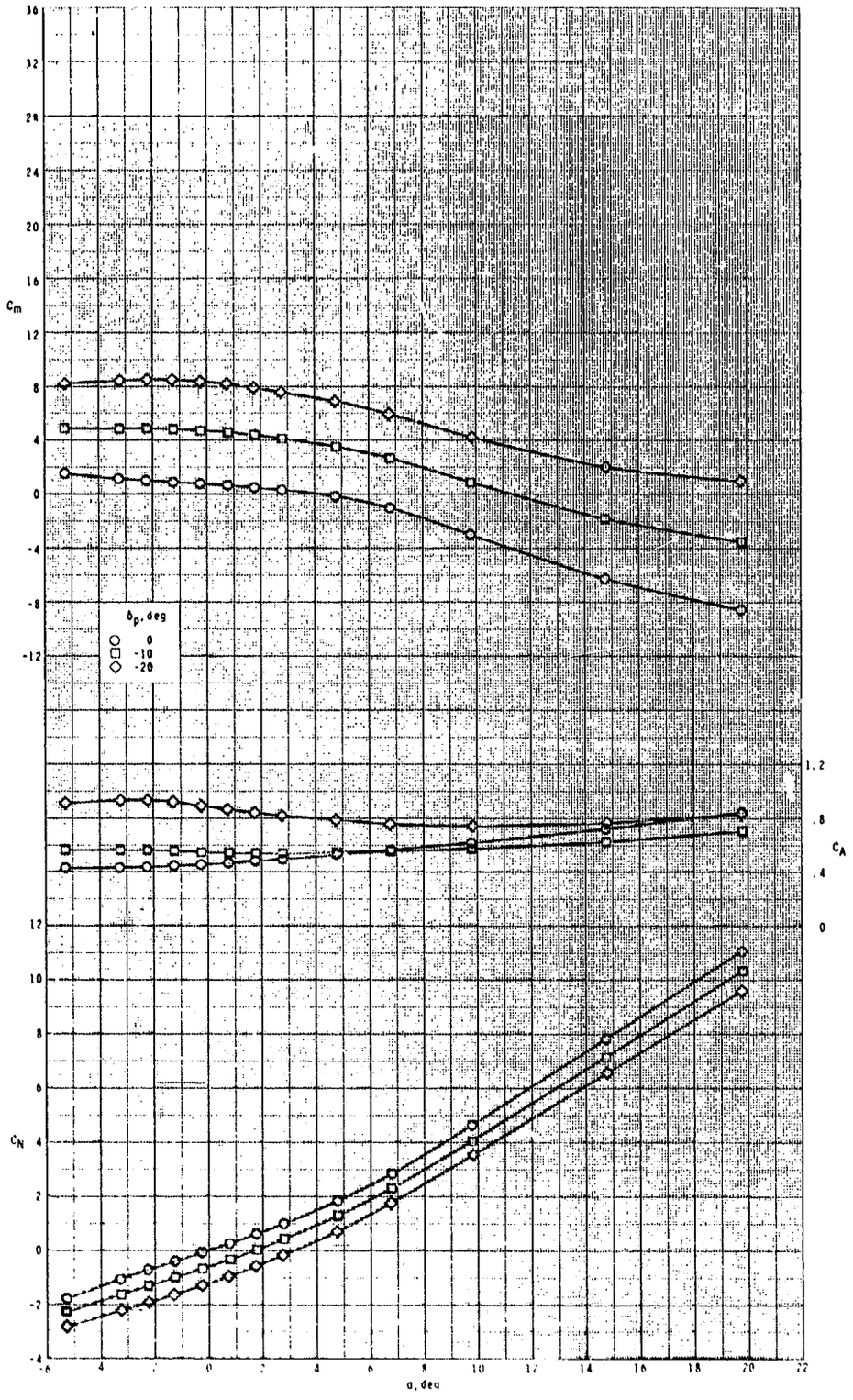

(b) M = 2.95.

Figure 36.- Continued.

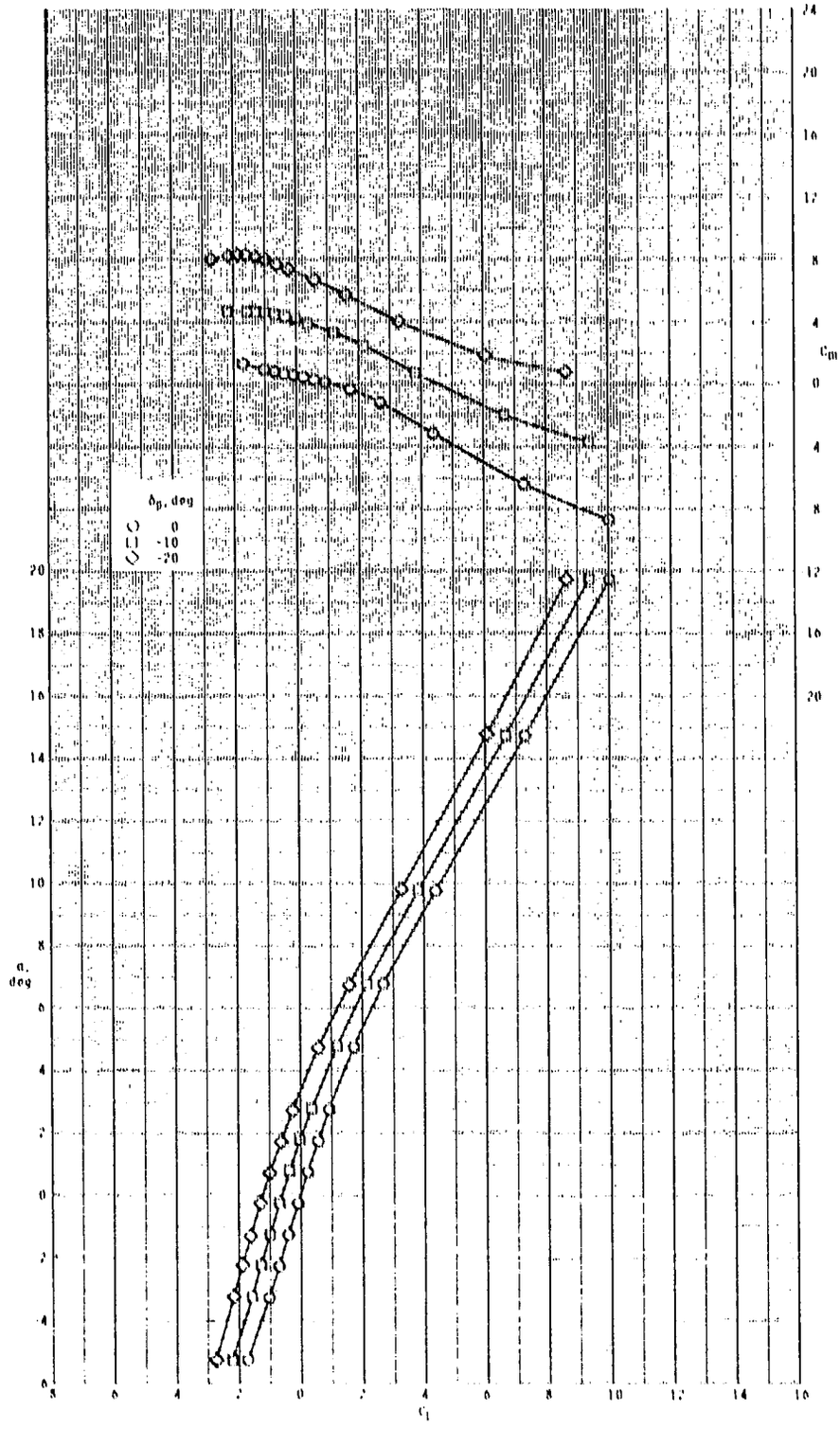

(b) Continued.

Figure 36.- Continued.

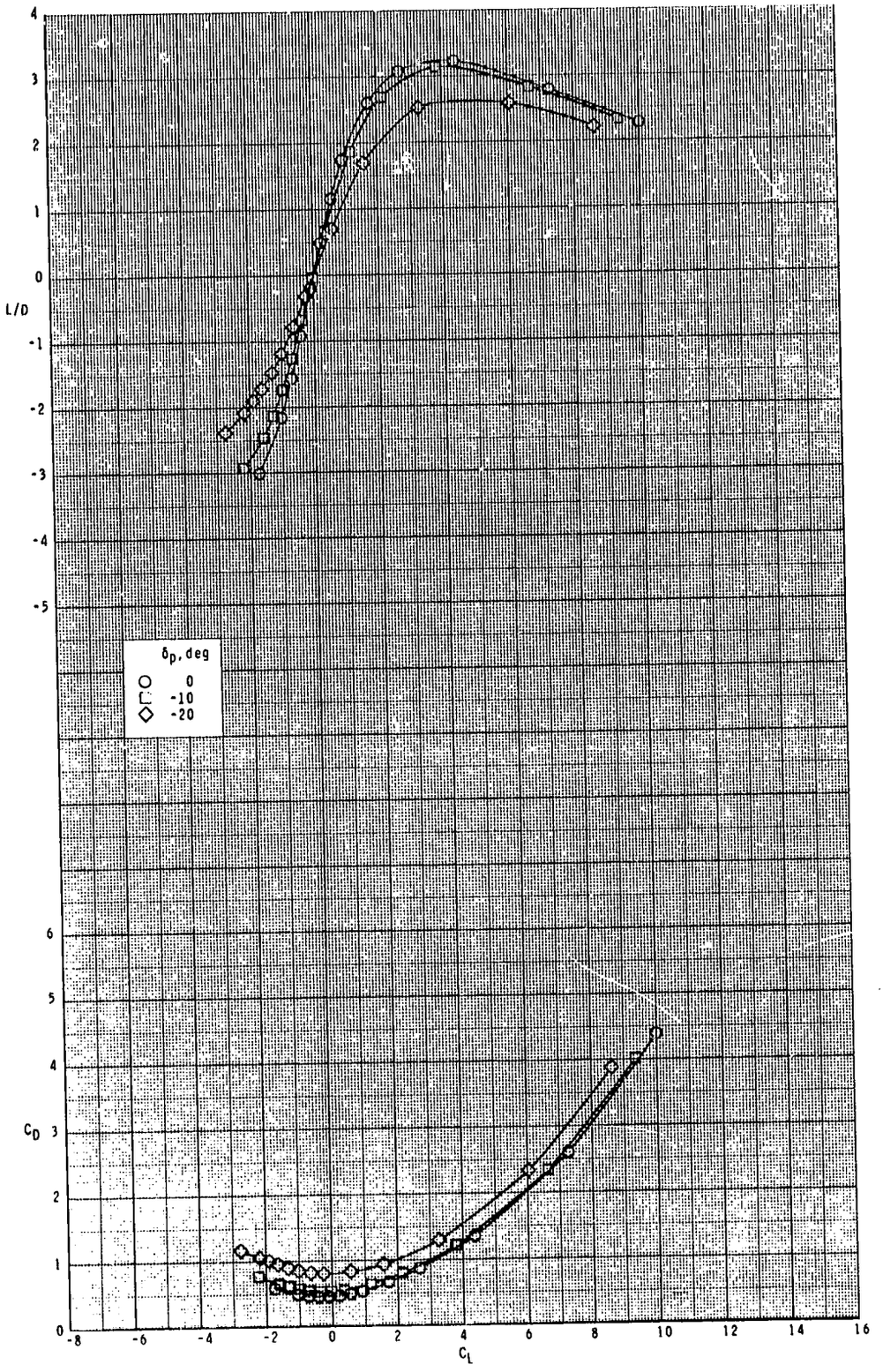

(b) Concluded.

Figure 36.- Continued.

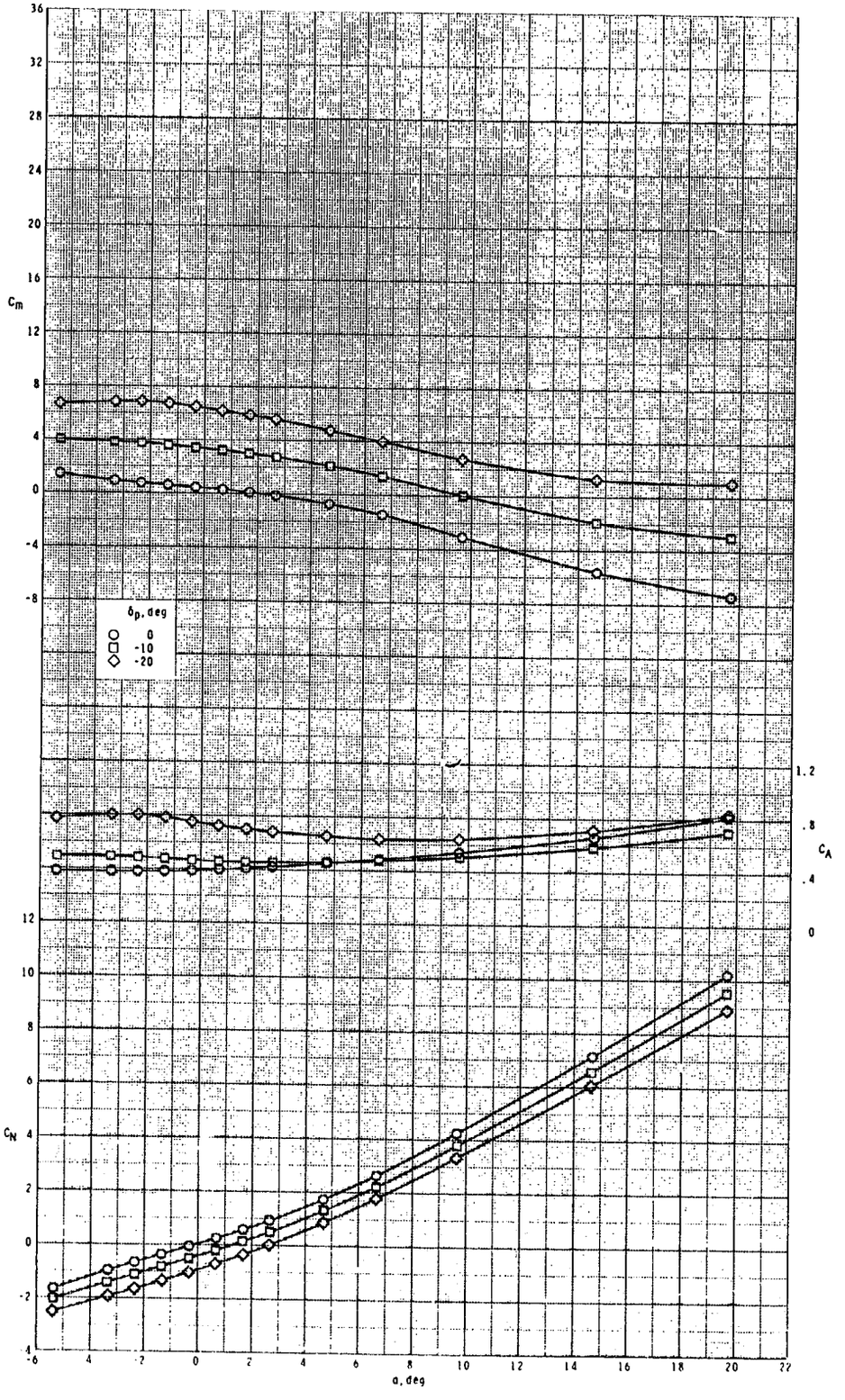

(c) M = 3.50.

Figure 36.- Continued.

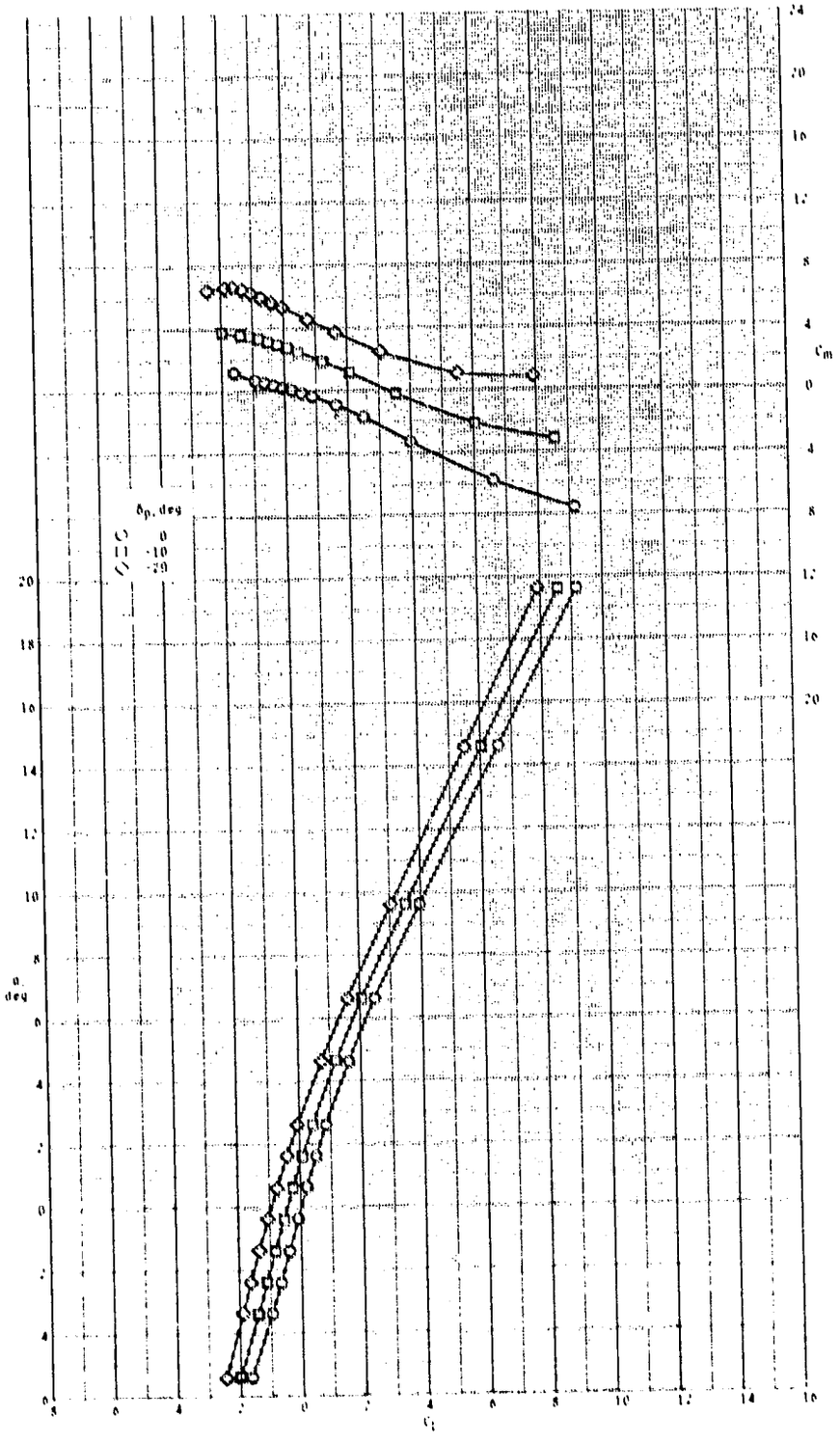

(e) Continued.

Figure 36.- Continued.

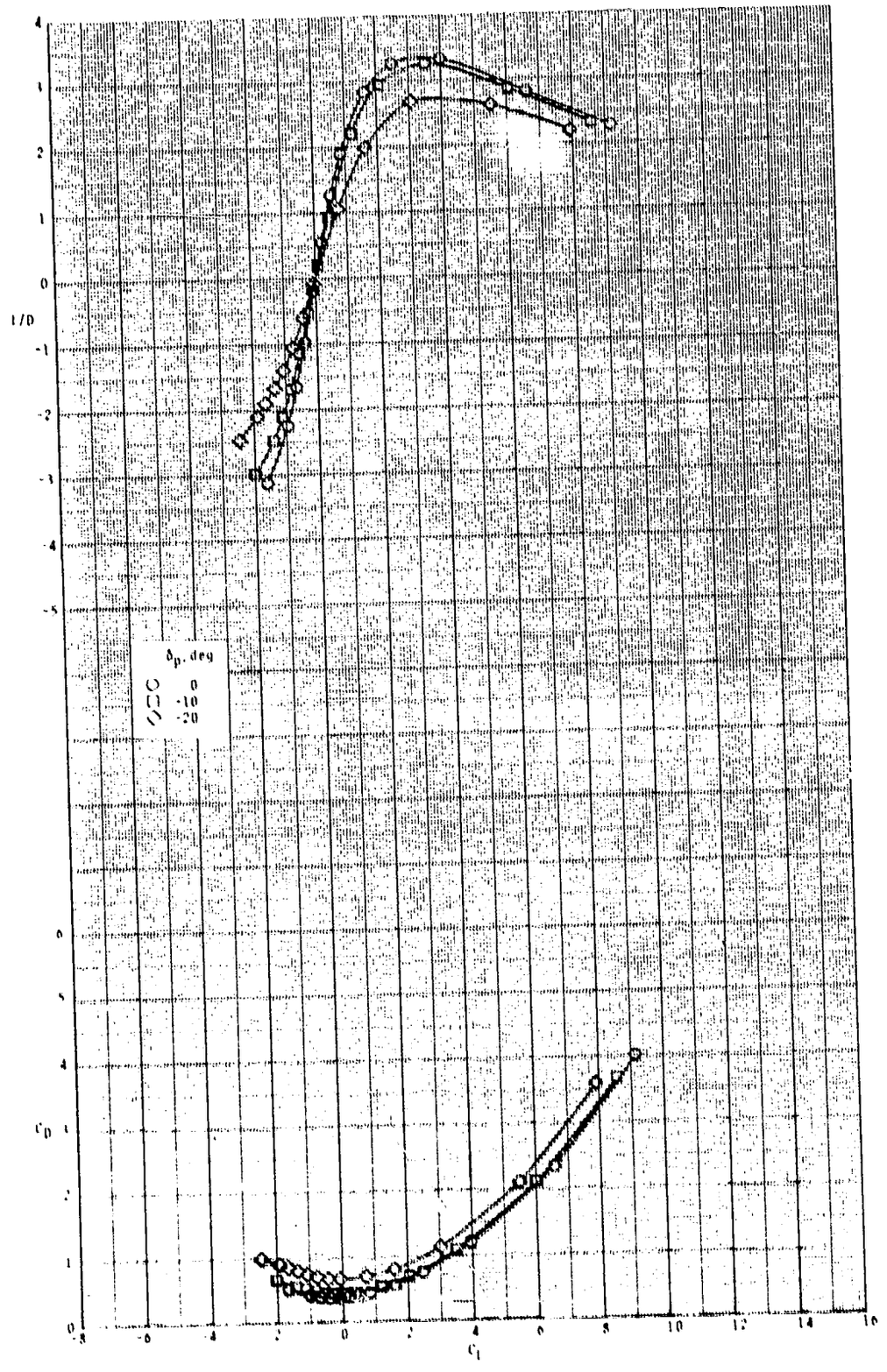

(c) Concluded.

Figure 36.- Continued.

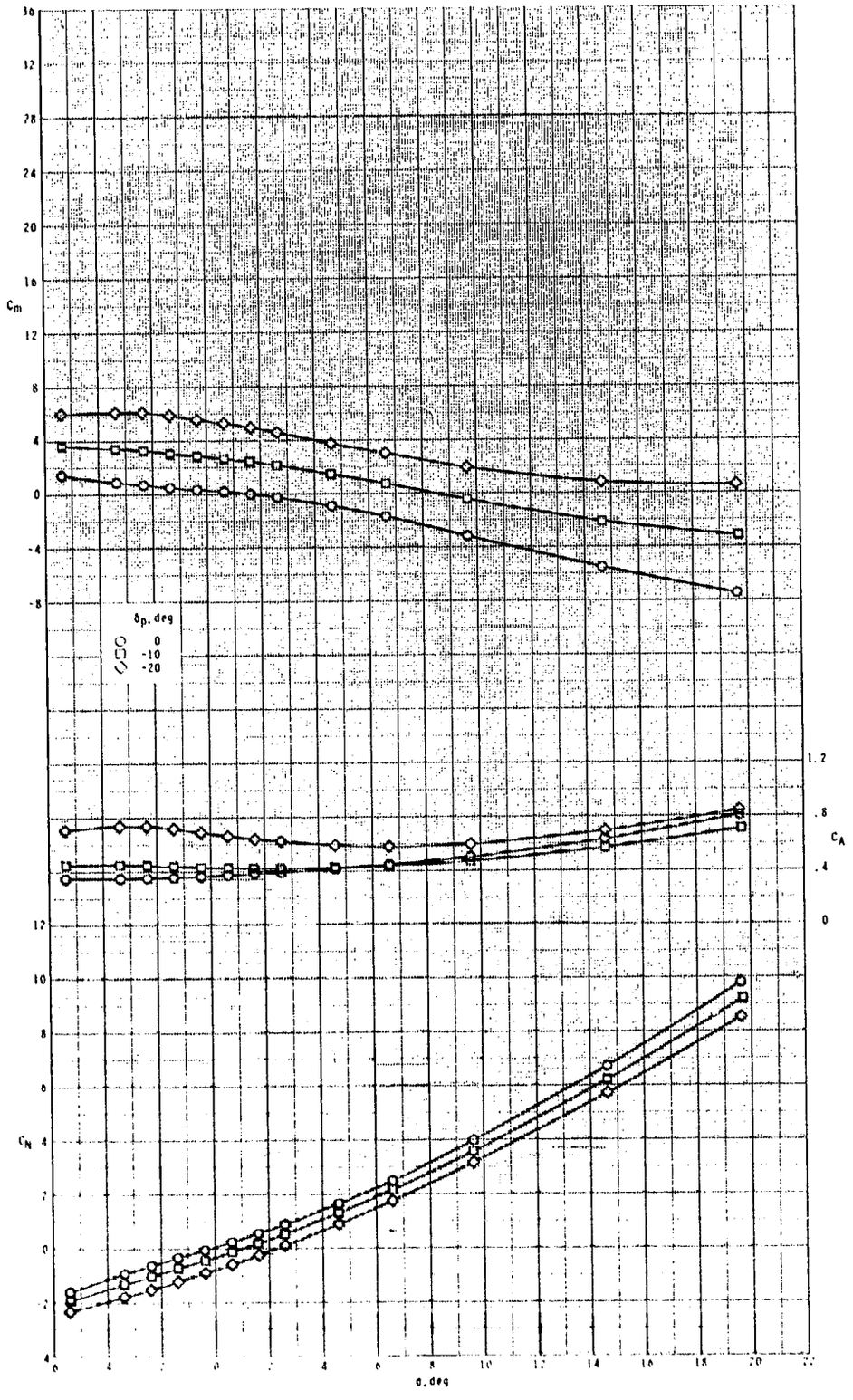

(d) M = 3.95.

Figure 36.- Continued.

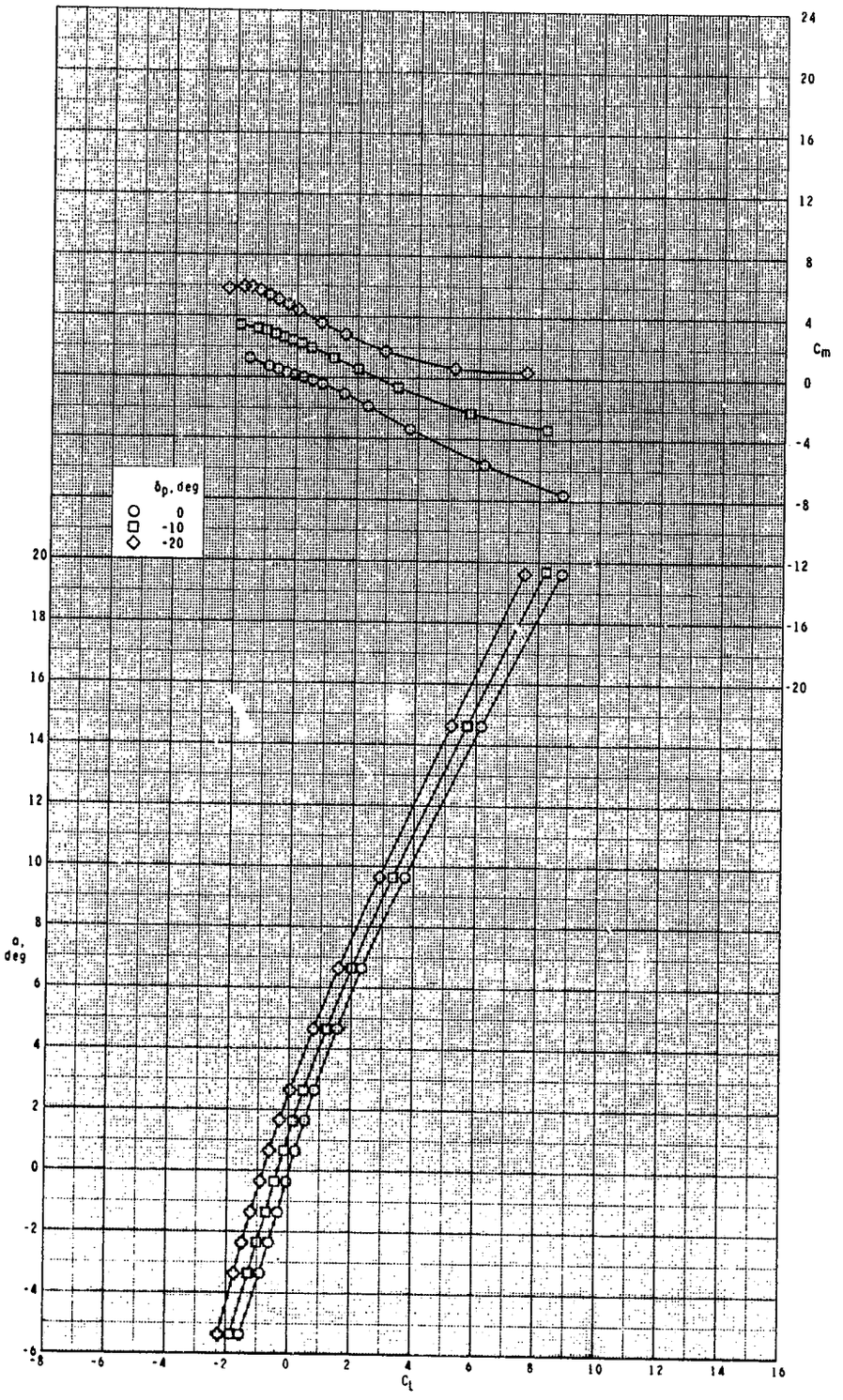

(d) Continued.

Figure 36.- Continued.

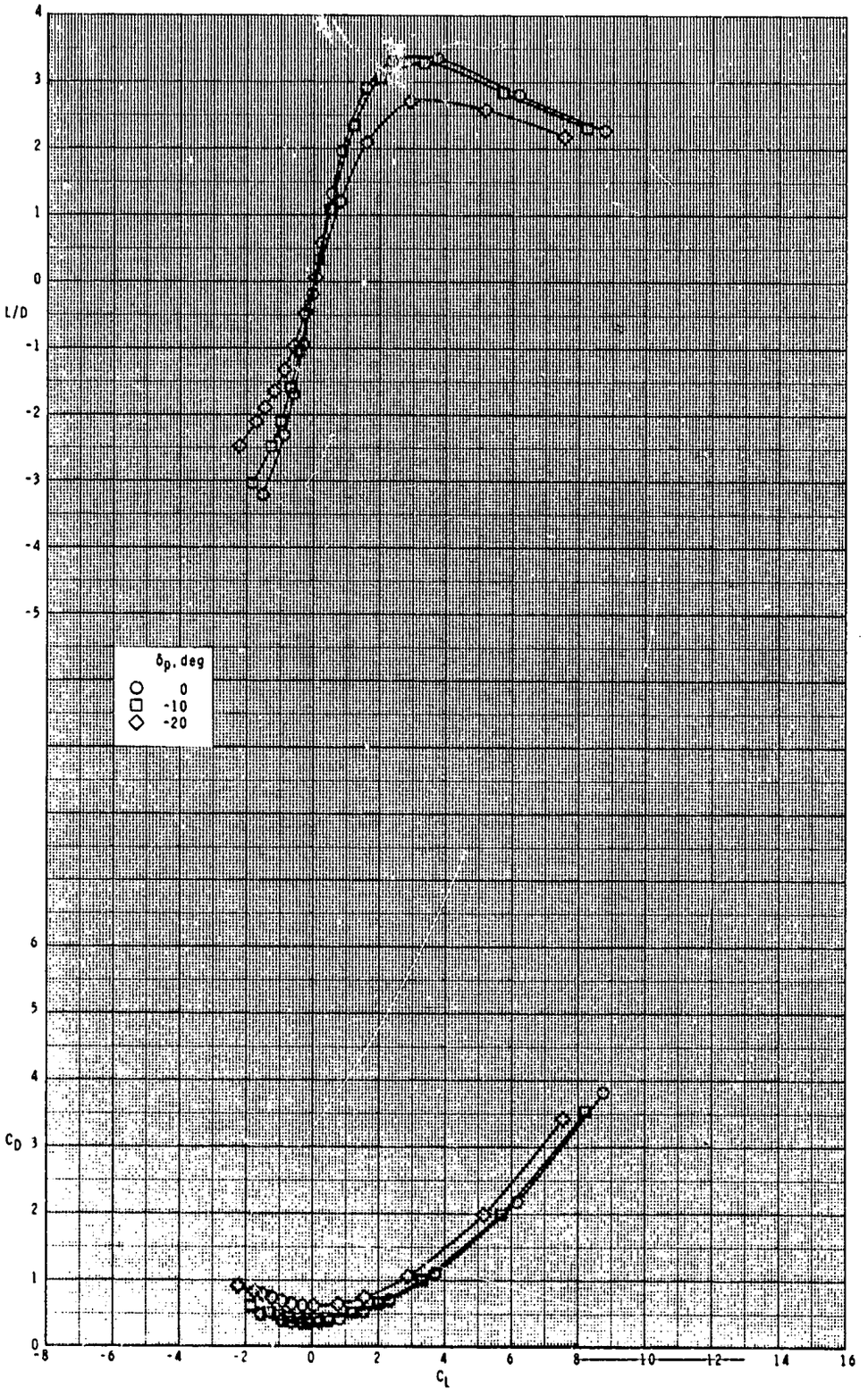

(d) Concluded.

Figure 36.- Concluded.

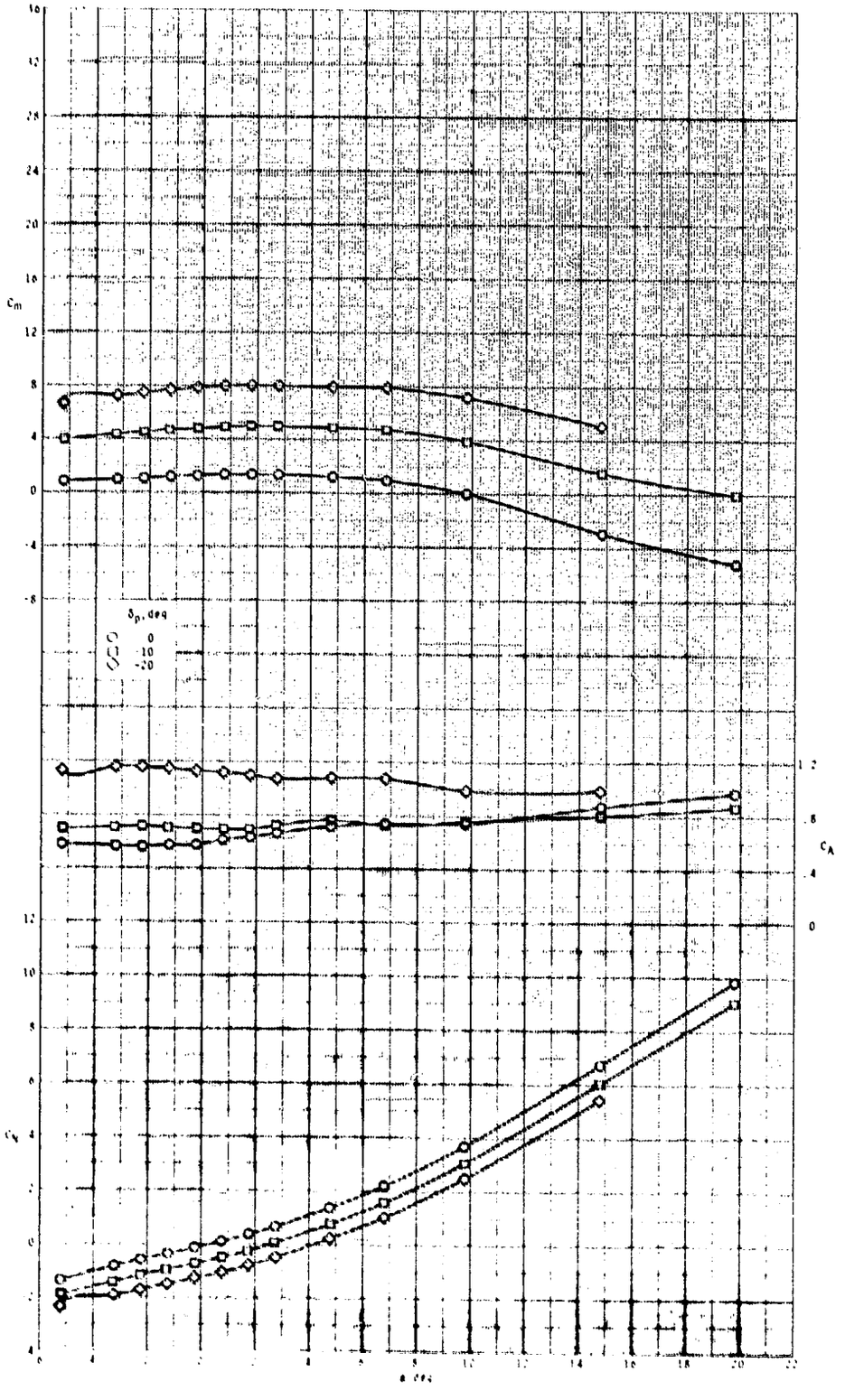

(a) M = 2.50.

Figure 37.- Pitch-control effectiveness of configuration $B_1I_3T_1$ with $\phi_I = 135°$.

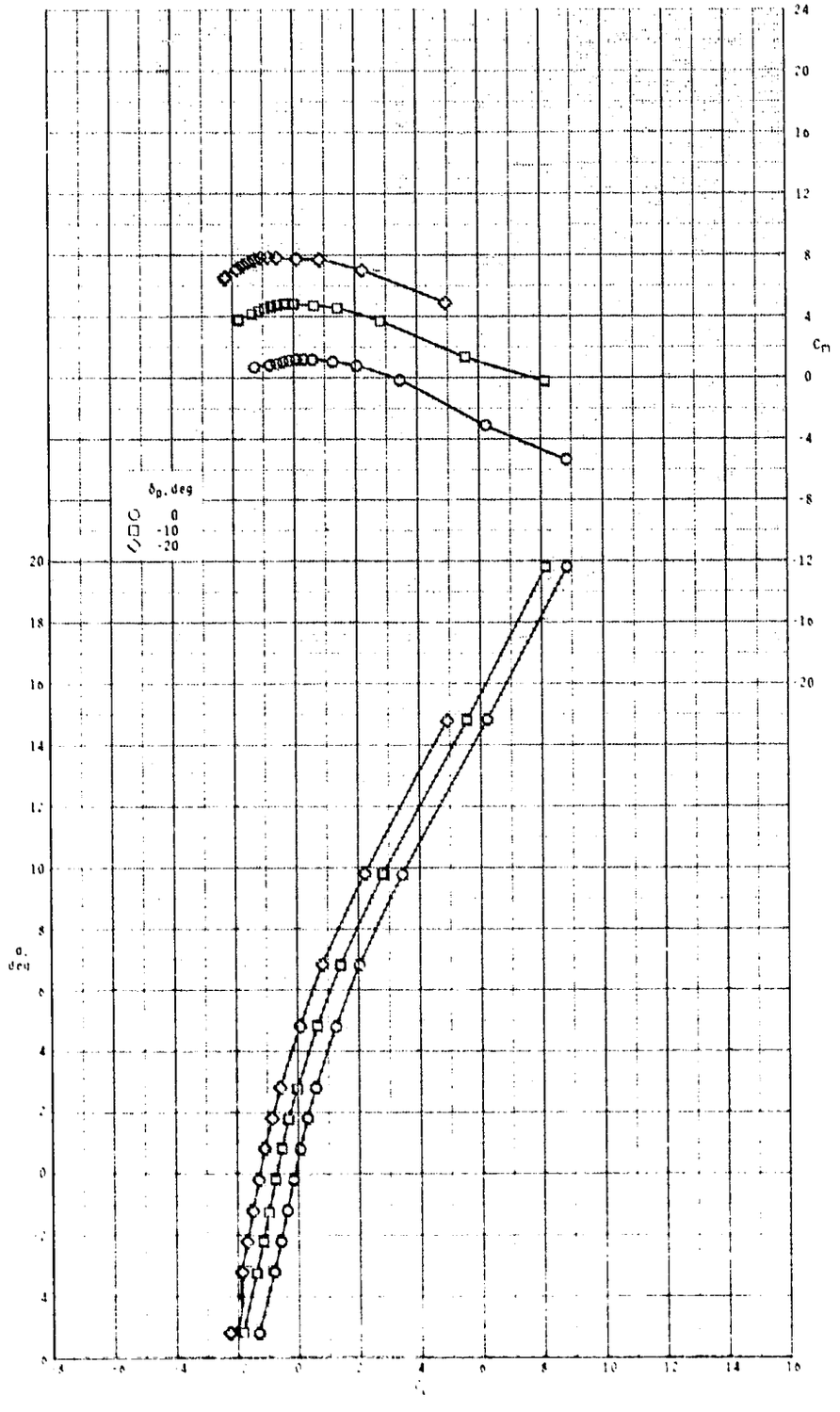

(a) Continued.

Figure 37.- Continued.

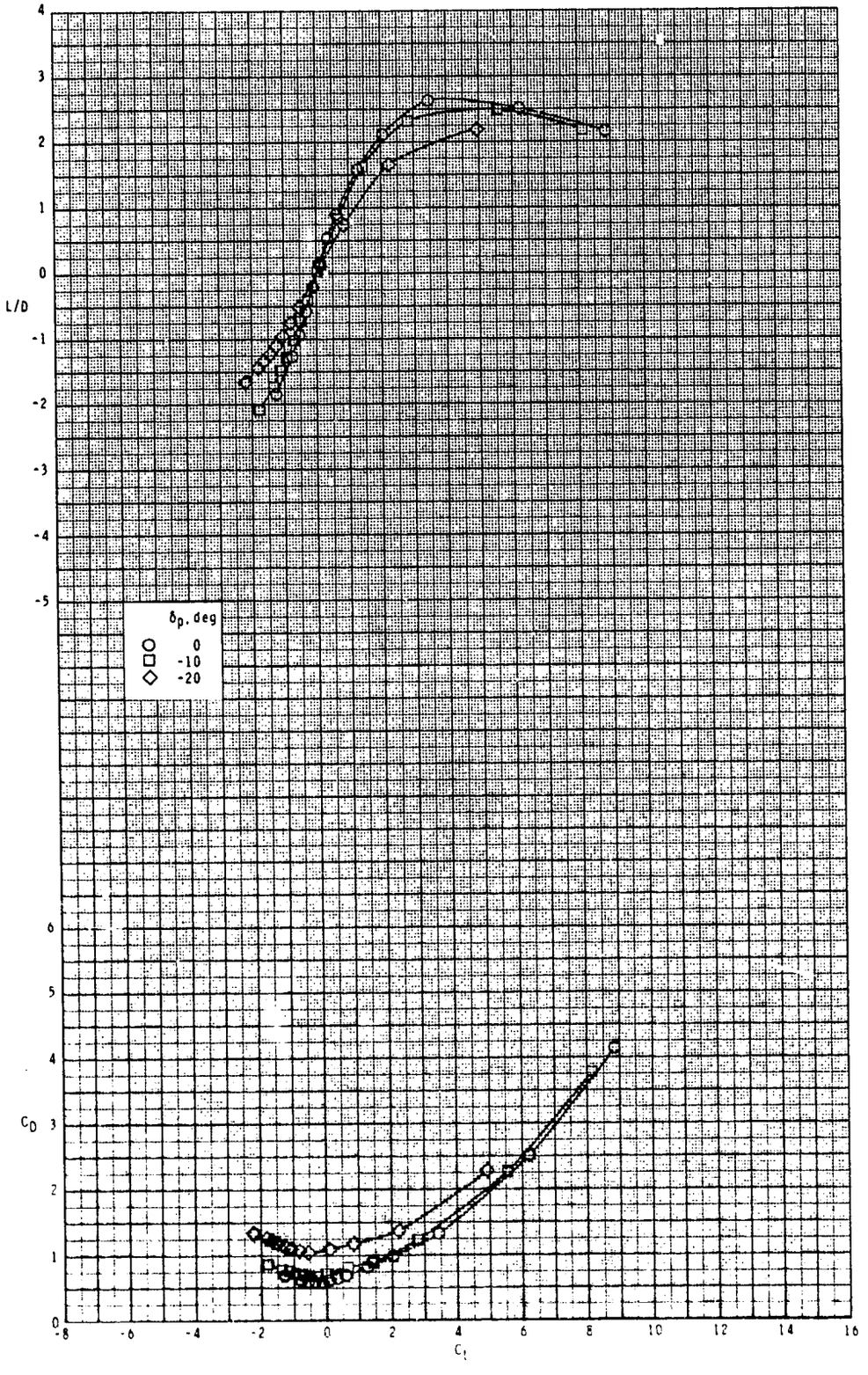

(a) Concluded.

Figure 37.- Continued.

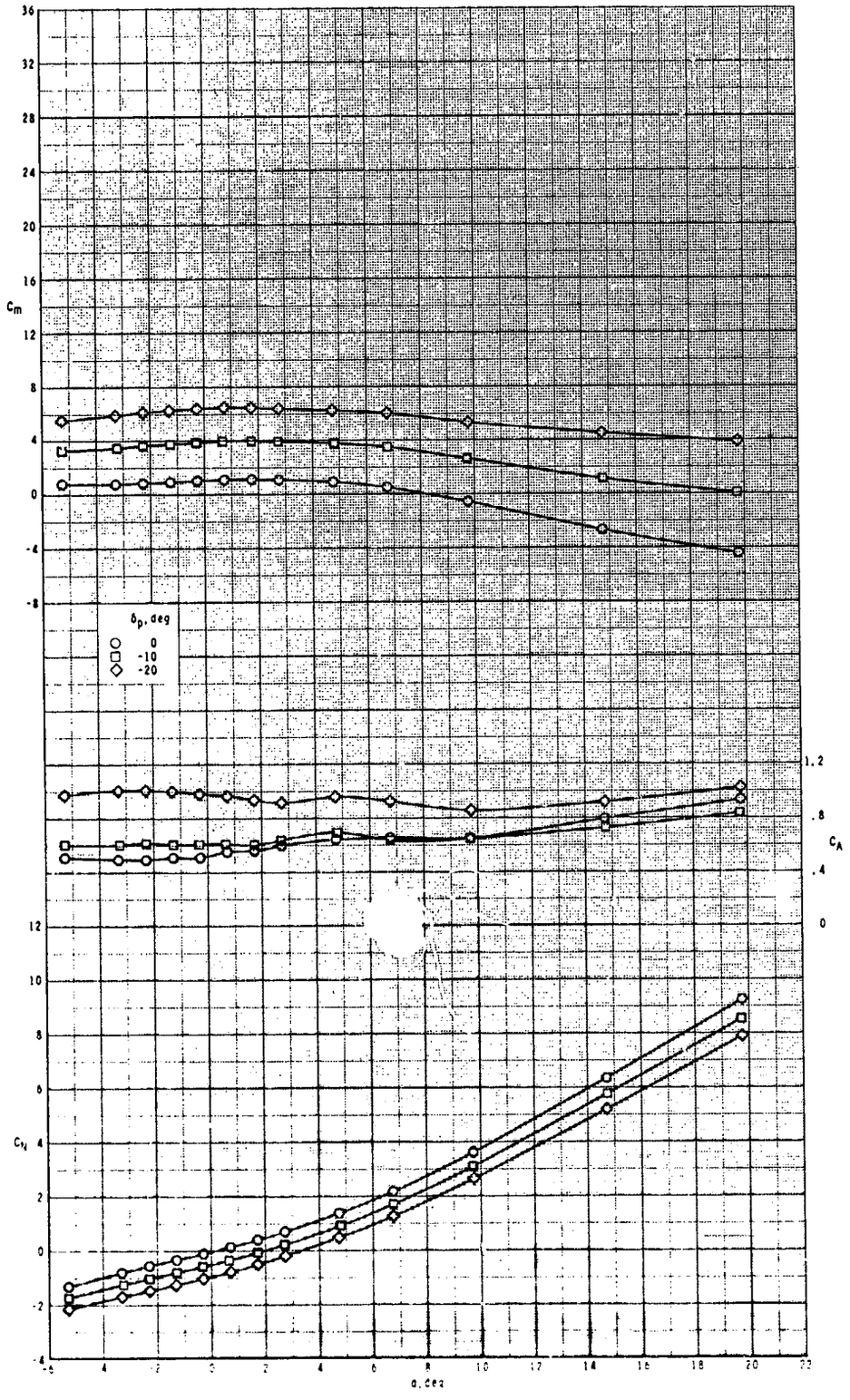

(b) M = 2.95.

Figure 37.- Continued.

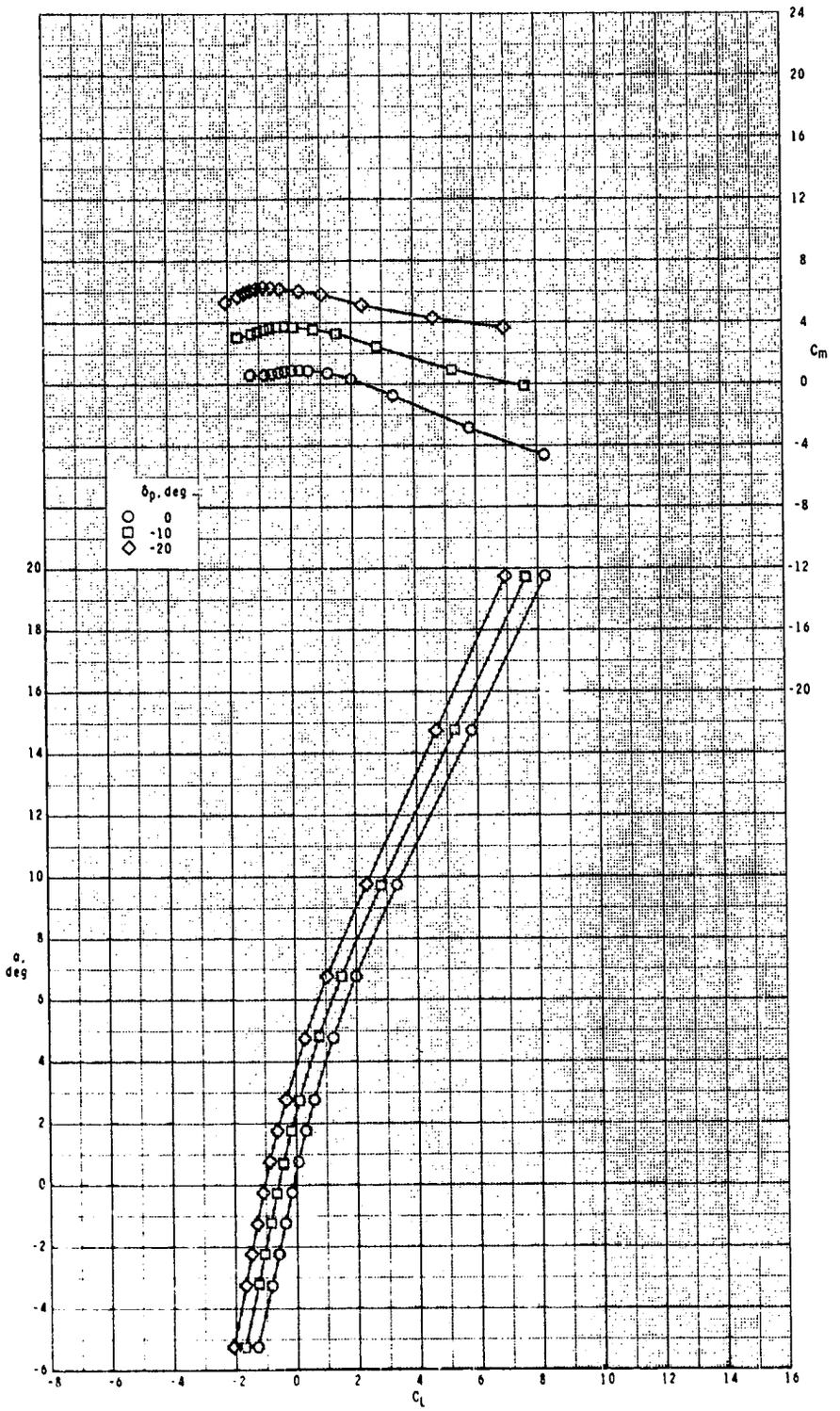

(b) Continued.

Figure 37.- Continued.

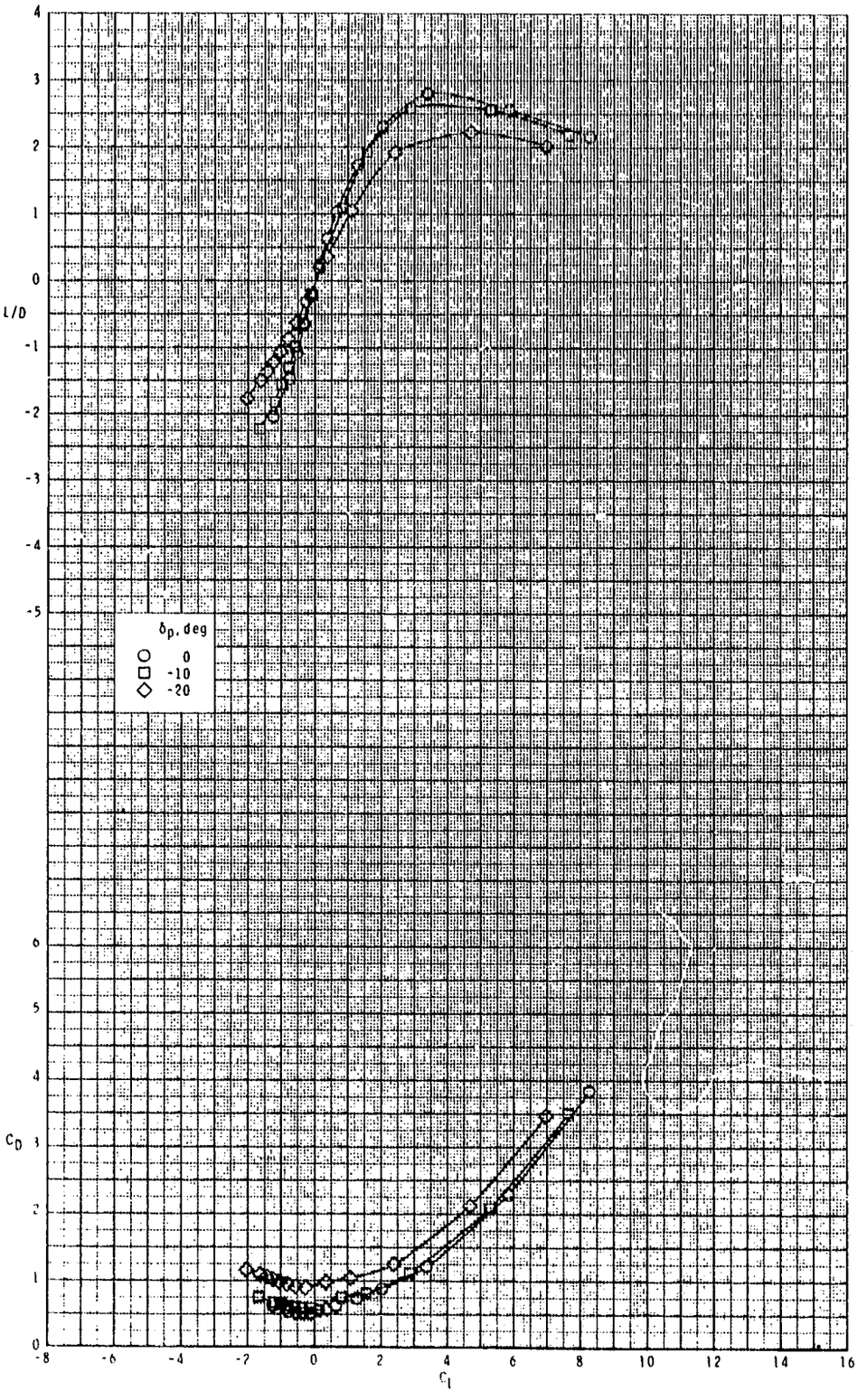

(b) Concluded.

Figure 37.- Continued.

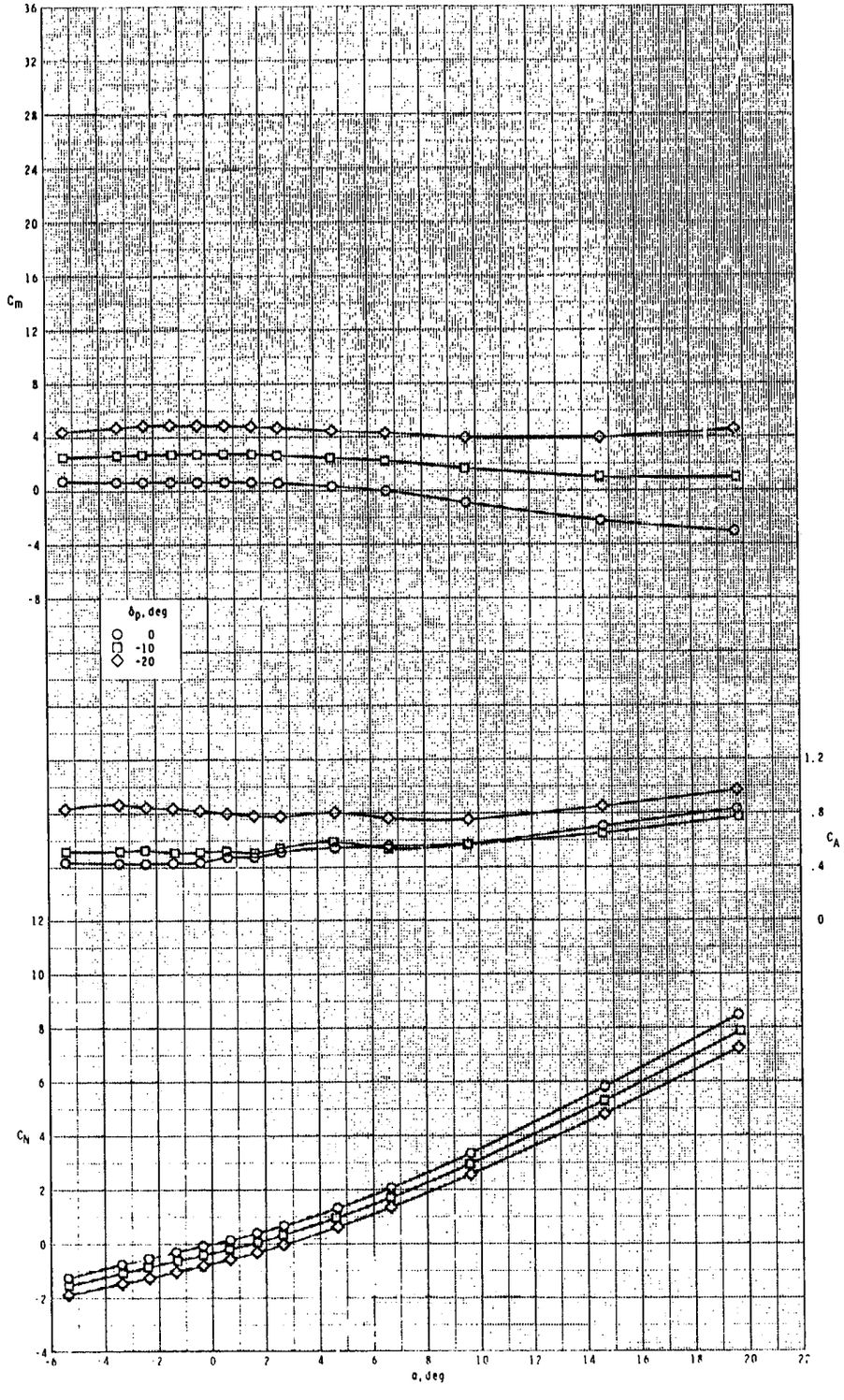

(c) M = 3.50.

Figure 37.- Continued.

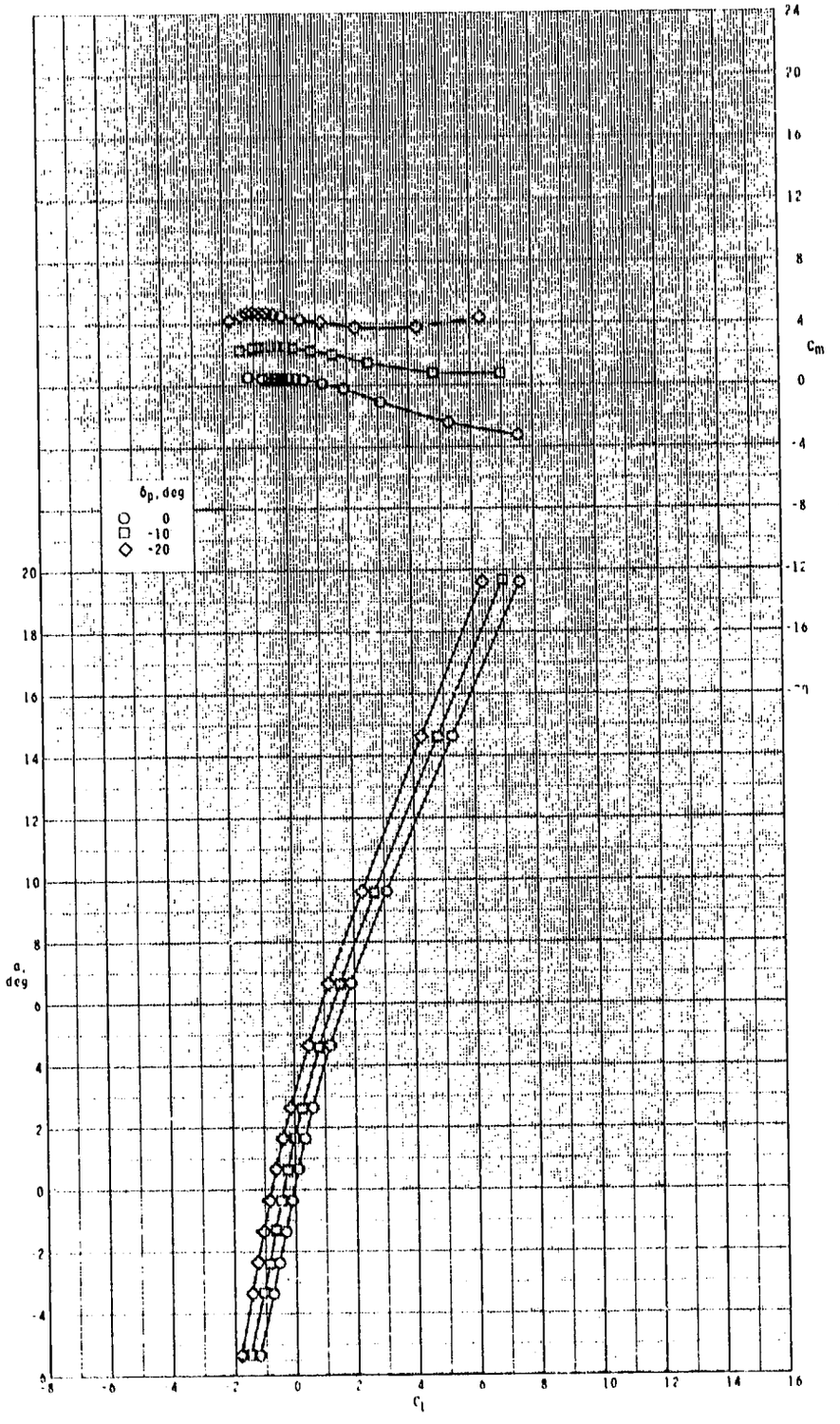

(c) Continued.

Figure 37.- Continued.

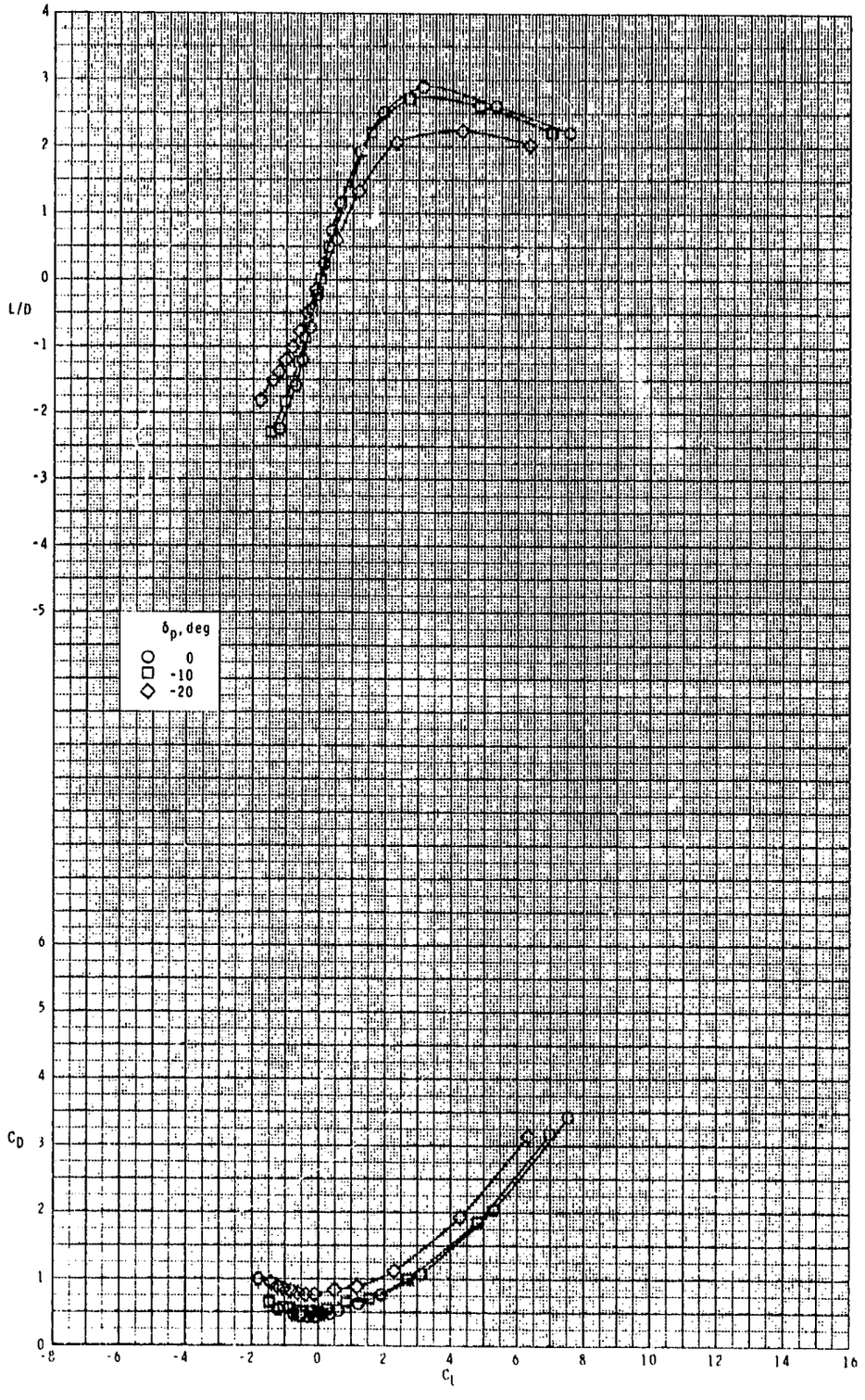

(c) Concluded.

Figure 37.- Continued.

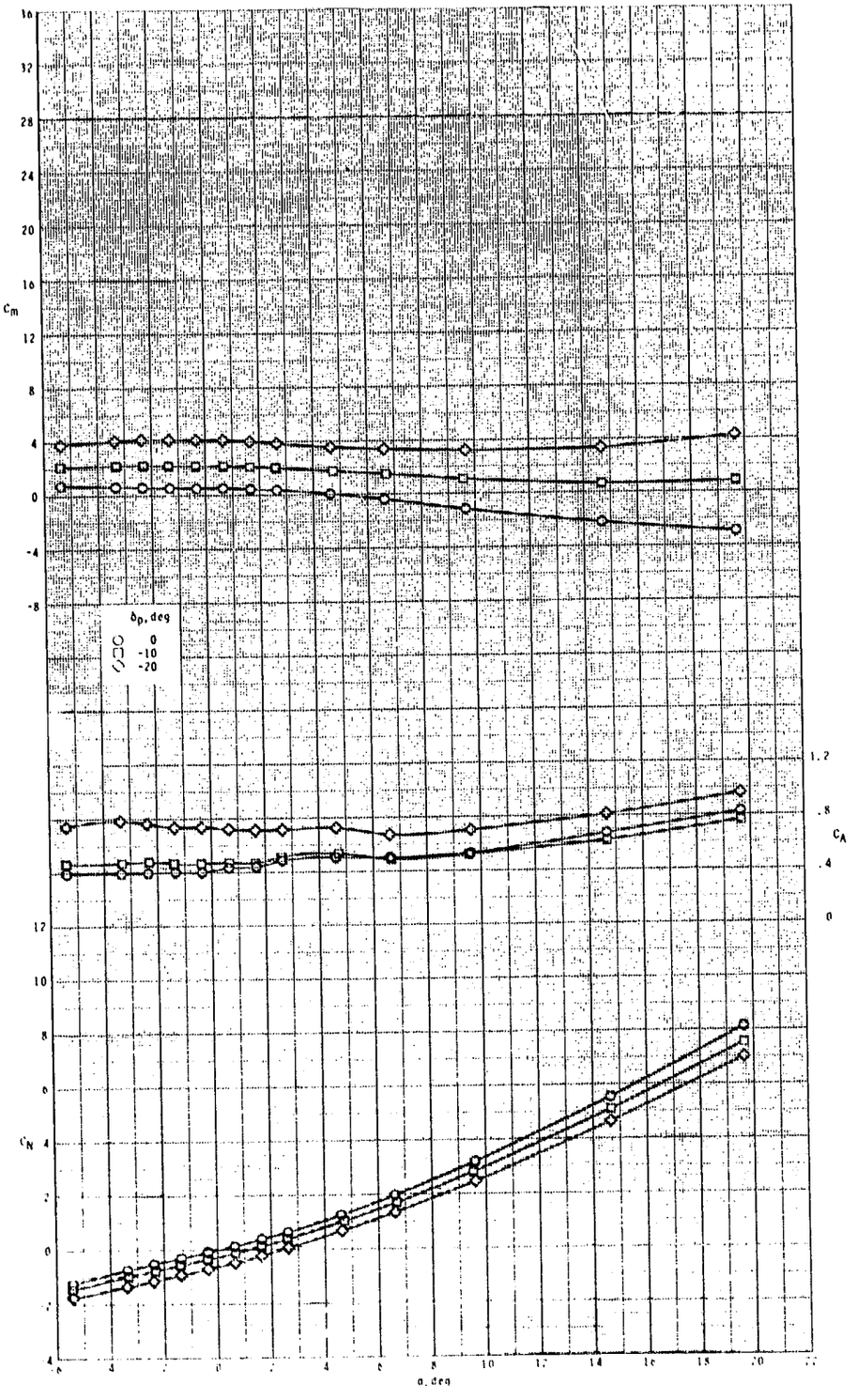

(d) M = 3.95.

Figure 37.- Continued.

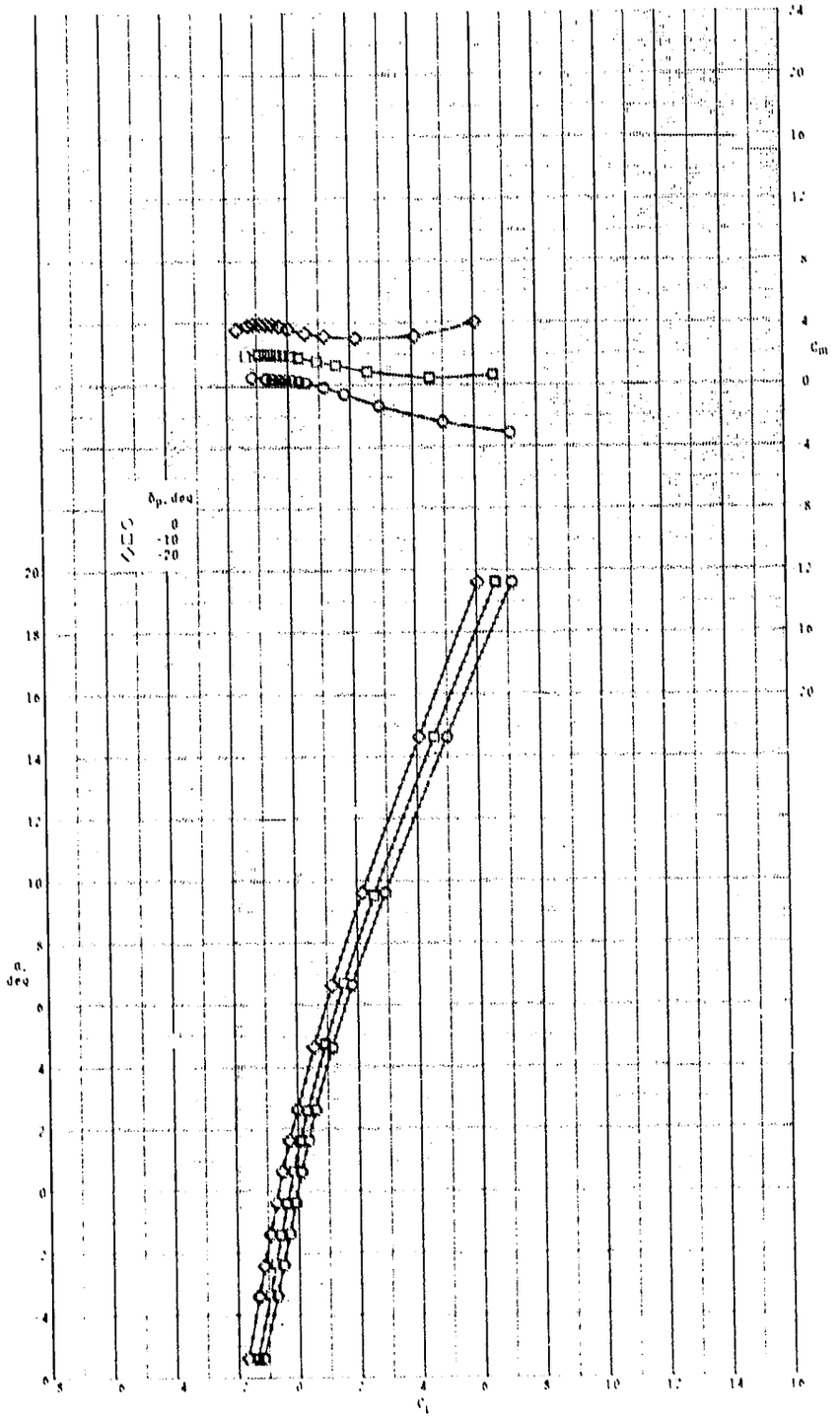

(d) Continued.

Figure 37.- Continued.

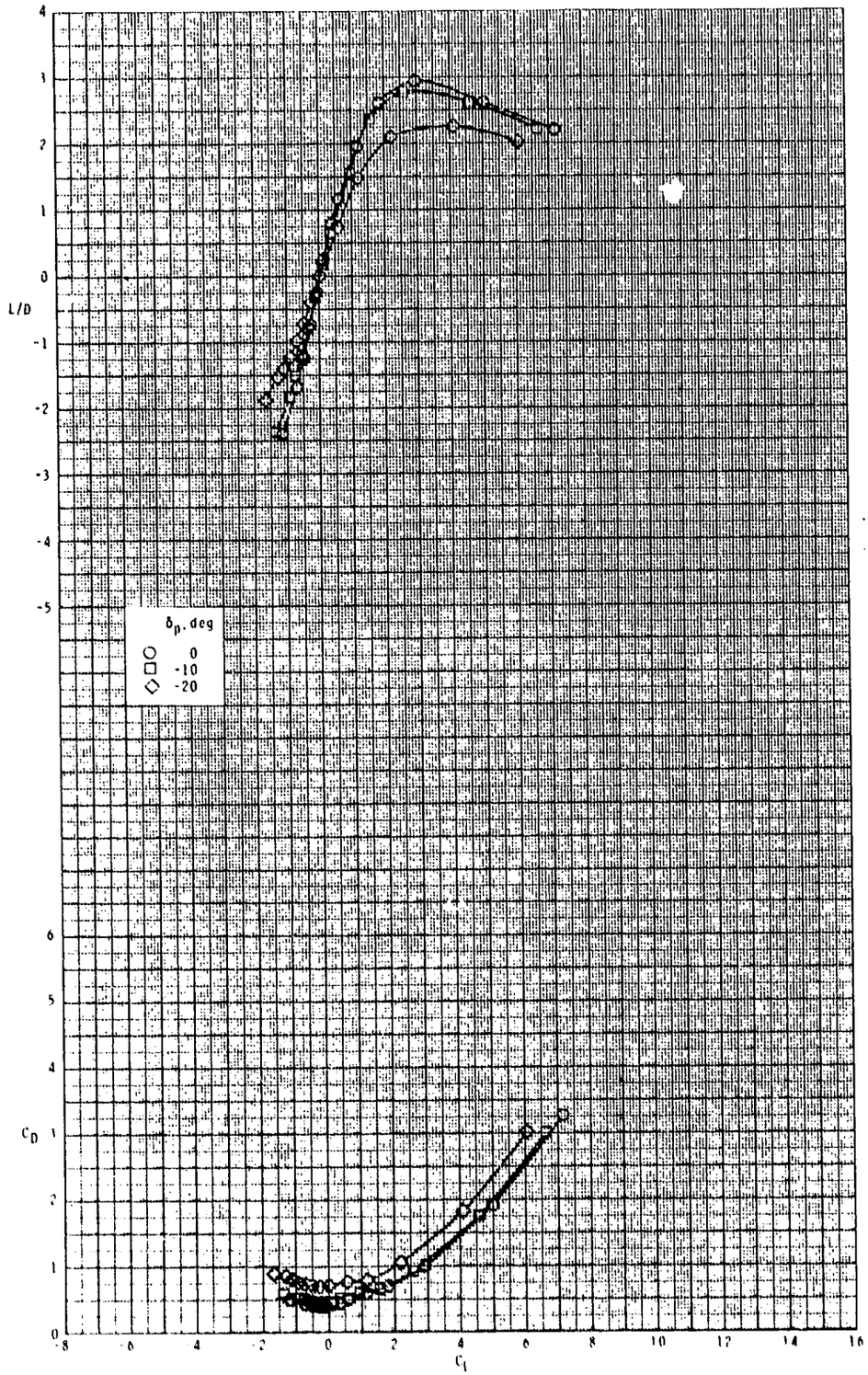

(d) Concluded.

Figure 37.- Concluded.

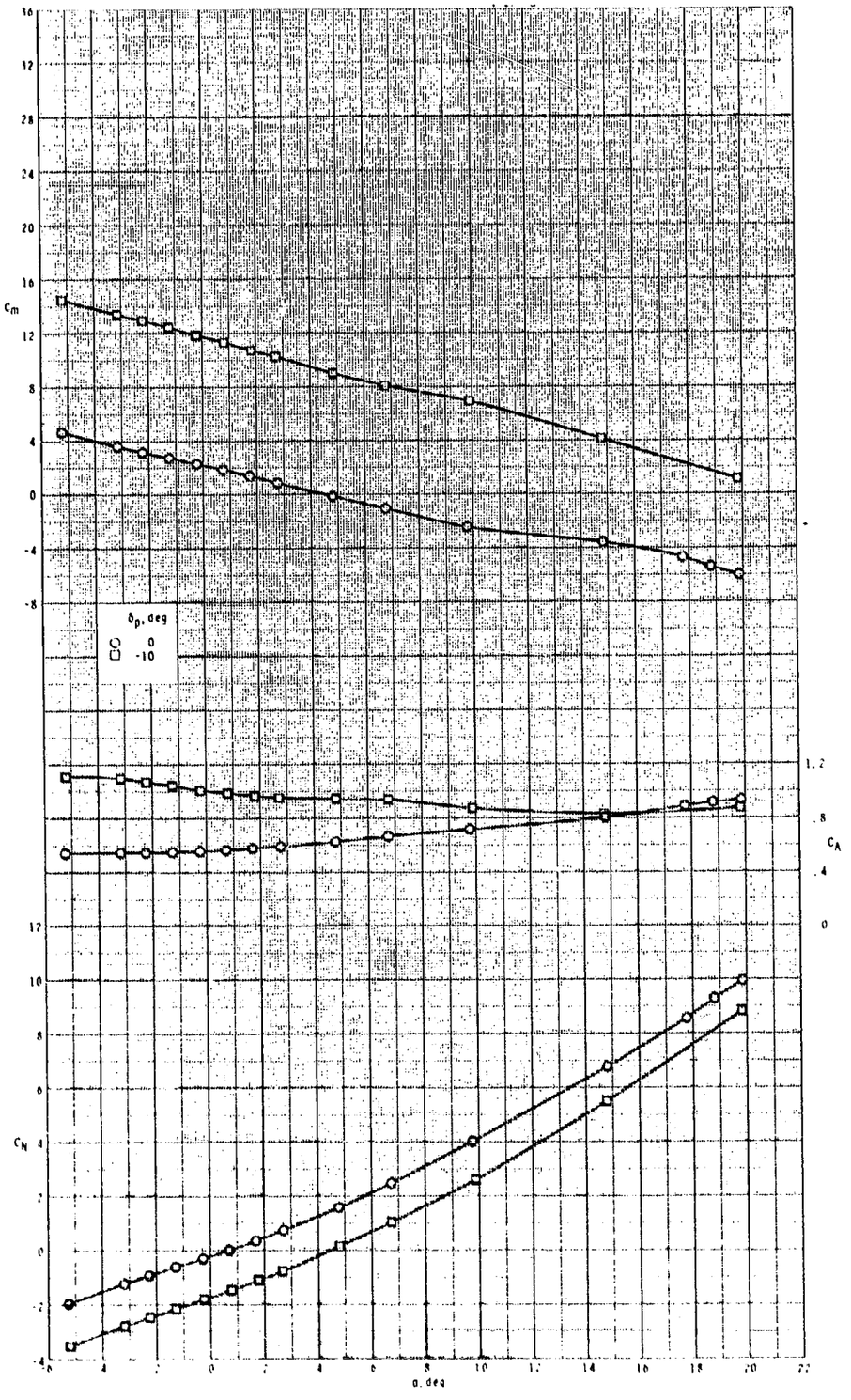

(a) M = 2.50.

Figure 38.- Pitch-control effectiveness of configuration $B_1I_3T_2$ with $\phi_I = 135°$.

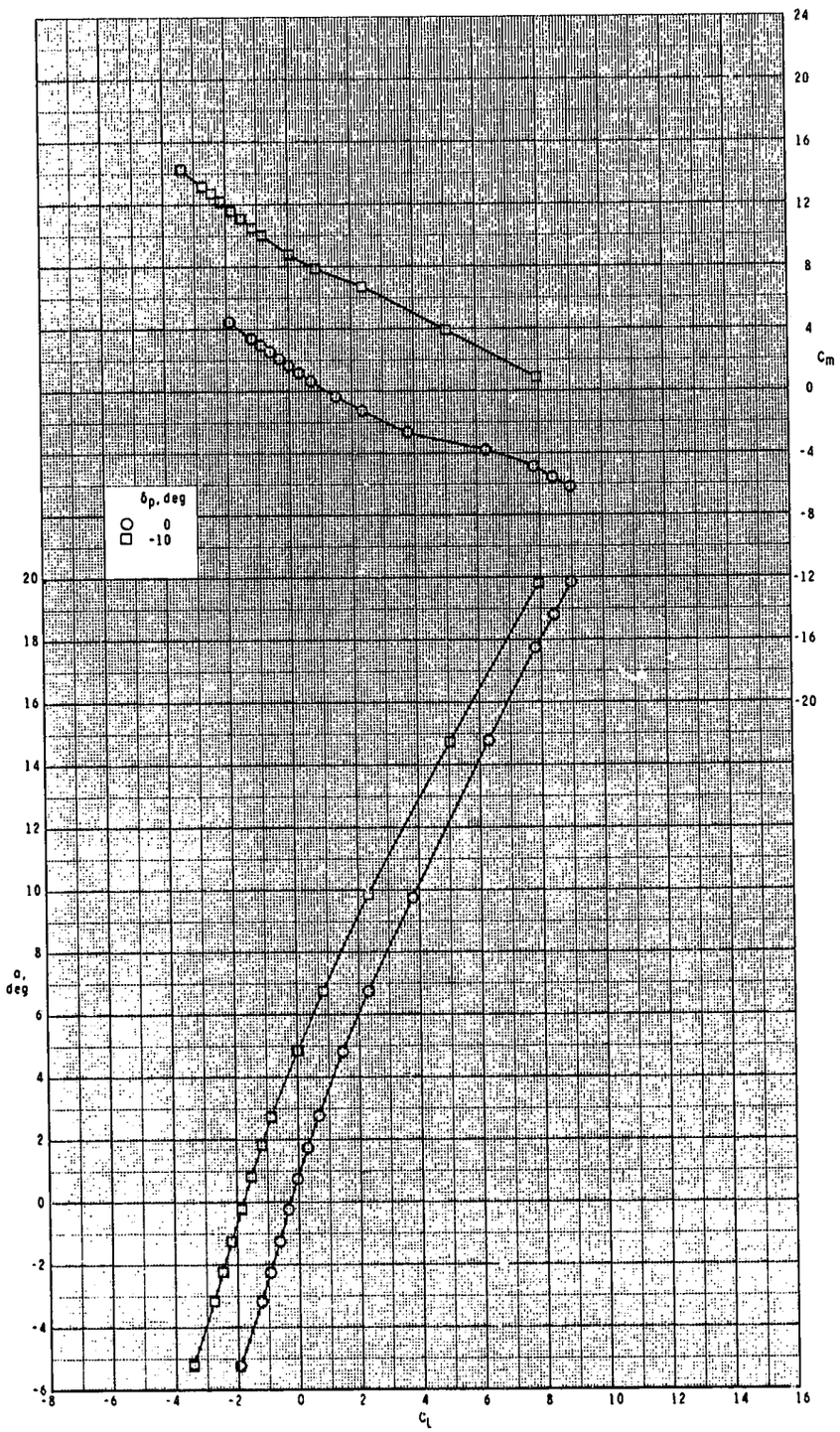

(a) Continued.

Figure 38.- Continued.

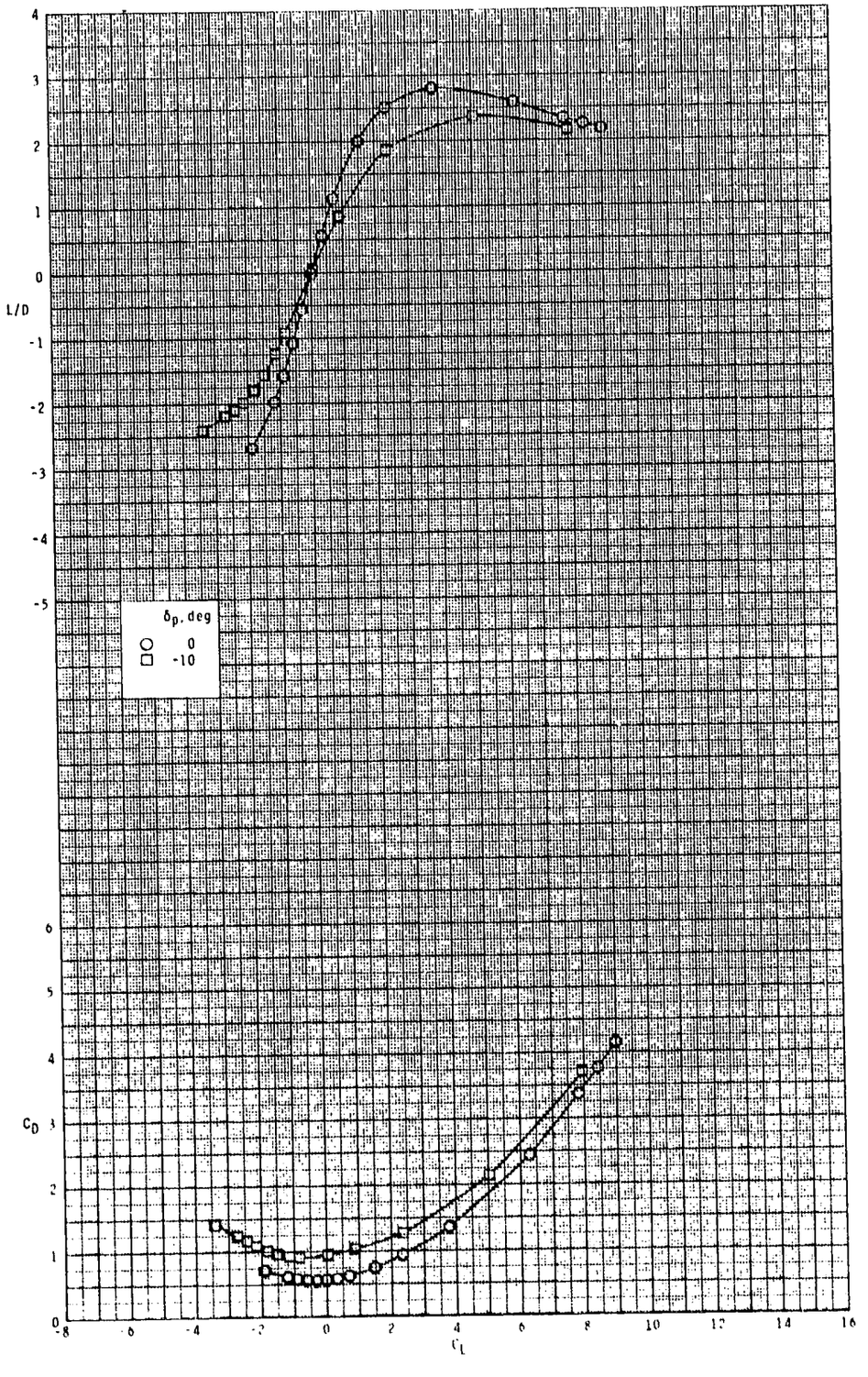

(a) Concluded.

Figure 38.- Continued.

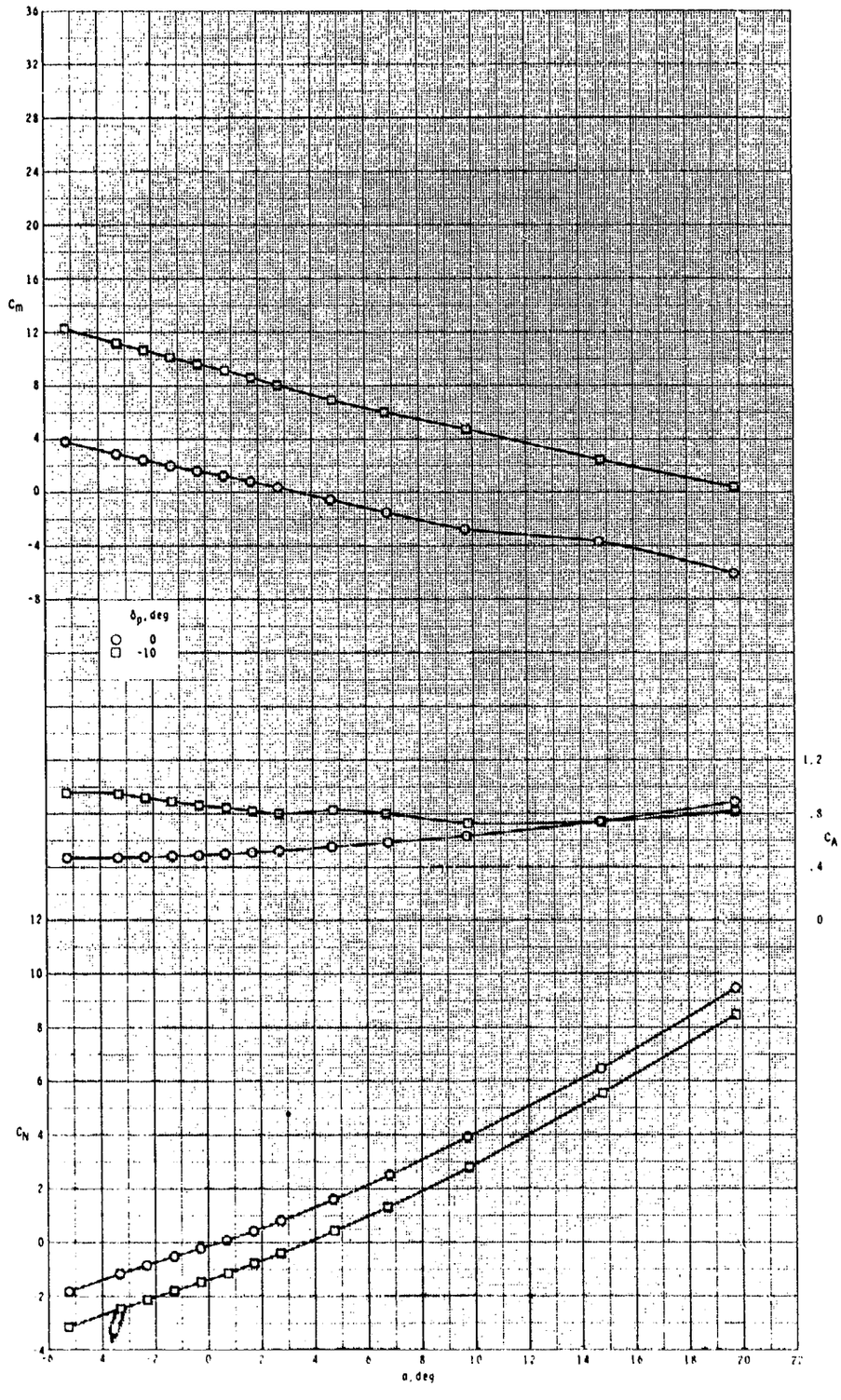

(b) M = 2.95.

Figure 38.- Continued.

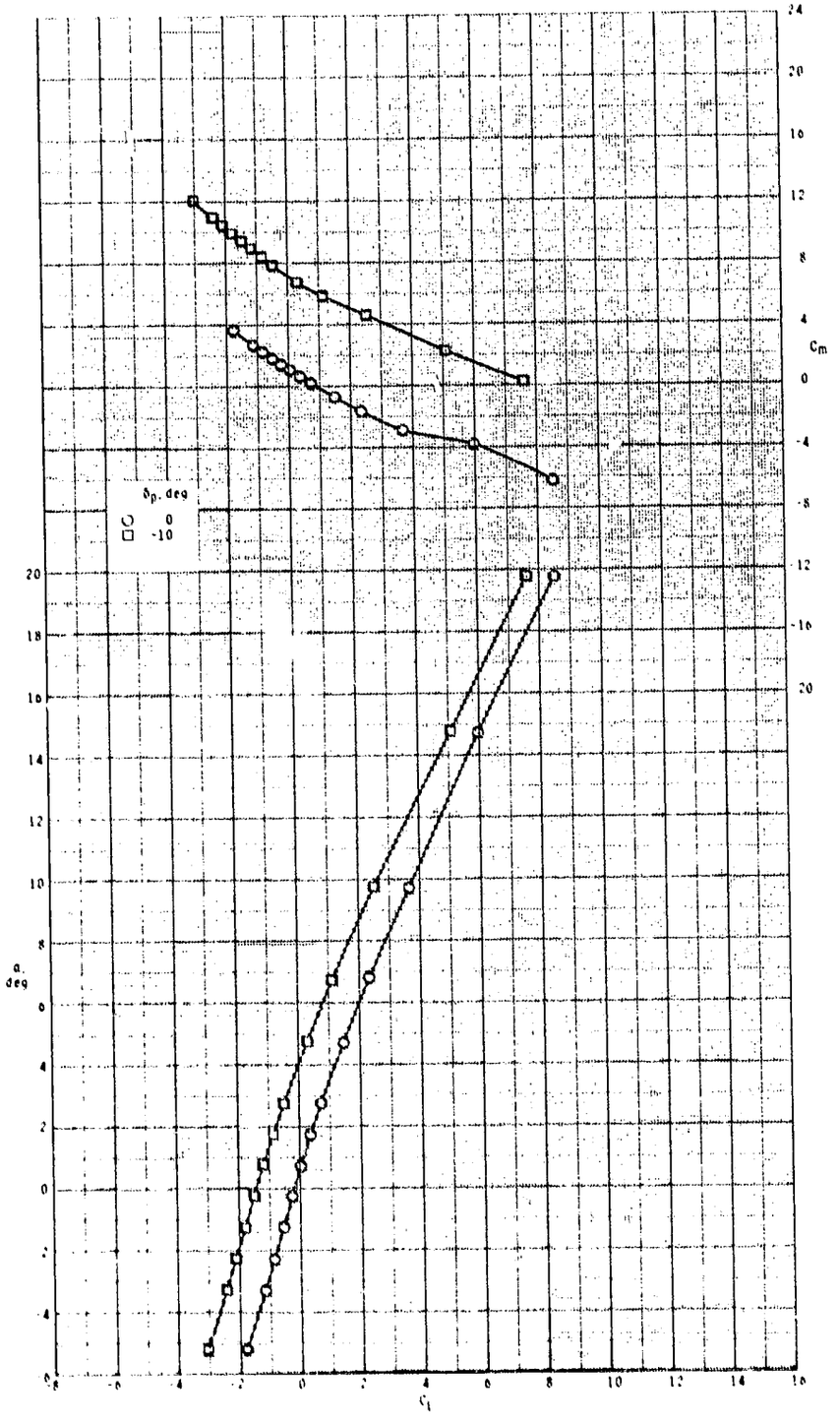

(b) Continued.

Figure 38.- Continued.

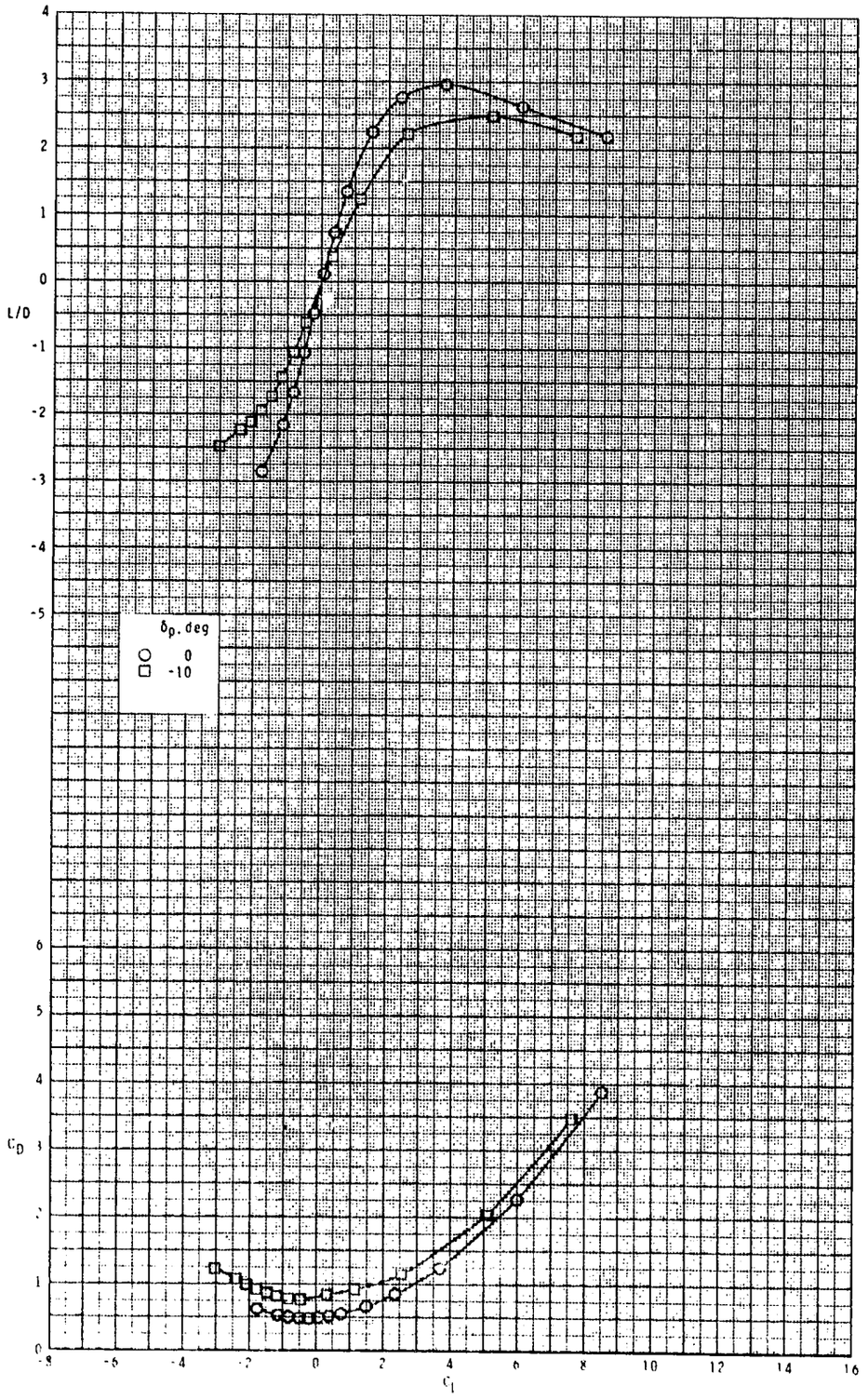

(b) Concluded.

Figure 38.- Continued.

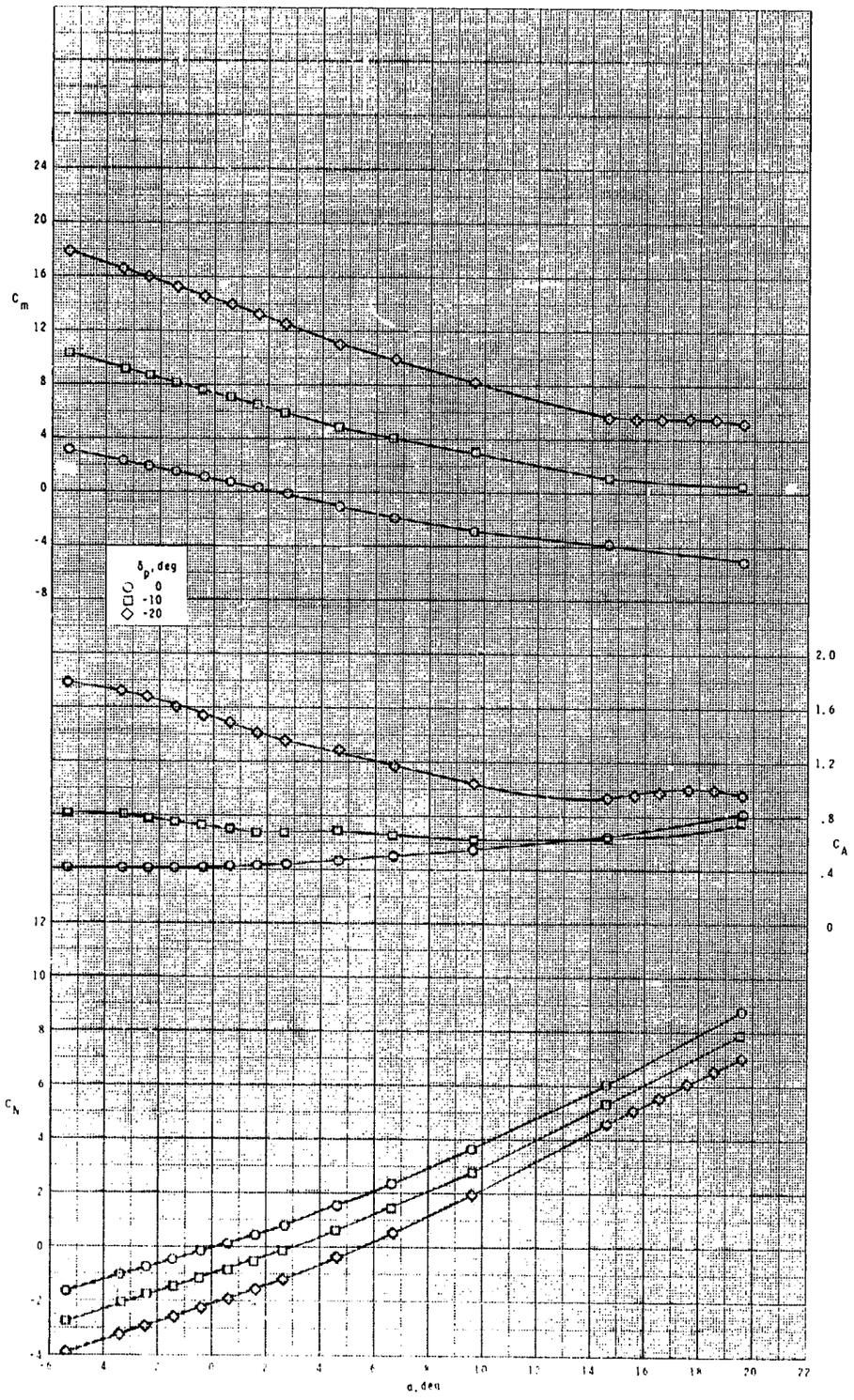

(c) M = 3.50.

Figure 38.- Continued.

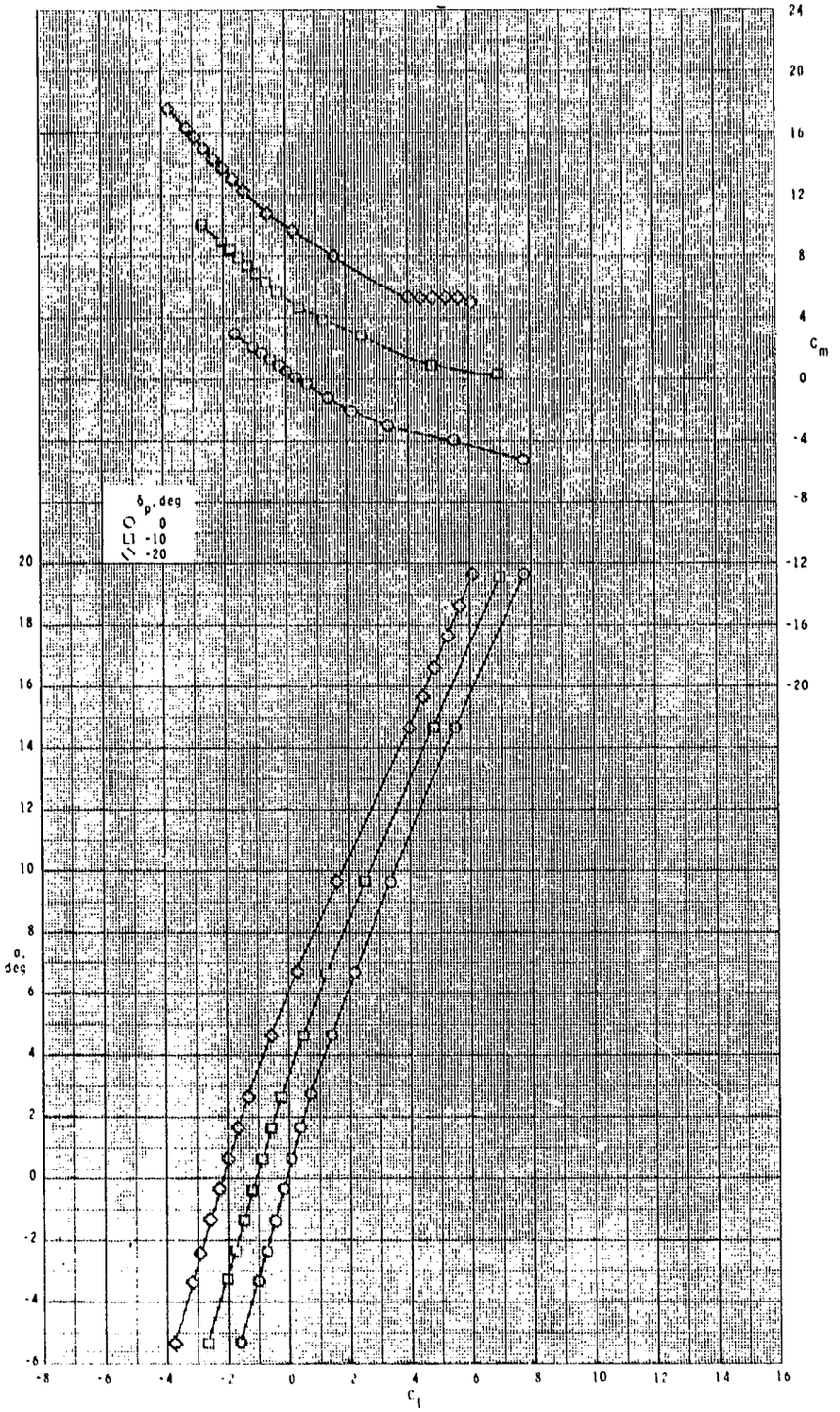

(c) Continued.

Figure 38.- Continued.

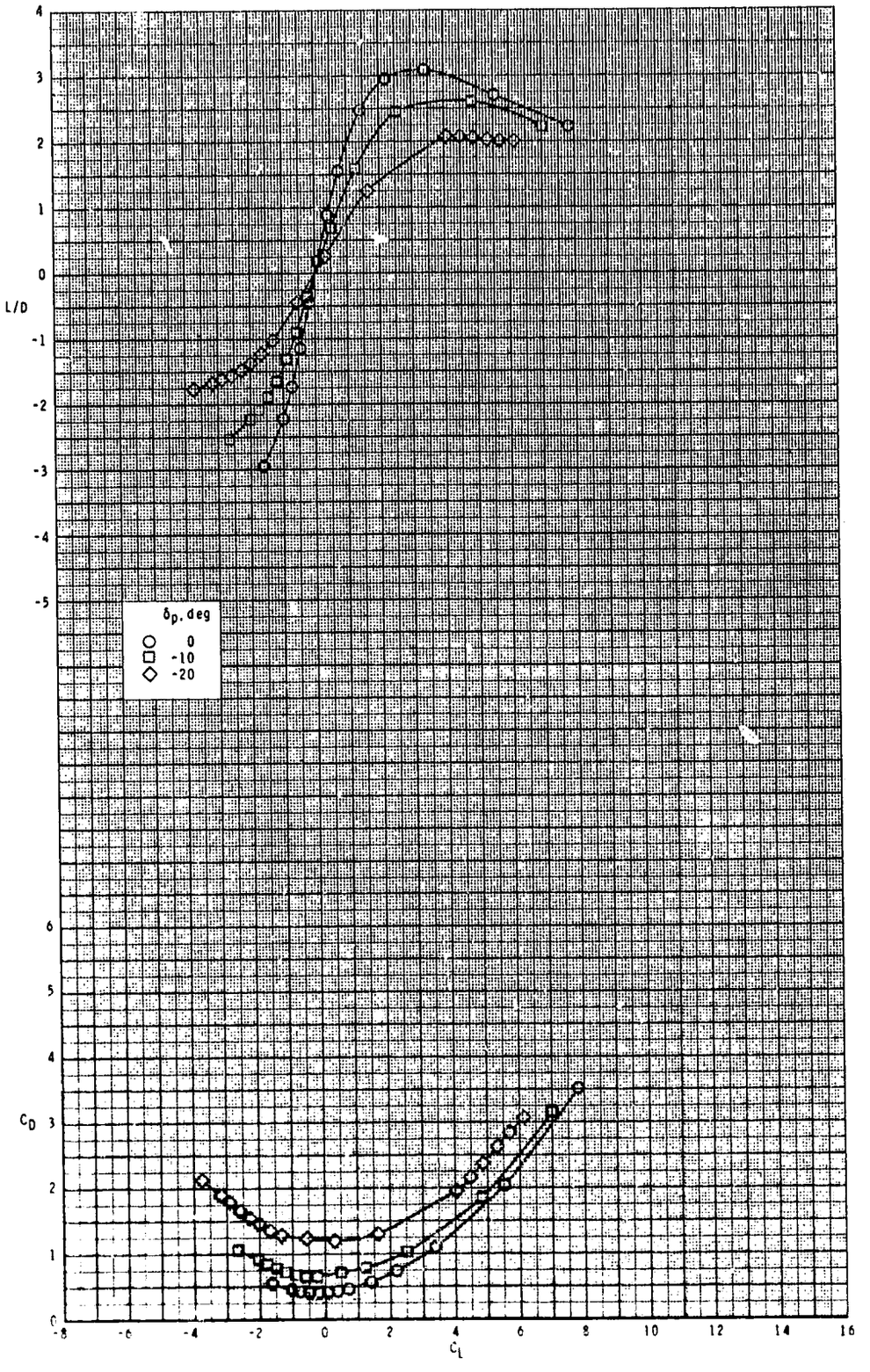

(c) Concluded.

Figure 38.- Continued.

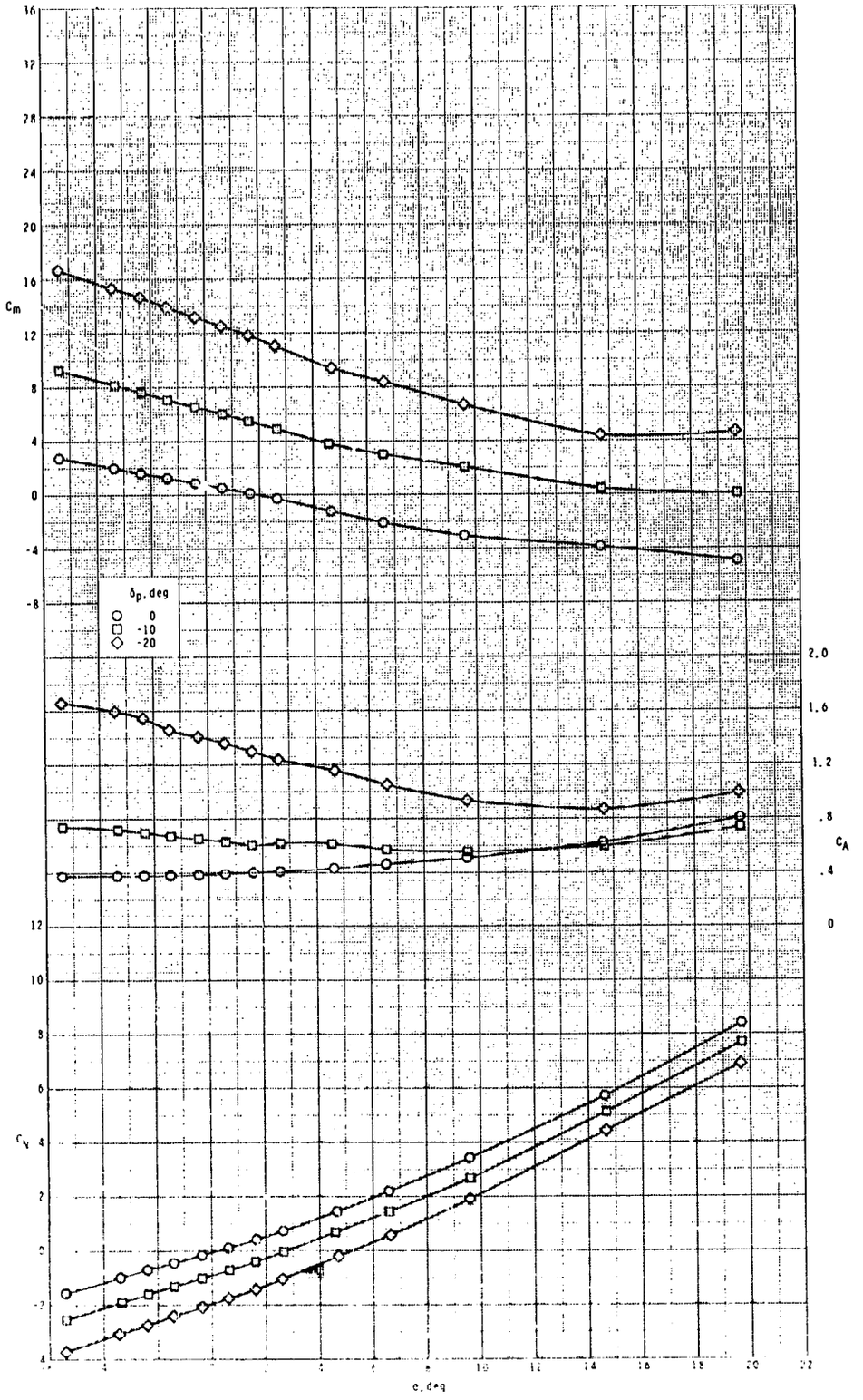

(d) M = 3.95.

Figure 38.- Continued.

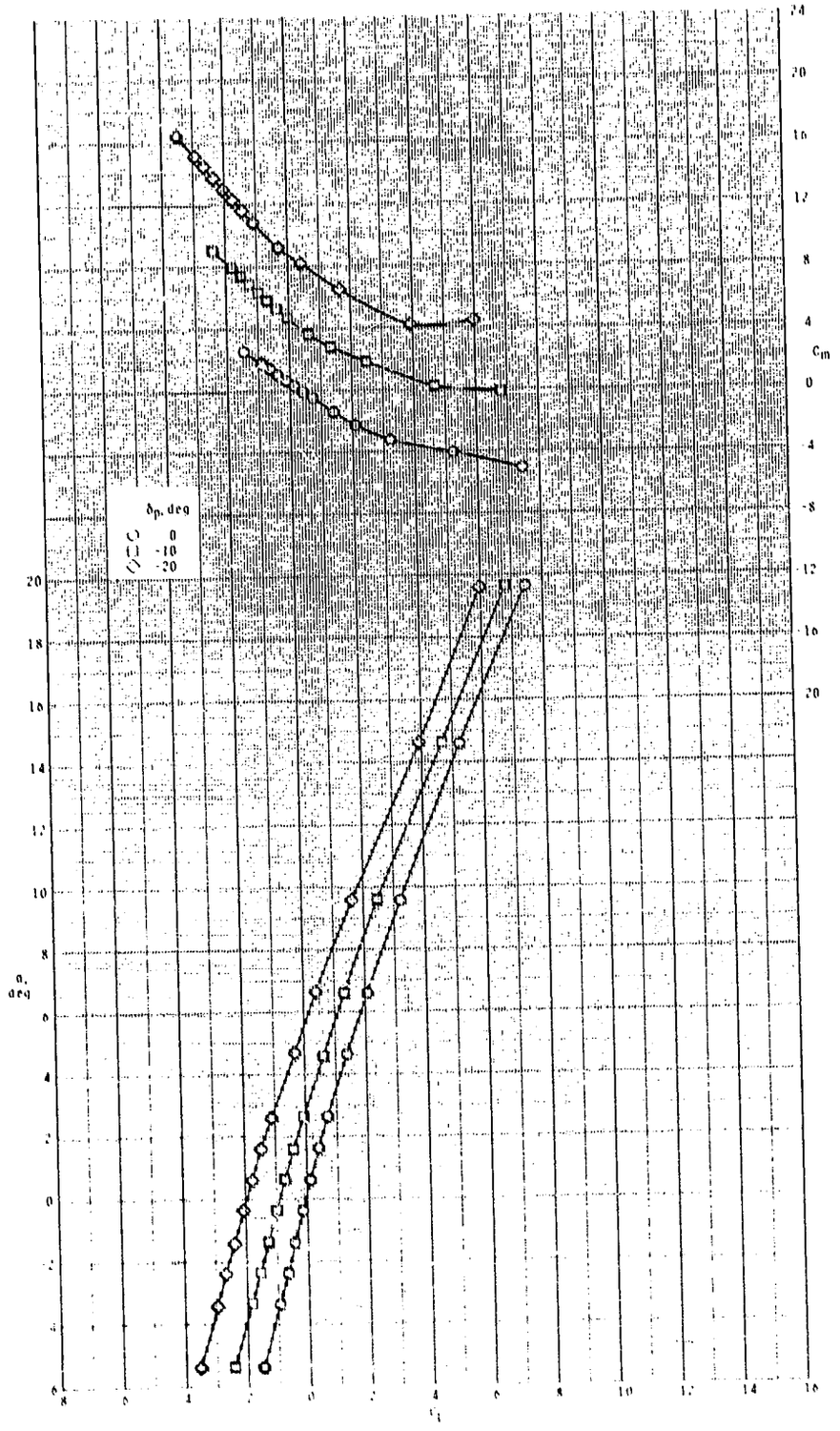

(d) Continued.

Figure 38.- Continued.

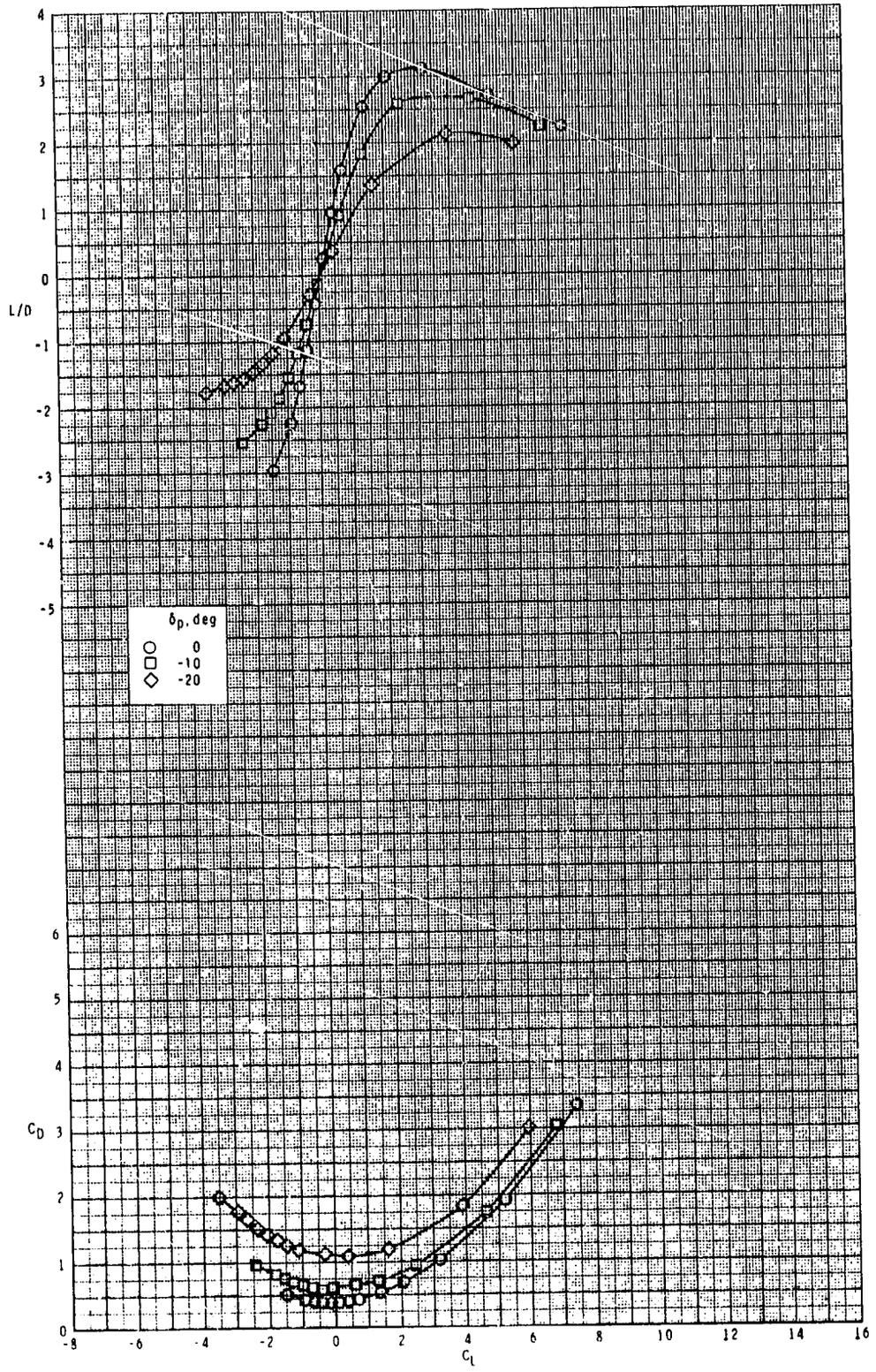

(d) Concluded.

Figure 38.- Concluded.

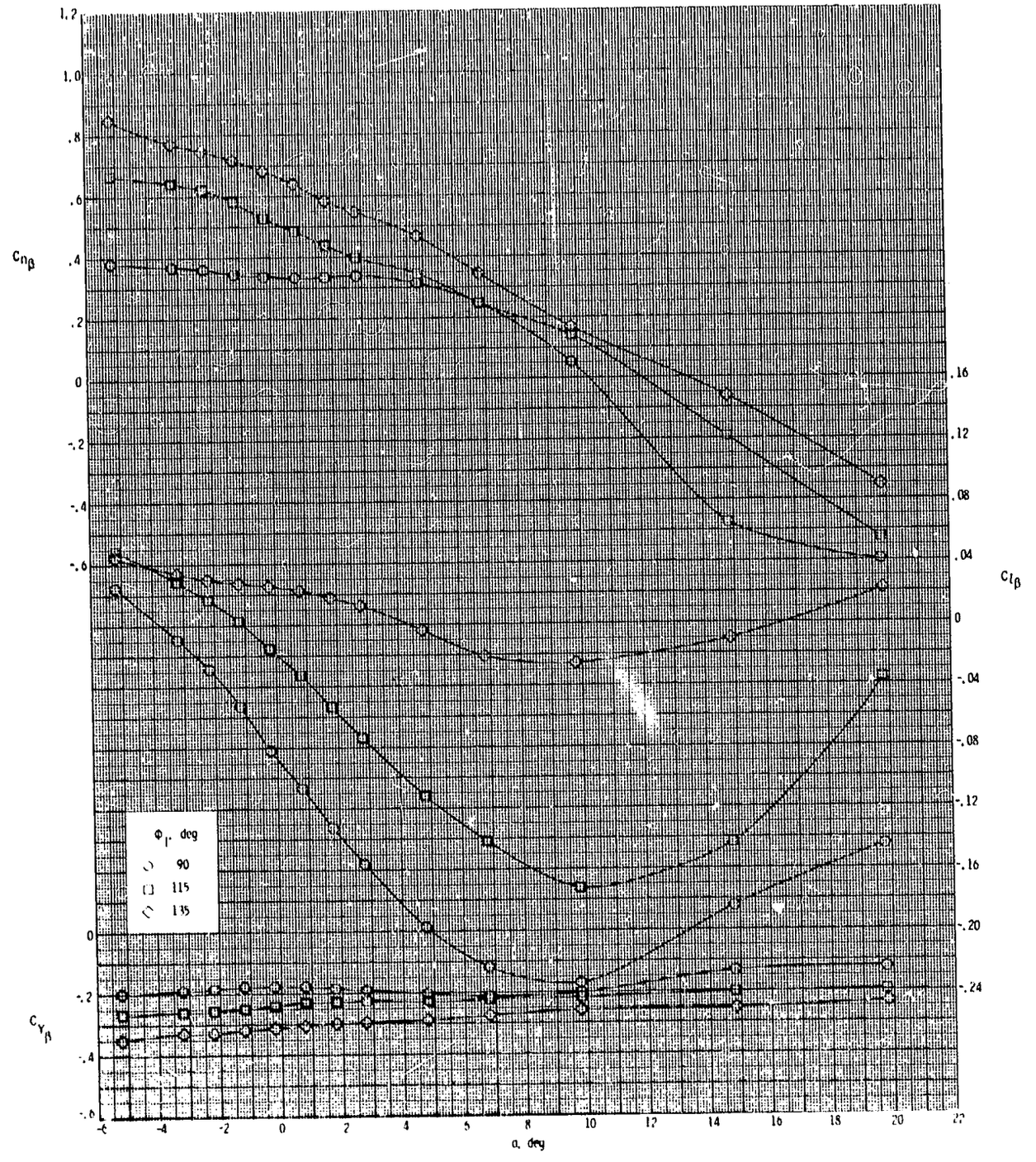

(a) M = 2.50.

Figure 39.- Effect of inlet orientation angle Φ_I on lateral-directional stability of configuration $B_1 I_3 T_1$ with $\delta_p = 0°$.

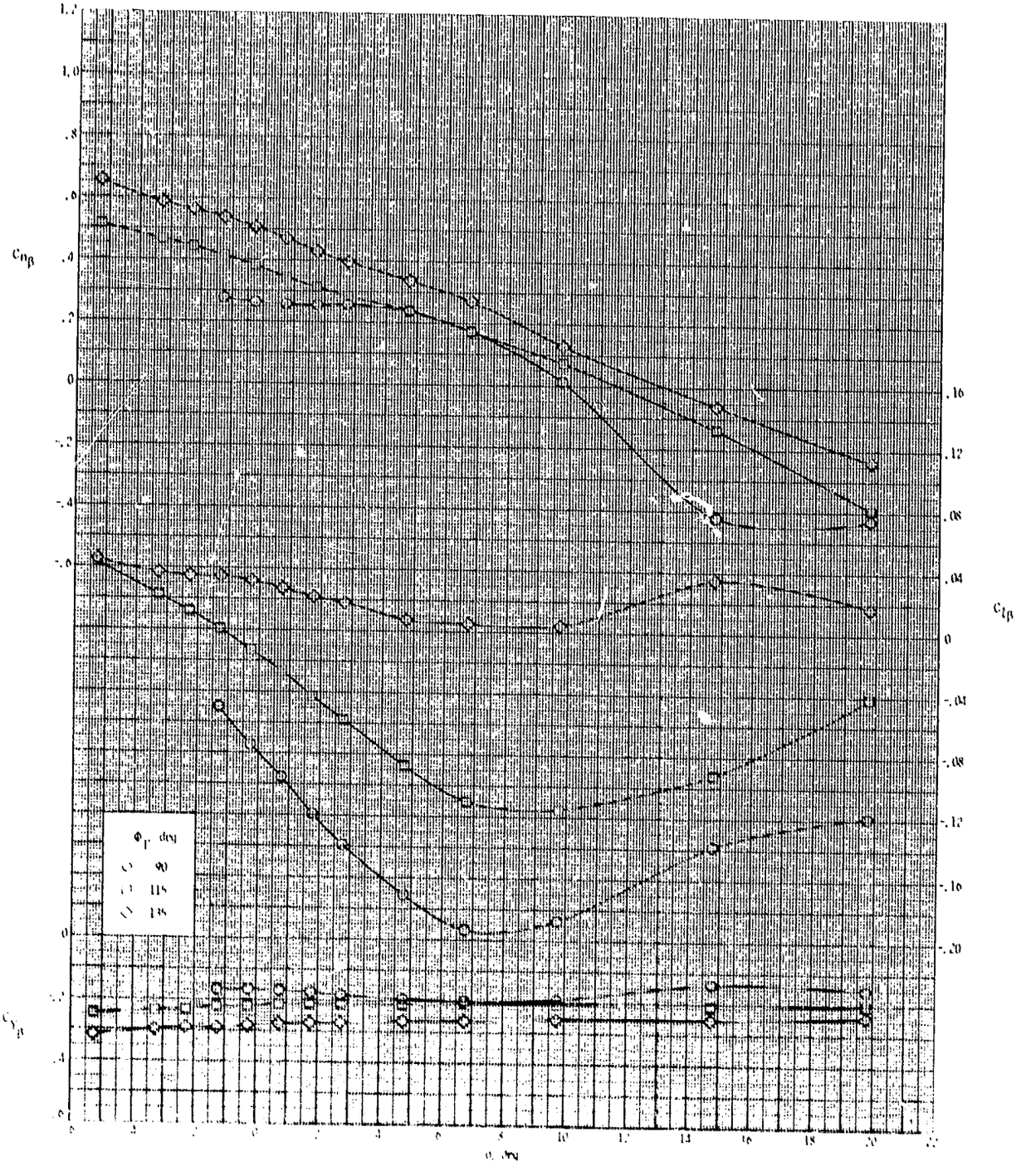

(b) M = 2.05.

Figure 39.- Continued.

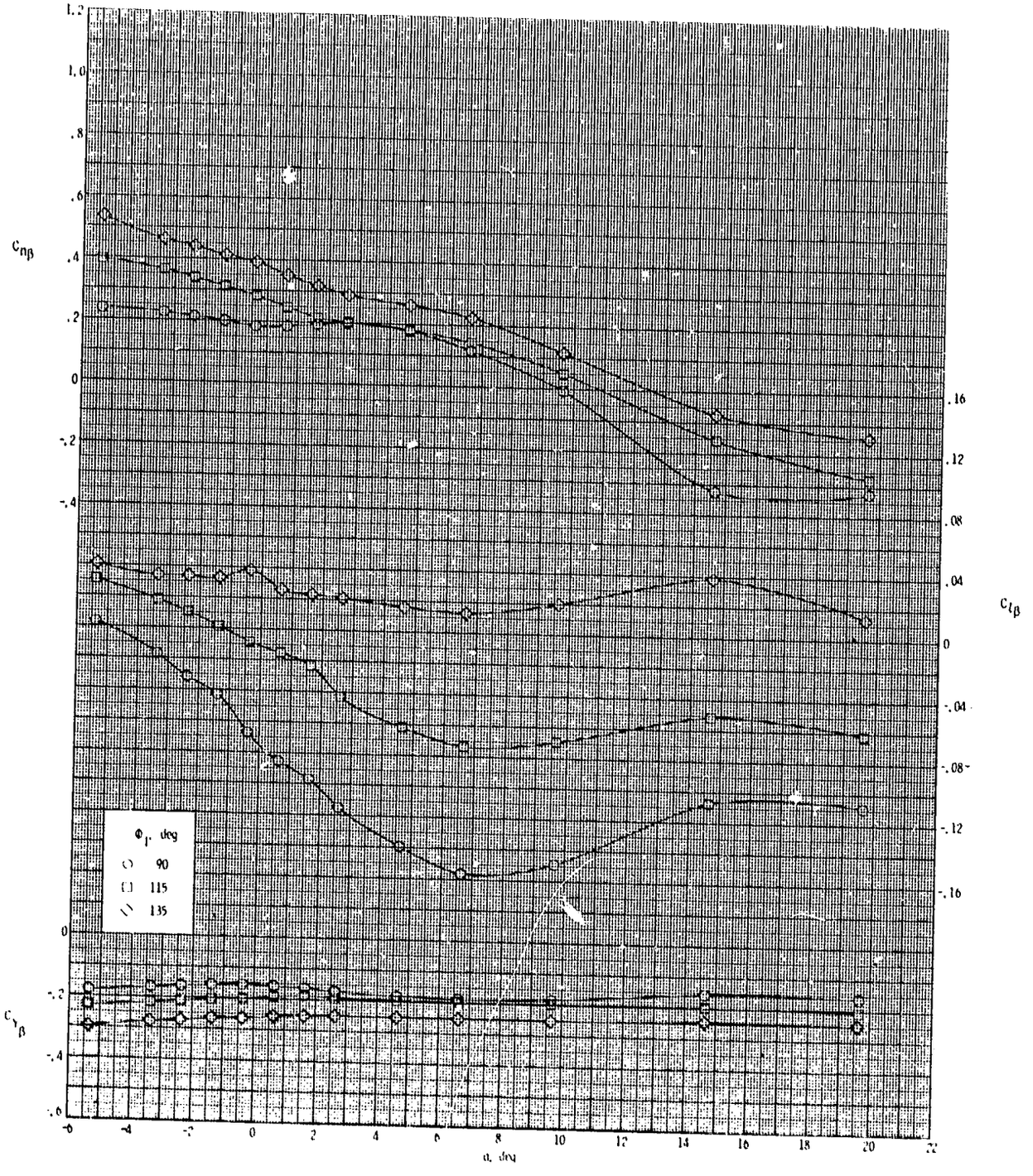

(c) M = 3.50.

Figure 39.- Continued.

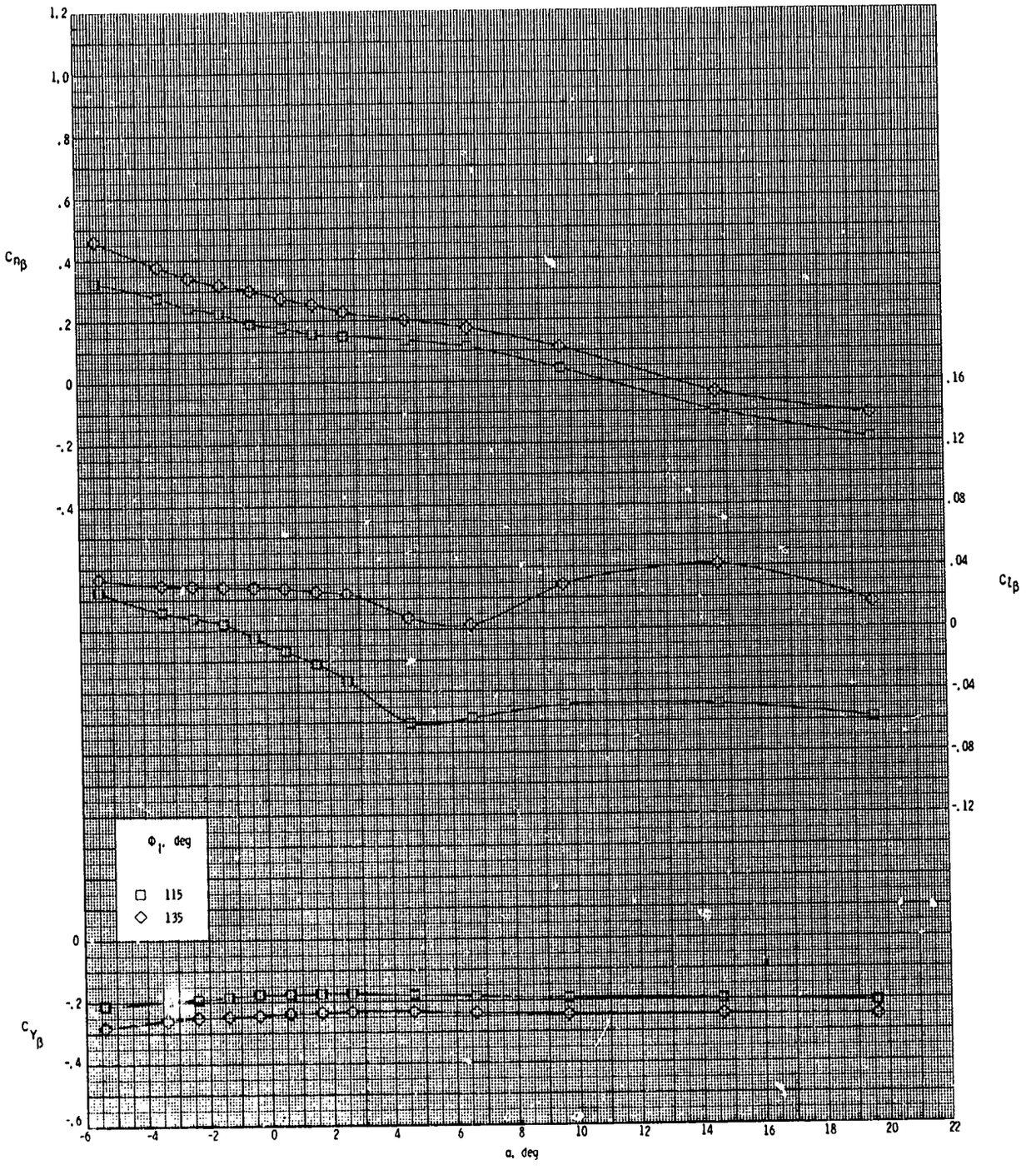

(d) M = 3.95.

Figure 39.- Concluded.

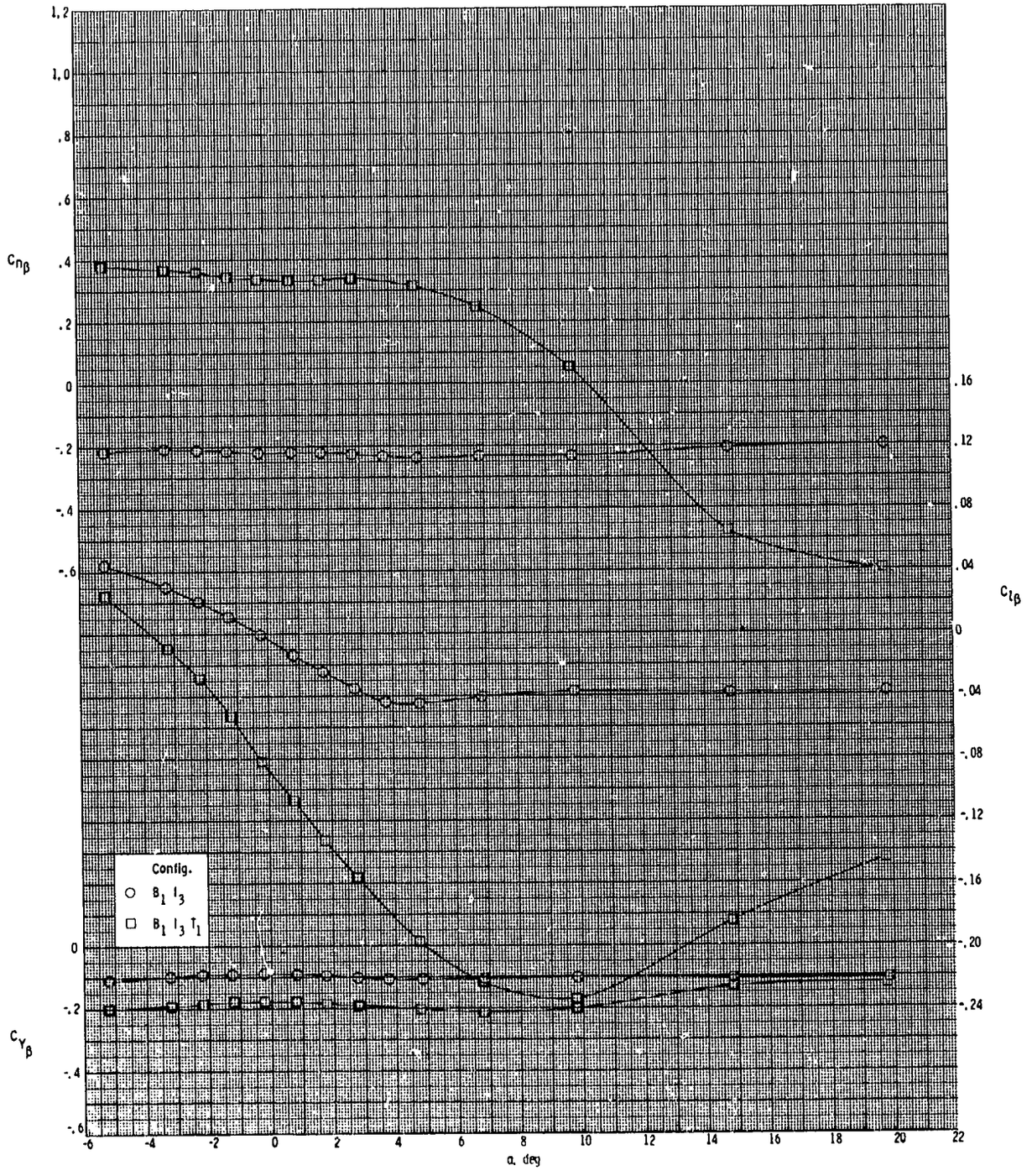

(a) M = 2.50.

Figure 40.- Effect of various model components on lateral-directional stability for two-dimensional extended inlets with $\phi_I = 90°$ and $\delta_p = 0°$.

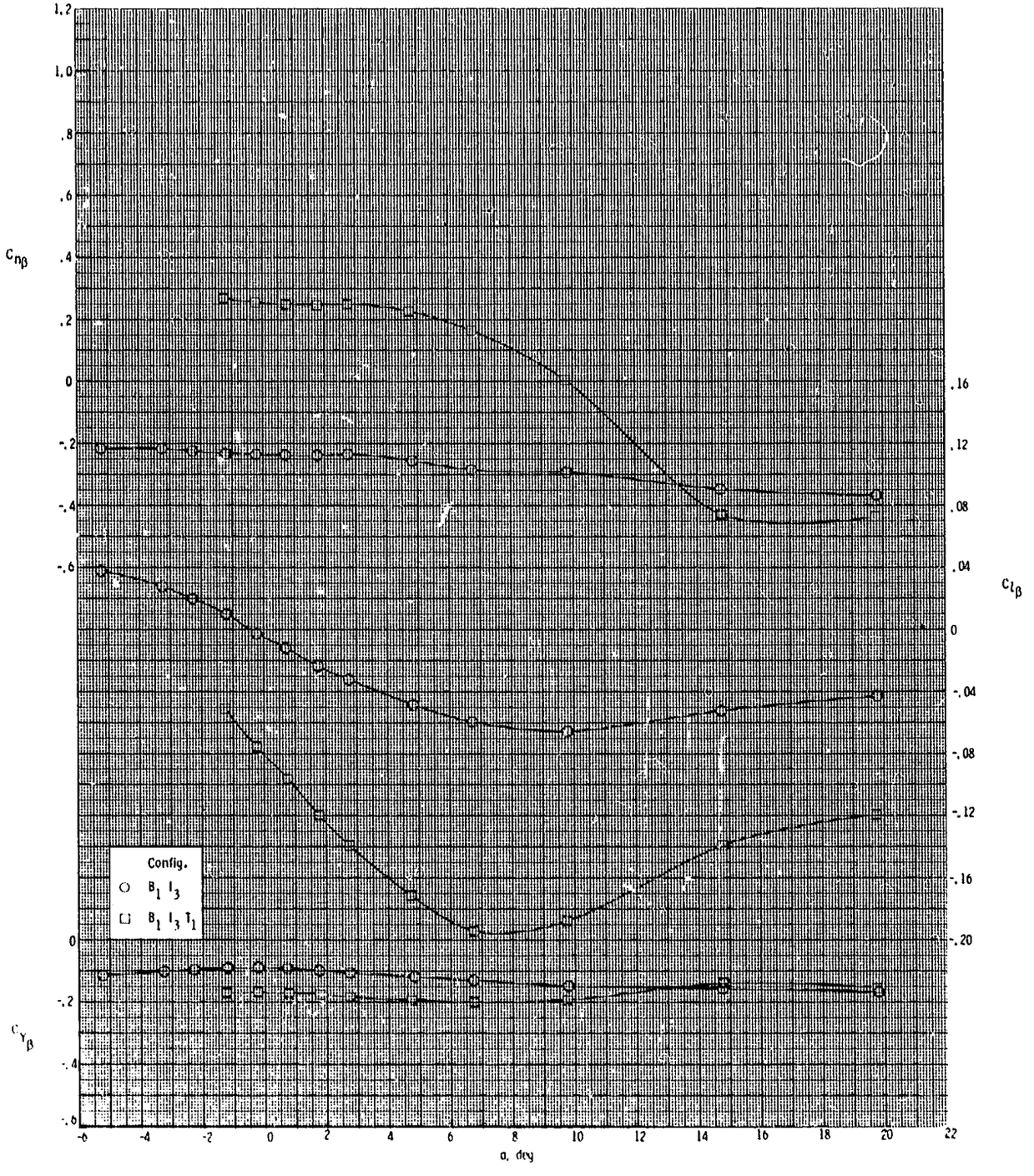

(b) M = 2.95.

Figure 40.- Continued.

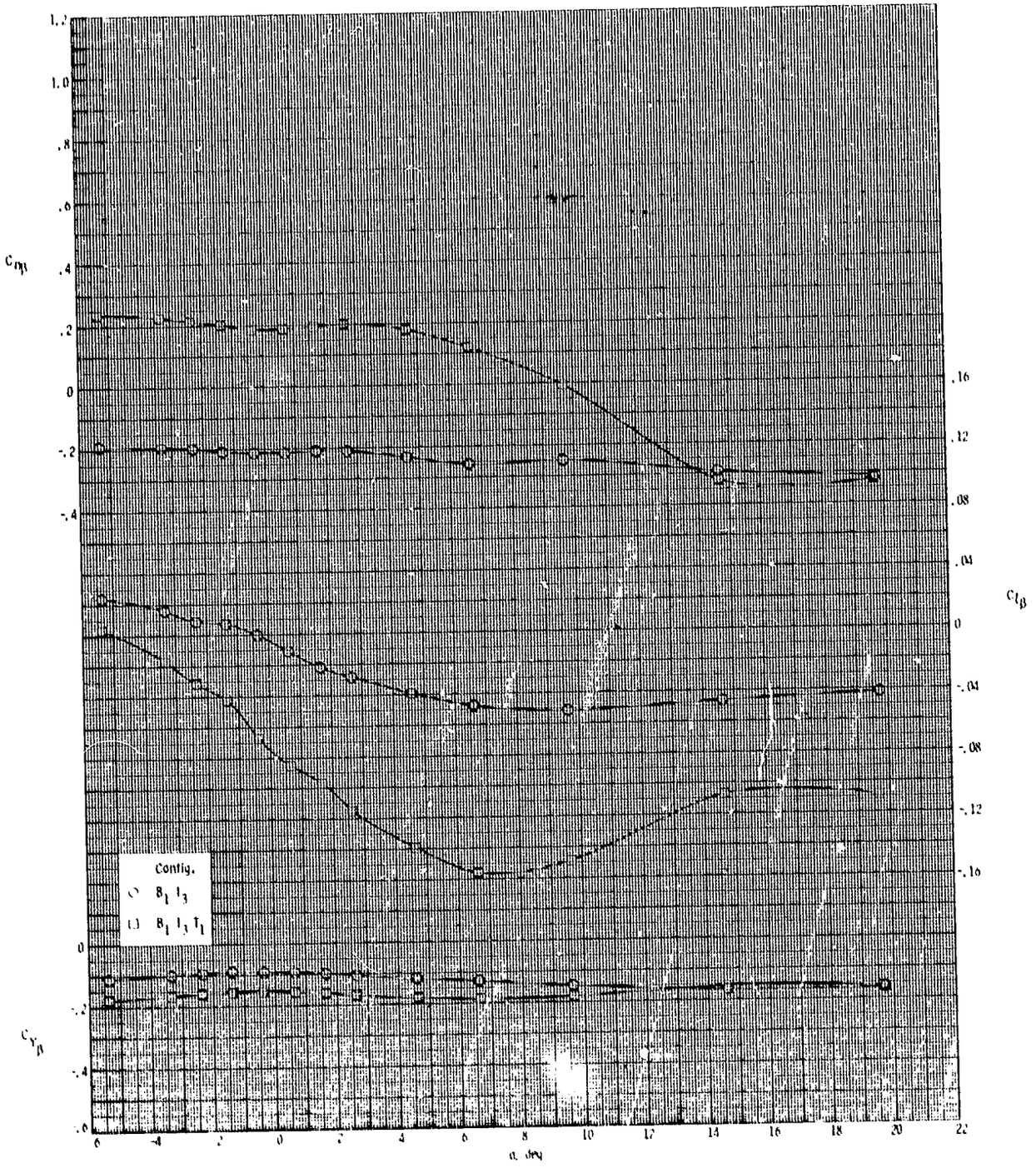

(c) M = 3.50.

Figure 40.- Continued.

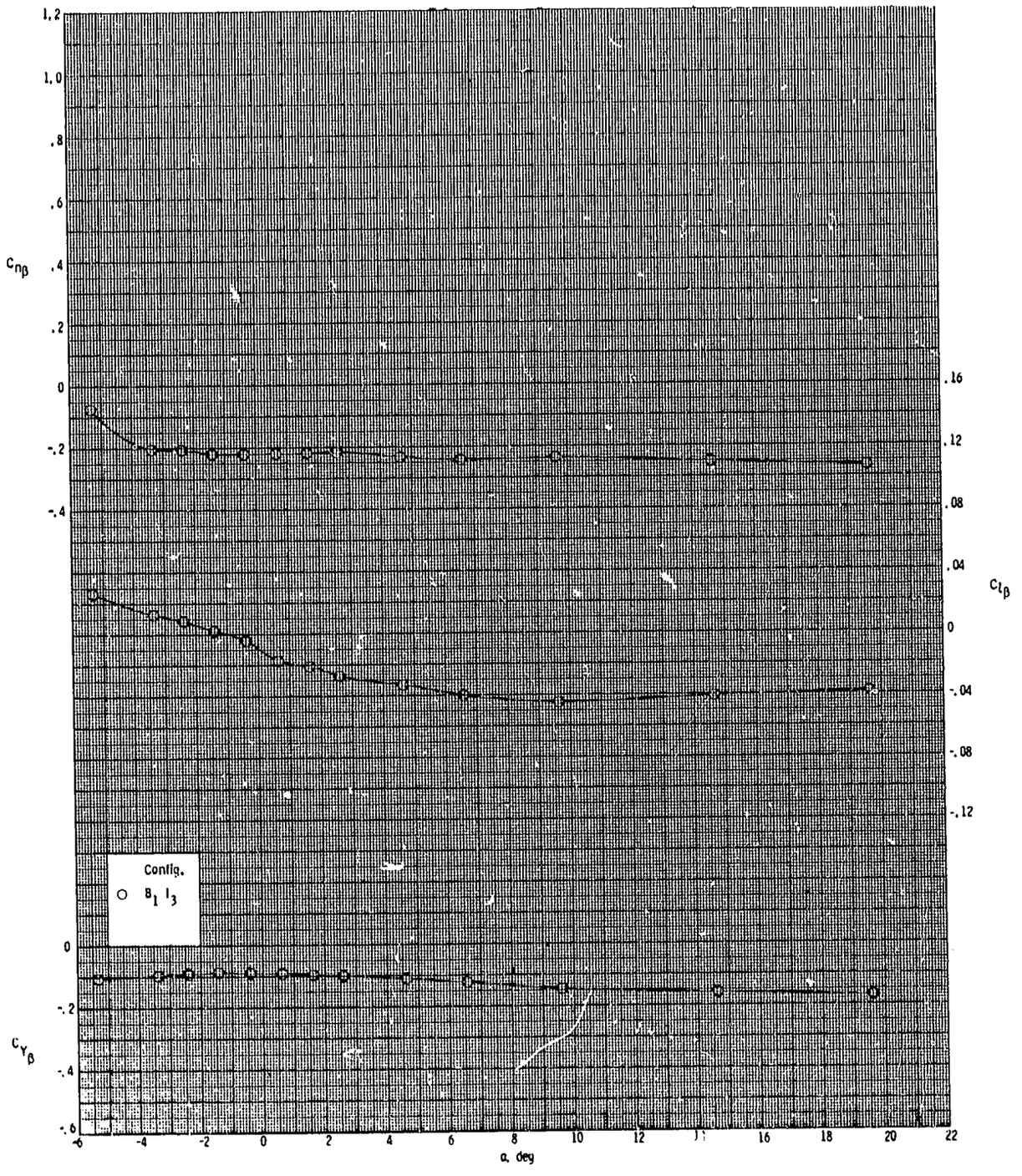

(d) M = 3.95.

Figure 40. Concluded.

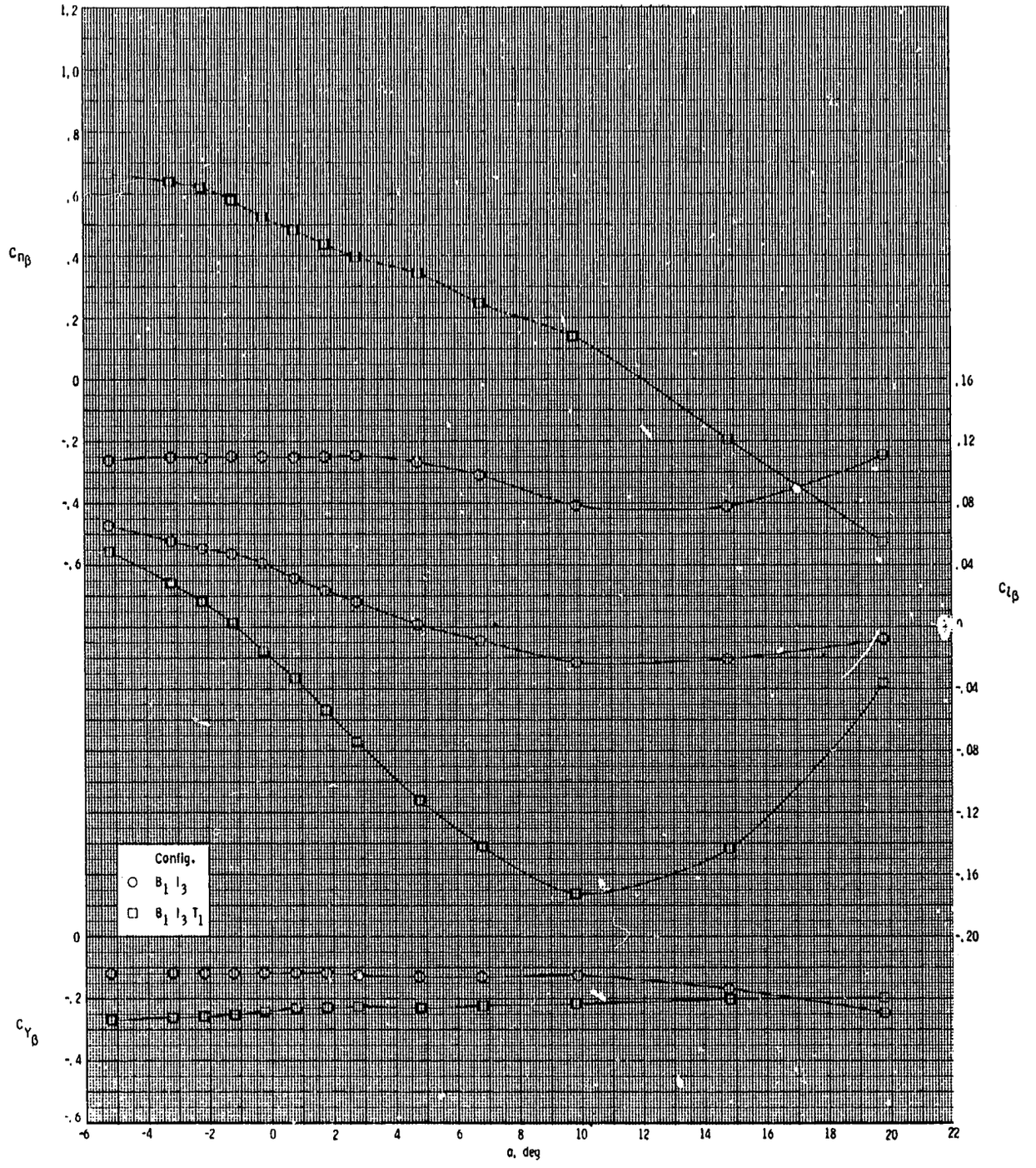

(a) M = 2.50.

Figure 41.- Effect of various model components on lateral-directional stability for two-dimensional extended inlets with ϕ_I = 115° and δ_p = 0°.

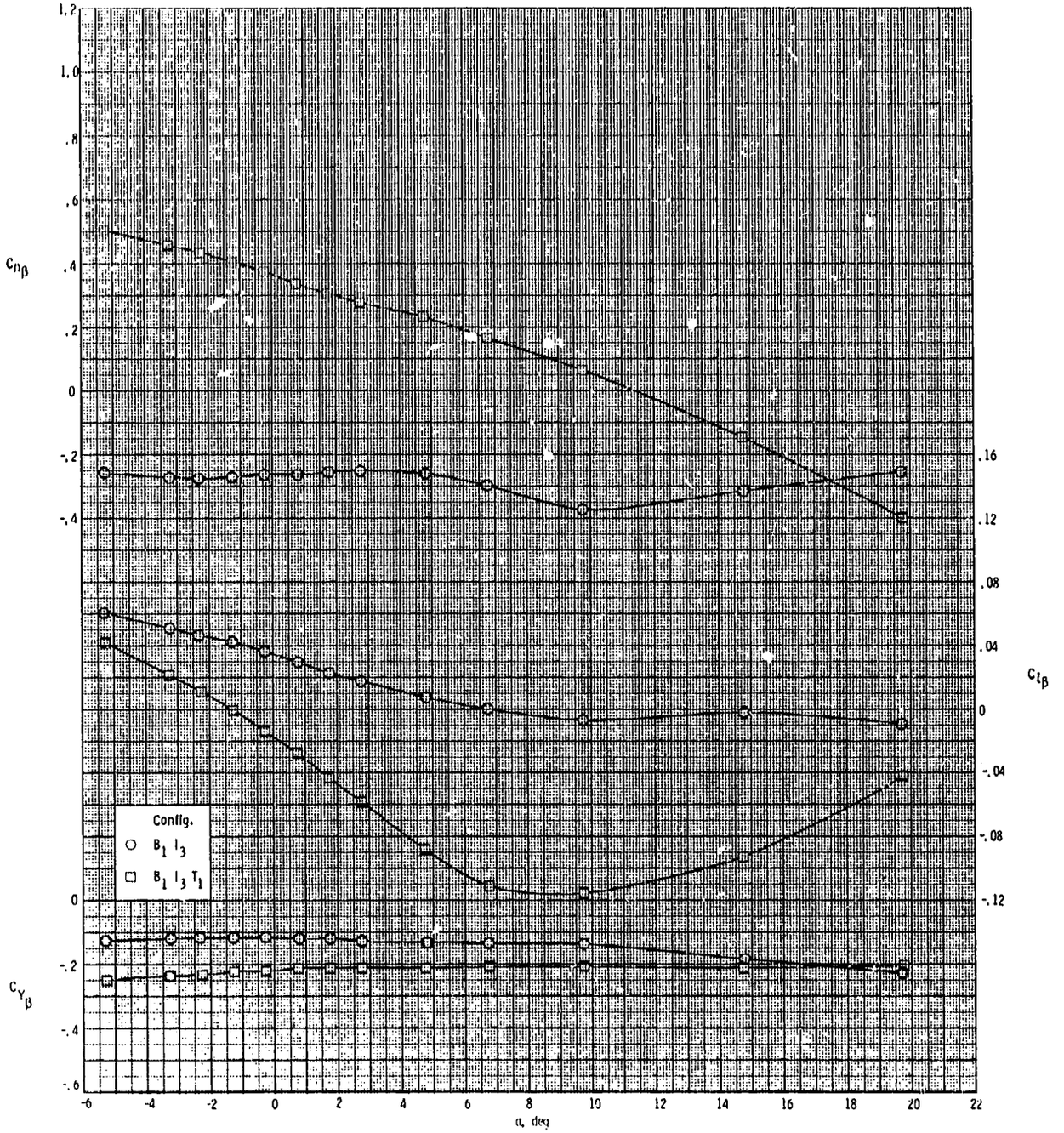

(b) M = 2.95.

Figure 41.- Continued.

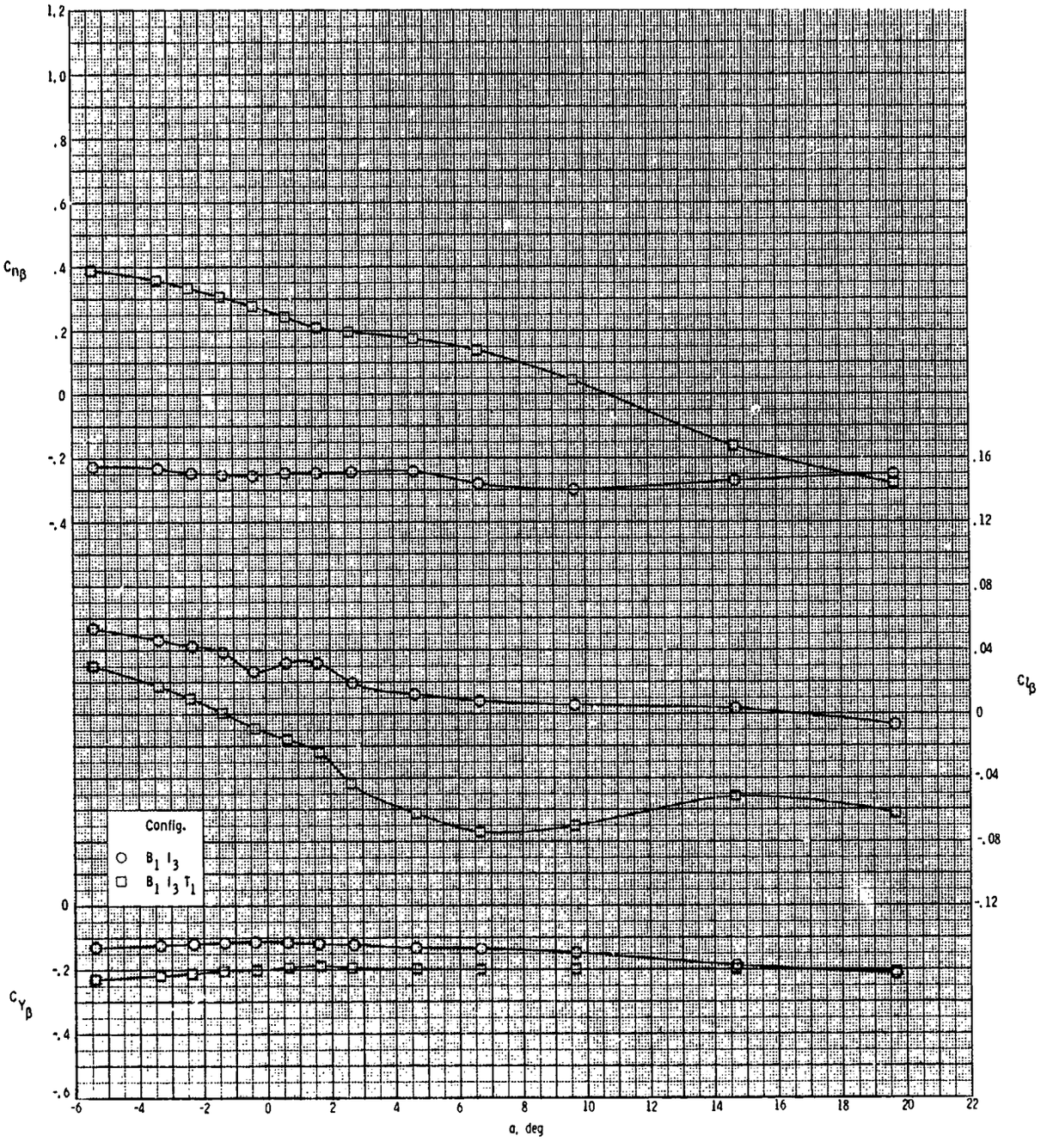

(c) M = 3.50.

Figure 41.- Continued.

C-5

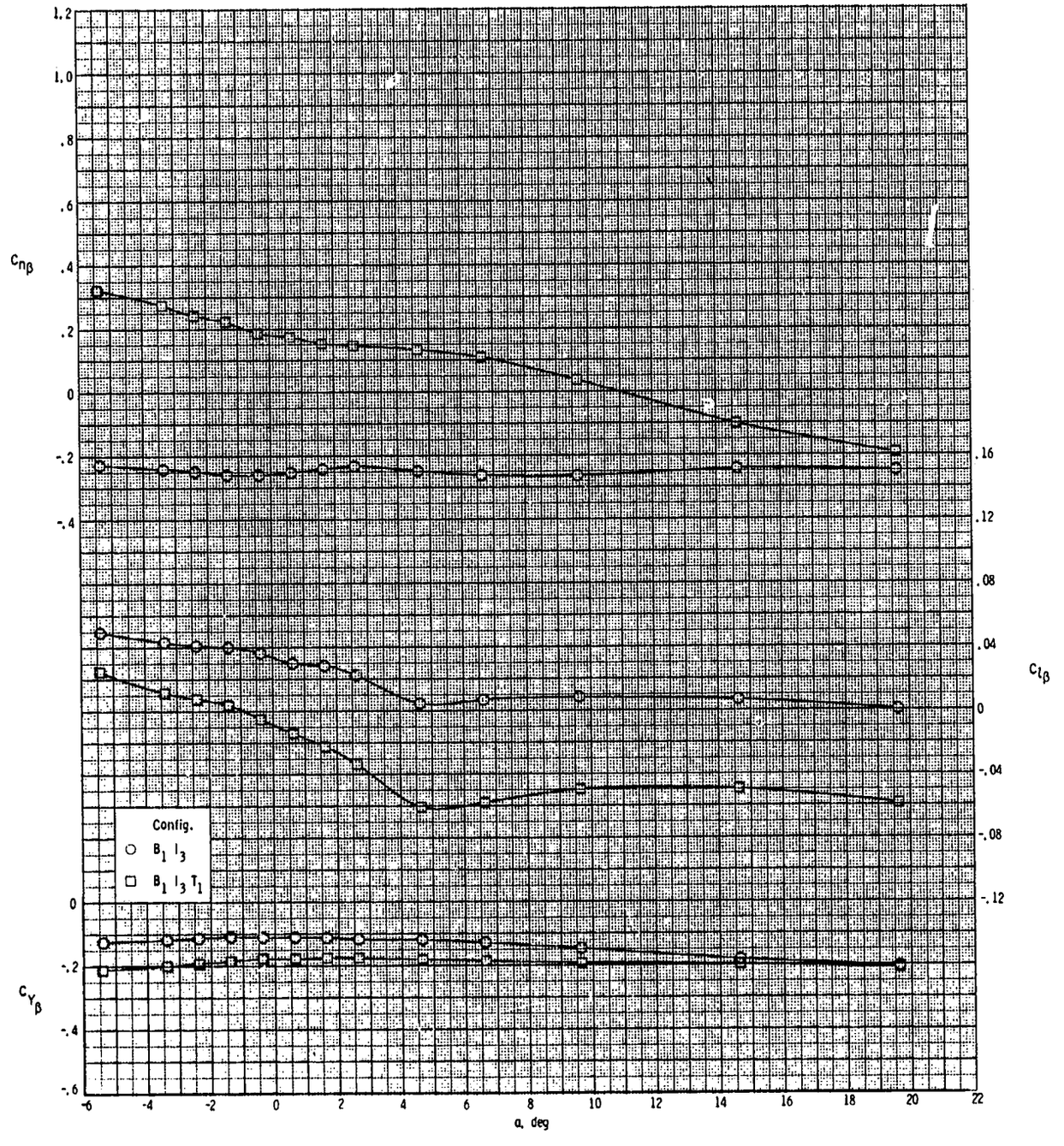

(d) M = 3.95.

Figure 41.- Concluded.

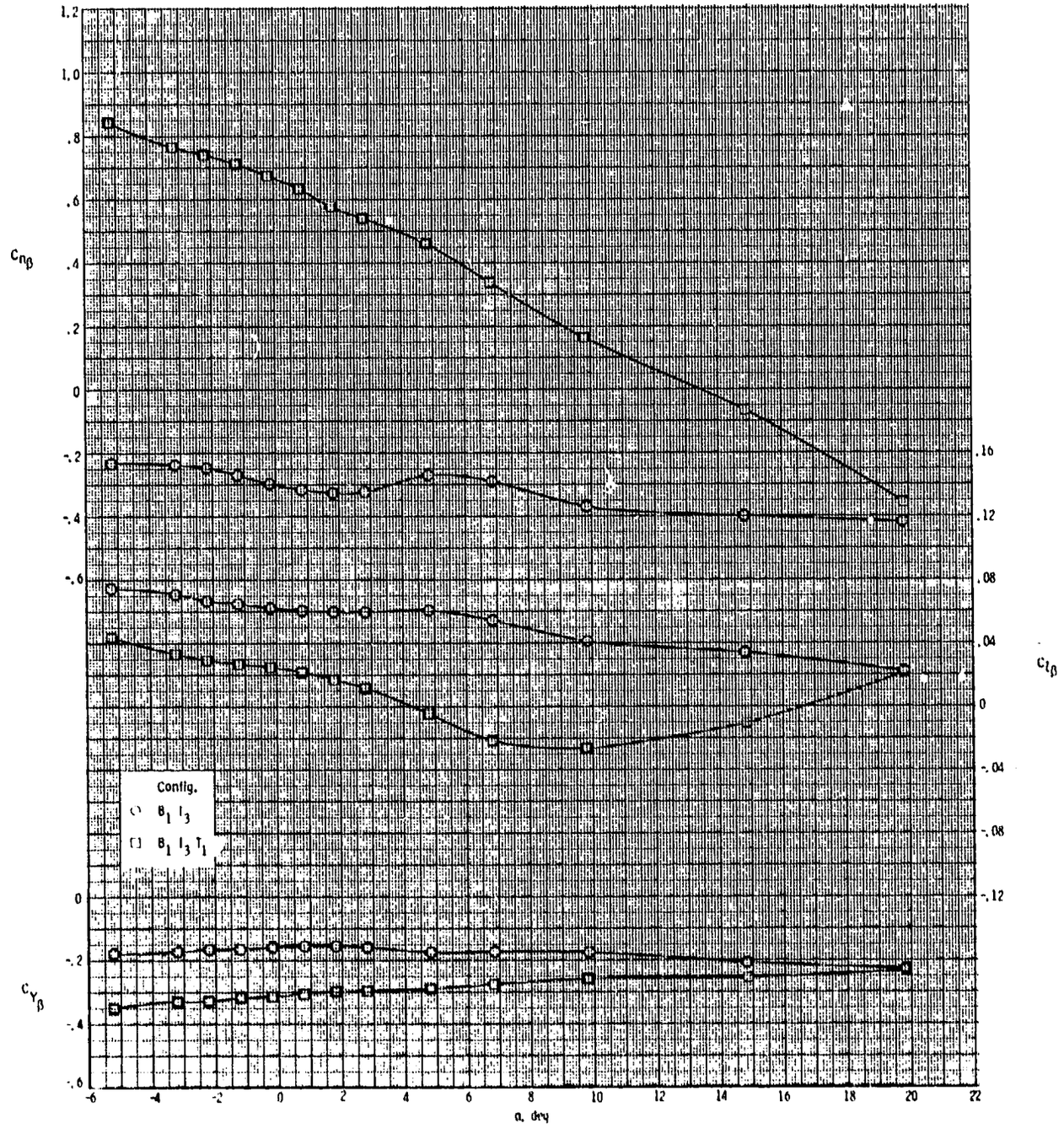

(a) M = 2.50.

Figure 42.- Effect of various model components on lateral-directional stability for two-dimensional extended inlets with ϕ_I = 135° and δ_p = 0°.

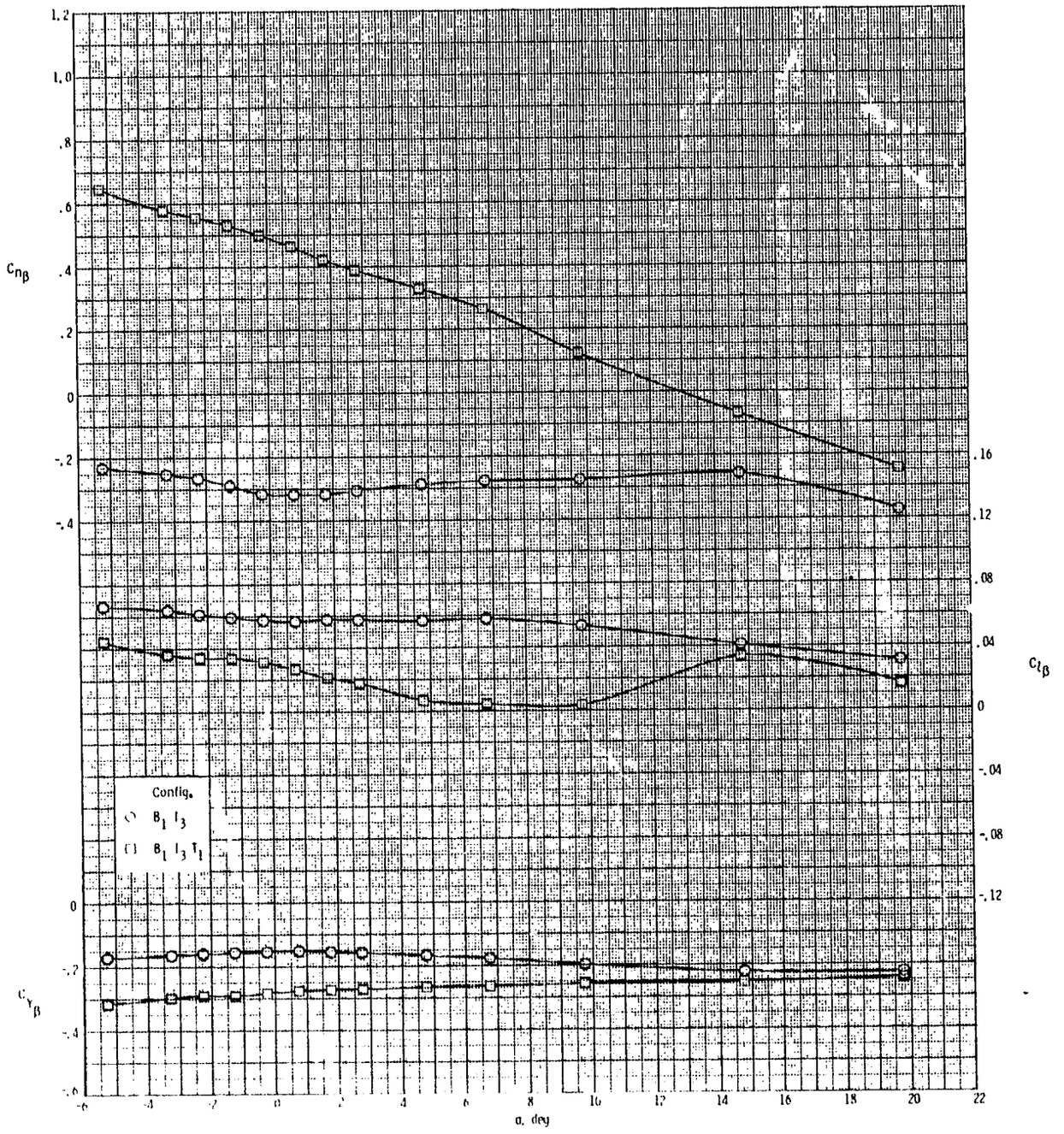

(b) M = 2.95.

Figure 42.- Continued.

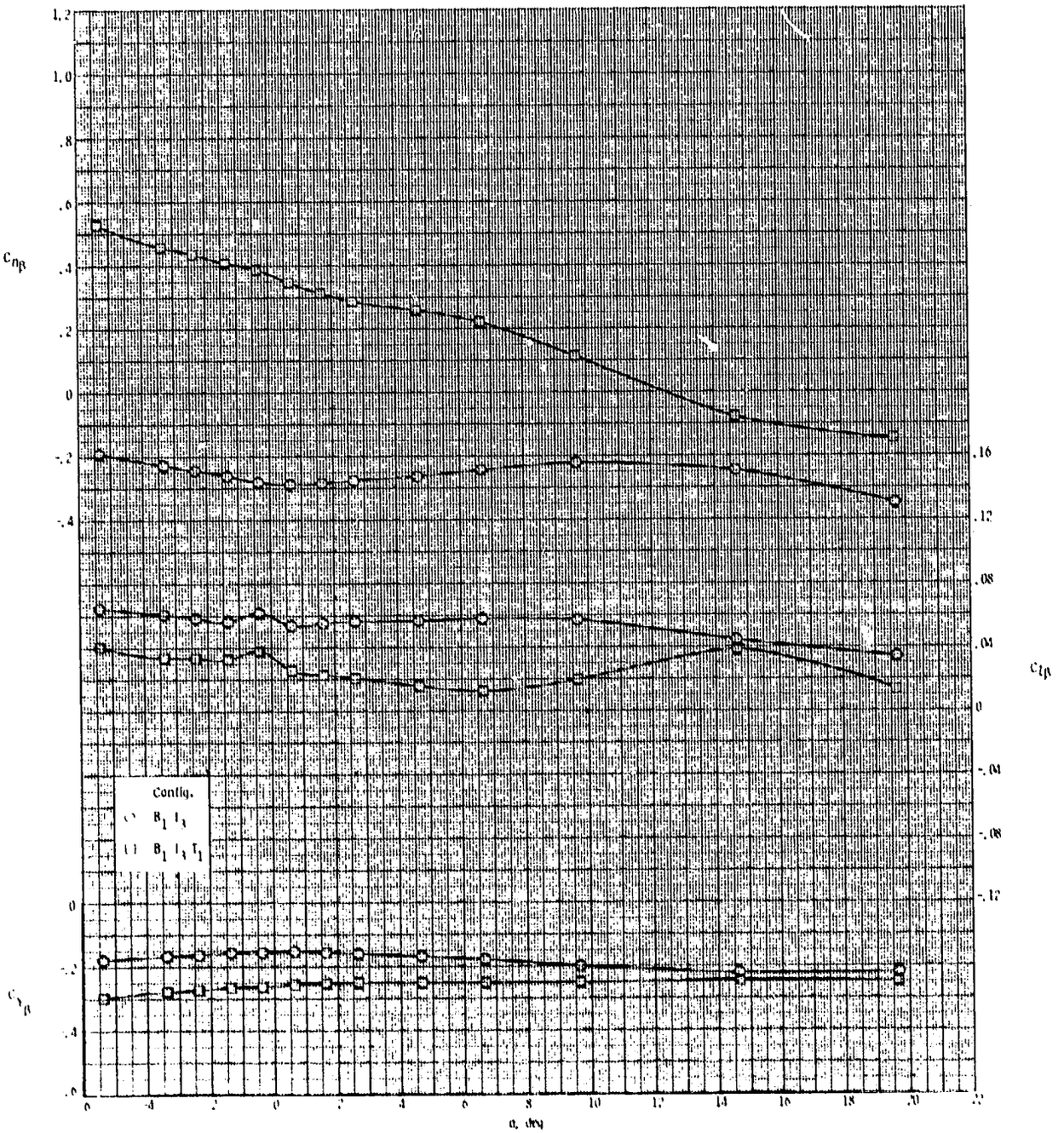

(c) M = 3.50.

Figure 42.- Continued.

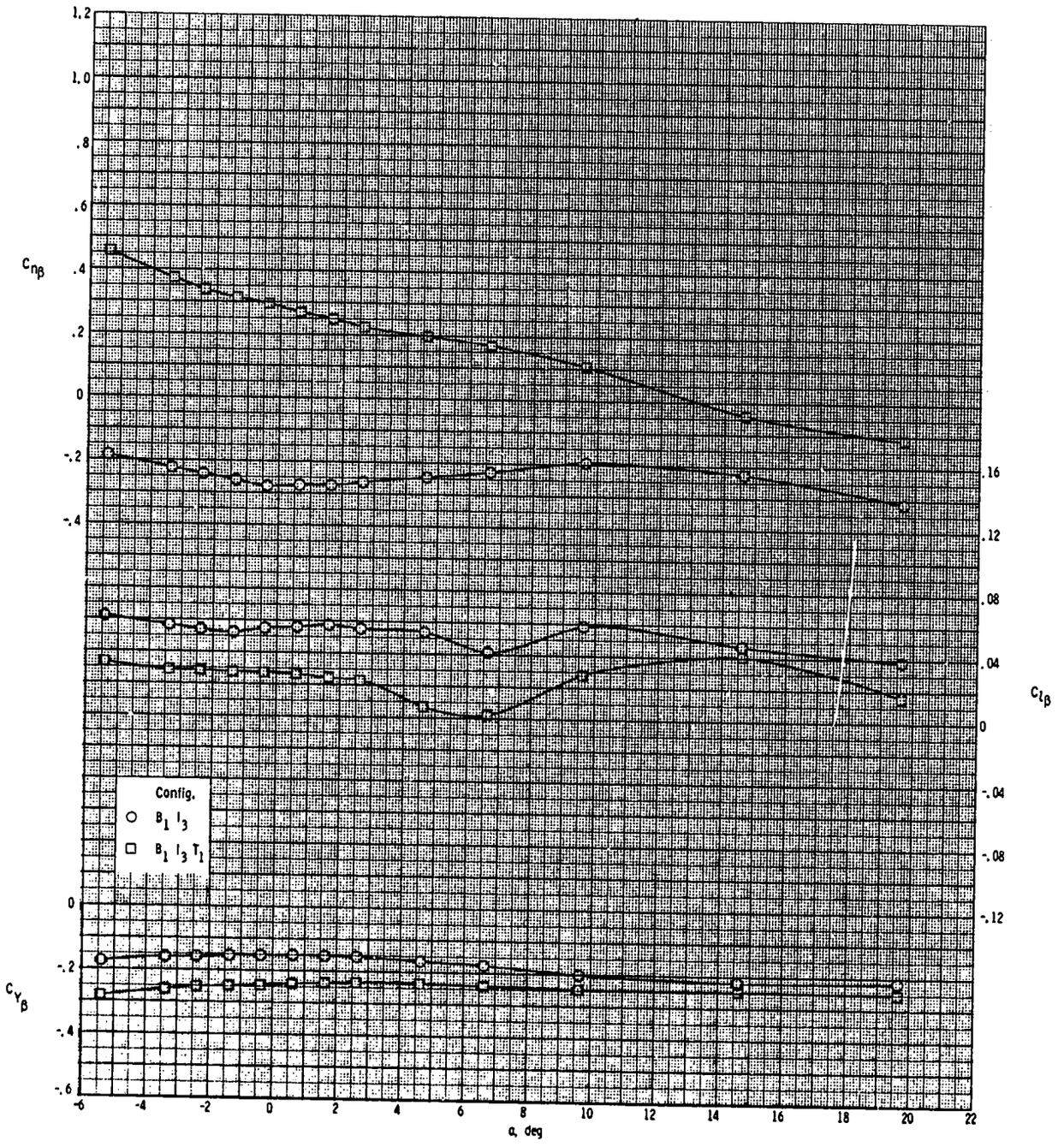

(d) M = 3.95.

Figure 42.- Concluded.